Научном већу Института за физику

Предмет: Молба за покретање поступка за реизбор у звање **Виши научни сарадник**

Молим Научно веће Института за физику да у складу са Правилником о поступку и начину вредновања и квантитативном исказивању научноистраживачких резултата истраживача, покрене поступак за мој реизбор у звање **Виши научни сарадник**.

У прилогу достављам:

1. Мишљење руководиоца пројекта са предлогом чланова комисије,
2. Биографске податке,
3. Преглед научне активности,
4. Елементе за квалитативну оцену научног доприноса,
5. Елементе за квантитативну оцену научног доприноса,
6. Списак објављених радова,
7. Копије радова објављених после претходног избора у звање,
8. Податке о цитираности,
9. Фотокопију решења о претходном избору у звање,
10. Додатне прилоге.

У Београду, 25.05. 2021. године

Са поштовањем
др Јелена Трајић

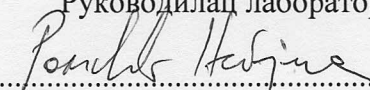**Научном већу Института за физику Београд**
Београд, 25.05.2021.

Предмет: Мишљење руководиоца лабораторије о реизбору др Јелене Трајић у звање виши научни сарадник

Др Јелена Трајић је запослена у Лабораторији за истраживање у области електронских материјала Института за физику. До краја пројектног циклуса Министарства просвете, науке и технолошког развоја Републике Србије је била ангажована на пројекту Интегралних интердисциплинарних истраживања Министарства просвете, науке и технолошког развоја ИИИ45003 – Оптоелектронски нанодимензиони системи – пут ка примени, у оквиру кога је руководила потпројектом Карактеризација наночестица и наноструктура.

С обзиром да испуњава све предвиђене услове, у складу са Правилником о поступку и начину вредновања и квантитативном исказивању научноистраживачких резултата Министарства просвете, науке и технолошког развоја, сагласан сам са покретањем поступка за реизбор др Јелене Трајић у звање виши научни сарадник.

За састав комисије за реизбор др Јелене Трајић у звање виши научни сарадник предлажем:

1. Др Небојша Ромчевић, научни саветник Института за физику
2. Др Милан Тадић, редовни професор Електротехничког факултета
3. Др Биљана Бабић, научни саветник Института за физику.

Руководилац лабораторије

....

др Небојша Ромчевић
Научни саветник

2. Стручна биографија

Јелена Трајић (рођена Миљковић) је рођена 19.07.1964. у Београду, где је завршила основну и средњу школу. На Електротехничком факултету у Београду, на одсеку Техничка физика, дипломирала је 1989. године. Последипломске студије на Електротехничком факултету, на смеру "Физичка електроника чврстог стања и плазме" успешно је окончала 1995. године одбраном магистарске тезе под називом *"Проучавање фазног прелаза код PbS – PbTe полупроводних легура спектроскопским методама"*.

Докторску дисертацију *"Оптичке, структурне и галваномагнетске особине чврстих раствора $PbTe_{1-x}S_x$ и $Pb_{1-x}Mn_xTe$"* одбранила је 2005. године на Електротехничком факултету. Од 1990. године је запослена у Институту за физику у Београду.

Научна звања:
Научни сарадник – Институт за физику, 28.02.2006. године
Виши научни сарадник – Институт за физику, 22.12.2010. године
Виши научни сарадник – Институт за физику, 28.09.2016. године (реизбор)

Све време рада у Институту за физику др Јелена Трајић је била ангажована на пројектима Министарства за науку Републике Србије као и на међународним пројектима.

До краја пројектног циклуса Министарства просвете, науке и технолошког развоја Републике Србије била је ангажована на пројекту Интегралних интердисциплинарних истраживања Министарства просвете, науке и технолошког развоја Републике Србије: *Оптоелектронски нанодимензиони системи – пут ка примени*, број III 45003 (2011-2020.) којим руководи др Небојша Ромчевић. У оквиру овог пројекта руководила је потпројектом *Карактеризација наночестица и наноструктура*.

3. Преглед научне активности

Научни рад др Јелене Трајић је везан за област физике материјала, у оквиру које се бави физиком полупроводних кристала, танких филмова, наночестица и наноструктура. Научне активности обухватају експериментални рад, обраду резултата, моделовање и теоријску анализу испитиваних материјала. Такође, бави се и примењеним истраживањима.

Према материјалима који су предмет изучавања, научне активности др Јелене Трајић се могу сврстати у следеће области:

Транспортне и оптичке особине ускозонских полупроводних материјала на основи олово-телурида

Олово-телурид је веома осетљив на допирање различитим примесама. Приликом допирања долази до појаве нових и другачијих, односно измењених особина материјала. Избором врсте и количине примесе се може у широком опсегу утицати на његове електричне, оптичке, магнетне и друге особине. На тај начин се код олово-телурида јављају и потпуно нове значајне особине као што су стабилизација Фермијевог нивоа, постојање дуговремених релаксационих процеса и задржана фотопроводност. Јелена Трајић се бавила истраживањем олово-телурида допраног сумпором, манганом, никлом, кобалтом, хромом и силицујумом. Применом галваномагнетних мерења, далеке ифрацрвене спектроскопије и Раман мерења детаљно су испитане особине ових система. Проучавала је електрон-фонон интеракције, са посебним нагласком на интеракције плазмона и више фонона, при чему је развила модел за анализу спектара рефлексије за случај плазмон – мулти фонон интеракције. На овај начин су поред значајног доприноса у експерименталном регистровању оптичких

особинаових система, са јединствене позиције објашњене фононске и галваномагнетне особине. Претходно поменути резултати су садржај радова:

- **J.M. Miljković**, N. Romčević, Z.V. Popović, W. König, and V.N. Nikiforov, *Transport and optical properties of PbTe$_{1-x}$S$_x$ (x=0.02 and x=0.05) mixed crystals*, phys. stat. sol. (b) 193, 43-51 (1996),

- **J. Trajić**, M. Romčević, N. Romčević, S. Nikolić, A. Golubović, S. Durić, V.N. Nikiforov, *Optical properties of PbTe:Mn*, Journal of Alloys and Compounds 365, 89 − 93 (2004),

- A. Golubović, S. Nikolić, **J. Trajić**, S. Đurić, N. Romčević, M. Romčević, A. J. Nadolny, B. Taliashvili, V. N. Nikiforov, *Structural Properties of Pb$_{1-x}$Mn$_x$Te Compounds*, Materials Science Forum 453 − 454, 99 − 102 (2004),

- N. Romčević**, J. Trajić**, M. Romčević, A. Golubović, S. Nikolić, V.N. Nikiforov, *Raman spectroscopy of PbTe$_{1-x}$S$_x$ alloys,* Journal of Alloys and Compounds 387, 24 − 31 (2005),

- N. Romčević**,** A. Golubović, M. Romčević, **J. Trajić**, S. Nikolić, S. Đurić, V.N. Nikiforov, *Raman spectra of Pb$_{1-x}$Mn$_x$Te alloys*, Journal of Alloys and Compounds 402, 36 − 41 (2005),

- N. Romčević, A.J. Nadolny, M. Romčević, T. Story, B Taliashvili, A. Milutinović, **J. Trajić**, E. Lusakowska, D. Vasiljevic−Radovic, V Domukhovski, V. Osinniy, B. Hadžić and P. Dziawa, *Far−infrared phonon spectroscopy of Pb$_{1-x}$Mn$_x$Te layers grown by molecular beam epitaxy*, Journal of Alloys and Compounds, 442, 324 − 327 (2007),

- **J. Trajić**, N. Romčević, M. Romčević, V. Nikiforov, *Plasmon − phonon and plasmon − two different phonon interaction in Pb$_{1-x}$Mn$_x$Te mixed crystals*, Materials Research Bulletin, 42, 2192 − 2201 (2007),

- N. Romčević, **J. Trajić**, T.A. Kuznetsova, M. Romčević, B. Hadžić, D.R. Khokhlov, *Far − infrared study of impurity local modes in Ni − doped PbTe*, Journal of Alloys and Compounds, 442, 324 − 327 (2007),

- D. Stojanović, N. Romčević, **J. Trajić**, B. Hadžić, M. Romčević, D.R. Khokhlov,*Investigation of Photoconductivity in n − type gallium doped PbTe*, Science of Sintering, 39, 169 − 175 (2007),

- **J. Trajić**, A. Golubović, M. Romčević, N. Romčević, S. Nikolić, V.N. Nikiforov, *Pb$_{1-x}$Mn$_x$Te and PbTe$_{1-x}$S$_x$ compounds and their optical properties*, Journal of the Serbian Chemical Society, 72 (1), 55 − 62 (2007),

- D. Stojanović**, J Trajić**, B. Hadžić, M. Romčević, I. Ivanchik, D. R. Khokhlov, N. Romčević, *Far−Infrared Study of DX−Like Centers in Pb$_{0.95}$Mn$_{0.05}$Te(Ga)*, Acta Physica Polonica A, 112 (5) 959 − 962 (2007),

- **J. Trajić**, N. Romčević, M. Romčević, V.N. Nikiforov, *Plasmon − two phonon interaction in PbMnTe and PbTeS alloys*, Journal of the Serbian Chemical Society, 73 (3), 369 − 376 (2008),

- N. Romčević, **J Trajić**, B. Hadžić, M. Romčević, D. Stojanović, Z. Lazarević, T. Kuznetsova, D. Khokhlov, R. Rudolf, I. Anžel, *Raman spectroscopy of multhiphonon emission process in Ni − doped PbTe*, Acta Physica Polonica A 116, 91 − 92 (2009),

- N. Romčević, **J Trajić**, M. Romčević, D. Stojanović, T. A. Kuznetsova, D.R Khokhlov, W.D Dobrowolski, R. Rudolf, I. Anzel, *Optical and magnetic properties of PbTe(Ni)*, Acta Physica Polonica A 115 (4), 765 − 767 (2009),

- **J. Trajić**, N. Romčević, M. Romčević, D. Stojanovic, R. Rudolf, T.A. Kuznetsova and D.R. Khokhlov, *Far − infrared study of impurity local modes in Co − doped PbTe*, Journal of Alloys and Compounds, 493, 41− 46 (2010),

- N. Romčević, **J. Trajić**, M. Romčević, D. Stojanović, T.A. Kuznetsova, D.R. Khokhlov, W.D. Dobrowolski, *Optical and magnetic properties of PbTe(Co)*, Optoelectronics and Advanced Materials – Rapid Communications 4 (4), 470 – 475 (2010),

- **J. Trajić**, N. Romčević, M. Gilić, M. Petrović Damjanović, M. Romčević, V.N. Nikiforov, *Optical properties of PbTe$_{0.95}$S$_{0.05}$ single crystal at different temperatures: far-infrared study*, Optoelectronics and Advanced Materials - Rapid Communications 6 (5-6), 543-546 (2012)

- **J. Trajić**, N. Romčević, M. Romčević, Z. Lazarević, T.A. Kuznetsova, D.R. Khokhlov, *Plasmon – ionized impurity – phonon interaction in PbTe doped with Ni*, Optoelectronic and advanced materials - rapid communications 7 (7-8), 536-540 (2013),

- **J. Trajić**, N. Romčević, M. Romčević, D. Stojanović, L.I. Ryabova, D.R. Khokhlov, *Galvanomagnetic and optical properties of chromium doped PbTe*, Journal of Alloys and Compounds 602, 300-305 (2014),

- **J. Trajic**, N. Paunovic, M. Romcevic, V.E. Slynko, Jasna L. Ristic-Djurovic, W.D. Dobrowolski, N. Romcevic, *Far infrared spectra of Si doped PbTe single crystals*, Optical Materials 91, 195-198 (2019).

Оптичке особине полумагнетних полупроводних II-VI материјала

Полупроводници типа A^{II}B^{VI} се интензивно истражују услед велике могућности примене у оптоелектронској индустрији. Монокристали *CdTe$_{0.97}$Se$_{0.03}$* и *CdTe$_{0.97}$Se$_{0.03}$(In)* су испитивани применом инфрацрвене спектроскопије. Спекти су анализирани применом диелектричне функције која истовремено урачунава просторну расподелу слободних носилаца и њихов утицај на плазмон-фонон интеракцију. У циљу одређивања понашања дуготаласних оптичких фонона коришћен је модификован Genzel-ов модел и установљено је да дуготаласни оптички фонони испољавају дво-модно понашање. Регистрован је локални мод индијума, а такође је установљено да код оба узорка долази до формирања осиромашеног површинског слоја тј. слоја са малом концентрацијом слободних носилаца. Резултат је садржан у следећој публикацији:

- M. Petrović, N. Romčević, **J. Trajić**, W.D. dobrowolski, M. Romčević, B. Hadžić, M. Gilić, A. Mycielski, *Far-infrared spectroscopy of CdT$_{1-x}$Se$_x$(In): Phonon properties*, Infrared Physics and Technology 67, 323-326 (2014)

Полумагнетни полупроводници *Zn$_{1-x}$Mn$_x$GeAs$_2$* (*p*-типа) су испитивани применом дифракције X-зрака и Раман спектроскопије. Установљено је постојање интеракције између плазме и фонона која доводи до померања неких модова као и до појаве нових. Експериментално су одређене учестаности фонона ZnGeAs$_2$. У узорцима са већом концентрацијом мангана је установљено формирање кластера MnAs у две фазе: феромагнетни α-MnAs са хексагоналном структуром и парамагнетни β-MnAs са орторомбичном структуром, и експериментално су одређене њихове учестаности. Овај материјал је посебно интересантан због својих магнетних својстава која му омогућавају примену у спинтроници. Наиме, допирање манганом доводи до појаве феромагнетизма на собној температури. Резултати су публиковани у:

- M. Romčević, N. Romčević, W. Dobrowolski, L. Kalinski, **J. Trajić**, D.V. Timotijević, E. Dynowska, I.V. Fedorchenko, S.F. Marenkin, *Optical properties and plasmon-Two different phonons coupling in ZnGeAs$_2$+Mn*, Journal of Alloys and Compounds 548, 33-37 (2013),

- N. Romcevic, M. Romcevic, W.D. Dobrowolski, L. Kilanski, M. Petrovic, **J. Trajic**, B. Hadzic, Z. Lazarevic, M. Gilic, J.L. Ristic-Djurovic, N. Paunovic, A. Reszka, B.J. Kowalski, I.V. Fedorchenko, S.F. Marenkin, *Far-infrared spectroscopy of Zn$_{1-x}$Mn$_x$GeAs$_2$ single crystals:*

Plasma damping influence on plasmon - Phonon interaction, Journal of Alloys and Compounds 649, 375-379 (2015).

Полумагнетни полупроводник $Hg_{0.91}Mn_{0.09}Te$-MnSe добијен Bridgman-овом методом је испитиван применом AFM, дифракције X-зрака и инфрацрене спектроскопије у циљу одређивања најбољих услова за раст кристала. Установљено је постојање нанокластера MnSe. Примењена је Maxwell-Garnett-ова апроксимација ефективног медијума и утврђено је да се MnSe јавља у α и β фази. Такође је одређен и проценат његовог садржаја у HgMnTe. Део резултата је публикован у:

- M. Petrović, N. Romčević, M. Romčević, G. Stanišić, D. Vasiljević-Radović, **J. Trajić**, Z. Lazarević, S. Kostić, *Spectroscopy characterization of MnSe nanoclasters randomly distributed in HgMnTe single crystal*, Journal of Crystal Growth 338, 75-79 (2012).

Поликристалан $ZnSnSb_2 + Mn$ је проучаван у циљу објашњавања повезаности између високе концентрације слободних носилаца и структуре и њиховог утицаја на оптичке особине материјала. Приликом анализе су коришћени XRD, оптичка микроскопија, AFM и IR спектроскопија. Регистровано је постојање неколико различитих фаза ($ZnSnSb_2$, ZnSb, SnSb), мали удео Sn и MnSb. Ове фазе формирају различите микроструктуре што је повезано са великим неправилностима у структури решетке. Установљено је да висока концентрација слободних носилаца проузрокује велики број дефеката. Такође је установљено да у овом систему долази до плазмон-мулти фонон интеракције. Резултат је представљен у публикацији:

- M. Romcevic, N. Paunovic, U. Ralevic, J. Pesic, J. Mitric, **J. Trajic**, L. Kilanski, W. Dobrowolski, I. V. Fedorchenko, S. Fedorovich Marenkin, N. Romcevic, *Plasmon – Phonon interaction in $ZnSnSb_2 + Mn$ semiconductors*, Infrared Physics and Technology 108, 103345 (2020).

$CdGeAs_2$ је значајан материјал због примене у оптоелектроници. Сама примена је повезана са квалитетом кристалне решетке. Снимани су и анализирани Раман и FIR спектри $Cd_{1-x}Mn_xGeAs_2$. Установљено је да допирање малом концентрацијом мангана (x = 0.004) доводи до врло благе деформације решетке $CdGeAs_2$ и значајно смањује појаву дефеката GeAs. Резултат истраживања је представљен у публикацији:

- M. Romcevic, N. Romcevic, **J. Trajic**, L. Kilanski, W. Dobrowolski, I. V. Fedorchenko, S. F. Marenkin, *Defects in $Cd_{1-x}Mn_xGeAs_2$ lattice*, Journal of Alloys and Compounds 688, 56-61 (2016).

Оптичке особине танких филмова, наночестица и наноструктура

Проучавани су танки филмови *CdS, CdTe* и *CuSe* добијени техником вакуумског напаравања.

Танки филмови *CdS* су испитивани применом AFM, FIR и Раман спектоскопије. Ефективна пермеабилност је моделована Maxwell-Garnet-овом апроксимацијом, док је приликом анализе инфрацрвених спектара рефлексије коришћен нумерички модел за израчунавање коефицијента рефлексије сложених система који укључује филм и супстрат. Регистрована је појава површинског оптичког фонона и одређена зависност његове учестаности од дебљине узорка. Такође је одређена и симетрија фонона који учествује у креирању површинског оптичког фонона. Ови филмови су посебно интересантни јер имају велику могућност примене и ниску цену производње. Резултати су публиковани у:

- M. Gilić, **J. Trajić**, N. Romčević, M. Romčević, D.V. Timotijević, G. Stanišić, I.S. Yahia, *Optical properties of CdS thin films*, Optical Materials 35, 1112-1117 (2013),

- **J. Trajić**, M. Gilić, N. Romčević, M. Romčević, G. Stanišić, Z. Lazarević, D. Joksimović, I.S. Yahia, *Far-infrared investigations of the surface modes in CdS thin film*, Physica Scripta T162, 014031 (4pp) (2014),

- **J. Trajić**, M. Gilić, N. Romčević, M. Romčević, G. Stanišić, B. Hadžić, M. Petrović, Y.S. Yahia, *Raman spectroscopy of optical properties in CdS thin films*, Science of Sintering, 47 145-152 (2015).

Струкурне и оптичке особине танких филмова *CdTe* су испитиване применом AFM, XRD, FIR и Раман спектроскопије. И у овом случају је приликом анализе спектара рефлексије коришћен модел који укључује филм и супстрат. Ефективна пермеабилност је моделована Maxwell-Garnet-овом апроксимацијом. Регистровано је постојање површинског оптичког фонона (SOP) као и спрегнути плазмон – SOP модови. Резултати су публиковани у:

- J. Mitric, N. Paunovic, M. Mitric, B. Vasic, U. Ralevic, **J. Trajic**, M. Romcevic, W.D. Dobrowolski, I.S. Yahia, N. Romcevic, *Surface optical phonon – Plasmon interaction in nanodimensional CdTe thin Films*, Physica E: Low-dimensional Systems and Nanostructures 104, 64-70 (2018).

Двофазни танки филмови *CuSe* су испитивани применом FESEM, UV–VIS–NIR и фотолуминисцентне спектоскопије. Ове методе су коришћене за идентификацију и квантификацију две фазе. Помоћу модела за конфајнмент оптичких фонона одређиване су величине честица $CuSe_2$ фазе. UV-VIS спектроскопијом су добијене вредности забрањених зона обе фазе. Фотолуминесцентним мерењима на ниским температурама је детектован дефектни ниво селена – негативни U-центар. Резултати су публиковани у:

- M. Petrović, M. Gilić, J. Ćirković, M. Romčević, N. Romčević, **J. Trajić**, I. Yahia, *Optical Properties of CuSe Thin Films – Band Gap Determination*, Science of Sintering, 49, 167-174 (2017),

- M. Gilić, M. Petrović, R. Kostić, D. Stojanović, T. Barudžija, M. Mitrić, N. Romčević, U. Ralević, **J. Trajić**, M. Romčević, I.S. Yahia, *Structural and optical properties of CuSe2 nanocrystals formed in thin solid Cu–Se film*, Infrared Physics & Technology 76, 276–284 (2016).

Истраживане су и наночестице у одговарајућим матрицама и нано-структуре. Проучавани су утицаји температуре, магнетног поља, таласне дужине и снаге ласера на оптичке особине наноматеријала. Добијени резултати су моделовани и објашњени.

Изучаване су оптичка и структурна својства наночестица *CdSe* у стакленој матрици добијене оригиналном техником која комбинује загревање и озрачивање УВ ласером. Узорци су анализирани применом AFM и UV–VIS апсорпционих мерења. Резултати проучавања фотолуминисценције *CdSe* квантних тачака у стакленој матрици и морфологија њихових површина су представљени у:

- M.Gilic, R. Kostic, D. Stojanovic, M. Romcevic, B. Hadzic, M. Petrovic, U. Ralevic, Z. Lazarevic, **J. Trajic**, J. Ristic-Djurovic, J. Cirkovic, N. Romcevic, *Photoluminescence spectroscopy of CdSe nanoparticles embedded in transparent glass*, Optical and Quantum Electronics 50:288 (2018).

Наночестице *ZnS* које су добијене високоенергетским млевењем су испитиване применом дифракције X-зрака, SEM и HRTEM микроскопије, Раман и FIR спектроскопије. Испитиван је утицај времена млевења на својства наночестица. Одређене су димензије нанчестица и њихова дефинисаност. Мале димензије квантних тачака доводе до јаког конфинирајућег режима. У циљу испитивања конфинирања оптичких фонона у квантним тачкама коришћен је модел ефективног медијума. Такође су испитиване и структурне и оптичке особине *ZnS/ Poli (metil metakrilat)* применом XRD, SEM, TEM, HRTEM, FIR и Раман спектроскопије. Анализа Раман спектара је вршена моделом заснованим на теорији

ефективног медијума. Утврђено је присуство површинског оптичог фонона, чији облик и позиција зависе од врсте композита. Резултати су публиковани у:

- **J. Trajić**, R. Kostić, N. Romčević, M. Romčević, M. Mitrić, V. Lazović, P. Balaž, D. Stojanović, *Raman spectroscopy of ZnS quantum dots*, Journal of Alloys and Compounds 637, 401-406 (2015),

- **J. Trajić**, M. Romčević, N. Romčević, B. Babić, B. Matović, P. Balaž, *Far-infrared spectra of mesoporous ZnS nanoparticles*, Optical Materials 57, 225-230 (2016),

- M. Curcic, B. Hadzic, M. Gilic, V. Radojevic, A. Bjelajac, I. Radovic, D. Timotijevic, M. Romcevic, **J. Trajic**, N. Romcevic, *Surface optical phonon (SOP) mode in ZnS/Poly (methylmethacrylate) nanocomposites*, Physica E: Low-dimensional Systems andNanostructures115, 113708 (2020).

Спектроскопским методама су испитиване структурне и оптичке особине слојевитих нано-структура *CdTe/ZnTe* у којима су формиране само-организоване квантне тачке. Утврђена је њихова енергетска структура као и постојање мултифононских процеса. При анализи инфра-црвених спектара рефлексије коришћена је теорија ефективног медијума. На основу добијених резултата одређени су услови за формирање квантних тачака. Овај резултат је значајан са гледишта практичне примене, тј. при дизајнирању и добијању квантних структура тачно одређених карактеристика. Резултати су публиковани у:

- N. Romčević, M. Romčević, R. Kostić, D. Stojanović, A. Milutinović, **J. Trajić**, G. Karczewski, R. Galazka, *Photoluminescence Spectroscopy of CdTe/ZnTe Self – Assembled Quantum Dots*, International Journal of Photoenergy ID 358790 4 pages (2009),

- M. Gilić, N. Romčević, M. Romčević, D. Stojanović, R. Kostić, **J. Trajić**, W.D. Dobrowolski, G. Karczewski, R. Galazka, *Optical properties of CdTe/ZnTe self-assembled quantum dots: Raman and photoluminescence spectroscopy*, Journal of Alloys and Compounds 579, 330-335 (2013).

Испитиван је и *ZnO* који је за разлику од претходних узорака широкозонски полупроводник. Анализирани су узорци нанокристала ZnO допираног кобалтом, са концентрацијама од 5% до 95%. Узорци су добијени хидротермалном методом и методом калцинације и анализирани применом дифракције X-зрака и Раман спектроскопије. Одређене су димензије нанокристала као и њихов састав који се мења при додавању веће количине примеса. Анализиране су две појаве на Рамановим спектрима. Регистровано је уширење и померање фонона основног кристала услед смањења димензија честица. Јасно су раздвојени фонони који потичу од ZnO од фонона који одговарају оксиду кобалта. У нискофреквентној области регистроване су структуре које потичу од акустичких фонона, који су забрањени селекционим правилима, али се код нано-димензионалних система виде услед нарушавања симетрије. Њихов положај је директно повезан са величином честица. Коришћен је модел заснован на апроксимацији еластичног континуума. Овако израчунате фреквенције се поклапају са експериментално добијеним.

ZnO је полупроводник хексагоналне структуре са широком "директном" забрањеном зоном и релативно великом енергијом ексцитације. Ове особине га стављају у центар многих истраживања због великих могућности примене како у електронским и оптоелектронским уређајима, тако и у магнетно-електронским и спинтроничким уређајима, док се посебна пажња посвећује могућности постизања виско-температурског феромагнетизма код ових материјала. Резултати су публиковани у:

- B. Hadžić, N. Romčević, M. Romčević, I. Kuryliszyn-Kudelska, W. Dobrowolski, **J. Trajić**, D. Timotijević, U. Narkiewicz, D. Sibera, *Surface optical phonons in ZnO(Co) nanoparticles: Raman study*, Journal of Alloys and compounds 540, 49-56 (2012),

- B. Hadžić, N. Romčević, M. Romčević, I. Kuryliszyn-Kudelska, W. Dobrowolski, M. Gilić, M. Petrović-Damjanović, **J. Trajić**, U. Narkiewicz, D. Sibera, *Raman study of surface optical phonons in ZnO(Co) nanoparticles prepared by calcinations method*, Journal of optoelctronics and advanced materials 16 (5-6) 508-512 (2014).

Проучаване су и *ZnO@ZnS* core-shell наноструктуре са применом дифракције X-зрака, Raman и далеке инфрацрвене спектроскопије. Регистрован је „*top*" површински оптички фонон мод (TSO) у ZnO који је карактеристичан за цилиндричне нано-објекте, као и површински оптички фонон мод (SOP) у ZnS. Такође су регистровани SOP модови у ZnO@ZnS core-shell наноструктури, као и локални модови који потичу од кисеоника у ZnS и gap моде сумпора у ZnO. Услед постојања активног слоја у простору између ZnO језгра и ZnS љуске ова истраживања су веома важна због примене ових материјала у термоелектроници. Истраживање је публиковано у:

- B. Hadzic, B. Matovic, M. Randjelovic, R. Kostic, M. Romcevic, **J. Trajic**, N. Paunovic, N. Romcevic, *Phonons investigation of ZnO@ZnS core- shell nanostructures with active* layer, Journal of Raman Spectroscopy 52, 616-625 (2021).

Европијумом је допиран нанопрах *Gd₂Zr₂O₇*, који је познат материјал као домаћин (*host*) за фотолуминесентну примену. Узорци добијени SCS (Solution Combustion Synthesis) методом су анализирани применом AFM, FIR и Раман спектроскопије. Регистрована је електрон фонон интеракција која доводи до кршења селекционих правила и до појаве нових фонона. Уочена су два фонона која до сада нису била регистрована, и њихова позиција је у складу са уоченом електрон-фонон интеракцијом. Регистровани мултифононски процеси су директна последица допирања, а то условљава и појаву бочне траке фонона. Резултати су публиковани у:

- G. Krizan, M. Gilic, J.L. Ristic-Djurovic, **J. Trajic**, M. Romcevic, J. Krizan, B. Hadzic, B. Vasic, N. Romcevic, *Raman spectroscopy and electron-phonon coupling in Eu³⁺ doped Gd₂Zr₂O₇ nanopowders*, Optical Materials 73, 541-544 (2017),

- J. Mitric, J. Krizan, **J. Trajic**, G. Krizan, M. Romcevic, N. Paunovic, B. Vasic, N. Romcevic, *Structural properties of Eu³⁺ doped Gd₂Zr₂O₇ nanopowders: Far-infrared spectroscopy*, Optical Materials 75, 662-665 (2018).

Испитивана су својства *YAG:Dy* (Итријум алуминијум граната допиран јонима диспрозијума) нанопраха и поређена са особинама YAG нанопраха и YAG монокристала. Морфологија, специфична површина, текстура и оптичка својства испитивани су применом SEM микроскопије, методом адсорпције азота и FIR спектроскопије. Установљено је да је и YAG допиран Dy као и недопиран YAG микропорозан. Регистроване су сферне, јасно дефинисане и одвојене наночестице. Такође је установљено да допирање YAG диспорзијумом не утиче значајно на вибрације решетке, али да доводи до смањења учестаности фонона у односу на учестаности фонона YAG нанопраха и YAG монокристала. Резултати су публиковани у:

- **J. Trajić**, M.S. Rabasović, S. Savić-Шевић, D. Шевић, B. Babić, M. Romčević, J.L. Ristić-Djurović, N. Paunović, J. Križan, N. Romčević, *Far-infrared spectra of dysprosium doped yttrium aluminum garnet Nanopowder*, Infrared Physics & Technology 77, 226–229 (2016).

Баријум-титанат допиран антимоном је добијен механохемијском активацијом у планетарном млину. Полазне компоненте су биле оксиди баријума и титанијума. Приликом млевења долази до образовања нових једињења у облику прахова. При карактеризацији су коришћени XRD, FIR рефлексија и Раманова спектроскопија. Утврђена је веза између дужине млевења и величине и састава добијених кристалита. Неки од прахова су синтеровани и испитане су особине добијених керамичких прахова. Резултати су публиковани у:

- Z. Lazarević, N. Romčević, M. Romčević, **J. Trajić**, M. Vijatović, J. Bobić, B. Stojanovic, *Infrared and Raman Spectroscopy Study of Antimony Doped Barium Titanate Prepared from Organometallic Complex*, International Journal of Modern Physics B, 24, 676 – 681 (2010).

Проучавани су и услови раста монокристала $Bi_{12}GeO_{20}$ и $Bi_{12}SiO_{20}$ добијених методом раста кристала по Чохралском (Czochralski). Израчунати су критични дијаметар и критична стопа ротације, а одређени су и погодни раствори за полирање и нагризање. При карактеризацији добијених монокристала је коришћен низ експерименталних метода: дифракције X - зрака, FIR рефлексија и Раманова спектроскопија. Ови материјали, захваљујући великој разноврсности физичких особина имају велику примену у електронским и оптоелектронским уређајима, где је неопходно да кристали имају малу густину дислокација и велику оптичку хомогеност. Стога се велика пажња посвећује начину и условима добијања узорака. Резултати су публиковани у:

- Z. Lazarević, S. Kostić, M. Romčević, **J. Trajić**, B. Hadžić, D. Stojanović and N. Romčević, *Study of $Bi_{12}SiO_{20}$ single crystals obtained by Czocharlski method*, Optoelectronics and Advanced Materials - Rapid Communications 5 (2), 150-152 (2011),

- Z. Ž. Lazarević, S. Kostić, V. Radojević, M.J. Romčević, B. Hadžić, **J. Trajić**, N.Ž. Romčević, *Spectroscopy study of $Bi_{12}GeO_{20}$ single crystals*, Optoelectronics and Advanced Materials - Rapid Communications 7 (1-2), 58-61 (2013),

- G.S.I. Abudagel, S. Petričević, P. Mihailović, A. Kovačević, J.L. Ristić-Djurović, M. Lekić, M. Romčević, S. Ćirković, **J. Trajić**, N. Romčević, *Improvement of magneto-optical quality of high purity $Bi_{12}GeO_{20}$ single crystal induced by femtosecond pulsed laser irradiation*, Optoelectronics and Advanced Materials-Rapid Communications, 11, 477-481 (2017).

Утицај локалног загревања проузрокованог ласером на *MnO* наночестице је проучаван применом AFM микроскопије и далеке инфрацрвене спектроскопије (FIR). Спектри рефлексије су анслизирани применом Maxwell-Garnet апроксимације. Установљено је да ласерско srачење загревање доводи до конверзије делова MnO наночестица у MnO_2, Mn_3O_4 and MnOOH као и до формирања Mn на површини узорка. Резултат је публикован у:

- B. Babic, B.Hadzic, I. Kuryliszyn-Kudelska, N. Paunovic, B. Vasic, W.D. Dobrowolski, M. Romcevic, **J.Trajic**, N. Romcevic, *Far-infrared spectroscopy of laser power modified MnO nanoparticles*, Optoelectronics and Advanced Materials-Rapid Communications, 13, 376-379 (2019).

Оптичке особине материјала анализираних у оквиру сарадње са колегама из других научних институција

У оквиру сарадње са колегама из других лабораторија испитиване су оптичке особине материјала којима се они баве. Поред снимања инфрацрвених спектара рефлексије и апсорпције и Раманових спектара дат је и допринос у њиховој анализи и објашњењу регистрованих оптичких карактеристика.

У оквиру сарадње са колегама из Марибора испитиване су оптичке и структурне особине *пластично деформисаног бакра*. При анализи је коришћена FIR и Раманова спектроскопија и мерења на елипсометру. Утврђено је да није дошло до потпуне аморфизације узорка већ да су присутни нано-кристали бакра. Резултати са елипсометра су анализирани коришћењем двослојног модела и Бругеманове апроксимације ефективног медијума и утврђено је постојање бакар-оксида као и параметри површинске храпавости. Резултати су публиковани у:

- M. Mirić, R. Rebeka, I. Anzel, B. Hadžić, M. Romčević, **J. Trajić**, N. Romčević, *Ellipsometric Measurements of Plastically Deformed Copper*, Acta Physica Polonica A, 116, 715 – 717 (2009),

- **J. Trajić**, R. Rudolf, I. Anžel, M. Romčević, N. Lazarević, M. Mirić, Z. Lazarević, B. Hadžić, and N. Romčević, *Optical properties of plastically deformed copper*, Acta Physica Polonica A 117 (5) 791 – 793 (2010),

- N. Romčević, R. Rudolf. J. **Trajić**, M. Romčević, B. Hadžić, D. Vasiljević-Radović, I. Anžel, *Optical properties of plastically deformed copper: an ellipsometric study*, Materials and technology 45 (5) 463-465 (2011).

Током сарадње са колегама из Геотехничког института Словачке Академије наука проучаван је Cu_2FeSnS_4 *(stannite)* нанокристал добијен поступком механохемијске синтезе. Применом далеке инфрацрвене и Раман спектроскопије детаљно су проучена вибрациона својства овог система и одређен је утицај дужине времена млевења на формирање Cu_2FeSnS_4 нанокристала. Ова сарадња је настављена у оквиру COST акције *Mech@SusInd – Mechanochemistry for Sustainable Industry*. Резултати су представљени у:

- P. Baláž, M. Baláž, A. Zorkovská, I. Škorvánek, Z. Bujnáková, **J. Trajic**, *Kinetics of Solid-State Synthesis of Quaternary Cu_2FeSnS_4 (Stannite) Nanocrystals for Solar Energy Applications*, Acta Physica Polonica A 131, 1153-1155 (2017),

- **J. Trajic**, M. Romcevic, M. Petrovic, M. Gilic, P. Balaz, A. Zorkovska, N. Romcevic, *Optical properties of the mechanochemically synthesized Cu_2FeSnS_4 (stannite) nanocrystals:Raman study*, Optical Materials 75, 314-318 (2018),

- **J. Trajic**, M. Romcevic, N. Paunovic, M. Curcic, P. Balaz, N. Romcevic, *Far-infrared study of the mechanochemically synthesized Cu_2FeSnS_4 (stannite) nanocrystals*, Infrared Physics & Technology 90, 66–69 (2018).

4. Елементи за квалитативну оцену научног доприноса кандидата

4.1 Квалитет научних резултата

4.1.1 Научни ниво и значај резултата, утицај научних радова

Др Јелена Трајић је у свом досадашњем раду објавила 57 радова у међународним часописима са ISI листе, од којих 8 у категорији М21а, 11 у категорији М21, 16 у категорији М22 и 22 у категорији М23. Поред ових радова објавила је и 2 рада у категорији М33, 26 у категорији М34, 2 у категорији М51 и 4 поглавља М14 у тематском зборнику међународног значаја М12.

У периоду након одлуке Научног већа о предлогу за стицање претходног научног звања др Јелена Трајић је објавила 28 радова у међународним часописима са ISI листе и саопштења на међународним конференцијама од којих је један у категорији М21а, 3 у категорији М21, 10 у категорији М22, 6 у категорији М23, један у категорији М33, 3 у категорији М34 и 4 поглавља М14 у тематском зборнику међународног значаја М12.

Као пет најзначајнијих радова могу се узети:

1. **J. Trajić**, N. Romčević, M. Romčević, V. Nikiforov
   Plasmon – phonon and plasmon – two different phonon interaction in $Pb_{1-x}Mn_xTe$ mixed crystals
   Materials Research Bulletin, 42, 2192-2201 (2007).
   М21, цитиран до сада 16 пута.

2. **J. Trajić**, N. Romčević, M. Romčević, D. Stojanovic, R. Rudolf, T.A. Kuznetsova and D.R. Khokhlov
   Far – infrared study of impurity local modes in Co – doped PbTe
   Journal of Alloys and Compounds, 493, 41− 46 (2010)
   М21а, цитиран до сада 8 пута.

3. **J. Trajić**, R. Kostić, N. Romčević, M. Romčević, M. Mitrić, V. Lazović, P. Balaž, D. Stojanović
Raman spectroscopy of ZnS quantum dots
Journal of Alloys and Compounds 637, 401-406 (2015),
M21a, цитиран до сада 36 пута.

4. **J. Trajić**, M. Romčević, N. Romčević, B. Babić, B. Matović, P. Balaž
Far-infrared spectra of mesoporous ZnS nanoparticles
Optical Materials 57, 225-230 (2016),
M21, цитиран до сада 3 пута.

5. N. Romčević, **J. Trajić**, M. Romčević, A. Golubović, S. Nikolić, V.N. Nikiforov
Raman spectroscopy of PbTe$_{1-x}$S$_x$ alloys
Journal of Alloys and Compounds 387, 24-31 (2005),
M21, цитиран до сада 9 пута.

У првом раду су испитивана вибрациона својства Pb$_{1-x}$Mn$_x$Te ($x = 0.0002$, 0.002, 0.02 and 0.1) мешаних кристала применом далеке инфрацрвене спектроскопије (FIR). Приликом анализе експерименталних резултата су коришћене диелектричне функције које узимају у обзир плазмон-фонон и плазмон-два различита фонона интеракције. Одређене су две учестаности плазмон-фонон спрегнутих модова и три учестаности плазмон-два различита фонона спрегнутих модова. Израчунате су вредности лонгитудиналних оптичких модова (LO) и плазма учестаности (ω_P). Применом модела који је развијен на основу Genzel-овог модела је установљено да дуготаласни оптички фонони испољавају и интермедијално и дво-модно понашање.

Кандидат је развила модел за плазмон-два различита фонона интеракцију, анализирала експерименталне резултате „*best fit*" методом и одредила учестаности плазмон-фонон спрегнутих модова и плазмон-два различита фонона спрегнутих модова. Такође је, на основу развијеног метода одредила вредности лонгитудиналних оптичких модова (LO) и плазма учестаности (ω_P).

У другом раду су фононска својства PbTe допираног Co проучавана применом далеке инфрацрвене спектроскопије (FIR). Коришћен је модел који узима у обзир постојање плазмон-јонизована примеса-фонон интеракцију. Одређене су учестаности три примесна локална мода Co и установљено да кобалт улази у решетку PbTe у три различита валентна стања. Наиме, на почетку допирања Co улази у решетку PbTe као неутрална примеса (Co^{2+}), да би како концентрација примеса расте постао донор (Co^{3+}) и на крају акцептор (Co^{1+}). Такође је установљено да поред спрезања фонона решетке PbTe и плазмона постоји и интензивно спезање примесних модова Co и слободних носилаца, те да у околини сваког примесног центра постоји дво-компонентна плазма.

Кандидат је применом „*best fit*" методе одредила учестаности примесних модова, установила њихова различита валентна стања и израчунала вредности фреквенција дво-компонентне плазме.

У трећем раду су представљени резултати проучавања ZnS добијеног механохемијском синтезом применом дифракције X-зрака, SEM и HRTEM микроскопије и Раман спектроскопије. Проучавани су узорци добијени после различитог времена млевења. Применом Раман спектроскопије је установљено да мале димензије ZnS квантних тачака доводе до појаве „*confinement*" режима. Коришћен је „*continuum model of the optical phonon confinement in QD*" за истраживања у области оптичких фонона тј. области од 275 cm^{-1} (ω_{TO}) до 350 cm^{-1} (ω_{LO}). И поред тога што се овај модел користи за идеалан случај, добијене вредности за мод на 345 cm^{-1} су у сагласности са предвиђеним вредностима. Овај мод је препознат као конфинирани LO мод. Као што је и очекивано његова учестаност знатно нижа од одговарајућих учестаности монокристалних ZnS. Такође су регистроване су мулти-модне

појаве на Раман спектрима у области од 130 до 180 cm^{-1} и 265 cm^{-1}, које су упоредиве са интензитетом конфинираног LO moda.

Кандидат је у овом раду урадила део који се односи на Раман спектроскопију тј. применом наведеног модела установила постојање конфинираног LO мода и мулти-модних структура. Одредила карактеристичне учестаности и објаснила њихову природу.

У четвртом раду су представљени резултати испитивања нанопрахова ZnS добијених механохемијском синтезом, при чему је време млевења било 5, 10 и 20 min. Специфична површина и текстура су испитивани методом адсорпције азота док су оптичка својства су проучавана применом далеке инфрацрвене спектроскопије.

Др Јелена Трајић је у одредила оптичка својства ZnS нанопрахова анализом спектара рефлексије. Спектре рефлексије је анализирала применом „*best fit*" методе. Диелектричну функцију ZnS нанопрахова је моделовала „*Maxwell – Garnet*" апроксимацијом, при чему је посматрала нанопрах као хомогене сфере које су „утиснуте" у ваздух. Установила је постојање комбинованих плазмон - LO фонон модова (CPPMs) и регистровала велико пригушење фонона које доводи до смањења спрегнутих плазмон-фонон учестаности.

У петом раду су дати резултати проучавања PbTe$_{1-x}$S$_x$ (x = 0.02 and 0.05) мешаних кристала применом, дифракције X-зрака, галваномагнетних и ултразвучних мерења и Раман спектроскопије. Установљено је постојање структурног фазног прелаза на T_c = 60K код узорка са x = 0.05. Одређена су два TO/LO парова модова PbTe$_{1-x}$S$_x$ мешаних кристала. Применом модела који је развијен на основу Genzel-овог модела је установљено да дуготаласни оптички фонони испољавају дво-модно понашање. Установљено је постојање „*off-center*" јона сумпора што директно доводи до појаве фазног прелаза.

Кандидат је анализом Раман спектара одредила карактеристичне TO/LO учестаности PbTe$_{1-x}$S$_x$ мешаних кристала. Анализом галваномагнетних мерења и Раман спектара установила постојање фазног прелаза код узорка са 5% сумпора као и да до њега не долази код узорка са 2% сумпора. Такође је установила појаву мода на 75 cm^{-1}, који је директна последица „*off-center*" јона сумпора.

У свим овим радовима се може сматрати да је др Јелена Трајић основни/најважнији аутор.

4.1.2. Позитивна цитираност научних радова кандидата

На дан 25.05.2021. године, научни радови које је објавила др Јелена Трајић су цитирани у међународним часописима више од 304 пута, Хиршов фактор: h = 9 (Google Scholar).

Прилог: извод из Google Scholar-a

4.1.3. Параметри квалитета часописа

У категоријама М21, М22, М23 и М33 кандидат је објавио радове у следећим часописима, при чему су подвучени случајеви који се односе на период након одлуке Научног већа о предлогу за стицање претходног научног звања:

- 1+12 радова у *Journal of Alloys and Compounds* (ИФ=3,133 за један рад, 3,104 за пет радова, 2,390 за два рада, 1,455 за четири рада и 1,562 за један рад)

- 5+1 радова у *Optical Materials* (ИФ=2,975 за један рад, 2,770 за два рада, 2,415; 2,367 и 2,075 за по један рад)

- 1 рад у *Materials Research Bulletin* (ИФ=1,484)

- 1 рад у *Journal of Raman Spectroscopy* (ИФ=2,809)

- 4+1 радова у *Infrared Physics and Technology* (ИФ=2,379 за један рад, 2,313 за један рад, 1,827 за два рада + један рад)

- 2 рада у *Physica E: Low-dimensional Systems and Nanostructures* (ИФ=3,795 и 3,161)

- 1+2 рада у *Science of Sintering* (ИФ=0,941; 0,812 и 0,481)

- 1 рад у *Physica Scripta* (ИФ=1,126)

- 1 рад у *Journal of Crystal Growth* (ИФ=1,858)

- 1 рад у *International Journal of Photoenergy* (ИФ=1,500)

- 4+6 радова у *Optoelectronics and Advanced Materials-Rapid Communications* (ИФ=0,452 за један рад, 0,470 за два рада, 0,449 за три рада и 0,447; 0,402 и 0,304 за по један рад)

- 1 рад у *Optical and Quantum Electronics* (ИФ=1,547)

- 1+5 радова у *Acta Physica Polonica* (ИФ=0,927 за један рад, 0,467 за један рад, 0,433 за три рада)

- 1 рад у *Materials and technology* (ИФ=0,804)

- 1 рад у *International Journal of Modern Physics* (ИФ=0,519)

- 2 рада у Journal of the Serbian Chemical Society (ИФ=0,611)

Укупан фактор утицаја радова кандидата је 82,08 а у периоду након одлуке Научног већа о предлогу за стицање претходног научног звања тај фактор је 39.348.

4.1.4. Степен самосталности и степен учешћа у реализацији радова у научним центрима у земљи и иностранству

Научни рад др Јелене Трајић представља оригиналан допринос физици материјала, посебно у области физике полупроводних кристала, танких филмова, наночестица и наноструктура. У току каријере је учествовала је у експерименталним мерењима спектара рефлексије у далекој инфра-црвеној области, снимањима Раман спектара, и галваномагнетним мерењима. Успешном применом постојећих и развијањем нових модела приликом анализе добијених експерименталних резултата научни рад др Јелене Трајић је довео до јасније слике о особинама испитиваних материјала.

Др Јелена Трајић је успоставила међународну сарадњу са групама др Матеја Балажа Геотехничког института Словачке Академије и др Ладислава Челка из Централног европског технолошког института. Ова сарадња је настављена у оквиру COST акције CA18112 - Mech@SusInd – Mechanochemistry for Sustainable Industry.

Радови на којима је др Јелена Трајић аутор или коаутор су публиковани у водећим научним часописима.

Др Јелена Трајић је током каријере објавила укупно 57 радова у међународним часописима са ISI листе, од чега 8 радова категорије М21а, 11 радова категорије М21, 16 радова категорије М22 и 22 рада категорије М23. Водећи је аутор на 18 радова.

У периоду након одлуке Научног већа о предлогу за стицање претходног звања, др Јелена Трајић је аутор или коаутор 20 радова категорије М20, од чега је један рад категорије М21а, 3 рада категорије М21, 10 радова категорије М22 и 6 радова категорије М23. Водећи је аутор на 6 радова.

4.2 Ангажованост у формирању научних кадрова

У оквиру потпројекта којим је др Јелена Трајић руководила урађена је докторска дисертација др Мартине Гилић под насловом „Оптичке особине нанодимензионих система формираних у пластично деформисаном бакру, танким филмовима CdS и хетероструктурама CdTe/ZnTe" која је одбрањена на Факултету за физичку хемију Универзитета у Београду. Током рада на изради поменутог доктората објављени су следећи радови:

- M. Gilić, **J. Trajić**, N. Romčević, M. Romčević, D.V. Timotijević, G. Stanišić, I.S. Yahia, *Optical properties of CdS thin films,* Optical Materials 35, 1112-1117 (2013),

- **J. Trajić**, M. Gilić, N. Romčević, M. Romčević, G. Stanišić, B. Hadžić, M. Petrović, Y.S. Yahia, *Raman spectroscopy of optical properties in CdS thin films,* Science of Sintering, 47 145-152 (2015),

- **J. Trajić**, M. Gilić, N. Romčević, M. Romčević, G. Stanišić, Z. Lazarević, D. Joksimović, I.S. Yahia, *Far-infrared investigations of the surface modes in CdS thin film,* Physica Scripta T162, 014031 (4pp) (2014).

У оквиру задатака којима је руководила др Јелена Трајић урађени су делови магистарске тезе и докторске дисертације др Бранке Хаџић и делови магистарске тезе др Ђорђа Јовановића, што је резултовало радовима:

- D. Stojanović**, J Trajić**, B. Hadžić, M. Romčević, I. Ivanchik, D. R. Khokhlov, N. Romčević, *Far–Infrared Study of DX–Like Centers in Pb$_{0.95}$Mn$_{0.05}$Te(Ga)*, Acta Physica Polonica A, 112 (5) 959 – 962 (2007),

- N. Romčević, **J. Trajić**, M. Romčević, B. Hadžić, V.N. Nikiforov, *Plasmon – two phonon interaction in PbMnTe and PbTeS alloy*, BPU6: 6 th International Conference of the Balkan Physical Union, August 22 – 26, Istanbul, Turkey, Book of Abstracts 861 (2006).

Такође је у оквиру потпројекта којим др Јелена Трајић руководи, Андреа Бучалина одбранила докторску дисертацију под називом "Компаративна анализа савремених светских токова у управљању инвестицијама у нанотехнолошке производе" на Факултету за пословне студије у Београду. Тема дисертације су били економски аспекти примене нанотехнологије. Колегиница Трајић је увела Андреу Бучалину у проблематику нанотехнологија и руководила деловима докторске дисертације који су се односили на трансфер технологије из науке у индустрију, као значајног аспекта при инвестирању у нанотехнологије.

Прилог: Релевантне странице из теза

Др Јелена Трајић је била ангажована на *Рачунарском факултету* Универзитета Унион у Београду на предмету *Карактеризација полупроводника* у оквиру докторских студија на студијском програму Рачунарско инжењерство.

Прилог: Уговор о допунском раду

4.3. Нормирање броја коауторских радова, патената и техничких решења

Сви радови др Јелене Трајић су експерименталне природе, што често подразумева сарадњу више институција. Имајући то у виду, број коаутора на појединим радовима је већи од 7 и нормирањем бодова тих радова у складу са Правилником Министарства о поступку, начину вредновања и квантитативном исказивању научноистраживачких резултата укупан нормирани број М радова које је др Јелена Трајић остварила након одлуке Научног већа о

предлогу за стицање претходног научног звања износи 101,51 од ненормираних 120,5, те је очигледно да нормирање не утиче значајано на број бодова, при чему др Јелене Трајић свакако има вишеструко већи број бодова од захтеваног.

4.4. Руковођење пројектима, потпројектима и пројектним задацима

У оквиру пројекта Интегралних интердисциплинарних истраживања Министарства просвете, науке и технолошког развоја Републике Србије: Оптоелектронски нанодимензиони системи – пут ка примени, број III 45003 (2011-2015.) којим руководи др Небојша Ромчевић, др Јелена Трајић је руководила потпројектом *Карактеризација наночестица и наноструктура*.

Прилог: Доказ о руковођењу научним потпројектом

4.5 Активност у научним и научно-стручним друштвима

Члан научног одбора конференције *Трансфер технологија и знања из научно-истраживачких организација у мала и средња предузећа* 2008. године

Члан организационог одбора конференције *Трансфер технологија и знања из научно-истраживачких организација у мала и средња предузећа* 2010. године.

Прилог: Доказ о учешћу у организационим и научним одборима конференција

Др Јелена Трајић је члан Management Commity текуће COST акције CA18112 - Mech@SusInd – Mechanochemistry for Sustainable Industry

Прилог: Доказ о учешћу

Члан је Друштва физичара, Друштва за ЕТРАН и Оптичког друштва Србије.

Др Јелена Трајић је рецензент у међународним часописима: Optical Materials, Journal of Electronic Materials, Materials Science & Engineering B, Applied Physics A, Journal of Applied Physics, Science of sintering, Revista Mexicana de Física, RSC Advances, Optoelectronics and Advanced Materials-Rapid Communications, Acta Physica Polonica...

Такође је била рецензент SONATA BIS grant пројека Narodowe Centrum Nauki – NCN, Пољска.

Прилог: Неке од електронских порука и захвалница

4.6. Утицај научних резултата

Утицај научних резултата кандидата је детаљно приказан у тачки 1. овог прилога, као и у прилогу о цитираности. Комплетан списак радова је дат у одељку 6.

4.7. Конкретан допринос кандидата у реализацији радова у научним центрима у земљи и иностранству

Др Јелена Трајић је значајно допринела сваком раду у чијој је изради учествовала. Њен допринос се огледа у експерименталном раду, обради добијених резултата развијањем и применом одговарајућих модела као и анализи добијених података.

Др Јелена Трајић активно учествује у међународној сарадњи од 1993. године.

У оквиру сарадње Института за физику и Low Temperature Physics Department, Moscow State University, Moscow, Russia, учествовала је на пројектима:

- *Electronic, magnetic and optical properties of high temperature superconductors and semiconductors; Institute of Physics, Belgrade – Moscow State University, Russian Federation, 1993-1997.*
- *Optical properties of PbTe based allows doped with III group elements*, 2000-2003.
- *Optical, magnetic and transport properties of magnetic and semimagnetic semiconductors nanoparticles, films and bulk*, 2004-2007.

У оквиру Споразума о научној сарадњи између Пољске академије наука и Српске академије наука и уметности учествовала је на пројектима:

- *Optical, magnetic and transport properties of semimagnetic semiconductors, 2003-2004.*
- *Elementary excitations in semimagnetic crystals and structures, 2005-2007.*
- *Elementary excitations in semimagnetic nanocrystals and nanostructures, 2008-2015.*

Такође је учествовала на међународним пројектима:

- *Center of excellence for optical spectroscopy application in physics, material science and environmental protection; European Commission, 2006-2009.*
- *Local structures, displacements, and phase transitions in $Pb_{1-x}A_xTe_{1-y}B_y$ (A=Mn, In, Ga, B=S) semiconductors, Deutsches Elektronen-Sinhrotron, project at HASYLAB, 2005.*
- *Local structures in PbTe:A (A=Ni, Co, Yb) semimagnetic semiconductors, Deutsches Elektronen-Sinhrotron, project at HASYLAB, 2008.*
- *Cost 539 – Electroceramics from Nanopowders Produced by Innovative Methods (ELENA); 2005-2009.*
- *Optical properties of metallic nanoparticles, Serbia and Slovenia, 2010-2011.*

Др Јелена Трајић је члан Management Commity текуће COST акције CA18112 - Mech@SusInd – Mechanochemistry for Sustainable Industry.

4.8. Уводна предавања на конференцијама и друга предавања

У периоду након одлуке Научног већа о предлогу за стицање претходног научног звања, није било промена у односу на период пре претходног избора.

5. Елементи за квантитативну оцену научног доприноса кандидата

5.1. Остварени резултати у периоду након одлуке Научног већа о предлогу за стицање претходног научног звања:

Категорија рада	М бодова по раду	Број радова	Укупан М број бодова	Нормирани број М бодова
М14	4	4	16	16
М21а	10	1	10	10
М21	8	3	24	21,71
М22	5	10	50	39,12
М23	3	6	18	13,4
М33	1	1	1	1
М34	0,5	3	1,5	0,28
Укупно			120,5	101,51

5.2. Табела са квантитативним показатељима радова категорија М20 објављеним након претходног избора у звање:

Редни број рада	М	ИФ	СНИП
1 М21а	10	3,133	1,326
1 М21	8	2,809	1,009
2 М21	8	2,415	1,054
3 М21	8	2,367	1,058
1 М22	5	2,379	1,274
2 М22	5	3,795	0,917
3 М22	5	2,975	1,068
4 М22	5	3,161	0,88
5 М22	5	2,313	1,296
6 М22	5	2,770	1,025
7 М22	5	2,770	1,025
8 М22	5	0,941	0,884
9 М22	5	1,827	1,140
10 М22	5	1,827	1,140
1 М23	3	0,452	0,22
2 М23	3	1,547	0,617
3 М23	3	0,470	0,268
4 М23	3	0,927	0,574
5 М23	3	0,470	0,268

6M23	3	0,470	0,268
Укупно	99	39,82	17,31

5.3. Поређење са минималним квантитативним условима за избор у звање виши научни сарадник:

Минималан број М бодова за реизбор (избор)		Остварено	Остварено нормираних
укупно	25 (50)	120,5	101,5
M10+M20+M31+M32+M33 M41+M42+M51 $\geq$	20 (40)	119	101,2
M11+M12+M21+M22 M23+M24+M31+M32 M41M42 $\geq$	30 (15)	102	84,2

6. СПИСАК НАУЧНИХ РАДОВА РАЗВРСТАНИХ ПРЕМА КАТЕГОРИЈАМА НАУЧНОГ РАДА (М КОЕФИЦИЈЕНТИ)

Радови након избора у претходно звање означени су са *

6.1. МОНОГРАФИЈЕ, МОНОГРАФСКЕ СТУДИЈЕ, ТЕМАТСКИ ЗБОРНИЦИ, ЛЕСКИКОГРАФСКЕ И КАРТОГРАФСКЕ ПУБЛИКАЦИЈЕ МЕЂУНАРОДНОГ ЗНАЧАЈА (М10)

М14 Монографска студија/поглавље у књизи М12 или рад у тематском зборнику међународног значаја:

1.* M. Gilic, M. Petrovic, B. Hadzic, M. Romcevic, **J. Trajic**, N. Romcevic, Z. Lazarevic,
"*Structural Properties of Cu-Se-CuSe$_2$ Thin Films*",
W. E. Lee et al. (eds.), Proceedings of the IV Advanced Ceramics and Applications Conference, Springer Atlantis Press (2017) 235-256.

2.* M. Gilic, M. Petrovic, B. Hadzic, Z. Lazarevic, M. Romcevic, **J. Trajic**, N. Romcevic,
"*Optical Properties of Plastically Deformed Copper: Ellipsometry and Raman Study*",
W. E. Lee et al. (eds.), Proceedings of the III Advanced Ceramics and Applications Conference, Springer Atlantis Press (2016) 173-182.

3.* M. Petrovic, **J. Trajic**, M. Gilic, M. Romcevic, B. Hadzic, Z. Lazarevic, D. Stojanovic,
"*Optical Properties and Electron–Phonon Interactions of CdTe$_{1-X}$Se$_x$(In) Single Crystal*",
W. E. Lee et al. (eds.), Proceedings of the III Advanced Ceramics and Applications Conference, Springer Atlantis Press (2016) 183-191.

4.* B. Hadžić, N. Romčević, **J. Trajić**, R. Kostić, G. Stanišić, D. Timotijević
"*Vibrational Spectroscopy of SOP Modes in ZnO Doped with CoO, MnO and Fe$_2$O$_3$*",
W. E. Lee et al. (eds.),Proceedings of the III Advanced Ceramics and Applications Conference, Springer International Publishing AG, Part of Springer Science+Business, Book 2016, ISBN: 978-94-6239-156-7 (Print) 978-94-6239-157-4 (Online), Pages 159-172

6.2. РАДОВИ ОБЈАВЉЕНИ У НАУЧНИМ ЧАСОПИСИМА МЕЂУНАРОДНОГ ЗНАЧАЈА (М 20)

М 21а Рад у међународном часопису изузетних вредности

1.* M. Romcevic, N. Romcevic, **J. Trajic**, L. Kilanski, W. Dobrowolski, I. V. Fedorchenko, S. F. Marenkin
Defects in Cd$_{1-x}$Mn$_x$GeAs$_2$ lattice
Journal of Alloys and Compounds 688 56-61 (2016).

2. **J. Trajić**, R. Kostić, N. Romčević, M. Romčević, M. Mitrić, V. Lazović, P. Balaž, D. Stojanović
Raman spectroscopy of ZnS quantum dots
Journal of Alloys and Compounds 637, 401-406 (2015).

3. N. Romcevic, M. Romcevic, W.D. Dobrowolski, L. Kilanski, M. Petrovic, **J. Trajic**, B. Hadzic, Z. Lazarevic, M. Gilic, J.L. Ristic-Djurovic, N. Paunovic, A. Reszka, B.J. Kowalski, I.V. Fedorchenko, S.F. Marenkin
Far-infrared spectroscopy of $Zn_{1-x}Mn_xGeAs_2$ single crystals: Plasma damping influence on plasmon - Phonon interaction
Journal of Alloys and Compounds 649, 375-379 (2015),

4. **J. Trajić**, N. Romčević, M. Romčević, D. Stojanović, L.I. Ryabova, D.R. Khokhlov
Galvanomagnetic and optical properties of chromium doped PbTe
Journal of Alloys and Compounds 602, 300-305 (2014),

5. M. Gilić, N. Romčević, M. Romčević, D. Stojanović, R. Kostić, **J. Trajić**, W.D. Dobrowolski, G. Karczewski, R. Galazka
Optical properties of CdTe/ZnTe self-assembled quantum dots: Raman and photoluminescence spectroscopy
Journal of Alloys and Compounds 579, 330-335 (2013),

6. M. Romčević, N. Romčević, W. Dobrowolski, L. Kalinski, **J. Trajić**, D.V. Timotijević, E. Dynowska, I.V. Fedorchenko, S.F. Marenkin
Optical properties and plasmon-Two different phonons coupling in $ZnGeAs_2+Mn$
Journal of Alloys and Compounds 548, 33-37 (2013),

7. B. Hadžić, N. Romčević, M. Romčević, I. Kuryliszyn-Kudelska, W. Dobrowolski, **J. Trajić**, D. Timotijević, U. Narkiewicz, D. Sibera
Surface optical phonons in ZnO(Co) nanoparticles: Raman study
Journal of Alloys and compounds 540, 49-56 (2012),

8. **J. Trajić**, N. Romčević, M. Romčević, D. Stojanovic, R. Rudolf, T.A. Kuznetsova and D.R. Khokhlov
Far − infrared study of impurity local modes in Co − doped PbTe
Journal of Alloys and Compounds, 493, 41− 46 (2010),

M 21 Радови у врхунским међународним часописима

1.* B. Hadzic, B. Matovic, M. Randjelovic, R. Kostic, M. Romcevic, **J. Trajic**, N. Paunovic, N. Romcevic
Phonons investigation of ZnO@ZnS core- shell nanostructures with active layer
Journal of Raman Spectroscopy 52, 616-625 (2021),

2.* G. Krizan, M. Gilic, J.L. Ristic-Djurovic, **J. Trajic**, M. Romcevic, J. Krizan, B. Hadzic, B. Vasic, N. Romcevic,
Raman spectroscopy and electron-phonon coupling in Eu^{3+} doped $Gd_2Zr_2O_7$ nanopowders
Optical Materials 73, 541-544 (2017),

3.* **J. Trajić**, M. Romčević, N. Romčević, B. Babić, B. Matović, P. Balaž
Far-infrared spectra of mesoporous ZnS nanoparticles
Optical Materials 57, 225-230 (2016),

4. M. Gilić, **J. Trajić**, N. Romčević, M. Romčević, D.V. Timotijević, G. Stanišić, I.S. Yahia
Optical properties of CdS thin films
Optical Materials 35, 1112-1117 (2013),

5. N. Romčević, M. Romčević, R. Kostić, D. Stojanović, A. Milutinović, **J. Trajić**, G. Karczewski, R. Galazka,
Photoluminescence Spectroscopy of CdTe/ZnTe Self – Assembled Quantum Dots,
International Journal of Photoenergy ID 358790 4 pages (2009),

6. N. Romčević, **J. Trajić**, T.A. Kuznetsova, M. Romčević, B. Hadžić, D.R. Khokhlov,
Far – infrared study of impurity local modes in Ni – doped PbTe
Journal of Alloys and Compounds, 442, 324 − 327 (2007),

7. **J. Trajić**, N. Romčević, M. Romčević, V. Nikiforov
*Plasmon – phonon and plasmon – two different phonon interaction in $Pb_{1−x}Mn_xTe$
mixed crystals*
Materials Research Bulletin, 42, 2192 − 2201 (2007),

8. N. Romčević, A.J. Nadolny, M. Romčević, T. Story, B Taliashvili, A. Milutinović, **J. Trajić**, E. Lusakowska, D. Vasiljevic–Radovic, V Domukhovski, V. Osinniy, B. Hadžić and P. Dziawa
*Far–infrared phonon spectroscopy of $Pb_{1−x}Mn_xTe$ layers grown by molecular beam
epitaxy*
Journal of Alloys and Compounds, 442, 324 − 327 (2007),

9. N. Romčević, A. Golubović, M. Romčević, **J. Trajić**, S. Nikolić, S. Đurić, V.N. Nikiforov,
Raman spectra of $Pb_{1−x}Mn_xTe$ alloys
Journal of Alloys and Compounds 402, 36 − 41 (2005),

10. N. Romčević, **J. Trajić**, M. Romčević, A. Golubović, S. Nikolić, V.N. Nikiforov, *Raman
spectroscopy of $PbTe_{1−x}S_x$ alloys*
Journal of Alloys and Compounds 387, 24 − 31 (2005),

11. **J. Trajić**, M. Romčević, N. Romčević, S. Nikolić, A. Golubović, S. Durić, V.N. Nikiforov,
Optical properties of PbTe:Mn
Journal of Alloys and Compounds 365, 89 − 93 (2004).

М 22 Радови у истакнутим међународним часописима

1.* M. Romcevic, N. Paunovic, U. Ralevic, J. Pesic, J. Mitric, **J. Trajic**, L. Kilanski, W. Dobrowolski, I. V. Fedorchenko, S. Fedorovich Marenkin, N. Romcevic
Plasmon – Phonon interaction in ZnSnSb2 + Mn semiconductors
Infrared Physics and Technology 108, 103345 (2020),

2.* M. Curcic, B. Hadzic, M. Gilic, V. Radojevic, A. Bjelajac, I. Radovic, D. Timotijevic, M. Romcevic, **J. Trajic**, N. Romcevic
Surface optical phonon (SOP) mode in ZnS/Poly (methylmethacrylate) nanocomposites
Physica E: Low-dimensional Systems and Nanostructures115, 113708 (2020),

3.* **J. Trajic**, N. Paunovic, M. Romcevic, V.E. Slynko, Jasna L. Ristic-Djurovic, W.D. Dobrowolski, N. Romcevic
Far infrared spectra of Si doped PbTe single crystals
Optical Materials 91, 195-198 (2019),

4.* J. Mitric, N. Paunovic, M. Mitric, B. Vasic, U. Ralevic, **J. Trajic**, M. Romcevic, W.D. Dobrowolski, I.S. Yahia, N. Romcevic
Surface optical phonon – Plasmon interaction in nanodimensional CdTe thin Films
Physica E: Low-dimensional Systems and Nanostructures 104, 64-70 (2018),

5.* **J. Trajic**, M. Romcevic, N. Paunovic, M. Curcic, P. Balaz, N. Romcevic
Far-infrared study of the mechanochemically synthesized Cu_2FeSnS_4 (stannite) nanocrystals
Infrared Physics & Technology 90, 66–69 (2018),

6.* J. Mitric, J. Krizan, **J. Trajic**, G. Krizan, M. Romcevic, N. Paunovic, B. Vasic, N. Romcevic
Structural properties of Eu^{3+} doped $Gd_2Zr_2O_7$ nanopowders: Far-infrared spectroscopy
Optical Materials 75, 662-665 (2018),

7.* **J. Trajic**, M. Romcevic, M. Petrovic, M. Gilic, P. Balaz, A. Zorkovska, N. Romcevic
Optical properties of the mechanochemically synthesized Cu_2FeSnS_4 (stannite) nanocrystals: Raman study
Optical Materials 75, 314-318 (2018),

8.* M. Petrović, M. Gilić, J. Ćirković, M. Romčević, N. Romčević, **J. Trajić**, I. Yahia
Optical Properties of CuSe Thin Films – Band Gap Determination
Science of Sintering, 49, 167-174 (2017),

9.* **J. Trajić**, M.S. Rabasović, S. Savić-Šević, D. Šević, B. Babić, M. Romčević, J.L. Ristić-Djurović, N. Paunović, J. Križan, N. Romčević
Far-infrared spectra of dysprosium doped yttrium aluminum garnet Nanopowder
Infrared Physics & Technology 77, 226–229 (2016),

10.* M. Gilić, M. Petrović, R. Kostić, D. Stojanović, T. Barudžija, M. Mitrić, N. Romčević, U. Ralević, **J. Trajić**, M. Romčević, I.S. Yahia
Structural and optical properties of $CuSe_2$ nanocrystals formed in thin solid Cu–Se film
Infrared Physics & Technology 76, 276–284 (2016),

11. **J. Trajić**, M. Gilić, N. Romčević, M. Romčević, G. Stanišić, B. Hadžić, M. Petrović, Y.S. Yahia
Raman spectroscopy of optical properties in CdS thin films
Science of Sintering, 47 145-152 (2015),

12. M. Petrović, N. Romčević, **J. Trajić**, W.D. dobrowolski, M. Romčević, B. Hadžić, M. Gilić, A. Mycielski
Far-infrared spectroscopy of $CdT_{1-x}Se_x(In)$: Phonon properties
Infrared Physics and Technology 67, 323-326 (2014),

13. **J. Trajić**, M. Gilić, N. Romčević, M. Romčević, G. Stanišić, Z. Lazarević, D. Joksimović, I.S. Yahia
Far-infrared investigations of the surface modes in CdS thin film
Physica Scripta T162, 014031 (4pp) (2014),

14. M. Petrović, N. Romčević, M. Romčević, G. Stanišić, D. Vasiljević-Radović, **J. Trajić**, Z. Lazarević, S. Kostić
Spectroscopy characterization of MnSe nanoclasters randomly distributed in HgMnTe single crystal
Journal of Crystal Growth 338, 75-79 (2012),

15. D. Stojanović, N. Romčević, **J. Trajić**, B. Hadžić, M. Romčević, D.R. Khokhlov,
Investigation of Photoconductivity in n – type gallium doped PbTe
Science of Sintering, 39, 169 – 175 (2007),

16. **J.M. Miljković**, N. Romčević, Z.V. Popović, W. König, and V.N. Nikiforov
Transport and optical properties of PbTe$_{1-x}$S$_x$ (x=0.02 and x=0.05) mixed crystals
phys. stat. sol. (b) 193, 43-51 (1996).

M23 Радови у међународним часописима

1.* B. Babic, B.Hadzic, I. Kuryliszyn-Kudelska, N. Paunovic, B. Vasic, W.D. Dobrowolski, M. Romcevic, **J.Trajic**, N. Romcevic
Far-infrared spectroscopy of laser power modified MnO nanoparticles
Optoelectronics and Advanced Materials-Rapid Communications, 13, 376-379 (2019),

2.* M.Gilic, R. Kostic, D. Stojanovic, M. Romcevic, B. Hadzic, M. Petrovic, U. Ralevic, Z. Lazarevic, **J. Trajic**, J. Ristic-Djurovic, J. Cirkovic, N. Romcevic
Photoluminescence spectroscopy of CdSe nanoparticles embedded in transparent glass
Optical and Quantum Electronics 50:288 (2018),

3.* G.S.I. Abudagel, S. Petričević, P. Mihailović, A. Kovačević, J.L. Ristić-Djurović, M. Lekić, M. Romčević, S. Ćirković, **J. Trajić**, N. Romčević,
Improvement of magneto-optical quality of high purity Bi12GeO20 single crystal induced by femtosecond pulsed laser irradiation
Optoelectronics and Advanced Materials-Rapid Communications, 11, 477-481 (2017),

4.* P. Baláž, M. Baláž, A. Zorkovská, I. Škorvánek, Z. Bujnáková, **J. Trajic**
Kinetics of Solid-State Synthesis of Quaternary Cu$_2$FeSnS$_4$ (Stannite) Nanocrystals for Solar Energy Applications
Acta Physica Polonica A 131, 1153-1155 (2017),

5.* M. Petrović, M. Romčević, R. Kostić, N. Romčević, W. D. Dobrowolski, **M. Gilić**. B. Hadžić, J. Trajić, D. Stojanović, Z. Lazarević
Optical properties of Cd$_{1-x}$Mn$_x$S nanoparticles: off-resonance Raman spectroscopy
Optoelectronics and advanced materials-rapid communications 10, 177-179 (2016),

6.* H.I. Elswie, S.Kostić, V. Radojević, N. Romčević, B. Hadžić, J. Trajić, Z. Lazarević
Growth, characterization and optical quality of calcium fluoride single crystals grown by the Bridgman method,
Optoelectronics and Advanced Materials-Rapid 10 (7-8) 522-525 (2016)

7. B. Hadžić, N. Romčević, M. Romčević, I. Kuryliszyn-Kudelska, W. Dobrowolski, M. Gilić, M. Petrović-Damjanović, **J. Trajić**, U. Narkiewicz, D. Sibera
Raman study of surface optical phonons in ZnO(Co) nanoparticles prepared by calcinations method
Optoelectronics and Advanced Materials-Rapid Communications 16 (5-6) 508-512 (2014),

8. **J. Trajić**, N. Romčević, M. Romčević, Z. Lazarević, T.A. Kuznetsova, D.R. Khokhlov
Plasmon – ionized impurity – phonon interaction in PbTe doped with Ni
Optoelectronics and Advanced Materials-Rapid Communications 7 (7-8),

536-540 (2013),

9. Z. Ž. Lazarević, S. Kostić, V. Radojević, M.J. Romčević, B. Hadžić, **J. Trajić**, N.Ž. Romčević
   Spectroscopy study of $Bi_{12}GeO_{20}$ single crystals
   Optoelectronics and Advanced Materials - Rapid Communications 7 (1-2), 58-61 (2013),

10. **J. Trajić**, N. Romčević, M. Gilić, M. Petrović Damjanović, M. Romčević, V.N. Nikiforov
    Optical properties of $PbTe_{0.95}S_{0.05}$ single crystal at different temperatures:
    far-infrared study
    Optoelectronics and Advanced Materials - Rapid Communications 6 (5-6), 543-546 (2012)

11. N. Romčević, R. Rudolf. J. **Trajić**, M. Romčević, B. Hadžić, D. Vasiljević-Radović, I. Anžel
    Optical properties of plastically deformed copper: an ellipsometric study
    Materials and technology 45 (5) 463-465 (2011),

12. Z. Lazarević, S. Kostić, M. Romčević, **J. Trajić**, B. Hadžić, D. Stojanović and N. Romčević
    Study of $Bi_{12}SiO_{20}$ single crystals obtained by Czocharlski method
    Optoelectronics and Advanced Materials - Rapid Communications 5 (2), 150-152 (2011),

13. **J. Trajić**, R. Rudolf, I. Anžel, M. Romčević, N. Lazarević, M. Mirić, Z. Lazarević, B. Hadžić, and N. Romčević
    Optical properties of plastically deformed copper
    Acta Physica Polonica A 117 (5) 791 – 793 (2010),

14. N. Romčević, **J. Trajić**, M. Romčević, D. Stojanović, T.A. Kuznetsova, D.R. Khokhlov, W.D. Dobrowolski
    Optical and magnetic properties of PbTe(Co)
    Optoelectronics and Advanced Materials – Rapid Communications 4 (4), 470 – 475 (2010),

15. Z. Lazarević, N. Romčević, M. Romčević, **J. Trajić**, M. Vijatović, J. Bobić, B. Stojanovic
    Infrared and Raman Spectroscopy Study of Antimony Doped Barium Titanate Prepared from Organometallic Complex
    International Journal of Modern Physics B, 24, 676 – 681 (2010),

16. M. Mirić, R. Rebeka, I. Anzel, B. Hadžić, M. Romčević, **J. Trajić**, N. Romčević,
    Ellipsometric Measurements of Plastically Deformed Copper
    Acta Physica Polonica A, 116, 715 – 717 (2009),

17. N. Romčević, **J Trajić**, B. Hadžić, M. Romčević, D. Stojanović, Z. Lazarević, T. Kuznetsova, D. Khokhlov, R. Rudolf, I. Anžel
    Raman spectroscopy of multiphonon emission process in Ni – doped PbTe
    Acta Physica Polonica A 116, 91 – 92 (2009),

18. N. Romčević, **J Trajić**, M. Romčević, D. Stojanović, T. A. Kuznetsova, D.R Khokhlov, W.D Dobrowolski, R. Rudolf, I. Anzel
    Optical and magnetic properties of PbTe(Ni)
    Acta Physica Polonica A 115 (4), 765 – 767 (2009),

19. **J. Trajić**, N. Romčević, M. Romčević, V.N. Nikiforov,
    Plasmon – two phonon interaction in PbMnTe and PbTeS alloys
    Journal of the Serbian Chemical Society, 73 (3), 369 – 376 (2008),

20. **J. Trajić**, A. Golubović, M. Romčević, N. Romčević, S. Nikolić, V.N. Nikiforov,
Pb$_{1-x}$Mn$_x$Te and PbTe$_{1-x}$S$_x$ compounds and their optical properties
Journal of the Serbian Chemical Society, 72 (1), 55 − 62 (2007),

21. D. Stojanović**, J Trajić**, B. Hadžić, M. Romčević, I. Ivanchik, D. R. Khokhlov,
N. Romčević
Far–Infrared Study of DX–Like Centers in Pb$_{0.95}$Mn$_{0.05}$Te(Ga)
Acta Physica Polonica A, Vol.112, no 5, 959 − 962 (2007),

22. A. Golubović, S. Nikolić, **J. Trajić**, S. Đurić, N. Romčević, M. Romčević, A. J. Nadolny, B. Taliashvili, V. N. Nikiforov
Structural Properties of Pb$_{1-x}$Mn$_x$Te Compounds
Materials Science Forum 453 − 454, 99 − 102 (2004).

6.3. ЗБОРНИЦИ СА МЕЂУНАРОДНИХ НАУЧНИХ СКУПОВА (М 30)

М 33 Саопштење са међународног скупа штампано у целини

1.* R. Kostić, D.Stojanović, **J.Trajić**, P.Balaž
Off-Resonant Raman Spectroscopy of ZnS Quantum Dots
In: Lee B., Gadow R., Mitic V. (eds) Proceedings of the IV Advanced Ceramics and Applications Conference. Atlantis Press, Paris. (2017),

2. N. Romčević**, J. Trajić**, M. Romčević, and V.N. Nikoforov,
Plasmon - two phonon interaction in PbTe$_{0.95}$S$_{0.05}$ alloy
11 th International Conference on Phonon Scattering in Condensed Matter, St Petersburg, Russia, July 25-30, 2004., phys, stat. sol. (c) 1 (11), 2832-2835 (2004).

М 34 Саопштење са међународног скупа штампано у изводу

1.* M. Ćurčić, M. Gilić, B. Hadžić, **J. Trajić**, Z. Lazarević, M. Romčević, V. Radojević, A. Bjelajac, I. Radovic, P. Balaž, N. Romčević
Preparation and optical properties of ZnS/Poly(methyl methacrylate) nanocomposite
The seventh Serbian Ceramic Society Conference »Advanced Ceramics and Application«, September 17-19, 2018, Serbian Academy of Sciences and Arts, Knez Mihailova 35, Belgrade, Serbia, Book of abstracts P17,

2.* **J. Trajic**, M. Romcevic, M. Petrovic, M. Gilic, N. Paunovic, P. Balaz, A. Zorkovska, N. Romcevic
Optical properties of the mechanochemically synthesized Cu$_2$FeSnS$_4$ (stannite) nanocrystals
The Sixth Serbian Ceramic Society Conference »Advanced Ceramics and Application«, September 18-20, 2017, Serbian Academy of Sciences and Arts, Knez Mihailova 35, Belgrade, Serbia, Book of abstracts P21,

3.* M. Gilić, R. Kostić, D. Stojanović, M. Romčević, B. Hadžić, Z. Lazarević, **J. Trajić**, J. Ristić-Đurović, N. Romčević,
Photoluminescence spectroscopy of CdSe nanoparticles embeded in transparent glass
PHOTONICA2017 6th INTERNATIONAL SCHOOL AND CONFERENCE ON PHOTONICS,
28. Aug. − 1. Sep. 2017, Belgrade, Serbia, Book of abstracts O.M.7 − pp. 86,

4. R. Kostić, D. Stojanović, **J. Trajić**, P. Balaž
   Off-resonant Raman spectroscopy of ZnS quantum dots
   Serbian Ceramic Society Conference "Advanced Ceramics and Application IV", New Frontiers
   in Multifunctional Material Science and Processing, September 21-23, 2015 Serban Academy of
   Science and Arts, Belgrade, Program and the Book of Abstracts, str. 71,

5. D. Stojanović, **J.Trajić**, R. Kostić, N. Romčević, M. Romčević, M. Mitrić, P. Balaž
   Raman spectroscopy of ZnS quantum dots obtained by mechanochemical synthesis
   Sustainable Materials Science and Technology, an International Conference, Paris, 15-17 July
   2015, General scientific program, p. 18,

6. M. Petrović, M. Gilić, B. Hadžić, M. Romčević, N. Romčević, **J. Trajić**, Z. Lazarević
   Structural and optical properties of chemically deposited copper selenide thin films
   Serbian Ceramic Society Conference "Advanced Ceramics and Application IV", New Frontiers
   in Multifunctional Material Science and Processing, September 21-23, 2015 Serban Academy of
   Science and Arts, Belgrade, Program and the Book of Abstracts , str. 79,

7. M. Gilic, N. Romcevic, M. Romcevic, D. Stojanovic, R. Kostic, **J. Trajic**, W.D. Dobrowolski,
   G. Karczewski, R. Galazka
   Optical Properties of CdTe/ZnTe Self-Assembled Quantum Dots
   43rd Jaszowiec 2014, International School & Conference on the Physics of
   Semiconductors, Visla, Poland, June 7th-12th, ThP1, 2007,

8. **J. Trajić**, M. Romčević, N. Romčević, R. Kostić, M.I. Čomor
   Phonon Properties of $Cd_{1-x}Mn_xS$ Nanoparticles
   2011 Spring Meeting Nice, France 9-13 May SYMPOSIUM C Size dependent properties of
   nanomaterials C-15 (2011),

9. N. Romčević, R. Rudolf, **J. Trajić**, M. Romčević, D. Stojanović, M. Mirić, Z. Lazarević, B.
   Hadžić, I. Anžel
   Optical properties of plastically deformed copper
   18th Conference on materials and technology, Portorož, Slovenia 15-17.11.2010.
   Programe and Book of Abstracts 98 (2010),

10. **J. Trajic** , N. Romcevic , M. Romcevic , D. Stojanovic , T. A. Kuznetsova, D. R. Khokhlov
    Plasmon-ionised impurity-interaction in Co and Ni doped PbTe
    YUCOMAT 2010 Herceg Novi, September 6- 10, 2010 Book of Abstract 115 (2010),

11. N. Romčević, M. Romčević, **J. Trajić**, D.Stojanović, Z.Lazarević, B. Hadžić,
    A. Mycielski
    Far – infrared and Raman Spectroscopy of $CdTe_{0.97}Se_{0.03}(In)$
    E –MRS 2008 FALL MEETENG Warsaw 15th – 19th September, Book of Abstract
    67 (2009),

12. R. Rudolf, I. Anžel, N. Romčević, M. Mirić, B. Hadžić, M. Romčević, **J. Trajić**,
    Optical properties of plastically deformed copper
    Eleventh annual conference YUCOMAT 2009 Herceg Novi, August 31 – September
    4, 2009 Book of Abstract 45, (2009),

13. N. Romčević, **J Trajić**, M. Romčević, D. Stojanović, B. Hadžić, T. Kuznetsova,
    D. Khokhlov,W. D. Dobrowolski
    Optical and magnetic properties of PbTe(Co)

Eleventh annual conference YUCOMAT 2009 Herceg Novi, August 31 – September 4, 2009 Book of Abstract 158 (2009),

14. N. Romčević, B. Hadžić, **J Trajić**, T. Kuznetsova, M. Romčević, Z. Lazarević, D. Stojanović, D. Khokhlov
Raman spectroscopy of multiphonon emission process in Ni – doped PbTe
E – MRS 2008 FALL MEETENG Warsaw 15th –19th September, Book of Abstract 36 (2008),

15. N. Romčević, **J Trajić**, M. Romčević, D. Stojanović, T. A. Kuznetsova and D.R. Khokhlov, W. D Dobrowolski
Optical and magnetic properties of PbTe(In)
Tenth Annual Conference "YUCOMAT 2008 ", September 8 – 12, 2008, Herceg Novi, Book of Abstracts, 107 (2008),

16. N. Romčević, M. Romčević, **J. Trajić**, W. Dobrowolski, T.A. Kuznetsova, D.R. Khokhlov
Optical and magnetic properties of PbTe(Ni) single crystals
Ninth Yugoslav Materials Research Society Conference YUCOMAT 2007, Herceg Novi, Montenegro, September 10 – 14, 2007, Programe and Book of Abstracts 107 (2007),

17. D. Stojanović**, J. Trajić**, B. Hadžić, M. Romčević, I. Ivanchik, D. R. Khokhlov, N. Romčević
Far – Infrared Study of DX – Like Centers in $Pb_{0.95}Mn_{0.05}Te(Ga)$
Proceedings of the International School and Conference on Optics and Optical Materials, ISCOM07, ABSTRACTS OF PLENARY AND INVITED LECTURES AND CONTRIBUTED PAPERS, Serbia, Belgrade, September, 3 – 7 (2007),

18. **J. Trajić**, N. Romčević, M. Romčević, V.N. Nikiforov
Plasmon – two phonon interaction in $Pb_{1-x}Mn_xTe$ and $PbTe_{1-x}S_x$ alloys
Eight Yugoslav Materials Research Society Conference YUCOMAT 2006, Herceg Novi, Montenegro, September 4 – 8. 2006, Programe and Book of Abstracts 94 (2006),

19. N. Romčević, **J. Trajić**, T.A. Kuznetsova, M. Romčević, B. Hadžić, and D.R. Khokhlov
Far –infrared study of impurity local modes in Ni – doped PbTe
15th International Conference on Solid Compounds of Transition Elements, 15 –20 July 2006, Krakow, Poland, Book of Abstracts 196 (2006),

20. N. Romčević, **J. Trajić**, M. Romčević, V.N Nikiforov
Plasmon – two phonon interaction in $Pb_{1-x}Mn_xTe$ and $PbTe_{1-x}S_x$ alloys
11 th International Conference on Phonon Scattering in Condensed Matter, St. Petersburg, Russia, July 25 – 30, 2004, Book of Abstracts pp162 (2004),

22. A. Golubović, S. Nikolić, M. Romčević, **J. Trajić**, N. Romčević, and V.N. Nikiforov
$Pb_{1-x}Mn_xTe$ and $PbTe_{1-x}S_x$ Alloys: Structural, Transpor and Optical Properties
4th International Conference of the Chemical Societies of the South –East European Countries on Chemical Sciences in Changing Times: Visions, Challenges and Solutions, Belgrade, Serbia and Montenegro July 18 – 21, 2004. Book of Abstracts Vol II A – P 45,

23. **J. Trajić**, V.N. Nikiforov, N. Romčević, M. Romčević and A.N. Vasil`ev
Off centers in $PbTe_{0.95}S_{0.05}$ single crystal: ultrasonic study

YUCOMAT 2003: Fifth Yugoslav Materials Research Society Conference, Herceg Novi, Serbia and Montenegro, september 15 – 19, 2003, Programme and the book of abstracts, 1, 93 (2003),

24. N. Romčević, **J. Trajić**, M. Romčević, A. Milutinović, A.J. Nadolny, B. Taliashvili and V.N. Nikiforov
Far – infrared spectroscopy of $Pb_{1-x}Mn_xTe$ alloys
YUCOMAT 2003: Fifth Yugoslav Materials Research Society Conference, Herceg Novi, Serbia and Montenegro, september 15 – 19, 2003, Programme and the book of abstracts, 1, 29 (2003),

25. N. Romčević, M. Romčević, D. Stojanović, **J. Trajić**, V. N. Nikiforov
Local modes of transition metal ions (Mn, Co, Ni) in lead – telluride
BPU – 5: Fifth General Conference of the Balkan Physical Union, August 25 – 29, 2003, Vrnjačka Banja, Serbia and Montenegro, Book of Abstracts, SP06 – 105,

26. **J. Trajić**, V.N. Nikiforov, N. Romčević, M. Romčević and A.N. Vasil`ev
Ultrasonic study of $PbTe_{1-x}S_x$,
BPU5: Fifth General Conference of the Balkan Physical Union, August 25 – 29, Vrnjačka Banja, Serbia and Montenegro, Book of Abstracts 1, 165 (2003).

6.5. ЧАСОПИСИ НАЦИОНАЛНОГ ЗНАЧАЈА (М 50)

М 51 Рад у водећем часопису националног значаја

1. D.P. Stojanović, R.S. Kostić, **J.M. Trajić**
Polarizacioni efekti u sfernim kvantnim nanočesticama
TEHNIKA-NOVI MATERIJALI 24, 5 (2015),

2. **J.M. Miljković**, N. Romčević, and Z.V. Popović
Transport proporties of $PbTe_{1-x}S_x$ alloys
Zbornik matice srpske za prirodne nauke 85, 155 – 158 (1993).

6.6. ЗБОРНИЦИ СКУПОВА НАЦИОНАЛНОГ ЗНАЧАЈА (М 60)

М 63 Саопштење са скупа националног значаја штампано у целини

1. N. Romčević, **J. Trajić**, M. Romčević, T.A. Kuznetsova, D.R. Khokhlov
Primesni lokalni modovi u PbTe dopiranom Ni
4 – 8. jun 2007, Herceg Novi – Igalo, Zbornik radova 51. Konferencije za ETRAN, MO1.3 (2007),

2. N. Romčević, R. Kostić, M. Romčević, **J. Trajić**
Ramanova spektroskopija $Cd_{1-x}Mn_xS$ nanočestica
6 – 8. jun 2006 Beograd, Zbornik radova 50. Konferencije za ETRAN, 4, (2006),

3. **J. Trajić**, N. Romčević, M. Romčević, V.N. Nikiforov
Plazmon – dvo fonon interakcija kod $PbTe_{0,95}S_{0,05}$ i $Pb_{0,98}Mn_{0,02}Te$ legura
5 –10. jun 2005 Budva, Zbornik radova 49. Konferencije za ETRAN, 4, 105 – 108 (2005),

4. **J. Trajić**, N. Romčević, M. Romčević

Fazni prelaz kod PbTe$_{0,95}$S$_{0.05}$ monokristala: ultrazvučna merenja
7–10. jun 2004 Čačak, Zbornik radova 48. konferencije za ETRAN, 4, 91 – 92 (2004),

5. **J. Trajić**, M. Romčević, N. Romčević, S. Nikolić, V.N. Nikiforov
   Optička svojstva PbTe:Mn
   8–13. jun 2003 Heceg Novi, Zbornik radova 47.konferencije za ETRAN, 4, 222 – 224 (2003),

6. M. Romčević, N. Romčević**, J. Trajić**
   Optički fononi kod Hg$_{1-x}$Mn$_x$Te
   8 – 13. jun 2003 Heceg Novi, Zbornik radova 47. konferencije za ETRAN, 4, 219 – 221 (2003),

7. N. Romčević, D.R. Khokhlov, M. Romčević, D. Stojanović, S.N. Chesnokov, **J. Trajić**, V. Nikorich
   Lead telluride based alloys doped with III group elements – new effects and aplication,
   Primenjena Fizika u Srbiji – PFS, Zbornik radova i apstrakata predavanja po pozivu, 27 – 29 maja 2002. Knjiga 2/1, pp. 113 – 116 (2002),

8. **J. M. Miljković**, N. Romčević, and Z.V. Popović
   Far–infrared study of PbTe$_{1-x}$S$_x$ (x=0.02 and x=0.05) alloys
   4 – 7. jun 1996. Budva: XL Konferencija ETRAN–a, 4, 30 – 32 (1996).

CrossMark

Defects in $Cd_{1-x}Mn_xGeAs_2$ lattice

Maja Romcevic [a], Nebojsa Romcevic [a, *], Jelena Trajic [a], Lukasz Kilanski [b],
Witold Dobrowolski [b], Irina Valentinovna Fedorchenko [c], Sergei Fedorovich Marenkin [c]

[a] *Institute of Physics, University of Belgrade, 11080 Belgrade, Serbia*
[b] *Institute of Physics, Polish Academy of Sciences, Al. Lotnikow 32/46, 02-668 Warsaw, Poland*
[c] *Kurnakov Institute of General and Inorganic Chemistry RAS, 119991 Mocow, Russia*

ABSTRACT

$CdGeAs_2$ is a promising material for optical applications. It has the wide transparency range between 2.3 and 18 μm except harmful absorption region at 5.5 μm. Its presence is related to the crystal lattice quality. The measurements of Raman and far infrared reflectivity spectra of the series of $Cd_{1-x}Mn_xGeAs_2$ samples ($0 \leq x \leq 0.037$) were carried out in spectral range from 60 to 400 cm^{-1}, at room temperature. Beside all expected optical modes three defect modes are registered at about 125, 170 and 235 cm^{-1}. Their intensities are related to tetragonal distortion of lattice (Δ) so we connected them with lattice defects Ge_{As}, usually formed in this material, and $CdAs_2$ and Cd_3As_2 clusters whose characteristic frequencies match these values. Antisite defects Ge_{As} are connected to energy level at about 200 meV and to absorption at 5.5 μm. Based on obtained results we can conclude that doping with small amount of manganese ($x = 0.004$) results in slight deformation of $CdGeAs_2$ crystal lattice and consequently considerably reducing the formation of antisite defects Ge_{As}.

© 2016 Elsevier B.V. All rights reserved.

1. Introduction

It has been shown that $II-IV-V_2$ semiconductors with chalcopyrite type lattice are very suitable for optoelectronics, quantum electronics and spintronics applications. These materials represent a crystallochemical and electronic analog of the III-V zincblende semiconductors. Their chalcopyrite crystal lattice is formed by doubling the unit cell of zinc-blende structure along the z-axis.

$CdGeAs_2$ is a very good candidate for nonlinear optical applications. It has the wide transparency range (2.3–18 μm) and significant birefringence ($n_e - n_o = 0.09$) [1–3] which make this material suitable for frequency conversion applications in the infrared range. But undesirable and harmful optical absorption was registered in 5.5 μm region. It was established that its appearance is related to growth conditions [4,5]. Also, this absorption is attributed to the intraband transition and connected to the antisite defects (Ge_{As}) [6,7]. Correlation between absorption at 5.5 μm and hole concentration was established too [8].

Such chalcopyrite materials doped with manganese exhibit room temperature ferromagnetism [9]. In $CdGeAs_2$ heavily doped with Mn this is due to formation of MnAs clusters [10]. But, by limiting content of manganese (x) to 0.037 the homogeneous distribution of Mn is provided [10]. Electrical and magnetic properties of the $Cd_{1-x}Mn_xGeAs_2$ samples ($0 \leq x \leq 0.037$) was investigated [10] and it was established that they have excellent crystallographic quality, that Mn ions are distributed randomly, substituting the Cd sites, and an impurity level associated with defect states, with activation energy $E_a = 200$ meV, was registered in energy gap.

In this paper we measured and analyzed optical spectra of the $Cd_{1-x}Mn_xGeAs_2$ samples ($0 \leq x \leq 0.037$) in far infrared region and tried to connect obtained optical properties with crystal structure and to establish influence of added manganese on crystal lattice quality. Connection between antisite defect formation and doping with Mn can be very important for possible applications.

2. Experiments and results

Investigated materials $Cd_{1-x}Mn_xGeAs_2$ were prepared by a vertical Bridgeman method [11]. Initial mixture consisted of stoichiometric ratios of fine $CdAs_2$, Ge and Mn high purity powders. The growth process was carried out in graphitized ampoules where were single-crystal $CdGeAs_2$ seed, under vacuum of 10^{-2} Pa. The growth process was carried out at a temperature of 950 ± 0.5 K. In

---

* Corresponding author. Institute of Physics, Pregrevica 118, 11080 Belgrade, Serbia.

E-mail address: romcevi@ipb.ac.rs (N. Romcevic).

the final stage temperature of the ampoule was gradually decreased (about 5–10 K/s) to the room temperature, in order to obtain more homogeneous crystal [12]. The obtained ingots of $Cd_{1-x}Mn_xGeAs_2$ were cut perpendicular to the growth direction into slices of 1 mm thickness, mechanically polished, chemically cleaned, and etched prior to further characterization.

The chemical composition of the as-grown crystals was measured using the energy dispersive X-ray fluorescence method (EDXRF). Measurements were done at room temperature with the use of the Tracor X-ray Spectrace 5000 EDXRF Spectrometer equipped with Si(Li) detector. The relative uncertainty of this method does not exceed 10%. The EDXRF spectra show that unintended impurity concentration in the alloy is less than 10^{15} cm^{-3}. The EDXRF measurements showed that the amount of Mn, x, changes in our samples from 0 up to 0.037.

The structural properties of our $Cd_{1-x}Mn_xGeAs_2$ samples were studied with the use of the high resolution X-ray diffraction method (HRXRD). We used multipurpose X'Pert PRO MPD, Panalytical diffractometer configured for Bragg-Brentano diffraction geometry, equipped with a strip detector and an incident-beam Johansson monochromator. The Cu $K_{\alpha 1}$ X-ray radiation with wavelength equal to 1.5406 Å was used. This instrument allows obtaining diffraction patterns with an excellent resolution and counting statistics. This analysis confirmed excellent crystalline quality of our samples. Obtained spectra were analyzed by the Rietveld refinement method and it was confirmed that all samples are a single phase materials of tetragonal chalcopyrite-type structure. Also, by this method we obtained the lattice parameters for all samples with different amount of Mn. Obtained results are presented in Table 1 [10,13].

It can be seen that the lattice parameters depend on x, i.e. with the addition of Mn a and c linearly decrease, except for the sample with the lowest quantity of Mn ($x = 0.004$) in which the lattice slightly deformed. The ionic radius of Mn is smaller than that of Cd [14] so the substitution of the Cd ions by the Mn ions in the crystal lattice results in decreasing of lattice parameters a and c [10,13].

Raman experiment was used for the study of structural, optical and electrical properties of the $Cd_{1-x}Mn_xGeAs_2$ samples. Jobin–Yvon T64000 monochromator was used for the measurements. Focus of the 514 nm radiation from Coherent Innova 99 Ar$^+$ laser on the sample was performed using an optical microscope with 100 × objective. The same microscope was used to collect the backscattered radiation. The dispersed scattering light was detected by a charge-coupled device (CCD) detection system. The average power density on the sample was 20 mWmm^{-2}. Raman spectra are measured in spectral range from 65 to 400 cm^{-1} at room temperature.

The additional study of the $Cd_{1-x}Mn_xGeAs_2$ has been made by measuring the far-infrared (FIR) reflection spectra in the spectral range of 70–350 cm^{-1}, at room temperature, using BOMEM DA 8 spectrometer.

Raman spectra of five $Cd_{1-x}Mn_xGeAs_2$ samples with different amount of Mn ($0 \leq x \leq 0.037$), measured at room temperature, are

shown in Fig. 1a. The spectra are shown overlapped for easier detection of changes of the modes intensities, depending on the concentration of manganese.

It is obvious that the spectra are mainly consistent. It is also evident that there are ranges with narrow and clear modes of basic material CdGeAs$_2$, indicated in Fig. 1a [15], as well as areas with wide structures (marked with Def.1,2,3). Spectrum of the sample with the lowest content of Mn ($x = 0.004$) has weakest intensity and stands out from the others. It can be connected to the weak lattice deformation in this sample, i.e. small deviation of parameters a and c (Table 1). Actually, the main difference of this spectrum is that the intensities of the broad structures at about 175 and 235 cm^{-1} are weaker, so the whole spectrum has less intensity.

IR reflection spectra of investigated samples are shown in Fig. 1b. These spectra are also consist of clear modes correspond to crystal CdGeAs$_2$, as it marked in Fig. 1b, and wide areas between them with some weak structures, which probably correspond to defects in these materials.

3. Discussion

The II-IV-V$_2$ class materials are derived from the III-V cubic zinc-blende structure (GaAs), space group T_d^2, by doubling their unite cell in the z direction, wherein one sublattice consists of group V atoms
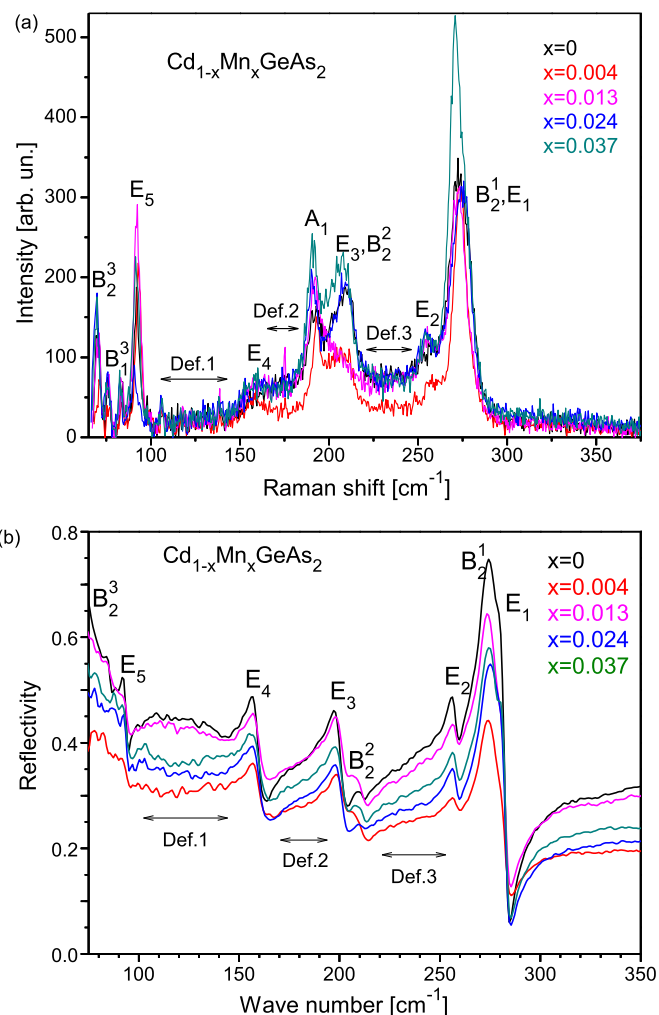
Table 1
The results of the EDXRF and HRXRD analyzes for the $Cd_{1-x}Mn_xGeAs_2$ samples including the chemical composition x, and lattice parameters a and c of a chalcopyrite structure [10].

$x \pm \Delta x$	$a \pm \Delta a$ (Å)	$c \pm \Delta c$ (Å)
0	5.9452 ± 0.0002	11.2153 ± 0.0003
0.004 ± 0.001	5.9425 ± 0.0002	11.2207 ± 0.0006
0.013 ± 0.001	5.9439 ± 0.0002	11.2156 ± 0.0006
0.024 ± 0.002	5.9436 ± 0.0002	11.2116 ± 0.0004
0.037 ± 0.003	5.9417 ± 0.0003	11.2082 ± 0.0006

Fig. 1. Raman spectra (a) and Far-infrared reflectivity spectra (b) of $Cd_{1-x}Mn_xGeAs_2$, at room temperature.

and the other one of equal amounts of groups II and IV atoms in a regular fashion. The $CdGeAs_2$ is ternary chalcopyrite semi-conductors and crystallize in the D_{2d}^{12} space group. There are eight atoms in the primitive unit cell. This means there are 24 dispersion curves, i.e. 24 normal vibrational modes at Γ point. They consist of 15 nonzero optical frequencies and 2 acoustic components.

$$\Gamma = A_1 + 2A_2 + 3B_1 + 3B_2 + 6E + (B_2 + E)_{aco}$$

All the optical modes, except A_2, are Raman active. But only B_2 and E are polar modes so they are infrared active too [16]. The literature data for phonon frequencies of $CdGeAs_2$ at zone-center are presented in Table 2.

In previous studies [10] was found that our samples $Cd_{1-x}Mn_xGeAs_2$ have good crystalline quality and relatively low free carrier concentration. In such a case Raman spectra should be very clear with strong narrow peaks. This is the case in some parts of our Raman spectra and these modes are labeled (Fig. 1a). All predicted modes of E and B_2 symmetry as well as A_1 and B_1^3 are registered in the spectra. Addition of Mn does not cause significant shift of the modes positions. Only for the sample with high amount of Mn ($x = 0.037$) the intensities of modes are increased.

On IR reflectivity spectra in Fig. 1b the modes of E and B_2 symmetry are obtained and labeled. Influence of adding of manganese on these modes is weak.

Besides, in areas between those known modes there are some wide structures, at about 110—140 cm^{-1} (Def.1), 165—185 cm^{-1} (Def.2) and 220—250 cm^{-1} (Def.3), as can be seen in Fig. 1. We have analyzed these modes to determine their origin.

For a precise analysis of the Raman spectra (Fig. 1a) the decomposition procedure was applied to extract individual peaks. Decomposition was implemented in the range from 60 to 380 cm^{-1} by using Lorentz profiles. Only Raman spectrum of $CdGeAs_2$ with individual peaks is shown in Fig. 2a because all others decomposed spectra are similar. Peaks that correspond to $CdGeAs_2$ lattice vibrations are labeled. Structures between them are modeled by wide Lorentz profiles and presented by green textured peaks. It can be seen that peaks labeled Def.2 and Def. 3 are stronger than Def.1.

Analysis of the reflection spectra was carried out by fitting frequency dependent dielectric function with experimental results. The dielectric function is taken in the factorized form:

$$\varepsilon = \varepsilon_\infty \prod_{j=1}^{n} \frac{\omega_{LOj}^2 - \omega^2 + i\gamma_{LOj}\omega}{\omega_{TOj}^2 - \omega^2 + i\gamma_{TOj}\omega} \qquad (1)$$

where ω_{TO} and ω_{LO} are transverse and longitudinal optical vibrations, γ_{TO} and γ_{LO} their dumping, n is number of oscillators taken into account and ε_∞ is high-frequency dielectric constant. Plasma frequency ω_P is not included in the equation because free carrier concentration is low and interaction between plasma and phonons is not observed on the spectra. In this way the phonon positions were obtained and they match literature values.

Fitted reflection spectra are shown in Fig. 2b. The theoretical

curves are presented by full lines. Besides known lattice phonons the influence of some imperfections had to be taken into account in order to get good fit. The best fit without this correction is presented on the reflection spectrum for $x = 0$ (Fig. 2b) by green line. The difference is not large but it is evident and most intense in section labeled Def.1.

Since $CdGeAs_2$ phonons are known and well investigated, we will analyze influence of lattice imperfections on Raman and reflection spectra.

There are several causes of a peak broadening on Raman spectra [17] such as electronic transition, electron-phonon interaction, amorphous state, nano-dimensions and others. X-ray measurements showed that the samples have regular crystal lattices and some other phases in the material have not been registered [10,13]. However, it is well established that the Raman experiment is more sensitive method for investigation of nano-clusters and different defects in semiconductors, so it cannot be excluded the existence of lattice defects or nano-formations composed of Cd, Ge and As atoms. But, Raman scattering on lattice defects is quite complex. Also optical phonons of nano-particles are broadened and shifted and depend on their size, shape and surroundings [17,18]. So such compounds are difficult for analysis, especially if there are more than one type of nanostructures with different sizes and shapes. In that case their cumulative effect is registered.

We analyzed dependence of intensities of defect modes on Mn concentration. The results are shown in Fig. 3. On Raman spectra an area under the Lorentz profile represents the mode intensity (A) (Fig. 3a,b). For IR reflection spectra the mode intensity is proportional to a ω_{LO}^2-ω_{TO}^2 (S) (Fig. 3c).

Intensities of optical modes of the $Cd_{1-x}Mn_xGeAs_2$ crystals are shown on Fig. 3a. The modes designations are on the right side of diagram, representing the vibrations of specified atoms. In cases of B_2^1 and E_1 (~210 cm^{-1}) as well as for E_3 and B_2^2 (~275 cm^{-1}) it was not possible to clearly separate modes so we presented their total intensities. From this diagram we can see that modes intensities decrease for sample with the lowest amount of manganese, the one with slightly deformed lattice, and then increase by adding more Mn.

The dependencies of intensities of defect modes on composition (x) are very interesting, as we can see on Fig. 3b,c. For Def.1 ($\approx 120\ cm^{-1}$) the huge difference between Raman and IR reflection results is evident. Obviously, this mod is IR active but has small Raman scattering cross-section. The other two defect modes Def.2 ($\approx 170\ cm^{-1}$) and Def.3 ($\approx 235\ cm^{-1}$) also have discrepancies between IR and Raman results - Def.2 for sample $x = 0.024$ and Def.3 for $x = 0.004$. The cause of this may be that these defect modes consist of two or more modes from different defects or clusters, which give different signals on IR and Raman measurements. So the defect modes, as the sums of few different defect modes, behave differently for different alloy compositions.

The change of lattice parameters a and c with composition is shown in Fig. 3d. The dependence of tetragonal distortion $\Delta = 2 - c/a$ is presented in the insert.

Diagrams of crystal lattice modes and defect modes (from Raman experiment, Fig. 3a, b) are similar, except for larger amount of Mn ($x = 0.037$). They have minimum for $x = 0.004$. Also it has been observed that dependence of defect modes intensity (A) on composition (x) (Fig. 3b) is very similar to dependence of tetragonal distortion of the lattice on x, which is shown in insert in Fig. 3d. This is a very strong indication that the defect modes are connected to, i.e. caused by intrinsic lattice conditions.

A brief overview of possible formations, which are registered in the literature and for which the optical phonons are known, is presented here. Characteristic frequencies of atoms, molecules or clusters of As - at about 200 and 250 cm^{-1} [19], Ge - at 300 cm^{-1} or

Table 2
Phonon frequencies experimentally obtained in Ref. [15].

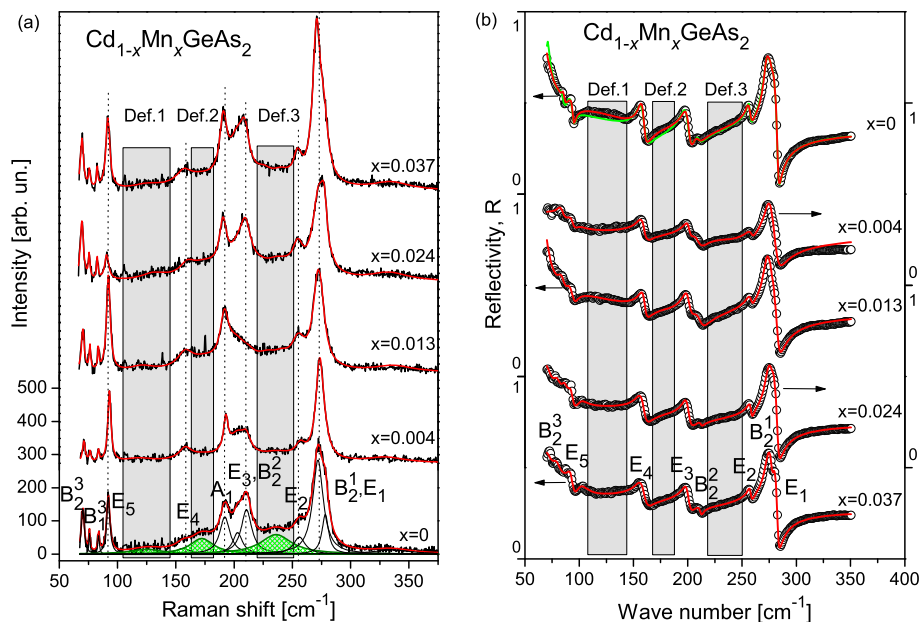| Mode	A_1	B_1	$B_2 - TO\ (LO)$	$E - TO\ (LO)$
$\omega\ (cm^{-1})$			273 (284)	275 (290)
		260		259 (264)
	196		205 (216)	203 (209)
		165		160 (165)
		75	73 (73)	96 (97)
				46 (48)

Fig. 2. Fitted Raman spectra (a) and Far-infrared reflectivity spectra (b) of $Cd_{1-x}Mn_xGeAs_2$, at room temperature. Red lines represent the best fits; gray regions mark lattice defects modes. (For interpretation of the references to colour in this figure legend, the reader is referred to the web version of this article.)
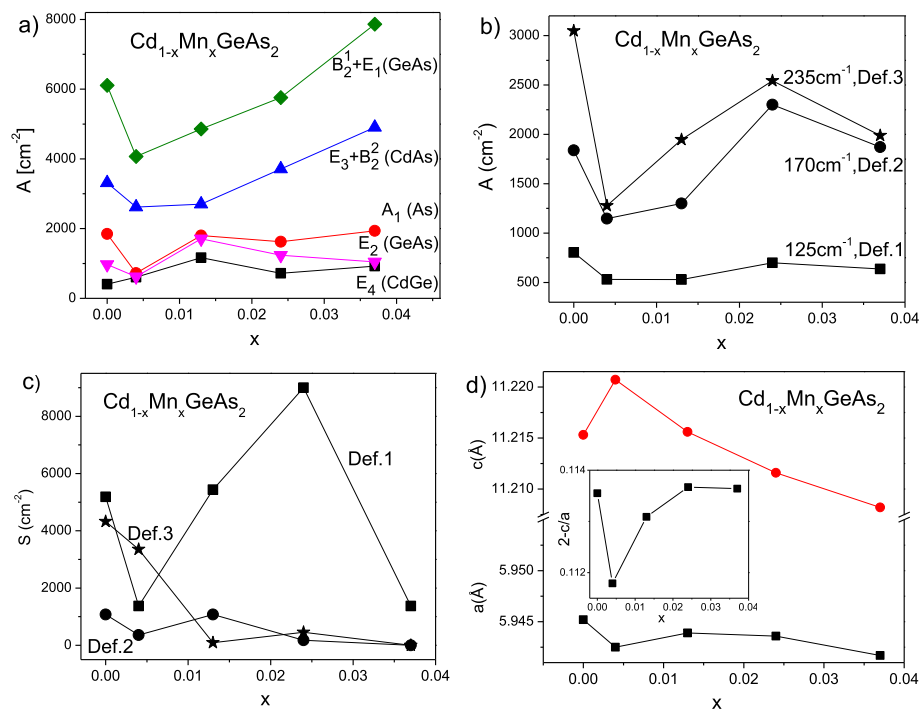

Fig. 3. Intensities of modes obtained from Raman spectra (a,b) and from IR reflectivity spectra (c); Dependence of lattice parameters and tetragonal distortion $\Delta = 2 - c/a$ (insert) on composition x (d).

little lower for nano dimensions [20], and Cd at 88 and 143 cm^{-1} [21], cannot be identified on our spectra (Fig. 1).

The strongest phonon of a GeAs compound is at 260 cm^{-1} [22] which coincides with GeAs sublattice vibrations in CdGeAs$_2$ (E$_2$ mode) [15]. So, it is not possible to distinguish these clusters even if they exist.

CdAs sublattice has frequencies in range 200–215 cm^{-1} [15]. Cadmium arsenide most commonly appears in forms CdAs$_2$ and Cd$_3$As$_2$. CdAs$_2$ has tetragonal crystalline structure. Each Cd atom is

surrounded with 4 As atoms, and each As atom with two Cd and two As atoms. CdAs$_2$ is a n-type semiconductor with significant anisotropy of electrical and optical properties [23]. Phonon modes of CdAs$_2$ are determined by analysis of reflectivity spectra [24] and they are at 83, 120, 202, and 245 cm^{-1}. On Raman spectra [23] the strongest modes are at 223 and 246 cm^{-1} and somewhat weaker at 80 and 125 cm^{-1}. These values are matching the ranges on our spectra at about 125 cm^{-1} and 220–250 cm-1 Cd$_3$As$_2$ is very interesting n-type semiconductor with narrow band gap (0.14 eV),

which attracted attention because it is three-dimensional Dirac topological semimetal [25]. It has tetragonal lattice where Cd is tetrahedrally coordinated with As atoms, while As atom is surrounded by six Cd atoms, located at 6 of the 8 corners of a cube, the 2 "vacant" sites are at diagonally opposite corners of one face of that cube [26]. These $Cd_6\square_2$ cubes group so that empty vertices form channels parallel to the a and b axes at different levels along the c axis [27]. It is very interesting that recent studies have shown that Cd_3As_2 crystals appear in the form of needles [26,27]. Cd_3As_2 appears in several crystal forms. The α"- Cd_3As_2 crystal has phonon frequencies at 189 and 244.5 cm^{-1} registered by Raman measurements [26] which approximately coincide with our results. There is a difference of more than 10 cm^{-1} but this can be attributed to nano dimensions, specific shape and boundary conditions of "defect" formations as to imprecision in the fitting process. Anyway, the 189 cm^{-1} is the closest frequency to the 173 cm^{-1} (179 cm^{-1} on IR spectra, Fig. 1b) that we could find in literature.

Research of native defects in p-type $CdGeAs_2$ was carried out and energies of the defect formation were calculated [28–30] and it was found that energy favorable intrinsic defects are vacancies of Cd (V_{Cd}) and antisite defects - Cd on a Ge place (Cd_{Ge}) and Ge on a As place (Ge_{As}), which are acceptor-type defects. Formation energies of two-component compounds $CdAs_2$ (−0.182 eV/formula unit) and Cd_3As_2 (−0.43 eV/formula unit) were calculated. Energies of formation of GeAs and $GeAs_2$ are positive so they are metastable compounds in this case.

For further analysis some findings related to the $Cd_{1-x}Mn_xGeAs_2$ materials published in other papers will be used. This can provide a right direction in determining the types of defects. In Ref. [10] paper it was establish existence of energy level at 200 meV probably caused by antisite defects in the materials. Another interesting and useful information about these materials are values of normalized molar fractions of the alloying elements and the Mn content (x) given in Ref. [13] and presented here in Table 3. It can be noted that amount of As atoms (≈ 0.488) is less than expected (0.5), while excess of Ge atoms is registered (≈ 0.27 instead 0.25). Also, there is a lack of Cd atoms (≈ 0.24). Such values are in good agreement with calculations and predictions of defect formations in $CdGeAs_2$ [28]: Cd → Ge → As resulting in the formation of V_{Cd}, Cd_{Ge}, Ge_{As} (acceptor intrinsic defects) and lack of As. Therefore, this material can be identified as Ge-rich and As-poor alloy.

In some papers that studied properties of p-type $CdGeAs_2$ the existence of Ge_{As} antisite defects is confirmed and that is connected with absorption band near 5.5 μm (225 meV) [5,30,31]. Also a direct correlation between that absorption and concentration of holes (p) was established [5,31]. The compositions of analyzed $CdGeAs_2$ samples and the atom percentages presented in Ref. [5] indicate that these materials also have excess of Ge and shortage of As atoms, as in our case.

We have assumed that a significant part of defect modes registered on Raman and IR reflectivity spectra (Figs. 1 and 2) are caused by these Ge_{As} intrinsic defects. Supports to this assumption are papers investigating Ga-rich p-type GaAs and correlations

between absorption at 5.5 μm, energy level at about 200 meV and antisite defects Ga_{As} [32,33], and papers in which Raman and Far-infrared spectra of such GaAs are presented [34−39]. GaAs is a material very similar to $CdGeAs_2$, wherein the Ga sublattice is replaced by sublattice consisting of regularly distributed Cd and Ge atoms, which results in a slight deformation of the crystal lattice. However, these two materials have very similar properties.

It is very interesting that optical spectra of Ga-rich p-type GaAs, doped and undoped, have modes in the same frequency ranges as the designated defect modes on the spectra of our Ge-rich p-type $Cd_{1-x}Mn_xGeAs_2$ samples − around 125, 170 and 235 cm^{-1}. In the paper [34] the far-infrared spectra of GaAs and GaAs doped with Zn, Mg, Si and C were analyzed. The same frequencies appear for different samples: 122, 156, 170, 220 and 235 cm^{-1}. In Ref. [35] Raman spectra of p-type GaAs are presented with modes at 120, 150, 175 and 225 cm^{-1} and they are attributed to transitions of bound holes on shallow acceptors in GaAs. Infrared absorption spectra shown in Ref. [36] have mode at 119 cm^{-1} and that is ascribed to the Ga_{As} antisite defect. Authors of [37] were measured Raman spectra of undoped GaAs. The modes at about 120, 150 and 170 cm^{-1} are clearly visible and they represent the transitions of bound holes from the ground state to the excited 2S and 2P states of the acceptors. The paper [38] − "Defect induced Raman transition in non-stoichiometric Ga − rich GaAs: A pseudolocalized vibrational mode of the Ga_{As} antisite?" is very useful for understanding this puzzle. They connected excess of Ga in GaAs, existing of 78/203 meV double acceptor levels, Raman mode at 225 cm^{-1} and determined Ga antisite defect as a probable common cause. Besides, on their Raman spectra the modes at 160−170 cm^{-1} stand out, determined as 2 TA, and at ≈ 130 cm^{-1}, not discussed. The same authors published new Raman spectra [39] in order to better examine 78 meV double acceptor. The modes at 95 and 120 cm^{-1} are clearly visible and explained as electronic excitations at the neutral 78 meV double acceptor. Modes at 148 and 174 cm^{-1} are connected to residual carbon and zinc acceptors or 2 TA.

According to these papers concerning Ga-rich p-type GaAs we can notice that different optical spectra contain modes on the same positions − about 120, 150, 170, 225 and 235 cm^{-1}, whereby the mode on 120 cm^{-1} is much stronger on IR spectra [38]. Also, the mode at 150 cm^{-1} coincides with E_4 mode of $CdGeAs_2$ so we cannot discuss it. These modes are connected to absorption at 5.5 μm, energy level at about 200 meV and antisite defects Ga_{As}.

Based on the matching of such GaAs optical modes with defect modes from our spectra and on established existence of antisite defects Ge_{As} in $CdGeAs_2$ it can be concluded that origin of the defect modes are Ge_{As}, as well as of impurity level at about 200 meV, i.e. absorption at 5.5 μm. This occurs in Ge-rich p-type $CdGeAs_2$ in which these defects are easily formed.

Also, the evident correlation between the modes intensity and the lattice tetragonal distortion (Δ) is very interesting (Fig. 3). It is important to notice that defect modes have the lowest intensity for the lowest distortion Δ, i.e. for the smallest difference between 2a and c. It is possible that low Δ is a consequence of adding a small amount of Mn, resulting in more regular lattice. The further addition of Mn leads to increase of $CdGeAs_2$ modes wherein the defect modes stay correlated to the distortion. For greater quantity of Mn they definitely decrease. Adding of Mn is not explicitly evident on the spectra (Figs. 1 and 2) but affect the lattice and for greater amount slight shift of modes positions becomes noticeable.

Different intensities of defect modes obtained from Raman and IR spectra can be explained by their multiple causes − lattice antisite defects and existing of clusters, whereby they have different cross sections for Raman scattering and for IR reflectivity. So we assume that in addition to antisite defects there are $CdAs_2$ and Cd_3As_2 small clusters in the $CdGeAs_2$ lattice.

Table 3
The results of the EDXRF analysis for the $Cd_{1-x}Mn_xGeAs_2$ samples including the normalized molar fractions of the alloying elements and the Mn content x, from Ref. [13].

x	Molar fraction of alloying elements			
	Cd	Mn	Ge	As
0	0.241	0	0.272	0.485
0.010	0.240	0.0023	0.268	0.488
0.023	0.236	0.0056	0.268	0.489
0.037	0.234	0.0088	0.268	0.489

4. Conclusions

The measurements of Raman spectra and far infrared reflectivity spectra of the series of $Cd_{1-x}Mn_xGeAs_2$ samples, with $0 \leq x \leq 0.037$, were carried out at room temperature, in spectral range from 60 to 400 cm^{-1}. The fitting procedures were done and all expected optical modes are registered. Results indicated that the samples are of high quality but also that some structural imperfections exist in them. Based on obtained results the three frequency ranges, at about 125, 170 and 235 cm^{-1}, are attributed to lattice imperfections and designated as defect modes. Small clusters and lattice defects are possible causes of these wide peaks at the spectra. These imperfections must have nanometer dimensions since they were not registered by X-ray measurements. It was determined that characteristic frequencies of $CdAs_2$ and Cd_3As_2 clusters correspond to obtained experimental results. By analogy with GaAs we concluded that registered defect modes for the most part correspond to antisite defects Ge_{As}, and connected this lattice defect to registered energy level at about 200 meV and to absorption at 5.5 μm. We determined the characteristic frequencies at about 125, 170 and 235 cm^{-1} that correspond to this Ge_{As} antisite defect. Also, we noticed a direct correlation between strength of defect modes and tetragonal distortion of lattice ($\Delta = 2 - c/a$).

Based on obtained results we can conclude that doping with small amount of manganese results in slight deformation of $CdGeAs_2$ crystal lattice and consequently considerably reducing the formation of antisite defects Ge_{As}. This can be very important for optical applications of this material in the infrared region.

Acknowledgments

References

[1] R.I. Byer, H. Kildal, R.S. Feigelson, CdGeAs$_2$ — a new nonlinear crystal phase-matchable at 10.6 μm, Appl. Phys. Lett. 19 (1971) 237–240.

[2] G. Krivaite, A.S. Borshchevskii, A. Sileika, Valence band structure of CdGeAs$_2$ from electroreflectance spectra, Phys. Status Solidi (b) 57 (1973) K39–K41.

[3] D.N. Nikogosyan, Nonlinear optics crystals (review and summary of data), Sov. J. Quantum Electron 7 (1977) 1–13.

[4] R.S. Feigelson, Improving optical transparency in CdGeAs$_2$ crystals by controlling crystalline defects, J. Cryst. Growth 292 (2006) 179–187.

[5] W. Huang, B. Zhao, S. Zhu, Z. He, B. Chen, Z. Zhen, Y. Pu, Correlation between dislocation etch pits, carrier concentration and optical absorption in CdGeAs2 grown by modified Vertical Bridgman method, J. Alloys Comp. 656 (2016) 818–824.

[6] L. Bai, N.Y. Garcesa, N. Yanga, P.G. Schunemanna, S.D. Setzlera, T.M. Pollaka, L.E. Halliburtona, N.C. Gilesa, Optical and EPR study of defects in cadmium germanium arsenide, Mater. Res. Soc. Symp. Proc. 744 (2003) 537–542.

[7] M.A. Blanco, A. Costales, V. Luana, R. Pandey, Theoretical study of the group-IV antisite acceptor defects in CdGeAs$_2$, Appl. Phys. Lett. 85 (2004) 4376–4378.

[8] L. Bai, N.C. Giles, P.G. Schunemanna, T.M. Pollak, K. Nagashio, R.S. Figelson, Donor-acceptor pair emission near 0.55 eV in CdGeAs$_2$, J. Appl. Phys. 95 (2004) 4840–4844.

[9] R. Demin, L. Koroleva, S. Marenkin, S. Mikhailov, T. Aminov, H. Szymczak, R. Szymczak, M. Baran, Room-temperature ferromagnetism in Mn-doped CdGeAs2 chalcopyrite, J. Magn. Magn. Mater 290–291 (2005) 1379–1382.

[10] L. Kilanski, M. Gorska, E. Dynowska, A. Podgorni, A. Avdonin, W. Dobrovolski, I.V. Fedorchenko, S.F. Marenkin, Homogeneous limit of Cd$_{1-x}$Mn$_x$GeAs$_2$ alloy: electrical and magnetic properties, J. Appl. Phys. 115 (2014), 133917-6.

[11] V.M. Novotortsev, K.K. Palkina, S.G. Mikhailov, A.V. Molchanov, L.I. Ochertyanova, S.F. Marenkin, Synthesis and structure of Mn-Doped CdGeAs2 single crystals, Inorg. Mater 41 (2005) 439–442.

[12] S.F. Marenkin, V.M. Novotortsev, K.K. Palkina, S.G. Mikhailov, V.T. Kalinnikov, Preparation and structure of CdGeAs$_2$ crystals, Inorg. Mater 40 (2004) 93–95.

[13] E. Dynowska, L. Kilanski, W. Paszkowicz, W. Dobrovolski, I.V. Fedorchenko, S.F. Marenkin, X-ray powder diffraction study of chalcopyrite-type Cd$_{1-x}$Mn$_x$GeAs$_2$ crystals, X-Ray Spectrom. 44 (2015) 404–409.

[14] P. Pyykko, Refitted tetrahedral covalent radii for solids, Phys. Rev. B 85 (2012) 024115–024117.

[15] J. Pascual, J. Pujol, L. Artus, J. Camassel, Alternating anion-cation bond strengths in CdGeAs2: application to the family of ternary pnictides, Phys. Rev. B 43 (1991) 9831–9842.

[16] You Yo, Beijun Zhao, Shifu Zhy, Tao Gao, Haijun Hou, Ab initio vibrational and dielectric properties of chalcopyrite CdGeAs2, Sol. St. Sci. 13 (2011) 422–426.

[17] G. Gouadec, P. Colomban, Raman Spectroscopy of nanomaterials: how spectra relate to disorder, particle size and mechanical properties, Prog. Cryst. Growth Charact. Mater 53 (2007) 1–56.

[18] I.H. Campbell, P.M. Fauchet, The effects of microcrystal size and shape on the one phonon Raman spectra of crystalline semiconductors, Sol. St. Comm. 58 (1986) 739–741.

[19] M. Romcevic, L. Kilanski, N. Romcevic, B. Hadzic, W. Dobrowolski, I.V. Fedorchenko, S.F. Marenkin, Raman spectra of ZnGeAs$_2$ highly doped with Mn, Mat. Res. Bull. 59 (2014) 300–304.

[20] P. Alfaro-Calderon, M. Cruz-Irisson, C. Wang-Chen, Theory of Raman scattering by phonons in germanium nanostructures, Nano. Res. Lett. 3 (2008) 55–59.

[21] T. Kutner, R. Dalgiewicz-Nowak, T. Grycuk, Fluorescence spectra of the Cd$_2$ dimer: transitions involving 0^+_u and 1_u Rydberg states and the lowest excited gerade states, Chem. Phys. Lett. 384 (2004) 171–178.

[22] D.G. Mead, Long wavelength study of semiconducting germanium arsenide, GeAs, Infrared Phys. 22 (1982) 209–213.

[23] J. Weszka, M. Balkanski, A.M. Raukhman, S.F. Marenkin, Raman scattering and lattice vibrations in tetragonal CdAs$_2$ crystals, Phys. Stat. Sol. (b) 194 (1996) 509–515.

[24] I. Gregora, J. Petzelt, Far infrared reflectivity of CdAs$_2$, Phys. Stat. Sol.(b) 49 (1972) 271–275.

[25] P. Schonherr, T. Hesjedal, Structural properties and growth mechanism of Cd$_3$As$_2$ nanowires, Appl. Phys. Lett. 106 (2015) 013115–013124.

[26] S. Wei, J. Lu, W. Yu, H. Zhang, Y. Qian, Isostructural Cd3E2 (E = P, As) microcrystals prepared via a hydrothermal Route, Cryst. Grow. Des. 6 (2006) 849–853.

[27] M.N. Ali, Q. Gibson, S. Jeon, B.B. Zhou, A. Yazdani, R. J Cava, The crystal and electronic structures of Cd$_3$As$_2$, the three-dimensional electronic analogue of graphene, Inorg. Chem. 53 (2014) 4062–4067.

[28] T.R. Paudel, W.R.L. Lambrecht, First-principles study of native defects in CdGeAs$_2$, Phys. Rev. B 78 (2008) 085214–085311.

[29] P.G. Schunemann, S.D. Setzler, T.M. Pollak, A.J. Ptak, T.H. Myers, Defect segregation in CdGeAs$_2$, J. Cryst. Grow. 225 (2001) 440–444.

[30] M.A. Blanco, A. Costales, V. Luana, R. Pandey, Theoretical study of the group-IV antisite acceptor defects in CdGeAs$_2$, App. Phys. Lett. 85 (2004) 4376–4378.

[31] L. Bai, C. Xu, N.C. Giles, K. Nagashio, R.S. Feigelson, Correlation of the electrical and optical properties of p-type CdGeAs$_2$, J. Appl. Phys. 99 (2006) 013512–013515.

[32] J. Wagner, Optical spectroscopy of impurity levels in GaAs, Phys. Scr. T29 (1989) 167–171.

[33] M. Bugajski, K.H. Ko, J. Lagowski, H.C. Gatos, Native acceptor levels in Ga-rich GaAs, J. Appl. Phys. 65 (1989) 596–599.

[34] R.F. Kirkman, R.A. Stradling, P.J. Lin-Chung, An infrared study of the shallow acceptor states in GaAs, J. Phys. C. Sol. St. Phys. 11 (1978) 419–433.

[35] K. Wan, R. Bray, Electronic Raman spectra of shallow acceptors in semi-insulating GaAs, Phys. Rev. B 32 (1985) 5265–5272.

[36] J.D. Collins, G.A. Gledhill, R.C. Newman, Ga antisite defects in neutron irradiated and annealed GaAs? Mat. Sci. Forum 10–12 (1986) 1081–1086.

[37] R. Bray, K. Wan, J.C. Parker, Insights into metastable defects in semi-insulating GaAs from electronic Raman studies of nonequilibrium holes, Phys. Rev. Lett. 57 (1986) 2434–2437.

[38] J. Wagner, M. Ramsteiner, R.C. Newman, Defect induced Raman transition in non-stoichiometric Ga-rich GaAs: a pseudolocalized vibrational mode of the GaAs antisite? Sol. St. Comm. 64 (1987) 459–463.

[39] J. Wagner, M. Ramsteiner, Ground-state splitting of the 78-meV double acceptor in GaAs, Phys. Rev. B 36 (1987) 6688–6690.

Journal of
RAMAN SPECTROSCOPY   WILEY

Phonons investigation of ZnO@ZnS core-shell nanostructures with active layer

Branka Hadzic[1] ⓘ | Branko Matovic[2] | Marjan Randjelovic[3] |
Radmila Kostic[1] | Maja Romcevic[1] ⓘ | Jelena Trajic[1] | Novica Paunovic[1] |
Nebojsa Romcevic[1]

[1]Institute of Physics, University of Belgrade, Belgrade, Serbia

[2]Institute Vinca, University of Belgrade, Belgrade, Serbia

[3]Faculty of Sciences and Mathematics, University of Nis, Nis, Serbia

Correspondence
Maja Romcevic, Institute of Physics, University of Belgrade, 11080 Belgrade, Serbia.
Email: romcevic@ipb.ac.rs

Abstract

In the present work experimental study of the ZnO@ZnS core-shell nanostructure with an active layer obtained by conversion of zinc oxide powders with H_2S is reported. The prepared structures were characterized by scanning electron microscopy, X-ray diffraction, Raman spectroscopy, and far-infrared spectroscopy. Top surface optical phonon (TSO) in ZnO, characteristic for the cylindrical nano-objects, the surface optical phonon (SOP) mode of ZnS, and SOP modes in ZnO@ZnS core-shell nanostructure are registered. Local mode of oxygen in ZnS and gap mode of sulfur in ZnO are also registered. This result is due to the existence of an active layer in the space between ZnO core and ZnS shell, which is very important for the application of these materials as thermoelectrics.

KEYWORDS
active layer, core-shell nanostructures, local mode, surface phonons, thermoelectric

1 | INTRODUCTION

ZnO and ZnS are two well-known and widely used wide-band gap semiconductors that are still in the focus of scientific research. Different combinations and changeable structures of ZnO and ZnS intrigue researchers all over the world due to the large possibility of their application as optoelectronic devices, sensors, lasers, and other novel devices. Both materials, ZnO and ZnS, are abundant, highly stable, non-toxic, environmentally friendly and intensively studied II-VI materials.[1-3] They can exist in the form of three crystallographic phases: cubic sphalerite, hexagonal wurtzite, or, in the rarest form, cubic rock salt. ZnO at the room temperature preferentially crystallizes in the hexagonal phase, while the ZnS structure depends on the temperature. At the room temperature ZnS crystallizes in the cubic phase but at temperatures above 1020°C ZnS is most stable in the hexagonal phase

form. However, there are also other differences between these two materials besides the difference in existing phases at room temperature. Although both of these materials are characterized by the wide direct band gaps, ZnS shows wider direct band gaps for both of its crystallographic phases. Nevertheless, ZnO is characterized by higher exciton binding energy. Band gaps for the ZnO hexagonal phase are reported to be 3.34, 3.37, and 3.4 eV with the binding energy of 60 mW, for the ZnS cubic phase band gaps are 3.54 and 3.68 eV, while for the ZnS hexagonal phase are 3.80 and 3.91 eV with the binding energy of 40 mW.[4-8]

Excellent features of ZnO and ZnS as individual components contribute to the favorable properties of the materials obtained combining these two components and make them good candidates for a wide range of applications, such are the thermoelectric components.[9,10] The most important parameter in the field of

thermoelectricity is the so-called figure of merit. It provides a connection between the material parameters and the maximum efficiency that will be achieved when this material is used as a thermoelectric generator. The goal of designing new materials or structures is to keep the phonon part of thermal conductivity in the material as small as possible, without changing the electrical parameters (electric conductivity, Seebeck coefficient, and electronic part of thermal conductivity). One possible way to achieve this is to use a ZnO/ZnS superlattice.[11] Another possibility is to use $ZnO_{1-x}S_x$ alloys. In the latter case, impurities act as local scatters that can alter the phonon transport.[12]

The general conclusion of all of the previously mentioned studies is summarized in the work of Bachmann et al.[13] where it is underlined that incorporation of sulfur in ZnO and incorporation of oxygen in ZnS can substantially reduce the thermal lattice conductivity and increase the figure of merit. However, a possible breakthrough in this field can be achieved with the usage of ZnO@ZnS core-shell system.

Core-shell nanostructures are a special class of the biphasic materials whose properties depend not only on the combination of the core and shell materials but also on their geometry, design, and core-shell volume ratio.[14–18] In previous studies of the ZnO@ZnS core-shell structures, this phenomenon was disregarded.[19–24] So far, the research focus was on the methods of synthesis and the quality of the spatial homogeneity of the obtained structures, such are the attempts to eliminate the existence of impurity throughout the system.

In addition, the focus has been on the application of these structures in solar cells,[23] as new materials for luminescence, and for magnetic applications.[24] Characterization methods were also selected for this purpose. Spectroscopic methods were used only to confirm X-ray measurements. Thus, in Sundararajan et al.[19] it was said that the Fourier-transform infrared spectroscopy (FT-IR) spectra confirmed starching vibrations of ZnO and ZnS, respectively. In Flores et al.[20] the same conclusion was reached using Raman spectroscopy. No attention was paid to the possibility of the formation of any layer between the ZnO core and the ZnS shell, which is the topic of our research.

While scanning electron microscopy, X-ray diffraction (XRD) and far-infrared spectroscopy give us information about the global structure, Raman spectroscopy is focused on the local environment, which is crucial for this type of research. The present work aims to determine the existence of the active layer doping phases in the space between the core and the shell by registering the surface, local, and gap modes, as well as by analyzing other structural and optical characteristics of the ZnO@ZnS core-shell system.

2 | EXPERIMENT

For the synthesis of ZnO/ZnS core-shell nanostructures, gas-phase sulfidation of ZnO (Merck) at elevated temperatures was exploited using flow reactor which is schematically presented in Figure S1 (Supporting Information). Hydrogen sulfide was initially obtained from iron (II) sulfide and hydrochloric acid and without further processing was introduced in the round-bottom flask containing 3 g of ZnO powder. Iron sulfide was added into a three neck round bottom flask (B) with mounted dropping funnel with Polytetrafluoroethylene (PTFE) key (A) containing 3 M HCl. Flow of HCl was adjusted to achieve required H_2S flow of 6.5 ml/min during 6 h. Evolved gas was passed into round-bottom flask with ZnS (C) which was heated at 340–400°C. Vinyl laboratory tubings were used to introduce gas into flow reactor.

Unreacted H_2S was collected and retained in two stages. First, the vessel containing $FeCl_3$ solution (D) was used to chemically convert H_2S gas into iron sulfides and small amount of remaining gas was caught in the next stage using solution of NaOH (E).

Morphology of the obtained powders and their evolution during calcination were studied by the field emission scanning electron microscope (FE-SEM) model FE-SEM JEOL-5200F (Japan).

The composition of investigated samples was investigated utilizing a Rigaku IV XRD diffractometer with Cu Kα radiation at room temperature. The present phases were identified by applying the PDXL2 software (version 2.0.3.0),[25] with the reference to the diffraction patterns present in the International Centre for Diffraction Data (ICDD).[26]

The far-infrared reflection spectra were measured at room temperature at the spectral range from 70 to 630 cm^{-1} with a BOMEM DA 8 spectrometer.

The micro-Raman spectra were taken in the backscattering configuration and analyzed by the TriVista 557 system equipped with a nitrogen-cooled charge-coupled-device detector. As an excitation source the Verdi G optically pumped semiconductor laser with the 532 nm line was used. Excitation energy is in the off-resonance regime for all the considered materials.

3 | RESULTS

SEM images of the two starting materials (ZnO and ZnS nanoparticles) and the obtained core-shell structure

(ZnO@ZnS) are given in Figure 1. In Figure 1a large ZnO particles are shown, in Figure 1b long narrow ZnS particles can be observed, while in Figure 1c large particles of the formed core-shell ZnO@ZnS structure are evident. This is confirmation that the core-shell structure usually shows the same morphology as a core. ZnO particles are cylindrical with the diameter ranging from 200 to 500 nm and length in the 300 to 500 nm range. ZnS particles are spiral wire-shaped structures with the diameter in the 20 to 30 nm range and length in the 300 to 500 nm range. The final structure contains mostly ZnO cylinders that originate from the starting ZnO material. ZnS is probably located at the surface of ZnO cylinders as a shell.

The formation of ZnS layer around ZnO particle surface is well known from sulfidation reaction: $ZnO(s) + H_2S(g) = ZnS(s) + H_2O(g)$, where ZnS growth an outward development during ZnO sulfidation. Such a process leads to a core-shell structure, which has been clearly demonstrated in many studies.[27–29]

The X-ray diffractograms of ZnO, ZnS nanoparticles, and ZnO@ZnS core-shell nanostructure are shown in Figure 2. The detailed phase composition investigations revealed the presence of crystalline phases of the hexagonal ZnO and cubic ZnS compounds in the starting materials, while in ZnO@ZnS the cubic ZnS transformed into hexagonal polymorph. Cubic-to-hexagonal phase transition of ZnS has been observed at very low temperatures at 250°C.[30] Since the experiment is conducted in range of 340–400°C, it is normal that a phase transformation takes place.

The plane identification (indexing) is done. The diffraction peaks correspond to the (1 1 1), (2 2 0), and (3 1 1) planes of the cubic phase of ZnS, matching with JCPDS 05-0566, and wurtzite (hexagonal phase) was found in JCPDS 36-1450. The XRD peaks are broadened because of nanocrystalline nature of the synthesized samples. On the other side, ZnO phase is hexagonal wurtzite phase, (JCPDS 01-089-0510). Obtained the core-shell structure consists of 88% ZnO (in core) and 12% ZnS

(shell). Williamson-Hall plots were used to separate the effect of the size and strain in the nanocrystals.[31] The results are shown in Table 1.

By means of the PDXL2 software (version 2.0.3.0),[25] it was calculated that the mean crystalline size $\tilde{a}$ of ZnO is determined as 57 nm, in the case of ZnS is 2.1 nm, while obtained the core-shell structure consists of 88% ZnO (core) with mean crystalline size of about 67 nm
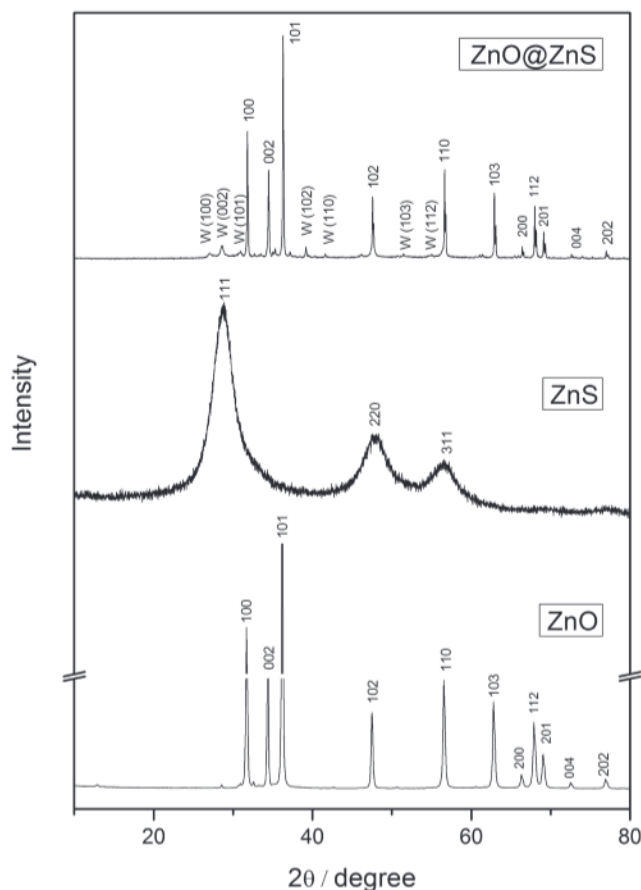
FIGURE 2 XRD spectra for all investigated samples. W = wurtzite (hexagonal) ZnS
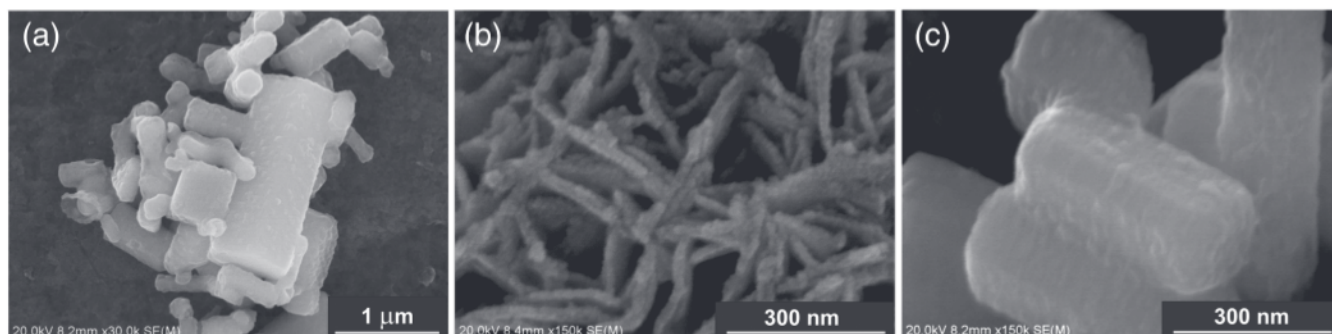
FIGURE 1 SEM images for (a) ZnO, (b) ZnS, and (c) ZnO@ZnS

TABLE 1 Unit cell parameters, crystallite size, and lattice strain of samples

Sample	Lattice parameter (nm)	Crystallite size (nm)	Strain (%)
starting material			
ZnS	$a = 0.53805(3)$	2.1	0.0075
ZnO	$a = b = 0.32521(4)$ $c = 0.52101(8)$	57	0.145
ZnO@ZnS core-shell			
ZnS	$a = b = 0.3848$ $c = 0.6317$ $\alpha = 90$ $\beta = 90$ $\gamma = 120$	11	0.001884
ZnO	$a = b = 0.32481(4)$ $c = 0.520044(7)$	69	0.00072

and 12% ZnS (shell) with mean crystalline size of about 11 nm.

The lattice strain of phases in core-shell structure is 0.001884 for ZnS and 0.00072 for ZnO. The value for stress in case of ZnS phase is lower than the stress for ZnO. It can be considered to be the consequence of an ordering of atomic arrangement during sulfidation, that is, the formation of zinc sulfide. The less ordering lead to an increasing strain due to the significant amount of strain that is localized at the surface of crystallites as a result of a high concentration of broken bonds.

The hexagonal phase of ZnO, the cubic, and hexagonal phase of ZnS were previously registered by the XRD analysis. Since the understanding of the bulk material vibrational properties is crucial for the analysis of the vibration properties of the core-shell structure, the vibrational properties analysis was initiated with a brief report of the literature data for the registered phases. The bulk modes are expected to be shifted and broadened as a consequence of the miniaturization.

The hexagonal structure of ZnO belongs to the space group C_{6v}^4, with the unit cell that contains four atoms, where all atoms occupy C_{3v} sites. From the factor group theory analysis existence of nine optical modes, that are classified by the following symmetries $\Gamma_{opt} = A_1 + 2B_1 + E_1 + 2E_2$, is evident.[32] Modes of symmetry A_1, E_1, and E_2 are Raman active, A_1 and E_1 are infrared active, while B_1 is inactive (silent) mode. Both A_1 and E_1 are polar modes and split into transverse (TO) and longitudinal (LO) phonons with different wavenumbers due to the macroscopic crystal field. Anisotropy of the ZnO crystal causes A_1 and E_1 modes to have different wavenumbers.

The cubic ZnS structure belongs to $F-43m$ (T_d^2) space group with a trigonal primitive unit cell containing one formula unit with two atoms. Thus, it has 6 degrees of freedom, three acoustic, and three optical phonons. The Brillouin zone center phonons, both acoustic and optical, are triply degenerate for this cubic structure and

have symmetry species $\Gamma_{15}(F_2)$. A macroscopic electric field in polar crystals, such as ZnS, is associated with LO vibrations and makes LO mode energy greater than the TO mode energy. This effect removes the degeneracy of the optical mode yielding a doubly degenerate TO mode and a LO mode. Both, the TO and LO modes are Raman active, while the TO mode is also infrared active.[33,34]

Wurtzite ZnS belongs to the space group P63mc (C46r) and all atoms occupy C3r sites. The nine possible optic modes of the four-atom primitive cell have the following symmetries: $1A_1 + 2B_1 + 1E_1 + 2E_2$. The A_1 and E_1 branches are both Raman and IR active, the E_2's are only Raman active, and the B_1's are neither IR nor Raman active.

3.1 | Far-infrared spectroscopy

The experimental data of two starting materials and the obtained core-shell structure are presented by circles in Figure 3. To analyze the far-infrared spectra the standard analysis, which applies the correlation between the reflection coefficient and dielectric function, was used. A theoretical model of the bulk dielectric function was discussed by several authors.[35,36]

The low-frequency dielectric properties of the single crystals are described by classical oscillators corresponding to the TO-modes, to which the Drude part is superimposed to take into the account the free carrier contribution:

$$\varepsilon_S(\omega) = \varepsilon_\infty + \sum_{k=1}^{l} \frac{\varepsilon_\infty S_k}{\omega_{TOk}^2 - \omega^2 - i\gamma_{TOk}\omega} - \frac{\varepsilon_\infty \omega_P^2}{\omega(\omega + i\Gamma_P)} \quad (1)$$

where ε_∞ is the bound charge contribution and it is assumed to be a constant, $\omega_{TOk}\omega_{TOk}$ is the transverse optical-phonon wavenumber, $\omega_P\omega_P$ the plasma
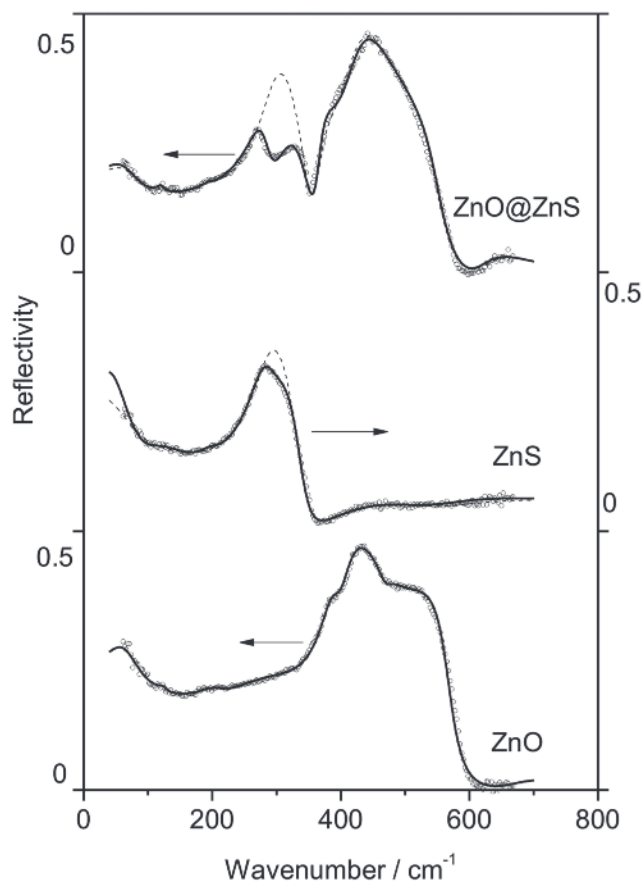
FIGURE 3 Far-infrared reflection spectra for all investigated samples. The experimentally obtained data points are depicted by circles. The theoretical spectra given as the solid lines are obtained with the model defined by Equations (1) and (2) and the fitting procedure

wavenumber, γ_{TOk} is damping, Γ_P is the plasmon mode damping coefficient, and S_k is an oscillator strength.

In general, the optical properties of an inhomogeneous material are described by the complex dielectric function that depends on the 3-D distribution of constituents. The investigated mixture consists of two dielectric components. One is treated as a host, and the other as the inclusion. The characterization of the inhomogeneous material by the two dielectric functions is not useful since the exact geometrical arrangement of the constituents of the material is needed. However, if the wavelength of the electromagnetic radiation is much larger than the size of inclusions, classical theories of inhomogeneous material presume that the material can be treated as a homogeneous substance with an effective dielectric function. In the literature, many mixing models can be found for the effective permittivity of such a mixture.[37] The optical properties of such materials depend

upon the properties of constituents, as well as their volume fraction.

The simplest model that describes an inhomogeneous material by an effective dielectric function can be written as $\varepsilon_{eff} = (1 - f) \, \varepsilon_1 + f \, \varepsilon_2$. This model is applicable in the case of bulk materials of dielectric constant ε_1 in which the second phase or the material of the dielectric constant ε_2, which occupies volume fractions f, is randomly distributed. In the case where nanoparticles are distributed in the air, or in an optically similar medium, the Maxwell–Garnett or Bruggeman formula is usually used.[37]

In general terms, the Maxwell–Garnett Effective Medium Approximation is expected to be valid at relatively low volume fractions f, since it is assumed that the domains are spatially separated and electrostatic interaction between the chosen inclusions and all other neighboring inclusions is neglected.

Since samples used in the present study are well defined with separated nanosized grains (as demonstrated on SEM images presented in Figure 1), the Maxwell–Garnet model was used for the present case. Effective permittivity of mixture, ε_{eff}, according to the Maxwell–Garnet mixing rule is as follows[38]:

$$\varepsilon_{eff} = \varepsilon_1 + 3f\varepsilon_1 \frac{\varepsilon_2 - \varepsilon_1}{\varepsilon_2 + 2\varepsilon_1 - f(\varepsilon_1 - \varepsilon_2)} \qquad (2)$$

In this case, nanoparticles of permittivity ε_2 are located randomly in the homogeneous environment ε_1 (air) and occupy a volume fraction f.

Solid lines presented in Figure 3 are calculated spectra obtained by a fitting procedure based on the previously presented model. The parameter adjustment was carried out automatically, using the least squares fitting of the theoretical (R_t) and experimental (R_e) reflectivity at q arbitrarily taken points:

$$\delta = \sqrt{\frac{1}{q}\sum_{j=1}^{q}\left(R_{ej} - R_{tj}\right)^2} \qquad (3)$$

The value of δ was minimized until it complied with the commonly accepted experimental error (less than 3%). For all the samples the determination errors of wavenumber and damping coefficients were in the range 3%–6% and 10%–15%, respectively. The agreement of the theoretical model obtained in this manner with the experimental results is excellent. In Table 2, the best fitting parameters are presented. In this case, the wavenumber indicated by ω_{TOk} in Equation 1 is perceived as the characteristic wavenumber for a given material.

TABLE 2 Calculated fit parameters obtained from the Raman and far-infrared spectra

	ZnS		ZnO		ZnO@ZnS		Description
	Raman (cm^{-1})	IR (cm^{-1})	Raman (cm^{-1})	IR (cm^{-1})	Raman (cm^{-1})	IR (cm^{-1})	
ω_P	-	82	-	94	-	91	
ω_1	132	119					$[TO_1–LA]_\Sigma$ or $2TA_2$
ω_2	145				152		$[TO_u–LA]_\Sigma$
ω_3	157						$[LO–LA]_\Sigma$
ω_4	174						2TAX
ω_5			203	210	203	190	2TA or E_2(low)
ω_6	206	197			219		LA
ω_7					**246**		**Gap-mode S in ZnO**
ω_8	263	281				269	TO
ω_9	**310**	**309**			**305**	**301**	**SOP**
ω_{10}			330	338	334		E_2(high)–E_2(low)
ω_{11}	**346**	**350**			**349**	**357**	**LO and LO+Plasma (IR)**
ω_{12}			379	379	380	386	A_1(TO)
ω_{13}			411	395	409	410	E_1(TO)
ω_{14}	415	420					$(LO_\Gamma + TA_L)$ or $(TO_\Gamma + LA_L)$
ω_{15}			436	436	436	438	E_2(high)
ω_{16}					**472**		**Local-mode O in ZnS**
ω_{17}			**484**	**469**			**TSO**
ω_{18}			**540**		**537**		**SOP**
ω_{19}			578	557	584	557	A_1(LO)

The parameters important for discussion are bold.

In Figure 3, the some phonon influence is evident at approximately 310 cm^{-1}. The experimental spectra are in complete agreement with the theoretical ones (please notice the solid lines in Figure 3) when the existence of this phonon is included, while inconsistency between the experimental and theoretical spectra (see the dashed lines in Figure 4) is clear when this phonon is omitted.

3.2 | Raman spectroscopy

The Raman spectra of the ZnO, ZnS, and zno@zns core-shell nanostructure, measured in the spectral range of 100–600 cm^{-1} at room temperature, are presented in Figure 4. Experimental Raman scattering spectra are analyzed by the deconvolution of the Lorentzian curve.[39] The thick red line presents a resulting spectral curve. Positions of Lorentzians are given in Table 2.

The Raman spectrum of the ZnO nanoparticle is presented in Figure 4a. Intense modes at 203, 330, 379, 411, 436, 484, 540, and 578 cm^{-1} were detected. The obtained results are in good agreement with the values given in the literature,[40] as it should be for the commercially supplied materials.

When ZnS is concerned the circumstances are more complex. In our previous research[41] the ZnS nanoparticles obtained by the mechanochemical synthesis dissolved in polymethyl methacrylate (PMMA) were studied. The experimental spectrum of the ZnS nanoparticle is characterized by several broader structures, broad multimodal features in 130–200 cm^{-1} region, along with the broad structures centered at 263, 346, and 425 cm^{-1}. Like in the far-infrared spectra analysis, the phonon influence at 310 cm^{-1} was observed. Congruence of the fitted spectrum with the experimental one is better when it is performed with this phonon.

Figure 4c shows the Raman spectra of the zno@zns core-shell nanostructure. Beside the phonons which originate from the initial constituents, there are two new structures evident at 246 and 472 cm^{-1}. In addition, the structure at approximately 310 cm^{-1} is shifted to the lower wavenumbers, while phonon observed at 346 cm^{-1} originating from ZnS is shifted at 349 cm^{-1}.
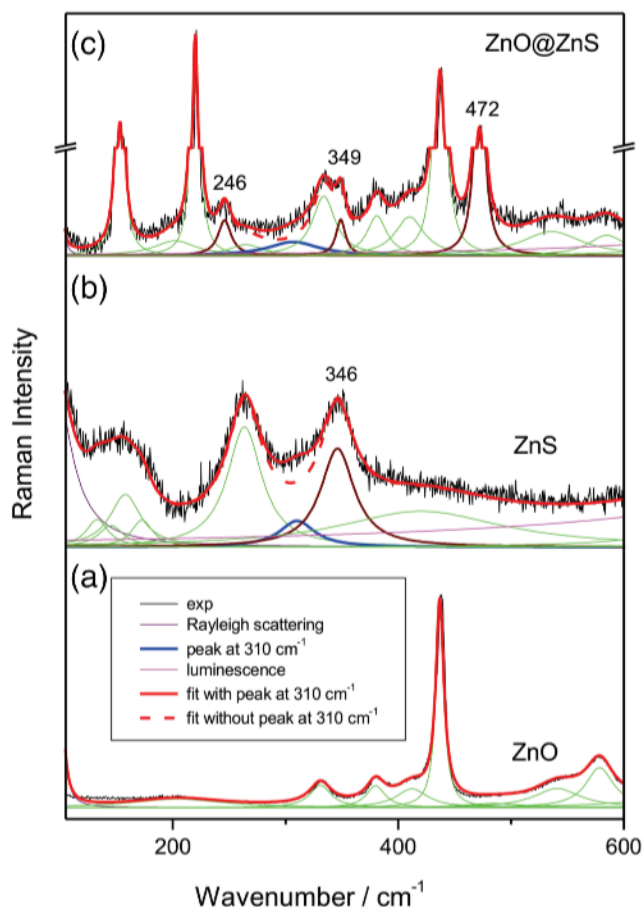
FIGURE 4 (a–c) Raman spectra for all investigated samples. The measured spectra are represented by dark line; theoretical spectra are convolution of Lorentzian curves [Colour figure can be viewed at wileyonlinelibrary.com]

4 | DISCUSSION

In the examined samples the ZnO particles are observed as big cylinders, few hundreds of nm in size. But even for the nanoparticles of few nanometers, as a consequence of the rather flat ZnO dispersion in the Brillouin zone, the effect of the optical phonons confinement is negligible, and the experimental spectra are almost the same as in the case of the bulk samples. This can also be applied to the ω_{LO} phonon of ZnS at about 350 cm^{-1}. Its shift toward the lower wavenumbers is expected and consistent with the corresponding nano dimension.[34]

Surface modes are difficult to be observed experimentally. But we roughly analyzed investigated nanoparticles (particle material, geometry, and dielectric permittivity if surrounding material), and we find that some feature in experimental spectra can be fairly good identified as surface modes. We used typical values of ZnO and ZnS dielectric parameters that are in our earlier papers: ZnO ($\varepsilon_0 = 10.24$, $\varepsilon_{besk} = 4.47$); ZnS($\varepsilon_0 = 8.1$; $\varepsilon_{besk} = 5$).

In principle, if nano-objects are present, then the surface of the whole particle is in contact with the matrix. Surface optical phonons (SOP) are characteristic when these nano-objects embedded in the matrix are concerned, and their activity becomes significant since they appear in the experimental spectra. Surface phonons are the most prominent in the spectra of the objects a few nanometers in size. The ZnO nanoparticles in the present study are cylindrical with axial symmetry. To find the wavenumbers of surface phonons the classic electrostatic equation for the appropriate geometry must be solved taking into account the interface conditions, that is, the object geometry must be treated properly.[42,43] Results of the study showed that for the cylinder-like nano-objects two types of surface phonons are characteristic: side surface optical phonons (SSO) and top surface optical phonons (TSO). SSO modes are related to the cylindrical interface (like in the cylindrical wire), and TSO modes are related to the planar interface (base of the cylinder).[42–44] There are two types of TSO mode: anti-symmetric and symmetric. Besides the geometry of the objects, surface optical frequencies are sensitive to the surface environment, that is, dielectric permittivity of the outer medium. All surface mode wavenumbers are in region $\omega_{TO} < \omega_{SOP} < \omega_{LO}$, that is, $\omega_{IITO} < \omega_{SOP} < \omega_{mixedLO} \approx 572$ cm^{-1}. In real samples spectra, surface optical wavenumbers depend on the surface quality, that is, surface roughness and arrangement and density of the nano-objects, resulting in the effective surrounding medium permittivity.

In the experimental ZnO spectra a wide feature of very low intensity is centered at ~484 cm^{-1}. This mode can be assigned as the surface optical mode,[42,43] or even more precise as TSO.[44] In the experimental spectra, a wide feature of middle low intensity centered at about 540 cm^{-1} can also be observed. This mode can be assigned as the surface optical mode.[45]

Surface mode wavenumbers for the ZnS particles are the solution of the same equation [43] but in the spherical case. If the non-polar matrix surrounds spherical QD (case of radial, i.e., central symmetry), there is one surface mode for each quantum number l. The wavenumber of these modes does not depend on the sphere radius. In the case of ZnS QD without matrix, that is, in a vacuum ($\varepsilon_{matrix} = 1$), wavenumbers of $l = 1$ and $l = 2$ surface phonons are ~330 and ~334 cm^{-1}, respectively. When the matrix is concerned, it must be noted that when the dielectric permittivity is increasing to the value higher than 1, then the surface modes wavenumbers are decreasing. The calculated surface mode wavenumber ($l = 1$, $\varepsilon_{matrix} = 2$) is 310 cm^{-1}. Mode in the spectral region from 300 to 330 cm^{-1} can be assigned as the ZnS nanoparticle surface mode.[34]

In the case of ZnO@ZnS, the surface optical ZnO mode at 484 cm^{-1} (TSO) is completely screened by the impurity mode. Surface optical ZnO mode at 540 cm^{-1} is at the same position and with the almost unchanged intensity as in the ZnO nanoparticles spectra. The surface optical ZnS mode of low intensity is at position 305 cm^{-1}. It is not clear if the ZnS shell is complete and uniform over the entire ZnO cylinder, but this decrease of the surface optical mode wavenumber is a sign that ZnS is effectively in $\varepsilon_{matrix} < 2$.

Surface optical modes are treated rudimentary, and this is not the main contribution in this paper. It is a possible explanation for these low-intensity features that appear in the experimental spectra. Position of these modes gives fairly good identification.

Raman active modes registered at 246 and 472 cm^{-1} for ZnO@ZnS core-shell nanostructure (Figure 3) were not observed in starting components. It can be assumed that in this case impurity modes are in question. Considering previous observation, it seems that in this case, during the formation of the ZnO@ZnS core-shell nanostructure the phenomenon indicated in Figure 3 occurred. To be precise, in the thin layer between ZnS and ZnO migration of oxygen and sulfur took place. This indicates that oxygen originated from ZnO migrated into the ZnS lattice where it substituted sulfur, while sulfur, in the same way, migrated into the ZnO lattice. New vibrational modes, separated from the host lattice modes, can appear when the supplementary atoms are integrated into the host lattice. When the amount of the impurity atoms is minor in comparison to the amount of the host lattice atoms, the generated mode is "localized." Namely, its eigenvector doesn't have a sinusoidal or wavelike dependence on space, but is strongly peaked at the impurity atom, and wanes rapidly on one or two lattice sites away.[46]

More precisely, when the lighter element (sulfur in this case) in the binary mixture ZnS ($m_S < m_{Zn}$) is replaced by the even lighter impurity (oxygen, $m_O < m_S$), a local mode is formed above the top of the optical band of ZnS. On the other hand, when the heavier impurity (sulfur) replaces the lighter element (oxygen) within the binary mixture (ZnO) a gap-mode is formed below the bottom of the optical band of the binary mixture.

Calculation of the local-mode and gap-mode wavenumbers [47] involves a comprehension of the eigenfrequencies and eigenvectors of the host-crystal vibrational modes, as well as changes in the mass and force constant caused by the impurity atom. The mass-defect parameter $\varepsilon_j = 1 - M/M_j$ plays an important role, where M is the mass of the impurity atom and M_j is the mass of the host/crystal atom. For the limited number of the polar diatomic crystals, the three-dimensional

mass-defect calculation was performed. Using the full lattice dynamics, the additional calculations were made for particular types of impurities in some host crystals.[48–50]

Lucovsky et al.[51] established a simple model for the calculation of local modes in three-dimensional crystals. In the present case, when sulfur in ZnS is substituted with oxygen the obtained position of the local mode is 471 cm^{-1}, which is in excellent agreement with the experimentally obtained result.

In the opposite case, when the gap mode is formed as a consequence of the replacement of oxygen with sulfur in ZnO, the situation is more complex and the mass-defect parameter is $\varepsilon_j = -1$. Consequently, for this parameter value, used models show singularity and that makes them inappropriate. Because of that, the simplest way to calculate gap mode position using only isotope effect was chosen[48]; that is, only mass variation is taken into account, while the gap mode is obtained by the separation from the TO phonons of the starting crystal. Applying this method enabled the obtainment of the position of the sulfur gap-mode in ZnO at approximately 268 cm^{-1}. That is in a good agreement (difference is 9%) with the experimentally obtained position at 246 cm^{-1}.

Few crystallographic planes of crystal material must be present in the crystallite to register particular crystallographic structure of crystallite by XRD. This is not the case in the ZnO-ZnS interface region. We did not observe any peak in the XRD that originates from ZnO-ZnS mixing region. This region seems to be very narrow. But characteristics of this interface region are clearly seen from very intensive new Raman modes of ZnO-ZnS, that is, appearance of local and gap modes. Raman spectroscopy is known as sensitive to the close surrounding.

The registered phonon properties are directly related to the existence of the active layer isolated impurities in the binary system, that is, sulfur in ZnO and oxygen in ZnS. Matching of the experimentally and theoretically obtained values indicates the complete incorporation of the impurities into the binary system with all the properties that this phenomenon brings. Obtained results will be a starting point for the continuation of the research in this field toward the application of these materials as thermoelectrics.

5 | CONCLUSION

The ZnO@ZnS core-shell nanostructure with an active layer is obtained by conversion of zinc oxide powders with H$_2$S. SEM images and XRD patterns shown the existence of a cylindrical nanostructure confirming at the

same time that core-shell structure is usually characterized by the same morphology as a core, in this case ZnO. Using Raman and Far-infrared spectroscopy the phonons characteristics of the starting components were registered. TSO in ZnO, characteristic for the cylindrical nano-objects, the surface optical phonon (SOP) mode of ZnS as well as SOP modes in ZnO@ZnS core-shell nano-structure are registered. Local-mode of oxygen in ZnS and gap-mode of sulfur in ZnO are also registered. These results are due to the existence of an active layer in the space between the ZnO core and the ZnS shell. These findings are very important for the potential application of these materials as thermoelectrics.

ORCID

Branka Hadzic https://orcid.org/0000-0001-5459-7461
Maja Romcevic https://orcid.org/0000-0002-5064-175X

REFERENCES

[1] S. S. Kumar, P. Ventakeswarlu, V. R. Rao, *Int. Nano Lett.* **2007**, *61*, 2054.

[2] A. Kushwaha, M. Aslam, *Electrochim. Acta* **2014**, *130*, 222.

[3] K. J. Klabude, *Nanoscale Materials in Chemistry*, Wiley Inter-cience, New York **2001**.

[4] N. Romcevic, R. Kostic, B. Hadzic, M. Romcevic, I. Kuryliszyn-Kudelska, W. D. Dobrowolski, U. Narkiewicz, D. Sibera, J. Alloys, *Compd.* **2010**, *507*, 386.

[5] J. M. Azpiroz, E. Mosconi, F. De Angelis, *J. Phys. Chem. C* **2011**, *115* (51), 25219.

[6] P. V. Raleaooa, A. Roodt, G. G. Mhlongo, D. E. Motaung, R. E. Kroon, O. M. Ntwaeaborw, *Physica B Condens. Matter* **2017**, *507*, 13.

[7] C. W. Raubach, Y. V. De Santana, M. M. Ferrer, P. G. Buzolin, J. R. Sambrano, E. Longo, *Dalton Trans.* **2013**, *42*, 11111.

[8] M. Sookhakian, Y. M. Amin, W. J. Basirun, M. Tajabadi, N. Kamarulzaman, *J. Lumin.* **2014**, *145*, 244.

[9] G. Homm, M. Piechotka, A. Kronenberger, A. Laufet, F. Gather, D. Hartung, C. Heiliger, B. Mayer, P. Klar, S. Steinmller, J. Janek, *J. Electron. Mater.* **2010**, *39*, 1504.

[10] G. Homm, J. Teubert, T. Henning, P. J. Klar, B. Szyszka, *Phys. Status Solidi C* **2010**, *7*(6), 1602.

[11] M. Bachmann, M. Czerner, S. Edalati-Boostan, C. Heiliger, *Eur. Phys. J. B* **2012**, *85*, 146.

[12] J. Huso, J. R. Ritter, L. Bergman, M. D. McCluskey, *Phys. Status Solidi B* **2019**, *256*, 1800607.

[13] M. Bachmann, M. Czerner, C. Heeliger, *Phys. Status Solidi A* **2013**, *210*(1), 125.

[14] K. L. Pisane, S. K. Singh, M. S. Seehra, *J. Appl. Phys.* **2015**, *117* (17), 17D708.

[15] A. V. Nomoev, S. P. Bardakhanov, M. Schreiber, D. G. Bazarova, N. A. Romanov, B. B. Baldanov, B. R. Radnaev, V. V. Syzrantsev, *Beilstein J. Nanotechnol.* **2015**, *6*, 874.

[16] A. M. El-Toni, M. A. Habila, J. P. Labis, Z. A. Althman, M. Alhoshan, A. A. Elzatahry, F. Zhangg, *Nanoscale* **2016**, *8*, 2510.

[17] S. Hou, Y. Chi, Z. Zhao, *IOP Conf. Ser. Mater. Sci. Eng.* **2017**, *182*, 012026.

[18] Y. F. Zhu, D. Fan, W. Shen, *J. Phys. Chem. C* **2008**, *112*, 10402.

[19] M. Sundararajan, P. Sakthivel, A. C. Fernandez, J. Alloys, *Compd.* **2018**, *768*, 553.

[20] E. M. Flores, C. W. Raubach, R. Gouvea, E. Longo, S. Cava, M. L. Moreira, *Mater. Chem. Phys.* **2016**, *173*, 347.

[21] K. T. Lee, B. H. Choi, J. U. Woo, J. S. Kang, J. H. Paik, B. U. Chu, S. Nahm, *J. Europ. Ceramic Soc.* **2018**, *38*, 4237.

[22] B. S. Rema Devi, R. Raveendrana, V. Vaidyan, *Pramana – J. Phys.* **2007**, *68*(4), 679.

[23] E. Zheng, Y. Wang, J. Song, X. F. Wang, W. Tian, G. Chen, T. Miyasaka, *J. Energy Chem.* **2018**, *27*(5), 1461.

[24] P. V. Raleaooa, A. Roodt, G. G. Mhlongo, D. E. Motaung, R. E. Kroon, O. M. Ntwaeaborwa, *Phys. B* **2017**, *507*, 13.

[25] Powder Diffraction File, PDF-2 Database, announcement of new data base release **2012**, International Centre for Diffraction Data (ICDD).

[26] C. Suryanarayana, M. Grant Norton, *X-ray Diffraction: A Practical Approach*, Springer, New York **1998** Version 2012.

[27] T. Ghrib, M. A. Al-Messiere, A. L. Al-Otaibi, *J. Nanomater.* **2014**, *2014*, 989632.

[28] J. Han, W. Liu, T. Zhang, K. Xue, W. Li, F. Jiao, W. Qin, *Sci. Rep.* **2017**, *7*, 42536.

[29] P. Banerjee, P. K. Jain, *RSC Adv.* **2018**, *8*, 34476.

[30] A. K. Kole, P. Kumbhakar, *Results Phys.* **2012**, *2*, 150.

[31] T. Ungar, *J. Mater. Sci.* **2007**, *42*, 1584.

[32] B. Hadzic, N. Romcevic, M. Romcevic, I. Kuryliszyn-Kudelska, W. Dobrowolski, J. Trajic, D. Timotijevic, U. Narkiewicz, D. Sibera, J. Alloys, *Compd.* **2012**, *540*, 49.

[33] P. Bruesch, *Phonons: Theory and experiments II* **1986**, 2. United States: Springer-Verlag New York Inc.

[34] J. Trajic, R. Kostic, N. Romcevic, M. Romcevic, M. Mitric, V. Lazovic, P. Balaz, D. Stojanovic, J. Alloys, *Compd.* **2015**, *637*, 401.

[35] G. Abstreiter, M. Cardona, A. Pinczuk, in *Light Scattering in Solids, IV*, Ed. By M. Cardona and G. Guntherodt (Springer-Verlag, Berlin, **1984**).

[36] E. Burstein, A. Pinczuk, R. F. Wallis, in *The Phys. of Semi-metals and Narrow-Gap Semicon*, (Eds: D. L. Carter, R. T. Bate), Pergamon, New York **1971**.

[37] A. Sihvola, *IEE Electromagnetic Waves Series* **1999**, *47*.

[38] J. C. Maxwell Garnett, *Phil. Trans. R. Soc. A.* **1904**, *203*, 385.

[39] B. H. Henry, J. R. During (Eds), *Raman spectroscopy: Sixty Years On*, Vol. 10, Elsevier, Amsterdam **1990**.

[40] B. Hadzic, N. Romcevic, M. Romcevic, I. Kuryliszyn-Kudelska, W. Dobrowolski, R. Wróbel, U. Narkiewicz, D. Sibera, J. Alloys, *Compd.* **2014**, *585*, 214.

[41] M. Curcic, B. Hadzic, M. Gilic, V. Radojevic, A. Bjelajac, I. Radovic, D. Timotijevic, M. Romcevic, J. Trajic, N. Romcevic, *Physica E Low Dimens. Syst. Nanostruct.* **2020**, *115*, 113708.

[42] P. M. Chassaing, F. Demangeot, V. Paillard, A. Zwick, N. Combe, *Appl. Phys. Lett.* **2007**, *91* (5), 053108.

[43] P. M Chassaing, F. Demangeot, V. Paillard, A. Zwick, N. Combe, C. Pagès, M. L. Kahn, A. Maisonnat, B. Chaudret, *J Phys Conf Ser.* **2007**, *92*, 012165.

[44] P. M. Chassaing, F. Demangeot, V. Paillard, A. Zwick, N. Combe, C. Pages, M. L. Kahn, A. Maisonnat, B. Chaudret, *Phys. Rev. B* **2008**, *77*, 153306.

[45] A. Pescaglini, E. Secco, A. Martin, D. Cammi, C. Ronning, A. Cantarero, N. Garrob, D. Iacopino, *J. Mater. Chem. C* **2016**, *4*, 1651.

[46] A. S. Baker, A. J. Sievers, *Rev. Mod. Phys.* **1975**, *47*, S1.

[47] P. G. Dawber, R. J. Elliott, *Proc. Roy. Soc. (London)* **1963**, *A273*, 222.

[48] J. Mitric, U. Ralevic, M. Mitric, J. Cirkovic, G. Krizan, M. Romcevic, M. Gilic, N. Romcevic, *J. Raman Spectrosc.* **2019**, *50* (6), 802.

[49] R. Kostic, M. Petrovic-Damjanovic, N. Romcevic, M. Romcevic, D. Stojanovic, M. Comor, J. Alloys, *Compd.* **2012**, *521*, 134.

[50] I. F. Chang, S. S. Mitra, *Phys. Rev.* **1968**, *172*(3), 924.

[51] G. Lucovsky, M. H. Brodsky, E. Burstein, *Phys. Rev. B* **1970**, *2*, 3295.

SUPPORTING INFORMATION

Additional supporting information may be found online in the Supporting Information section at the end of this article.

Raman spectroscopy and electron-phonon coupling in Eu^{3+} doped Gd$_2$Zr$_2$O$_7$ nanopowders

G. Krizan [a], M. Gilic [b], J.L. Ristic-Djurovic [b], J. Trajic [b], M. Romcevic [b], J. Krizan [a], B. Hadzic [b], B. Vasic [b], N. Romcevic [b, *]

[a] AMI, d. o. o., Ptuj, Slovenia
[b] Institute of Physics, University of Belgrade, Pregrevica 118, 11080, Belgrade, Serbia

ARTICLE INFO

ABSTRACT

The Raman spectra of Eu^{3+} doped Gd$_2$Zr$_2$O$_7$ nanopowders were measured. We registered three phonons at 177 cm^{-1}, 268 cm^{-1}, and 592 cm^{-1}, as well as their overtones at 354 cm^{-1}, 445 cm^{-1}, 708 cm^{-1}, 1062 cm^{-1}, 1184 cm^{-1}, ~1530 cm^{-1}, and ~1720 cm^{-1}. The phonon at 592 cm^{-1} is known to be characteristic for Gd$_2$Zr$_2$O$_7$ fluorite-type structure; however, the other two have not been registered so far. We found that the position of the newly detected phonons agrees well with the observed electron-phonon interaction. On the other hand, the registered multiphonon processes were a consequence of miniaturization that further induced changes in electronic structure of Eu^{3+} doped Gd$_2$Zr$_2$O$_7$ nanopowders.

© 2017 Elsevier B.V. All rights reserved.

1. Introduction

The rare earth zirconates (Re$_2$Zr$_2$O$_7$) were identified as attractive candidates for TBC (thermal barrier coatings) applications, high temperature heating devices, and host materials for luminescence applications [1,2]. Europium is one of many trivalent rare-earth ions that can be used for luminescence doping of both zirconia and zirconates [3]. Also Eu^{3+} ions within a doped compound of [Xe] 4f^6 configuration in different host lattices are found to give rise to strong luminescence emitting red light. The material in question shows typical f-f transitions of europium ions only. It is known [4] that luminescence is relatively independent on the host crystal field in trivalent rare earth ions because the optically active 4f electrons of the ions are shielded from the rest of the ions by the outer 5s and 5p shells [5].

Nanophosphors based on quantum dots have significant advantages over conventional bulk phosphor powders [6]. In quantum dots the optical properties such as light absorbance are determined by the size of the dots, whereas the optical properties of conventional bulk phosphor powders are determined solely by the phosphor's chemical composition. Changing the size produces dramatic changes in color. A small dot size also means that,

typically, over 70% of the atoms are at the surface sites so that chemical changes at these sites allow adjustment of the light-emitting properties of the dots and enabling emission of multiple colors from a single-size dot [6].

Raman spectroscopy is found to be a suitable method for investigations in this field of science. The method is highly effective in establishing the relation between the electronic structure and structural changes caused by miniaturization [7]. This method can be used to register all the aspects of electron − phonon interaction as well [8].

2. Sample and characterization

The combustion method was used for the synthesis of Eu^{3+} doped Gd$_2$Zr$_2$O$_7$ nanopowders. The chemicals Gd(NO$_3$)$_3$ * 6H$_2$O, Zr(NO$_3$)$_2$ * H$_2$O, Eu(NO$_3$)$_3$ * 6H$_2$O with purity of 99.99% were purchased from ABCR, Gd$_2$O$_2$ (99.9%) from the NOAH Technologies, and urea (NH$_2$)$_2$CO from Sigma−Aldrich. Europium doped cubic Gd$_2$Zr$_2$O$_7$ nanopowders were prepared by Solution Combustion Synthesis (SCS) method. The flame combustion process is used most frequently due to its simplicity and low cost of the synthesis procedures as well as because it enables adjustments of particle size and morphology.

After the synthesis, the nanopowder was annealed in air at 1200 °C for 2 h. The morphology analysis of the synthesized

materials indicated irregular crystallite size distribution and existence of agglomerated grains which were in the submicron size [9]. Annealing of the material is needed in order to achieve complete crystallinity. The Eu^{3+} concentration in $Gd_2Zr_2O_7$ was 2 mol%.

In our previous paper [9] we performed X-ray powder diffraction (XRD) and photoluminescence measurements of the same material. The diffractogram confirmed that monophased sample was crystallized in fluorite (F) type structure (space group Fm3m). The photoluminescence spectra gave an insight into a number of electronic transitions, among them were those at 705 nm and 713 nm ($^5D_0 - {}^7F_4$), 654 nm ($^5D_0 - {}^7F_3$), 611 nm and 630 nm ($^5D_0 - {}^7F_2$), 593 nm ($^5D_0 - {}^7F_1$), 584 nm ($^5D_0/^5D_1 - {}^7F_1$), and 578 nm ($^5D_0/^5D_1 - {}^7F_0$), which were also helpful here in Raman spectra analysis.

In this work we use the Raman spectroscopy as a tool to register the effects linked with the electron − phonon interaction in the Eu^{3+}-doped-$Gd_2Zr_2O_7$-nanoparticle.

3. Results and analysis

Atomic force microscopy (AFM) was done in tapping mode using NTEGRA Prima from NT-MDT and NSG01 probes. AFM results are summarized in Fig. 1. Two dimensional and three dimensional topographies are given in Fig. 1(a) and (b). They reveal grain structure of the sample. In order to further emphasize grain structure and grain boundaries, AFM phase image is given in Fig. 1c. Grain boundaries are mostly visible as a bright lines between neighbouring grains. Histogram of the grain size is given in Fig. 1d. By approximating grains as spherical particles, we conclude that the mean grain size (diameter) is around 50—60 nm.

Raman spectra were obtained with Micro Raman Chromex 2000 using 532 nm line of frequency doubled Nd:YAG laser. The spectral resolution was 1 cm^{-1}. Micro-Raman spectra were recorded at room temperature in the spectral range of 100−1900 cm^{-1}. The results are presented in Fig. 2.

The Raman spectrum of Eu^{3+} doped $Gd_2Zr_2O_7$ nanopowders in the frequency range 100−1900 cm^{-1} is shown in Fig. 2a. Very intensive lines were distinguished at 1530 cm^{-1} and 1729 cm^{-1}. Due to high intensity of these peaks the structures at lower wave numbers are practically invisible. To overcome this problem, the lower range of the same spectrum up to 1300 cm^{-1} is given in Fig. 2b on the 15 times smaller intensity scale. As a result a very interesting spectral structure became visible.

The spectrum in Fig. 2b is rather complex; therefore, we used the deconvolution method to separate Raman lines. Raman spectra are usually analyzed using either Lorentzian or Gaussian curves, so here we assumed that all phonon lines are of the Lorentzian type. The spectrum is described with 9 Lorentzians with positions at 177 cm^{-1}, 268 cm^{-1}, 354 cm^{-1}, 445 cm^{-1}, 592 cm^{-1}, 708 cm^{-1}, 1062 cm^{-1}, and 1184 cm^{-1}. It now became clear that there were 3 phonons, namely at $\omega_1 = 177$ cm^{-1}, $\omega_2 = 268$ cm^{-1} and $\omega_3 = 592$ cm^{-1}, and that the other modes were their overtones at $2\omega_1 = 354$ cm^{-1}, $4\omega_1 = 708$ cm^{-1}, $6\omega_1 = 1062$ cm^{-1}, $2\omega_3 = 1184$ cm^{-1}, and $\omega_1+\omega_2 = 445$ cm^{-1}. We assigned the dominant structures in Fig. 2a to $8\omega_1$ (1530 cm^{-1}) and $3\omega_3$ (1720 cm^{-1}). These structures have not been reported about so far in literature for Eu^{3+} doped $Gd_2Zr_2O_7$. However, similar results were recorded for some other systems with the same dopant, Eu^{3+} [10].

As other authors [11], we started our analysis from the bulk material, since vibrational properties of a bulk material are crucial

Fig. 1. Results of AFM analysis: (a) two dimensional and (b) three dimensional topography, (c) phase contrast image, and (d) grain distribution size.

Fig. 2. Raman spectra of $Gd_2Zr_2O_7(Eu)$ nanopowders. a) range 100—1900 cm^{-1}, b) range 100—1300 cm^{-1}.

Despite clear theoretical predictions, experimental results found in literature are quite diverse. For example, in Ref. [17] Raman spectra showed that only the A_{1g} mode exhibits a significant change between F and P phase. In numerous experimental spectra, only four phonons in P phase could be distinguished. These are E_g at about 320 cm^{-1}, A_{1g} at 520 cm^{--1}, F_{2g} band at about 405 cm^{-1}, and 600 cm^{-1}. This problem has been discussed for a long time, a good review of experimental data is published in 1983 in Ref. [12], but the dilemmas are still present nowadays [17—19]. It has been widely accepted, especially for nanomaterials, that results point to both the cation and anion pyrochlore-type ordering in the nano-domains inside the well-defined crystalline fluorite matrix. Therefore in most systems with the F structure, the phonons that are excluded by selection rules can be found. In most works, the existence of the phonon modes at ~140 cm^{-1} assigned to O-A-O vibrations and at ~220 cm^{-1} assigned to O−B−O vibrations is documented [12,17—19].

The main question in this work is why the frequencies of the phonon modes we obtained differ from the frequencies obtained by other authors. Moreover, the nature of the multiphonon processes is also to be explained. Only the phonon detected at $\omega_3 = 592$ cm^{-1} (F_{2g} symmetry) needed no special attention, since it was registered many times before in F − structured $Gd_2Zr_2O_7$ [17—19].

Based on our results [9], we think that the answer lies in the influence of doping with Eu^{3+}. As other authors [20] we as well came to the conclusion that Eu^{3+}, in relatively small concentrations/amounts, did not induce changes in phonon spectra of $Gd_2Zr_2O_7$. Another issue arises from the dimension of our powder. Although we were not in the strong quantum confinement regime, shifts in photoluminescence lines position occurred in comparison with the bulk material [5,9]. The electronic structure of $Gd_2Zr_2O_7(Eu)$ with the experimental values from Ref. [9] is given in Fig. 3. It can be seen that the transitions at 705 nm and 713 nm ($^5D_0 − {}^7F_4$) differ by the energy of the phonon $\omega_1 = 177$ cm^{-1}, whereas the transitions at 593 nm ($^5D_0 − {}^7F_1$) and 588 nm ($^5D_0/{}^5D_1 − {}^7F_1$) differ by the energy $2\omega_1 = 254$ cm^{-1}. The appropriate electronic transitions can be found in the same manner for the other phonons and their overtones. Specific structure at ($^5D_0 − {}^7F_2$) transition, i. e. the presence of two lines at 611 and 630 nm, appeared due to the existence of the second harmonic of ω_2 phonon.

for understanding vibrational properties of small particles. As a consequence of miniaturization, we expected the bulk modes to be shifted and broadened.

According to the Subramanian's theory [12], the disordered fluorite (F) and ordered pyrochlore (P) are two isometric structures important for $Gd_2Zr_2O_7$. The F structure has the space group of Fm3m and all cations are distributed randomly inside. The P structure with the space group of Fd3m is isometric and closely related to the ideal F structure, except that there are two cation sites, three anion sites $48f(O_1)$, $8a(O_2)$, and $8b(O_3)$, and one-eighth of the anions in 8b site are absent [13,14]. According to the group theoretical analysis, they are [15,16]:

$$\Gamma(Raman)_P = A_{1g} + E_g + 4F_{2g} \tag{1}$$

$$\Gamma(Raman)_F = F_{2g} \tag{2}$$

The group theory indicates disappearance between A_{1g} and E_g modes and reduction in the number of F_{2g} mode with the phase transition from $A_2B_2O_6O'$ P (Fm3m space group, Z = 8) to perfect AO_2 F (Fm3m, Z = 4) structure. For the ideal F structure, there is only one vibrational mode (F_{2g}), which involves oxygen vibration in the tetrahedral cage formed by four A cations.

Fig. 3. Schematics of electronic structure of $Gd_2Zr_2O_7(Eu)$. The phonons and their harmonics that participate in photoluminescence are indicated.

Fig. 4. Schematic potential energy diagram.

4. Conclusion

We used Raman spectroscopy to obtain phonon properties of Eu^{3+} doped $Gd_2Zr_2O_7$ nanopowders. The registered electron − phonon interaction led to the breakdown of the selection rules and appearance of the new phonons in fluorite structure $Gd_2Zr_2O_7$(Eu) spectrum. Registered multiphonon processes were a direct consequence of certain peculiarities in electronic structure of Eu^{3+} doped $Gd_2Zr_2O_7$ nanopowders, which caused the phonon side band appearance.

Acknowledgments

References

[1] J. Wu, X. Wei, N.P. Padture, P.G. Klemens, M. Gell, E. Garcia, P. Miranzo, M.I. Osendi, J. Am. Ceram. Soc. 85 (12) (2002) 3031–3035.
[2] R. Zhang, Q. Xu, W. Pan, C.L. Wan, L.H. Qi, H.Z. Miao, Structure and ionic conductivity of Ln2Zr2O7-type rare earth zirconates, Key Eng. Mater. 336–338 (2007) 420–423.
[3] M.M. Gentleman, D.R. Clarke, Surf. Coat. Technol. 93 (2004) 188–189.
[4] M.M. Gentleman, D.R. Clarke, Surf. Coat. Technol. 200 (2005) 1264–1269.
[5] Y.–S. Chang, H.–J. Lin, Y.–L. Chai, Y.-C. Li, J. Alloys Comp. 460 (2008) 421–425.
[6] A. Lakshmanan, Luminescence and Display Phosphors, Phenomena and Applications, Nova Science Publishers, Inc, New York, 2008, p. 146.
[7] M. Cardona, G. Guntherodt (Eds.), Light scattering in solids: v. 8: Fullerenes, Semiconductor Surfaces, Coherent Phonons, Springer-Verlag Berlin and Heidelberg GmbH & Co. K, 2010.
[8] M. Cardona, G. Guntherodt (Eds.), Light Scattering in Solids I: Introductory Concepts, Springer-Verlag Berlin and Heidelberg GmbH & Co. K, 1982.
[9] M.S. Rabasovic, D. Sevic, J. Krizan, M. Terzic, J. Mozina, B.P. Marinkovic, S. Savic-Sevic, M. Mitric, M.D. Rabasovic, N. Romcevic, J. Alloys Comp. 622 (2015) 292–295.
[10] S. Karthika, Synthesis and Characterization of Titania-zirconia Based Nanocomposites, Mahatma Gandhi University, 2014. PhD Thesis, http://shodhganga.inflibnet.ac.in/bitstream/10603/42089/15/15_chapter4.pdf.
[11] Challa S.S.R. Kumar (Ed.), Raman Spectroscopy for Nanomaterials Characterization, Springer-Verlag Berlin and Heidelberg GmbH & Co. K, 2012.
[12] M.A. Subramanian, G. Aravamudan, G.V. Subba Rao, Prog. Solid State Chem. 15 (1983) 55–143.
[13] F.X. Zhang, J. Lian, J.M. Zhang, K.J. Moreno, A.F. Fuentes, Z. Wang, R.C. Ewang, J. Alloys Comp. 494 (2010) 34–39.
[14] A. Garbout, I. Ben Taazayet-Belgacem, M. Ferid, J. Alloys Comp. 573 (2013) 43–52.
[15] M.T. Vandenborree, E. Husson, J.P. Chatry, D. Michel, J. Raman Spectrosc. 14 (1983) 63–71.
[16] B.E. Scheez, W.B. White, J. Am. Ceram. Soc. 62 (1979) 468–470.
[17] L. Zhou, Z. Huang, J. Qi, Z. Feng, D. Wu, W. Zhang, X. Yu, Y. Guan, X. Chen, L. Xie, K. Sun, T. Lu, Metall. Mat. Trans. A 47A (2016) 623–630.
[18] V.V. Popov, A.P. Menushenkov, A.A. Yastrebtsev, YaV. Zubavichus, R.D. Svetogorov, N.A. Kolyshkin, J. Phys. Conf. Ser. 747 (2016) 012042.
[19] F.X. Zhang, M. Lang, R.C. Ewing, Appl. Phys. Lett. 106 (2015) 191902.
[20] X. Xia, J. Ouyang, Z. Liu, J. Am. Ceram. Soc. 93 (4) (2010) 1074–1080.
[21] J.M. Ziman, Electron-phonon Interaction, September 2007. Published to Oxford Scholarship 2001, Online.
[22] M. Capone, C. Castellani, M. Grilli, Adv. Condens. Matter Phys. 2010 (2010) 18, 920860.
[23] J.J. Friedrich, D. Haarer, Photochemical hole burning: a spectroscopic study of relaxation processes in polymers and glasses, Angew. Chem. Int. Ed. Engl. 23 (23) (1984) 113–140.
[24] A. Chernikov, T. Feldtmann, S. Chatterjee, M. Koch, M. Kira, S.W. Koch, Solid State Commun. 150 (37, 38) (2010) 1733–1736.
[25] J. Pieper, A. Freiberg, in: J. Golbeck, A. van der Est (Eds.), The Biophysics of Photosynthesis, Chapter 2: "Electron−phonon and Exciton−phonon Coupling" in Light Harvesting, Insights from Line-narrowing Spectroscopies, Springer Science+Business Media New York, 2014.

We believe that above mentioned phonons at ~140 cm^{-1} (O-A-O vibrations) and ~220 cm^{-1} (O−B−O vibrations) underwent certain changes caused by the electron − phonon interaction; and were shifted to 177 cm^{-1} and 268 cm^{-1}, respectively. There are many papers that deal with the theoretical calculations concerning electron − phonon interaction [21,22]. Of our interest are those associated with the formation of phonon side band as a result of electron − phonon interaction [23–25]. In principal, we observed the surrounding of the dopant atom, in our case Eu^{3+}, for the $\omega_1 = 177$ cm^{-1} phonon as presented in Fig. 4. The potential energy curves of a selected nuclear motion are plotted as a function of its conformational coordinate q_k in the electronic ground and excited states E_i and E_f, respectively. The most probable transitions, according to the Franck-Kondon principle are given by red solid arrows for the cases of absorption (A) and fluorescence (C). In our case, the most probable absorption (A) was the one closest to the laser energy. Schematic vibronic wavefunctions are given as grey lines for selected vibrational energies. Red dashed arrows (B, D) indicate fast vibrational relaxation following the initial electronic transition. As presented in the right part of Fig. 4, the transition (B) was in our case the most intense for the $8\omega_1$ and $3\omega_3$. Other registered transitions were much weaker; therefore, the intensity of the corresponding phonons was much smaller than that for $8\omega_1$ and $3\omega_3$, which is in accordance with the Franck − Kondon principal rule and experimentally registered results given in Fig. 2. This further leads to the occurrence of the phonon side band, as described for the Eu^{3+}, Eu^{3+}/CdS, Eu^{3+}/CdTe doped TiO$_2$−ZrO$_2$ matrices [10].

We can say that the phonons of the main crystal have changed their energy, so that they now have the energy needed for intra/zonal transitions, while the phonon symmetry remained unchanged.

CrossMark

Far-infrared spectra of mesoporous ZnS nanoparticles

J. Trajić [a, *], M. Romčević [a], N. Romčević [a], B. Babić [b], B. Matović [b], P. Baláž [c]

[a] *Institute of Physics, University of Belgrade, 11080 Belgrade, Serbia*
[b] *Institute Vinca, University of Belgrade, 11000 Belgrade, Serbia*
[c] *Institute of Geotechnics, Slovak Academy of Sciences, 043 53 Košice, Slovakia*

ARTICLE INFO

ABSTRACT

ZnS nanoparticles were synthesized mechanochemically by high-energy milling, with three different milling times (5 min, 10 min and 20 min). Nitrogen adsorption method was used for examining specific surface area and texture of obtained powders. It was found that all samples are completely mesoporous. The optical properties were studied by far-infrared spectroscopy at room temperature in spectral region of $50-600$ cm^{-1}. The analysis of the far-infrared reflectivity spectra was made by the fitting procedure. The dielectric function of ZnS nanoparticles is modeled as a mixture of homogenous spherical inclusions in air by the Maxwell-Garnet formula. In the analysis of the far-infrared reflection spectra, appearance of combined plasmon-LO phonon modes (CPPMs) with high phonon damping are observed, which causes decrease of coupled plasmon-phonon frequencies.

1. Introduction

Research on semiconductor nanoparticles has significant scientific and practical interest because of their unique optical and electrical properties [1–4]. Zinc sulfide (ZnS) is an important II–VI semiconductor which semiconductor nanoparticles has been investigated extensively because of its broad spectrum of potential applications such as in catalysts, cathode-ray tubes (CRT), field emission display (FED) phosphors for a long time. It can also be used for electroluminescent devices and photodiodes [5–12].

The differences between the nanoparticles and bulk particles are caused by a high surface to volume ratio, which induces the structural and electronic changes. These differences depend on particle sizes, shape and surface characteristics. The decrease of particle sizes causes an extremely high surface area to volume ratio. The enhanced surface area increases surface states, which change the activity of electrons and holes, and affects the chemical reaction dynamics. Consequently, much research on ZnS nanoparticles and their physicochemical properties has been carried out and various methods have been used for the preparation of these nanoparticles [13–16].

The plasmons of free carriers and the longitudinal-optical (LO) phonons interact via their macroscopic electric fields, and as the

result the coupled LO phonon-plasmon modes (CPPMs) appears. The coupling of elementary excitations in solids has been investigated by many authors, and the phenomenological approach to this problem is formulated by several authors [17,18]. The most of published studies are devoted to the interaction of a single phonon with effective plasmons as well as the influence of the plasmon damping on the CPPM [19,20]. Our intention is to use far-infrared spectroscopy to study the fundamental properties of the coupled plasmon-phonons modes in the ZnS nanoparticles as well as to investigate these coupled modes under different phonon damping conditions.

In this paper, we present the results obtained by using far-infrared spectroscopy (FIR) to study optical properties of the ZnS nanoparticles which are mechanochemical synthesized using high-energy milling. Specific surface area and texture of obtained nanoparticles were examined using nitrogen adsorption method. The dielectric function of ZnS nanoparticles is modeled as a mixture of homogenous spherical inclusions in air, by the Maxwell-Garnet formula.

2. Samples preparation and characterization

Mechanochemical synthesis of ZnS nanoparticles was performed in a Pulverisette 6 planetary mill. The milling condition were: 50 balls of 10 mm diameter; weight charge of total powder mixture in the mill was 14.2 g, ball charge in the mill was 360 g, material of milling chamber and balls was tungsten carbide and

---

* Corresponding author.
  E-mail address: jelena@ipb.ac.rs (J. Trajić).

rotation speed of the planet carrier was 500 rpm. Milling time was 5, 10 and 20 min using an argon atmosphere as a protective medium in the mill. Initial characterization of ZnS powders is presented in detail in Ref. [21]. We will briefly review results of these investigations.

The morphology of samples has been investigated by SEM using high resolution electron microscope MIRA3 FEG-SEM, Tescan at accelerating voltage lower than 29 kV. From micrographs (Fig. 1) we conclude that ZnS powder is composed by well-defined and separated nanoparticles. These nanoparticles are spherical and have about 2 nm of diameter.

High resolution TEM (HRTEM-Philips Tecnai 200 operated at 200 kV) images provide the determination of the size of the nanoparticles, the type of structures produced and also the possibly induced morphologies (Fig. 2) [22]. Several clusters are clearly identified, and particularly three of them are having sizes of 2.6, 3.7 and 3.4 nm respectively. The corresponding fast Fourier transform (FFT) denotes a polycrystalline material, which must be composed of the nanocrystals.

The structural characteristics were obtained by the XRD powder technique. All samples were examined under the same conditions, using a Philips PW 1050 diffractometer equipped with a PW 1730 generator, 40 kV × 20 mA, using Ni filtered CoKα radiation of 0.1778897 nm at room temperature. Diffraction patterns show mainly the reflection of cubic phase (Fig. 3). The refracting planes denoted with (hkl) indices are 111, 220 and 311, respectively. Crystallite sizes were estimated as 1.9 nm (after 5 min milling time), 2.3 nm (10 min) and 2.4 nm (20 min).

3. Results and discussion

3.1. Adsorption isotherms - BET experiments

The specific surface area and the pore size distribution (PSD) of ZnS were analyzed using the Surfer (Thermo Fisher Scientific, USA). PSD was estimated by applying BJH method [23] to the desorption branch of isotherms and mesopore surface and micropore volume were estimated using the t-plot method [24]. Nitrogen adsorption isotherms for ZnS nanoparticles, as the amount of N_2 adsorbed as function of relative pressure at $-196\ °C$, are shown in Fig. 4. According to the IUPAC classification [25] isotherms of ZnS samples are of type IV and with a hysteresis loop which is associated with mesoporous materials. In all samples, the shape of hysteresis loop is of type H3. Isotherms revealing type H3 hysteresis do not exhibit any limiting adsorption at high P/P₀, which is observed with non-rigid aggregates of particles giving rise to slit-shaped pores [26].

Specific surface areas calculated by BET equation, S_{BET}, are listed in Table 1. S_{BET} values, for all samples, lie within $41-72 m^2 g^{-1}$. Overall specific surface decrease with the increase of milling time. r_{med} is the median pore radius and this value is the largest in the case of the sample obtained after 10 min of the mechanochemical treatment. PS confirms this conclusion i.e., pore radii are in the wide region from 2 to 45 nm.

Pore size distribution (PSD) of samples is shown in Fig. 5. Figure shows that samples are mesoporous with most pore radius between 2 and 46 nm. Mean pore radius for all samples, as well as cumulative pore volume (CpV) are presented in Table 1. As expected, CpV decrease with increasing the milling time.

t-plots, obtained on the basis of the standard nitrogen adsorption isotherms, are shown in Fig. 6. The straight line in the medium t-plot region gives a mesoporous surface area including the contribution of external surface, S_{meso}, determined by its slope, and the micropore volume, V_{mic}, is given by the intercept. The calculated porosity parameters (S_{meso}, S_{mic}) are given in Table 1 t-plot analysis confirmed that all samples are completely mesoporous (pore radius is between 2 and 50 nm).

3.2. Far-infrared spectroscopy

The far-infrared measurements were carried out with a BOMEM DA − 8 FIR spectrometer. A DTGS pyroelectric detector was used to cover the wave number range from 50 to 600 cm^{-1}.

When visible light interacts with semiconducting nanoparticles (characteristic size d, dielectric function ε_2) which are distributed in a medium with the dielectric constant ε_1 in the limit $\lambda \gg d$, the heterogeneous composite can be treated as a homogeneous medium and effective medium theory is applied. There are many mixing models for the effective dielectric permittivity of such a mixture [27]. Since our samples are well defined and separated nanosized grains we used Maxwell-Garnet model for present case. For the spherical inclusions case, the prediction of the effective permittivity of mixture ε_{eff} according to the Maxwell-Garnet mixing rule is [28]:

$$\varepsilon_{eff} = \varepsilon_1 + 3f\varepsilon_1 \frac{\varepsilon_2 - \varepsilon_1}{\varepsilon_2 + 2\varepsilon_1 - f(\varepsilon_1 - \varepsilon_2)} \tag{1}$$

Here, spheres of permittivity ε_2 are located randomly in homogeneous environment ε_1 and occupy a volume fraction f.

The ZnS nanoparticles are situated in air, therefore the ε_1 is 1. Dielectrical function of ZnS nanoparticles (ε_2) we obtain by applying following procedure. The low-frequency dielectric
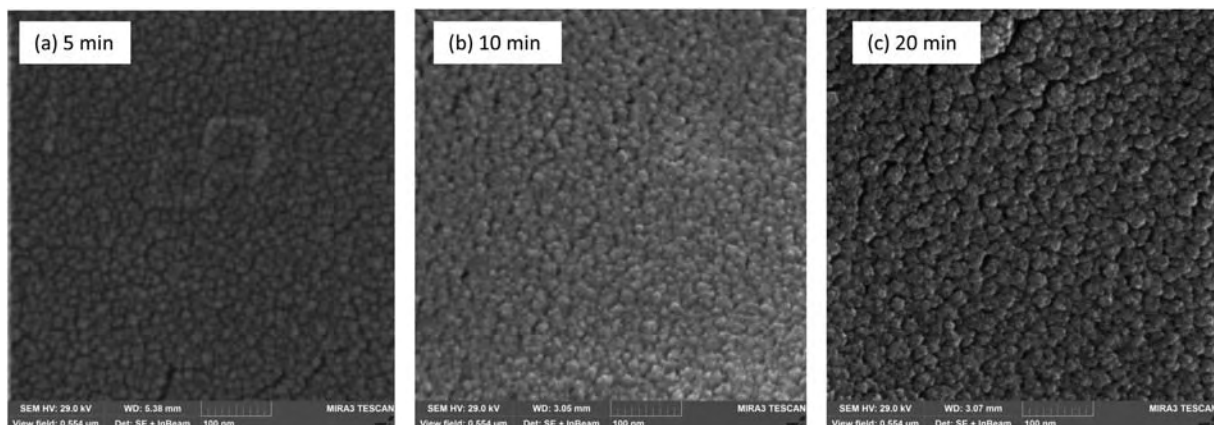
Fig. 1. SEM images of ZnS nanoparticles obtained after milling time of 5 min (a), 10 min (b) and 20 min (c) [21].
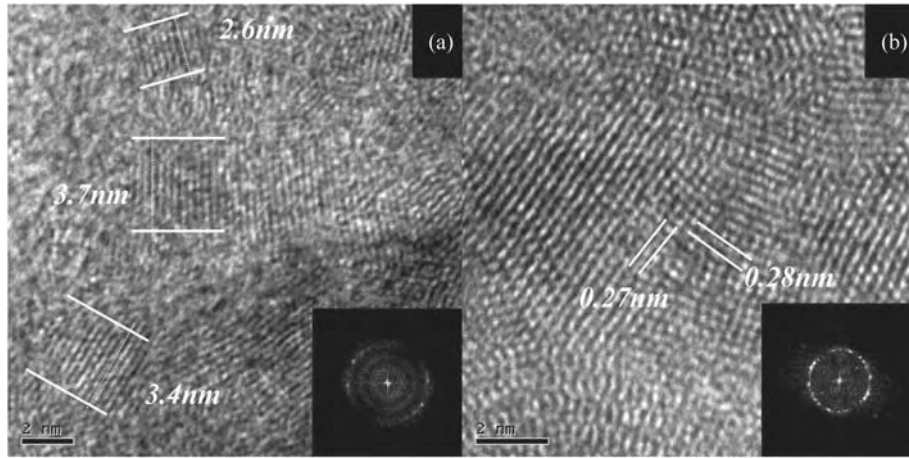
Fig. 2. HRTEM analysis of mechanochemically synthesized ZnS nanoparticles: (a) identification of nanoparticle with size around 3 nm and (b) determination of structure using the interplanar distance measurement [21].
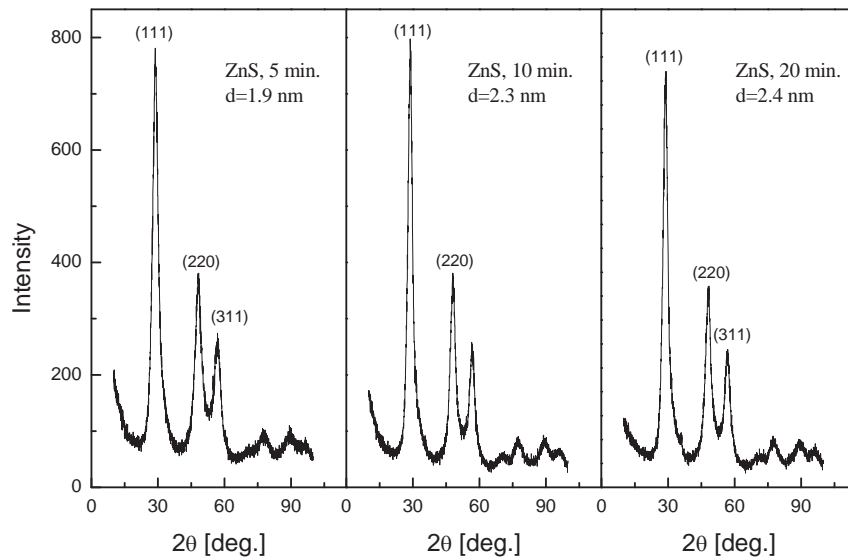

Fig. 3. XRD spectra of ZnS powders obtained after various milling times [21].

properties of single crystals are described with classical oscillators corresponding to the TO-modes, to which the Drude part is superimposed taking into account the free carrier contribution [29]:

$$\varepsilon_s(\omega) = \varepsilon_\infty + \sum_{k=1}^{l} \frac{\varepsilon_\infty \left(\omega_{LOk}^2 - \omega_{TOk}^2 \right)}{\omega_{TOk}^2 - \omega^2 - i\gamma_{TOk}\omega} - \frac{\varepsilon_\infty \omega_P^2}{\omega(\omega + i\Gamma_P)} \quad (2)$$

where ε_∞ is the bound charge contribution and it is assumed to be a constant, ω_{LOk} and ω_{TOk} are the longitudinal and transverse optical phonon frequencies, ω_P the plasma frequency, γ_{TOk} indicate the damping of uncoupled modes of the host crystal, and Γ_P is the plasmon mode damping coefficient.

In the case of ZnS nanoparticles the pure LO modes of the lattice are strongly influenced by the plasmon mode (ω_P) of the free carrier, which causes appearance a combined plasmon-LO phonon mode (CPPM) [18]. Consequently, the determination of LO mode is connected with the elimination of free carrier influence. Hence, in analysis of far-infrared reflection spectra of our samples we used the dielectric function that includes the interaction between LO

phonon and a plasmon, i.e. the plasmon-phonon interaction [30].

$$\varepsilon_2(\omega) = \varepsilon_\infty \frac{\prod_{j=1}^{2} \left(\omega^2 + i\gamma_{lj}\omega - \omega_{lj}^2 \right)}{\omega(\omega + i\Gamma_P)(\omega^2 + ig\omega - \omega_t^2)} \prod_{k=1}^{s} \frac{\omega^2 + i\gamma_{kLO} - \omega_{kLO}^2}{\omega^2 + i\gamma_{kTO} - \omega_{kTO}^2} \quad (3)$$

The ω_{lj} and γ_{lj} ($j = 1, 2$) parameters of the first numerator are the eigenfrequencies and damping coefficients of the longitudinal plasmons-phonon (LP + LO) waves, that arise as a result of the interaction of the initial ($\omega_{LO,ZnS}$ and ω_P) modes. The parameters of the first denominator correspond to the similar characteristics of the transverse (TO) vibrations. The second term represents uncoupled mode of the crystal (s), where ω_{LO} and ω_{TO} are the longitudinal and transverse frequencies, and γ_{LO} and γ_{TO} are the damping coefficients of the k-th crystal mode.

In that manner the TO mode frequencies obtained directly from fit, while the LO modes are determined by the maximum of the dielectric loss function. As a result the combined plasmon-LO phonon modes ($\omega_{l1,l2}$) were observed. In the experimental spectra
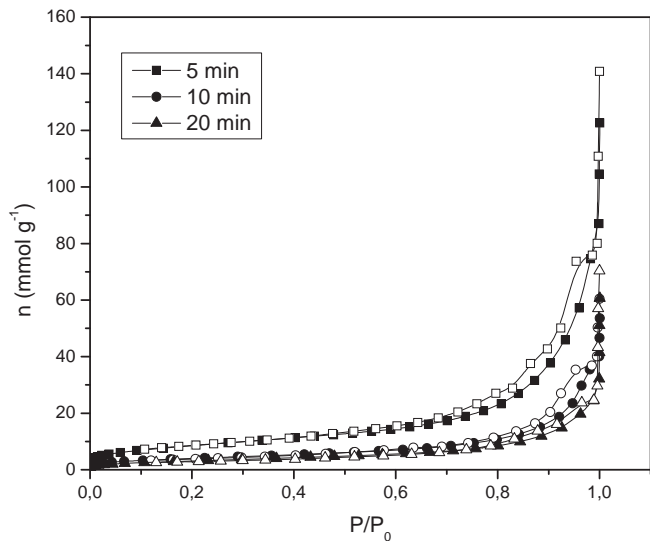
Fig. 4. Nitrogen adsorption isotherms as the amount of N_2 adsorbed as a function of relative pressure for ZnS samples. Solid symbols-adsorption, open symbols-desorption.

Table 1
Porous properties of ZnS nanoparticles.

Sample	S_{BET} (m^2/g)	S_{meso} (m^2/g)	S_{mic} (m^2/g)	CpV (cm^3/g)	r_{med} (nm)
5 min	72	72	0	0.194	6.3
10 min	58	58	0	0.112	7.9
20 min	41	41	0	0.085	5.6
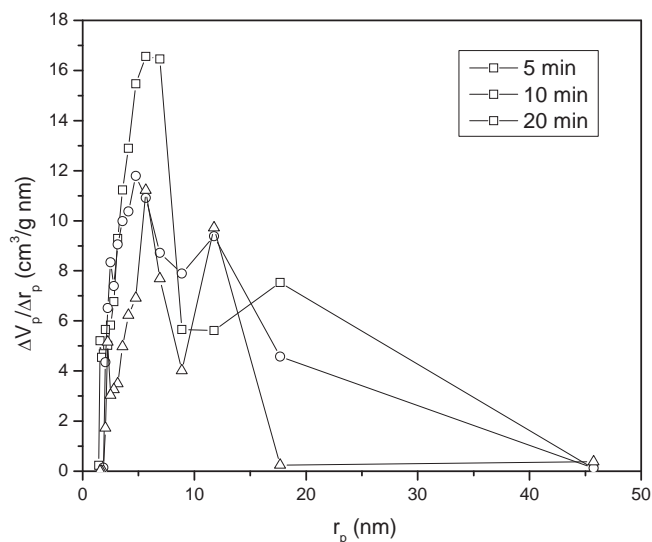
Fig. 5. Pore size distribution (PSD) for ZnS nanoparticles.

only coupled mode positions are observable. Therefore the determination of LO-modes is connected with the decoupled procedure.

The far-infrared spectra of ZnS powders obtained after various milling times, in the spectral range of 50–600 cm^{-1}, at room temperature are presented in Fig. 7. The experimental data are presented by circles, while the solid line was obtained using the dielectric function from Eq. (3), where s = 3.

Analyzing the reflection spectra we determine the values of filling factors. In Fig. 7 the calculated spectra for different filling factor are presented. Calculated spectrum for ZnS nanoparticles
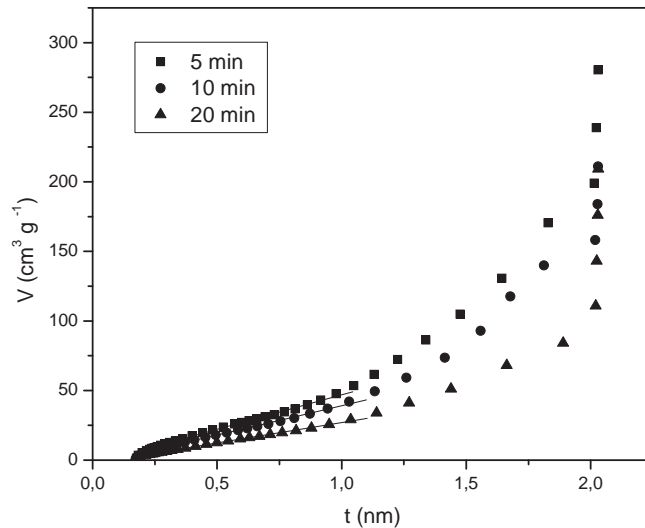
Fig. 6. t-plot for nitrogen adsorption isotherm of ZnS samples.

filling factor 0.52 is presented by dashed line, for 0.5 by solid line and for 0.48 by doted line. The figure shows that for different thickness there is a significant variance in calculated spectra. Main volume fractions f obtained as the best fit parameter estimation are presented in Table 2. These results are consistent with results obtained by BET experiment (chapter 3.1). Namely, the increase of milling time causes the mean pore radius to decrease, meaning that the filling factor is increased and cumulative pore volume (CpV) is decreased.

As we already said, calculated spectrum for ZnS nanoparticles (solid line) was obtained using the dielectric function from Eq. (3), where s = 3 This means that in the samples besides ZnS TO/LO pair exist three phonons which do not interact with the free carriers. These phonons at ~125 cm^{-1}, ~220 cm^{-1} and ~295 cm^{-1} originated from cubic ZnS, and corresponding to sums and differences of two phonons (overtones and combinations). Mode at about 125 cm^{-1} we identified as [TO$_l$–LA]$_\Sigma$, mode at about 220 cm^{-1} as [TO–TA]$_X$, and mode at ~295 cm^{-1} as [LA + TA$_u$]$_{W,\Sigma}$ [31]. The subindices "u" and "l" indicate the upper and lower transverse branches, respectively.

Characteristic parameters for plasmon-LO phonon interaction are presented in Fig. 8. As a result of the best fit we obtained the frequencies of coupled modes (ω_{l1} and ω_{l2}) marked by open circles and transverse mode frequencies which is denoted by stars. The solid lines are solutions of a real part of the Eq. (2) (Re{ε_S} = 0) where l = 1. Dashed lines represent theoretical predicted values of LO and TO frequencies of ZnS cubic crystal. As we already said, in the experimental spectra only coupled plasmon-LO phonon modes ($\omega_{l1,l2}$) were observed. The reflection spectra minima occurred at area of $\omega_{l1,l2}$ eigenfrequencies, while their maximum was at ω_t (Fig. 7.). These modes are classified in a lower branch (L$_-$) and an upper branch (L$_+$). With the increase in plasma frequency the nature of the upper mode changes in energy from the LO phonon-like to a plasmon-like. The change in the lower frequency mode occurs in the reaching the transverse-optical (TO) phonon energy for large plasmon energy. In the case of ZnS nanoparticles CPPM frequencies values (ω_{l2}) is lower than longitudinal optical frequencies of ZnS crystal, which means that interaction between free carriers and LO phonon causes frequency decrease. In Fig. 9 eigenfrequencies of plasmon phonon modes for single crystal ZnS, for different values of transverse phonon damping are presented. It is clearly seen that increase of phonon damping causes decrease of coupled plasmon-
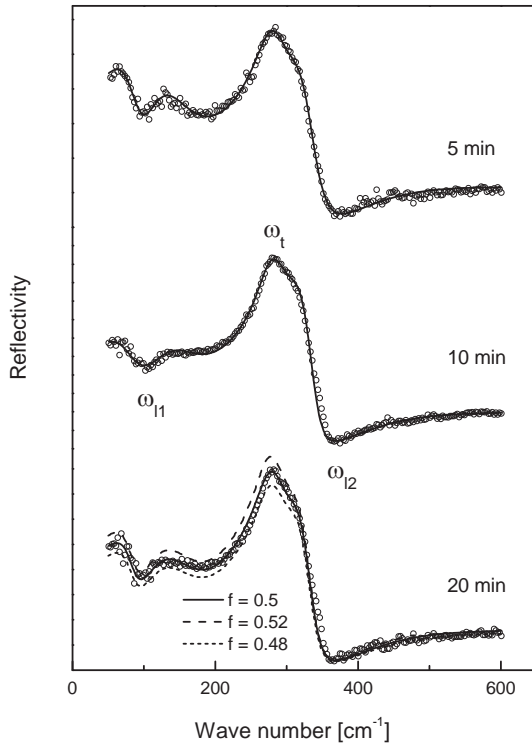
Fig. 7. Far-infrared reflection spectra of ZnS nanoparticles. The experimentally obtained data points are depicted by circles. The theoretical spectra obtained with the model defined by Eq. (3) and fitting procedure are given as solid lines. Three different samples were considered which are obtained after various milling times.
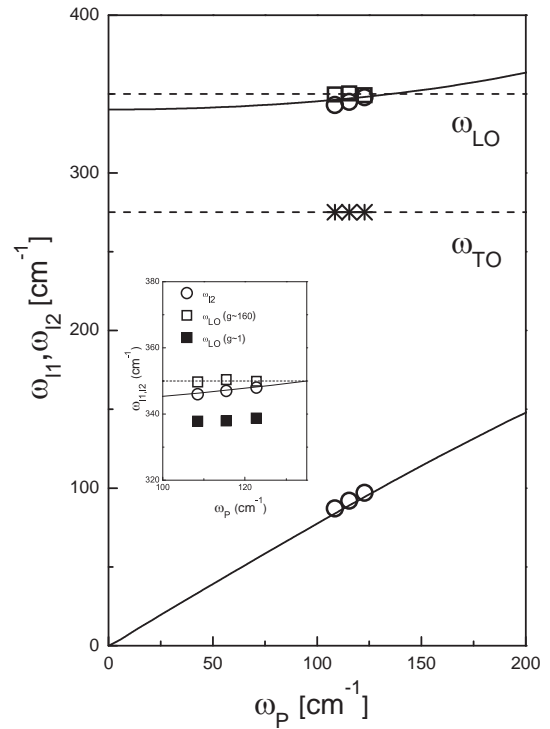

Fig. 8. The eigenfrequencies of the plasmon-phonon modes for ZnS nanoparticles obtained after various milling times. The solid lines are calculated spectra from Re $\{\varepsilon_S\} = 0$, where ε_S is given by Eq. (2); $\bigcirc - \omega_{l1,l2}$, $^* - \omega_{TO}$ and $\square - \omega_{LO}$. Inset: $\blacksquare - \omega_{LO}$ ($g \sim 1$ cm^{-1}), $\square - \omega_{LO}$ ($g \sim 160$ cm^{-1}) and $\bigcirc - \omega_{l2}$.

Table 2
Main volume factor for ZnS nanoparticles obtained after different milling time.

ZnS nanoparticles	t = 5 min	t = 10 min	t = 20 min
f	0.47	0.49	0.50

phonon frequencies. In the case of ZnS nanoparticles we discuss phonon damping is about 160 cm^{-1}, consequently it is obvious that the high value of phonon damping cause decrease of plasmon-LO coupled frequencies. High values of the phonon damping are caused by small dimensions of nanoparticles, namely the amount of damping is inversely proportional to the crystallite size [32].

Determination of LO mode is connected with the elimination of free carrier influence, i.e. with the decoupled procedure [30]. This procedure is explained in detail in our previous work [33]. The numerically calculated values for LO$_{ZnS}$ frequencies, as the solutions of a real part of Eq. (2) (Re$\{\varepsilon_S\} = 0$) and $g \sim 160$ cm^{-1} is presented in Fig. 8 by open squares. However, on the contrary to our previous articles, in this case we must take into account high values of phonon damping. Difference between values of LO frequencies calculated in this manner and values obtained when the value of damping is neglectable is shown in the inset Fig. 8. Values determined in this way, taking into account high values of the phonon damping are in excellent agreement with theoretically predicted values.

4. Conclusion

As a method to investigate phonon properties of ZnS nanocrystals we used far-infrared spectroscopy. ZnS nanoparticles were synthesized mechanochemically by high-energy milling, wherein
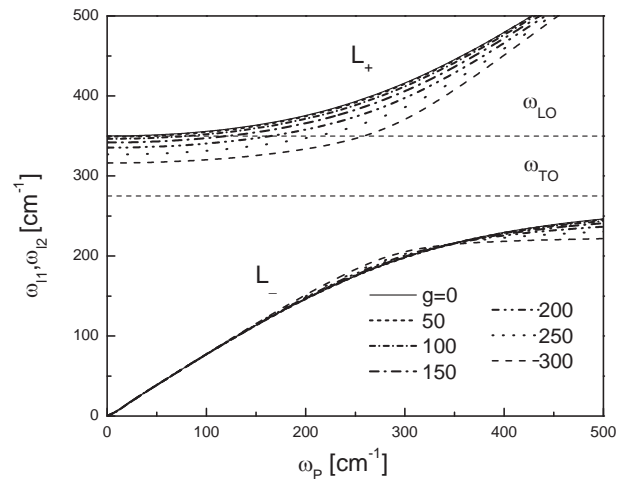
Fig. 9. Eigenfrequencies of plasmon-phonon modes for ZnS nanoparticles. The solid lines are spectra calculated from Re$\{\varepsilon_S\} = 0$, where ε_S is given by Eq. (2) while parameter l is set to 1. Seven different values of plasma damping were considered, i.e., $g = 0$, 50, 100, 150, 200, 250, and 300 cm^{-1}.

the milling time was varied. All samples are completely mesoporous, the nanoparticles are spherical, well-defined and separated. The increase of milling time causes the increase of filling factor and decrease of cumulative pore volume (CpV). We threat the ZnS nanoparticles as a mixture of homogenous spherical inclusion in air modeled by Maxwell-Garnet formula. Far-infrared measurements reveal, besides modes characteristic for the ZnS cubic crystal lattice and their multiphonon combinations, combined plasmon-LO phonon modes (CPPMs) with high phonon damping. As a

consequence the specific nature of the behavior of the coupled phonons frequency is determined.

Acknowledgments

References

[1] K.J. Klabunde, Nanoscale Materials in Chemistry, Wiley Interscience, New York, 2001.
[2] M. Fayette, R.D. Robinson, J. Mater. Chem. A 2 (2014) 5965–5978.
[3] X.R. Rui, H.T. Tan, Q.G. Yan, Nanoscale 69 (2014) 9889–9924.
[4] J. Chang, E.R. Waclawik, RSC Adv. 4 (2014) 23505–23527.
[5] H. Wang, X. Lu, Y. Zhao, C. Wang, Mater. Lett. 60 (2006) 2480–2484.
[6] N. Habubi, M. Hashim, A. Al-Yasiri, Baghdad Sci. J. 7 (2010) 1421–1425.
[7] J.S. Jie, W.J. Zhang, I. Bello, Ch-S. Lee, S.T. Lee, Nano Today 5 (2010) 313–336.
[8] X. Fang, T. Zhai, U.K. Gautam, L. Li, L. Wu, Y. Bando, D. Golberg, Prog. Mater. Sci. 56 (2011) 175–287.
[9] M. Nirmal, L. Brus, Acc. Chem. Res. 32 (1999) 407–414.
[10] D.C. Look, B. Claflin, Y.L. Alivov, S.J. Park, Phys. Status Solid (A) 201 (2004) 2203–2212.
[11] J.S. Hu, L.L. Ren, Y.G. Guo, H.P. Liang, A.M. Cao, L.J. Wan, et al., Angew. Chem. Int. Ed. 44 (2005) 1269–1273.
[12] M. Kanemoto, H. Hosokawa, Y. Wada, K. Murakoshi, S. Yanagida, T. Sakata, et al., J. Chem. Soc. Faraday Trans. 92 (1996) 2401–2411.
[13] P. Balaz, M. Balintova, Z. Bastl, J. Briancin, V. Sepelak, Solid State Ionics 101 (1997) 45–51.
[14] S.A. Chen, W.M. Liu, Langmuir 15 (1999) 8100–8104.
[15] N.R. Pawaskar, S.D. Sathaye, M. Bhadbhade, K.R. Patil, Mater. Res. Bull. 37 (2002) 1539–1546.
[16] J. Chen, Y. Li, Y. Wang, J. Yun, D. Cao, Mater. Res. Bull. 39 (2004) 185–194.
[17] M. Cardona, G. Gunterodt (Eds.), Light Scattering in Solids, Top. Appl. Phys., vol. 8, Springer, Berlin, 1975.
[18] J. Trajic, N. Romcevic, M. Romcevic, D. Stojanovic, R. Rudolf, T.A. Kuznetsova, D.R. Khokhlov, J. Alloys Compd. 493 (2010) 41–46.
[19] G. Irmer, M. Wenzel, J. Monecke, Phys. Rev. B 56 (15) (1997) 9524–9538.
[20] N. Romcevic, et al., J. Alloys Compd. 649 (2015) 375–379.
[21] J. Trajić, R. Kostić, N. Romčević, M. Romčević, M. Mitrić, V. Lazović, P. Balaž, D. Stojanović, J. alloys Compd. 637 (2015) 401–406.
[22] E. Dutkova, P. Balaz, P. Pourghahramani, S. Velumani, J.A. Ascencio, N.G. Kostova, J. Nanosci. Nanotechnol. 9 (2009) 6600–6605.
[23] E.P. Barret, L.G. Joyner, P.P. Halenda, J. Am. Chem. Soc. 73 (1951) 373–380.
[24] B.C. Lippens, B.G. Linsen, J.H. de Boer, J. Catal. 3 (1964) 32–37.
[25] K.S.W. Sing, D.H. Everett, R.A.W. Haul, L. Moscou, R.A. Pierotti, J. Rouquerol, et al., Pure Appl. Chem. 57 (1985) 603–619.
[26] S. Lowell, J.E. Shields, M.A. Thomas, M. Thommes, in: Characterization of Porous Solids and Powders: Surface Area, Pore Size and Density, Kluwer Academic Publishers, Dordrecht Netherlands, 2004, p. 44.
[27] K. Karkkainen, A. Saviola, K. Nikoskinen, IEEE Trans. Geosci. remote Sens. 39 (5) (2001) 1013–1018.
[28] J.C.M. Garnett, Trans. R. Soc. Vol. CCIII, A (1994) 385–420.
[29] V. Gopal, Infrared Phys. 18 (1978) 121.
[30] A.A. Kukharskii, Solid State Commun. 8 (1970) 1275–1279.
[31] J. Serrano, A. Cantarero, M. Cardona, N. Garro, R. Lauck, R.E. Tallman, T.M. Ritter, B.A. Weinstein, Phys. Rev. B 69 (2004) 14301–14312.
[32] H. Frase, B. Fultz, J.L. Robertson, Phys. Rev. B 57 (2) (1998) 898–905.
[33] J. Trajić, N. Romčević, M. Romčević, V.N. Nikiforov, Mater. Res. Bull. 42 (2007) 2192–2201.

Plasmon – Phonon interaction in ZnSnSb$_2$ + Mn semiconductors

Maja Romcevic[a,*], Novica Paunovic[a], Uros Ralevic[a], Jelena Pesic[a], Jelena Mitric[a], Jelena Trajic[a],
Lukasz Kilanski[b], Witold Dobrowolski[b], Irina Valentinovna Fedorchenko[c,d],
Sergey Fedorovich Marenkin[c,d], Nebojsa Romcevic[a]

[a] *Institute of Physics, University of Belgrade, Belgrade, Serbia*
[b] *Institute of Physics, Polish Academy of Sciences, Warsaw, Poland*
[c] *Kurnakov Institute of General and Inorganic Chemistry, Russian Academy of Science, Moscow, Russian Federation*
[d] *College of New Materials and Nanotechnologies, National University of Science and Technology, Moscow, Russian Federation*

ARTICLE INFO

ABSTRACT

Semiconductors of II-IV-V$_2$ type with chalcopyrite structure have been studied for several decades. Due to advances in materials synthesis technologies, and doping with various elements, the possibilities of their application have expanded. In this paper, polycrystalline ZnSnSb$_2$ + Mn was examined with the aim to explain the connection of its high free carrier concentration with the material structure and influence on optical properties. Two samples of Zn$_{1-x}$Mn$_x$SnSb$_2$ with different compositions ($x = 0.027$ and $x = 0.076$) and significant difference in carrier concentrations were analyzed. Their structural properties were examined by x-ray diffraction, optical microscopy, and AFM. The existence of several different phases - ZnSnSb$_2$, ZnSb, SnSb, and small amounts of Sn and MnSb, as well as very complex microstructures, were registered. It was found that the high free carrier concentrations are caused by a large number of defects, especially zinc vacancies. Optical properties were analyzed using IR spectroscopy at room temperature. Based on the analysis of IR reflection spectra, the presence of plasmon - phonons interaction was registered. It was determined that three ZnSnSb$_2$ phonons of B$_2$ symmetry interact with plasma, which then leads to the change of their positions. A detailed analysis of this interaction provides insight into the behavior of some other material parameters. Also, vibration modes of ZnSb and SnSb phases were registered on the spectra. Knowledge of phonon behavior and their interaction with plasma is important for possible applications, especially as a thermoelectric material.

1. Introduction

Semiconductors have been widely used thanks to the ability to adapt to different requirements. The II-IV-V$_2$ chalcopyrite semiconductors have been intensively studied in recent decades [1]. The fields of their application are considerably expanded by doping with various impurities. A significant breakthrough was achieved by the addition of magnetic impurities, whereby ferromagnetism at room temperature was achieved [2,3]. The synthesis technology of this class of compounds has been developed, but it is still adapting to new requirements [4]. Zn-Sn-Sb based alloys have required thermoelectric properties and find application as low-toxic thermoelectric materials [5,6,7]. The engineering of structural, transport, electrical, optical, magnetic properties as well as other material parameters, goes along with the increasing application of this class of semiconductors.

ZnSnSb$_2$ is II-IV-V$_2$ type material with the tetragonal chalcopyrite structure, narrow gap of 0.7 eV at room temperature, high

concentration of free carriers (10^{21}–10^{22} cm^{-3}) and inhomogeneous structure [8,9]. In this paper we analyzed ferromagnetic semiconductor ZnSnSb$_2$ + Mn, which has interesting magnetic properties, such as paramagnet-ferromagnet transition with the Curie temperature about 522 K and the cluster-glass behavior with the transition temperature about 465 K, caused by the formation of MnSb clusters in the material [10]. The Zn$_{1-x}$Mn$_x$SnSb$_2$ samples were obtained using direct fusion method, and characterization of their structural, magnetic, optical and phonon properties were done [9]. We chose two samples with different chemical contents, x = 0.027 and x = 0.076, which we labeled as samples A and B respectively, with the aim to examine their properties in more detail. Main reason was a ten times difference in their free-carrier concentrations ($p_A = 13 \times 10^{21}$ cm^{-3} and $p_B = 1.2 \times 10^{21}$ cm^{-3}). We wanted to determine what the cause of this difference in concentration is, and whether there is a reaction between the free carriers and the crystal lattice. The question of plasmon-phonon interaction is particularly interesting in the study of thermoelectric

---

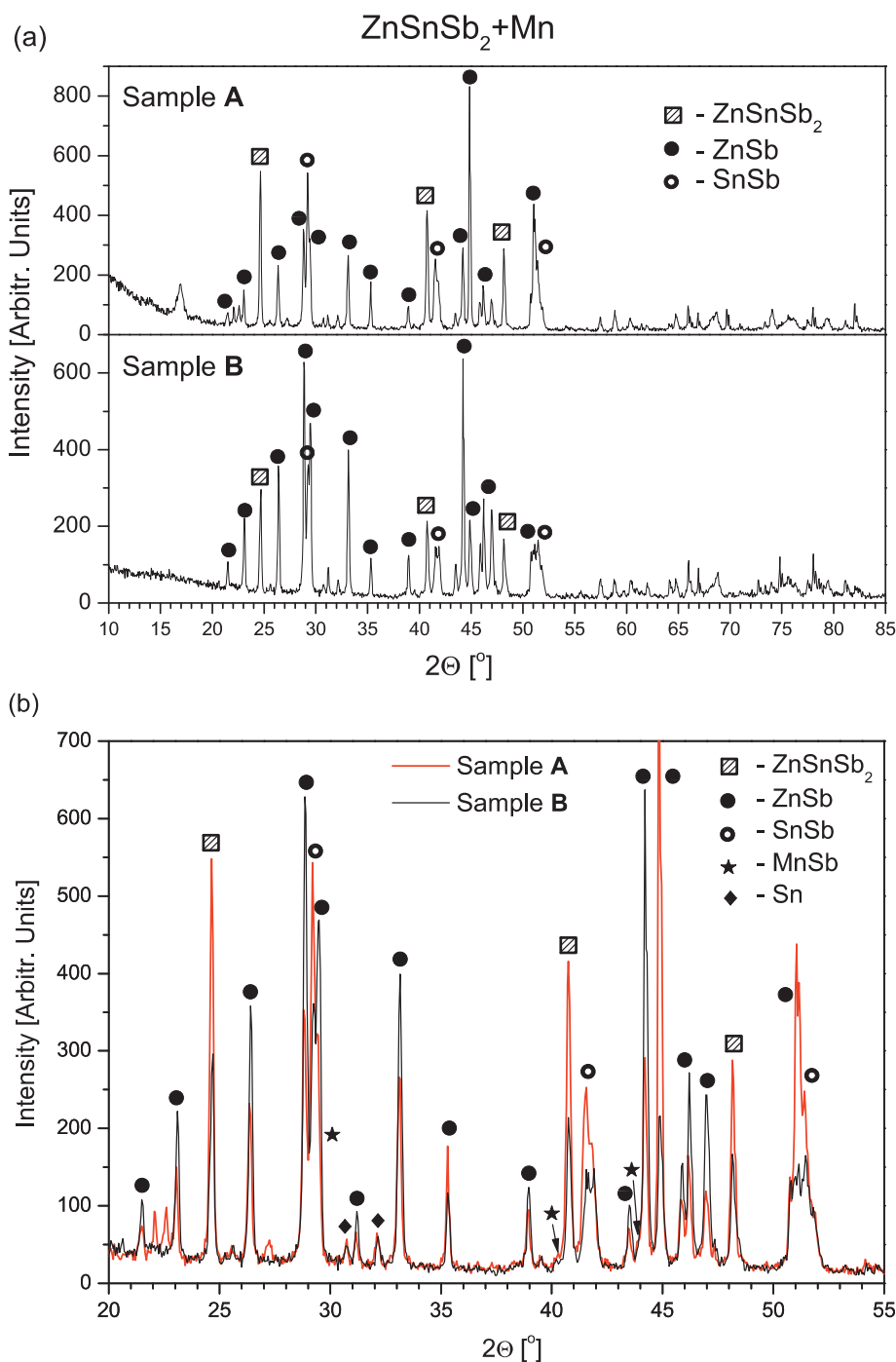**Fig. 1.** (a) X-ray diffraction pattern for ZnSnSb$_2$ + Mn samples which contain different amounts of Mn. The registered crystal phases are marked; (b) The two spectra are overlapped to compare their relative intensities.

materials, as well as their electrical and thermal conductivity, and their interdependence.

ZnSnSb$_2$ is not a homogeneous material, and the consequence is that even two samples from the same crystal can have significantly different properties. This is not surprising given the complicated ZnSnSb$_2$ microstructure. Our goal was to analyze the relationship between microstructures, their phonons and free carriers, their conditionality and interactions. For this purpose we used x-ray diffraction, optical microscopy, AFM and IR spectroscopy measurements. Obtained results were analyzed by applying the model for plasmon-phonon interaction.

2. Samples and characterization

ZnSnSb$_2$ semiconductor has a chalcopyrite structure, spatial group I42d, with lattice parameters $a \approx 6.275$ Å and $c \approx 12.55$ Å and ratio c/a close to 2. ZnSnSb$_2$ melts by a peritectic reaction at $T = 362$ °C with a possible phase transformation of the cubic modification into a tetragonal one at $T = 348$ °C [11,12]. The ZnSnSb$_2$ + Mn ferromagnetic semiconductors were synthesized using the method that makes it possible to obtain single crystals at temperatures below the temperature of the peritectic reaction.

The analyzed samples of Zn$_{1-x}$Mn$_x$SnSb$_2$ were synthesized by the direct fusion method. High purity components were used for the

synthesis: zinc single crystals (99.999%), shots of tin (99.999%), antimony single crystals (99.999%), and manganese powder (99.999%). They were mixed in stoichiometric ratios.

The reaction mixture was put into a quartz glass tube and heated up to 631 ˚C. After that, ampoules were quenched to 355 ˚C and then annealed at 355 ˚C. This is described in more detail in the papers [12,13]. The synthesized crystals were cut into slices of about 1.5 mm thickness.

The chemical composition of the samples (x) was determined using the energy dispersive x-ray fluorescence method (EDXRF) [10]. Obtained results showed that average Mn content (x) in the samples is between 0.027 and 0.138. All the studied crystals had the correct stoichiometry of $Zn_{1-x}Mn_xSnSb_2$ alloy equal to $1-x : x : 1 : 2$, within our measurement accuracy of about 10% of the x value.

Based on the magnetotransport measurements [10] it was found that electrical and magnetotransport parameters, such as resistivity, carrier concentration, and carrier mobility, do not depend linearly on composition, i.e. on the Mn content. Therefore, as mentioned above, two samples with a considerable difference in free-carrier concentrations were selected. The sample with $x = 0.027$ and $p = 13 \times 10^{21}$ cm^{-3} was labeled as sample A and the one with $x = 0.076$ and $p = 1.2 \times 10^{21}$ cm^{-3} as sample B. In this way we wanted to determine the connection between the free carriers and the structural and optical properties of the alloy.

The structural properties of these samples were investigated by the XRD powder technique. Measurements were done using a Philips PW 1050 diffractometer equipped with a PW 1730 generator, 40 kV $\times$ 20 mA, using Ni filtered Co Ka radiation of 0.1778897 nm at room temperature. The x-ray diffraction patterns were collected during 2 h in the range of $10 - 100°$ with a scanning step of 0.05˚ and 10 s scanning time per step. Phase analysis showed that besides the main phase of chalcopyrite $ZnSnSb_2$, the orthorhombic ZnSb, rhombohedral SnSb, and hexagonal MnSb phases are present in the samples. This is consistent with the literature [8,10].

An optical microscope was used to get an insight into the distribution of different phases of the material along the surface. Images were captured using Olympus BH series modular microscope with UIS objective lenses with 50x and 400x enhancement.

The surfaces of $ZnSnSb_2$ + Mn samples were examined in detail using Atomic Force Microscope (AFM), NTEGRA prima from NTMDT. The topography and phase images were acquired simultaneously by operating the AFM in semi-contact mode. NSG01 probes with a typical resonant frequency of 150 kHz and 10 nm tip apex curvature radius were used.

The far-infrared (FIR) reflectivity measurements were done with a BOMEM DA-8 Fourier-transform infrared spectrometer in the spectral range from 40 to 450 cm^{-1} at room temperature. A Hyper beamsplitter and deuterated triglycine sulfate (DTGS) pyroelectric detector were used.

3. Results and discussion

It is known that during the preparation of $ZnSnSb_2$ the polycrystalline material is formed, consisting of the main phase and ZnSb, SnSb and β-Sn inclusions [11].

The structure of the two selected samples was investigated by X-ray diffraction measurements. Obtained results with marked phases are presented in Fig. 1. In Fig. 1(b) the overlap of the results is shown, with the aim to compare their relative intensities. The list of XRD peaks positions and their corresponding Miller indices and phases is given in Table 1 in Supplementary Materials.

Besides the chalcopyrite $ZnSnSb_2$ phase the orthorhombic ZnSb, rhombohedral SnSb, Sn have also been registered, as well as weak lines from hexagonal MnSb inclusions. The idea was to detect differences in the structures of these two samples. It is obvious that diffraction lines corresponding to the $ZnSnSb_2$ phase (squares) are stronger for sample A

Table 1

Expected values of $ZnSnSb_2$ phonons of B_2 and E symmetries, from literature [26].

Phonon	B_2^1	B_2^2	B_2^3	E^1	E^2	E^3	E^4	E^5	E^6
Estimated value [cm^{-1}]	189	199	70	189	185	195	111	88	54

as well as lines of SnSb phase (open circles). Also, it is clear that lines corresponding to ZnSb (black circles) are mostly stronger for sample B. Existence of the Sn phase is evident, but lines corresponding MnSb phase are barely visible.

In order to examine the spatial distribution of the existing different crystal phases, the samples were recorded by an optical microscope with two different magnifications (50 $\times$ and 400 $\times$). Obtained micrographs are presented in Fig. 2.

Existing phases are clearly visible and they form multiphase structures. It should be noted that this is a very non-homogeneous material and that images from different parts of the samples differed, so the characteristic ones are selected and shown in Fig. 2.

In our previous work [9] is determined that gray fields are $ZnSnSb_2$ crystal, white ones correspond SnSb phase and that dark parts consist of ZnSb. Micrometric crystals of MnSb in the shape of dark circles were registered also.

Although microstructures of similar shapes have been formed in both samples, it is apparent that the surfaces significantly differ. Based on previous work [8,9,14], it can be concluded that these spherical and needle like microcrystals are ZnSb, MnSb, Sn, and Sb phases formed during crystallization of the material. As can be seen from Fig. 2. the sample B contains a lot of micron-sizes phases relatively evenly distributed over the surface (volume).

In order to more accurately examine the surface of the samples, we used atomic force microscopy (AFM) measurements. The characteristic results are presented in Fig. 3.

The surfaces of both samples have a granular structure. The sample A has evenly distributed grains over the entire surface with a few larger clusters and an average grain height of around ~100 nm (see Fig. 3(a) and the profile in Fig. 3(c)). The phase contrast in Fig. 3(b) originates exclusively from the abrupt changes in the height, indicating that the material properties of the sample A surface are homogeneous. The grains on the surface of the sample B are exclusively arranged into clusters which are not evenly distributed over the surface. The majority of the clusters reach several tens of nm in height, with a few exceptions having a height of ~100 nm (see Fig. 3(d) and the profile in Fig. 3(f)). The phase contrast of the sample B surface shows that the larger clusters have a distinct phase shift, seen as dark and white regions in Fig. 3(e), so that clusters have different material properties than the remainder of the surface.

This material is known to be difficult to synthesize and beside $ZnSnSb_2$ the ZnSb and SnSb phases are formed [11,15]. The series of $Zn_{1-x}Mn_xSnSb_2$ samples were synthesized under the same conditions with the only difference being the starting amounts of manganese and zinc [10]. Obviously, the small variation in the starting mixture causes rather different structures and properties of the materials.

It was found that a large concentration of lattice defects, especially in the cation sublattice, in $ZnSnSb_2$, as well as in other II-IV-V_2 semiconductors [16,17], causes a high hole concentration. In particular, Zn vacancies are those defects that lead to a very high concentration of holes [18,19,20]. Typical hole concentration in $ZnSnSb_2$ is 10^{20} cm^{-3} [15–20], in two-component p-type ZnSb it is 10^{19} cm^{-3} [18,19], while SnSb is a n-type material with metallic character and electron concentration of about 10^{22} cm^{-3} at 1.8 K [21]. Evidently, the electronic structure is very complex in this material.

It is difficult to say exactly what is the cause of different hole concentrations in the $Zn_{1-x}Mn_xSnSb_2$ samples, but it could be assumed that Zn vacancies are the main reason. Sample A has a higher content of
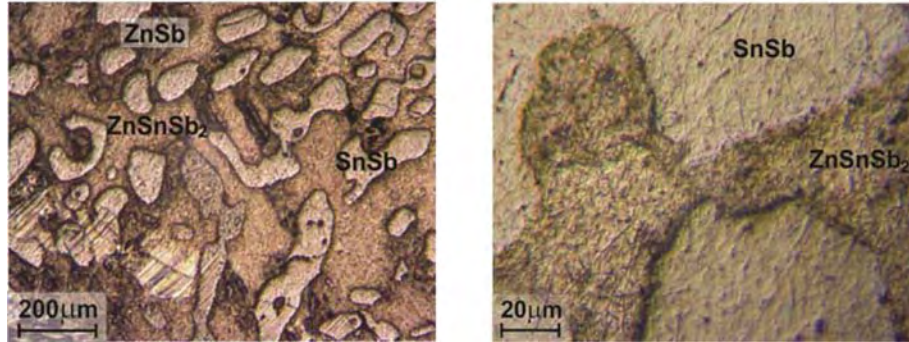
Sample A
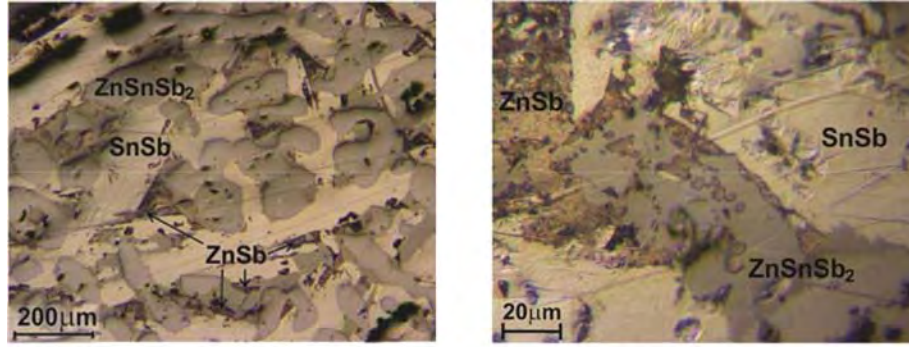
Sample B

Fig. 2. Micrographs of the ZnSnSb$_2$ + Mn samples surfaces with magnifications of 50 × and 400×.

SnSb, which is related to a higher deficiency of Zn atoms, and therefore higher hole concentration. So, the different concentrations of free carriers in the samples are a consequence of various defects and microstructures which are formed.

In order to examine the interaction of free carriers and a lattice, the far-infrared reflectivity spectra in the range 40–450 cm^{-1} at room temperature have been recorded. Obtained spectra are shown in Fig. 4.

It is obvious that the most distinct difference between the spectra relates to wave numbers above 220 cm^{-1}, where the high carrier concentration has a main influence. Also, in the range from 120 to 180 cm^{-1} the spectrum for sample B (black line) contains some phonon lines which are absent or attenuated in the spectrum for sample A (red line).

A detailed analysis of the obtained results was necessary. For the analysis of the spectra the fitting procedure which includes plasmon - phonon interaction was applied.

4. Plasmon - phonon interaction

In materials with high free carrier concentration a plasmon-phonon interaction should be taken into account, as it significantly affects the properties of the material. Its influence on the dielectric properties of the material is important for the analysis of the reflection spectra.

A theoretical model of the dielectric function in bulk materials [22] has been applied. The dielectric function $\varepsilon(\omega)$ describes dielectric properties of single crystal and includes classical oscillators corresponding to the TO-modes, and Drude part which takes into account the free carrier contribution:

$$\varepsilon(\omega) = \varepsilon_\infty + \sum_{k=1}^{l} \frac{\varepsilon_\infty(\omega_{LOk}^2 - \omega_{TOk}^2)}{\omega_{TOk}^2 - \omega^2 - i\gamma_{TOk}\omega} - \frac{\varepsilon_\infty \omega_P^2}{\omega(\omega + i\Gamma_P)} \quad (1)$$

In this equation ε_∞ is the high-frequency dielectric constant, ω_{TOk} and ω_{LOk} are the transverse and longitudinal optical-phonon frequencies, l is the number of phonons, ω_P is the plasma frequency, γ_{TOk}

and Γ_P are the phonon and plasmon damping. The use of such a dielectric function is valid in multiphase materials, since it is based on a phenomenological approach where the effective values of the material parameters are used, e.g. $\omega_p^2 = \omega_{p1}^2 + \omega_{p2}^2 + \omega_{p3}^2 + \cdots$.

As our ZnSnSb$_2$ + Mn samples have high concentration of free-carriers (p), and therefore high values of ω_P ($\omega_P^2 \sim p$), it is expected that plasma interacts with phonons. As a result the phonon frequencies are changed, i.e. their positions are shifted from the expected values. The phonon lines observed at the reflection spectra are these shifted modes i.e. coupled plasmon-phonon modes. So, the situation is much clearer if the dielectric function which takes a plasmon–phonon interaction in advance is used [23,24]. It also allows the possibilities that more than one phonon interact with plasma as well as existence of uncoupled phonons. That dielectric function is:

$$\varepsilon(\omega) = \varepsilon_\infty \frac{\prod_{j=1}^{n+1} (\omega^2 + i\gamma_{lj}\omega - \omega_{lj}^2)}{\omega(\omega + i\Gamma_P) \prod_{i=1}^{n} (\omega^2 + i\gamma_{ti}\omega - \omega_{ti}^2)} \cdot \prod_{k=1}^{s} \frac{\omega^2 + i\gamma_{LOk}\omega - \omega_{LOk}^2}{\omega^2 + i\gamma_{TOk}\omega - \omega_{TOk}^2}$$

$$(2)$$

The first fraction in Eq. (2) describes coupling of a plasmon and n LO phonons, where parameters ω_{lj} and γ_{lj} are eigenfrequencies and damping coefficients of the longitudinal component of the coupled phonons. ω_{ti} and γ_{ti} are frequencies and damping of transverse component of these phonons. Γ_P is the plasma damping. The second factor in Eq. (2) represents s uncoupled phonons of the crystal, wherein ω_{LOk} (ω_{TOk}) and γ_{LOk} (γ_{TOk}) are LO (TO) frequencies and damping coefficients of the k-th uncoupled phonon of the crystal.

The analysis of the obtained reflection spectra was performed by a fitting procedure, by adjusting the parameters of Eq. (2) in order to obtain a match between the experimental and theoretical curves. The values of ω_{lj} and ω_{ti} are directly obtained in this way while the ω_P and ω_{LO} values are calculated [25]. It can be seen that the positions of the ω_{l2} and ω_{l4} are significantly different for samples A and B. The behavior of phonons and interactions with plasma were analyzed based on the data thus obtained.
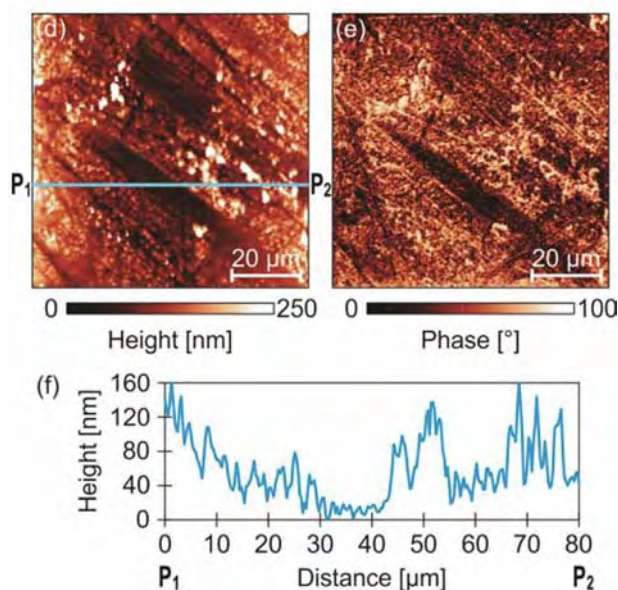
Sample A
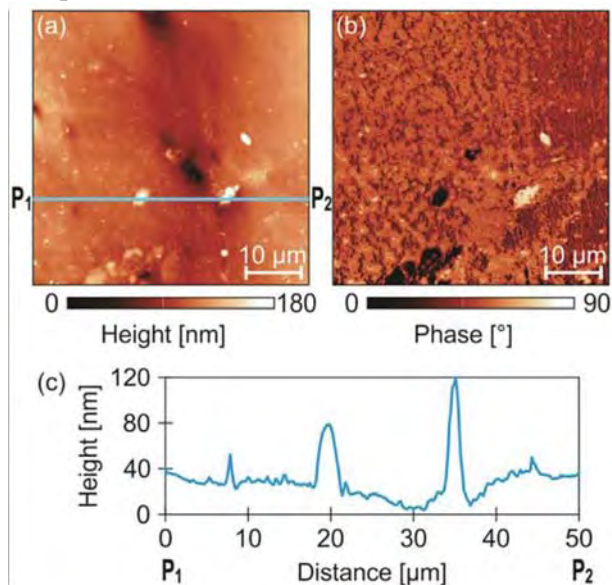
Sample B

Fig. 3. (a) AFM topography and (b) corresponding phase-contrast image of sample A; (c) Height profile taken along the straight solid line in (a) from point P_1 to point P_2; Figures (d), (e), and (f) refer to sample B in the same way.

The phonons of $ZnSnSb_2$ which are IR active are known from literature [26], and they are of B_2 and E symmetries. Their estimated values are given in Table 1.

Plasmon - phonon interaction commonly refers to the coupling of the plasma and one phonon [27]. In that case two coupled modes appear ω_{l1} and ω_{l2}, often labeled as ω_+ and ω_-. In the case of $ZnSnSb_2$, based on data obtained by fitting procedure, it was established that the plasma interacts with three phonons of B_2 symmetry [28,29,30]. As a result of that their positions are shifted and instead three B_2 modes there are four coupled modes ω_{l1}, ω_{l2}, ω_{l3} and ω_{l4}. Obtained values are shown as black points in Fig. 6. Their positions are different for the two samples because of the different influences of the plasma ($\omega_P^2 \sim p$). Because of the high plasma frequency of sample A, the ω_{l4} has high value of 675 cm^{-1} which is outside of the measured range.

For ease of analysis, it is common to draw a dependency diagram of obtained parameters (ω_{lj}, ω_t, ω_{TO}, ω_{LO}) on plasma frequency ω_P, as
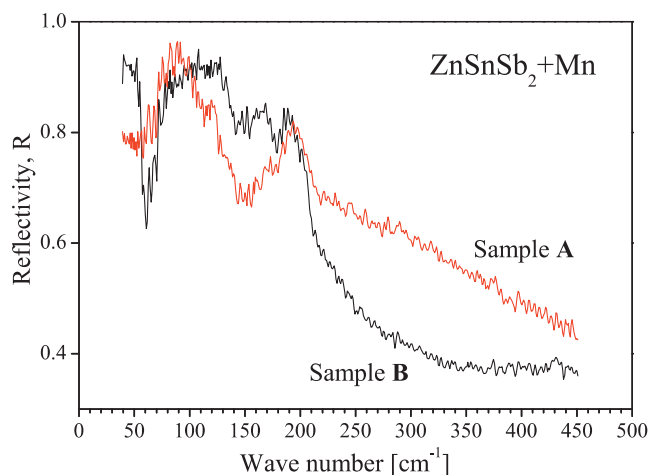
Fig. 4. Far-infrared reflectivity spectra of $ZnSnSb_2$ + Mn.
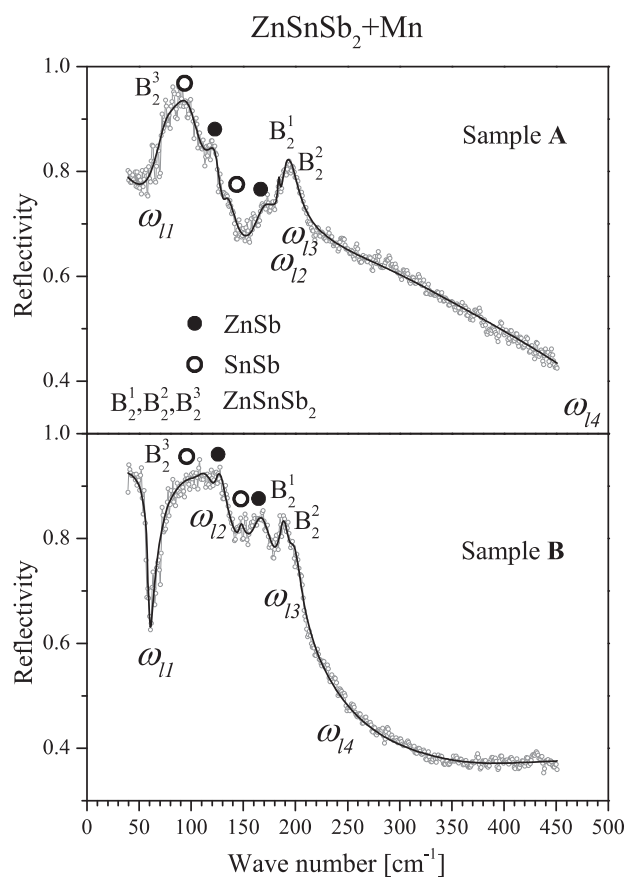
Fig. 5. Analyzed reflection spectra; experimental data are represented by circles while black lines are theoretical curves; registered optical phonons are indicated on the spectra.

shown in Fig. 6. The full lines are solutions of $Re\{\varepsilon(\omega)\} = 0$ from Eq. (1). It should be noted that line ω_{l3} between B_2^1 and B_2^2 phonons is barely visible because they are very close. The lines are calculated for five different values of plasma damping Γ_p (Fig. 6) ($\Gamma_p = 1/\tau$, where τ is a lifetime of plasmon). This was done to determine Γ_p interdependence with plasmon - phonon interaction.

The obtained values of plasma damping and plasma frequency of samples A and B are: $\Gamma_{pA} = 500$ cm^{-1}, $\Gamma_{pB} = 375$ cm^{-1}, $\omega_{pA} = 837$ cm^{-1} and $\omega_{pB} = 405$ cm^{-1}. It should be noted that these parameters represent the effective values that describe the sample as a
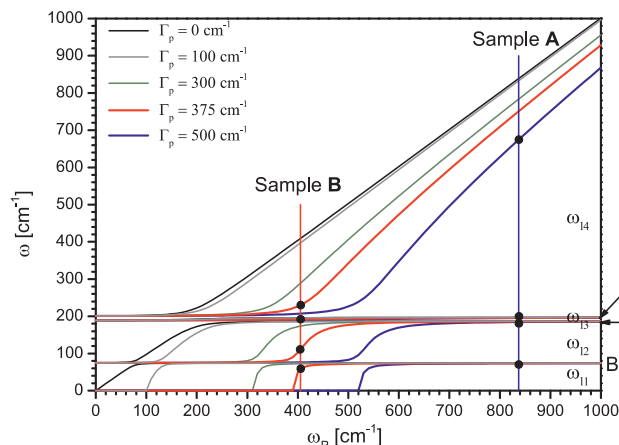
Fig. 6. Analysis of plasmon - three-phonons interaction; Full lines are obtained from Eq.(1), as the solutions of Re$\{\varepsilon(\omega)\}$ = 0, for various values of Γ_p; Black points represent experimentally obtained data for ω_{lj} for both samples (Eq. (2)).

whole. It could be expected (based on p_A and p_B values and $\omega_p^2 \sim p$) that ω_{pA} and ω_{pB} differ about three times, which was not established. Plasma frequency is defined as $\omega_p^2 = (n_p e^2)/(\varepsilon_0 \varepsilon_\infty m_h^*)$, i.e. it includes other parameters of the material. Thus, by determining the plasma frequency and plasma damping the other properties of the material can be analyzed.

Besides phonons of B_2 symmetry which interact with plasma, other ZnSnSb$_2$ phonons are not registered on the IR reflectivity spectra. However, characteristic phonons of the other phases can be identified, as can be seen in Fig. 5. It was necessary that these phonons are not covered by the plasmon - phonon interaction. ZnSb modes are noticed at about 125 and 165 cm^{-1}, which is in agreement with results from the literature [31]. Two modes that correspond to SnSb phase are at about 94 and 145 cm^{-1}, which matches the previously obtained data [9,32]. The appearance of these modes is expected due to the significant presence of ZnSb and SnSb phases in the samples. MnSb phonons are not registered, i.e. it was not possible to discern them due to the small amount of that phase.

Based on the performed analyses, it can be seen that different microstructures formed in the investigated samples lead to high concentrations of free carriers, but which are ten times different from each other. Those high values cause plasmon - B_2 phonons interaction. That can be used to analyze optical and electrical properties of the materials, as well as other parameters, such as dielectric constants, effective mass of charge carriers and phonon lifetimes. In this way, the multiphase material with different microstructures was analyzed as a whole.

Investigation of thermoelectric properties of ZnSnSb$_2$ is a current issue [5,15,33]. The analysis of plasmon - phonon interaction performed in this paper can significantly assist in the study and understanding of thermoelectric processes in this as in other semiconducting polycrystalline materials [34].

5. Conclusion

Two samples of ZnSnSb$_2$ + Mn with different amounts of manganese were analyzed in this paper. The small difference in the initial composition of the material led to a difference of ten times in the free carrier concentrations. Their structural properties were examined by x-ray diffraction, optical microscopy, and AFM. Several different phases were registered - ZnSnSb$_2$, ZnSb, SnSb, and small amounts of Sn and MnSb. These phases form different microstructures, which is related to the large irregularities of the lattice. It was found that the high free carrier concentrations are caused by a large number of defects, especially zinc vacancies.

The optical characteristics of these multiphase materials were

examined, whereby the samples were considered as a whole. Based on the analysis of IR reflection spectra the presence of a plasmon - phonons interaction was confirmed. It was determined that three ZnSnSb$_2$ phonons of B_2 symmetry interact with plasma, which led to the change of their positions. It is clear that strong plasmon - phonon interaction modifies optoelectronic properties of the ZnSnSb$_2$ + Mn samples, and that phonon positions depend on a free carrier concentration. A detailed analysis of this interaction also provides insight into the behavior of other material parameters, such as dielectric constants, effective mass of charge carriers and phonon lifetimes. Also, vibration modes of ZnSb and SnSb phases were registered on the spectra. Knowledge of phonon behavior in a material, as well as interaction with plasma, is very important for studying its thermoelectric properties.

Declaration of competing interest

The authors declare that there is no conflict of interest in this paper.

Acknowledgement

Appendix A. Supplementary material

Supplementary data to this article can be found online at https://doi.org/10.1016/j.infrared.2020.103345.

References

[1] J.L. Shay, J.H. Wernick, Ternary Chalcopyrite Semiconductors: Growth, Electronic Properties, and Applications, Chapter 3 - Electronic Structure of II-IV-V$_2$ Compounds, Pergamon Press, New York, 1975, pp. 79–109 https://doi.org/10.1016/B978-0-08-017883-7.50008-1.

[2] W. Dobrowolski , J. Kossut, T. Story. II–VI and IV–VI Diluted Magnetic Semiconductors – New Bulk Materials and Low-Dimensional Quantum Structures. Handbook of Magnetic Materials 15 (2003) pp. 289-377, (Elsevier, Amsterdam, 2003). https://doi.org/10.1016/S1567-2719(03)15003-2.

[3] L. Kilanski, M. Górska, W. Dobrowolski, E. Dynowska, M. Wójcik, B.J. Kowalski, J.R. Anderson, C.R. Rotundu, D.K. Maude, S.A. Varnavskiy, I.V. Fedorchenko, S.F. Marenkin, Magnetism and magnetotransport of strongly disordered Zn$_{1-x}$Mn$_x$GeAs$_2$ semiconductor: The role of nanoscale magnetic clusters, J. Appl. Phys. 108 (2010) 073925, , https://doi.org/10.1063/1.3490231.

[4] S.F. Marenkin, A.D. Izotov, I.V. Fedorchenko, V.M. Novotortsev, Manufacture of magnetic granular structures in semiconductor-ferromagnet systems, Russ. J. Inorg. Chem. 60 (2015) 295300, , https://doi.org/10.1134/S0036023615030146.

[5] M. Ito, Y. Ohishi, H. Muta, K. Kurosaki, S. Yamanaka, Thermoelectric properties of Zn-Sn-Sb based alloys, Mater. Res. Soc. Symp. Proc. 1314 (2011), https://doi.org/10.1557/opl.2011.618.

[6] P. Balasubramanian, M. Battabyal, D. Sivaprahasam, R. Gopalan, On the formation of phases and their influence on the thermal stability and thermoelectric properties of nanostructured zinc antimonide, J. Phys. D: Appl. Phys. 50 015602 (11 (2017) pp), https://doi.org/10.1088/1361-6463/50/1/015602.

[7] G. Coquil, B. Fraisse, S. Biscaglia, D. Ayme-Perrot, M.T. Sougrati, L. Monconduit, ZnSnSb$_2$ anode: A solid solution behavior enabling high rate capability in Li-ion batteries, J. Power Sour. 441 (2019) 227165, , https://doi.org/10.1016/j.jpowsour.2019.227165.

[8] O. Zobac, J. Sopousek, J. Bursik, A. Zemanova, P. Roupcova, Experimental Study of the Sb-Sn-Zn Alloy System, Metall. Mater. Trans. 45A (2014) 1181–1188, https://doi.org/10.1007/s11661-013-2104-1.

[9] M. Romcevic, M. Gilic, L. Kilanski, W. Dobrowolski, I.V. Fedorchenko, S.F. Marenkin, N. Romcevic, Phonon properties of ZnSnSb$_2$ + Mn semiconductors: Raman spectroscopy, J. Raman Spectrosc. 49 (2018) 1678–1685, https://doi.org/10.1002/jrs.5421.

[10] L. Kilanski, M. Gorska, A. Slawska-Waniewska, S. Lewinska, R. Szymczak, E. Dynowska, A. Podgorni, W. Dobrowolski, U. Ralevic, R. Gajic, N. Romcevic, I.V. Fedorchenko, S.F. Marenkin, High temperature magnetic order in Zn$_{1-x}$Mn$_x$SnSb$_2$ + MnSb nanocomposite ferromagnetic semiconductors, J. Phys.:Condens. Matter. 28 (2016) 336004, , https://doi.org/10.1088/0953-8984/28/33/336004.

[11] A. Tenga, F.J. Garcia-Garcia, A.S. Mikhaylushkin, B. Espinosa-Arronte, M. Andersson, U. Haussermann, Sphalerite − Chalcopyrite Polymorphism in Semimetallic ZnSnSb$_2$, Chem. Mater. 17 (2005) 6080–6085, https://doi.org/10.

1021/cm0516053.

[12] A. Tenga, F.J. Garcia-Garcia, Y. Wu, N. Newman, U. Haussermann, Metal-nonmetal transition in the sphalerite-type solid solution $[ZnSnSb_2]_{1-x}[2(InSb)]_x$, J. Solid State Chem. 182 (2009) 1438–1442, https://doi.org/10.1016/j.jssc.2009.03.015.

[13] M. Bostrom, S. Hovmoller, Preparation and Crystal Structure of the Pseudo-Decagonal Approximant Mn_3Ga_5, J. Solid State Chem. 153 (2000) 398–403, https://doi.org/10.1006/jssc.2000.8790.

[14] C. Wang, Y. Xu, S. Yang, H. Jiang, J. Li, J. Zhu, S. Yang, X. Liu, Experimental Determination of Phase Equilibria in the Sn-Zn-Sb System, J. Phase Equil. Diff. 36 (2015) 350–356, https://doi.org/10.1007/s11669-015-0387-1.

[15] A. Nomura, S. Choi, M. Ishimary, A. Kosuga, T. Chasapis, S. Ohno, G.J. Snyder, Y. Ohishi, H. Muta, S. Yamanaka, K. Kurosaki, Chalcopyrite $ZnSnSb_2$: A Promising Thermoelectric Material, ACS Appl. Mater. Interf. 10 (2018) 43682–43690, https://doi.org/10.1021/acsami.8b16717.

[16] V.N. Brudnyi, Electronic properties and pinning of the Fermi level in irradiated $II–IV–V_2$ semiconductors, Semiconductors 43 (2009) 1146–1154, https://doi.org/10.1134/S1063782609090085.

[17] V.G. Voevodin, S.N. Grinyaev, O.V. Voevodina, Nonstoichiometry and point defects in nonlinear optical crystals $A^2B^4C_2^5$, Mater. Sci. Semicond. Proces. 6 (2003) 385–388, https://doi.org/10.1016/j.mssp.2003.07.006.

[18] X. Song, M. Schrade, N. Maso, T.G. Finstad, Zn vacancy formation, Zn evaporation and decomposition of ZnSb at elevated temperatures: Influence on the microstructure and the electrical properties, J. Alloys Comp. 710 (2017) 762–770, https://doi.org/10.1016/j.jallcom.2017.03.339.

[19] L.V. Prokofieva, P.P. Konstantinov, A.A. Shabaldin, On the tin impurity in the thermoelectric compound ZnSb: Charge-carrier generation and compensation, Semicond 50 (2016) 741–750, https://doi.org/10.1134/S1063782616060208.

[20] L. Bjerg, G.K.H. Madsen, B.B. Iversen, Ab initio Calculations of Intrinsic Point Defects in ZnSb, Chem. Mater. 24 (2012) 2111–2116, https://doi.org/10.1021/cm300642t.

[21] B. Liu, J. Wu, Y. Cui, H. Wang, Y. Liu, Z. Wang, Z. Ren, G. Cao, Superconductivity in SnSb with a natural superlattice structure, Supercond. Sci. Technol. 31 (2018) 7, https://doi.org/10.1088/1361-6668/aae6fe 125011.

[22] Abstreiter G., Cardona M., Pinczuk A. Light scattering by free carrier excitations in semiconductors. In: Cardona M., Güntherodt G. (eds) Light Scattering in Solids IV. Topics in Applied Physics, vol 54. Springer, Berlin, Heidelberg. (1984) https://doi.org/10.1007/3-540-11942-6_20.

[23] A.A. Kukharskii, Plasmon-phonon coupling in GaAs, Solid State Commun. 13 (1973) 1761–1765, https://doi.org/10.1016/0038-1098(73)90724-2.

[24] N. Romcevic, M. Romcevic, W.D. Dobrovolski, L. Kilanski, M. Petrovic, J. Trajic,

B. Hadzic, Z. Lazarevic, M. Gilic, J.L. Ristic-Djurovic, N. Paunovic, A. Reszka, B.J. Kowalski, I.V. Fedorchenko, S.F. Marenki, Far-infrared spectroscopy of $Zn1 − xMnxGeAs2$ single crystals: Plasma damping influence on plasmon – Phonon interaction, J. Alloys Comp. 649 (2015) 375–379, https://doi.org/10.1016/j.jallcom.2015.07.087.

[25] J. Trajic, N. Romcevic, M. Gilic, M. Petrovic Damjanovic, M. Romcevic, V.N. Nikiforov, Optical properties of $PbTe_{0.95}S_{0.05}$ single crystal at different temperatures: Far - infrared study, Optoelec. Adv. Mater. Rap. Comm. 6 (2012) 543–546.

[26] F.W. Ohrendorf, H. Haeuseler, Lattice Dynamics of Chalcopyrite Type Compounds. Part I. Vibrational Frequencies, Cryst. Res. Technol. 34 (1999) 339–349, https://doi.org/10.1002/(SICI)1521-4079(199903)34:3 < 339:: AID-CRAT339 > 3.0. CO;2-E.

[27] Klein M.V. Electronic Raman Scattering. In: Cardona M. (eds) Light Scattering in Solids. Topics in Applied Physics, vol 8. Springer, Berlin, Heidelberg (1975). https://doi.org/10.1007/978-3-540-37568-5_4.

[28] M. Petrovic, N. Trajic, W.D. Dobrowolski, M. Romcevic, B. Hadzic, M. Gilic, A. Mycielski, Far-infrared spectroscopy of $CdTe_{1−x}Se_x$(In): Phonon properties, Infrared Phys. Tech. 67 (2014) 323–326, https://doi.org/10.1016/j.infrared.2014.08.010.

[29] M. Romcevic, N. Romcevic, W. Dobrowolski, L. Kilanski, J. Trajic, D.V. Timotijevic, E. Dynowska, I.V. Fedorchenko, S.F. Marenkin, Optical properties and plasmon – Two different phonons coupling in ZnGeAs2 + Mn, J. Alloys Comp. 548 (2013) 33–37, https://doi.org/10.1016/j.jallcom.2012.09.017.

[30] I.J. Luxmoore, C.H. Gan, P.Q. Liu, F. Valmorra, P. Li, J. Faist, G.R. Nash, Strong coupling in the far-infrared between graphene plasmons and the surface optical phonons of silicon dioxide, ACS Photonics 1 (2014) 1151, https://doi.org/10.1021/ph500233s.

[31] D.V. Smirnov, D.V. Mashovets, S. Pasquier, J. Leotin, P. Puech, G. Landa, Yu.V. Roznovan, Long-wavelength optical phonons of $Cd_x Zn_{1-x}Sb$ mixed crystals, Semicond. Sci. Technol. 9 (1994) 333–337.

[32] P. Nithyadharseni, M.V. Reddy, B. Nalini, M. Kalpana, B.V.R. Chowdari, Sn-based Intermetallic Alloy Anode Materials for the Application of Lithium Ion Batteries, Electrochim. Acta 161 (2015) 261–268, https://doi.org/10.1016/j.electacta.2015.02.057.

[33] Yu M. Basalaev, Ab Initio Study of the $ZnSnSb_2$ Semiconductor, Semiconductors 52 (2018) 1715–1720, https://doi.org/10.1134/S1063782618130043.

[34] Q. Xu, J. Zhou, T.H. Liu, G. Chen, Effect of electron-phonon interaction on lattice thermal conductivity of SiGe alloys, Appl. Phys. Lett. 115 (2019) 023903, , https://doi.org/10.1063/1.5108836.
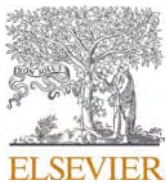
Surface optical phonon (SOP) mode in ZnS/Poly (methylmethacrylate) nanocomposites

Milica Curcic [a], Branka Hadzic [a], Martina Gilic [a,*], V. Radojevic [b], Andjelika Bjelajac [c], Ivana Radovic [d], Dejan Timotijevic [a], Maja Romcevic [a], Jelena Trajic [a], Nebojsa Romcevic [a]

[a] Institute of Physics Belgrade, University of Belgrade, 11080, Belgrade, Serbia
[b] Faculty of Technology and Metallurgy, University of Belgrade, 11000, Belgrade, Serbia
[c] Inovation Center of Faculty of Technology and Metallurgy, 11000, Belgrade, Serbia
[d] Vinča Institute of Nuclear Sciences, University of Belgrade, 11000, Belgrade, Serbia

ABSTRACT

The polymer nanocomposite ZnS/Poly (methylmethacrylate) was prepared by the solution casting method and its structural and optical properties were investigated using XRD, SEM, TEM, HRTEM, and Raman spectroscopy. The basic material, ZnS, has the cubic structure and its crystallite size was estimated to be 2.3 nm, which implies that a strong confinement regime is in effect. Analysis of Raman spectra was performed using the fitting procedure based on effective medium theory. As a result, the surface optical phonon (SOP) mode was detected. It was found that the shape and position of the SOP mode depend on the type of the composite.

1. Introduction

As a semiconductor, the zinc sulfide (ZnS) has gained considerable attention and is found to be applicable in optoelectronic, electroluminescent, and blue light emitting diode devices [1–8]. ZnS has two available allotropic forms – the wurtzite and zinc blende. The crystallographic form of wurtzite is hexagonal, whereas the zinc blende has the cubic crystallographic structure, is more stable and as such, is more common of the two. The ZnS in the form of the bulk material has a direct band gap positioned primarily in the UV region [9,10]. The wurtzite and the zinc blende forms have the band gaps of 3.77 and 3.72 eV, respectively. The band gap increases with a decrease in size from the bulk to the nanoscale [11,12]. Since ZnS easily absorbs moisture and oxidizes in air [13], it is not very stable as a pure compound in the atmosphere. Therefore, surfactants or capping agents are added to the ZnS nanoparticles to prevent structural transformation and surface reactions.

A nanocomposite consists of two or more different materials in which at least one of the components has a dimension smaller than 100 nm [14]. In polymer nanocomposites, the composing elements are an organic polymermatrix and inorganic components (semiconductors). Nanocomposites can include three dimensional metal matrix composites, lamellar composites, colloids, porous materials, gels, as well as copolymers in which nanosized material is dispersed within the bulk matrix. The properties of the nanocomposites depend on their components, morphology, and interface characteristic. In order to extend the area of their potential applications, mechanical, thermal, and electronic properties of conventional polymer materials had to be improved [15, 16]. As a thermoplastic polymer, Poly (methylmethacrylate) i.e. PMMA has many excellent properties. Its favorable properties include excellent transparency and ultraviolet resistance, as well as good abrasion resistance, hardness, and stiffness. Consequently, it is widely used in many applications, for example in lenses, light pipes, bathroom fittings, skylights, toys, etc. In addition, PMMA is non-degradable and biocompatible, which qualifies it for use in tissue engineering where typical applications are fracture fixations, intraocular lenses, and dentures [17].

For nanocrystals of relatively small dimensions, surface modes and the effects of dimension are expected to appear, along with the normal modes of an infinite lattice. Namely, in the frequency range between longitudinal optical phonon frequency (ω_{LO}) and transversal optical phonon frequency (ω_{TO}), a new mode known as a surface optical phonon (SOP) mode appears.

In our previous papers [18–22] we worked on investigating surface optical phonons (SOP) in semiconducting nanoparticles or thin films. In all those cases, SOP appeared because the nano-objects of investigated materials were well separated in the air.

In this paper we report the synthesis and structural and optical

* Corresponding author.
  E-mail address: martina@ipb.ac.rs (M. Gilic).

studies of polymer nanocomposites prepared by the incorporation of ZnS nanoparticles (pure and functionalized with silane) into the matrices of polymer PMMA. The studies of the metal sulfides/polymer nanocomposites were carried out by XRD, SEM, TEM, HRTEM and Raman spectroscopy. By extending our research to nanoparticles embedded in polymer matrix we would like to complete the knowledge about the SOP properties in A_2B_6 semiconducting materials.

2. Materials and methods

2.1. Initial components

Commercially available PMMA pellets (Acryrex® CM205, Chi Mei Corp. Korea, Mw ≈ 90400 g/mol, n = 1.49, λ = 633 nm) were used as a matrix in sample preparation. Dimethylformamide (DMF, anhydrous, 99.8%, Sigma-Aldrich) was used as a solvent. For surface modification with QD3-Mercaptopropyltrimethoxysilane (MPTMS) – Dynasylane, Evonik Industries and toluene, hexane (Sigma Aldrich) were used.

Mechanochemical synthesis of ZnS nanoparticles was performed in a Pulverisette 6 planetary mill. The milling parameters were: the weight charge of total powder mixture in the mill of 14.2 g, 50 balls with the diameter of 10 mm and ball charge in the mill of 360 g, milling chamber and balls made of tungsten carbide, and rotation speed of the planet carrier of 500 rpm. The milling time was 10 min and the argon atmosphere was used as a protective medium in the mill.

The X-ray diffraction measurements of the ZnS powders obtained after 10 min milling times were performed using Philips 1050 X-ray powder diffractometer with Ni-filtered Cu Kα radiation and Brag-Bretano focusing geometry. XRD pattern is presented in Fig. 1a and shows mainly the reflection of cubic phases (JCPDS 03-0524). The space group of the cubic unit cell is $F\bar{4}3m$ (T_d^2) and the cell contains four formula weights of ZnS [23]. The refracting planes denoted with (hkl) indices are (111), (220), and (311). Using the X-ray Line Profile Fitting

Program (XFIT) with a Fundamental Parameters convolution approach to generating line profiles the coherent domain size of the synthesized powder was determined to be 2.3 nm.

In Fig. 1b, the TEM analysis was employed to identify regions with pure zinc, pure sulfur, or homogeneous ZnS distribution. In the bright field image the morphology looks like an aggregate produced by smaller clusters compacted during milling.

The high resolution TEM (HRTEM-Phillips Tecnai 200 operated at 200 kV), is an excellent method to study metal sulfide semiconductor nanostructures, where core–shell or stoichiometric system can be distinguished [24,25]. In Fig. 1c an area of 16 nm × 16 nm is observed. Several clusters are clearly identifiable, in particular, three of them of sizes of 2.6, 3.7, and 3.4 nm.

2.2. Modification of ZnS QDs

ZnS nanoparticles were dispersed in 150 ml of toluene round-bottom flask equipped with a reflux condenser under the flow of nitrogen. When the boiling point of toluene was achieved, 1 g of 3-Mercaptopropyltrimethoxysilane (MPTMS), which is further on referred to as silane, was added and the resulting white suspension was stirred and refluxed for 22 h. After the completion of the reaction, the particles were filtrated and washed with hexane to remove the excess of silane. The particles were dried at 40 °C in the oven for 12 h and then used in the preparation of nanocomposites.

2.3. Preparation of PMMA and ZnS/PMMA nanocomposites

In the preparation of precursor solutions, DMF was used as the solvent for the PMMA. In a typical process, homogenous solution of polymer with respect to the amount of composite films was prepared by dissolving the polymeric granules (PMMA, m = 10.65 g) in 40 ml of DMF under magnet stirring for 48 h at room temperature on the mixture. The concentration of PMMA in DMF solution was 22 % wt. Therefore, PMMA was produced in the form of a film by solvent casting method. Namely, the resulting PMMA solution was casted in a horizontally positioned Petri dish. The solution was air dried for 24 h at room temperature and the obtained film was kept in a dryer for additional 24 h at 60 °C in order to eliminate the residual solvent.

In the synthesis of quantum dots/polymer (ZnS/PMMA) composite films the solutions were obtained in a similar manner. The concentration of PMMA in the DMF solution was 22 % wt. The concentration of ZnS particles in the films was 0.06 % wt. The mixture was stirred for 24 h. The ZnS/PMMA films were produced using the identical procedure as was the case with the PMMA. Namely, the solution was casted by placing it on a Petri dish and drying it for 24 h at room temperature, which was followed by drying in a dryer oven for additional 24 h at 60 °C.

The morphology of samples was investigated by SEM using the high resolution electron microscope MIRA3 TESCAN with accelerating voltage of 5, 12, and 20 kW. The SEM micrographs of ZnS nanoparticles and ZnS/PMMA nanocomposite are presented in Fig. 2. The micrographs of ZnS nanoparticles and nanoparticles in silane are given in Fig. 2a and b. The micrographs show that the powder is composed of well-defined and separated nanoparticles as well as of nanoparticle clusters that have spherical shape and approximate size of 17–30 nm. There are no macroscopic defects like a pinhole, peeling, or cracks. The clusters of about 60 nm, are visible in Fig. 2c and d.

3. Results and discussion

The Raman spectra of the PMMA, ZnS nanoparticles, ZnS nanoparticles in silane, ZnS/PMMA nanocomposite, and ZnS in silane/PMMA nanocomposite, measured in the spectral range of 200–650 cm^{-1} at room temperature, are presented in Fig. 3. The micro- Raman spectra were taken in the backscattering configuration and analyzed by the TriVista 557 system equipped with a nitrogen cooled charge-coupled-
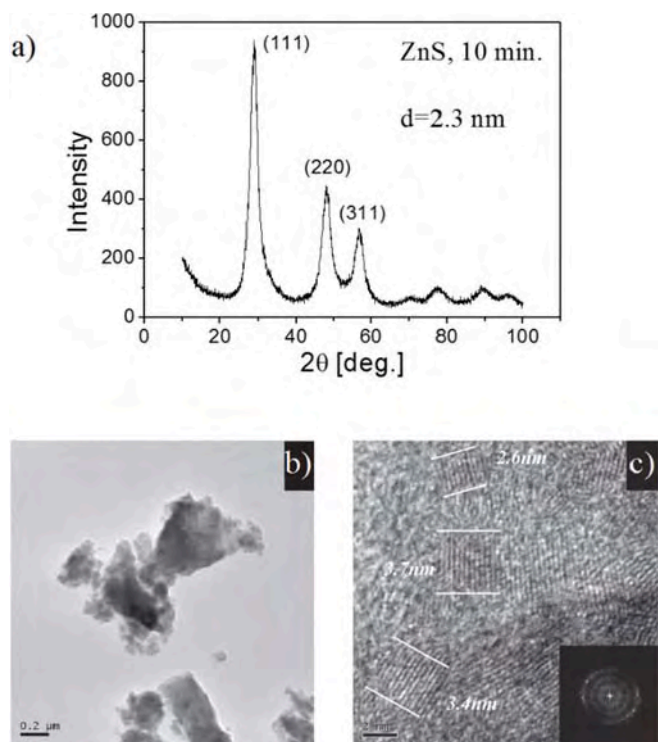

Fig. 1. (a) The XRD spectra of the ZnS powder after 10 min milling time, (b) the TEM analysis of mechanochemically synthesized ZnS nanoparticles – bright field, and (c) the HRTEM analysis of ZnS nanoparticles. The size of nanoparticles is determined to be approximately 3 nm.
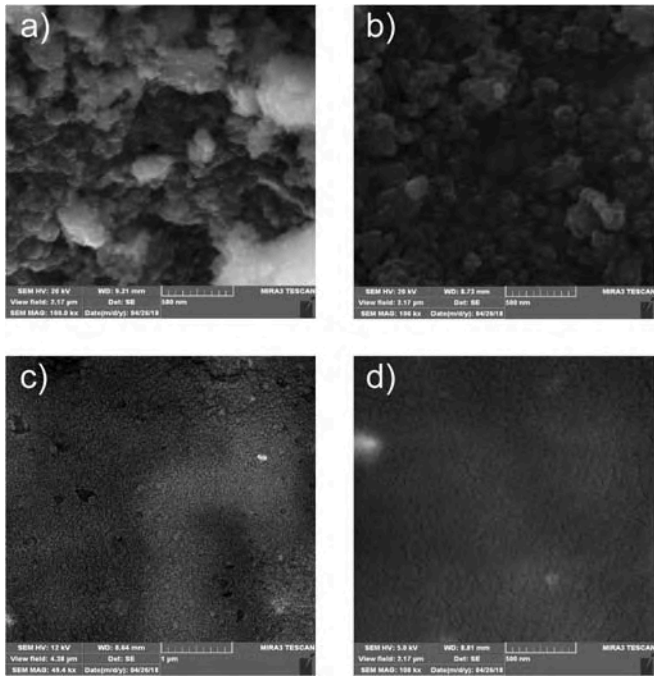
Fig. 2. SEM images. (a) ZnS nanoparticles, (b) ZnS nanoparticles in silane, (c) ZnS/PMMA nanocomposite, and (d) ZnS in silane/PMMA nanocomposite.

device detector. As an excitation source, the 532 nm line of Ti:Sapphire laser was used. This excitation energy is in the off-resonance regime for all the considered materials; consequently, for the ZnS nanoparticles as well. Since Raman spectra are usually analyzed by decomposing them into Lorentzian or Gaussian shape elements, we chose to assume that all phonon lines are of the Lorentzian type.

The Raman spectrum of PMMA is presented in Fig. 3a. Intense modes at 236, 299, 362, 402, 481, 555, and 599 cm^{-1}, as well as 4 modes of lesser intensity at about 278, 318, 382, and 505 cm^{-1} were detected. The theoretically fitted curve, which is obtained by convolving 11 Lorentz profiles and the line that describes Rayleigh scattering is also given in Fig. 3a. The obtained result is in a good agreement with the values given in the literature [26,27].

Fig. 3b shows the Raman spectrum of cubic ZnS nanoparticles. In the experimentally obtained spectrum the dominant wide structures are detected at 218, 264, 347, and 483 cm^{-1}.

As determined in Refs. [23,28–30], the Raman frequency of 347 cm^{-1} is associated to the A_1 and E_1 symmetry LO modes. At a lower frequency, a resolvable doublet with the peak at 264 cm^{-1} is observed. These peaks are assigned to the A_1 and E_1 TO modes. The mode at 218 cm^{-1} can be assigned to the LA symmetry. The appearance of this mode in the spectrum is a consequence of the violation of the selection rules due to the nanodimension. The Raman active mode at 347 cm^{-1} is asymmetrical, and the asymmetric peak broadening occurs toward the low-frequency side of the Raman spectrum. The dashed curve in Fig. 3b is obtained as the convolution of the Lorentz shapes of the known phonons of ZnS. Due to the discussed asymmetry of LO phonon at 347 cm^{-1}, this theoretically obtained curve differs from the experimental results.

Similar effect is registered in the Raman spectra of other samples. In the spectrum corresponding to the ZnS in silane, the modes at 259, 345, 489, 520, and 576 cm^{-1} are registered and are depicted in Fig. 3c. Fig. 3d shows that the modes of ZnS nanoparticles in PMMA are located at 262, 353, 364, 408, 488, 559, and 601 cm^{-1}. The intense modes at 260, 301, 354, 362, 406, 488, 559, and 601 cm^{-1} in Fig. 3e correspond to the ZnS nanoparticles in silane/PMMA. In all these cases the registered phonons can be attributed to either the pure ZnS or the pure PMMA. The difference between the experimentally measured spectrum
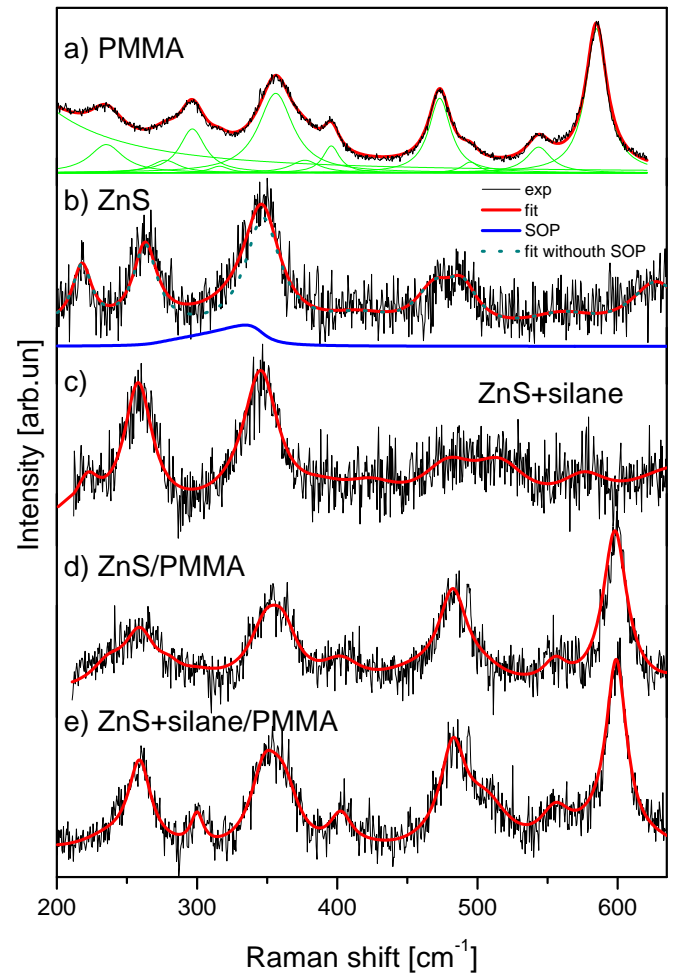
Fig. 3. Fitted and experimental Raman spectra. (a) The PMMA, (b) ZnS nanoparticles, (c) ZnS in silane, (d) ZnS/PMMA, and (e) ZnS in silane/PMMA.

and the curve obtained by convolving the Lorentz shapes located at the determined frequencies is the most noticeable for the pure ZnS.

The asymmetry and broadening around the Raman peak at 347 cm^{-1}, which is in the symmetric stretching vibration region, undoubtedly correspond to the variation of a secondary-structure. In a nanocrystal, this is usually considered to be a surface effect, and a "surface optical" phonon (SOP) mode is assigned to it. In order to analyze the surface optical phonon we have to take into account that nanoparticles are surrounded by silane and PMMA.

The part of spectra in Fig. 3 where the discrepancy between the experimental and theoretical spectra is located, is adjusted using the effective medium theory. Namely, the surface phonon modes are observed for particle sizes smaller than the wavelength of the exciting laser light. Usually these modes of small particles appear in polar crystals [31]. The dielectric function for the polar semi-insulating semiconductor:

$$\varepsilon_1(\omega) = \varepsilon_\infty \Pi_{i=1}^{n} \frac{\omega_{LO_i}^2 - \omega^2 - i\omega\gamma_{iLO}}{\omega_{TO_i}^2 - \omega^2 - i\omega\gamma_{iTO}}, \tag{1}$$

describes its optical properties in the IR region. Here, ω_{TO} and ω_{LO} are the frequencies of the transverse and longitudinal optical bulk phonons, respectively; ε_∞ is the dielectric constant at high frequencies, and γ is the damping constant. The bulk phonons in small particles have properties similar to those of the corresponding phonons in an infinite nanocomposite; however, their wave functions are adapted to the geometry of a small particle.

There are many mixing models for the effective dielectric permittivity of such a mixture. The Bruggeman model is preferred for high concentration of the inclusions since there are no restrictions for volume fraction (*f*) [32,33]. The effective dielectric function of the Bruggeman nanocomposite is given by:

$$(1-f)\frac{\varepsilon_1 - \varepsilon_{eff}}{\varepsilon_{eff} + g(\varepsilon_1 - \varepsilon_{eff})} + f\frac{\varepsilon_1 - \varepsilon_{eff}}{\varepsilon_{eff} + g(\varepsilon_2 - \varepsilon_{eff})} = 0, \qquad (2)$$

where *g* is a geometric factor depending on the shape of the inclusions. For three dimensional spherical particles $g = 1/3$ and for two-dimensional circles $g = 1/2$. Our nanoparticles of ZnS are clustered and not well separated in silane/PMMA, namely, they occupy a significant volume. Consequently, the condition for Bruggeman formula with $g = 1/3$ is satisfied. Due to a narrow range of the spectra, the effective medium theory is applicable and ε_2 is taken to be constant. In our case, spherical nanoparticles of ZnS with dielectric function given by Eq. (1), are characterized with $\varepsilon_2 = 1$, 1.5, and 2.1 if they are homogeneously distributed in air (for ZnS nanoparticles obtained by mechanochemical synthesis); in air and silane; and in air, silane, and PMMA; respectively. The intensity of Raman spectrum related to SOP is described with

$$I_{SOP}(\omega) \sim I_m\left(-\frac{1}{\varepsilon_{eff}}\right) \qquad (3)$$

In Fig. 3 SOP mode is shown with the blue line. The solid line in Fig. 3b–e is obtained by joining the contributions of SOPs and the phonons described with Lorentz curves. The agreement of the theoretical model obtained in this manner with the experimental results is excellent.

The parameters adjusment was carred out automatically, by means of the least-square fitting of theoretical (I$_t$) and experimental (I$_e$) intensity at q arbitrarly taken points:

$$\delta = \sqrt{\frac{1}{q}\sum_{j=1}^{q}\left(I_{ej} - I_{tj}\right)^2} \qquad (4)$$

The value of δ was minimized until it became with the usual experimental error (less than 2%). For all samples the determination errors of the frequencies and damping coeficients were about 3–6 and 10–15% respectively.

The significant change in the intensity and line shape of simulated SOP mode, described with Eq. (3), is caused predominantly by the variation of the main volume fraction (*f*) and damping rate γ_{LO}, as illustrated in Fig. 4 ($\varepsilon_2 = 1$). In our case, the position of the SOP mode's maximum directly follows the change in the filling factor (Fig. 4a), whereas its dependence on the dumping (Fig. 4b) is noticeably weaker.

From Fig. 4 it can be seen that SOP mode moves toward higher wavenumbers when filling factor increases. The position of surface optical phonon (SOP) mode frequencies is obtained from Ref. [18] to be

$$\omega_{SOP} = \max\left(I_m\left(-\frac{1}{\varepsilon_{eff}}\right)\right)$$

The SOP mode dependences on the type of environment and filing factor are shown in Fig. 5a and b, respectively. The four lines in Fig. 5a are the best fit lines for SOP mode in Fig. 3. Fig. 5a illustrates the change in the SOP mode for different environments. The peak positions for ZnS, ZnS in silane, ZnS/PMMA, and ZnS in silane/PMMA move consecutively toward higher wavenumbers. The dependence of the SOP mode position on the filing factor *f* is obtained to be practically linear, as can be seen in Fig. 5b. Having in mind the linearity of this dependence, one can further conclude that the filling factor and dumping g$_2$ increase when ZnS is embedded in silane, and are even bigger when ZnS in silane is embedded in PMMA.

The obtained results lead to the conclusion that the studied nanocomposites obtained from nanodimensional ZnS and PMMA exhibit significant surface effects.
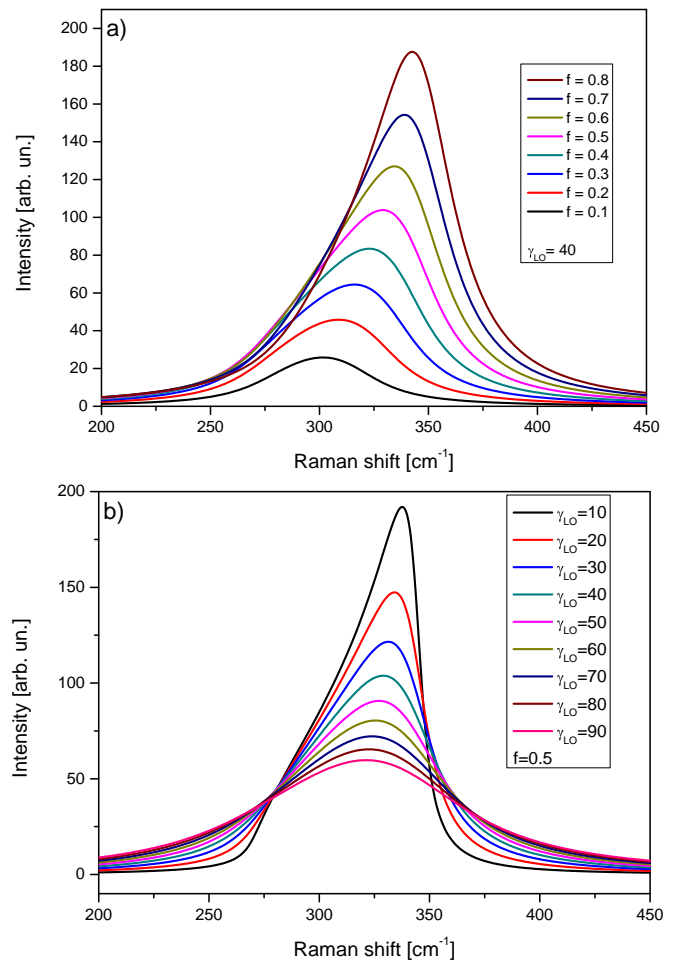
Fig. 4. Surface optical phonon (SOP) mode position. (a) The dependence on the filing factor and (b) the dependence on the phonon damping.

In comparison with SOP registered at similar nano-objects embedded in air there is a significant difference, i.e. in case of nanoparticles embedded in polymer matrix, the clusters of nanoparticles are created, and consequently, the cluster dimensions are larger than the dimensions of nanoparticles in air. However, those clusters are well separated one from others, so there is no interaction between them. Effectively, the value of filling factor is increased, and the surface phonon is weakened.

Moreover, by choosing the right polymer matrix and synthesis parameters, one can adjust the position and intensity of SOP, which is an advantage in application of these materials in electronic and sensor industry [34].

4. Conclusion

The results of studying optical and structural properties of ZnS nanoparticles and polymer nanocomposites ZnS in silane/PMMA and ZnS/PMMA are presented. The X-ray diffraction (XRD) analysis of the synsized nanocrystal identified its structure to be cubic. The size of initial ZnS crystallite of the cubic structure was estimated to be 2.3 nm, and it was determined that it is randomly distributed in the PMMA matrix. The optical properties were studied by the Raman spectroscopy at room temperature. The analysis of the Raman spectra was conducted using the fitting procedure. Since, nanoparticles were surrounded by the silane and PMMA, the Bruggeman model of effective medium was applied. The Raman measurements revealed the asymmetry and broadening around the peak at 347 cm^{-1} that is located in the symmetric stretching vibration region, and led to the conclusion that this peak
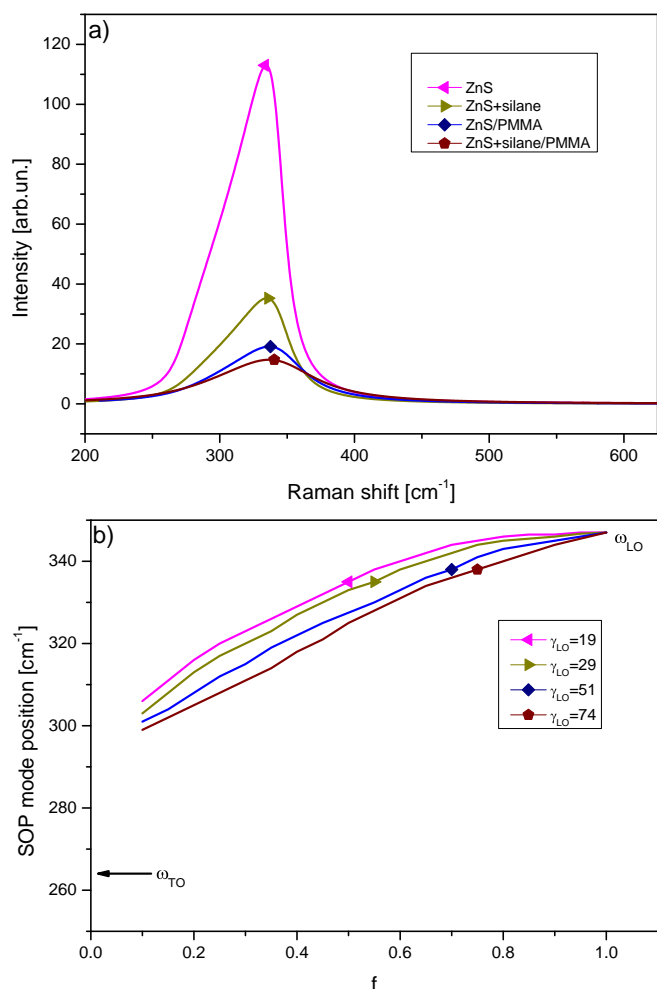
Fig. 5. (a) The Raman spectra of SOP modes for different environments and (b) the surface optical phonon (SOP) mode position dependence on the filling factor.

undoubtedly corresponds to the surface optical phonon (SOP) mode. The dependence of the SOP mode position on the filling factor (f) was analyzed for different composite materials, and it was determined that the SOP mode is moving towards higher wavenumbers when the filling factor increases.

Acknowledgements

References

[1] J.-M. Hwang, M.-O. Oh, I. Kim, J.-K. Lee, C.-S. Ha, Preparation and characterization of ZnS based nano-crystalline particles for polymer light-emitting diodes, Curr. Appl. Phys. 5 (2005) 31–34. https://doi.org/10.1016/j.cap.2003.11.075.

[2] H. Naz, R. Nauman Ali, X. Zhu, B. Xiang, Effect of Mo and Ti doping concentration on the structural and optical properties of ZnS nanoparticeles, Physica E 100 (2018) 1–6.

[3] Y.W. Jun, J.W. Seo, J.O. Sang, J. Cheon, Recent advances in the shape control of inorganic nano-building blocks, Coord. Chem. Rev. 249 (2005) 1766–1775. https://doi.org/10.1016/j.ccr.2004.12.008.

[4] S. Bhattacharyya, I. Perelshtein, O. Moshe, D.H. Rich, A. Gedanken, One-step solvent-free synthesis and characterization of Zn1− xMnxSe@ C nanorods and nanowires, Adv. Funct. Mater. 18 (2008) 1641–1653. https://doi.org/10.1002/adfm.200700653.

[5] A. Dev, S. Chaudhuri, B.N. Dev, ZnO 1-D nanostructures: low temperature synthesis and characterizations, Bull. Mater. Sci. 31 (2008) 551–559.

[6] G. Murugadoss, B. Rajamannan, U. Madhusudhanan, Synthesis and characterization of water-soluble ZnS: Mn2+nanocrystals, Chalcogenide Lett. 6 (2009) 197–201.

[7] P. Vinotha Boorana Lakshmi, K. Sakthi Raj, K. Ramachadran, Synthesis and characterization of nano ZnS doped with Mn, Cryst. Res. Technol. 44 (2009) 153–158. https://doi.org/10.1002/crat.200800271.

[8] H. Yang, S. Santra, P.H. Holloway, Syntheses and applications of Mn-doped II-VI semiconductor nanocrystals, J. Nanosci. Nanotechnol. 5 (2005) 1364–1375.

[9] N. Üzar, M.Ç. Arikan, Synthesis and investigation of optical properties of ZnS nanostructures, Bull. Mater. Sci. 34 (2011) 287–292. https://doi.org/10.1007/s12034-011-0085-5.

[10] R. John, S.S. Florence, Structural and optical properties of ZnS nanoparticles synthesized by solid state reaction method, Chalcogenide Lett. 6 (2009) 535–539.

[11] R. Seoudi, S.H.A. Allehyani, D.A. Said, A.R. Lashin, A. Abouelsayed, Preparation, characterization, and size control of chemically synthesized CdS nanoparticles capped with poly(ethylene glycol), J. Electron. Mater. 44 (2015) 3367–3374. https://doi.org/10.1007/s11664-015-3838-x.

[12] T.T.Q. Hoa, L.V. Vu, T.D. Canh, N.N. Long, Preparation of ZnS nanoparticles by hydrothermal method, J. Phys. Conf. Ser. 187 (2009) 012081–012086, https://doi.org/10.1088/1742-6596/187/1/012081.

[13] W. Hertl, Surface chemical properties of zinc sulfide, Langmuir 4 (1988) 594–598.

[14] T.E. Twardowski, Introduction to Nanocomposites Material Properties, Processing, Characterization, Destech Publications, Lancaster, Pa, USA, 2007.

[15] M. Tamborra, M. Striccoli, R. Comparelli, M.L. Curri, A. Petrella, A. Agostiano, Optical properties of hybrid composites based on highly luminescent CdS nanocrystals in polymer, Nanotechnology 15 (2004) S240–S244.

[16] F. Hussain, M. Hojjati, M. Okamoto, R.E. Gorga, Review article: polymer-matrix nanocomposites, processing, manufacturing, and application: an overview, J. Compos. Mater. 40 (2006), https://doi.org/10.1177/0021998306067321, 1511-1175.

[17] N.A. Peppas, R. Langer, New challenges in biomaterials, Science 263 (1994) 1715–1720.

[18] B. Hadžić, N. Romčević, M. Romčević, I. Kuryliszyn-Kudelska, W. Dobrowolski, J. Trajić, D. Timotijević, U. Narkiewicz, D. Sibera, Surface optical phonons in ZnO (Co) nanoparticles: Raman study, J. Alloy. Comp. 540 (2012) 49–56, https://doi.org/10.1016/j.jallcom.2012.06.076.

[19] M. Gilić, J. Trajić, N. Romčević, M. Romčević, D.V. Timotijević, G. Stanišić, I.S. Yahia, Optical properties of CdS thin films, Opt. Mater. 35 (2013) 1112–1117, https://doi.org/10.1016/j.optmat.2012.12.028.

[20] B. Hadžić, N. Romčević, M. Romčević, I. Kuryliszyn-Kudelska, W. Dobrowolski, R. Wróbel, U. Narkiewicz, D. Sibera, Raman study of surface optical phonons in ZnO(Mn) nanoparticles, J. Alloy. Comp. 585 (2014) 214–219, https://doi.org/10.1016/j.jallcom.2013.09.132.

[21] B. Hadžić, N. Romčević, M. Romčević, I. Kurylisyn-Kudelska, W. Dobrowolski, U. Narkiewicz, D. Sibera, Influence of SOP modes on Raman spectra of ZnO(Fe) nanoparticles, Opt. Mater. 42 (2015) 118–123, https://doi.org/10.1016/j.optmat.2014.12.029.

[22] J. Mitric, N. Paunovic, M. Mitric, B. Vasic, U. Ralevic, J. Trajic, M. Romcevic, W.D. Dobrowolski, I.S. Yahia, N. Romcevic, Surface optical phonon – plasmon interaction in nanodimensional CdTe thin films, Physica E 104 (2018) 64–70, https://doi.org/10.1016/j.physe.2018.07.021.

[23] J. Trajic, R. Kostic, N. Romcevic, M. Romcevic, M. Mitric, V. Lazovic, P. Balaz, D. Stojanovic, Raman spectroscopy of ZnS quantum dots, J. Alloy. Comp. 637 (2015) 401–406, https://doi.org/10.1016/j.jallcom.2015.03.027.

[24] F. Paraguay-Delgado, W. Antunez-Flores, M. Miki-Yoshida, A. Aguilar-Elgueyabal, P. Santiago, J.R. Diaz, J.A. Ascencio, Structural analysis and growing mechanisms for long SnO2 nanorods synthesized by spray pyrolysis, Nanotechnology 16 (2005) 688–694, https://doi.org/10.1088/0957-4484/16/6/011.

[25] O. Solcova, Ch D. Uecker, U. Steinike, K. Jiratova, Effect of the support on the reducibility of high-loaded nickel catalysts, Appl. Catal., A 94 (1994) 153–160. https://doi.org/10.1016/0926-860X(93)85004-9.

[26] R.M. Dukali, I. Radovic, D.B. Stojanovic, P.S. Uskokovic, N. Romcevic, V. Radojevic, R. Aleksic, Preparation, characterization and mechanical properties of Bi12SiO20/PMMA composite films, J. Alloy. Comp. 583 (2014) 376–381. https://doi.org/10.1016/j.jallcom.2013.08.206.

[27] K.J. Thomas, M. Sheeba, V.P.N. Nampoori, C.P.G. Vallabhan, P. Radhakrishnan, Raman spectra of polymethyl methacrylate optical fibres excited by a 532 nm diode pumped solid state laser, J. Opt. A Pure Appl. Opt. 10 (2008) 055303–055305, https://doi.org/10.1088/1464-4258/10/5/055303.

[28] J. Trajić, M. Romčević, N. Romčević, B. Babić, B. Matović, P. Balaž, Far-infrared spectra of mesoporous ZnS nanopaticles, Opt. Mater. 57 (2016) 225–230, https://doi.org/10.1016/j.optmat.2016.05.004.

[29] J. Serrano, A. Cantarero, M. Cardona, N. Garro, R. Luck, R.E. Tallman, T.M. Ritter, B.A. Weinstein, Raman scattering in β-ZnS, Phys. Rev. B 69 (2004), 014301.

[30] Y.C. Cheng, C.Q. Jin, F. Gao, X.L. Wu, W. Zhong, S.H. Li, P.K. Chu, J. Appl. Phys. 106 (2009) 123505, https://doi.org/10.1103/PhysRevB.69.014301.

[31] G. Irmer, Raman scattering of nanoporous semiconductors, J. Raman Spectrosc. 38 (2007) 634–646, https://doi.org/10.1002/jrs.1703.

[32] J. Saarinen, E.M. Vartiainen, K. Peiponen, On tailoring of nonlinear spectral properties of nanocomposites having Maxwell Garnett or Bruggeman structure, Opt. Rev. 10 (2003) 111–115.

[33] X.C. Zeng, D.J. Bergman, P.M. Hui, D. Stroud, Effective-medium theory for weakly nonlinear composites, Phys. Rev. B 38 (1988) 10970–10973. https://doi.org/10.1103/PhysRevB.38.10970.

[34] I. Kuryliszyn-Kudelska, W. Dobrowolski, M. Arciszewska, N. Romcevic, M. Romcevic, B. Hadzic, D. Sibera, U. Narkiewicz, Superparamagnetic and ferrimagnetic behavior of nanocrystalline ZnO(MnO), Physica E 98 (2018) 10–16. https://doi.org/10.1016/j.physe.2017.12.008.
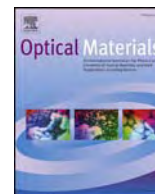
Far infrared spectra of Si doped PbTe single crystals

J. Trajic[a,*], N. Paunovic[a], M. Romcevic[a], V.E. Slynko[b], Jasna L. Ristic-Djurovic[a], W.D. Dobrowolski[c], N. Romcevic[a]

[a] Institute of Physics, University of Belgrade, Pregrevica 118, 11080, Belgrade, Serbia
[b] S.P.Timoshenko Institute of Mechanics, National Academy of Sciences, Kiev, Ukraine Nesterov st., 03680, MSP, Kiev 57, Ukraine
[c] Institute of Physics, Polish Academy of Sciences, Al. Lotnikow 32/46, 02-668, Warsaw, Poland

ARTICLE INFO

ABSTRACT

The far-infrared spectroscopy was used to analyze optical properties of PbTe single crystals doped with different amounts of Si. A dielectric function that takes into account the plasmon-phonon interaction was employed in the measured data manipulation. Two frequencies of plasmon-phonon coupled modes were obtained with the best-fit method, whereas the values for LO mode and plasma frequency (ω_p) were calculated. The best-fit to the experimentally obtained spectra agrees very well with the theoretical prediction.

1. Introduction

Specific physical and chemical properties of PbTe draws attention of numerous scientific studies. In particular, small band gap and high carrier mobilities qualify it for application in infrared optoelectronic devices [1] and thermoelectric materials [2]. The PbTe is also a good candidate for topological insulators materials. For instance, there are theoretical predictions that Te antisite defects in nonstoichiometric Te-rich PbTe could induce a band inversion, turning it into a topological crystalline insulator [3].

Thermoelectric materials found use in searches for alternative and complementary energy sources due to their ability to convert heat to electricity and *vice versa* [4–7]. Advantages of thermoelectric systems for direct heat-to-electricity conversion are environmental friendliness, absence of pollutants, small size, reliability, and large operating temperature range. Performance efficiency of a thermoelectric material, ZT, is expressed as ZT = $(S2\sigma/\kappa)T$, where S, T, ρ, and κ are the Seebeck coefficient, temperature, electrical resistivity, and thermal conductivity, respectively. The rocksalt-structured PbTe and related materials of n-as well as of p-type are shown to be good thermoelectric materials that operate in the mid-temperature range. As a matter of fact, PbTe-based materials have the highest recorded ZT among the bulk TE materials [8]. However, the materials based on PbTe have low mechanical strength, which can be improved by using Si as a dopant [9].

In order to absorb electromagnetic radiation, free carriers have to interact with a lattice. Transitions of an individual carrier as well as formation of collective plasma oscillators (plasmons) can contribute to the absorption. Consequently, the free-carrier absorption contains individual-carrier excitations (individual-carrier scattering), as well as collective carrier excitations (plasmon generation). Coupling of elementary excitations in solids has been investigated in a number of studies [10–13]. Studies of photon-plasmon processes usually start with a dielectric function for free carriers in a perfect crystal. Our approach [14,15] is to create a dielectric function that explains registered processes, and to compare it to the parameters obtained with the classical approach [13,16,17]. Comparison of the two yields to the physical explanation of the processes that take place in the doped semiconductors.

Raman spectroscopy is the commonly used technique to analyze optical properties of different materials. But, acquiring information about the coupled plasmon-phonon modes from the Raman spectra of PbTe samples is closely related to the ability to eliminate the influence of the oxide layer that is being formed at the sample surface. For film-samples, an additional problem can be removal of the substrate influence [18]. Further, analysis of the obtained results must be performed with elaborate mechanisms related to the microscopic approach in calculation of the Raman scattering cross-section [11] because the position of plasmon-phonon modes does not always coincide with the spectral maximum. Use of the IR spectroscopy in the analysis of the coupled plasmon-phonon modes takes into account all of these issues. In addition, in IR spectroscopy the position of global minimum remains directly related to the frequency of the coupled plasmon-phonon modes.

In this paper far-infrared spectroscopy (FIR) is used to study optical properties of PbTe single crystals doped with Si. Three values of Si

---

* Corresponding author.
E-mail address: jelena@ipb.ac.rs (J. Trajic).

concentration in the samples were considered, namely 1, 3, 5.6 at.%. Analysis of the reflection spectra in a wide spectral range was used to detect plasmon-phonon coupling in the studied system.

2. Experiment

Single crystal ingots of PbTe(Si) were grown by the modified Bridgman method. The samples were synthesized using high purity components. The impurity content in the starting mixture was from 3 to 8 at.%. The Si concentration in the crystals used here was 1, 3, and 5.6 at.%. Distribution of silicon along ingots was determined by the XRF (X-ray fluorescence) analysis. Prior to analysis, the ingots were cut into discs of the same thicknesses. The XRF measurements were carried out on both sides of each disc and the spectra are given as the average of the two. Distribution of silicon along these ingots is in accordance with the model given in Ref. [19] according to which impurities always moves back to the end of the ingot.

The infrared reflectivity measurements were carried out at room temperature with a BOMEM DA-8 Fourier-transform IR spectrometer. A deuterated triglycine sulfate (DTGS) pyroelectric detector was used to cover the wave number region from 50 to 450 cm^{-1}.

3. Results and discussion

The low-frequency dielectric properties of single crystals are described by classical oscillators corresponding to the TO-modes and the Drude part which takes into account the free carrier contribution [10,17]:

$$\varepsilon_S(\omega) = \varepsilon_\infty + \sum_{k=1}^{n} \frac{\varepsilon_\infty(\omega_{LOk}^2 - \omega_{TOk}^2)}{\omega_{TOk}^2 - \omega^2 - i\gamma_{TOk}\omega} - \frac{\varepsilon_\infty\omega_P^2}{\omega(\omega + i\gamma_P)} \quad (1)$$

where ε_∞, ω_{LOk}, ω_{TOk}, ω_P, γ_{TOk}, and γ_P are the bound charge contribution taken to be constant, longitudinal and transverse optical-phonon frequencies, plasma frequency, and phonon and plasma damping. Therefore, the TO mode frequency is obtained directly from the fit, whereas the LO modes are determined from the maximum of the dielectric loss function.

In the PbTe doped with Si the pure LO-mode of the lattice is strongly influenced by the plasmon mode of the free carriers, which causes appearance of a combined plasmon-LO phonon mode [12]. Consequently, only coupled mode positions are observable in the experimental spectra and the LO-modes are detectable only if the influence of the free carrier is eliminated [13]. Therefore, in the analysis of far-infrared reflectivity spectra of PbTe doped with Si we used the dielectric function that includes the interaction between LO phonon and a plasmon, i.e. the plasmon-phonon interaction in its initial form [13, 15]. Namely, the expression for dielectric function is

$$\varepsilon_f(\omega) = \varepsilon_\infty \frac{\prod_{j=1}^{2}(\omega^2 + i\gamma_{lj}\omega - \omega_{lj}^2)}{\omega(\omega + i\gamma_P)(\omega^2 + i\gamma_t\omega - \omega_t^2)} \cdot \prod_{p=1}^{l} \frac{\omega^2 + i\gamma_{LOp}\omega - \omega_{LOp}^2}{\omega^2 + i\gamma_{TOp}\omega - \omega_{TOp}^2} \quad (2)$$

The parameters ω_{lj} and γ_{lj} in the first numerator represent the eigenfrequencies and damping coefficients of the coupled plasmon-longitudinal phonon waves. The parameters in the first denominator correspond to the similar characteristics of the transverse (TO) vibrations. The second term in Eq. (2) represents l uncoupled modes of the crystal. Consequently, ω_{LOp} and ω_{TOp} are the longitudinal and transverse frequencies, whereas γ_{LOp} and γ_{TOp} are the corresponding damping parameters. Therefore, the determination of LO-mode and plasma frequency is connected with the decoupled procedure.

The far-infrared reflection spectrum at room temperature of the PbTe single crystal doped with 1 at.% Si is presented in Fig. 1. The experimental data are depicted with circles, whereas the solid line represents the calculated reflectivity spectrum, which is obtained by the fitting procedure that is based on the model for plasmon-phonon coupling given by Eq. (2). In the fitting procedure, the modes characteristic
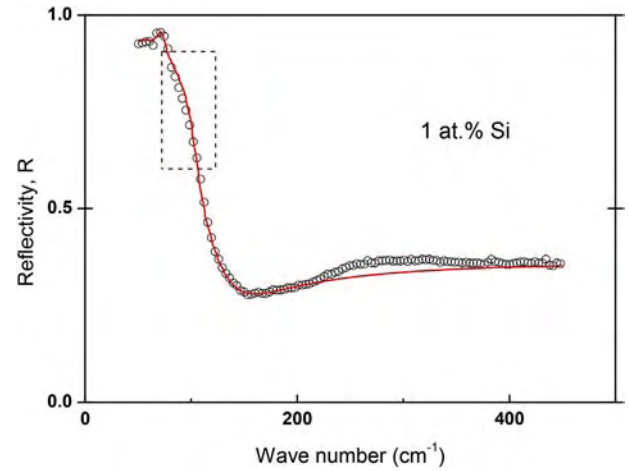
Fig. 1. Far-infrared reflection spectra of PbTe single crystal doped with 1 at.% Si. The spectrum obtained experimentally at room temperature is presented with circles. The solid lines depict the calculated spectrum obtained by the fitting procedure that is based on the model given by Eq. (2) where $p = 1$.

for this type of material are included, namely the pair of PbTe TO/LO modes and the mode at about 73 cm^{-1}, which is the PbTe Brillouin zone edge mode. These modes are considered because the phonon density of PbTe has a maximum at their frequencies [20].

Slight discrepancy between the theoretical spectrum and the experimental results in the frequency range at about 100 cm^{-1} (marked by dashed lines) indicates the existence of the mode that corresponds to the Si impurity. Fig. 2 shows the same spectrum as Fig. 1; however, in addition to the modes considered previously, the fitting procedure contains the Si impurity mode at about 90 cm^{-1}. Note that lead telluride grows with rather high concentration of native defects (vacancies, etc). In the PbTe lattice Si is a substitute for Pb and as such is a substitution impurity ion. Consequently, every ion in PbTe is no longer in the center of inversion symmetry and PbTe vibration modes could be Raman as well as far-infrared active. The impurity mode can arise simply because of the difference between masses and force constants of the impurity ion and the ion of the host material [21]. Their appearance can be caused by more complex mechanism of electron-phonon interaction [22]. When the semiconductor is doped with a substitution impurity [10] (in our case Si), and if the substitution takes place with the atoms of the heavier mass (Pb), lighter impurity leads to two modes: a
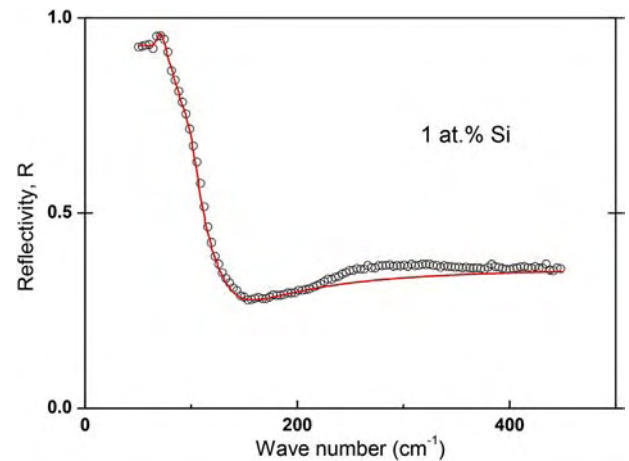

Fig. 2. Far-infrared reflection spectra of PbTe single crystal doped with 1 at.% Si. The experimental spectrum obtained at room temperature is presented with circles. The solid lines are calculated spectrum with additional Si impurity mode, obtained by the fitting procedure that is based on the model given by Eq. (2) where $p = 2$.
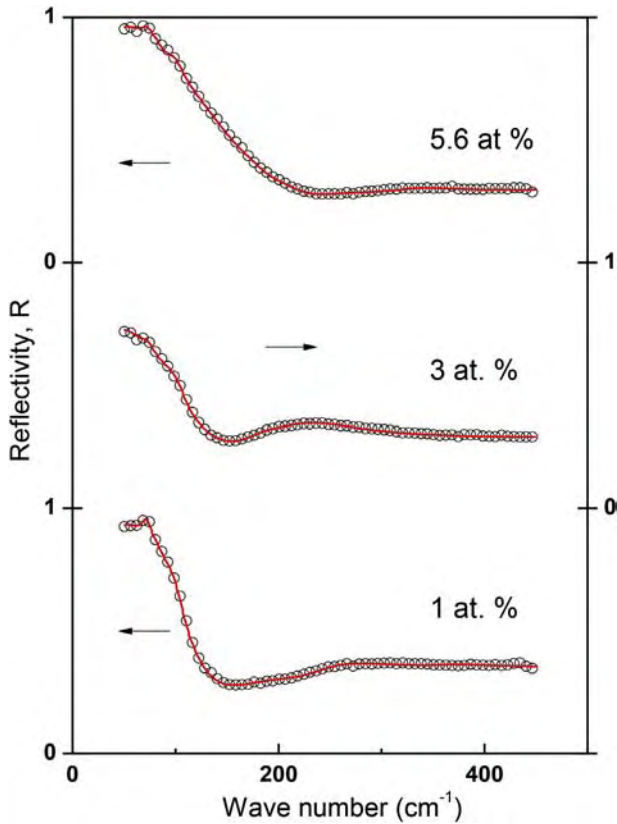
Fig. 3. Far-infrared reflection spectra of PbTe single crystals doped with 1, 3 and 5.6 at.% Si. The experimental spectra obtained at room temperature are depicted with circles. The solid lines are calculated spectra obtained by the fitting procedure that is based on the model given by Eqs. (2) and (4).

local mode situated above the optical band and a gap mode situated above the acoustic band and below the optical band of the host lattice. The position of Si impurity mode in PbTe was estimated in the manner described in detail in Ref. [23], namely with the expression

$$\omega_I(Si) = \omega_{TO}(PbTe)\sqrt{\frac{M_{Pb}}{M_{Si}}} \tag{3}$$

where M_{Pb} and M_{Si} are the masses of the atoms Pb and Si, respectively.

We did not manage to determine the set of parameters that provide good spectrum overlapping in the whole range of frequencies. Registered discrepancy between the experimental and the calculated reflectivity spectra is obvious, and the new structure is observable above 220 cm^{-1} In order to remove this discrepancy, Eqs. (1) and (2) were extended to include the term [24]:

$$\frac{\omega_{loc}^2}{\omega_0^2 - \omega^2 - i\omega G} \tag{4}$$

where ω_0, G, and ω_{loc} are the characteristic frequency, damping, and "strength" of the additional oscillator. According to Ref. [24], $(\omega_{loc})^2$ is proportional to the N_{loc} carrier concentration at the localized level.

In Fig. 3 we compare the experimental results to the theoretical spectrum at room temperature of PbTe single crystals doped with 1, 3 and 5.6 at.% Si, which take into account additional term described with Eq. (4) in Eq. (2).

We obtained the value of $\omega_0 = 235 \pm 8$ cm^{-1} as the result of the best fit procedure. In the SiTe electron transition from the excited state E to the ground state X exists in the range above 220 cm^{-1} [25]. It seems that during the process of doping PbTe with Si, localization of electrons occurs in the vicinity of Si impurity atom as a consequence of the appearance of Te−SiTe clusters with cubic symmetry. As one can
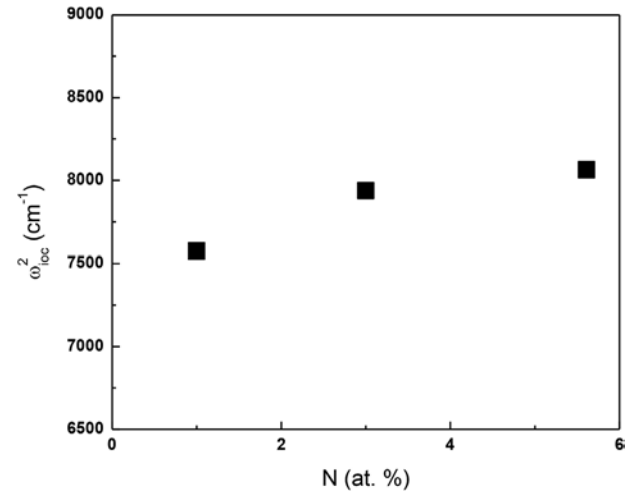
Fig. 4. The "strength" of the oscillator described by Eq. (4) vs silicon concentration.
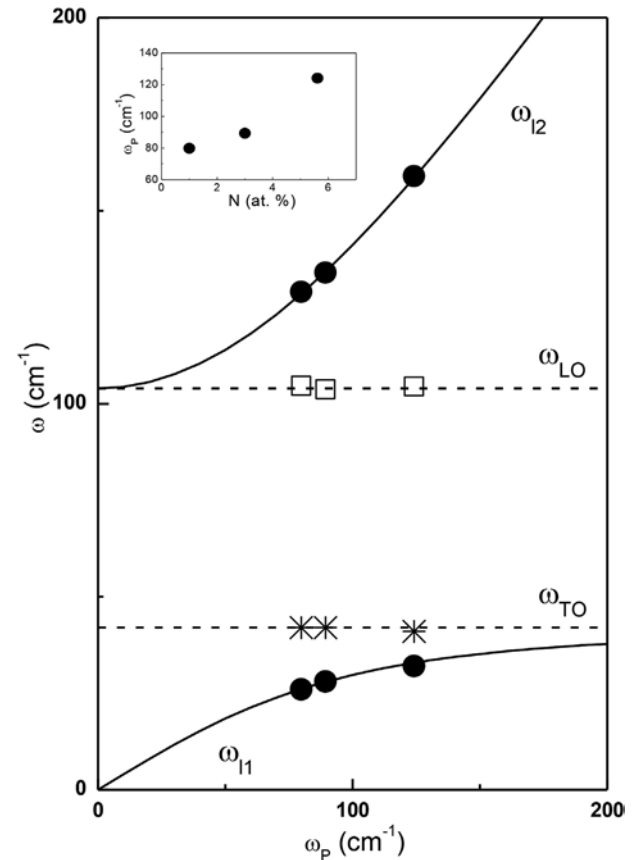
Fig. 5. The eigenfrequencies of the plasmon-LO phonon modes (full lines - Eq. (1)); ● - eigenfrequency spectra ω_{lj} obtained by procedure based on Eq. (2); □ - calculated values for ω_{LO} and * - experimentally determined values for ωTO. Inset: plasma frequencies (ω_P) vs. Si concentration.

see from Fig. 4, the "strength" of the oscillator connected with electron transition increases with the increase of Si concentration.

In Fig. 5 characteristic spectra for plasmon-phonon interaction are presented. Obtained results describe the relationship between the results obtained with Eq. (2) and those resulting from the traditional approach described with Eq. (1). The solid lines represent coupled frequencies, and as it was given in Ref. [13], the positions of the coupled modes were defined as the solutions of Eq. (1) (Re{ε} = 0). Dashed

lines, obtained experimentally as the best fit, correspond to the well-known values for PbTe LO and TO phonon positions [19]. As a result of the best fit, using Eq. (2) with additional term given by Eq. (4), we obtained the frequencies of coupled modes (ω_{l1} and ω_{l2}), and then we calculated the values for ω_{LOPbTe} and ω_P, as is described in Ref. [15]. The value for the ω_{LOPbTe} obtained in this manner is in good agreement with the literature. The characteristic parameters obtained as the best fit are shown in Fig. 5. The plasma frequencies (ω_P) dependence on Si concentration is presented in the inset of Fig. 5.

As we already said, localization of electrons occurs in the vicinity of the impurity, i.e. Si atom. Localization of electrons leads to the decrease of electrical conductivity. Since the thermal and electrical conductivities are proportional (Wiedemann-Franz Law), the decrease of electrical conductivity causes the decrease of thermal conductivity. Also, electrons localized around this impurity cause the localization of phonons. Since phonons are responsible for heat transmission, their localization also leads to the decrease of phonon thermal conductivity. As it is well known, a good thermoelectric material must have low thermal conductivity in order to retain the heat and to reduce the heat transfer losses. This lead us to conclude that localization of electrons in the vicinity of Si atom impurity makes PbTe doped with Si a good thermoelectric material.

These results are very significant since they represent the basis for investigation these effects in nanocrystals [26].

4. Conclusion

The far-infrared spectroscopy was employed to investigate phonon properties of PbTe single crystal doped by 1, 3, and 5.6 at.% Si. The spectra were analyzed using the dielectric function that takes into account the existence of plasmon-phonon interaction in advance. As a result of the best fit procedure the two frequencies corresponding to the coupled modes (ω_{l1} and ω_{l2}) were obtained, whereas the frequency values for LO mode (ω_{LO}) and plasma frequency (ω_P) were calculated. In addition to the modes that are characteristic for this type of material, we registered the Si impurity mode as well as the localization of electrons in the vicinity of Si impurity atom.

Declaration of interests

The authors declare that they have no known competing financial interests or personal relationships that could have appeared to influence the work reported in this paper.

Acknowledgements

References

[1] A.M. Samylov, M.K. Saharov, S.A. Buchnev, A.M. Khoviev, E.A. Dolgopolova, Crystal structure, carrier concentration and IR-sensitivity of PbTe thin films doped with Ga by two different methods, J. Cryst. Growth 240 (3) (2002) 340–346.

[2] M.S. Dresselhaus, G. Dresselhaus, X. Sun, Z. Zhang, S. Cronin, T. Koda, Y.I. Ying, The promise of low-dimensional thermoelectric materials, Microscale Thermophys. Eng. 3 (2) (1999) 89–100.

[3] M. Songsong, G. Chunyu, X. Chengcheng, W. Fan, S. Michael, L. Yunhao, Y. Huiqiu, W. Huizhen, Adv. Funct. Mater. 28 (2018) 1803188.

[4] X. Shi, L. Chen, C. Uher, Recent advances in high-performance bulk thermoelectric materials, Int. Mater. Rev. 61 (6) (2016) 379–415.

[5] G. Tan, L.D. Zhao, M.G. Kanatzidis, Rationally designing high-performance bulk thermoelectric materials, Chem. Rev. 116 (19) (2016) 12123–12149.

[6] J. He, T.M. Tritt, Advances in thermoelectric materials research: looking back and moving forward, Science 357 (2017) 1369.

[7] L. Yang, Z.G. Chen, M.S. Dargusch, High performance thermoelectric materials: progress and their applications, Adv. Energy Mater. 8 (6) (2017) 1701797.

[8] B. Cai, J. Li, H. Sun, L. Zhang, B. Xu, W. Hu, D. Yu, J. He, Z. Zhao, Z. Liu, Y. Tian, Enhanced thermoelectric performance of Na-doped PbTe synthesized under high pressure, Sci. China Mater. 61 (9) (2018) 1218–1224.

[9] Q. Zhang, H. Wang, Q. Zhang, W. Liu, B. Yu, H. Wang, D. Wang, G. Ni, G. Chen, Z. Ren, Effect of silicon and sodium on thermoelectric properties of thallium-doped lead telluride-based materials, Nano Lett. 12 (5) (2012) 2324–2330.

[10] E. Burstein, A. Pinczuk, R.F. Wallis, By D.L. Carter, R.T. Bate (Eds.), The Physics of Semimetals and Narrow-Gap Semiconductors, Pergamon, New York, 1971, p. 251.

[11] M. Cardona, G. Gunterodt (Eds.), Light Scattering in Solids, Top. Appl. Phys. vol. 8, Springer, Berlin, 1975.

[12] S. Takaoka, T. Hamaguchi, S. Shimomura, K. Murase, Observation of the coupled plasmon-lo phonon mode energy in photo-excited Pb1-xSnxTe doped with indium impurities, Solid State Commun. 54 (1) (1985) 99–102.

[13] A.A. Kuharskii, Solid State Commun. 8 (1970) 1275.

[14] J. Trajic, N. Romcevic, M. Romcevic, D. Stojanovic, R. Rudolf, T.A. Kuznetsova, D.R. Khokhlov, Far-infrared study of impurity local modes in Co-doped PbTe, J. Alloy. Comp. 493 (1–2) (2010) 41–46.

[15] J. Trajić, N. Romčević, M. Romčević, V.N. Nikiforov, Plasmon-phonon and plasmon-two different phonon interaction in Pb1-xMnxTe mixed crystals, Mater. Res. Bull. 42 (12) (2007) 2192–2201.

[16] V. Gopal, Analysis of the infrared plasma reflectivity spectra of semiconductors, Infrared Phys. 18 (2) (1978) 121–125.

[17] G. Abstreiter, M. Cardona, A. Pinczuk, M. Cardona, G. Guntherodt (Eds.), Light Scattering in Solids, IV, Springer-Verlag, Berlin, 1984.

[18] H. Wu, C. Cao, J. Si, T. Xu, H. Zhang, H. Wu, J. Chen, W. Shen, N. Dai, Observation of phonon modes in epitaxial PbTe films grown by molecular beam epitaxy, J. Appl. Phys. 101 (10) (2007) 103505.

[19] B.A. Volkov, L.I. Ryabova, D.R. Khokhlov, Mixed-valence impurities in lead telluride-based solid solutions, Uspekhi Fizicheskih Nauk 172 (8) (2002) 875–906 [Phys. Usp. 45 (8) (2002) pp. 819–846].

[20] W. Cochran, R.A. Cowley, G. Dolling, M.M. Elcombe, The crystal dynamics of lead telluride, Proc. R. Soc. A 293 (1966) 433–451.

[21] A.A. Maradudin, F. Seitz, D. Turnball (Eds.), Solid State Physics, vol. 19, Academic, New York, 1966.

[22] D.E. McCumber, One-phonon collision corrections to the high-frequency dielectric function of semiconductors, Phys. Rev. 154 (1967) 790.

[23] S. Venigopalan, A. Petrov, R.R. Galazka, A.K. Ramdas, S. Rodriguez, Raman scattering by phonons and magnons in semimagnetic semiconductors: Cd1−xMnxTe, Phys. Rev. B 25 (1982) 2681.

[24] N. Romcevic, Z.V. Popovic, D. Khokhliv, A.V. Nikorich, V. Konig, Far-infrared study of localized states in In-doped Pb0. 75Sn0.25Te single crystals, Phys. Rev. B 43 (8) (1991) 6712–6716.

[25] S. Chattopadhyaya, A. Pramanik, A. Banerjee, K. Kumar Das, Electronic states and spectroscopic properties of SiTe and SiTe⁺, J. Phys. Chem. A 110 (44) (2006) 12303–12311.

[26] J. Mitric, N. Paunovic, M. Mitric, B. Vasic, U. Ralevic, J. Trajic, M. Romcevic, W.D. Dobrowolski, I.S. Yahia, N. Romcevic, Surface optical phonon – plasmon interaction in nanodimensional CdTe thin films, Phys. E Low-dimens. Syst. Nanostruct. 104 (2018) 64–70.

Surface optical phonon – Plasmon interaction in nanodimensional CdTe thin films

J. Mitric[a],[*], N. Paunovic[a], M. Mitric[b], B. Vasic[a], U. Ralevic[a], J. Trajic[a], M. Romcevic[a], W.D. Dobrowolski[c], I.S. Yahia[d],[e], N. Romcevic[a]

[a] Institute of Physics, University of Belgrade, Pregrevica 118, 11080 Belgrade, Serbia
[b] Institute Vinca, University of Belgrade, P.O. Box 522, 11001 Belgrade, Serbia
[c] Institute of Physics, Polish Academy of Science, al. Lotnikov 32/46, 02-668 Warsaw, Poland
[d] Department of Physics, Faculty of Science, King Khalid University, P.O. Box 9004, Abha, Saudi Arabia
[e] Nano-Science & Semiconductor Labs, Department of Physics, Faculty of Education, Ain Shams University, Roxy, Cairo, Egypt

ABSTRACT

Structural and optical properties of CdTe thin films were investigated applying atomic force microscopy (AFM), XRD powder technique, Raman spectroscopy and far–infrared spectroscopy. CdTe thin films were prepared by using thermal evaporation technique. In the analysis of the far – infrared reflection spectra, numerical model for calculating the reflectivity coefficient for system which includes films and substrate has been applied. Effective permittivity of film mixture (CdTe and air) was modeled by Maxwell – Garnet approximation. We reveal the existence of surface optical phonon (SOP) mode and coupled plasmon-SOP modes (CPSOPM).

1. Introduction

II – VI semiconductor compounds, especially thin films, have become very popular because of their applications in numerous electronic and optoelectronic devices. Due to low production cost, thin films nowadays enjoy great attention in basic research and solid state technology.

The interest in various properties of photonic CdTe is well justified, as this material plays an important role in expanding variety of applications as in: integrated optics, optoelectronics, or solar energy conversion [1].

Two main properties of CdTe thin film are its high optical absorption coefficient (a thin film of CdTe with thickness of approximately 2 μm will absorb nearly 100% of the incident solar radiation) and its near ideal band gap for photovoltaic conversion efficiency of 1.45eV [2]. Also, its ease of film fabrication and low cost make it a representative material among II – VI semiconductors.

For fabrication of the CdTe films, various techniques have been applied: RF magnetron sputtering [3], molecular beam epitaxy (MBE) [4], pulsed laser deposition (PLD) [5], successive ionic layer adsorption and reaction method (SILAR) [6], metal organic chemical vapor deposition [7], screen printing [8], thermal evaporation method [9] etc. Thermal evaporation method shows some advantages such as: minimalization of impurities proportional to the growing layer, reduced

chances of oxidation and direction of propagation (occurs from the source to the substrate) [9,10]. This makes thermal evaporation technique the most suitable method, thanks to very high deposition rate, low material consumption and low cost of fabrication [11].

In the case of crystal with relatively small dimension, in the frequency range between bulk longitudinal optical phonon frequency (ω_{LO}) and transversal optical phonon frequency (ω_{TO}), a new mode known as a surface phonon mode appears [12,13]. It is known for the case of real crystal, that when its dimension is relatively small, surface modes and effects of dimension will be manifested in addition to the normal modes of infinite lattice. But, when crystal is reduced to extremely small dimensions, only the surface mode will persevere [12–14].

On the other side, electron – phonon interaction takes an important place in semiconducting materials [15]. In our earlier work we have registered plasmon (collective electron excitation) and LO phonons interaction in different systems [16–19]. Besides that, we have studied the impact of damping on interaction appearance [20], interaction between plasmon and different phonons [21,22], as well as interaction between plasmon and impurity local phonons [23–25].

In this work we report experimental studies of CdTe thin films prepared by thermal evaporation technique. Existence of nanodimensional structures in these thin films enabled us to observe effects associated with interactions between surface optical phonon (SOP) and

---

* Corresponding author.
  E-mail address: jmitric@ipb.ac.rs (J. Mitric).

plasmon for the first time.

Samples characterization was performed using atomic force microscopy (AFM). Structural properties were analyzed using XRD powder technique, and optical properties were characterized using Raman and far–infrared spectroscopy.

2. Sample preparation and characterization methods

CdTe single crystal was grown by the Bridgman technique. Different thickness of CdTe thin films were deposited by thermal evaporation from a resistance heating quartz glass crucible onto glass substrates using high vacuum coating unit type Edward 306 A. Films were grown at a pressure of 106 Pa. The mechanical rotation of the substrate holder during deposition produced homogeneous film. The distance between the source heater and substrates holder is 21 cm, in order to avoid any heat flow from the source to the substrates.

The morphology of the four CdTe thin films of different thicknesses was investigated by Atomic force microscopy (AFM). Atomic force microscopy measurements were performed using NT-MDT system NTEGRA Prima. Imaging was done in tapping mode using NSG01 probes. All AFM measurements were done at ambient conditions. For the sake of statistical analysis of sample surface, we calculated histograms and bearing ratios for each topographic image. The histogram represents a height distribution density of all points in a two-dimensional topographic image, or in other words, it is a number of points with height given on x-axis. On the other hand, the bearing ratio curve gives a percent of points in a corresponding two-dimensional topographic image with a height less than the number given on x-axis.

The structural characteristics were obtained by the XRD powder technique. All samples were examined under the same conditions, using a Philips PW 1050 diffractometer equipped with a PW 1730 generator, $40 \, kV \times 20 \, mA$, using Ni filtered Co Kα radiation of 0.1778897 nm at room temperature. Measurements were carried out in the 2 h range of 10–100° with a scanning step of 0.05° and 10 s scanning time per step. Crystallite size was determined by using XFIT computing program which is based on Fundamental Parameter convolution approach [26].

Raman measurements were performed using commercial NTegra Spectra system from NT-MDT. A linearly polarized semiconductor laser operating at a wavelength of 532 nm was used. All the spectra were obtained by setting the laser power to 2 mW within the $\sim 0.5 \times 0.5 \, \mu m$ sized focus with exposure time of 600 s.

The far-infrared (FIR) reflectivity measurements were performed at room temperature with a BOMEM DA-8 Fourier-transform infrared spectrometer. A Hyper beamsplitter and deuterated triglycine sulfate (DTGS) pyroelectric detector were used to cover the wave number region from 80 to 650 cm^{-1}.

3. Results and discussion

3.1. Atomic force microscopy

Three dimensional topographic images of all four samples are shown in the left side of Fig. 1. As can be seen, sample surfaces are rather flat, but still they are characterized with bright protrusions and dark holes (which represent air) resulting in a small surface roughness of several nanometers.

In order to characterize fraction of both observed topographic features, the statistical analysis have been performed by calculating histograms and bearing ratios from two dimensional topographic images. The results for all four samples are given in the right side of Fig. 1. They show that the peaks in the histograms are positioned in the middle of bearing ratio curves. Therefore, from these curves we can conclude that the fraction of holes and protrusions are rather similar, around 50%.

In order to estimate thicknesses of studied films, their step edges were measured by AFM. 3D AFM topographic images of the step edges are depicted in Fig. 2(a1-d1). The films are brighter and the substrates

are dark in the images, while the step edges are clearly resolved. Based on the AFM images, height distributions were calculated and presented in Fig. 2 (a2-d2). In all histograms, there are two characteristic peaks: a lower one corresponds to the substrate, while a higher one corresponds to the film. Therefore, the film height can be then approximately calculated as a difference between these two peaks. Estimated film thicknesses are given in Fig. 2 (a2-d2). The best resolved height peaks were found on CdTe 1 in Fig. 2 (a2) due to a smooth sample surface as can be seen in Fig. 2 (a1).

3.2. XRD

Structures of four synthesized CdTe thin films with different thicknesses were identified by XRD pattern as shown in Fig. 3. The diffractograms confirm that all samples are monophased, and that they crystallized in sphalerite type structure in 216. space group, $F\bar{4}3m$. All of the observed diffraction peaks are indexed according to this space group. Therefore, in our thin film samples there is no other structures other than CdTe. In this structural type, Cd ions occupy $4a$ Wyckoff positions, [[0, 0, 0]] with local symmetry $\bar{4}3m$, while Te ions occupy $4c$ Wyckoff positions [[1/4, 1/4, 1/4]] with the same local symmetry. Cd ions are in tetrahedral surrounding of Te ions (and vice versa). The tetrahedrons are regular and share common vertices. Crystallite size (R) is determined and presented in Fig. 2 and Table 1.

3.3. Raman spectroscopy

The cubic face-centered structure of bulk crystal CdTe is characterized by the 216. space group $F\bar{4}3m$ and contains four formula units, while the primitive cell is one fourth as many. Optical modes consist of one three fold –degenerated mode F_2 which is active in IR and Raman spectra. The dipole mode F_2 is split into the transverse (TO) and longitudinal (LO) modes in the vibrational spectra. It is very well known that reduction of the particle dimensions to nanoscale results in a breakdown of phonon selection rules and allows phonons with $l \neq 0$ to contribute to Raman scattering [27–31]. Consequently, some new forbidden vibration modes (low frequency region, acoustic modes, and high frequency region, surface optical modes) occur due to imperfections, impurity, valence band mixing and/or nonspherical geometry of the nanostructures [14].

TO (142 cm^{-1}) and LO (170.5 cm^{-1}) modes for the CdTe bulk crystal are both active in the Raman spectra. Also, the modes in band near 120 cm^{-1} correspond to phonons of Te on the CdTe surface and can be seen in the Raman spectra [32].

Raman spectra of CdTe thin films of different thickness at room temperature are presented in Fig. 4.

For analyzing obtained spectra Lorentz profiles were used. Solid lines are their sums. In the top right corner Raman spectra of bulk CdTe crystal for ambient conditions is presented [32]. The observed Raman spectra for all samples among characteristic CdTe TO mode at 142 cm^{-1} and phonon of Te of the CdTe surface (127 cm^{-1}), show the LO phonon like frequency shift from 170.5 cm^{-1} to 164 cm^{-1}. That can be attributed to the surface optical phonon (SOP) mode effect [33–38]. It is clear that SOP phonon is wider compared to LO phonon of bulk crystal, as well as when it's compared to phonon of nanodimensional film. This effect is associated with interaction between SOP and plasmon, which will be mentioned later on.

In order to analyze the surface optical phonon we have to take into account that a part of crystallites are surrounded by air. We will analyze the dependence of the SOP mode position on filling factor (f) of the mixed material.

Surface phonon modes can be detected in systems where particle size is much smaller when compared to wavelength of exciting light source [39]. These modes can be obtained for in the case of polar crystals [40], so we consider expression for dielectric function which describes optical properties of polar semi – insulating semiconductor in
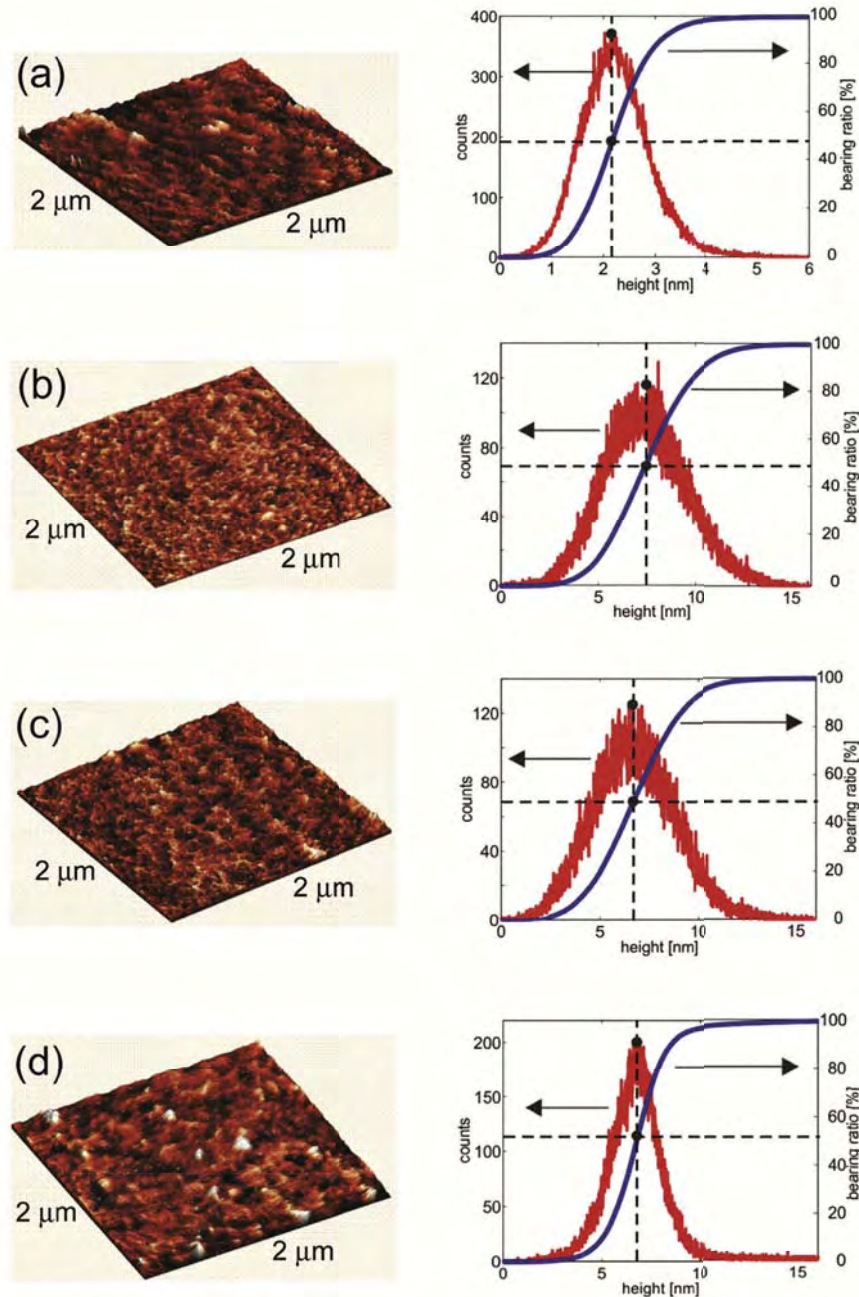
Fig. 1. Three-dimensional topographic image (left) and corresponding histogram and bearing ratio (right) for (a) CdTe 1, (b) CdTe 2, (c) CdTe 3, and (d) CdTe 4. Scan size is 2 μm.

IR region [24]:

$$\varepsilon_2(\omega) = \varepsilon_\infty \left(1 + \sum_{k=1}^{n} \frac{\omega_{LOk}^2 - \omega_{TOk}^2}{\omega_{TOk}^2 - \omega^2 - i\gamma_{TOk}\omega} - \frac{\omega_P^2}{\omega(\omega + i\Gamma)} \right) \quad (1)$$

ωTO and ωLO represent transverse and longitudinal optical bulk phonons, respectively; $\varepsilon\infty$ is the dielectric constant at high frequencies, ωP is plasma frequency and γ and Γ are the damping constants. Surface phonons can be considered similarly to phonons in infinite crystals, but with adapted wave functions to the geometry of the small particle.

Here, we will apply effective medium theory: Because the size of semiconducting nanoparticles, L, (with dielectric function ε_2, and are distributed in a medium with dielectric constant ε_1) is considerably

smaller than the interacting wavelength of visible light, λ ($\lambda \gg L$), we treat the heterogeneous composite as a homogeneous medium.

Even though there are numerous models for the effective dielectric permittivity for these kinds of mixtures [41], we decided to use Maxwell – Garnet model, because all our samples are thin films with well defined and separated nanosized grains. According to the Maxwell – Garnet mixing rule [42,43], effective permittivity of mixture, including spherical geometry of particles is given with:

$$\varepsilon_{eff} = \varepsilon_1 + 3f\varepsilon_1 \frac{\varepsilon_2 - \varepsilon_1}{\varepsilon_2 + 2\varepsilon_1 - f(\varepsilon_1 - \varepsilon_2)} \quad (2)$$

In this case, nanoparticles are spheres with permittivity ε_2 and are randomly distributed in homogeneous environment, with permittivity
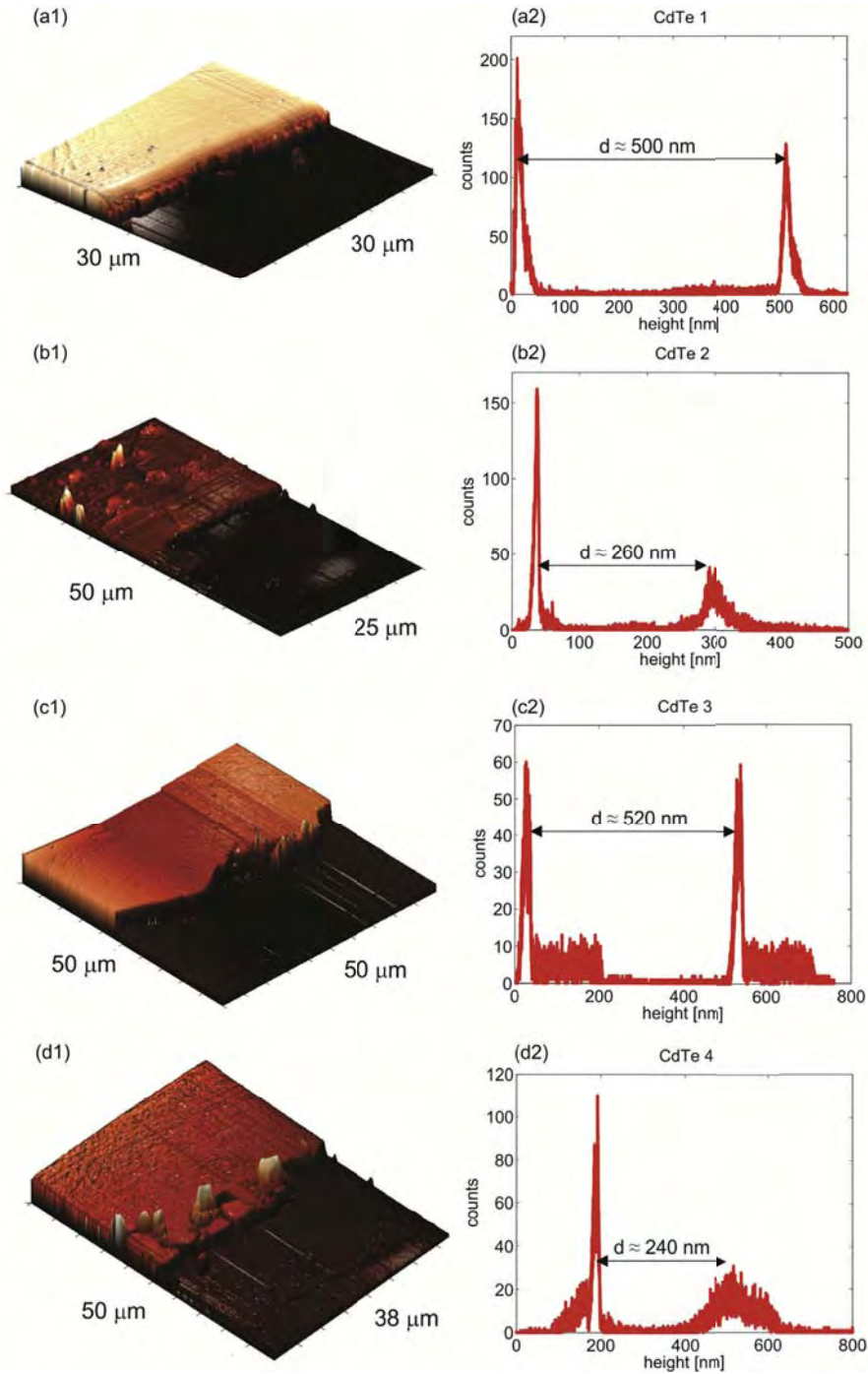
Fig. 2. (a1-d1) 3D AFM topographic images of step edges of studied films, and (a2-d2) corresponding height histograms. Average films thicknesses are denoted in the histograms.

ε_1 and occupy a volume fraction f.

Position surface optical phonon (SOP) mode frequencies are obtained from Ref. [44]:

$$\omega_{SOP} = max\left(I_m\left(-\frac{1}{\varepsilon_{eff}} \right) \right) \tag{3}$$

The result is shown in Fig. 5. The practical liner dependence of the position of the SOP mode on the filing factor f has been obtained. For the frequency of the SOP mode determined in Fig. 4 we have $f = 0.53$. This result is in accordance with the one obtained from the AFM measurements.

3.4. Far-infrared spectroscopy

Thicknesses of our films, as we will see, are in a range from $\sim 0.39\,\mu m$ to $\sim 0.72\,\mu m$, so reflectivity spectra contain information about CdTe films together with information about substrate. Representative scheme of our layered structure can be presented in Fig. 6 [45]. Medium 1 is air, medium 2 is thin bulk CdTe crystal layer and medium 3 is substrate glass, with dielectric functions ε_1 ($\varepsilon_1 = 1$), ε_2 and ε_3, respectively. We can now write [46]:

$$R_A = \frac{A_r}{A_i} = \frac{r_{12}e^{-i\alpha} + r_{23}e^{i\alpha}}{e^{-i\alpha} + r_{12}r_{23}e^{i\alpha}} \tag{4}$$
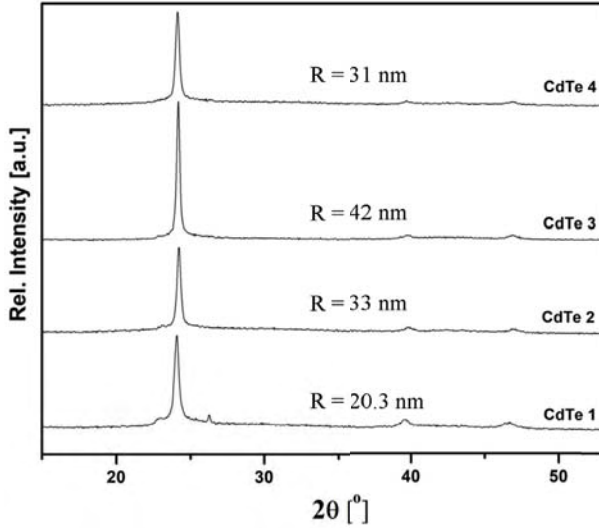
Fig. 3. XRD analysis of CdTe thin films of different thickness. Obtained crystallite sizes (R) are presented too.

Table 1
Parameters obtained from XRD measurements and FIR reflection spectroscopy. Thin films thickness - d, Crystallite size – R.

Name	d [μm]	R [nm]	ω_{l1} (ω_+) [cm^{-1}]	ω_{l2} (ω_-) [cm^{-1}]	ω_P [cm^{-1}]	ω_t [cm^{-1}]	f
CdTe 4	0.39	31.0	187	103	137.5	140.0	0.53
CdTe 2	0.43	33.0	174	78	96.6	140.5	0.53
CdTe 3	0.71	42.0	170	65	79.5	139	0.53
CdTe 1	0.72	20.3	165	30	35.2	140.5	0.53
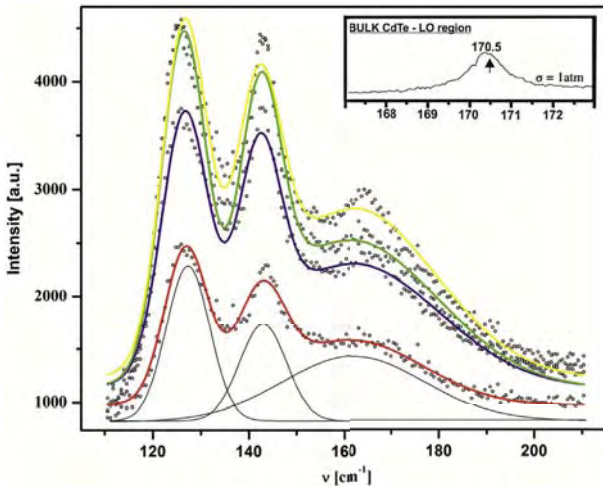
Fig. 4. Raman spectra of CdTe thin films of different thickness. Experimental spectra are shown by open dots. Solid lines are sums of three Lorentz profiles as it shown for spectrum of CdTe 1. In the top right corner LO region of bulk CdTe is presented, taken from the literature [32].

$r_{ij} = (n_i − n_j)/(n_i + n_j) = (\sqrt{\varepsilon_i} − \sqrt{\varepsilon_j})(\sqrt{\varepsilon_i} + \sqrt{\varepsilon_j})$ describe Fresnel coefficients, A_i and A_r represent amplitudes of incident and reflection beams, n is complex index of refraction, ε is the dielectric constant and $\alpha = 2\pi\omega d(\varepsilon_2)^{1/2}$ is the complex phase change related to the absorption in the crystal layer with the thickness d.

Reflectance, R, is given with:

$$R = |R_A|^2 \tag{5}$$

In this case we decided to use dielectric function which takes into

consideration the existence of plasmon – phonon interaction in advance.

The dielectric function of the CdTe crystal layer is:

$$\varepsilon_2(\omega) = \varepsilon_{\infty CdTe} \prod_{j=1}^{2} \frac{\omega^2 + i\gamma_{lj}\omega − \omega_{lj}^2}{\omega(\omega + i\Gamma_p)(\omega^2 + i\gamma_t\omega − \omega_t^2)} \tag{6}$$

The ω_{lj} and γ_{lj} ($j = 1, 2$), parameters of the first numerator are the eigenfrequencies and damping coefficients of the longitudinal plasmon-phonon (LP + LO) waves, that arise as a result of the interaction of the initial phonon ($\omega_{LO,CdTe} = 170.5$ cm^{-1}) and plasmons (ω_P) modes. The parameters of the denominator correspond to the similar characteristics of the transverse vibrations (ω_t, γ_t) and plasmon damping Γ_P. As a result of the best fit, we obtain coupled mode frequencies (ω_{l1} and ω_{l2}).

The dielectric function of the glass substrate is:

$$\varepsilon_s(\omega) = \varepsilon_{\infty\,sup} \prod_{k=1}^{n} \frac{\omega_{LOk}^2 − \omega^2 + i\gamma_{LOk}\omega}{\omega_{TOk}^2 − \omega^2 + i\gamma_{TOk}\omega} \tag{7}$$

where ω_{TO} and ω_{LO} are the transversal and longitudinal optical vibrations, and γ_{TO} and γ_{LO} are damping parameters, respectively.

In our case, layer 2 consists of a CdTe crystals and air (see Fig. 6). The size of the crystallites (R) is given in Fig. 2 and Table 1. These crystallites are described by a dielectric function given in Eq. (1) or Eq. (6) and located randomly in homogeneous environment ε_1 (air) and occupy a volume fraction f, so we can use effective medium theory and Maxwell - Garnet mixing rule, given with Eq. (2).

The far – infrared reflectivity spectrum of the glass substrate is shown in Fig. 7(e). The calculated spectrum, presented by solid line, was obtained using the dielectric function given by equation (7). As a result of the best fit we obtained three modes, whose characteristic frequency are $\omega_{TO1} = 60$ cm^{-1}, $\omega_{LO1} = 140$ cm^{-1}, $\omega_{TO2} = 441$ cm^{-1}, $\omega_{LO1} = 443$ cm^{-1} and $\omega_{TO3} = 471$ cm^{-1}, $\omega_{LO3} = 522$ cm^{-1}. Frequency values of these modes have remained the same during the fitting procedure for all CdTe thin film samples.

The parameters obtained by the best fit between the experimental results and the models for CdTe film described earlier are also given in Table 1. The far-infrared spectra of CdTe thin films, in the spectral range of 80–600 cm^{-1}, at room temperature, are presented in Fig. 7. Experimental data are presented by circles, while the solid lines are calculated spectra obtained by a fitting procedure based on the previously presented model. Experimental and theoretical spectra show an excellent match.

The thicknesses of our films obtained by Far – infrared spectroscopy are 20% greater, which is within the limits of error for both techniques. When using Far – infrared spectroscopy for calculating thickness of layered structured, we bring errors in absolute measurements, because we calculate effective thickness. The important thing is, the trend is the same, the films does not differ in the relative thickness, i.e. thickness ratios between films are the same.

We note that the thickness (d) of the film changes in the range of $\sim 0.39–\sim 0.7$ μm. While the thickness of the film is in the 0.40 μm region, the crystallite size is about 32 nm, and for a film thickness of about 0.72 μm, we have two sizes of crystallites different for a factor of 2. In addition, from Table 1, we have for thicker films CdTe 1 and CdTe 3, that the position of the coupled plasmon-phonon mode ω_{l1} is below the values of $\omega_{LO,CdTe} = 170.5$ cm^{-1}. On the other hand, these values are above $\omega_{LO,CdTe}$ for thin films CdTe 2 and CdTe 4. In both cases plasmon damping (Γ_p) is relatively low. The obtained eigenfrequencies of the plasmon – phonon coupled modes for CdTe thin films are presented in Fig. 8. As a result of the best fit from Fig. 7, we obtained the frequencies of coupled modes (ω_{l1} and ω_{l2}) marked by open circles and transverse mode frequencies which are denoted by - x. Value of ω_P are calculated by Refs. [16–18]:

$$\omega_P = \frac{\omega_{l1}\omega_{l2}}{\omega_t} \tag{8}$$
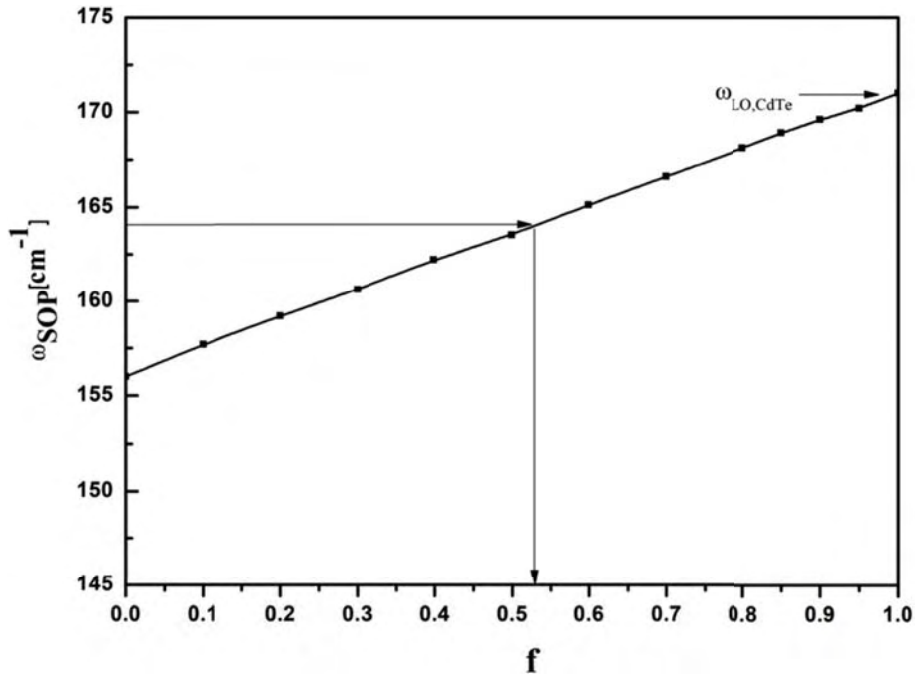
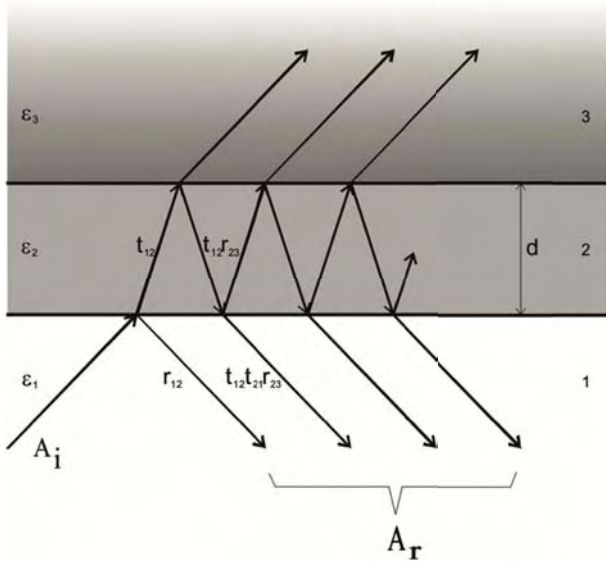Fig. 5. Surface optical phonon (SOP) mode position vs. filing factor.

Fig. 6. Schematic presentation of a three layer structure [46].
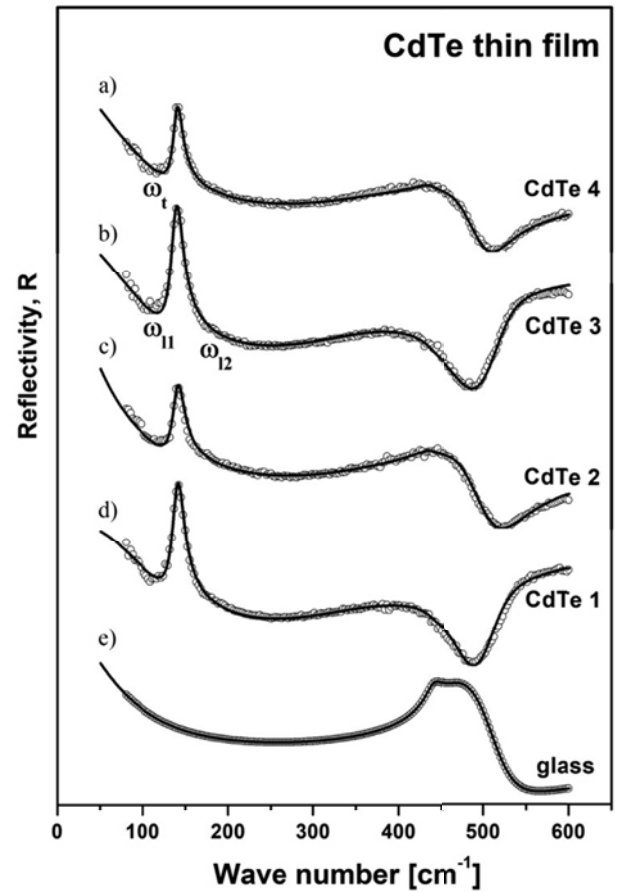

Fig. 7. Far – infrared reflection spectra of: CdTe thin films with thickness of (a) 0.39 μm, (b) 0.71 μm, (c) 0.43 μm, (d) 0.72 μm, and glass substrate (e). Experimental spectra are presented by circles while solid lines are calculated spectra obtained by a fitting procedure based on the model given by Eqs. (2) and (4)–(7).
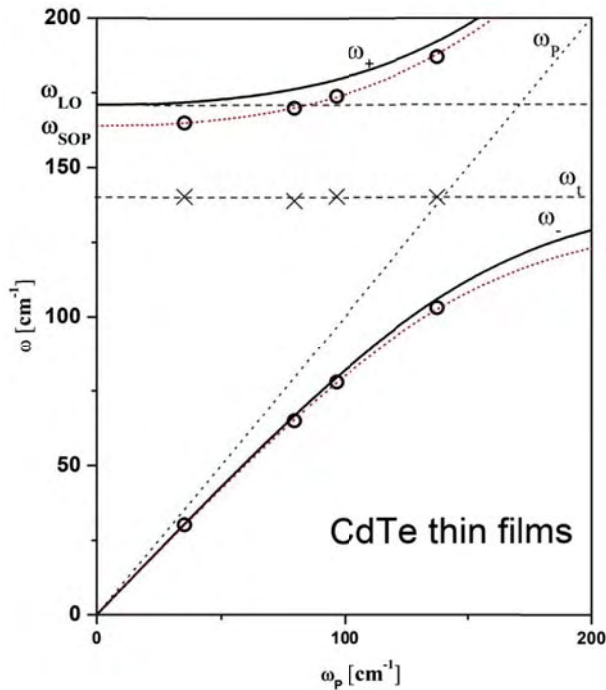
The calculated lines at Fig. 7 are solution of a real part of uncoupled dielectric function (Eq. (1)). However, for plasma-phonon modes positions are obtained:

$$\omega_{\pm} = \frac{\omega_P^2 + \omega_{LO}^2}{2} \pm \sqrt{\frac{(\omega_P^2 + \omega_{LO}^2)^2 - \omega_P \omega_{TO}}{4}} \qquad (9)$$

The full lines in Fig. 7 were obtained for the case $\omega_{LO,CdTe} = 170.5 \, \text{cm}^{-1}$. It is clear that all values of ω_{l1} and ω_{l2} are out of this theoretical model. Best fit, dashed lines in Fig. 7, was obtained for $\omega_{SOP} = 164 \, \text{cm}^{-1}$ which in Eq. (9) plays a role ω_{LO}. Shift of about $7 \, \text{cm}^{-1}$ is registered in relation to $\omega_{LO,CdTe}$, just like in the case of Raman spectra. As we said earlier, the LO phonon shift of CdTe crystal is attributed to the surface optical phonon (SOP) mode effect.

Based on these results, it is clear that in the case of CdTe thin films, prepared by using thermal evaporation technique, the filing factor is constant and does not depend on film thickness, crystallite size and

Fig. 8. The eigenfrequencies of the plasmon–phonon modes for CdTe thin films. The lines are calculated spectra [Re{ε_2} = 0; ε_2 is given by Eq. (1)]: solid line with $\omega_{LO,CdTe} = 170.5$ cm^{-1}; dashed line with $\omega_{SOP} = 164$ cm^{-1}; $\bigcirc$ - ω_{l1}, ω_{l2}; x – ω_t.

concentration of free carriers. On the other hand, the reflection spectra depend on the thickness of the film and the concentration of free carriers in the film, which is expected. In general, thin films have a higher concentration of free carriers ($\sim \omega_p$) (see Table 1). The linear dependence of the position of the SOP mode on the filing factor causes the existence of a modified plasmon – phonon interaction, where the SOP has the role of the LO phonon.

Of course, there are many models that can describe the registered frequency shift of the LO phonon in CdTe e.g. a continuum model of the optical phonon confinement [47,48] would also give a shift of 7 cm^{-1}, but for spherical nanoparticles of about 5 nm, which is far from our case.

4. Conclusion

In this paper, we present results of investigation of CdTe thin films prepared with thermal evaporation technique, with different thicknesses. Sample's surfaces are rather flat, but still they are characterized with bright protrusions and dark holes (air) resulting in a small surface roughness of several nanometers. We showed that, when using thermal evaporation technique we get high quality thin films, especially for thicker films with greater crystallite size. We conclude that the filling factor of our thin films is constant and does not depend on film thickness, crystallite size or concentration of free carriers, but yet has linear dependence on SOP position. This kind of morphology, with filling factor of ~50% causes existence of surface optical phonon and its interaction with plasmon, because of the free surface around nanoparticles. A numerical model for calculating the reflectivity coefficient for complex system, which includes films and substrate, has been applied, and CdTe thin film were treated as a mixture of homogenous spherical inclusion in air modeled by Maxwell – Garnet formula.

Acknowledgements

References

[1] S. Chandra Ray, K. Mallick, Int. J. Chem. Eng. Appl. 4 (2013) 183–186.
[2] C.S. Ferekides, U. Balasubramanian, R. Mamazza, V. Viswanathan, H. Zhao, D.L. Morel, Sol. Energy 77 (2004) 823–830.
[3] R. Kulkarni, et al., Energy Procedia 110 (2017) 188–195.
[4] A. Arnoult, J. Cibert, Appl. Phys. Lett. 66 (1995) 2397–2399.
[5] P. Bhattacharya, D.N. Bose, Semicond. Sci. Technol. 6 (1991) 384–387.
[6] A.U. Ubale, D.K. Kulkarni, Indian J. Pure Appl. Phys. 44 (2006) 254–259.
[7] T.L. Chu, S.S. Chu, C. Ferekides, J. Britt, C.Q. Wu, J. Appl. Phys. 71 (1992) 3870.
[8] A. Nakano, et al., Sol. Cell. 17 (1986) 233.
[9] K.S. Rahman, F. Haque, 3rd International Conference on the Developments in Renewable Energy Technology (ICDRET), 2014, pp. 29–31.
[10] S. Lalitha, S. Zh Karazhanov, P. Ravindran, S. Senthilarasu, R. Sathyamoorthy, J. Janabergenov, Physica B 387 (2007) 227–238.
[11] S. Singh, et al., Thin Solid Films 519 (2010) 1078–1081.
[12] D.S. Chuu, C.M. Dai, W.F. Hsieh, C.T. Tsai, J. Appl. Phys. 69 (1991) 12.
[13] A. Singha, B. Satpati, P.V. Satyam, A. Roy, J. Phys. Condens. Mater. 17 (2005) 5708–5967.
[14] M. Gilić, J. Trajić, N. Romčević, M. Romčević, D.V. Timotijević, G. Stanišić, I.S. Yahia, Opt. Mater. 35 (2013) 1112–1117.
[15] M. Cardona (Ed.), Top. Appl. Phys, vol. 8, Springer, Berlin, 1975.
[16] N. Romčević, M. Romčević, A. Golubović, Le Van Khoi, A. Mycielski, Đ. Jovanović, D. Stojanović, S. Nikolić, S. Đurić, J. Alloy. Compd. 397 (2005) 52–57.
[17] M. Romčević, N. Romčević, V.N. Nikiforov, Infrared Phys. Technol. 42 (2001) 541–545.
[18] N. Romčević, M. Romčević, A. Milutinović, S. Kostić, J. Alloy. Compd. 478 (2009) 41–44.
[19] J. Trajić, M. Romčević, N. Romčević, B. Babić, B. Matović, P. Balaž, Opt. Mater. 57 (2016) 225–230.
[20] N. Romčević, M. Romčević, W.D. Dobrowolski, L. Kilanski, M. Petrović, J. Trajić, B. Hadžić, Z. Lazarević, M. Gilić, J.L. Ristic-Djurović, N. Paunović, A. Reszka, B.J. Kowalski, I.V. Fedorchenko, S.F. Marenkin, J. Alloy. Compd. 649 (2015) 375–379.
[21] J. Trajić, N. Romčević, M. Romčević, V.N. Nikiforov, Mater. Res. Bull. 42 (2007) 2192–2201.
[22] M. Romčević, N. Romčević, W. Dobrowolski, L. Kalinski, J. Trajić, D.V. Timotijević, E. Dynowska, I.V. Fedorchenko, S.F. Marenkin, J. Alloy. Compd. 548 (2013) 33–37.
[23] N. Romčević, J. Trajić, T.A. Kuznetsova, M. Romčević, B. Hadžić, D.R. Khokhlov, J. Alloy. Compd. 442 (2007) 324–327.
[24] J. Trajić, N. Romčević, M. Romčević, D. Stojanović, R. Rudolf, T.A. Kuznetsova, D.R. Khokhlov, J. Alloy. Compd. 493 (2010) 41–46.
[25] J. Trajić, N. Romčević, M. Romčević, D. Stojanović, L.I. Ryabova, D.R. Khokhlov, J. Alloy. Compd. 602 (2014) 300–305.
[26] R.W. Cheary, A. Coelho, J. Appl. Crystallogr. 25 (1992) 109–121.
[27] R. Triboulet & P. Siffert, first ed., Elsevier, 2010.
[28] H. Zeng, W. Cai, B. Cao, J. Hu, Y. Li, P.S. Liu, Appl. Phys. Lett. 88 (2006) 181905.
[29] A. Ghosh, R.N.P. Chodhary, J. Phys. D Appl. Phys. 42 (2009) 075416.
[30] F. Friedrich, N.H. Nickel, Appl. Phys. Lett. 91 (2007) 111903.
[31] J. Xu, W. Ji, X.B. Wang, H. Shu, Z.X. Shen, S.H. Tang, J. Raman Spectrosc. 29 (1998) 613.
[32] V.C. Stergiou, Y.S. Raptis, E. Anastassakis, N. Pelekaneos, A. Nahmani, J. Cibert, Phys. Status Solidi 223 (2001) 237.
[33] J.F. Scott, T.C. Damem, Optic Commun. 5 (1972) 410.
[34] R. Rossetti, S. Nakahara, L.E. Bru, J. Chem. Phys. 79 (1983) 1086.
[35] B.F. Variano, N.E. Schlotter, D.M. Hwangand, C.J. Sandroff, J. Chem. Phys. 88 (1988) 2848.
[36] A.V. Baranov, Y.S. Bobovich, N.I. Grebenshchikova, V.I. Petrov, M.Y. Tsenter, Optic Spectrosc. 60 (1986) 685.
[37] H. Jerominek, M. Pigeon, S. Patela, Z. Jakubczk, C. Delisle, R.J. Tremblay, Appl. Phys. 63 (1986) 957.
[38] E.F. Hilinski, P.A. Lucas, J. Chem. Phys. 89 (1988) 3435.
[39] J. Trajić, M. Gilić, N. Romčević, M. Romčević, G. Stanišić, B. Hadžić, M. Petrović, Y.S. Yahia, Sci. Sinter. 47 (2015) 145–152.
[40] G. Irmer, J. Raman Spectrosc. 38 (2007) 634.
[41] K. Karkkainen, A. Saviola, K. Nikoskinen, IEEE Trans. Geosci. Rem. Sens. 39 (5) (2001) 1013.
[42] J.C.M. Garnett, Trans. Roy. Soc. Can. CIII (1904) 385420.
[43] A. Saviola, I. Lindell, A. Priou (Ed.), Dielectric Properties of Heterogeneous Materials PIER 6 Progres in Electromagnetic Research, Elsevier, Amsterdam, 1992, pp. 101–115 1.
[44] B. Hadžić, N. Romcević, M. Romcević, I. Kuryliszyn-Kudelska, W. Dobrowolski, J. Trajić, D.V. Timotijević, U. Narkiewicz, D. Sibera, J. Alloy. Compd. 540 (2012) 49–56.
[45] M. Gilić, et al., Infrared Phys. Technol. 76 (2016) 276–284.
[46] J. Trajić, M. Gilić, N. Romčević, M. Romčević, G. Stanišić, Z. Lazarević, D. Joksimović, I.S. Yahia, Phys. Scr., T 162 (2014) 014031.
[47] R. Roca, C. Trallero-Giner, M. Cardona, Phys. Rev. B 49 (1994) 13704.
[48] M.P. Chamberlain, C. Trallero-Giner, M. Cardona, Phys. Rev. B 51 (1995) 1680.

Regular article

Far-infrared study of the mechanochemically synthesized Cu$_2$FeSnS$_4$ (stannite) nanocrystals

J. Trajic [a,*], M. Romcevic [a], N. Paunovic [a], M. Curcic [a], P. Balaz [b], N. Romcevic [a]

[a] Institute of Physics, University of Belgrade, 11080 Belgrade, Serbia
[b] Institute of Geotechnics, Slovak Academy of Sciences, 043 53 Kosice, Slovakia

HIGHLIGHTS

- Stannite Cu$_2$FeSnS$_4$ nanocrystals were synthesized mechanochemically.
- Optical properties and compositional purity of Cu$_2$FeSnS$_4$ nanocrystals were characterized.
- Optical properties were investigated by Far-infrared spectroscopy.
- The influence of the milling time on synthesis of the stannite Cu$_2$FeSnS$_4$ was observed.

GRAPHICAL ABSTRACT
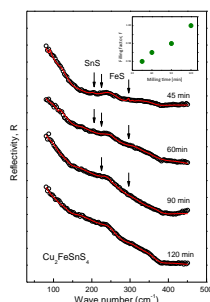
ARTICLE INFO

ABSTRACT

The analysis of the optical properties of mechanochemically synthesized stannite Cu$_2$FeSnS$_4$ nanocrystals has been performed using far-infrared spectroscopy. The Cu$_2$FeSnS$_4$ stannite nanocrystals were synthesized mechanochemically from elemental precursors Cu, Fe, Sn, and S. Milling time was 45, 60, 90 and 120 min. Reflectivity spectra were analyzed using the classical form of the dielectric function, which includes the phonon and the free carrier contribution. The influence of milling time on synthesis of stannite Cu$_2$FeSnS$_4$ is observed. Among the modes that are characteristic for the stannite Cu$_2$FeSnS$_4$, we registered the modes of binary phases of FeS and SnS. The total disappearance of the binary phases of FeS and SnS and forming pure Cu$_2$FeSnS$_4$ is observed when the milling time is 120 min. Effective permittivity of Cu$_2$FeSnS$_4$ and binary phases of FeS and SnS were modeled by Maxwell – Garnet approximation.

1. Introduction

Stannite (Cu$_2$FeSnS$_4$) is one of the best-known sulphide minerals, not only because of its economic importance as a tin ore, but also because of its structural and physical characteristics [1] such as adequate direct band gap (1.0–1.5 eV), low toxicity and a relatively high abundance of the elements in the Earth's crust [2]. Its constituents are abundantly available [3].

To deal with the increasingly severe energy crisis, research on high-efficient and low-cost solar cells is of pressing need and of great significance. Various types of semiconductors such as CdTe, Cu(In,Ga)Se$_2$ and TiO$_2$, have been extensively studied for thin film solar cells. Nevertheless, due to the toxicity of Cd and the limited availability of In and Ga, naturally abundant and non-toxic photo-voltaic materials are of considerable interest [4]. Quaternary semiconductor Cu$_2$FeSnS$_4$ is one of promising photovoltaic materials as an alternative absorber layer for the development of low-cost and environment-friendly thin film solar cells due to its analogous crystal structures to Cu(In,Ga)Se$_2$, suitable band gap and high absorption coefficient [5].

Several low-cost, highly efficient, environmental friendly and easy-to operate methods have been developed for preparation of Cu$_2$FeSnS$_4$, such as pulse laser and electro deposition [6], hot

injection [7], electrospinning [8], dip coating [9], microwave assisted approach [4,10,11] and oxide-nanoparticles-based process [12]. However, these techniques are complex as well as time-consuming, and require high temperature, while in some cases it is necessary to use the toxic organic solvents. Mechanochemical treatment is a powerful technique for synthesis of a wide range of materials where the high energy milling is being applied to induce and speed up chemical reactions [13,14]. This approach is simple, solvent-free, and reproducible, and also the synthesis might be easily scaled up. However, the control of stoichiometry and crystal structure during synthesis of the quaternary nanocrystals remains a challenge.

In this paper, the optical and structural properties of Cu_2FeSnS_4 nanoparticles which are mechanochemically synthesized have been investigated using far-infrared spectroscopy. The reflectivity spectra of the tetragonal Cu_2FeSnS_4 obtained after different milling time have been analyzed using the Maxwell–Garnett approximation. We have determined the influence of the milling time on the purity of the Cu_2FeSnS_4 nanocrystals.

2. Samples preparation and characterisation

The elemental precursors (Cu, Fe, Sn and S) were used to obtain stannite (CFTS) by a solid state one-pot mechanochemical synthesis. The starting materials were elemental Cu (99%), Fe (99%), Sn (99.9%), and S (99%). These materials were weighed and mixed in atomic ratios of 2:1:1:4, according to the stoichiometry Cu_2FeSnS_4. The particularities of synthesis and initial characterization of Cu_2FeSnS_4 nanoparticles were presented previously in Refs. [15,16], and will be briefly discussed here.

The mechanochemical synthesis of Cu_2FeSnS_4 nanoparticles was performed in a Pulverisette 6 planetary mill (Fritsch, Germany). The milling conditions were as follows: milling pot volume-250 ml, material of milling pot – tungsten carbide (WC) with 50 WC balls of 10 mm diameter in it, total weight of reactants – 5 g, ball-to-powder mass ratio – 70, milling speed – 500 min^{-1}. Milling time was 45, 60, 90 and 120 min using an argon protective atmosphere in the mill. Using the described synthesis process, the unique nanostructures and properties are developed. Cu_2FeSnS_4 polymorphs with tetragonally body-centred structure with crystallite sizes of 18–19 nm were obtained.

X-ray diffraction (XRD) is the most commonly used technique to characterize the crystal structure and compositional purity of stannite Cu_2FeSnS_4 nanoparticles. All samples were examined under the same conditions, using a D8 Advance Bruker X-ray diffractometer in the Bragg-Brentano geometry, using the Cu Kα radiation of 0.15418 nm and a scintillation detector at room temperature. The commercial Bruker tools have been used for data processing.

The XRD patterns of the elemental mixture (Cu, Fe, Sn and S powders) obtained after various milling times are shown in the Fig. 1. Diffraction patterns show the reflection of the tetragonal body-centred stannite Cu_2FeSnS_4 according to card JCPDS 44-1476 in the tetragonal space group I-42m. The XRD spectra shows three most intensive peaks at 2θ = 28.5°, 47.5° and 56.0° that can be assigned to the (1 1 2), (2 0 4), and (3 1 2) planes of the tetragonal crystals. Besides mentioned peaks, the peak of the Fe is observed at the Cu_2FeSnS_4 nanocrystal samples obtained after 45 and 60 min milling time. This peak disappears with increasing milling time.

In the attempt to characterize compositional purity of stannite, and observe the influence of the milling time on the mechanochemical synthesis of Cu_2FeSnS_4 nanocrystals we used far-infrared (FIR) spectroscopy. The infrared reflectivity measurements were carried out at room temperature with a BOMEM DA-
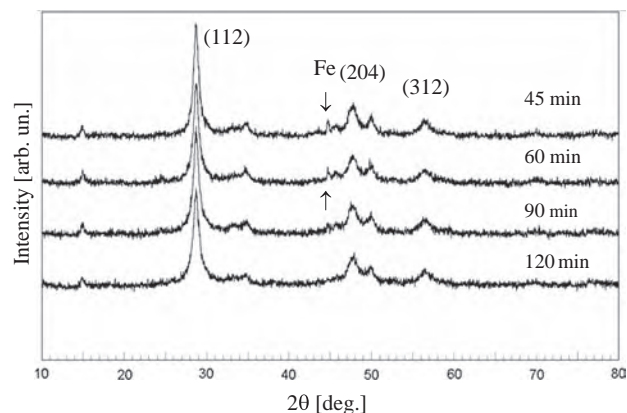

Fig. 1. XRD spectra of Cu_2FeSnS_4 nanocrystals obtained after various milling times.

8 Fourier-transform IR spectrometer. A deuterated triglycine sulfate (DTGS) pyroelectric detector was used to cover the wave number region from 80 to 450 cm^{-1}.

3. Results and discussion

The Cu_2FeSnS_4 is a tetrahedrally coordinated semiconductor in which each sulphur anion is bonded to four cations and each cation is bonded to four sulphur anions [17]. The factor group analysis of the allowed zone-centre vibrations for the I-42m tetragonal crystallographic structures of Cu_2FeSnS_4, indicates that ten infrared (IR) and fourteen Raman active phonon modes of irreducible representations are expected for this compound [18]:

$$\Gamma = 2A_1 + A_2 + 2B_1 + 4B_2 + 6E \tag{1}$$

The B_2 and E modes are IR active and they represent LO-TO splitting due to their polar character. The modes A_1, B_1, B_2 and E are Raman active.

Reflectivity spectra were analyzed using the classical form of the dielectric function, which includes several oscillators and the free carrier contribution to the dielectric function [19]. Whereas the analysis of the far IR reflectivity spectrum of Cu_2FeSnS_4 nanopowders revealed a presence of a plasmon mode, it was necessary to include both contributions of the phonon and the plasmon (free carrier contribution) to the dielectric function:

$$\varepsilon_s(\omega) = \varepsilon_\infty \left(\sum_{j=1}^{l} \frac{\omega_{LOk}^2 - \omega^2 + i\gamma_{LOk}\omega}{\omega_{TOk}^2 - \omega^2 + i\gamma_{TOk}\omega} - \frac{\omega_{P2}}{\omega(\omega + i\Gamma_P)} \right) \tag{2}$$

where ε_∞ is the high-frequency dielectric constant, ω_{LOk}, and ω_{TOk} are longitudinal and transverse frequencies of the k-th oscillator, γ_{LOk} and γ_{TOk} are their corresponding dampings, ω_p and Γ_p are the plasma frequency and damping. The first term in Eq. (2) is the lattice contribution whereas the second term is the Drude expression for the free carrier contribution to the dielectric constant. The far-infrared reflection spectrum of Cu_2FeSnS_4 nanocrystal obtained after 45 min milling time is presented in Fig. 2. The experimental data are presented by circles, while the solid line represents the calculated reflectivity spectra obtained by the fitting procedure based on Eq. (2). In the fitting procedure we included modes at about 93, 120, 144, 250, 315 and 350 cm^{-1} that are in accordance with the reported values for tetragonal Cu_2FeSnS_4 [18,20] as well as, plasma term. We did not succeed to determinate the set of parameters that provide good spectrum overlapping in the whole range of frequencies. Discrepancy between experimental and calculated reflectivity spectra in some regions is obvious,
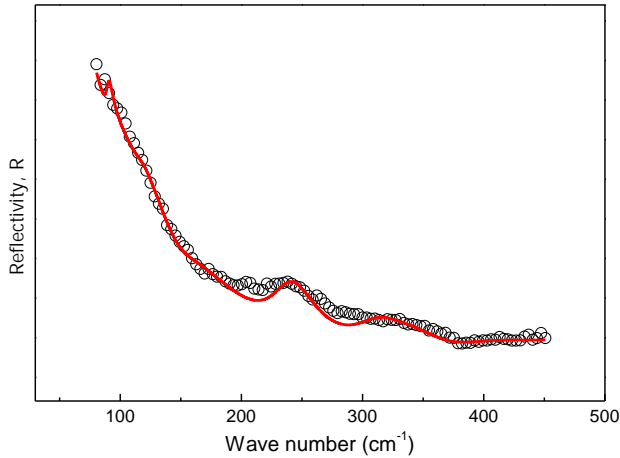
Fig. 2. Far-infrared reflection spectra of stannite Cu_2FeSnS_4 obtained after 45 min milling time. Experimental spectra are presented by circles. The solid lines are calculated spectra obtained by a fitting procedure based on the model given by Eq. (2).
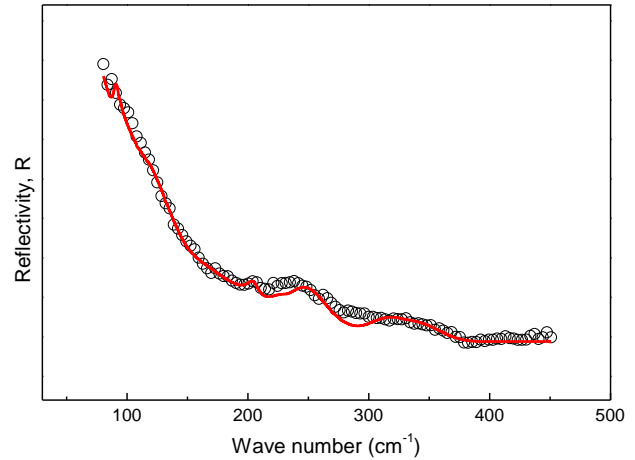

Fig. 3. Far-infrared reflection spectra of stannite Cu_2FeSnS_4 obtained after 45 min milling time. Experimental spectra are presented by circles. The solid lines are calculated spectra obtained by a fitting procedure based on the model given by Eq. (3).

which indicates that in this system among the nanocrystals of Cu_2FeSnS_4 exists another mixtures of starting elements and their phases.

Because our sample consists of Cu_2FeSnS_4 nanoparticles and binary and/or ternary phases of starting elements we have applied the effective medium approximation method to calculate infrared reflectivity spectra. The widely used effective medium theory is the Maxwell–Garnett approximation which treats the effective medium as consisting of a matrix in which are embedded inclusions and where the fraction of the inclusions is very small, so that the inclusions are spatially separated and can be treated as a perturbation [21,22]. For the spherical inclusions case, the prediction of the effective permittivity of mixture ε_{eff} according to the Maxwell-Garnet mixing rule reads [23,24]:

$$\varepsilon_{ff} = \varepsilon_1 + 3f\varepsilon_1 \frac{\varepsilon_2 - \varepsilon_1}{\varepsilon_2 + 2\varepsilon_1 - f(\varepsilon_1 - \varepsilon_2)} \tag{3}$$

Here, spheres of permittivity ε_2 are located randomly in homogeneous environment ε_1 and occupy a volume fraction f. In the case of mechanochemicaly sintesized Cu_2FeSnS_4, multicomponent phases of starting elements with dielectrical function ε_2 are randomly located in pure Cu_2FeSnS_4 with dielectrical function ε_1, where ε_1 and ε_2 are defined by Eq. (2).

In Fig. 3 is presented the far-infrared reflection spectrum of Cu_2FeSnS_4 nanocrystal obtained after 45 min milling time where the solid line is obtained by applying Maxwell–Garnett approximation. In the fitting procedure, besides modes which originated from tetragonal Cu_2FeSnS_4 we included mode at about $215\ cm^{-1}$ which is corresponding to infrared frequency of SnS binary component [25]. Occurrence of SnS binary phase is in accordance with the observation of Bernardini et al, where, by thermal synthesis, also, the minor traces of herzenbergite SnS have been detected, besides stannite [1,26].

Taking into account this mode, corresponding to infrared frequency of SnS binary component, we obtained better overlapping, but it is obvious that besides binary phase of SnS the other multicomponent phases are formed. Satisfactory overlapping of experimental and theoretical spectra is achieved when in the fitting procedure the modes at about 225 and $297\ cm^{-1}$ (Fig. 4a) are added. These two modes are originated from impurity FeS binary phases [17,27]. Slight difference in frequencies between available literature data as well as data we gathered probably arises from the differences in the cation-anion bond distances. Also, disordered
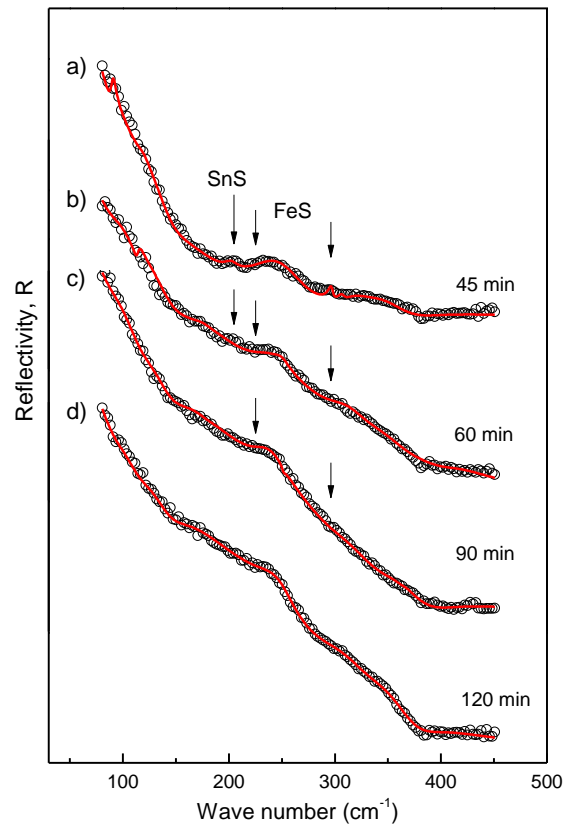

Fig. 4. Far-infrared reflection spectra of stannite Cu_2FeSnS_4 obtained after different milling times. Experimental spectra are presented by circles. The solid lines are calculated spectra obtained by a fitting procedure based on the model given by Eq. (3).

distribution of Cu and Fe atoms leads to the presence of a high content of Cu_{Fe} and Fe_{Cu} anti-site defects that would degrade the crystalline quality of these regions. The existence of a highly disordered distribution of cations in these domains would lead to a shift of the peak towards lower frequencies [28].

The far-infrared reflection spectra of Cu_2FeSnS_4 nanocrystals obtained after various milling times, in the spectral range from 80 to $450\ cm^{-1}$, are presented in Fig. 4. The experimental data

Table 1
Volume fraction of tetragonal Cu_2FeSnS_4 as a function of milling time.

Milling time [min]	Filling factor, f
45	0.96
60	0.97
90	0.98
120	1

are presented by circles, while the solid line represent the calculated reflectivity spectra obtained by the fitting procedure based on Eq. (3).

The spectrum of Cu_2FeSnS_4 nanocrystals obtained after 60 min milling time is presented in Fig. 4b. In the case of this nanocrystal the same modes are registered as in the sample obtained after 45 min milling time. Namely, modes originated from tetragonal Cu_2FeSnS_4, together with modes originated from binary phases FeS and SnS are registered at infrared spectra samples obtained after 45 and 60 min milling time. In infrared spectrum of sample obtained after 90 min milling time (Fig. 4c), the mode that corresponds to SnS was not observed, whereas in the case of the nanocrystal obtained after 120 min milling time (Fig. 4d), only the modes originated from pure tetragonal Cu_2FeSnS_4 are registered. This spectrum, obtained after 120 milling time, is calculated with the set of parameters corresponding to the pure Cu_2FeSnS_4 sample.

The total disappearance of the mode originated from SnS binary phase is observed after 60 min milling time, and FeS modes disappear when the milling time is 120 min (longer than 90 min). Absence of those modes excluded the presence of FeS and SnS binary phases, which indicates that after 90 min milling time pure stannite Cu_2FeSnS_4 is synthesized.

Volume fraction of tetragonal Cu_2FeSnS_4 obtained as estimation of the best fit parameter are presented in Table 1. As milling time increases, the filling factor increase also, which indicates that during miling the contribution of impurity binary phases FeS and SnS decrease, while contribution of pure, tetragonal Cu_2FeSnS_4 increases. Namely, Cu_2FeSnS_4 is synthesized from elemental precursors Cu, Fe, Sn and S by applying the high-energy milling. During synthesis besides tetragonal Cu_2FeSnS_4 nanocrystal the binary phases of starting elements FeS and SnS occur. In our case where the multicomponent phases of starting elements are randomly located in Cu_2FeSnS_4, the filling factor f gives us information about the contribution (volume fraction) of pure Cu_2FeSnS_4.

4. Conclusion

We have measured the far-infrared reflectivity spectra of the mechanochemically synthesized Cu_2FeSnS_4 nanocrystals obtained after different milling time. Reflectivity spectra were analyzed using the classical form of the dielectric function, which includes the phonon and plasmon contribution to the dielectric function. The best fit spectra are obtained using the Maxwell–Garnett approximation. Besides modes which are characteristic for tetragonal Cu_2FeSnS_4 nanocrystals we registered the existence of modes that originates from binary phases of FeS and SnS. The total disappearance of the mode originated from SnS binary phase is observed after 60 min milling time, and FeS modes disappear when the milling time is longer than 90 min. Absence of those modes excluded the presence of FeS and SnS binary phases, which indi-

cates that after 90 min milling time pure stannite Cu_2FeSnS_4 is synthesized. As a best fit parameter we determined volume fraction of tetragonal Cu_2FeSnS_4 as a function of milling time. Analyzing the reflectivity spectra we determine not only which impurity components occur during the synthesis of Cu_2FeSnS_4, and we find out the change in contribution of these impurity components as the miling time is varied.

Conflict of interest

None.

References:

[1] G.P. Bernardini, D. Borrini, A. Caneschi, F. Di Benedetto, D. Gatteschi, S. Ristori, M. Romanelli, Phys. Chem. Miner. 27 (2000) 453–461.
[2] B. Zhou, X. Yan, P. Li, L. Yang, D. Yu, Eur. J. Inorgan. Chem. 1 (2015) 2690–2694.
[3] H. Guan, H. Shen, B. Jiao, Xu Wang, Mater. Sci. Semicond. Process. 25 (2014) 159–162.
[4] X. Meng, H. Deng, J. He, L. Sun, P. Yang, J. Mater. Lett. 151 (2015) 61–63.
[5] X. Zhang, N. Bao, K. Ramasamy, Y.A. Wang, Y. Wang, B. Lin, A. Gupta, Chem. Commun. 48 (2012) 4956–4958.
[6] Y. Li, T.F. Yuan, L.X. Jiang, Z.H. Su, F.Y. Liu, J. Alloys Comp. 610 (2014) 331–336.
[7] L. Li, B.L. Zhang, M. Cao, Y. Sun, J.C. Jiang, P.F. Hu, Y. Shen, J. Alloys Comp. 551 (2013) 24–29.
[8] F. Ozel, M. Kus, A. Yar, E. Arkan, M. Can, A. Aljabour, N.M. Varal, M. Ersoz, J. Mater. Sci. 50 (2015) 777–783.
[9] G. Rajesh, N. Muthukumarasamy, E.P. Subramaniam, S. Agilan, D. Velauthapillai, J. Sol-Gel Sci. Technol. 66 (2013) 288–292.
[10] M. Sabet, M.S. Niasari, D. Ghanbari, O. Amiri, M. Yousefi, Mater. Sci. Semicond. Process. 16 (2013) 696–704.
[11] S.M.H. Mashkani, F. Mohandes, M.S. Niasari, K.V. Rao, Mater. Res. Bull. 47 (2012) 3148–3159.
[12] G. Chen, J. Li, S. Chen, Z. Huang, M. Wu, Mater. Chem. Phys. 188 (2017) 95–99.
[13] P. Baláž, Mechanochemistry in Nanoscience and Minerals Engineering, Springer, Berlin Heidelberg, 2008, p. 413.
[14] P. Baláž, M. Achimovičová, M. Baláž, P. Billik, Z. Cherkezova-Zheleva, J.M. Criado, F. Delogu, E. Dutková, E. Gaffet, F.J. Gotor, R. Kumar, I. Mitov, T. Rojac, M. Senna, A. Streletskii, K. Wieczorek-Ciurowa, Chem. Soc. Rev. 42 (2013) 7571–7637.
[15] P. Baláž, M. Baláž, M.J. Sayagués, I. Škorvánek, A. Zorkovská, E. Dutková, J. Briančin, J. Kováč, J. Kováč Jr, Y. Shpotyuk, Nanoscale Res. Lett. 12 (2017) 256–266.
[16] P. Baláž, M. Baláž, A. Zorkovská, I. Škorvánek, Z. Bujnáková, J. Trajić, Acta Phys. Polon. 131 (4) (2017) 1153–1155.
[17] C. Yan, C. Huang, J. Yang, F. Liu, J. Liu, Y. Lai, J. Li, Y. Liu, Chem. Commun. 48 (2012) 2603–2605.
[18] T. Gürel, C. Sevik, T. Cagin, Phys. Rev. B 84 (2011) 205201.
[19] R.J. Gonzalez, R. Zallen, H. Berger, Phys. Rev. B 55 (11) (1997) 7014–7017.
[20] M. Himmrich, H. Haeuseler, Spectrochim. Acta 47A (7) (1991) 933–942.
[21] J.E. Spanier, I.P. Herman, Phys. Rev. B 61 (15) (2000) 10437.
[22] J.J. Saarinen, E.M. Vartiainen, K.E. Peiponen, Opt. Rev. 10 (2) (2003) 111.
[23] J.C.M. Garnett, Transaction of the Royal Society CCIII 385420, 1904.
[24] A. Saviola, I. Lindell, Dielectric Properties of Heterogeneous Materials PIER 6 Progres in Electromagnetic Research ed. A. Priou, Amsterdam, Elsevier, 1992, pp. 101–151.
[25] J.M. Chamberlain, P.M. Nikolic, M. Merda, P. Mihailovic, J. Phys. C: Solid State Phys. 9 (1976) L637–L642.
[26] G.P. Bernardini, P. Bonazzi, M. Corazza, F. Corsini, G. Mazzetti, L. Poggi, G. Tanelli, Eur. J. Mineral. 2 (1990) 219–225.
[27] Y. El Mendili, B. Minisini, A. Abdelouas, J.-F. Bardeau, RSC Adv. 4 (2014) 25827–25834.
[28] X. Fontané, V. Izquierdo-Roca, E. Saucedo, S. Schorr, V.O. Yukhymchuk, M.Ya. Valakh, A. Pérez-Rodríguez, J.R. Morante, J. Alloys Comp. 539 (2012) 190–194.
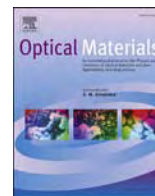
Structural properties of Eu^{3+} doped Gd$_2$Zr$_2$O$_7$ nanopowders: Far-infrared spectroscopy

J. Mitrić [a, *], J. Križan [b], J. Trajić [c], G. Križan [b], M. Romčević [c], N. Paunović [c], B. Vasić [c], N. Romčević [c]

[a] *School of Computing, University Union, Knez Mihailova 6, Belgrade 11 000, Serbia*
[b] *AMI, d. o. o., Ptuj, Slovenia*
[c] *Institute of Physics, University of Belgrade, Pregrevica 118, 11080 Belgrade, Serbia*

ARTICLE INFO

ABSTRACT

The Solution Combustion Synthesis (SCS) method was used to prepare nanopowders of europium doped cubic Gd$_2$Zr$_2$O$_7$ nanopowders. The surface of the samples have been investigated using atomic force spectroscopy (AFM) and far-infrared spectroscopy (FIR). Far-infrared reflectivity spectra of Eu^{3+} doped Gd$_2$Zr$_2$O$_7$ nanopowders were measured at room temperature in spectral region between 80 and 650 cm^{-1}. The Maxwell–Garnet formula was used to model dielectric function of Eu^{3+} doped Gd$_2$Zr$_2$O$_7$ nanopowders as mixtures of homogenous spherical inclusions in air.

© 2017 Elsevier B.V. All rights reserved.

1. Introduction

A$_2$B$_2$O$_7$ type of pyrochlores are important class of materials because of their diverse scientific and technological applications like in nuclear waste storage [1], electro/photo catalysis [2,3], luminescence [3], CO$_2$ hemisorption [4], photoluminescence hosts [5], topological Mott insulator [6] etc.

Pyrochlore oxides which occur in various crystalline phases, manifest numerous interesting and important physicochemical properties which make them eligible for potential hosts for the chemical substitution [7].

Rare earth based zirconates (Re$_2$Zr$_2$O$_7$) pyrochlores have wide scientific and technological applications as: potential thermal barrier coatings (TBC), high temperature heating devices or luminescence hosts [8].

Among all rare earth based pyrochlores, Gd$_2$Zr$_2$O$_7$ stands out as a material with a distinctively low thermal conductivity and high phase stability [9]. Besides that, Gd$_2$Zr$_2$O$_7$ could be an excellent candidate for potential photoactive materials [10].

As shown through our previous work [4,11], there are two different crystal structures for Gd$_2$Zr$_2$O$_7$, pyrochlore and the fluorite type.

Rare earth ions are widely used as activators for various phosphors and other organic and inorganic luminescent materials, because they offer high color purity, high luminescence lifetime and also a narrow emission profile, thanks to its optically active 4f electrons which are strongly shielded from the rest of ions by the other 5s and 5p shells [12].

Among all lanthanides, Eu^{3+} ion is in advantage as a dopant ion for structural probing, as well as for synthesis of red light emitting phosphor [8]. The reason this ion is a useful spectroscopic probe is because of its main source of luminescence - single level, ^{5}D$_0$ state, which prevents the convolution of overlapping emission peaks from different levels [13]. Also, doping any aliovalent ion in these oxides is not only used for structural probing, but it could also generate significant changes in photophysical behavior of those materials in such way that doping creates various kinds of defects like ion/oxygen vacancies, which can alter the band gap of materials, i.e. photophysical characteristics of one material. Particularly for Gd$_2$Zr$_2$O$_7$, it is proven that efficient doping results in tuning of thermal [14], electrical [15], optical [4] and other properties.

In this paper, we present the results obtained by using far – infrared spectroscopy (FIR) to study optical properties of the Eu^{3+} doped Gd$_2$Zr$_2$O$_7$ nanopowders which were prepared by the Solution Combustion Synthesis (SCS) method. The dielectric function of Eu^{3+} doped Gd$_2$Zr$_2$O$_7$ nanopowder is modeled as a mixture of

---

* Corresponding author.
    E-mail address: jmitric@ipb.ac.rs (J. Mitrić).

homogenous spherical inclusions in air, by the Maxwell-Garnet formula.

2. Sample and characterization

Europium doped cubic $Gd_2Zr_2O_7$ nanopowders were prepared by Solution Combustion Synthesis (SCS) method. Starting chemicals $Gd(NO_3)\cdot 6H_2O$, $Zr(NO_3)_2\cdot H_2O$, $Eu(NO_3)\cdot 6H_2O$ with the purity of 99,99% were purchased from ABCR, Gd_2O_2 (99,9%) from the NOAH Technologies and urea $(NH_2)_2CO$ from Sigma-Aldrich.

Due to its simplicity and low cost of the synthesis procedures and possibility of tailoring the size and morphology of particles, the flame combustion process is the most frequently used. After the synthesis, the nanopowder was annealed, in order to achieve the full crystallinity, in air atmosphere at 1200 °C for 2 h. The Eu^{3+} concentration in $Gd_2Zr_2O_7$ was 2 mol%. The morphology analysis of the synthesized materials indicates the irregular crystallite size distribution and existence of agglomerated grains which are in the submicron size.

In our previous work [4,11] we performed X − ray powder diffraction (XRD) and photoluminescence measurements of the same material. XRD analysis confirmed that sample was crystallized in fluorite (F) type structure (space group Fm3m). The photoluminescence spectra showed a number of electronic transitions, among them were those at 705 nm and 713 nm ($^5D_0 - {}^7F_4$), 654 nm ($^5D_0 - {}^7F_3$), 630 and 611 nm ($^5D_0 - {}^7F_2$), 593 nm ($^5D_0 - {}^7F_1$), 584 nm ($^5D_0/{}^5D_1 - {}^7F_1$) and 578 nm ($^5D_0/{}^5D_1 - {}^7F_0$).

The Raman spectra of Eu^{3+} doped $Gd_2Zr_2O_7$ nanopowders were measured. We registered three phonons at 177 cm^{-1}, 268 cm^{-1} and 592 cm^{-1}, as well as their overtones at 354 cm^{-1}, 445 cm^{-1}, 708 cm^{-1}, 1062 cm^{-1}, 1184 cm^{-1}, ~1530 cm^{-1} and ~1720 cm^{-1}. The phonon at 592 cm^{-1} was already known to be characteristic for $Gd_2Zr_2O_7$ fluorite − type structure, and we found that other two phonon positions to be characteristic with the observed electron − phonon observed interaction and that the registered multiphonon processes were a consequence of miniaturization that further induces changes in electronic structure of Eu^{3+} doped $Gd_2Zr_2O_7$ nanopowders. All the above mentioned results will be useful in the far − infrared spectroscopy analysis of Eu^{3+} doped $Gd_2Zr_2O_7$ nanopowders.

3. Results and analysis

3.1. AFM

Atomic force microscopy (AFM) measurements were done using NTEGRA Prima system from NT-MDT at room temperature and ambient conditions. Imaging was done in tapping mode using NSG01 probes. Phase lag of AFM cantilever was recorded simultaneously during tapping mode imaging.

Two dimensional and three dimensional topography of the sample surface are shown in Fig. 1(a) and (b), respectively (scan size is 5 × 5 μm^2). As can be seen, the surface is rather flat with characteristic holes represented with dark color. Cross section of one characteristic hole (along dashed line in Fig. 1(a)) is given in the inset of Fig. 1(a). Hole width and depth are around 1 μm and 200 nm, respectively. Apart from this holes, the sample surface consists of small grains. They are better visualized in Fig. 1(c) and (d) showing the topography and phase contrast image of a zoomed part (scan size is 1 × 1 μm^2). Grains are clearly visible, especially
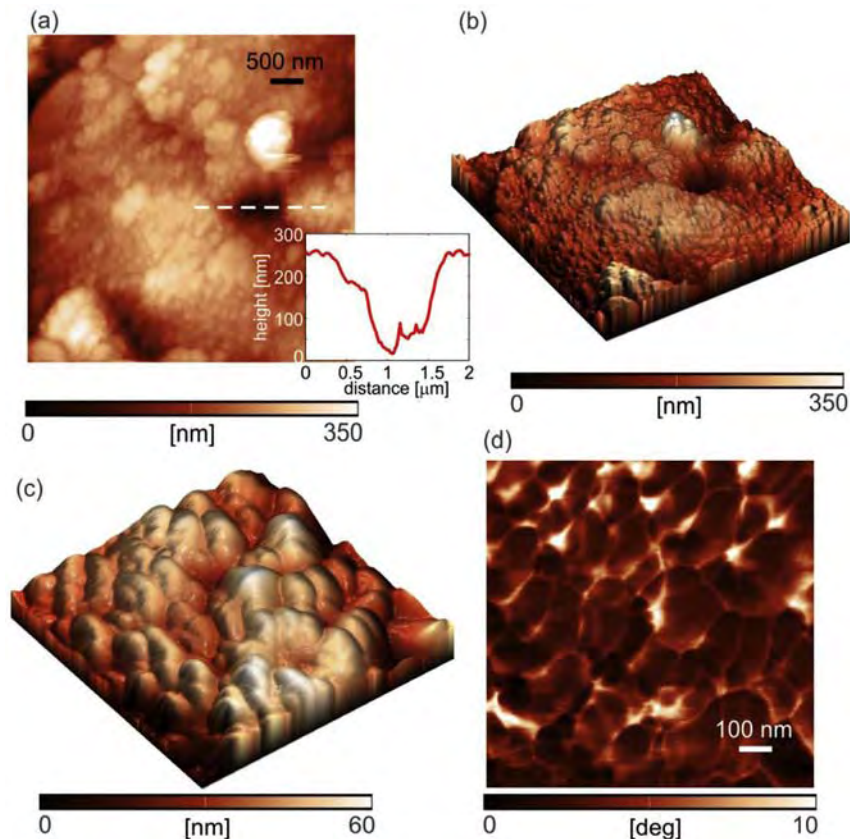

Fig. 1. (a) Two-dimensional and (b) three-dimensional topography of the sample surface. The inset in part (a) shows the cross-section along the corresponding dashed line. (c) Three-dimensional topography and (b) corresponding phase contrast image of a zoomed region from part (a).

grain boundaries in the phase contrast image since the phase is very sensitive to abrupt changes in the topography. Dispersion of grain size is rather wide, but still we can conclude that the characteristic grain size is in the order of 100 nm.

3.2. Far-infrared spectroscopy

The infrared reflectivity measurements were performed at room temperature with a BOMEM DA-8 Fourier-transform infrared spectrometer. A Hyper beamsplitter and deuterated triglycine sulfate (DTGS) pyroelectric detector were used to cover the wave number region from 80 to 650 cm^{-1}. Spectra were collected with 2 cm^{-1} resolution and with 500 interferometer scans added for each spectrum.

When visible light, λ, interacts with semiconducting nanoparticles (characteristic size d, dielectric function ε_2) which are distributed in a medium with the dielectric constant ε_1 in the limit $\lambda \gg d$, the heterogeneous composite can be treated as a homogeneous medium and effective medium theory is applied. There are many mixing models for the effective dielectric permittivity of such mixture [16]. Since our samples are well defined and separated nanosized grains, we used Maxwell-Garnet model for present case. For the spherical inclusions case, the prediction of the effective permittivity of mixture, ε_{eff}, according to the Maxwell-Garnet mixing rule is [17]:

$$\varepsilon_{eff} = \varepsilon_1 + 3f\varepsilon_1 \frac{\varepsilon_2 - \varepsilon_1}{\varepsilon_2 + 2\varepsilon_1 - f(\varepsilon_1 - \varepsilon_2)} \tag{1}$$

Here, spheres of permittivity ε_2 are located randomly in homogeneous environment ε_1 and occupy a volume fraction f. The observed nanoparticles are situated in air, therefore the ε_1 is 1. For dielectrical function of observing nanoparticles (ε_2) we used the standard model [18]:

$$\varepsilon_2(\omega) = \varepsilon_\infty \left(\prod_{k=1}^{n} \frac{\omega_{LOk}^2 - \omega^2 + i\gamma_{LOk}\omega}{\omega_{TOk}^2 - \omega^2 + i\gamma_{TOk}\omega} - \frac{\omega_P^2}{\omega(\omega - i\tau^{-1})} \right) \tag{2}$$

where ε_∞ is the bound charge contribution and it is assumed to be a constant, ω_{TOk} and ω_{LOk} are transverse and longitudinal frequencies, γ_{TOk}, and γ_{LOk} are their dampings, ω_P is the plasma
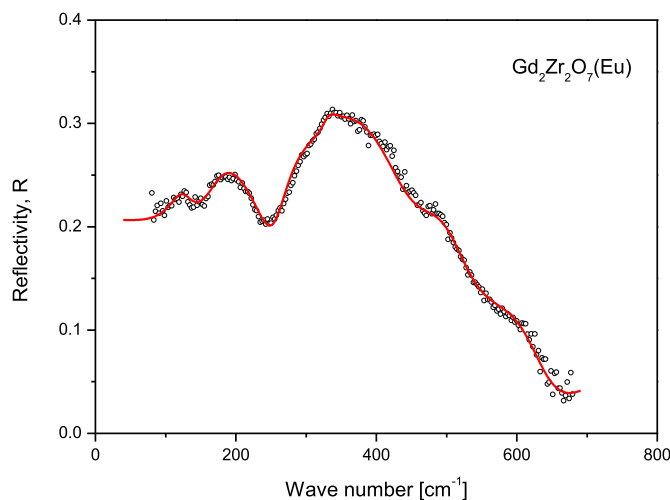
Fig. 2. Far − infrared reflection spectra of Eu^{3+} doped $Gd_2Zr_2O_7$ nanopowder. The experimental data are represented by circles. The solid lines are the calculated spectra obtained with the parameter values given in Table 1 and the fitting procedure based on the model given by Eqs. (1) and (2).

frequency and τ is the free carrier relaxation time. The first term in (2) is the lattice contribution, whereas the second term is the Drude expression for the free carrier contribution to the dielectric constant. In this case, we will consider ω_{TOk} as a characteristic frequency of material (ν_k), and we will link ω_{LOk} with oscillator strength ($S_k \sim \omega_{LOk}^2 - \omega_{TOk}^2$) which does not have big influence on discussion.

The far-infrared spectra of Eu^{3+} doped $Gd_2Zr_2O_7$ nanopowders, in the spectral range of 80–650 cm^{-1}, at room temperature, are presented in Fig. 2. The experimental data are presented by circles, while the solid lines are calculated spectra obtained by a fitting procedure based on the previously presented model. In Table 1 the best fit parameters are presented. Values for Eu^{3+} doped $Gd_2Zr_2O_7$ single crystal are taken from literature [11,19−22].

McCauley [23], and Vandenborre [24] came to the result that of the total number of 26 normal modes ($\Gamma = A_{1g} + E_g + 2F_{1g} + 4F_{2g} + 3A_{2u} + 3E_u + \underline{\textbf{8F_{1u}}} + 4F_{2u}$) only those of F_{1u} vibrations are active in the IR absorption. One of the eight F_{1u} modes is associated with three degrees of translation of the unit cell and refers to the acoustic branch of the crystal vibrations and thus analysis predict 7 IR − active optic modes [22]. Our results confirm all of the seven active vibrations and their assignations are shown in Table 1 and also indicate that anharmonicity factors are not significant. The analysis [23,24] also predicts that six vibrations of the types A_{1g}, E_g and $4F_{2g}$ are Raman − active modes. As per the selection rules, the remaining modes (F_{1g}, A_{2u}, E_u and F_{2u}) are inactive both in the IR and Raman spectra. According to the group-theoretical analysis, all the atoms of the crystal lattice are involved in the seven IR active F_{1u} vibrations (and six Raman − active modes) of the pyrochlore [22−24].

Following other authors' and our previous work [11,25] we started our analysis from the bulk material, considering that understanding bulk properties will lead to better understanding of properties of small particles, and therefore, as a result we expect the bulk modes to be shifted and broadened.

All modes are shifted compared to literature data. We believe that this is not because of the doping with Eu^{3+} and that in relatively small concentrations/amounts, doping did not induce changes in phonon spectra of $Gd_2Zr_2O_7$ [26]. We confirm our previous work [11] where we used Raman spectroscopy to obtain modes at 177 cm^{-1} and 268 cm^{-1} which noticeably differed from results obtained by many other authors who claimed that these modes occur at ~140 cm^{-1} (O-A-O vibrations) and ~220 cm^{-1} (O-B-O vibrations), respectively. Using FIR spectroscopy we obtained significant modes at 175 cm^{-1} and 255 cm^{-1} which describe O-A-O and O-B-O vibrations, respectively. The reason for this shift, as we believe, is electron − phonon interaction which led to the breakdown of the selection rules and appearance of the new phonons in fluorite structure $Gd_2Zr_2O_7$:Eu spectrum [11].

Interesting thing is, FIR spectrum shows two modes characteristic for pyrochlore type of structure, at 365 cm^{-1} and 490 cm^{-1}, although they are weak [19]. These two modes correspond to the vibrations of GdO_8 and ZrO_6 polyhedra, respectively. This confirm some earlier thoughts of P phase and F phase co-existing in the sample [19]. As it was said earlier [4,11], $Gd_2Zr_2O_7$ has two isometric structures, disordered fluorite (F) and ordered pyrochlore (P). In general, disordered fluorite structure type for this compound is confirmed [4]. But, it is also known that $Ln_2Zr_2O_7$ (Ln = elements of lanthanide series) have a pyrochlore-type structure stable at low temperature [19]. The Raman activity allowed for the pyrochlore structure results from oxygen vibrations, and only four bands are observed in the Raman spectra of $Ln_2Zr_2O_7$ pyrochlore-type compounds (Table 1 [21]). In the ordered structure there is no evidence of the significant band at 125 cm^{-1}, like our FIR spectrum shows.

Table 1
Best fit parameters of far − infrared spectra of Eu^{3+} doped $Gd_2Zr_2O_7$.

Exp. results: $Gd_2Zr_2O_7$: Eu^{3+} nanopowder	Literature: $Gd_2Zr_2O_7$: Eu^{3+} single crystal	Assignment
50	−	$\mathbf{v_7}$: O′-Gd-O′ bending vibrations
126	−	$\mathbf{v_6}$: Gd-ZrO_6 streching vibrations
175	177 [11]	$\mathbf{v_5}$: O-Gd-O bending vibrations
255	268 [11]	$\mathbf{v_4}$: O-Zr-O bending vibrations
330	310 [20], 315 [21]	$\mathbf{v_3}$: Zr-O + O-Zr-O vibrational mode (O-Zr-O bending)
365	370 [19], 400 [21]	$\mathbf{v_2}$: vibrations of GdO_8 polyhedra
490	500 [19], 538 [21]	$\mathbf{v_1}$: Zr-O stretching vibration, vibrations of ZrO_6 polyhedra
610	599 [20], 592 [21]	$\mathbf{E_g}$: Zr-O′ stretching vibration

The thing is, for $Ln_2Zr_2O_7$ compounds, an order − disorder transition pyrochlore ↔ defective fluorite may occur when the temperature is raised [21]. This confirms that in $Gd_2Zr_2O_7$:Eu nanopowder P- and F- phase coexist. At first, this is not in agreement with XRD results for $Gd_2Zr_2O_7$:Eu nanopowder [4], but using FIR spectroscopy in reflectivity mode, we concern mainly the surface of material and coexistence of two phases is characteristic for the surface, but not for the general structure which is generally investigated using XRD.

Modes at 330 cm^{-1} and 610 cm^{-1} are clearly visible in both F phase and P phase spectra [20] and they correspond to Zr-O + O-Zr-O vibrational mode.

The rest of well known IR active vibrations, O-Gd-O and O′-Gd-O′ (O′ represents the 8(a) site oxide ion [27,28]) bending vibrations, are not yet assigned for Gd - zirconates. We assume that these vibrations correspond to 50 cm^{-1}, 126 cm^{-1} modes, respectively. The mode at 50 cm^{-1} clearly could not be obtained with our spectrometer which works in 80–650 cm^{-1} region, but that mode is well-suited to the fitting procedure based on the model given by Eqs. (1) and (2). Value of 50 cm^{-1} for Gd-zirconate is expected, regarding [[22], pg. 78, Table VII] which shows O′-Gd-O′ assignments for lanthanide series from La to Sm, but not for the Gd. We find answer in the isotope effect. The change in spectrum is conditioned with the mass of nuclei, and if the mass of some element is greater, spectral lines will move to lower values of wave number. Therefore, considering the increase in mass from La to Gd, we assume that previously unknown wave number value of O′-Gd-O′ vibration for Gd-zirconates corresponds to our result of 50 cm^{-1} (value of wave numbers from La to Gd are decreasing). We also use isotopic shift to explain the 126 cm^{-1} for which we assume corresponds to O-Gd-O vibration band and it also may suggest the possibility of a lowered local symmetry for some crystallographic sites [24] (that is in agreement with our assumptions with order ↔ disorder transition).

4. Conclusion

In this paper far-infrared reflectivity measurements were used to obtain phonon properties of Eu^{3+} doped $Gd_2Zr_2O_7$ nanopowders. We registered phonons of both isomeric structures characteristic for $Gd_2Zr_2O_7$ nanopowder and concluded coexistence of these two phases on the surface of the material, whereas fluorite structure is typical for the general structure. Low frequency modes were registered and regarding isotope effect they have been assigned.

Acknowledgments

References

[1] C. Fischer, S. Finkeldei, F. Brandt, D. Bosbach, A. Luttge, Direct measurement of surface dissolution rates in potential nuclear waste forms: the example of pyrochlore, ACS Appl. Mater. Interfaces 7 (32) (2015) 17857−17865.
[2] M.C. Hsieh, G.C. Wu, W.G. Liu, W.A. Goddard, C.M. Yang, Nanocomposites of tantalum-based pyrochlore and indium hydroxide showing high and stable photocatalytic activities for overall water splitting and carbon dioxide reduction, Angew. Chem. Int. Ed. 53 (51) (2014) 14216−14220.
[3] J. Parrondo, M. George, C. Capuano, K.E. Ayers, V. Ramani, Pyrochlore electrocatalysts for efficient alkaline water electrolysis, J. Mater. Chem. A 3 (20) (2015) 10819−10828.
[4] M.S. Rabasovic, D. Sevic, J. Krizan, M. Terzic, J. Mozina, B. Marinkovic, N.R.M. Mitric, M.D. Rabasovic, Characterization and luminescent properties of Eu^{3+} doped $Gd_2Zr_2O_7$ nanopowders, J. Alloys Compd. 622 (3) (2014) 292−295.
[5] R.J. Walker, et al., Surface termination and CO2 adsorption onto bismuth pyrochlore oxides, Chem. Mater. 28 (1) (2016) 90−96.
[6] T. Kondo, et al., Quadratic Fermi node in a 3D strongly correlated semimetal, Nat. Commun. 6 (2015) 10042.
[7] S.K. Gupta, P.S. Ghosh, C. Reghukumar, N. Pathak, R.M. Kadam, Experimental and theoretical approach to account for green luminescence from $Gd_2Zr_2O_7$ pyrochlore: exploring the site occupancy and origin of host-dopant energy transfer in $Gd_2Zr_2O_7$, RSC Adv. 6 (50) (2016) 44908−44920.
[8] J. Wu, et al., Thermal-barrier-coating applications, J. Am. Ceram. Soc. 35 (2002) 3031−3035.
[9] L. Wang, J.I. Eldridge, S.M. Guo, Thermal radiation properties of plasma-sprayed $Gd_2Zr_2O_7$ thermal barrier coatings, Scr. Mater. 69 (9) (2013) 674−677.
[10] K.-J. Hu, Z.-G. Liu, J.-Y. Wang, T. Wang, J.-H. Ouyang, Synthesis and photoluminescence properties of Eu^{3+}- doped $Gd_2Zr_2O_7$, Mater. Lett. 89 (2012) 276−278.
[11] G. Križan, M. Gilić, J.L. Ristić - Đurović, J. Trajić, M. Romčević, J. Križan, B. Hadžić, B. Vasić, N. Romčević, Raman Spectroscopy and electron - phonon coupling in Eu^{3+} doped $Gd_2Zr_2O_7$ nanopowders, Opt. Mater. 73 (2017) 541−544.
[12] Y.S. Chang, H.J. Lin, Y.L. Chai, Y.C. Li, Preparation and luminescent properties of europium-activated $YInGe_2O_7$ phosphors, J. Alloys Compd. 460 (1−2) (2008) 421−425.
[13] W. Zheng, P. Huang, D. Tu, E. Ma, H. Zhu, X. Chen, Lanthanide-doped upconversion nano-bioprobes: electronic structures, optical properties, and biodetection, Chem. Soc. Rev. (6) (2015) 1379−1415.
[14] K.S. Lee, K.I. Jung, Y.S. Heo, T.W. Kim, Y.G. Jung, U. Paik, Thermal and mechanical properties of sintered bodies and EB-PVD layers of Y_2O_3 added $Gd_2Zr_2O_7$ ceramics for thermal barrier coatings, J. Alloys Compd. 507 (2) (2010) 448−455.
[15] X.L. Xia, Z.G. Liu, J.H. Ouyang, S. Gao, X.M. Liu, Effect of Ce substitution for Zr on electrical property of fluorite-type $Gd_2Zr_2O_7$, Solid State Sci. 13 (6) (2011) 1328−1333.
[16] J. Trajić, M.S. Rabasović, S. Savić-Šević, D. Šević, B. Babić, M. Romčević, J.L. Ristić-Djurović, N. Paunović, J. Križan, N. Romčević, Far-infrared spectra of dysprosium doped yttrium aluminium garnet nanopowder, Infrared Phys. Technol. 77 (2016) 226−229.
[17] J.C.M. Garnett, Colours in metal glasses and in metallic films i (1904).
[18] I.J. Uhanov, Opt. Svojstva Poluprovodnikov, Nauka, Moskva, 1977.
[19] L. Zhou, et al., Thermal-driven fluorite−pyrochlore−fluorite phase transitions of $Gd_2Zr_2O_7$ ceramics probed in large range of sintering temperature, Metall. Mater. Trans. A Phys. Metall. Mater. Sci. (2015) 1−8.
[20] T. Moriga, S. Emura, A. Yoshiasa, S. Kikkawa, F. Kanamaru, X-ray and Raman study on coordination states of fluorite- and pyrochlore- type compounds in the system ZrO_2-Gd_2O_3 50 (1990) 357−361.
[21] D. Michel, M.P.Y. Jorba, R. Collongues, Study by Raman spectroscopy of order-disorder phenomena occurring in some binary oxides with fluorite-related structures, J. Raman Spectrosc. 5 (2) (1976) 163−180.
[22] M.A. Subramanian, G. Aravamudan, G.V. Subba Rao, Oxide pyrochlores - a review, Prog. Solid State Chem. 15 (2) (1983) 55−143.
[23] R.A. McCauley, Infrared-absorption characteristics of the pyrochlore structure, J. Opt. Soc. Am. 63 (6) (1973) 721.
[24] R.A. McCauley, Infrared-absorption characteristics of the pyrochlore structure, J. Opt. Soc. Am. 63 (6) (1973) 721.
[25] C.S.S.R. Kumar, Raman Spectroscopy for Nanomaterials Characterization, Springer-Verlag, Berlin Heidelberg, 2012.
[26] X.L. Xia, J.H. Ouyang, Z.G. Liu, Electrical properties of gadolinium-europium zirconate ceramics, J. Am. Ceram. Soc. 93 (4) (2010) 1074−1080.
[27] M.T. Vandenborre, E. Husson, J.P. Chatry, D. Michel, Rare-earth titanates and stannates of pyrochlore structure; vibrational spectra and force fields, J. Raman Spectrosc. 14 (2) (1983) 63−71.
[28] M.T. Vandenborre, E. Husson, Comparison of the force field in various pyrochlore families II. Phases presenting structural defects, J. Solid State Chem. 5359 (1984) 253−262.
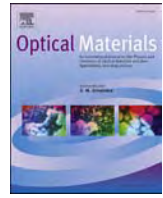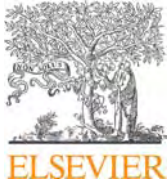
Optical properties of the mechanochemically synthesized Cu$_2$FeSnS$_4$ (stannite) nanocrystals: Raman study

J. Trajic [a], [*], M. Romcevic [a], M. Petrovic [a], M. Gilic [a], P. Balaz [b], A. Zorkovska [b], N. Romcevic [a]

[a] Institute of Physics, University of Belgrade, 11080 Belgrade, Serbia
[b] Institute of Geotechnics, Slovak Academy of Sciences, 043 53 Kosice, Slovakia

ABSTRACT

The analysis of the vibrational properties of mechanochemically synthesized stannite Cu$_2$FeSnS$_4$ nanocrystals has been performed. X-ray diffraction (XRD) and Raman spectroscopy are techniques used to characterize the crystal structure and compositional purity of stannite Cu$_2$FeSnS$_4$ nanoparticles. The detailed analysis of the experimental spectra has allowed us to determine the frequency and symmetry assignment of the main and weaker peaks. The milling time influence on synthesis stannite Cu$_2$FeSnS$_4$ from elemental precursors Cu, Fe, Sn and S is observed. Among the peaks that are characteristic for the stannite Cu$_2$FeSnS$_4$, we registered the modes of binary phases of FeS and SnS. The total disappearance of the binary phases of FeS and SnS is observed when the milling time is longer than 90 min.

© 2017 Elsevier B.V. All rights reserved.

1. Introduction

Intensive research has been conducted on the development of earth-abundant solar cells to replace high-efficiency solar cells, which use the rare and expensive elements like In, Ga and Te and toxic elements like Cd and Se. Recently, a new approach has emerged for a large-scale fabrication of solar cells based on the synthesis of nanocrystals that can be either annealed into large-grain thin films for the second generation solar cells, or used it to fabricate into nanocrystal arrays for the third generation solar cells.

The quaternary chalcogenide Cu$_2$FeSnS$_4$ (CFTS) is important and interesting material because it has many suitable characteristics for photovoltaic and optoelectronic applications, such as adequate direct band gap (1.0–1.5 eV), low toxicity and a relatively high abundance of the elements in the Earth's crust [1], and its constituents are abundantly available [2].

Theoretical calculations have demonstrated that the presence of tetrahedrally coordinated copper atoms is a critical feature for the exhibition of good photovoltaic properties of chalcogenide absorbers [3]. Cu$_2$FeSnS$_4$ (CFTS) is a tetrahedrally coordinated semiconductor in which each sulphur anion is bonded to four cations and each cation is bonded to four sulphur anions, which enabled

Cu$_2$FeSnS$_4$ to be another possible earth-abundant alternative material for solar cell applications [4–6]. Compared with inefficient traditional sputtering [7] or evaporation [8] methods of preparing Cu$_2$-II–IV–VI$_4$ group semiconductor materials, low-cost, highly efficient, environmental friendly and easy-to operate solution approaches have been studied widely, such as pulse laser and electro deposition [9], hot injection [10], electrospinning [11], dip coating [12], and microwave assisted approach [13–15]. However, these techniques are complex as well as time-consuming, and require high temperature, while in some cases it is necessary to use the toxic organic solvents. Mechanochemical treatment is a powerful technique for synthesis of a wide range of materials where the high energy milling is being applied to induce and speed up chemical reactions [16,17]. This approach is simple, solvent-free, and reproducible, and also the synthesis might be easily scaled up.

X-ray diffraction (XRD) and Raman spectroscopy are the most commonly used techniques to characterize the crystal structure and compositional purity of stannite Cu$_2$FeSnS$_4$ nanoparticles. In contrast with XRD based techniques, Raman scattering can provide more reliable information about the crystalline structure of the samples and the potential presence of structural and chemical inhomogenities as secondary phases or polytypes, and also localize them spatially [18]. Various methods, including Raman spectroscopy of quaternary crystals have been the subject of intensive researches over the last few years. For example, Raman spectroscopy was used to analyze polycrystalline thin films of Cu$_2$ZnSnS$_4$ [2,19],

* Corresponding author.
E-mail address: jelena@ipb.ac.rs (J. Trajic).

nanoparticles of Cu_2FeSnS_4 synthesized by thermal decomposition of metal precursors [20], nanospheres of Cu_2FeSnS_4 synthesized by a facile solvothermal method [5], or simple hot-injection method [21]. However, contrary to cited authors, in this work we report the systematic analysis performed by Raman scattering measurements of the vibrational properties of Cu_2FeSnS_4 nanoparticles which are mechanochemically synthesized during different milling time. By Raman spectroscopy we have analyzed and determined the influence of the milling time on the purity of the nanocrystals of Cu_2FeSnS_4.

2. Samples preparation and characterization

The elemental precursors (Cu, Fe, Sn and S) were used to obtain stannite (CFTS) by a solid state one-pot mechanochemical synthesis. The starting materials were elemental Cu (99%), Fe (99%), Sn (99.9%), and S (99%). These materials were weighed and mixed in atomic ratios of 2:1:1:4, according to the stoichiometry Cu_2FeSnS_4.

The mechanochemical synthesis of Cu_2FeSnS_4 nanoparticles was performed in a Pulverisette 6 planetary mill. The milling conditions were: milling pot volume 250 ml, milling pot material tungsten carbide with 50 tungsten carbide balls of 10 mm diameter, total weight of reactants 5 g, ball-to-powder mass ratio 70, milling speed was 500 min^{-1}. Milling time was 45, 60, 90 and 120 min using an argon atmosphere as a protective medium in the mill [22]. Using the described synthesis process, the unique nanostructures and properties are developed. Cu_2FeSnS_4 polymorphs with tetragonally body-centred structure with crystallite sizes of 18–19 nm were obtained.

The widespread used techniques to characterize the crystal structure and compositional purity of Cu_2FeSnS_4 nanoparticles are X-ray diffraction (XRD) and Raman spectroscopy.

The crystal structure was characterized by a D8 Advance Bruker X-ray diffractometer in the Bragg-Brentano geometry, using the Cu Kα radiation of 0.15418 nm and a scintillation detector. The commercial Bruker tools have been used for data processing.

The XRD patterns of the elemental mixture (Cu, Fe, Sn and S powders) milled for 45, 60, 90 and 120 min are shown in Fig. 1. The XRD pattern matches well with the tetragonal body-centred stannite Cu_2FeSnS_4 according to JCPDS card 44-1476 in the tetragonal

space group I-42m. The XRD spectra shows three most intensive peaks at $2\theta = 28.5°$, $47.5°$ and $56.0°$ that can be assigned to the (112), (204), and (312) planes of the tetragonal crystals.

Together with peaks corresponding to stannite Cu_2FeSnS_4 structure, peaks corresponding to tetragonal body-centred rhodostannite $Cu_2FeSn_3S_8$ (JCPDS 85-0378) are visible. In nature, rhodostannite can be often seen as replacement of stannite [23]. This transformation may also happen in preparation of synthetic crystals by applying the high-energy milling. This synthesis technique often leads to the products with extraordinary properties [17]. With increasing the milling time, the phase content of stannite increases while phase content of rhodostannite decreases [24].

Besides intrinsic peaks of Cu_2FeSnS_4 nanocrystals, the peak of the non-consumed Fe is observed at all samples milled for 45 and 60 min. This peak disappears with increasing milling time.

3. Results and discussion

To eliminate the possibility that the sample was a coincidental stoichiometric mixture of starting elements and their phases, Raman characterization of the nanocrystals was performed.

The Raman spectra of Cu_2FeSnS_4 powders were measured in the spectral range 50–600 cm^{-1} at room temperature. The micro-Raman spectra were taken in the backscattering configuration and analyzed by Jobin Yvon T64000 spectrometer, equipped with nitrogen cooled charge − coupled − device detector. As an excitation source we used the 514.5 nm line of an Ar − ion laser. Method precision is ±1 cm^{-1} in the range 450−850 nm, and reproducibility is better than 1 pixel.

Optical properties of Cu_2FeSnS_4 stannite are defined by valence band which is formed by p chalcogenide sulphur and the conduction band which is formed by cationic states. Namely, conduction band minimum state is mainly hybridization between the Sn s-like and S p-like states, while Cu d-like states hybridize with S p-like states in a wide energy range in the valence band below the valence band maximum [25,26].

Cu_2FeSnS_4 is a tetrahedrally coordinated semiconductor in which each sulphur anion is bonded to four cations and each cation is bonded to four sulphur anions [27]. The factor group analysis of the allowed zone-centre vibrations for the I-42m tetragonal
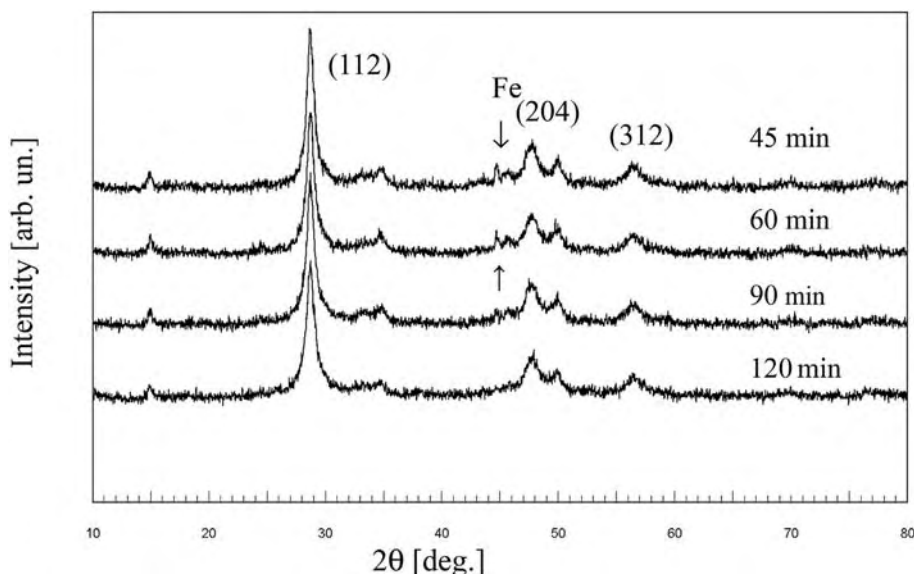

Fig. 1. XRD spectra of Cu_2FeSnS_4 nanocrystals obtained after various milling times.

crystallographic structures of Cu_2FeSnS_4, indicates that ten infrared (IR) and fourteen Raman active phonon modes of irreducible representations are expected for this compound [28]:

$$\Gamma = 2A_1 + A_2 + 2B_1 + 4B_2 + 6E \qquad (1)$$

The modes A_1, B_1, B_2 and E are Raman active. The B_2 and E modes are also IR active, and they represent LO-TO splitting due to their polar character. From all these modes the A_1 symmetry are expected to be the strongest lines in the Raman spectra [4]. In these type crystals strong phonon anharmonic effect is registered. For instance, in Cu_2CoSiS_4 the very strong broadening of the mode at 505 cm^{-1} point to a relative large TO/LO splitting for this vibration. Similar observations are made for chalcopyrite type compounds where one finds TO/LO splittings of 50 cm^{-1} for $CuAlS_2$ and about 20 cm^{-1} for the corresponding gallium and indium compounds $CuGaS_2$ and $CuInS_2$ [29]. In case of Cu_2FeSnS_4 [29] and binary compounds FeS [30] and SnS [31] TO/LO splitting is much smaller, consequently, phonon anharmonic effect is not observed [32].

The Raman spectra of Cu_2FeSnS_4 nanocrystals obtained after various milling times, in the spectral range from 50 to 600 cm^{-1}, are presented in Fig. 2. Experimental Raman scattering spectra are analyzed by the deconvolution to Lorentzian curves [33]. This Figure shows the Raman spectra measured from the Cu_2FeSnS_4 samples, together with the fitting of the peaks with Lorentzian curves. Positions of Lorentzians are given above the spectral and fitted curves.
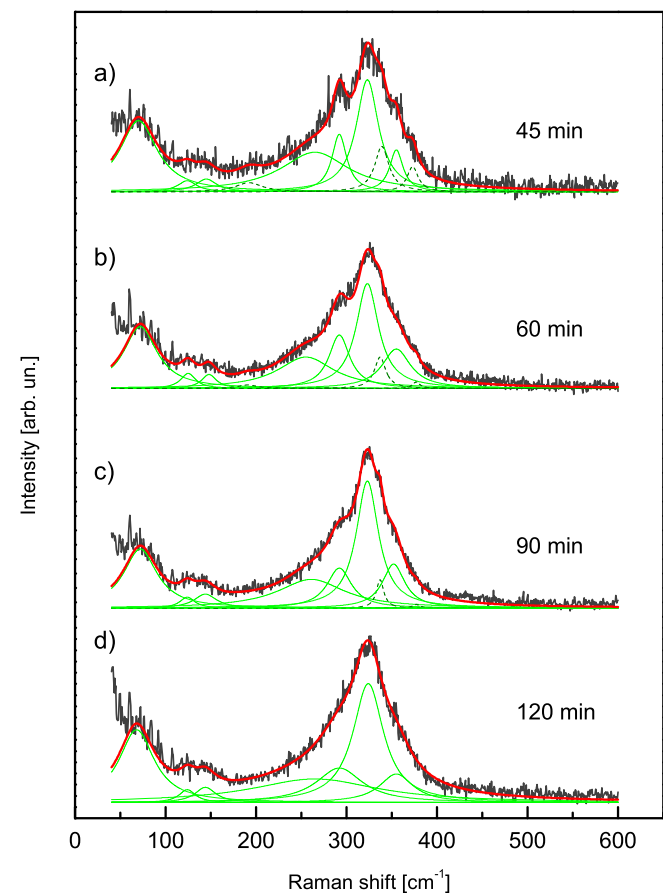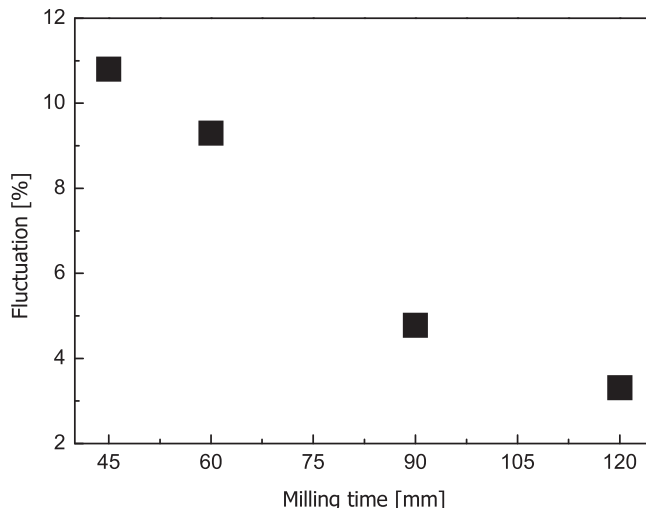
Fig. 3. Raman spectra fluctuation versus milling time.

Before beginning of the Raman spectra analysis we shall consider the quality of the spectra. In Fig. 3 one can see that fluctuations of measured value decrease as milling time increases. Keeping in mind that all spectra are recorded under the same conditions the observed change of fluctuations of the measured values gives us information about the quality of the nanocrystals after prolonged milling, and it is obvious that after 120 min of milling the nanocrystal has the best quality.

The spectrum of Cu_2FeSnS_4 nanocrystals obtained after 45 min milling time is presented in Fig. 2a. The spectrum show two dominant peaks at 322 cm^{-1} and 292 cm^{-1}, which are in accordance with the reported values for tetragonal Cu_2FeSnS_4. The peaks originate from the motion of the S anions around fixed cations and they are identified as A_1 symmetry modes. Dominant structure at about 322 cm^{-1} in experimental spectra is vibration of pure anion mode of S anions around fixed Sn cations [28], while the mode at approximately 292 cm^{-1} can be considered as a pure S anion mode around the Cu cation. The other observed Raman modes could be derived from the combined motion of anions and cations [34].

Fitting the spectra with the Lorentzian curves allowed identification of additional weaker contributions at 73, 122, 145, 255 and 355 cm^{-1}. The peaks located at approximatively 73, 122, 145 and 355 cm^{-1} are in good agreement with the frequencies of the IR peaks reported for this compound [28]. These peaks are tentatively attributed to E symmetry modes. There are, also, a few week peaks around the mode at 255 cm^{-1}, but we fitted them with a broad peak at the same frequency.

In addition, other possible binary and ternary phases can be distinguished by Raman spectroscopy. We represent them by dashed lines in Fig. 2. Shoulder peaks at approximately 339 and 377 cm^{-1} originates from FeS binary phase [35]. Existence of these modes is confirmed by XRD measurements. Weak, broad peak at about 192 cm^{-1} originates from the binary intermediate phase SnS [36]. Occurrence of SnS binary phase is in accordance with the observation of Bernardini et al., where, by thermal synthesis, also, the minor traces of herzenbergite SnS besides stannite have been detected [37,38]. The fact that the component is not visible (Sn) or the component is very weak (Fe) on XRD spectra indicates that the content of binary components SnS and FeS is very small.

Slight difference in frequencies between available literature data as well as data we gathered probably arises from the differences in the cation-anion bond distances. Also, the significant role have cationic defects which are always presented. Namely, disordered

Fig. 2. Raman spectra of Cu_2FeSnS_4 obtained after various milling times.

distribution of Cu and Fe atoms leads to the presence of a high content of Cu_{Fe} and Fe_{Cu} anti-site defects that would degrade the crystalline quality of these regions. The existence of a highly disordered distribution of cations in these domains would lead to a relaxation of the q-conservation rule, with a shift of the Raman peak towards lower frequencies [4].

By XRD measurements the rhodostannite $Cu_2FeSn_3S_8$ is also registered. Comparing the Raman spectrum of stannite and rhodostannite from the RRUFF database, one can see that Raman spectrum of rhodostannite approximately overlaps with stannite spectrum.

The spectrum of Cu_2FeSnS_4 nanocrystals obtained after 60 min milling time is presented in Fig. 2b. In case of this nanocrystal the same modes are also registered as in the sample obtained after 45 min milling time, but nevertheless it is noticed that intensity of the modes originated from the stannite increases (solid lines), and that the modes originated from FeS and SnS binary phases (dashed lines) decreases. The trend is also seen in the sample obtained after 90 min milling time (Fig. 2c). However besides further increase of the intensity of the modes originated from stannite, and decrease of the intensity of the modes originated from binary phase FeS, in this nanocrystal the mode at 192 cm^{-1} was not observed. This fact means that after 60 min milling time SnS binary phase disappears. Cu_2FeSnS_4 nanocrystals obtained after 120 min milling time is presented in Fig. 2d. The spectrum is characterized by the strongest line at 322 cm^{-1}, two prominent lines at 292 and 355 cm^{-1}, and several weak spectral features corresponding to IR peaks. Absence of Raman peaks positioned at 192, 339 and 377 cm^{-1} excluded the

presence of other binary or ternary impurity phases, such as FeS and SnS, which implicates that after 90 min of milling the total synthesis of tetragonal Cu_2FeSnS_4 nanocrystals occur, without any additional components.

Intensity dependencies of the mode originated from the binary phases of FeS and SnS, from the milling time are presented in Fig. 4a. One can perceive that their intensities decrease while the milling time increase, as well as that after 60 min binary phase of SnS disappears, whereas intensities of the FeS modes continues to decrease until total disappearance when the milling time is longer than 90 min. Absence of those Raman peaks excluded the presence of FeS and SnS binary phases, which indicates that after 90 min milling time pure stannite Cu_2FeSnS_4 is synthesized. Contrary the modes originated from the binary phases FeS and SnS, intensities of the modes originated from Cu_2FeSnS_4 predominantly increases while milling time increases (Fig. 4b.).

4. Conclusion

Raman scattering measurements have been applied in an attempt to characterize compositional purity of stannite, and observe the influence of the milling time on the mechanochemical synthesis of Cu_2FeSnS_4 nanocrystals. The stannite Cu_2FeSnS_4 is mechanochemically synthesized from elemental precursors Cu, Fe, Sn, and S. We registered the peaks located at approximately 73, 122, 145, 255, 292, 322 and 355 cm^{-1}, which are in good agreement with the frequencies of the peaks reported for tetragonal Cu_2FeSnS_4. Among the peaks that are characteristic for the stannite Cu_2FeSnS_4, we also registered the modes at about 192, 339 and 377 cm^{-1} that originates from binary phases of FeS and SnS, respectively. Intensities of these modes decreases while the milling time increase. The total disappearance of the mode originated from SnS binary phase is observed after 60 min milling time, and FeS modes disappear when the milling time is longer than 90 min. Absence of those Raman peaks excluded the presence of FeS and SnS binary phases, which indicates that after 90 min milling time pure stannite Cu_2FeSnS_4 is synthesized. We present relatively simple, cheap solvent-free, and reproducible method to synthesize the pure stannite Cu_2FeSnS_4, comparing to the methods suggested by other researchers.

Fig. 4. Intensity of the modes originated from the binary phases FeS and SnS (a) and Cu_2FeSnS_4 (b) versus milling time.

References

[1] B. Zhou, X. Yan, P. Li, L. Yang, D. Yu, Eur. J. Inorg. Chem. 1 (2015) 2690–2694.
[2] H. Guan, H. Shen, B. Jiao, Xu Wang, Mater. Sci. Semicond. Process. 25 (2014) 159–162.
[3] C. Domain, S. Laribi, S. Taunier, J.F. Guillemoles, J. Phys. Chem. Solids 64 (2003) 1657–1663.
[4] X. Fontané, V. Izquierdo-Roca, E. Saucedo, S. Schorr, V.O. Yukhymchuk, M.Ya Valakh, A. Pérez-Rodríguez, J.R. Morante, J. Alloys Compd. 539 (2012) 190–194.
[5] M. Cao, C. Li, B. Zhang, J. Huang, L. Wang, Y. Shen, J. Alloys Compd. 622 (2015) 695–702.
[6] L. Ai, J. Jiang, J. Mater. Chem. 22 (2012) 20586–20592.
[7] J.S. Seol, S.Y. Lee, J.C. Lee, H.D. Nam, K.H. Kim, Sol. Energy Mater. Sol. Cells 75 (2003) 155–162.
[8] C.W. Shi, G.Y. Shi, Z. Chen, P.F. Yang, M. Yao, Mater. Lett. 73 (2012) 89–91.
[9] Y. Li, T.F. Yuan, L.X. Jiang, Z.H. Su, F.Y. Liu, J. Alloys Compd. 610 (2014) 331–336.
[10] L. Li, B.L. Zhang, M. Cao, Y. Sun, J.C. Jiang, P.F. Hu, Y. Shen, J. Alloys Compd. 551 (2013) 24–29.
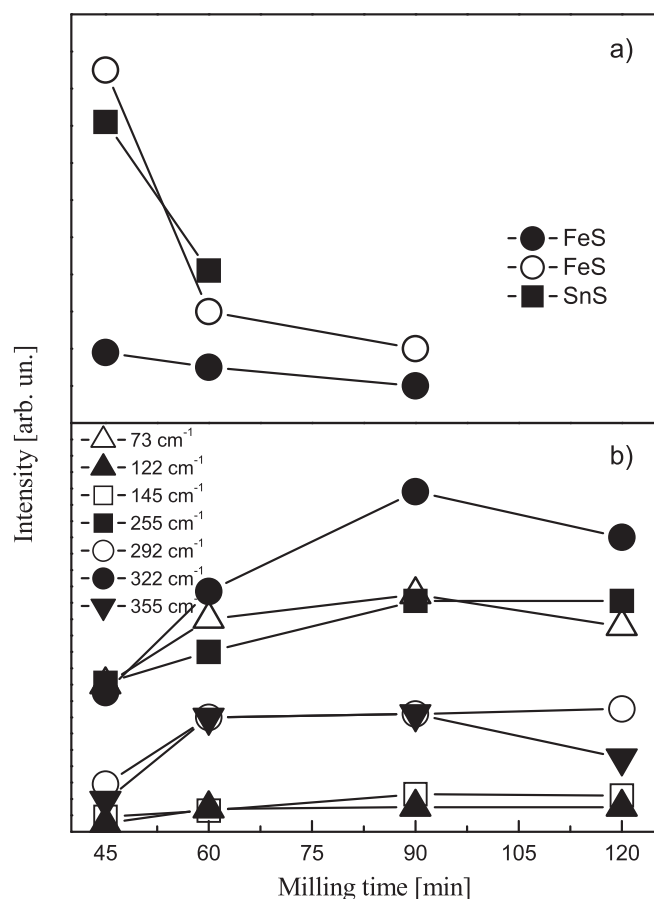[11] F. Ozel, M. Kus, A.Yar, E. Arkan, M. Can, A. Aljabour, N.M. Varal, M. Ersoz,

J. Mater. Sci. 50 (2015) 777–783.

[12] G. Rajesh, N. Muthukumarasamy, E.P. Subramaniam, S. Agilan, D. Velauthapillai, J. Sol-Gel Sci. Technol. 66 (2013) 288–292.

[13] X.K. Meng, H.M. Deng, J. He, L. Sun, P.X. Yang, J.H. Chu, Mater. Lett. 151 (2015) 61–63.

[14] M. Sabet, M.S. Niasari, D. Ghanbari, O. Amiri, M. Yousefi, Mater. Sci. Semicond. Process. 16 (2013) 696–704.

[15] S.M.H. Mashkani, F. Mohandes, M.S. Niasari, K.V. Rao, Mater. Res. Bull. 47 (2012) 3148–3159.

[16] P. Baláž, Mechanochemistry in Nanoscience and Minerals Engineering, Springer, Berlin Heidelberg, 2008, p. 413.

[17] P. Baláž, M. Achimovičová, M. Baláž, P. Billik, Z. Cherkezova-Zheleva, J.M. Criado, F. Delogu, E. Dutková, E. Gaffet, F.J. Gotor, R. Kumar, I. Mitov, T. Rojac, M. Senna, A. Streletskii, K. Wieczorek-Ciurowa, Chem. Soc. Rev. 42 (2013) 7571–7637.

[18] Z. Lazarevic, B. Stojanovic, M. Romcevic, M. Mitric, C. Jovalekic, N. Romcevic, J. Alloys Compd. 453 (2008) 499–502.

[19] P.A. Fernandes, P.M.P. Salomé, A.F. da Cunha, J. Alloys Compd. 509 (2011) 7600–7606. H. Guan, H. Shen, B.Jiao, X. Wang, Materials Science in Semiconductor Processing 25(2014) 159–162.

[20] K. Mokurala, P. Bhargava, S. Mallick, Mater. Chem. Phys. 147 (2014) 371–374.

[21] C. Yan, C. Huang, J. Yang, F. Liu, J. Liu, Y. Lai, J. Li, Y. Liu, Chem. Commun. 48 (2012) 2603–2605.

[22] P. Baláž, M. Baláž, M.J. Sayagués, I. Škorvánek, A. Zorkovská, E. Dutková, J. Briančin, J. Kováč, J. Kováč Jr., Y. Shpotyuk, Nanoscale Res. Lett. 12 (2017) 256–266.

[23] H. Hey, Mineral. Mag. 37 (1970) 954.

[24] P. Baláž, M. Baláž, A. Zorkovská, I. Škorvánek, Z. Bujnáková, J. Trajic, Acta Phys. Pol. A 131 (2017) 1153–1155.

[25] X. Meng, H. Deng, J. Tao, H. Caoa, X. Lia, L. Suna, P. Yang, J. Chu, J. Alloys Compd. 680 (2016) 446–451.

[26] A.H. Reshak, K. Nouneh, I.V. Kityk, Jiri Bila, S. Auluck, H. Kamarudin, Z. Sekkat, Int. J. Electrochem. Sci. 9 (2014) 955–974.

[27] C. Yan, C. Huang, J. Yang, F. Liu, J. Liu, Y. Lai, J. Li, Y. Liu, Chem. Commun. 48 (2012) 2603–2605.

[28] T. Gürel, C. Sevik, T. Cagin, Phys. Rev. B 84 (2011) 205201.

[29] M. Himmrich, H. Haeuseler, Spectrochim. Acta 47A (1991) 933–942.

[30] Y. El Mendili, B. Minisini, A. Abdelouas, J.-F. Bardeau, RSC Adv. 4 (2014) 25827–25834.

[31] J.M. Chamberlain, P.M. Nikolic, M. Merda, P. Mihailovic, J. Phys. C Solid State Phys. 9 (1976) L637–L642.

[32] Yu P. Cyathchenko, G.E. Krasnyatskii, Opt. Spectrosc. 47 (1979) 911 (in Russian).

[33] B.H. Henry, J.R. During (Eds.), Raman Spectroscopy: Sixty Years, vol. 10, Elsevier, Amsterdam, 1990, p. 933.

[34] C. Rincó, M. Quintero, E. Moreno, Ch Power, E. Quintero, J.A. Henao, M.A. Macías, G.E. Delgado, R. Tovar, M. Morocoima, Solid State Commun. 151 (2011) 947–951.

[35] A.K. Kleppe, A.P. Jephcoat, Mineral. Mag. 68 (2004) 433–441.

[36] L.S. Price, I.P. Parkin, A.M.E. Hardy, R.J.H. Clark, Chem. Mater. 11 (1999) 1792–1799.

[37] G.P. Bernardini, D. Borrini, A. Caneschi, F. Di Benedetto, D. Gatteschi, S. Ristori, M. Romanelli, Phys. Chem. Minerals 27 (2000) 453–461.

[38] G.P. Bernardini, P. Bonazzi, M. Corazza, F. Corsini, G. Mazzetti, L. Poggi, G. Tanelli, Eur. J. Mineral. 2 (1990) 219–225.

Optical Properties of CuSe Thin Films – Band Gap Determination

Milica Petrović[1*)], Martina Gilić[1], Jovana Ćirković[2], Maja Romčević[1], Nebojša Romčević[1], Jelena Trajić[1], Ibrahim Yahia[3]

[1]Institute of Physics, University of Belgrade, Pregrevica 118, Belgrade, Serbia
[2]The Institute for Multidisciplinary Research, University of Belgrade, Belgrade, Serbia
[3]Nano-Science and Semiconductors Labs., Physics department, Faculty of Education, Ain Shams University, Roxy, Cairo, Egypt

Abstract:

    Copper selenide thin films of three different thicknesses have been prepared by vacuum evaporation method on a glass substrate at room temperature. The optical properties of the films were investigated by UV–VIS–NIR spectroscopy and photoluminescence spectroscopy. Surface morphology was investigated by field-emission scanning electron microscopy. Copper selenide exhibits both direct and indirect transitions. The band gap for direct transition is found to be ~2.7 eV and that for indirect transition it is ~1.70 eV. Photoluminescence spectra of copper selenide thin films have also been analyzed, which show emission peaks at 530, 550, and 760 nm. The latter corresponds to indirect transition in investigated material.

Keywords: *Copper selenide; Thin films; Semiconductors; UV–VIS–NIR spectroscopy; Photoluminescence spectroscopy.*

1. Introduction

    Copper selenides are interesting metal chalcogenide semiconductor materials. They exist in many phases and structural forms: different stoichiometry such as CuSe (klockmannite), Cu_2Se_x, $CuSe_2$ (marcasite), α - Cu_2Se (bellidoite), Cu_3Se_2 (umagnite), Cu_5Se_4 (athabaskite), Cu_7Se_4 etc., as well with non-stoichiometric form such as $Cu_{2-x}Se$ (berzelianite), and can be constructed into several crystallographic forms (monoclinic, cubic, tetragonal, hexagonal, etc.). Their color ranges from blue black to bluish green depending on the type of stoichiometric composition. Special constitutions of these compositions make copper selenide an ideal candidate for scientific research.

    Copper selenide is a semiconductor with p-type conductivity. It has both direct and indirect transitions so the presence of both band gaps, direct and indirect, is observed. The band gap of copper selenide is not well defined. Literature data are quite controversial: direct allowed transitions are reported to have corresponding band gap in the range of 2 to 3 eV, and indirect band gap between 1.1 and 1.5 eV [1-4]. The indirect band gap being near the optimum value for solar cell applications makes this material capable to potentially offer a high efficiency of conversion. However, copper selenide nanoparticles have been reported to

_____

*)**Corresponding author:** milicap@ipb.ac.rs

_____

possess a direct band gap of 4 eV [5] and indirect one of 1.87 eV. The reasons of such variation in band gaps could lie in the sharp cut off of the wavelength with the spectral transmittance instead of the slow increase, the presence of large number of dislocations, wide range of stoichiometric deviation and quantum confinement effect.

Copper chalcogenide thin films have numerous applications in various devices such as solar cells [6-8], photodetectors [9], optical filters [10], microwave shielding [11], thermoelectric converters [12]. Photovoltaic cells and Shottky diodes are associated with these metal chalcogenide compound [13, 14]. Copper selenide is a precursor material of $CuInSe_2$, used for highly efficient photovoltaic elements [15]. Also, $CuSe_2$ is served as a typical anion conductor and significant Cu-Se alloys targets for the preparation of CIGS/CIS thin film solar cells in RF magnetic sputtering [16].

A number of methods have been reported for the deposition of thin films of different crystalline modifications and varying stoichiometries such as anelectrodeposition [17], selenisation [18], vacuum evaporation [19], solid state reaction [20], and chemical bath deposition [21].

In this paper, we report the preparation of CuSe thin films deposited onto glass substrate using vacuum evaporation techniqueat room temperature and their characterization trough FESEM, UV–VIS–NIR and photoluminescence spectroscopy.

2. Experimental

The vacuum evaporation technique was used to deposit thin films of copper selenide onto glass substrate. Copper selenide alloy of high purity (99.99 %) was purchased from Aldrich Company. With use of a Mo boat, the powder was deposited onto highly pre-cleaned glass substrates at vacuum ~3 mPa at room temperature, with use of conventional coating unit-Edwards, E-306 A. During the evaporation of CuSe thin films, the rate of deposition was kept constant ~10 nm/s. The film thickness was controlled with use of a quartz crystal thickness monitor - FTM4, Edwards. Films of three different thicknesses: 56 nm (CuSe1), 79 nm (CuSe2), and 172 nm (CuSe3) were obtained by deposition onto glass substrates.

Field–emission scanning electron microscopy (FESEM) images were obtained for CuSe thin films deposited on glass substrate in order to study the surface morphology of the thin films. A Jeol JSM-7600F with a Schottky-type emitter was used at an accelerating voltage of 1.5 kV.

The UV–VIS–NIR diffusion reflectance and transmittance spectra were recorded in the wavelength range of 300 – 1000 nm on a Shimadzu UV-2600 spectrophotometer equipped with an integrated sphere. The diffuse reflectance and transmittance spectra were measured relative to a reference sample of $BaSO_4$.

Photoluminescence emission measurements were obtained using Jobin–Yvon U1000 spectrometer, equipped with RCA-C31034A photomultiplier with housing cooled by Peltier element, amplifiers and counters. As an excitation source we used the 488 nm laser line of Argon laser.

3. Results and discussion
3.1. FESEM

Fig. 1 shows representative FESEM image of sample CuSe2 at room temperature and images of two other films are similar. As we may observe, film is packed and continuous without the presence of porosity or voids. The surface is rather smooth with no cracking observed.
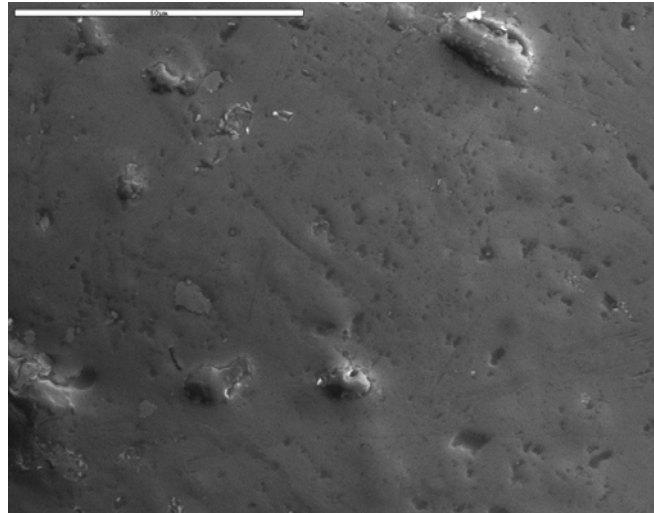
Fig. 1. Top view micrograph of CuSe2 thin film at room temperature using SEM.

3.2. UV–VIS–NIR spectroscopy

In Fig. 2. diffuse reflectance (R) and transmittance (T) spectra of our thin films samples in the wavelength range 200–1000 nm are presented. As we can see, the transmittance increases with decrease in the film thickness, which is not the case for reflectance. This is typical for films with high electrical conductivity and implies a reflection coefficient nearing 1 for films of metallic conductivity.
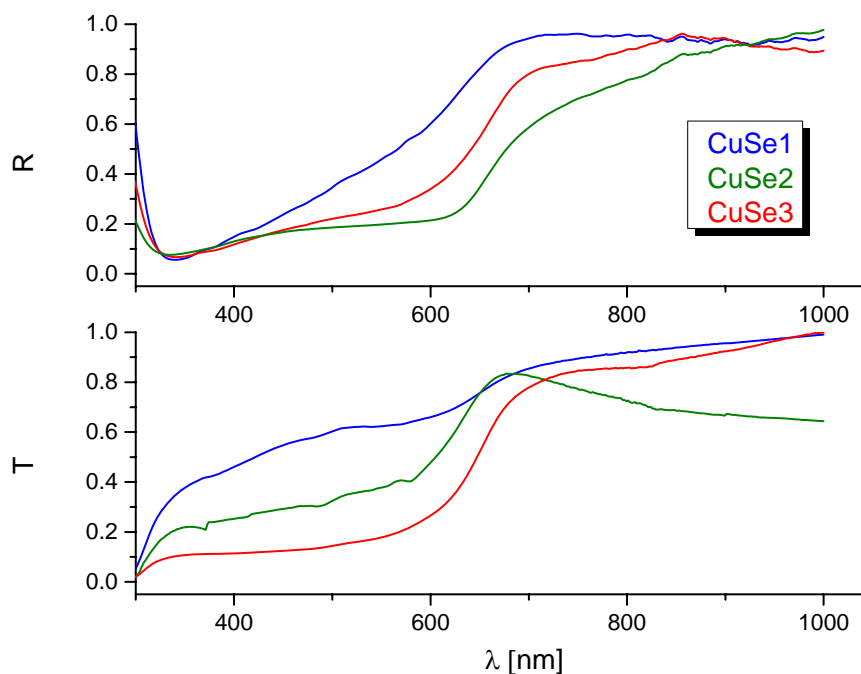
Fig. 2. Diffuse reflectance and transmittance spectra.

In this study we used Tauc plot for the determination of optical band gap from diffuse reflectance measurements. The determination of band gap in semiconductors is significant for obtaining the basic solid state physics. The relation expression proposed by Tauc, Davis and

Mott [22-24] is following:

$$\alpha h\nu = A\left(h\nu - E_g\right)^{\frac{1}{n}} \qquad (1)$$

where h is a Planck's constant, A is the transition probability constant depending on the effective mass of the charge carriers in the material, E_g is the band gap, $h\nu$ is the photon energy and α is absorption coefficient which is defined as the relative rate of decrease in light intensity along its propagation path, i.e. a property of a material that defines the amount of light absorbed by it. The value of n denotes the nature of the transition. In case of direct transitions n equals *1/2* and *3/2* for allowed and forbidden transitions, respectively. As for indirect transitions, n equals *2* and *3* for allowed and forbidden transitions, respectively. Since CuSe exhibits both direct and indirect allowed transitions, $n = 1/2$ and $n = 2$.

Then, the acquired diffuse reflectance spectra are converted to Kubelka–Munk function [25]:

$$\alpha = \frac{(1-R)^2}{2R} \qquad (2)$$

So using this function, a plot of $(\alpha h\nu)^{1/n}$ against $h\nu$ is obtained. The energy band gap is determined by extrapolating the linear portion of $(\alpha h\nu)^{1/n}$ vs. $h\nu$ to the energy axis at $(\alpha h\nu)^{1/n} = 0$. The intercept of these plots on the energy axis gives the energy band gap. Such plots are given in Fig. 3a) – direct transitions and Fig. 3b) – indirect transitions.
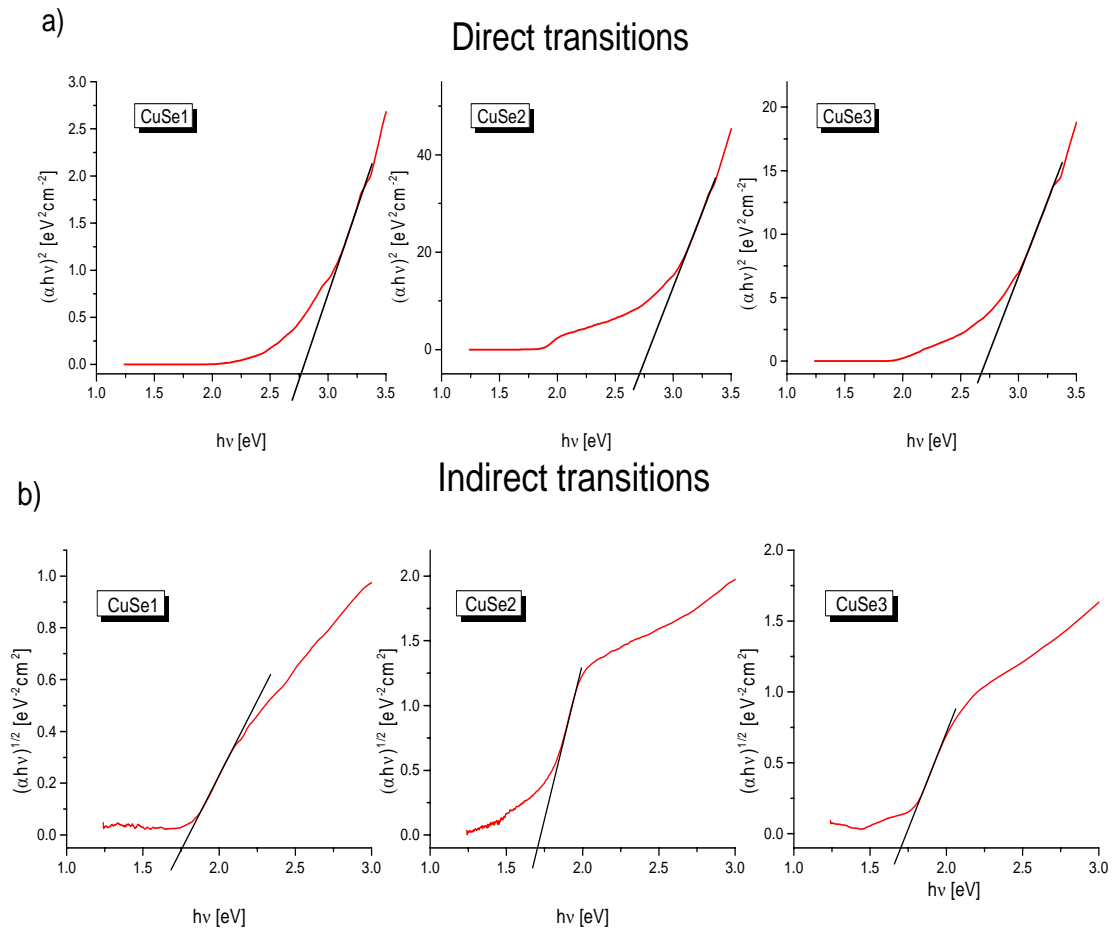
Fig. 3. a) Dependence of the $(\alpha h\nu)^2$ of the photon energy ($h\nu$), b) Dependence of the $(\alpha h\nu)^{1/2}$ of the photon energy ($h\nu$).

Tab. I The estimated band gap energies of CuSe thin films.

	CuSe1	CuSe2	CuSe3
Direct transition (eV)	2.77	2.71	2.69
Indirect transition (eV)	1.75	1.70	1.70

The experimentally determined values of energy gaps for CuSe thin films slightly differ from each other on second decimal place, their values range from 2.69 to 2.77 eV for direct transitions, and from 1.70 to 1.75 eV in the case of indirect transitions. The estimated band gap positions of each sample are given in Table I. It seems that despite the difference in film thicknesses, their optical properties such as band gap energies are quite similar.

References report a large range of energy band gap values for CuSe. For direct transitions that values usually go between 2 and 3 eV. R. Bari et al. [26] obtained the value of 2.51 eV for the sample thickness of 150 nm, and with the increase of film thickness they reported the decrease of band gap width. I. Grozdanov [27], V. Garcia et al. [2] and G. B. Sakr et al. [28] obtained the value of 2.33, 2.13–2.38 and 2.74 eV, respectively. The latter is very similar to the results obtained in this paper. D. Rajesh et al. [29] got a diversity of band gaps ranging from 1.95 (the thickest film) to 3.70 eV (the thinnest film). As for indirect transitions, they received less attention. In [2] the obtained values are 1.22–1.34 eV, whereas in [12] the value is about 1.4 eV. The values we obtained, ~1.7 eV, are bigger than reported in literature. In our opinion, the larger indirect band gap values are due to quantum confinement effect [30, 31] whereby the electrons are localized in individual crystallites.

3.3. Photoluminescence spectroscopy

Photoluminescence emission spectra can be used for investigation of the possible outcomes of photoinduced electrons and holes in a semiconductor, since photoluminescence emission results from the recombination of free charge carriers. A semiconductor is characterized with the electronic band structure and its main features – the valence band or the highest occupied molecular orbital (HOMO) and the conduction band or the lowest unoccupied molecular orbital (LUMO). The difference between the valence band and the conduction band in the means of energy is called band gap (E_g). We talk about two types of photoluminescence phenomenon according to its attributes and formation mechanism: the band–to–band photoluminescence and the excitonic photoluminescence [32-34]. The band–to–band PL spectrum regards the separation situation of photogenerated charge carriers. The excitonic PL spectrum, however, cannot directly reflect the separation situation of photoinduced carriers. If discrete energy levels are present in the band gap, these may dominate the optical spectrum. PL measurements then yield information about the energetic positions of the electronic states in the gap. Such localized states can originate from various types of imperfections like vacancies, interstitial atoms, atoms at surfaces and grain boundaries. However, it is often difficult to determine the exact position and origin of these states.

Photoluminescence spectra of CuSe thin films of three different thicknesses at room temperature are presented in Fig. 4. In all spectra, the band in the red spectral region, positioned at about 760 nm (1.63 eV), is clearly seen. According to the UV–VIS results (see previous chapter), we can attribute this PL peak to indirect band–to–band transition for indirect transition in CuSe. Since the excitation energy (488 nm = 2.54 eV) is lower than the energy for direct transitions (460 nm = 2.7 eV), peak that corresponds to direct transitions cannot be observed. In green area, a broad band is observed which consists of two peaks, at

_____

about 530 nm and about 550 nm. These localized states must originate from native defects of Se or Cu.
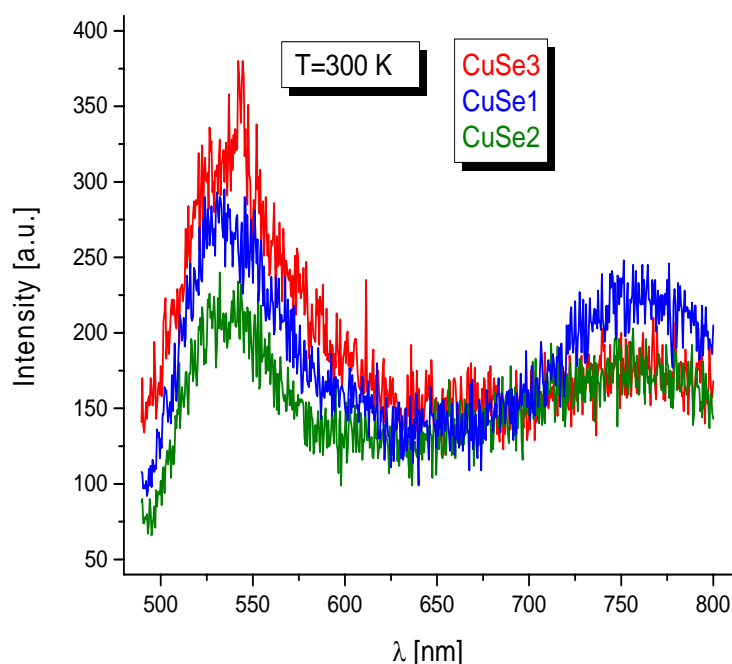

Fig. 4. Photoluminescence emission spectra of CuSe thin films at room temperature.

4. Conclusions

CuSe thin films of three different thicknesses, obtained by vacuum evaporation technique on glass substrate, underwent through photoluminescence investigation along with UV–VIS–NIR measurements and FESEM analysis. Reflectance measurements revealed values for both direct and indirect band gap: ~2.7 and 1.7 eV, respectively. The existence of indirect band gap on this value, somehow wider then in literature, is confirmed by photoluminescence measurements. Presence of localized states between the direct and indirect band gap is discovered from luminescence measurements. In this paper we proved that simple and low cost technique as vacuum evaporation is capable of producing high quality thin films.

Acknowledgements

5. References

1. P. Hankare, A. Khomane, P. Chate, K. Rathad, K. Garadkar, J. Alloys and Comp., 469 (2009) 478.
2. V. Garcia, P. Nair, M. Nair, J. Cryst. Growth, 203 (1999) 113.
3. O. Arellano–Tanori, M. Acosta–Enriquez, R. Ochoa–Landin, R. Iniguez–Palomares, T. Mendivil–Reynoso, M. Flores–Acosta, S. Castillo, Chalcogenide Letters, 11 (2014) 13.

_____

4. A. Jagminas, R. Juskenas, I. Gailiute, G. Statkute, R. Tomasinuas, J. Cryst. Growth, 294 (2006) 343.
5. D. Patidar, N. S. Saxena, J. Cryst. Growth, 343 (2012) 68.
6. T. P. Hsieh, C. C. Chuang, C. S. Wu, J. C. Chang, J. W. Guo, W. C. Chen, Solid State Elec., 56 (2011) 175.
7. M. Singh, J. Jiu, T. Sugahara, K. Suganuma, ACS Appl. Mater. Interfaces, 6 (2014) 16297.
8. J. H. Scofielda, A. Dudaa, D. Albina, B. L. Ballardb, P. K. Predeckib, Thin Solid Films, 260 (1995) 26.
9. S. Lei, A. Sobhani, F. Wen, A. George, Q. Wang, Y. Huang, P. Dong, B. Li, S. Najmaei, J. Bellah, G. Gupta, A. D. Mohite, L. Ge, J. Lou, N. J. Halas, R. Vajtai, P. Ajayan, Adv. Mater., 45 (2014) 7666.
10. G. Juska, V. Gulbinas, A. Jagminas, Lithua. J. Phys., 50 (2010) 233.
11. C. Levy-Clement, M. Neumann-Spallart, S. K. Haram, K. S. V. Santhanam, Thin Solid Films, 12 (1997) 302.
12. V. M. Bhuse, P. P. Hankare, K. M. Garadkar, A. S. Khomane, Mater. Chem. Phys., 80 (2003) 82.
13. S. Y. Zhang et al., Cryst. Growth Des., 6 (2006) 2809.
14. H. M. Pathan, C. D. Lokhande, D. P. Amalnerkar, T. Seth, Appl. Surf. Sci., 211 (2003) 48.
15. R. R. Pai, T. T. John, M. Lakshimi, K. P. Vijayakumar, C. S. Kartha, Thin Solid Films, 473 (2005) 208.
16. N. H. Kim, S. Oh, W. S. Lee, J. Korean Phys. Soc., 61 (2012) 1177.
17. G. Sokolsky, N. Ivanova, S. Ivanov, T.Tomila, Y. Boldyrev, Science of Sintering, 39 (2007) 273.
18. X. Ji, L. J. Wang, J. Y. Teng, Y. M. Mi, C. M. Zhang, Surf. Eng., 29 (2013) 356.
19. J. Trajić, M. Gilić, N. Romčević, M. Romčević, G. Stanišić, B. Hadžić, M. Petrović, Y. S. Yahia, Science of Sintering, 47 (2015) 145.
20. Zhi-Peng Sun, Lang Liu, Li Zhang and Dian-Zeng Jia, Nanotechology, 17 (2006) 2266.
21. R. Palomino-Merino, O. Portillo-Moreno, L. A. Chaltel-Lima, R. Gutiérrez Pérez, M. de Icaza-Herrera, and V. M. Castaño, J. Nanomat., 2013 (2013) 6.
22. J. Tauc, R. Grigorovici, A. Vancu, Phys. Status Solidi, 15 (1966) 627.
23. J. Tauc (F. Abeles ed.), Optical Properties of Solids, North Holland (1972)
24. E. Davis, N. Mott, Philos. Mag., 22 (1970) 903.
25. P. Kubelka, F. Munk, Zeits F. teckn. Physik., 12 (1931) 593-601.
26. R. Bari, V. Ganesan, S. Potadar, L. Patil, Bull. Mater. Sci., 32 (2009) 37.
27. I. Grozdanov, Synthetic Metals, 63 (1994) 213.
28. G. Sakr, I. Yahia, M. Fadel, S. Fouad, N. Romčević, J. Alloys and Comp., 507 (2010) 557.
29. D. Rajesh, R. Chandrakanth, C. Sunandana, Journal of Applied Physics, 4 (2013) 65.
30. G. Hodes, A. Albu-Yayor, F. Decker, P. Motisuke, Phys. Rev., B 36 (1987) 4215.
31. V. García, M. Nair, P. Nair, R. Zingaro, Semicond. Sci. Technol., 12 (1997) 645.
32. F. B. Li, H. Z. Li, Appl. Catal. A, 228 (2002) 15.
33. P. Kumar, K. Singh, J. Opto. Biomed. Mater., 1 (2009) 59.
34. J. G. Yu, Y. R. Su, B. Cheng, Adv. Funct. Mater., 17 (2007) 1984.

_____

Садржај: *Танки филмови бакар селенида три различите дебљине добијени су техником вакуумског напаравања на супстрат од стакла на собној температури. Оптичке особине филмова испитиване су методама UV–VIS–NIR и фотолуминесцентне спектроскопије. Морфологија површине испитивана је методом*

_____

скенирајуће електронске микроскопије са ефектом поља. У бакар селениду се догађају и директни и индиректни прелази. Измерена забрањена зона која одговара директним прелазима је ~2.7 eV, док је забрањена зона која одговара индиректним прелазима ~1.70 eV. Анализирани су и спектри фотолуминесценције танких филмова бакар селенида, и уочени су пикови на 530, 550 и 760 nm. Последњепоменути пик одговара индиректним прелазима у изучаваном материјалу.

Кључне речи: *Бакар селенид; Танки филмови; Полупроводници; UV–VIS–NIR спектроскопија; Фотолуминесцентна спектроскопија.*

_____
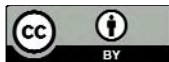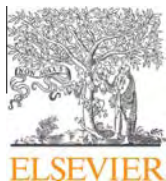
Far-infrared spectra of dysprosium doped yttrium aluminum garnet nanopowder

J. Trajić [a,*], M.S. Rabasović [a], S. Savić-Šević [a], D. Ševic [a], B. Babić [b], M. Romčević [a], J.L. Ristić-Djurović [a], N. Paunović [a], J. Križan [c], N. Romčević [a]

[a] Institute of Physics, University of Belgrade, Pregrevica 118, 11080 Belgrade, Serbia
[b] Vinca Institute of Nuclear Sciences, University of Belgrade, 11001 Belgrade, Serbia
[c] AMI, d.o.o., Ptuj, Slovenia

HIGHLIGHTS

- YAG:Dy nanopowder was produced by Solution Combustion Synthesis (SCS) method.
- Powders are composed by well-defined and separated nanoparticles.
- Some particles are agglomerated but there are also separated particles.
- The dielectric function was modeled by the Maxwell–Garnet formula.
- Optical phonon confinement is registered.

GRAPHICAL ABSTRACT
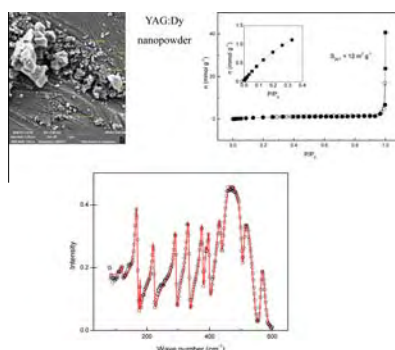
ARTICLE INFO

ABSTRACT

The solution combustion synthesis was used to prepare nanopowders of yttrium aluminum garnet (YAG) and YAG doped with dysprosium ions, Dy^{3+}, (YAG:Dy). The morphology, specific surface area, texture, and optical properties of the prepared materials were studied by the means of scanning electron microscopy (SEM), nitrogen adsorption method, and far-infrared spectroscopy at room temperature in the spectral region between 80 and $600 \, cm^{-1}$. It was established that all the examined samples were microporous. The Maxwell–Garnet formula was used to model dielectric function of YAG and YAG:Dy nanopowders as mixtures of homogenous spherical inclusions in air.

© 2016 Elsevier B.V. All rights reserved.

1. Introduction

Importance of yttrium aluminum garnet, $Y_3Al_5O_{12}$, commonly abbreviated as YAG, arises from its high chemical stability as well as excellent optical and high-temperature mechanical properties [1]. It is a ceramic material with a cubic garnet crystallographic structure whose thermal expansion is isotropic, whereas its optical properties are homogeneous, without birefringence effects [2,3]. Over the last five decades the structural properties of YAG were the subject of numerous studies, which proved its technological relevance and led to its use in a broad range of applications. For example, YAG has found its role as a host material in solid-state lasers of different kinds, luminescence materials, and scintillators [4–6].

Two prospective applications particularly draw attention toward trivalent dysprosium-activated optical materials. Namely,

---

if the phonon energy of host matrix is low, these materials could be an alternative to praseodymium-doped optical amplifiers used in the second telecommunication window [7]. The second promising area of application, the solid-state lasers operating in the visible part of the spectrum [8], is based on the blue and yellow emissions originating from $^4F_{9/2}$ level of Dy^{3+}. These emissions are much more probable than the non-radiative relaxation to the next lower energy level, $^6F_{3/2}$, that corresponds to large energy gap of approximately 7500 cm^{-1}. Consequently, relatively high phonon energy of yttrium aluminum garnet presents YAG crystal as a prospective host material for dysprosium ions [9].

We used solution combustion synthesis (SCS) method to prepare nanopowder samples of YAG and YAG doped with 2 mol% Dy. Optical properties of the samples were analyzed by far-infrared spectroscopy (FIR), whereas nitrogen adsorption method was employed to examine specific surface area and texture. The dielectric function of the nanopowders was modeled using the Maxwell–Garnet formula.

2. Samples preparation and characterization

The SCS method used to prepare the YAG and YAG:Dy nanopowder samples was performed in several steps. Yttrium oxide (Y_2O_3) and aluminum oxide (Al_2O_3) of 99.99 % purity was purchased from the NOAH Technologies. The oxides were dissolved in HNO_3 followed by the addition of carbohydrazide to the solution of aluminum nitrate and yttrium nitrate:

$$3Y(NO_3)_3 + 5Al(NO_3)_3 + 15CH_6N_4O$$
$$\rightarrow YAG + 42N_2 + 15CO_2 + 45H_2O.$$
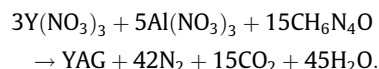
Good reactivity of the raw materials provided absence of the intermediate phases, e.g., YAM ($Y_4Al_2O_9$) or YAP (YAlO$_3$), in the obtained YAG powder. The YAG:Dy samples were produced by doping YAG host with Dy^{3+} ions using the concentration of 2 mol %. Further, YAG:Dy nanopowder was annealed in the air atmosphere at 1300 °C with the aim to obtain full crystallinity [10].

The morphology of the prepared YAG and YAG:Dy nanopowders was examined using a high resolution scanning electron microscope (SEM) equipped with the high brightness Schottky Field Emission gun (FEGSEM, TESCAN) operating at 4 kV. In order to provide conductivity of the samples needed for SEM analysis, the samples were coated with gold/palladium. The SEM images of our YAG and YAG:Dy samples are given in Fig. 1. The powders are composed of well-defined and separated nanoparticles,

clusters, and agglomerated particles. The size of individual spherical particles is in the range of about 30–50 nm. The spherical shape of particles is of great importance because it provides lower light scattering and brighter luminescence performance [11].

3. Results and discussion

3.1. Adsorption isotherms – BET experiments

The analyzer Surfer (Thermo Fisher Scientific, USA) was used to examine YAG and YAG:Dy nanopowders.

The dependences of the adsorbed amount of N_2 on the relative pressure, P/P_0, at the temperature of −196 °C, i.e., the nitrogen adsorption isotherms, for the YAG and YAG:Dy samples are given in Fig. 2. The adsorptions at low relative pressures, given in the graph inserts, indicate that there are micropores on the particle surfaces. According to the IUPAC classification pores are classified as macropores (pore width above 50 nm), mesopores (pore width 2–50 nm) and micropores (pore width below 2 nm) [12]. At the same time, non-limiting adsorption at high P/P_0, was found to correspond to non-rigid aggregates of particles giving rise to slit-shaped pores [13]. Note that these conclusions are in agreement with the SEM images given in Fig. 1, which show that our samples contain agglomerated as well as separated particles. The separated particles are found to be spherical with the diameter of approximately 40 nm. The specific surface areas calculated by the BET equation, S_{BET}, are found to be 5 $m^2\,g^{-1}$ and 12 $m^2\,g^{-1}$ for the YAG and YAG:Dy samples, respectively. Since the radius of Dy^{3+} ion of 0.1167 nm is larger than the radius of Y^{3+} ion, which is 0.1159 nm, it comes as no surprise that the presence of Dy led to increase of the overall specific surface of particles. Also, dopants introduce defects into the structure of the material which results in different charge on the particle surface when doped and undoped are compared. This charge on the particle surface leads to differences in packaging particles and their greater or lesser agglomeration, which on the other hand have significant role on the porosity and specific surface area. Incorporated dopants have a tendency to concentrate at the surface of nanomaterials. All these have significant role on the increasing of the specific surface area.

3.2. Far-infrared spectroscopy

The far-infrared measurements were carried out with the BOMEM DA – 8 FIR spectrometer. The wave number range between 80 and 600 cm^{-1} was covered with the DTGS pyroelectric detector.
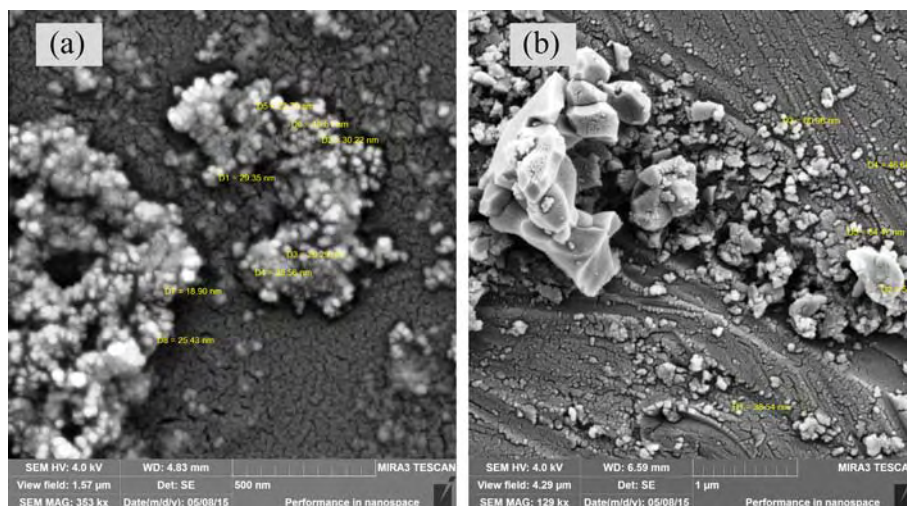

Fig. 1. SEM micrographs. The micrographs of YAG and YAG:Dy nanopowders are given in part (a) and (b), respectively.
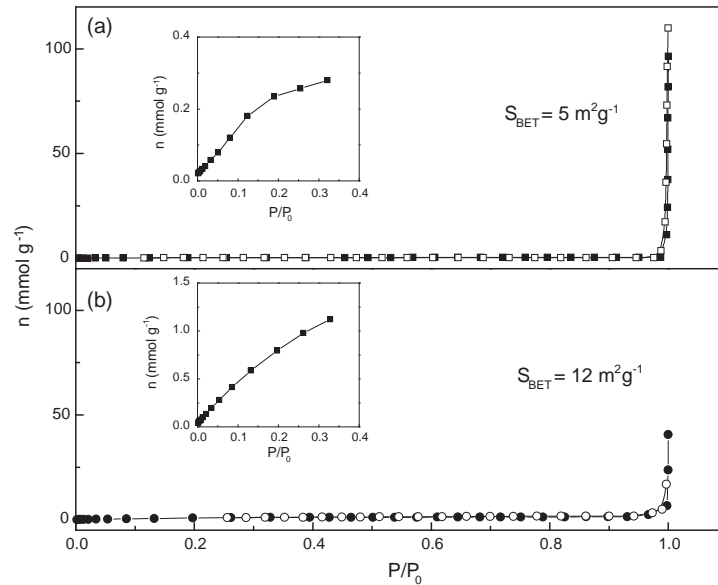
Fig. 2. Nitrogen adsorption isotherms. The amount of adsorbed N_2 given as a function of the relative pressure is shown in graphs (a) and (b) for YAG and YAG:Dy nanopowders, respectively. Solid symbols correspond to adsorption, whereas open symbols represent desorption. The shapes of the curves around zero are enlarged in the inserts.

If the visible light wavelength, λ, is much larger than the characteristic size of semiconducting nanoparticles, d, i.e., if $\lambda \gg d$, the heterogeneous composite of nanoparticles with the dielectric function ε_2 distributed in a medium with the dielectric constant ε_1 can be treated as a homogeneous medium and effective medium theory is applicable. The effective dielectric permittivity of such a mixture can be modeled by a number of mixing models [14]. We chose the Maxwell–Garnet model since our samples are well defined and separated nanosized spherical grains. Consequently, the predicted effective permittivity of the mixture becomes [15]:

$$\varepsilon_{eff} = \varepsilon_1 + 3f\varepsilon_1 \frac{\varepsilon_2 - \varepsilon_1}{\varepsilon_2 + 2\varepsilon_1 - f(\varepsilon_1 - \varepsilon_2)}, \tag{1}$$

where spheres of permittivity ε_2 were taken to occupy a volume fraction f as well as to be randomly located in a homogeneous environment characterized with ε_1. In the considered nanopowders, nanoparticles are situated in air, therefore $\varepsilon_1 = 1$. To determine the dielectric function of the nanoparticles, i.e., ε_2, we used the plasmon–phonon interaction model [16]:

$$\varepsilon_2(\omega) = \varepsilon_\infty \left(\prod_{k=1}^{n} \frac{\omega_{LOk}^2 - \omega^2 + \imath\gamma_{LOk}\omega}{\omega_{TOk}^2 - \omega^2 + \imath\gamma_{TOk}\omega} - \frac{\omega_P^2}{\omega(\omega - \imath\tau^{-1})} \right) \tag{2}$$

where ε_∞ is the bound charge contribution and it is assumed to be a constant, ω_{TOk} and ω_{LOk} are the transverse and longitudinal frequencies, γ_{TOk} and γ_{LOk} are their dampings, ω_P is the plasma frequency and τ is the free carrier relaxation time. The first term in Eq. (2) is the lattice contribution, whereas the second term corresponds to the Drude expression for the free carrier contribution to the dielectric constant.

The measured and calculated far-infrared spectra of YAG and YAG:Dy nanopowders, in the spectral range between 80 and 600 cm^{-1}, at room temperature are shown in Fig. 3. The experimental data are depicted by circles, whereas the solid lines are used to draw the calculated spectra obtained by the fitting procedure based and the model defined by Eqs. (1) and (2). The best fit parameters corresponding to YAG and YAG:Dy nanopowders are given in Table 1. The values corresponding to the YAG single crystal are taken from [17].
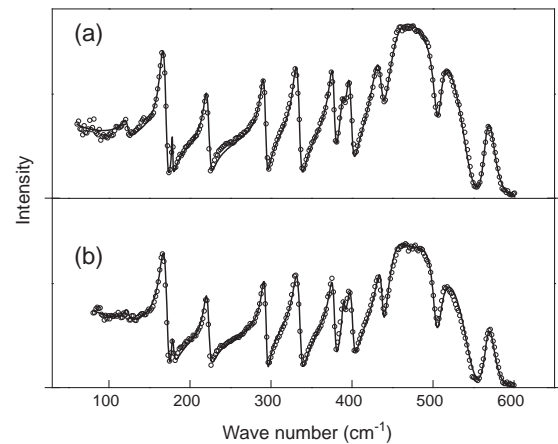

Fig. 3. Far-infrared reflection spectra of YAG nanopowder (a) and YAG:Dy nanopowder (b) at room temperature. The experimental data are represented by circles. The solid lines are the calculated spectra obtained with the parameter values given in Table 1 and the fitting procedure based on the model given by Eqs. (1) and (2).

YAG crystallizes in the cubic structure, it has the symmetry of O_h^{10}–$Ia3d$ space group, and eight molecules of $Y_3Al_5O_{12}$ per primitive unit cell. Out of the ninety-eight theoretically predicted Brillouin zone center modes that correspond to the O_h structure in the YAG group, $3A_{1g} + 5A_{2g} + 8E_g + 14T_{1g} + 14T_{2g} + 5A_{1u} + 5A_{2u} + 10E_u + 18T_{1u} + 16T_{2u}$, only the eighteen T_{1u} modes are IR-active [19]. Further, out of these eighteen theoretically predicted IR-active modes, fourteen are visible in the experimental and modeled far-infrared reflectivity spectra of the YAG and YAG:Dy nanopowders, and in the data corresponding to the YAG single crystal retrieved from literature, see Fig. 3 and Table 1. The bands at around 430, 453, 477, 510 and 566 cm^{-1} represent the characteristic metal–oxygen vibrations, which are in our example Y–O and Al–O. Our data are in agreement with the previous reports regarding single crystals [18,19] as well as with the results on nanocrystals of YAG [20,21]. The peaks located in the vicinity of 477, 510 and 566 cm^{-1} are the asymmetric stretching vibrations, whereas the peak at approximately 453 cm^{-1} is the symmetric vibration

Table 1
Best fit parameters of far-infrared spectra of YAG single crystal, YAG nanopowder and YAG:Dy nanopowder.

	YAG single crystal	YAG nanopowder	YAG:Dy nanopowder	Vibrations
ω_{TO} (cm^{-1})	122	122	122	T (+T$_d$) translations of tetrahedral and dodecahedral cation
	165	165	163	T$_d$ translations of dodecahedral cation
	180	178	178	T$_d$ (+T) translations of tetrahedral and dodecahedral cation
	221	220	219	T$_d$ translations of dodecahedral cation (translations of cations in YO$_3$ and AlO$_4$)
	291	290	289.5	T$_0$
	327	330	328	T translations of tetrahedral cation
	375	375	373	R libration of tetrahedral cation
	390	388.5	389	T$_0$ translations of octahedral cation
	396	399.5	396	R libration of tetrahedral cation
	432	431	431	T$_0$ translations of octahedral (translations + libration) cations in AlO$_6$ and AlO$_4$
	453	447	444	ν_2 symmetric
	477	465	465	ν_4 symmetric
	510	508	507	ν_4
	566	563	564	ν_4 (symmetric and asymmetric stretching of Al–O in octahedrons)
ω_p (cm^{-1})	220	190	220	–
τ (cm^{-1})	0.001	0.002	0.035	–
f	1	0.96	0.80	–

of Al–O bond in the octahedral arrangement of garnet structure. The four lowest energy peaks correspond to the translation and vibration of cations in different coordination – tetrahedral, octahedral and dodecahedral [22]. The peaks around 165, 220, 375 and 396 cm^{-1} have been attributed to the translator motion of Y^{3+} ions within the distorted cube that has eight oxygen ions at its vertices, as well as to the heavy mixing of the translational, rotational, and ν_3 mode of the (AlO$_4$) unit.

Differences in the structure of YAG single crystal and YAG nanopowder cause changes in the phonon frequencies. Namely, decrease in the crystallite size causes optical phonon confinement. The influence of doping of YAG by Dy^{3+} on the spectral properties and lattice vibrations is not significant. Compared to the spectra of YAG single crystal and YAG nanopowder, there are no new phonon modes corresponding to the YAG:Dy nanopowder; however, further decrease of phonon frequencies is registered. Since Dy^{3+} ions are by 0.69%, larger than Y^{3+} ions, substitution of Y^{3+} with Dy^{3+} leads to further distortion of the cubic cell, and consequently to the shift of characteristics frequencies toward lower frequencies, as can be seen in Fig. 3 and Table 1.

The values of filling factors were determined from the analysis of reflection spectra. The main volume fraction, f, obtained as the best fit parameter estimation, is listed in Table 1. These results are consistent with the results obtained by the BET experiment described in Section 3.1. Namely, high values of the filling factor are associated with the existence of micropores.

4. Conclusions

Due to their prospective application in optical amplifiers for the second telecommunication window and solid-state lasers that operate in the visible part of the spectrum, properties of the YAG:Dy nanopowder were investigated and compared to those corresponding to the YAG nanopowder and YAG single crystal. The nanopowders were synthetized by the solution combustion synthesis technique and the samples were analyzed by the scanning electron microscopy, nitrogen adsorption method as well as by the far-infrared spectroscopy. The measured far-infrared spectra were in complete agreement with the modeled spectra obtained with the Maxwell–Garnet formula, plasmon–phonon interaction model, and fitting procedure. It was determined that the Dy doped as well as non-doped YAG nanopowders are microporous. Spherical, well-defined and separated nanoparticles as well as agglomerated particles were detected. The far-infrared measurements revealed that the YAG nanopowder has lower phonon

frequencies than the YAG single crystal as well as that doping of YAG by Dy^{3+} does not have significant influence on the spectral properties and lattice vibrations. However, the doping caused further decrease of phonon frequencies, with respect to the frequencies that correspond to the YAG single crystal and YAG nanopowder.

References

[1] Ji-Guang Li, Takayasu Ikegami, Jong-Heun Lee, Toshiyuki Mori, J. Am. Ceram. Soc. 83 (4) (2000) 961–963.
[2] L. Wen, X. Sun, Z. Xiu, S. Chen, Chi-Tay Tsai, J. Eur. Ceram. Soc. 24 (2004) 2681–2688.
[3] J.W.G.A. Vrolijk, J.W.M.M. Willems, R. Metselaar, J. Eur. Ceram. Soc. 6 (1990) 47–51.
[4] Y. Fujimoto, T. Yanagida, H. Yagi, T. Yanagidani, V. Chani, Opt. Mater. 36 (2014) 1926–1929.
[5] C.R. Varney, D.T. Mackay, S.M. Reda, F.A. Selim, J. Phys. D Appl. Phys. 45 (2012) 015103–015106.
[6] A. Senyshyn, L. Vasylechko, Acta Phys. Pol., A 124 (2013) 329–335.
[7] B. Cole, L.B. Shaw, P.C. Pureza, R. Mossadegh, J.S. Sanghera, I.D. Aggarwal, J. Non-Cryst, Solids 256–257 (1999) 253–259.
[8] A. Kaminskii, U. Hommerich, D. Temple, J.T. Seo, K.-I. Ueda, S. Bagayev, A. Pavlyulk, Jpn. J. Appl. Phys., Part 2: Lett. 39 (3A/B) (2000). L208-11.
[9] M. Klimczak, M. Malinowski, J. Sarnecki, R. Piramidowic, J. Lumin. 129 (2009) 1869–1873.
[10] M.S. Rabasovic, D. Sevic, J. Krizan, M.D. Rabasovic, S. Savic-Sevic, M. Mitric, M. Petrovic, M. Gilic, N. Romcevic, Opt. Mater. 50 (2015) 250–255.
[11] Joo-Yun Chong, Yuelan Zhang, Brent K. Wagner, Zhitao Kang, J. Alloys Compd. 581 (2013) 484–487.
[12] K.S.W. Sing, D.H. Everett, R.A.W. Haul, L. Moscou, R.A. Pierotti, J. Rouquerol, et al., Pure Appl. Chem. 57 (4) (1985) 603–619.
[13] S. Lowell, J.E. Shields, M.A. Thomas, M. Thommes, Charactrization of Porous Solids and Powders: Surface Area, Pore Size and Density, Kluwer Academic Publishers, Dordrecht Netherlands, 2004. 44.
[14] K. Karkkainen, A. Saviola, K. Nikoskinen, IEEE Trans. Geosci. Remote Sensors 39 (5) (2001) 1013–1018.
[15] J.C.M. Garnett, Trans. R. Soc. Vol. CCIII (1904) 385–420.
[16] I.J. Uhanov, Opt. svojstva poluprovodnikov, Nauka, Moskva (1977).
[17] S. Kostić, Z.Ž. Lazarević, V. Radojević, A. Milutinović, M. Romčević, N.Ž. Romčević, A. Valčić, Mater. Res. Bull. 63 (2015) 80–87.
[18] J.P. Hurrel, P.S. Porto, I.F. Chang, S.S. Mitra, R.P. Bauman, Phys. Rev. 173 (1968) 851–856.
[19] G.A. Slack, D.W. Oliver, R.M. Chrenko, S. Roberts, Phys. Rev. 177 (1969) 1308–1314.
[20] Z.H. Chen, Y. Yang, Z.G. Hu, J.-T. Li, S.L. He, J. Alloys Compd. 433 (2007) 328–331.
[21] E. De la Rosa, L.A. Díaz-Torres, P. Salas, A. Arredondo, J.A. Montoya, C. Angeles, R.A. Rodríguez, Opt. Mater. 27 (2005) 1793–1799.
[22] A.M. Hofmeister, K.R. Campbell, J. Appl. Phys. 72 (1992) 638–646.
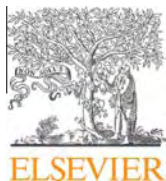
Structural and optical properties of CuSe$_2$ nanocrystals formed in thin solid Cu–Se film

M. Gilić [a,*], M. Petrović [a], R. Kostić [a], D. Stojanović [a], T. Barudžija [b], M. Mitrić [b], N. Romčević [a], U. Ralević [a], J. Trajić [a], M. Romčević [a], I.S. Yahia [c]

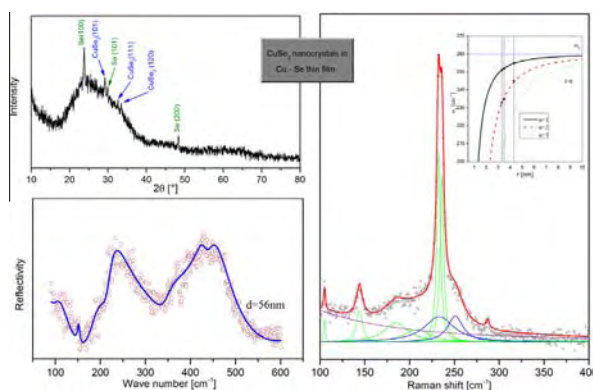[a] Institute of Physics, University of Belgrade, Pregrevica 118, 11080 Belgrade, Serbia
[b] Vinca Institute of Nuclear Sciences, University of Belgrade, Belgrade, Serbia
[c] Nano-Science & Semiconductor Labs., Physics Department, Faculty of Education, Ain Shams University, Roxy, Cairo, Egypt

HIGHLIGHTS

- Two-phase-system, low-pressure modification of CuSe$_2$ and solid solution Cu in Se.
- Raman and far-infrared spectra show 10 modes that belong to hexagonal Se and CuSe$_2$.
- Continuum medium model of optical phonon confinement in CuSe$_2$ nanocrystal.
- Maxwell-Garnett mixing rule was applied.

GRAPHICAL ABSTRACT

ARTICLE INFO

ABSTRACT

This paper describes the structural and optical properties of Cu–Se thin films. The surface morphology of thin films was investigated by atomic force microscopy (AFM) and scanning electron microscopy (SEM). Formation of Cu–Se thin films is concluded to proceed unevenly, in the form of islands which later grew into agglomerates. The structural characterization of Cu–Se thin film was investigated using X-ray diffraction pattern (XRD). The presence of two-phase system is observed. One is the solid solution of Cu in Se and the other is low-pressure modification of CuSe$_2$. The Raman spectroscopy was used to identify and quantify the individual phases present in the Cu–Se films. Red shift and asymmetry of Raman mode characteristic for CuSe$_2$ enable us to estimate nanocrystal dimension. In the analysis of the far-infrared reflection spectra, numerical model for calculating the reflectivity coefficient of layered system, which includes film with nanocrystalite inclusions (modeled by Maxwell-Garnett approximation) and substrate, has been applied.

1. Introduction

Copper selenide is a metal chalcogenide semiconductor which exists in many phases and crystallographic forms:

different stoichiometric such as CuSe (mineral klockmannite), Cu$_2$Se, CuSe$_2$ (mineral marcasite), Cu$_3$Se$_2$ (mineral umangite), Cu$_5$Se$_4$ (mineral athabaskite), Cu$_7$Se$_4$ as well as in non-stoichiometric form as Cu$_{2-x}$Se (mineral berzelianite) and can be constructed into several crystallographic forms (monoclinic, cubic, tetragonal, orthorhombic, hexagonal, etc.). The phase diagram of copper–selenium system [1] shows us that the

thermal stability of these compounds is highly dependent on the stoichiometric form.

Cu–Se thin films are p-type semitransparent highly conducting semiconductors [2,3] that found numerous applications in devices such as thin film solar cells, photodetectors, superionic materials, optical filters [4,5]. Moreover, $CuSe_2$ is superconductor at low temperatures with a transition temperature $T_C \sim 2.4$ K [6]. $CuSe_2$ is reported to be weak ferromagnetic below 31 K [7,8] implying the possible coexistence of ferromagnetism and superconductivity in this compound.

The attraction of this material also lies in feasibility of producing the ternary material $CuInSe_2$ (CIS) and quaternary material Cu(In,Ga)Se_2 (CIGS) as they are the leading candidates for absorber material in large-scale photovoltaic application system [9–11]. CIGS technology laboratory demonstrations reached a submodule power conversion of 20.4% [12].

The optical and electrical properties of copper selenide films depend on the used fabrication method due to compositional complexity of this compound, and possible phase transitions. Numerous methods have been reported for the deposition of these films of different crystalline modifications and varying stoichiometry. These methods can be primarily categorized in two processes. One is solution-based process: chemical bath deposition [3,13,14], solution growth [2], hydrothermal method [15], etc. Another one is vacuum based process: vacuum evaporation techniques [16–19].

Despite of numerous works concerning CuSe in last few decades, there is no much information about its optical properties. This paper reports optical and structural characterization of Cu–Se thin films of three different thicknesses. These films are obtained by rather simple and low-cost vacuum evaporation technique, using Mo boat onto glass substrate at room temperature. Characterization was performed using XRD, AFM, SEM, Raman and far-infrared reflection measurements. The structure of the obtained films is discussed on the basis of XRD data along with AFM measurements. The above properties have been reviewed with respect to the results of the Raman and far-infrared spectroscopy.

2. Samples and characterization

2.1. Preparation of Cu–Se thin films

Copper selenide alloy of high purity (99.99%) was purchased from Aldrich Company. With use of a Mo boat, the powder was deposited onto a highly pre-cleaned glass substrates at vacuum better than 2.67 mPa and at room temperature, with use of a conventional coating unit – Edwards, E-306 A. During the evaporation of Cu–Se thin films, the rate of deposition was kept constant −10 nm/s. The film thickness was controlled with use of a quartz crystal thickness monitor – FTM4, Edwards. Films of three different thicknesses: 56 nm (CuSe A), 79 nm (CuSe B) and 172 nm (CuSe C) were obtained by deposition onto glass substrates.

2.2. AFM and SEM surface characterization

The surface morphology of thin films was investigated by atomic force microscopy (AFM) and scanning electron microscopy (SEM). AFM imaging was done using the NTEGRA Prima system from NT-MDT. Typical tip curvature radius was 8–10 nm. All AFM measurements were performed at room temperature and under ambient conditions. SEM imaging was done using scanning electron microscope equipped with a high brightness Schottky Field Emission gun (FEGSEM, TESCAN) operating at 4 kV. The samples were coated with gold/palladium to make them conductive.

The atomic force microscopy was used to determine the general cell wall structure, together with the assembly of particular components into the wall structure as a whole. Areas of 10×10 μm were investigated. AFM images for Cu–Se thin films are presented in Fig. 1. For the quantitative estimation of the surface, the standard programs of the view treatment were used. Values of the average height, average roughness (R_a), root mean squared (RMS) roughness and surface skewness (Ssk) were analyzed, and the results are presented in Table 1.

From the RMS values, it is clear that the surface of our samples is relatively uneven and rather rough (RMS ranging from 14 to 22 nm), which implies the existence of more than one phase in the system. Unlike the RMS values and average roughness, the average height of our samples grows linearly with film thickness. That trend is expected from the crystal growth. Formation of Cu–Se thin films is concluded to proceed unevenly, in the form of islands which later grew into agglomerates.

SEM analysis confirms the uneven growth of our samples, resulting in rather rough surface with cracks and voids. SEM images of CuSe A sample are presented in Fig. 2, being the representative ones. Agglomerated clusters of few hundreds nanometers in diameter are distributed non-uniformly along the surface. In order to obtain the film thicknesses, the samples are tilted at 30°. The estimated thicknesses are: (56 ± 4) nm for CuSe A (Fig. 2c), (78 ± 4) nm for CuSe B and (171 ± 4) nm for CuSe C (not presented). These values are in good agreement with the ones obtained during samples preparation.

2.3. XRD

The structural characterization of Cu–Se thin film was investigated by using X-ray diffraction pattern. X-ray diffraction measurements were performed on a Philips 1050 X-ray powder diffractometer using a Ni-filtered Cu Kα radiation and Bragg-Brentano focusing geometry. The patterns were taken in the 10–80° 2θ range with step of 0.05° and exposure time of 6 s per step.

X-ray diffraction patterns of our samples are presented in Fig. 3. There is wide diffraction structure in region 20–40° characteristic for noncrystal materials. Good defined peaks are signs of crystal structure formation.

Reflections are clearly seen at Bragg angles (2θ) of about 24°, 29°, 30°, 32.6°, 33.4°, 42°*, 44°*, 46°* and 48.5°. Reflections at angles with asterisk are noticed only for the sample CuSe C. The inset in Fig. 3c presents the full intensity spectrum of CuSe C. The intensities of peaks that rise up with film thickness are signs of the crystal growth. The structural phase analysis was performed on the obtained diffractograms by using EVA 9.0 computing program. It has been observed that the two-phase samples are obtained. Two crystal structures were identified. More prominent one is selenium and less prominent is orthorhombic marcasite structure of $CuSe_2$.

The dominant phase is solid solution of Cu in Se. Namely, according to phase diagrams in works of Chakrabarti and Laughlin [20] and Heyding [1], selenium and copper make solid solution even at 67% of Se. Selenium, the solvent, has hexagonal structure [21] which is by no means the only stable phase of Se under normal conditions of temperature and pressure, with $Z = 3$ atoms per unit cell (S.G. No. 152; $P3_121$ – Schoenflies symbol: D_3^4, $a = 4.3662$ Å, $c = 4.9536$ Å). Selenium atoms (Wyckloff site 3a, with local point symmetry 2 (Schoenflies symbol D_3)) are arranged in helical chains which are oriented along the c-axis of the hexagonal elementary cell (Fig. 4a). One chain is always surrounded by six chains in corners of a hexagon to yield the 3D structure (Fig. 4b). The bonding of atoms within a given chain is covalent whereas the bonding between neighboring chains is by weaker Van der Waals forces.
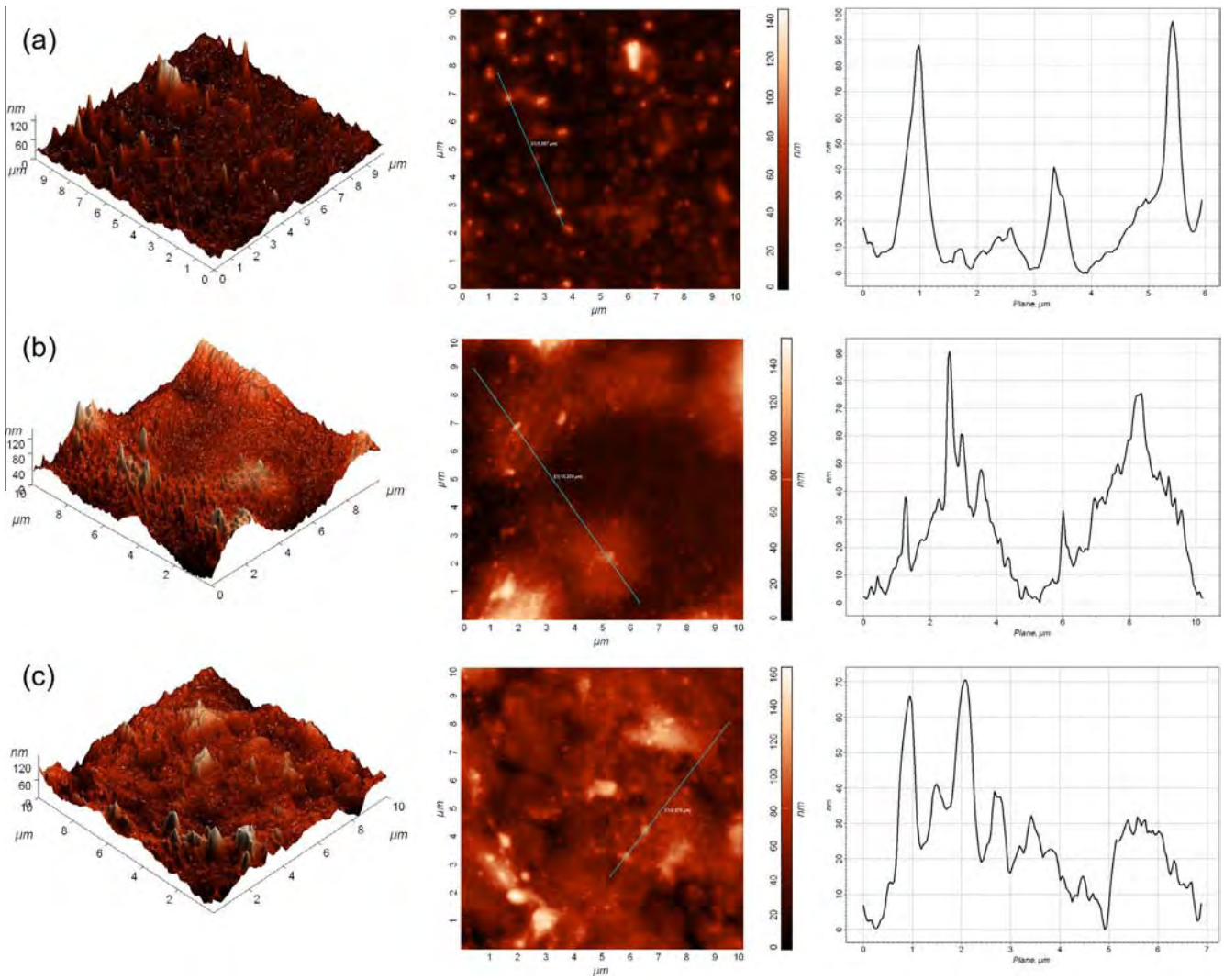
Fig. 1. 3D, 2D AFM images and profile along direction assigned on the 2D image: (a) CuSe A, (b) CuSe B and (c) CuSe C.

Table 1
Quantitative results of AFM.

	Average height (nm)	R_a (nm)	RMS (nm)	Ssk
CuSe A	24	10	14	2
CuSe B	45	17	22	1
CuSe C	61	14	19	1

Reflections at 24° (1 0 0), 30° (1 0 1), 42°* (1 1 0), 44°* (0 1 2), 46°* (1 1 1) and 48.5° (2 0 0) are attributed to this phase.

The second one is low-pressure modification of CuSe$_2$, with Bragg reflections at 29° (1 0 1), 32.6° (1 1 1) and 33.4° (1 2 0) [PDF-2 74-0280]. This modification of CuSe$_2$ has the orthorhombic marcasite structure with Z = 2 formula units per unit cell (S.G. No. 58; *Pnnm* – Schoenflies symbol D_{2h}^{12}, a = 5.103 Å, b = 6.292 Å,
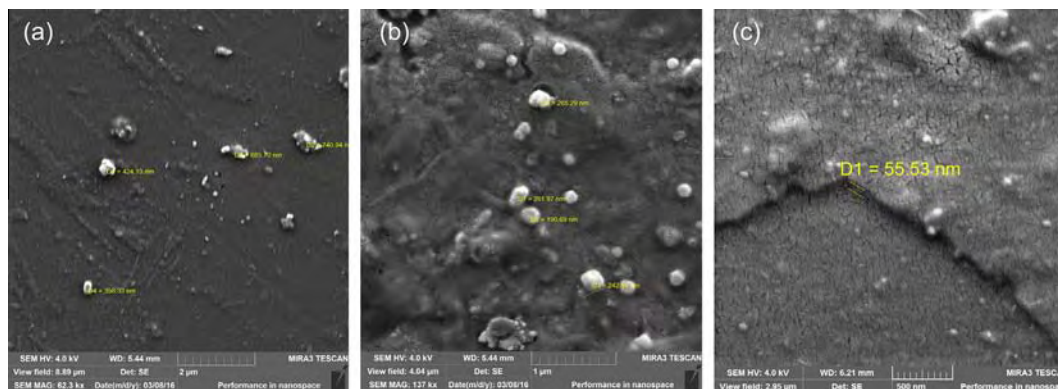
Fig. 2. SEM images of CuSe A sample.
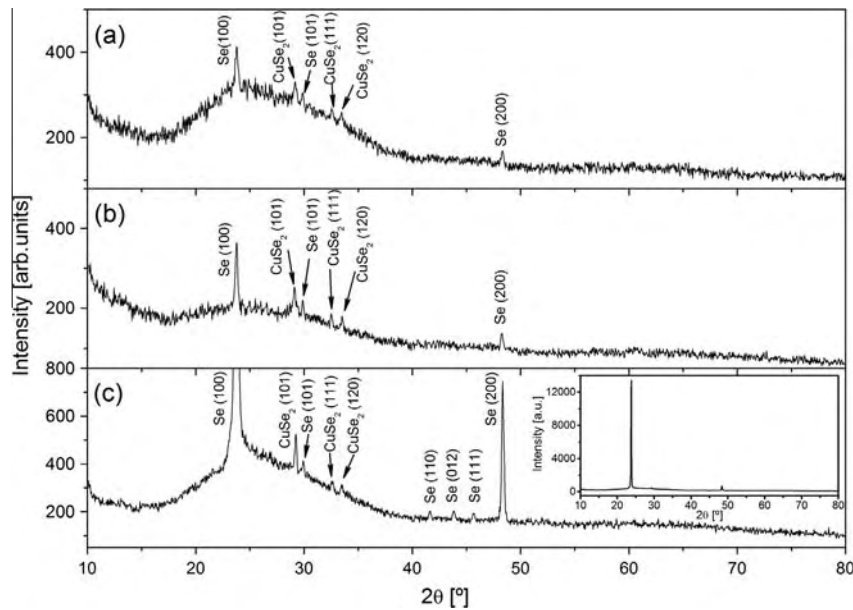
Fig. 3. XRD spectra of (a) CuSe A (b) CuSe B and (c) CuSe C; inset: full intensity spectrum of CuSe C.
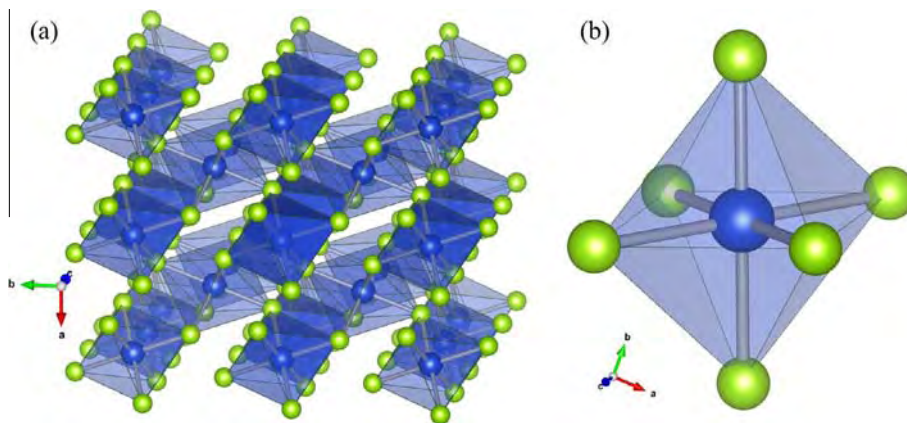
Fig. 4. Crystal structure of hexagonal Se; (a) atoms oriented along *c*-axis; (b) one chain surrounded by six nearest – neighbor helices.

c = 3.812 Å) [22,23] Fig. 5. In this structure each Cu atom (Wyckoff site 2*a*, with local point symmetry 2/*m* (Schoenflies symbol C_{2h})) is surrounded by six Se atoms in a distorted octahedral arrangement, in plane by 4 Se with Cu–Se distance 2.62 Å and out of plane by two more Se neighbors with Cu–Se distance 2.60 Å. These octahedra are corner-sharing in the (*ab*) plane and edge-sharing along *c* axis. Each Se atom (Wyckoff site 4*g*, local point symmetry m (Schoenflies symbol C_s)) is in a distorted tetrahedral configuration, surrounded by three Cu neighbors and one Se neighbor (Se–Se distance 2.29 Å).

Small intensity of Bragg reflections characteristic for $CuSe_2$ indicates small amount of $CuSe_2$, probably in a form of crystallites of very small dimension. The absence of great number of peaks characteristic for the diffractograms of these phases indicates there is no random distribution of crystallites, but the preferentially oriented structures – which indeed was expected for thin films.

3. Results and discussion

XRD identifies two crystal phases: hexagonal Se and small amount of orthorhombic $CuSe_2$. These two crystal phases should contribute to Raman and FIR spectra. We will briefly elaborate already known vibrational properties of these two crystal structures.

As we pointed out in the previous chapter, selenium crystallizes in hexagonal structure of the D_3^4 space group, with three (Z = 3) formula units per unit cell, that results in nine dimensional representation. Factor-group analysis yields a normal modes distribution at the center of Brillouin zone (BZ):

$$\Gamma = A_1 + 2A_2 + 3E$$

The translational motion in *x, y* direction transforms as *E* and in *c* direction as A_2. Optical modes are: A_1 (Raman) + A_2 (IR) + 2*E* (Raman, IR). So three modes of symmetry A_2 + 2*E* are infrared active, and three modes of symmetry A_1 + 2*E* are Raman active. In experimental spectra first order i.e. fundamental modes are expected to dominate. Two two-dimensional modes of the same symmetry *E* are additionally assigned as E^1 (lower energy) and E^2 (higher energy). Forms of vibrations and frequencies of these modes are well known [24,25].

In the second order modes, momentum conservation involves two phonons. The second order selection rules must be satisfied. The selection rules of the two phonon states at critical points are derived from the reducible direct product representation of the
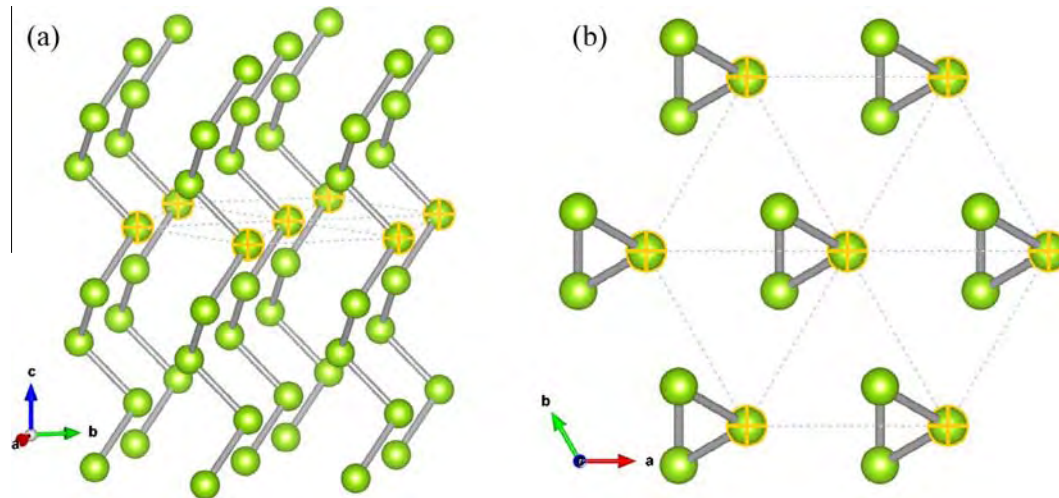
Fig. 5. Crystal structure of orthorhombic $CuSe_2$; blue spheres – copper ions, green spheres – selenium ions; (a) $2 \times 2 \times 2$ unit cells – coordination polyhedra around Cu^{2+} ions; (b) one separated coordination polyhedron around Cu^{2+} ion. (For interpretation of the references to color in this figure legend, the reader is referred to the web version of this article.)

corresponding one phonon states. Scattering process originates from the BZ center (Γ point) or from the BZ boundary points. As wave vectors at the BZ boundary are much larger than the wave vector of the excitation used in experiments, two phonons created or destroyed in the second order scattering that satisfy momentum conservation, originate from the same point of the BZ. We will follow experimental results of Lucovsky et al. [24] to identify the first and second order modes in the center of BZ.

As we established in previous section $CuSe_2$ crystallizes in the orthorhombic (marcasite type) structure, space group *Pnnm* i.e. D_{2h}^{12}, with two formula units ($Z = 2$) per unit cell. Two formula units give 18 degrees of freedom. Factor group analysis gives symmetry of normal modes, in the center of the Brillouin zone:

$$\Gamma = 2A_g + 2B_{1g} + B_{2g} + B_{3g} + 2A_u + 2B_{1u} + 4B_{2u} + 4B_{3u}$$

The translational motion in x, y and z direction transforms as $B_{1u} + B_{2u} + B_{3u}$. Two modes of A_u symmetry are silent modes. Only gerade modes (index g, even parity) are Raman active. Copper ions are located in the center of inversion of *Pnnm* space group so they do not contribute to even parity modes i.e. to the Raman scattering process. So the Raman active modes originate only from the selenium atom vibrations [26]. In the Raman scattering experiment one can expect 6 Raman active modes: $\Gamma_{Raman} = 2A_g + 2B_{1g} + B_{2g} + B_{3g}$. There are 7 infrared active (ungerade) modes: $\Gamma_{IR} = B_{1u} + 3B_{2u} + 3B_{3u}$.

To distinguish modes of the same symmetry, we additionally assign them by superscript in the order of appearance. The A_g^1 mode represents in-phase stretching vibration of Se_2 units. Frequency of this mode depends on Se–Se distance. This is the strongest mode in Raman spectra of marcasite type structures [26–28]. Stretching vibration of chalcogenide ions is characteristic for materials of alike crystallographic structures: pyrite [26,29,30], hexagonal [31] and the others [32]. The A_g^2 mode represents the twisting of Se ions, which tends to rotate Se ions around c axes [26–28]. B_{2g} and B_{3g} are the same type of vibrations, the chain rotations around a and b axis, their frequencies are low, should be close to each other and of small intensity.

There is variety of Cu–Se based crystals. Despite the fact they are of different symmetries, there is characteristic vibration i.e. Raman active mode that represents the stretching vibration of Se ions. In case Cu–Se crystals, Se–Se distance is practically the same for structures pyrite $CuSe_2$ [23], marcasite $CuSe_2$ [23], hexagonal

CuSe [31] or Cu_2Se [32]. In Raman spectra of these structures there is a dominant mode at $\sim$260 cm^{-1}.

Symmetry considerations predict 7 IR active modes, but there are no results about position and activity of these modes in marcasite $CuSe_2$.

3.1. Raman spectroscopy

The micro-Raman spectra were taken in the backscattering configuration and analyzed by Jobin-Yvon T64000 spectrometer, equipped with nitrogen cooled charged-coupled-device detector. As an excitation source we used the 532 nm line of Ti:Sapphire laser, with laser power 20 mW. The measurements were performed in the spectrum range 100–400 cm^{-1}.

The Raman spectra of Cu–Se thin films of different thickness are shown in Fig. 6. Experimental Raman scattering spectra (presented as open dots) are analyzed by the deconvolution to Lorentzian curves. The dominant structure is in region 230–240 cm^{-1}. Ten modes can be reconstructed.

Eight modes (thick green[1] lines on Fig. 6a) are recognized as fundamental and second order modes of hexagonal selenium and listed in Table 2. Factor-group analysis predicts three fundamental Raman active modes. The dominant structure is mainly formed of two fundamental selenium modes of close energy that are assigned as E^2 ($\sim$232 cm^{-1}) and A_1 ($\sim$236 cm^{-1}) modes of hexagonal Se structure. Mode at $\sim$143 cm^{-1} is identified as E^1 mode. Low intense mode at $\sim$105 cm^{-1} is identified as A_2 mode. This fundamental mode is IR active and Raman forbidden. This mode was already registered in hexagonal Se Raman spectra [24]. Wide structures of small intensity at $\sim$185 cm^{-1}, $\sim$208 cm^{-1}, $\sim$287 cm^{-1} and $\sim$354 cm^{-1} are assigned as second order modes and listed in Table 2, as in [24].

Two modes of low intensity, denoted with blue lines in Fig. 6, are in spectral region close to dominant selenium fundamental modes. These two lines i.e. Raman active modes are associated to $CuSe_2$. The more intense one is at $\sim$255 cm^{-1}, $\sim$252 cm^{-1} and $\sim$251 cm^{-1} for samples CuSe A, CuSe B and CuSe C respectively. In Raman spectra of marcasite type $CuSe_2$ one expects dominant scattering structure centered at $\sim$260 cm^{-1} mostly from A_g^1 stretching mode activity. A_g^1 phonon branch goes down in all

---

[1] For interpretation of color in Fig. 6, the reader is referred to the web version of this article.
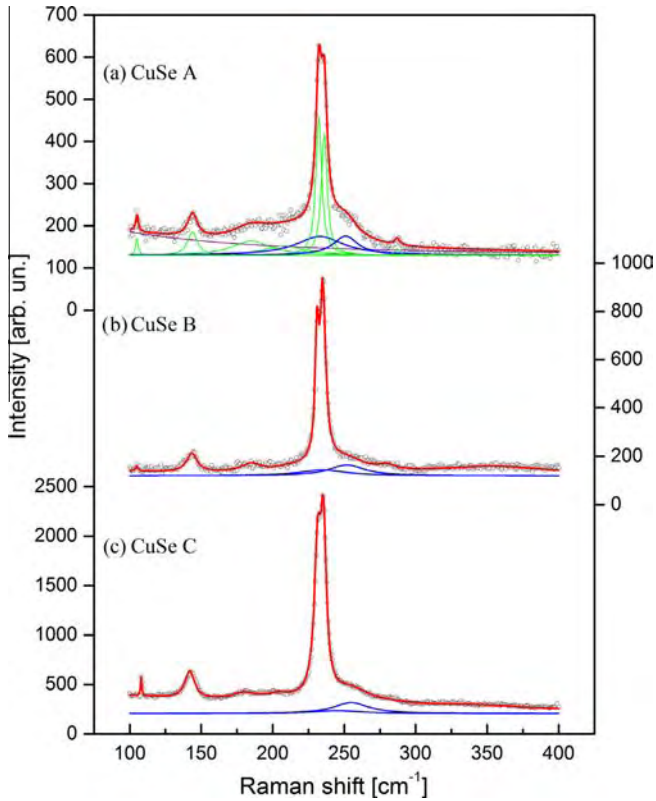
Fig. 6. Raman spectra of Cu–Se thin films of different thicknesses: (a) CuSe A; (b) CuSe B; (c) CuSe C.

Table 2
Position of registered Raman (infrared) active modes (cm^{-1}) of hexagonal Se.

CuSe A	CuSe B	CuSe C	[24]	Assignment
Fundamental modes				
105 (105)	105 (105)	108 (105)	102	A_2 (IR)
144 (152)	143.5 (–)	142.6 (–)	143	E^1 (Raman, IR)
232 (230)	232 (230)	232 (230)	233	E^2 (Raman, IR)
236	236	236	237	A_1 (Raman)
Second order modes				
185	185	183	183	–
208 (200)	208 (200)	206 (205)	206	$2A_2$ (IR)
287 (272)	280 (280)	273 (270)	273	$2E^1$ (Raman, IR)
345 (350)	345 (358)	345 (358)	345	–

directions in BZ. In the case of very small particles i.e. nanoparticles, effects of confinement is to push A_g^1 mode to lower frequencies. In nanocrystals optical modes are confined, bulk selection rules are ruined, high surface to volume ratio increases the role of surface properties, but there is fundamental track of bulk properties. As A_g^1 dispersion relation decreases in all directions in BZ, we expect the frequencies of confined mode to be below $260 \; cm^{-1}$. Analysis of the Raman spectra presented in Fig. 6 concerns to the spectral region below $260 \; cm^{-1}$ (ω_{Ag^1}).

A continuum model of the optical phonon confinement in nanocrystal is used. Parameters were transferred from the bulk phonon dispersion curves. It is limited to nanoparticles of regular shape. Although this is not the case in real nano-crystalites, we present results of calculation for ideal spherical $CuSe_2$ nanocrystals. One small spherical $CuSe_2$ crystal, isotropic and homogeneous inside, is considered. This consideration of confined optical vibrations in nanocrystals is based on macroscopic equation for the relative displacement of the positive and negative ions [33,34]. This equation is solved in spherical coordinates. The spherically

symmetric solutions of equation must belong to the irreducible representations of the three-dimensional rotation–inversion group $O(3)$ labeled as D_l^g (even) and D_l^u (odd upon inversion). Raman transition operator for allowed scattering belongs to D_0^g and D_2^g [35]. Frequencies of the spherical ($l = 0$) and spheroidal quadrupolar modes ($l = 2$) can be calculated and generally observed by resonant Raman scattering.

If we assume, as in [36,37], that at the surface of the sphere all components of displacement are almost zero, the electrostatic potential and the normal component of the electric displacement are continuous. Then one can obtain frequencies of the Raman active modes ($l = 0$ and $l = 2$, $n = 1, 2, 3, \ldots$), l and n being the spherical quantum numbers. The most important contribution to one-phonon Raman scattering corresponds to $l = 0$. This mode is excited for parallel polarizations of the incident and scattered light. The corresponding frequencies are:

$$\omega_n^2 = \omega_0^2 - \beta^2 \left(\frac{\mu_n}{r} \right)^2 \tag{1}$$

ω_0 is the optical bulk frequency i.e. $\omega_0 = 260 \; cm^{-1}$ in $CuSe_2$, r is the radius of the sphere, μ_n is the nth node of the Bessel spherical function j_1 ($\mu_1 < \mu_2 < \mu_3 < \ldots$). Frequency shift (difference between ω_n and ω_0) for fixed r depends on β. $\beta_1 = 1.5 \; 10^3 \; m/s$ for bulk $CuSe_2$. ω_n increases as the radius of the dot (r) increases, and in the limit: $r \to \infty$ frequencies ω_n converge to ω_0. Fig. 7 presents the optical vibration modes frequencies dependence ($l = 0$, $n = 1, 2, 3$) on the radius of $CuSe_2$ nanocrystals. The smaller the radius, the lower is the frequency of confined mode. As for intensity, this model predicts the most intensive peak in Raman spectra to be the mode ω_n ($n = 1$).

Exact positions of modes at $\sim 251 \; cm^{-1}$, $\sim 252 \; cm^{-1}$ and $\sim 255 \; cm^{-1}$ (Table 3 and Fig. 6), for three samples: CuSe A, CuSe B and CuSe C respectively, are marked with stars in Fig. 7. These modes are tentatively assigned as $l = 0$, $n = 1$. It is evident that experimental values determine nanocrystals dimension. Modes at frequencies $\sim 233 \; cm^{-1}$, $\sim 235 \; cm^{-1}$ and $\sim 246 \; cm^{-1}$ (Table 3 and Fig. 6), for samples CuSe A, CuSe B and CuSe C respectively, fall on the calculated curves. These modes are tentatively assigned as $l = 0$, $n = 2$. Nanocrystals dimension established by $l = 0$, $n = 1$ modes is definitely confirmed. Despite the situation that in reality there is nanocrystal size distribution, nanocrystal shape irregularity, inhomogeneity inside, Raman spectroscopy enable detection of average particle size as: $r \sim 3.3 \; nm$ (CuSe A), $r \sim 3.4 \; nm$ (CuSe B) and $r \sim 4.3 \; nm$ (CuSe C).

The mode from $CuSe_2$ is broadened and shifted toward lower frequencies in comparison to the bulk system [26,27]. Shift toward lower frequencies is characteristic for modes of decreasing phonon dispersion relation in bulk. The results of Raman spectroscopy are in good agreement with XRD results. The presence of two crystal phases in synthesized film, the hexagonal Se and orthorhombic $CuSe_2$, is confirmed once again. Small amount of $CuSe_2$ evidenced by XRD is confirmed by low intensity of $CuSe_2$ modes.

3.2. Far-infrared spectroscopy

The far-infrared measurements were carried out with a BOMEM DA-8 FIR spectrometer. A DTGS pyroelectric detector was used to cover the wave number range from 90 to $600 \; cm^{-1}$.

The penetration depth of the infrared electromagnetic waves into a nontransparent crystal is approximately 3 μm. Thickness of our films is from 56 nm to 172 nm, so reflectivity spectra contain information about films together with information about substrate. Three-layer structure is schematically presented in Fig. 8, where medium 1 is air with dielectric function ε_1 ($\varepsilon_1 = 1$), medium 2 is thin Se–$CuSe_2$ mixture layer with corresponding dielectric
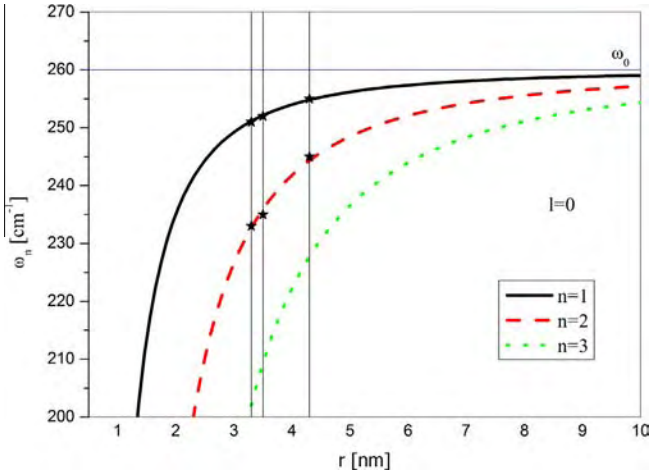
Fig. 7. The radial dependence of $l = 0$ optical modes for CuSe$_2$ spherical nanocrystals.

Table 3
Position of registered Raman (IR) active modes (cm^{-1}) of marcasite CuSe$_2$.

$l = 0$	CuSe A	CuSe B	CuSe C	[26,27]	Assignment
$n = 1$	251 (251)	252 (252)	255 (255)	260	A_g^1
$n = 2$	233	235	243		

function ε_2 and medium 3 is substrate (glass) with dielectric function ε_3. In this case:

$$R_A = \frac{A_r}{A_i} = \frac{\mathbf{r}_{12}e^{-i\alpha} + \mathbf{r}_{23}e^{i\alpha}}{e^{-i\alpha} + \mathbf{r}_{12}\mathbf{r}_{23}e^{i\alpha}} \tag{2}$$

where A_i and A_r are amplitudes of incident and reflection beams, $r_{ij} = (n_i - n_j)/(n_i + n_j) = (\sqrt{\varepsilon_i} - \sqrt{\varepsilon_j})/(\sqrt{\varepsilon_i} + \sqrt{\varepsilon_j})$ are Fresnel coefficients, n_i is complex refractive index of corresponding medium, ε_i complex dielectric constant and $\alpha = 2\pi\omega d(\varepsilon_2)^{1/2}$ is the complex phase change related to the absorption in the medium 2 with the thickness d. The corresponding reflectance (R) is:

$$R = |R_A| \tag{3}$$

The dielectric function of homogeneous medium is:

$$\varepsilon(\omega) = \varepsilon_\infty \prod_{k=1}^{k=N} \frac{\omega_{LOk}^2 - \omega^2 + i\gamma_{LOk}\omega}{\omega_{TOk}^2 - \omega^2 + i\gamma_{TOk}\omega} \tag{4}$$

where ω_{TO} and ω_{LO} are the transversal and longitudinal optical vibrations, and γ_{TO} and γ_{LO} are damping parameters.

The Se–CuSe$_2$ thin films we threat as a mixture of uniformly distributed spherical inclusions of CuSe$_2$ in homogeneous Se. Namely, when visible light interacts with semiconducting nanoparticles (characteristic size L, dielectric function ε'') which are distributed in a medium with the dielectric constant ε', the heterogeneous composite can be treated as a homogeneous medium, and so-called effective medium theory applies.

There are many mixing models for the effective dielectric permittivity of such a mixture [38]. XRD and Raman measurements imply that the structure of our films can be treated as Se film with separated nanocrystals of CuSe$_2$ inside. We decided to use Maxwell-Garnett model for present case. For the spherical inclusions case, the prediction of the effective permittivity of mixture ε_{eff} according to the Maxwell-Garnett mixing rule reads [39,40]:

$$\varepsilon_2 = \varepsilon_{eff} = \varepsilon' + 3f\varepsilon' \frac{\varepsilon'' - \varepsilon'}{\varepsilon'' + 2\varepsilon' - f(\varepsilon' - \varepsilon'')} \tag{5}$$

Here, spheres of permittivity ε'' are located randomly in homogeneous environment of permittivity ε'. Spheres of permittivity ε'' occupy a volume fraction f. ε' and ε'' are also in form of Eq. (4).
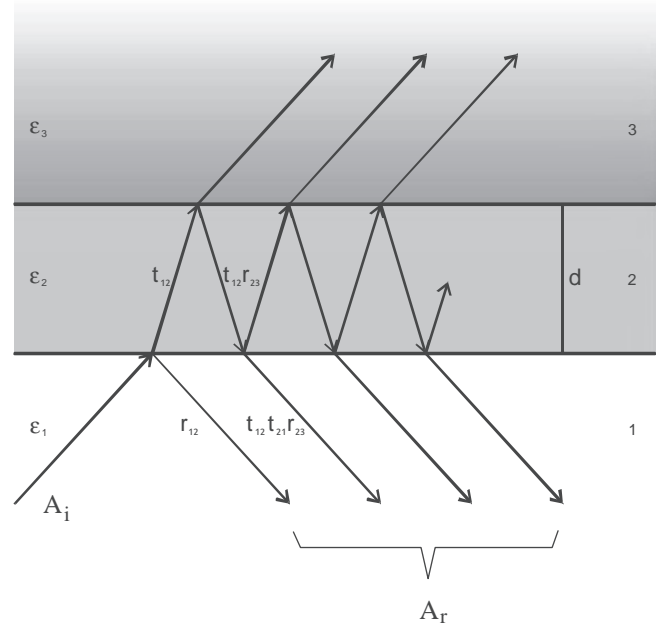

Fig. 8. Schematic presentation of a three layer structure.

The far-infrared reflection spectra of Se–CuSe$_2$ thin films mixture on glass are presented in Fig. 9. Film thickness increases from the bottom to the top of Fig. 9. Experimental data are presented by circles, while the solid lines are calculated spectra obtained by a fitting procedure based on the previously presented model.

The far-infrared reflectivity spectrum of the glass substrate is shown in Fig. 9 (bottom). The calculated spectrum, presented by solid line, was obtained using the dielectric function given by Eq. (4). As a result of the best fit we obtained two modes ($N = 2$). Frequencies of these two modes are $\omega_{TO1} = 438$ cm^{-1}, $\omega_{LO1} = 439$ cm^{-1} and $\omega_{TO2} = 471$ cm^{-1}, $\omega_{LO2} = 523$ cm^{-1}. Frequency values of these modes have remained the same during the fitting procedure for all thin film samples. As the thickness of the film increases (from the bottom to the top of Fig. 9), these substrate reflectivity structures become weaker. As concerns fitting procedure, this weakening is the consequence of increasing the film thickness d.

As we already know from the symmetry analysis of Se structure, there are three infra-red active modes: A_2, E^1 and E^2. We assumed ε' (permittivity of Se), in form given by Eq. (4) ($N = 3$) at positions $\omega_{A2} \sim 105$ cm^{-1}, $\omega_{E1} \sim 152$ cm^{-1} and $\omega_{E2} \sim 230$ cm^{-1}. To achieve coinciding with the experimental spectra, we modeled ε'', (permittivity of CuSe$_2$) in form given by Eq. (4) ($N = 1$) at positions 250–255 cm^{-1}. Volume fraction f is of the order of few percentages. Effective permittivity of film is $\varepsilon_2 = \varepsilon_{eff}$ given by Eq. (5). Additional parameter is the thickness d of the film. Reflectance of the whole structure was calculated by using Eqs. (2) and (3). The best fitting parameters are listed in Tables 2 and 3.

FIR reflectivity measurements are in accordance with the XRD and Raman spectroscopy results. Synthesized films are thin (few tenths of nanometers) and CuSe$_2$ particles are small (few nanometers). There is certain roughness of the sample surface, established by AFM. That is why the most phonon structures in FIR reflectivity spectra are wide and of low intensity. In the central region, 200–300 cm^{-1}, the modes overlap each the other. As a result there is wide and complex structure in this spectral region. Low reflectivity level and high noise compared to it, results in the shape of experimental spectra presented in Fig. 9. Phonon characteristics are practically transferred from Raman measurements. After careful and demanding fitting procedure we achieved that calculated FIR
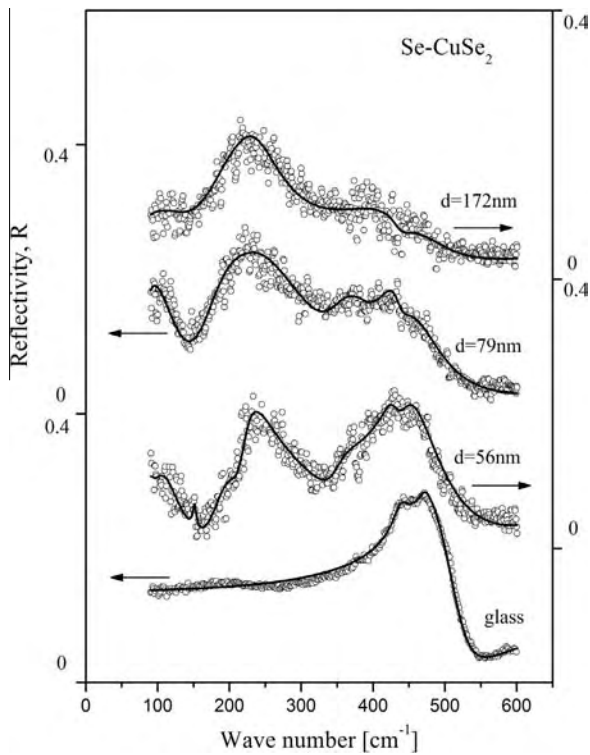
Fig. 9. Far-infrared reflectivity spectra of Se–CuSe$_2$ thin films mixture on glass substrate. Reflectivity spectra from the bottom to the top: glass substrate; CuSe A (d = 56 nm); CuSe B (d = 79 nm); CuSe C (d = 172 nm).

reflectivity spectra reproduce experimental results completely. FIR results, in this case, are used as kind of control and confirmation of samples structure established by XRD and Raman spectroscopy.

4. Conclusions

The optical and structural parameters have been studied for Cu–Se thin films. The surface morphology of thin films was investigated by AFM and SEM. X-ray diffraction results indicate that Cu–Se thin films have two phases, the first one solid solution of Cu in Se and second phase is low-pressure modification of CuSe$_2$. The Raman and far-infrared spectroscopy were used to identify and quantify the individual phases presented in the Cu–Se films.

Raman active modes of hexagonal Se are clearly seen and assigned. We tentatively assign modes at 251–255 cm^{-1} and 233–243 cm^{-1} as l = 0, n = 1 and n = 2 confined CuSe$_2$ A_g^1 mode. Assumed model concerns to an ideal spherical nanocrystal, but it works good in real samples where there is nanocrystal size distribution, shape irregularity, inhomogeneity inside. Raman spectroscopy enables detection of average particle size as: $r \sim 3.3$ nm (CuSe A), $r \sim 3.4$ nm (CuSe B) and $r \sim 4.3$ nm (CuSe C). As the thickness of the film increase, the size of the CuSe$_2$ nanocrystals increases too. Calculated frequencies are in a very good agreement to experimental results.

Infrared active modes of hexagonal Se that dominate in the reflectivity spectra are identified. Presence of CuSe$_2$ nanocrystals in predominantly Se film was modeled by effective medium theory. We tentatively assign mode at 251–255 cm^{-1} as CuSe$_2$ nanocrystal mode. Calculated FIR reflectivities reproduce completely experimental spectra. FIR reflectivity results confirm the sample structure established by XRD and Raman spectroscopy.

References

[1] R.D. Heyding, The copper/selenium system, Can. J. Chem. 44 (1966) 1233–1236.
[2] S. Gosavi, N. Deshpande, Y. Gudage, R. Sharma, Physical, optical and electrical properties of copper selenide (CuSe) thin films deposited by solution growth technique at room temperature, J. Alloy. Compd. 448 (2008) 334–338.
[3] P. Hankare, A. Khomane, P. Chate, K. Rathad, K. Garadkar, Preparation of copper selenide thin films by simple chemical route at low temperature and their characterization, J. Alloy. Compd. 469 (2009) 478–482.
[4] V.J. Fulari, V.P. Malekar, S.A. Gangawane, Measurement of properties of copper telluride thin films using holography, Prog. Electromag. Res. C 12 (2010) 53–64.
[5] H.M. Pathan, C.D. Lokhande, D.P. Amalnerkar, T. Seth, Modified chemical deposition and physicochemical properties of copper (I) selenide thin films, Appl. Surf. Sci. 211 (2003) 48–56.
[6] Y. Takana, N. Uchiyama, S. Ogawa, N. Mori, Y. Kimishima, S. Arisawa, A. Ishii, T. Hatano, K. Togano, Superconducting properties of CuS$_{2-x}$Se$_x$ under high pressure, Physica C 341–348 (2000) 739–740.
[7] G. Krill, P. Panissod, M.F. Lapierre, F. Gautier, C. Robert, M.N. Eddine, Magnetic properties and phase transitions of the metallic CuX$_2$ dichalcogenides (X = S, Se, Te) with pyrite structure, J. Phys. C 9 (1976) 1521–1533.
[8] M. Kontani, T. Tutui, T. Moriwaka, T. Mizukoshi, Specific heat and NMR studies on the pyrite-type superconductors CuS$_2$ and CuSe$_2$, Physica B 284 (2000) 675–676.
[9] K. Matsunaga, T. Komaru, Y. Nakayama, T. Kume, Y. Suzuki, Mass-production technology for CIGS modules, Sol. Energy Mater. Sol. Cells 93 (2009) 1134–1138.
[10] I. Repins, M. Contreras, B. Egaas, C. DeHart, J. Scharf, C. Perkins, B. To Bobby, R. Noufi, 19·9%-efficient ZnO/CdS/CuInGaSe$_2$ solar cell with 81·2% fill factor, Prog. Photovolt.: Res. Appl. 16 (2008) 235–239.
[11] A. Romeo, M. Terheggen, D. Abou-Ras, D. Batzner, F. Haug, M. Kalin, D. Rudmann, A. Tiwari, Development of thin-film Cu(In, Ga)Se$_2$ and CdTe solar cells, Prog. Photovolt.: Res. Appl. 12 (2004) 93–111.
[12] P. Jackson, D. Hariskos, E. Latter, S. Paetel, R. Wuerz, R. Menner, W. Wichmann, M. Powalla, Polycrystalline Cu(InGa)Se$_2$/CdS thin film solar cells made by new precursors, Prog. Photovolt. 19 (2011) 894–897.
[13] V. Garcia, P. Nair, M. Nair, Copper selenide thin films by chemical bath deposition, J. Cryst. Growth 203 (1999) 113–124.
[14] R. Bari, V. Ganesan, S. Potadar, L. Patil, Structural, optical and electrical properties of chemically deposited copper selenide films, Bull. Mater. Sci. 32 (2009) 37–42.
[15] A. Sobhani, M. Salavati-Niasari, A new simple route for the preparation of nanosized copper selenides under different conditions, Ceram. Int. 40 (2014) 8173–8182.
[16] P. Peranantham, Y. Jeyachandran, C. Viswanathan, N. Praveena, P. Chitra, D. Mangalaraj, S.K. Narayandass, The effect of annealing on vacuum-evaporated copper selenide and indium telluride thin films, Mater. Charact. 58 (2007) 756–764.
[17] H. Okimura, T. Matsumae, Electrical properties of Cu$_{2-x}$Se thin films and their application for solar cells, Thin Solid Films 71 (1980) 53–59.
[18] G.G. Rusu, M. Rusu, M. Girtan, Optical characterization of vacuum evaporated CdZnTe thin films deposited by a multilayer method, Vakuum 81 (2007) 1476–1482.
[19] A.M. Hermman, L. Fabick, Research on polycrystalline thin-film phtovoltaic devices, J. Cryst. Growth 61 (1983) 658–664.
[20] D.J. Chakrabarti, D.E. Laughlin, The Cu–Se (copper–selenium) system, Bull. Alloy Phase Diagrams 2 (1981) 305–315.
[21] P. Cherin, P. Unger, The crystal structure of trigonal selenium, Inorg. Chem. 6 (1967) 1589–1591.
[22] G. Gattow, Z. Arong, Allg. Chem. 340 (1965) 312 (Calculated from ICSD using POWD-12++ (1997)).
[23] R.D. Heyding, R.M. Murray, The crystal structures of Cu$_{1.8}$Se, Cu$_3$Se$_2$, α- and γ-CuSe, CuSe$_2$ and CuSe$_2$II, Can. J. Chem. 54 (1976) 841–848.
[24] G. Lucovsky, A. Mooradian, W. Taylor, G.B. Wright, R.C. Keezer, Identification of the fundamental vibrational modes of trigonal, α-monoclinic and amorphous selenium, Solid State Commun. 5 (1967) 113–117.
[25] W.D. Teuchert, R. Geick, G. Landwehr, H. Wendel, W. Weber, Lattice dynamics of trigonal selenium. I. Phonon spectra, J. Phys. C 8 (1975) 3725–3736.
[26] C. Sourisseau, R. Cavagnat, M. Fouassier, The vibrational properties and valence force fields of FeS$_2$, RuS$_2$ pyrites and FeS$_2$ marcasite, J. Phys. Chem. Solids 52 (1991) 537–544.
[27] X. Wu, M. Kanzaki, S. Qin, G. Steinle-Neumann, L. Dubrovinsky, Structural study of FeP$_2$ at high pressure, High Pressure Res. 29 (2009) 235–244.

[28] J. Li, Z. Jin, T. Liu, J. Wang, X. Zheng, J. Lai, Chemical synthesis of MSe_2 (M = Ni, Fe) particles by triethylene glycol solution process, Crys. Eng. Comm. 16 (2014) 6819–6822.

[29] M. Blanchard, M. Alfreddsson, J. Brodholt, G.D. Price, K. Wright, C.R.A. Catlow, Electronic structure study of the high-pressure vibrational spectrum of FeS_2 pyrite, J. Chem. B 109 (2005) 22067–22073.

[30] A.K. Kleppe, A.P. Jephcoat, High-pressure Raman spectroscopic studies of FeS_2 pyrite, Mineral. Mag. 68 (2004) 433–441.

[31] E.M. Ishii, K. Shibata, H. Nozaki, Anion distributions and phase transitions in $CuS_{1-X} Se_X$ ($x = 0–1$) studied by Raman spectroscopy, J. Solid State Chem. 105 (1993) 504–511.

[32] B. Mincareva-Sukarova, M. Najdoski, I. Grozdanov, C.J. Chunnailall, Raman spectra of thin solid films of some metal sulfides, J. Mol. Struct. 410–411 (1997).

[33] M.P. Chamberlain, C. Trallero-Giner, M. Cardona, Theory of one-phonon Raman scattering in semiconductor microcrystallites, Phys. Rev. B 51 (1995) 1680–1693.

[34] R. Roca, C. Trallero-Giner, M. Cardona, Polar optical vibrational modes in quantum dots, Phys. Rev. B 49 (1994) 13704–13711.

[35] E. Duval, Far-infrared and Raman vibrational transitions of a solid sphere: selection rules, Phys. Rev. B 46 (1992) 5795–5797.

[36] C. Trallero-Giner, A. Debernardi, M. Cardona, E. Menendez-Proupin, A.I. Ekimov, Optical vibrons in CdSe dots and dispersion relation of the bulk material, Phys. Rev. B 57 (1998) 4664–4669.

[37] J. Trajic, R. Kostic, N. Romčević, M. Romčević, M. Mitric, V. Lazovic, P. Balaz, D. Stojanovic, Raman spectroscopy of ZnS quantum dots, J. Alloy. Compd. 637 (2015) 401–406.

[38] K. Karkkainen, A. Saviola, K. Nikoskinen, IEEE Trans. Geosci. Remote Sens. 39 (5) (2001) 1013–1018.

[39] J.C.M. Garnett, Colours in metal glasses and in metallic films, Trans. R. Soc. CCIII (1904) 385–420.

[40] A. Saviola, I. Lindell, Dielectric Properties of Heterogeneous Materials PIER 6 Progress in Electromagnetic Research, in: A. Priou (Ed.), Elsevier, Amsterdam, 1992, pp. 101–151.

Far-infrared spectroscopy of laser power modified MnO nanoparticles

B. BABIC[a], B. HADZIC[a], I. KURYLISZYN-KUDELSKA[b], N. PAUNOVIC[a], B. VASIC[a], W. D. DOBROWOLSKI[b], M. ROMCEVIC[a], J. TRAJIC[a,*], N. ROMCEVIC[a]

[a]Institute of Physics, University of Belgrade, Pregrevica 118, 11080 Belgrade, Serbia
[b]Institute of Physics, Polish Academy of Science, al. Lotnikow 32/46, 02-668 Warszawa, Poland

The influence of the locally induced laser heating on MnO nanoparticles were investigated by atomic force microscopy (AFM) and far-infrared spectroscopy (FIR) at room temperature, in the spectral region between 80 and 600 cm^{-1}. The FIR spectra were analyzed by using Maxwell-Garnet formula, where MnO nanoparticles are modeled as a mixture of homogeneous spherical inclusions in air. Laser induced heating leads to the conversion of the part MnO nanoparticles into the MnO_2, Mn_3O_4 and $MnOOH$, along with possible formation of elemental Mn on the sample surface.

1. Introduction

MnO is transitional metal oxide which crystallizes in the simple rock salt structure. It is well known that this structure has a certain number of defects, usually in the cationic sublattice, what leads to the formation of structure which can be described as an ordered Mn vacancy cubic structure with the formula $Mn_{1-\delta}O$, where $0 \leq \delta \leq 0.15$ [1-3].

Due to this non-stoichiometry, MnO has unique electrical, magnetic, optical and mechanical properties, characteristic for the rock salt structure [1, 2]. Recently, Hiramoto and co-workers proposed a new synthetic route which enables the control of the non-stoichiometric defects in the structure [4]. Bulk MnO acts as a p-type semiconductor and has anti-ferromagnetic properties [5]. But, the presence of impurities can significantly change the magnetic properties of the MnO [6 - 9].

The size of the particles has considerable influence on the properties of MnO. For instance, literature data shows that nanometric MnO has ferromagnetic characteristics [5]. New characteristics on nanometric scale can be explained with significant changes into the surface to volume ratio. The decreasing of the particle size increases the amount of edge atoms and, consequently, the number of unsaturated chemical bonds which, further, changes the physical and chemical properties of the material. Manganese can exists in the several oxidation states among which Mn(II) is the lowest. By different oxidation treatment, manganese can be transverse in to the different, higher, oxidation states.

Recently, we have investigated the influence of the lacer induced heating of ZnO(Co) [10], $Bi_{12}GeO_{20}$ [11] and MnO [12] nanoparticles, with different laser powers. It has been shown that laser induced heating leads to creation of new phases, depending on laser power.

In order to further investigate the influence of the locally induced laser heating on MnO nanoparticles, non-irradiated, as well as irradiated MnO sample, were investigated by using far-infrared spectroscopy (FIR) and atomic force microscopy (AFM).

2. Sample characterization

Commercially available polycrystalline MnO powder of the analytical grade (Sigma-Aldrich Co) was pressed into a pellet. Verdi G optically pumped semiconductor laser with wavelenght of 532 nm was used as excitation source. In this paper we analyzed one sample, at first before laser treatment and afterwards after treatment with a laser with a power of 24 mW.

AFM measurements of non-irradiated and irradiated sample with the highest energy were done using NT-MDT system NTEGRA Prima at ambient conditions. AFM images were recorded in tapping mode, using NSG01 probes from NT-MDT.

The far-infrared measurements on non-irradiated and irradiated sample with laser power (24mV) were carried out with a BOMEM DA-8 FIR spectrometer. A DTGS pyroelectric detector was used to cover the wave number range from 80 to 600 cm^{-1}.

3. Results and analysis

3.1. AFM measurements

AFM topographies of non-irradiated (a) and irradiated (b) MnO samples are presented on Fig. 1. Fig. 1 shows a clear difference between the surfaces of the sample before and after irradiation. Prior to irradiation, a granulated structure, with well recognized grain boundaries, is visible.

Grains size is about few tens of nanometers. In our previous investigations X-ray analysis showed that mean crystallite size is about 44 nm [12] which is in good agreement with results obtained with AFM.

After irradiation, the topography of the surface was significantly changed. The grain boundaries are not visible and surface is smooth. Due to the laser induced heating and increasing of the energy, MnO particles on the surface of the samples interact with the elements and compounds from the vicinity (mostly oxygen and water) and create compounds in which manganese is in the higher oxidation state. Process is spontaneous and these different species are inhomogeneously arranged on the surface of the sample and, consequently, clear boundaries between grains are lost.

surface of the sample and, consequently, clear boundaries between grains are lost.

3.2. Far-infrared spectroscopy

When visible light, of wavelength λ interacts with semiconducting nanoparticles (characteristic size d, dielectric function ε_2) which are distributed in a medium with the dielectric constant ε_1 in the limit $\lambda \gg$ d, the heterogeneous composite can be treated as a homogeneous medium and effective medium theory is applied. There are many mixing models for the effective dielectric permittivity of such a mixture [13]. Since our samples are well defined and separated nanosized grains, we used Maxwell-Garnet model for present case. For the spherical inclusions case, the prediction of the effective permittivity of mixture ε_{eff} according to the Maxwell-Garnet mixing rule is [14]:

$$\varepsilon_{eff} = \varepsilon_1 + 3f\varepsilon_1 \frac{\varepsilon_2 - \varepsilon_1}{\varepsilon_2 + 2\varepsilon_1 - f(\varepsilon_1 - \varepsilon_2)} \qquad (1)$$

Here, spheres of permittivity ε_2 are located randomly in homogeneous environment ε_1 and occupy a volume fraction f. The observed nanoparticles are situated in air, therefore the ε_1 is 1. For dielectric function of observing nanoparticles (ε_2) we are using the standard model [15]:

$$\varepsilon_2(\omega) = \varepsilon_\infty + \sum_{k=1}^{l} \frac{\varepsilon_\infty(\omega_{LOk}^2 - \omega_{TOk}^2)}{\omega_{TOk}^2 - \omega^2 - i\gamma_{TOk}\omega} - \frac{\varepsilon_\infty \omega_P^2}{\omega(\omega + i\tau^{-1})} \qquad (2)$$

where ε_∞ is dielectric constant at high frequencies, ω_{TOk} and ω_{LOk} are transverse and longitudinal frequencies, γ_{TOk} is the phonon damping, ω_P is the plasma frequency and τ is the free carrier relaxation time. The first term in (2) is the lattice contribution whereas the second term is the Drude expression for the free carrier contribution to the dielectric constant. In this case, ω_{TOk} is considered as characteristic frequency of the material and ω_{LOk} is connected with the oscillator strength ($S_k \sim \omega_{LOk}^2 - \omega_{TOk}^2$).

The far-infrared spectra of non-irradiated and irradiated MnO nanopowders, in the spectral range of 80 to 600 cm^{-1}, at room temperature are presented in Fig. 2. The experimental data are presented by circles, while the solid lines are calculated spectra obtained by a fitting procedure based on the previously presented model. Obviously, a very good correlation between experimental data and calculated spectra is achieved. Parameters, such as: filling factors, f, plasma frequencies, ω_P, effective permittivity of mixtures, ε_{eff}, and transversal and longitudinal frequencies ω_{TO}/ω_{LO}, for the non-irradiated and irradiated sample, estimated from the reflection spectra, are presented in Table 1. Induced laser heating leads to the increasing of the filling factor. Result is expected and in agreement with result obtained by AFM. Namely, phase transformation and loss of the grain boundaries leads to the decreasing of the space between particles. In accordance with that, the dielectric constant at high frequencies and plasma frequency decrease. Also, we should keep in mind that surface affected by the laser beam

Fig. 1. AFM 3D topography of (a) non-irradiated and (b) irradiated sample of MnO nanoparticles

After irradiation, the topography of the surface was significantly changed. The grain boundaries are not visible and surface is smooth. Due to the laser induced heating and increasing of the energy, MnO particles on the surface of the samples interact with the elements and compounds from the vicinity (mostly oxygen and water) and create compounds in which manganese is in the higher oxidation state. Process is spontaneous and these different species are inhomogeneously arranged on the

is significantly smaller (radius 1 mm) in comparison with the overall surface of the pallet (radius 6 mm) which means that, in the case of the irradiation of the whole sample the differences would be more significant.

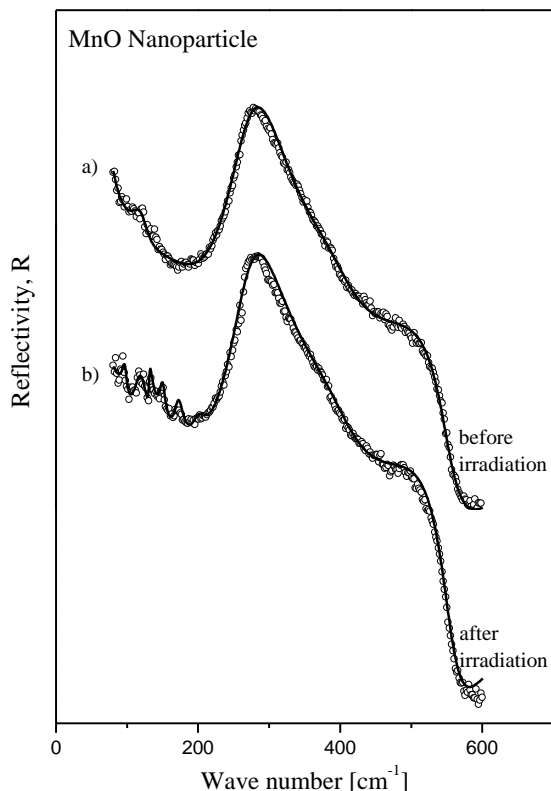MnO Nanoparticle

a)

b)

before irradiation

after irradiation

Fig. 2. Far – infrared reflection spectra of (a) non-irradiated and (b) irradiated MnO nanoparticles. The experimental data are represented by circles. The solid lines are the calculated spectra obtained by fitting procedure based on the model given by Eqs. (1,2)

Five vibration modes were determined for both non-irradiated and irradiated sample and their values are presented in Table 1. To our knowledge, there are no literature data for the FIR characterization of the MnO and we compared these results with data collected by Raman spectroscopy. By summarizing different literature data [12, 16-24], three characteristics peaks for MnO are obtained in the range 520-545, 559-595 and 645-660 cm^{-1}. First two peaks we registered by using FIR spectroscopy, also. In both cases, non-irradiated and irradiated sample, additional two peaks, in the range of 310-410 cm^{-1} are recorded. According to literature data, these peaks can be attributed to the β-MnO_2 (TO/LO pair at 324/330cm^{-1}) [18, 22, 23] and α-MnO_2 (395/405cm^{-1}) [20, 21]. Additionally, according to Kim at al. [24] peak at 324 cm^{-1} can be attributed to Mn_3O_4.

Additional vibration peaks that appear in FIR spectra of irradiated samples can be identified in the following way: peaks at 131, 140, 171 and 199.5 cm^{-1} could be attributed to a α–MnOOH [20, 21] and peak at 171.5 cm^{-1} could be attributed to α–MnO_2 [20, 21].

Some authors peak at 171 cm^{-1} attributed to Mn_5O_8 phase (binary $Mn_2^{2+}Mn_3^{4+}O_8$ oxide with layer structure) [25]. These peaks are also registered at Raman spectra of the irradiated samples.

Table 1. Calculated fit parameters obtained from the far - infrared spectra of non - irradiated and irradiated MnO nanoparticles

	Before irradiation [cm^{-1}]	After irradiation [cm^{-1}]
f	0.81	0.89
ω_P	301	291
ε_∞	2.8	2.5
ω_{TO}/ω_{LO}	120/123	116.8/117
ω_{TO}/ω_{LO}	140/148	140/140
ω_{TO}/ω_{LO}	324/330	320/330
ω_{TO}/ω_{LO}	395/405	398/407
ω_{TO}/ω_{LO}	520/526	515/558
ω_{TO}/ω_{LO}	575/590	579/584
ω_{TO}/ω_{LO}	-	96.8/97.4
ω_{TO}/ω_{LO}	-	131/131.3
ω_{TO}/ω_{LO}	-	140/141
ω_{TO}/ω_{LO}	-	171.5/172
ω_{TO}/ω_{LO}	-	199.5/200

Mode at about 100 cm^{-1} (TO/LO pair is 116.8/117 cm^{-1} in our case) was registered before for this group of materials [26] as a "defect mode". Mod at 96.8/97.4 cm^{-1}, in the some region, can be describe us „defect mode", also. However, since it occurs only in an irradiated sample, we can assume that we have a case of disorder-enabled phonon (DAP) mode [27]. This is the case registered in a large number of A^2B^6 semiconductors [28].

Finally, it was shown that FIR spectroscopy is a useful technique for the characterization of laser power induced phase changes in MnO nanoparticles.

4. Conclusion

MnO nanoparticles modified by laser heating are investigated by using far-infrared spectroscopy. Effective permitivity of MnO nanoparticles (mixture of homogeneous spherical inclusions in air) are modeling by Maxwell-Garnet formula. In consequence of laser irradiation, volume fraction of nanoparticles increase while dielectric constant and plasma frequencies decrease, due to the formation of the different species on the surface of the MnO sample.

Additional vibration modes characteristic for the irradiated samples, were confirmed by using FIR method.

Acknowledgments

References

[1] M. Jimenez-Melendo, A. Dominguez-Rodriguez, J. Castaing, Acta Metallurgica et Materialia **43**, 3589 (1995).

[2] R. Aragon, Physical Review B **46,** 5328 (1992).

[3] M. J. Radler, J. B. Cohen, G. P. Sykora, T. Mason, D. E. Ellis, J. Faber Jr., Journal of Physics and Chemistry of Solids **53**, 141 (1992).

[4] M. Hiramoto, N. Okinaka, T. Akyimam, Materials Chemistry and Physics **134**, 98 (2012).

[5] I. Djerdj, D. Arcon, Z. Jaglicic, M. Niederberger, Journal of Physical Chemistry C **111**, 3614 (2007).

[6] N. Mironova-Ulmane, A. Kuzmin, M. Grube, Journal of Alloys and Compounds **480**, 97 (2009).

[7] J. Park, E. Kang, C. J. Bae, J. G. Park, H. J. Noh, J. Y. Kim, J. H. Park, H. M. Park, T. Hyeon, Journal of Physical Chemistry B **108**, 13594 (2004).

[8] A. E. Berkowitz, G. F. Rodriguez, J. I. Hong, K. An, T. Hyeon, A. Agarwal, D. J. Smith, E. E. Fullerton, Physical Review B **77**, 024403 (2008).

[9] J. J. Hauser, J. V. Waszczak, Physical Review B **30**, 5167 (1984).

[10] B. Hadžić, N. Romčević, D. Sibera, U. Narkiewicz, I. Kurylisyn-Kudelska, W. Dobrowolski, M. Romčević, Journal of Physics and Chemistry of Solids **91**, 80 (2016).

[11] A. Kovačević, J. Ristić-Djurović, M. Lekić, B. Hadžić, G. Saleh Isa Abudagel, S. Petričević, P. Mihailović, B. Matović, D. Dramlić, Lj. Brajović, N. Romčević, Materials Research Bulletin **83**, 284 (2016).

[12] B. Hadzic, B. Vasic, B. Matovic, I. Kuryliszyn-Kudelska, W. Dobrowolski, M. Romcevic, N. Romcevic, Journal of Raman Spectroscopy (2018) in press.

[13] K. Karkkainen, A. Sihvola, K. Nikoskinen, IEEE Transactions on Geoscience and Remote Sensing **39**, 1013 (2001).

[14] J. C. M. Garnett, Philosophical Transactions of the Royal Society of London, Series A **203** 385 (1904).

[15] J. Trajic, N. Romcevic, M. Romcevic, V. N. Nikiforov, Materials Research Bulletin **42**, 2192 (2007).

[16] F. Buciuman, F. Patcas, R. Cracium, D. R. T. Zahn, Physical Chemistry Chemical Physics **1**, 185 (1999).

[17] C. Julien, M. Massot, R. Baddour-Hadjean, S. Franger, S. Bach, J. P. Pereira-Ramos, Solid State Ionics **159**, 345346 (2003).

[18] C. M. Julien, M. Massot, C. Poinsignon, Spectrochimica Acta Part A **60**, 689 (2004).

[19] B. K. Pandey, A. K. Shahi, R. Gopal, Materials Focus **2**, 221 (2013).

[20] T. Gao, H. Fjellvag, P. Norby, Analytica Chimica Acta **648**, 235 (2009).

[21] S. Cheng, L. Yang, D. Chen, X. Ji, Z.-J. Jiang, D. Ding, M. Liu, Nano Energy **9** 161 (2014).

[22] C. M. Julien, M. Massot, Proceedings of the International Workshop Advanced Techniques for Energy Sources Investigation and Testing, Sofia, Bulgaria, September 2004, pp. 1–17.

[23] S. Kumar, A. K. Ojha, R. K. Singh, Journal of Raman Spectroscopy **45**, 717 (2014).

[24] M. Kim, X. M. Chen, X. Wang, C. S. Nelson, R. Budakian, P. Abbamonte, S. L. Cooper, Physical Review B **84**, 174424 (2011).

[25] J. Gao, M. A. Lowe, H.D. Abruna, Chemistry of Materials **23**, 3223 (2011).

[26] H. Kepa, T. Giebultowicz, B. Buras, B. Lebech, K. Clausen, Physica Scripta **25**(6A), 807 (1982).

[27] V. Dzagan, I. Lokteva, C. Himcinschi, X. Jin, J. Kolny-Olesik, D. R. T. Zahn, Nanoscale Research Letters **6**, 79 (2011).

[28] A. Ingale, K. C. Rustagi, Physical Review B **58**, 7197 (1998).

*Corresponding author: jelena@ipb.ac.rs

CrossMark

Photoluminescence spectroscopy of CdSe nanoparticles embedded in transparent glass

M. Gilic[1] · **R. Kostic**[1] · **D. Stojanovic**[1] · **M. Romcevic**[1] · **B. Hadzic**[1] · **M. Petrovic**[1] ·
U. Ralevic[1] · **Z. Lazarevic**[1] · **J. Trajic**[1] · **J. Ristić-Djurovic**[1] · **J. Cirkovic**[2] · **N. Romcevic**[1]

Abstract

In this paper we present photoluminescence measurements of CdSe nanoparticles embedded in transparent glass. Sample is prepared using an original technique, which combines both heat treatment and ultraviolet laser irradiation. Photoluminescence spectra displayed one main emission band at 2.14 eV. We identify this bands energy as basic interband transition in CdSe nanoparticle. We calculated energy of basic ($1s_h$–$1s_e$) transition in spherical CdSe quantum dot (QD), within infinite potential barrier, in effective-mass approximation. On the basis of this model, average radius of synthesized CdSe QDs is about 3 nm, which is in consistence with AFM measurements and UV–VIS absorption measurements.

Keywords Cadmium selenide · Nanoparticles · Photoluminescence · AFM · Effective mass approximation

1 Introduction

Glasses doped with nanosized inclusions of metals or semiconductors are known since a very long time. The first glasses containing metal nanoparticles were fabricated by Roman glassmakers in the fourth century A.D. Mediaval cathedral windows through several European countries witness the attention drawn by stained glasses containing metal aggregates as artistic work (Poole et al. 2003). They exhibit great varieties of beautiful colors owing to the nanosized metal particles which were embedded in the glass matrix.

Semiconductor-doped glasses were, however, not so widespread used. One very important application of semiconductor-doped glasses are sharp cut-off glass filters. In most cases, Cd

✉ M. Gilic
   martina@ipb.ac.rs

1 Institute of Physics Belgrade, University of Belgrade, Pregrevica 118, Zemun 11080, Serbia

2 Institute for Multidisciplinary Research, University of Belgrade, Kneza Viseslava 1, Belgrade 11000, Serbia

(S_x,Se_x) nanocrystals are used for this purpose. By varying× the position of the cut-off wavelength can be precisely tuned between ~400 and 1000 nm.

These glass filters are easily available from different glassmakers, such as Schott, Corning, Hoya, or Toshiba. This is an import point, as it allowed a great number of optics groups to study this kind of composite material without the need for skills in material preparation.

From technological perspective, CdSe nanoparticles are of significant interest because of their unique quantum confinement properties, bright photoluminescence, narrow emission band, and photostability (Srivastava and Singh 2012). CdSe-polymer nanocomposites find potential applications in the fabrication of devices like photovoltaic cells, laser, thin film transistors, light emitting diodes (Yu et al. 2006; Oertel et al. 2005), catalysis (Ahmadi et al. 1996) and biological fluorescence labels (Bruchez et al. 1998; Chan and Nie 1998). In particular, CdSe nanocrystals have been proposed as working elements for nanotransistors (Klein et al. 1997), electrohromic materials (Wang et al. 2001), and charge-coupling devices (Woo et al. 2002).

In the present paper we studied photoluminescence characteristics of CdSe quantum dots in glass matrix along with investigating surface morphology of the system using AFM measurements.

2 Experimental details

CdSe nanoparticles embedded in transparent silicate-based glasses was successfully fabricated by a novel technique consisting in joined utilization of the thermal annealing below glass crystalization temperature, and the UV continuous wave laser irradiation (Argon laser at 244 nm). This innovative fabrication method exploits adapted combination of thermal annealing and UV laser power density that allows controlling the spatial localization of the nanocrystals formation inside the glass sample. The originality of the technique is that the required thermal energy needed for the precipitation of CdSe into crystals is brought by thermal annealing in association to UV absorption, which leads to the control of the spatial crystallization. Further information about samples fabricating can be found elsewhere (Mekhlouf et al. 2007).

The surface morphology of our sample was investigated by atomic force microscopy (AFM). AFM imaging was done using the NTEGRA Prima system from NT MDT. AFM measurements were performed at room temperature and under ambient conditions.

The UV–VIS absorbance spectrum was recorded on the room temperature in the wavelength range 200–800 nm on a Shimadzu UV-2600 spectrophotometer equipped with an integrated sphere. The absorbance spectrum was measured relative to a reference sample of $BaSO_4$.

Photoluminescence measurements on room temperature were obtained by Jobin-Yvon U1000 spectrometer equipped with RCA-C31034A photomultiplier with housing cooled by Peltier element, amplifiers and counters. As an excitation sources, the 488 and 514.5 nm lines of Argon laser were used.

3 Results and discussion

3.1 Results of AFM surface characterization

The surface morphology of our sample was investigated by atomic force microscopy, in order to determine the general cell wall structure, together with the assembly of particular components into the wall structure as a whole. Areas of 2×2 and 5×5 μm were investigated, and AFM images of our sample are presented in Fig. 1a, b. From Fig. 1 it is clear that the sample is packed and continuous without the presence of porosity and voids. The surface is rather smooth with no cracks observed. The small islands of several nm to several tenths of nm in diameter are distinguished, which corresponds to the nanoparticles of CdSe. According to the height bars at the right side of Fig. 1a, b, the surface height of our sample is up to 14 nm. Figure 1c, d show the histograms of the nanostructure height in 2×2 and 5×5 μm areas of AFM images, respectfully. The sample exhibits an ensemble of nanostructures with an average height of (4.9 ± 0.2) nm for chosen area of 2×2 μm, and (6.4 ± 0.2) nm for 5×5 μm area.
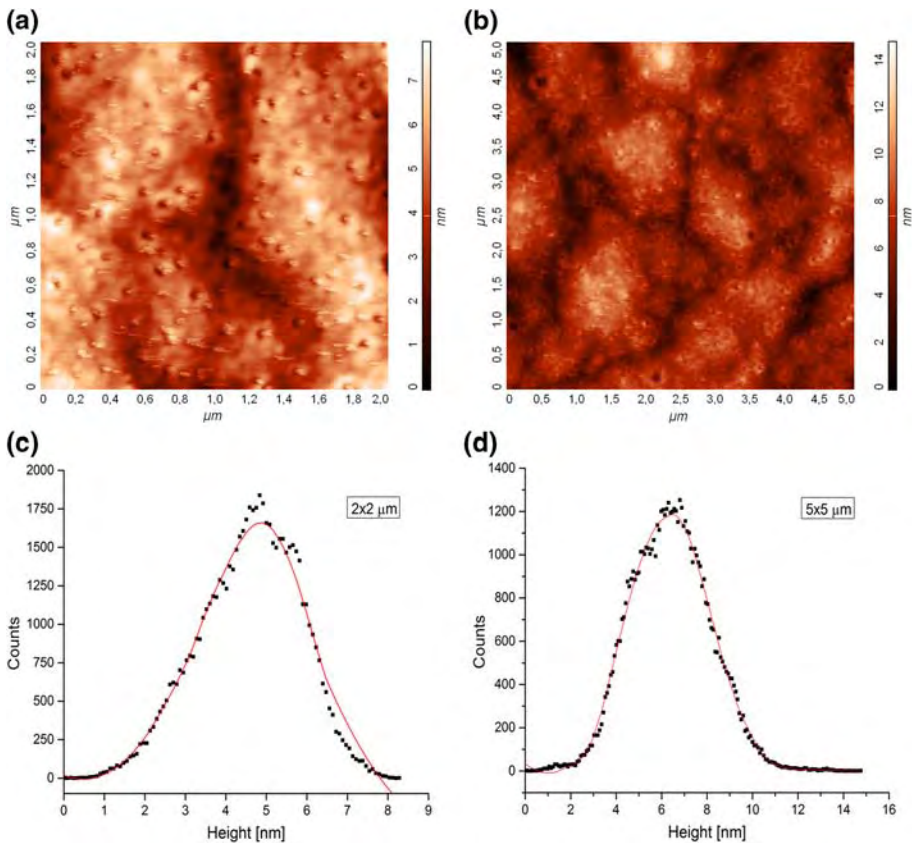
Fig. 1 2D AFM images and histograms of CdSe nanoparticles embeded in transparent silicate-based glasses, **a** 2×2 μm image, **b** 5×5 μm image, **c** 2×2 μm histogram, **d** 5×5 μm histogram

3.2 Optical characterization: photoluminescence and UV–VIS absorbance measurements

UV–VIS absorbance spectrum of our sample is presented in Fig. 2. The position of the first optical transition is at 520 nm. The position of a peak is related to the size of the absorbing nanocrystal and to the band gap. The average size of the nanocrystal of interest can be obtained using the relation (Yu et al. 2003):

$$D = 1.6122 \times 10^{-9} \times \lambda^4 - 2.6575 \times 10^{-6} \times \lambda^3 + 1.6242 \times 10^{-3} \times \lambda^2 - 0.4277 \times \lambda + 41.57 \tag{1}$$

where λ (nm) is the first exciton peak of CdSe absorbance spectrum. From the $\lambda = 520$ nm the calculated size of our nanoparticles is 2.6 nm.

There are several approaches in literature to determine the band gap from the absorbance spectra. In the present study we employ the approach of Yu et al. (2003) and Hegazy and Abd (2014) where the E_g is calculated directly from the absorption maximum of the first exciton absorption peak. Using formula

$$E_g = h\nu = hc/\lambda, \tag{2}$$

the obtained band gap is 2.39 eV.

Normally, the absorption of light by CdSe QDs increases with decreasing wavelength (Kongkanand et al. 2008; Debgupta et al. 2014). In present case, we must conclude that the glass matrix modify the spectrum of CdSe QDs—the absorption spectrum of glass matrix: CdSe QDs hybrid composite differ from those of individual components, as in Dayneko et al. (2016) where the CdSe QDs were incorporated in poly[N-9′-heptadecanyl-2,7-carbazole-alt-5,5-(4′,7′-di-2-thienyl-2′,1′,3′-benzothiadiazole)].

PL spectra of CdSe QDs in glass matrix are presented in Fig. 3. The dominant band in both spectra is very broad and has a maximum at ~2.14 eV. Such a broad band implies the existence of vast size distribution of CdSe QDs. We assigned this transition as direct band-to-band transition in CdSe. Due to the Stokes shift, this value is smaller than the band gap observed
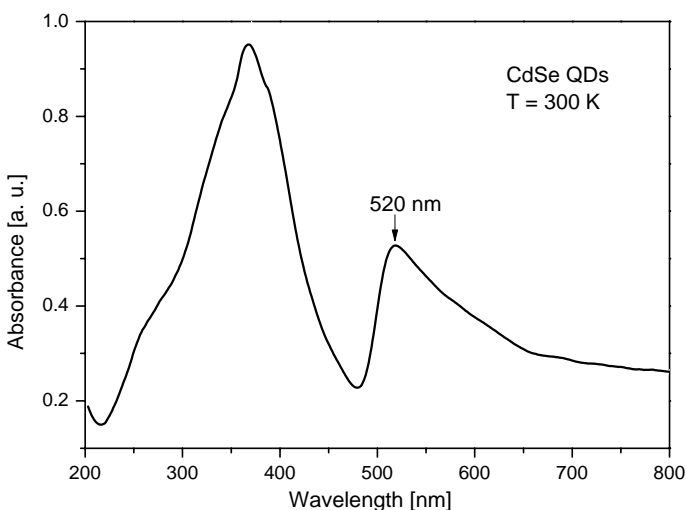

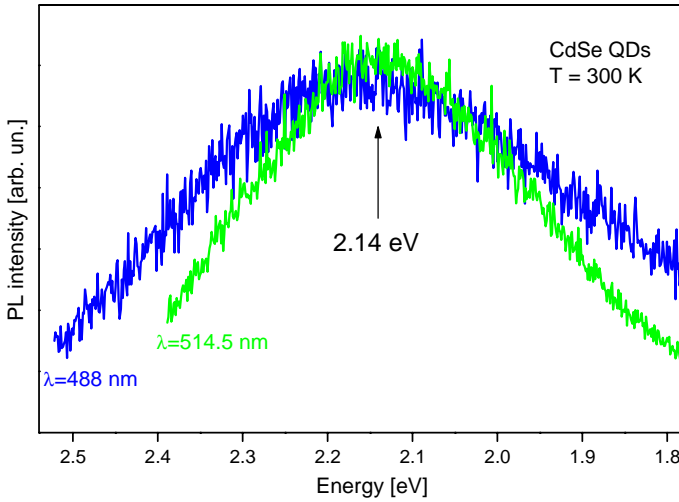**Fig. 2** UV–VIS absorbance spectrum of CdSe QDs

Fig. 3 Photoluminescence spectra of CdSe QDs excited with 488 nm (blue) and 514.5 nm (green) lines of Ar–laser and recorded on the room temperature. (Color figure online)

from absorption spectrum. However, the band gap of bulk CdSe is reported to be 1.75 eV. The observed blue shift of this band is ~ 0.39 eV, and its position can be explained in the following manner.

3.3 Model

The single quantum dot we consider is spherical CdSe core surrounded by transparent glass. R is the core radius and the dot center is center of coordinates (Schoss et al. 1994; Kostić and Stojanović 2011). Electron and hole i.e. carriers, in such a system are characterized by their effective masses. In this case m_e^* and m_h^* are electron and hole effective masses of CdSe. Rectangular potential through the structure, having in mind that CdSe is surrounded by glass, is assumed as:

$$V(r) = \begin{cases} 0 & r \leq R \\ \infty & r > R \end{cases} \tag{3}$$

Considering that the carrier spectra are mainly formed by size quantization, the stationary Schrödinger equation for a single particle (electron or hole).

$$\left(-\frac{\hbar^2}{2m_i^*}\nabla^2 + V(r) \right)\Psi(\vec{r}) = E_i\Psi_i(\vec{r}), \ i = e, \ h \tag{4}$$

is solved in spherically symmetric potential $V(r)$, described by (3). Separation of radial and angular coordinates leads to $\Psi_{lm}(r) = R_l(r)Y_{lm}(\theta, \phi)$. $R_l(r)$ is the radial wave function, and $Y_{lm}(\theta, \phi)$ is a spherical harmonic. l and m are orbital and magnetic quantum numbers. For a spherical potential with stepwise constant value 0, in the core, and ∞, outside the core, the radial function $R_l(r)$ is given by:

$$R_l(r) = \begin{cases} Aj_l(kr) & r \leq R \\ 0 & r > R \end{cases}, \tag{5}$$

j_l, are Bessel spherical functions. These solutions already satisfy conditions that the wave function is regular when $r=0$. Each solution must satisfy boundary conditions. In case of infinitely high potential barrier, wave function does not penetrate into the surrounding medium and must satisfy trivial boundary condition: to be zero at $r=R$. This trivial boundary condition leads to equation characteristic for each l ($l=0$, 1, 2,…). There is series of solutions (eigensolutions i.e. eigenenergies) characteristic for each l. Number n numerates eigenenergies E_{nl}. For an electron E_{nl} shows the energy above core conductive band, and for hole energy below valence band of core material.

As it is common, the lowest energy among solution for each l is numerated as $n=1$. Among all states, state $l=0$, $n=1$ is the lowest energy solution i.e. it is the ground state.

Once the eigenvalues E_{nl} are determined, the coefficients A_{nl} in Eq. (5) are determined by using the normalization condition for $R_{nl}(r)$, $\int_0^\infty R_{nl}^2(r) \cdot r^2 dr = 1$. Result of these calculations is the complete information about eigenenergies E_{nl} and corresponding wave functions $R_{nl}(r)$.

One state can be identified by characteristic energy, denoted as E_{nl} and wave function, denoted as ψ_{nl} or just (n, l). As it is usual all $l=0$ states are assigned as s, $l=1$ states as p and $l=2$ states as d. In all papers $l=0$ (s) states are assigned: ($l=0$, $n=1$) as $1s$, ($l=0$, $n=2$) as $2s$, ($l=0$, $n=3$) as $3s$ etc. For the $l=1$ (p) states, some authors assigned states in the same manner as for $l=0$, i.e. ($l=1$ $n=1$) as $1p$, ($l=1$, $n=2$) as $2p$, ($l=1$, $n=3$) as $3p$ etc. For the $l=2$ (d) states, assignation is: ($l=2$ $n=1$) is $1d$, ($l=2$, $n=2$) is $2d$, ($l=2$, $n=3$) is $3d$ etc. In this assignation number in front s, p or d numerates if it is the first, second or higher order solution. It is possible, having in mind wave functions properties, to use hydrogen like assignation: ($l=1$ $n=1$) is $2p$, ($l=1$ $n=2$) is $3p$, ($l=1$ $n=3$) is $4p$…; ($l=2$ $n=1$) is $3d$, ($l=2$ $n=2$) is $4d$, ($l=2$ $n=3$) is $5d$… Hydrogen like assignation is even more desirable if we deal with charged impurities inside QD.

These calculations were performed for electrons and holes in similar procedure, giving the confinement energies E_{nl}^e and E_{nl}^h, and wave functions R_{nl}^e and R_{nl}^h. Once the electron and hole wave functions are known, radial probability in the system give an illustrative picture, especially in more complex structures, of electron and hole spatial localization.

We focused our analysis to transition between $l=0$, $n=1$ hole ($1s_h$) and electron ($1s_e$) states, because this is the basic interband transition.

From the electron and hole wave functions, the Coulomb interaction of electron and hole can be calculated. In the frame of perturbation theory energy of Coulomb interaction is given by:

$$E_C = -e^2 \int \int \frac{\left|R^e\left(r_e\right)\right|^2 \left|R^h\left(r_r\right)\right|^2}{4\pi\varepsilon\left|r_e - r_h\right|} r_e^2 r_h^2 dr_e dr_h \tag{6}$$

ε is the high energy dielectric permittivity.

The transition electronic energy (E_{10}) is sum of the core gap energy, corresponding electron and hole eigenvalues and the Coulomb energy:

$$E_{10} = E_g + E_{10}^e + E_{10}^h + E_C \tag{7}$$

The parameters characteristic for CdSe bulk are presented in Table 1. Calculation parameters, effective masses of carriers and dielectric permittivity, are transferred from literature (Kostić and Stojanović 2011; Sahin et al. 2009). Calculated transition energy is presented in Fig. 4.

Table 1 The material parameters used in the calculations

Material	m_e^*/m_0	m_h^*/m_0	ε_r	E_g (eV)
CdSe	0.13	0.45	9.3	1.75

m_e^* is electron effective mass in material, m_h^* is hole effective mass in material, m_0 is electron mass, ε_r is relative dielectric permittivity, E_g is the energy gap of the material
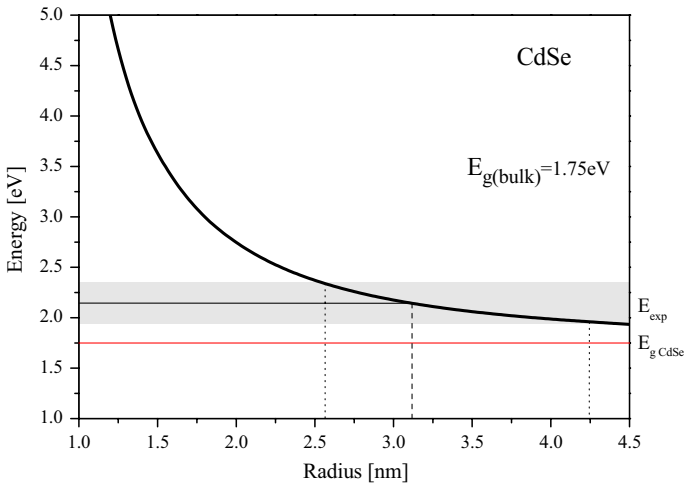
Fig. 4 $1s_h$–$1s_e$ interband transition energy in CdSe QD as function on the dot radius

Energy of basic interband transition ($1s_h$–$1s_e$) in the quantum dots increases as the dimension of the dot decreases. Simple model based on effective mass approximation can estimate transition energy of QD. This energy depends on the dimension of the dot, and parameters of the bulk material like energy gap, dielectric permittivity, and electron and hole effective masses. Due to the very broad band, we consider that trere is an ensemble of quantum dots with a wide range of sizes. As a provisional borders, we used the energy values of FWHM of the band obtained by 514.5 nm laser line, which is less broad than the one obtained with 488 nm. These borders are 1.94–2.32 eV, and corresponding QD dimensions are 2.5–4.2 nm. The band maximum at 2.14 eV corresponds to the QD size of 3.1 nm. These results are in agreement with the calculations for UV–VIS absorbance.

4 Conclusions

The photoluminescence measurements along with AFM measurements of CdSe nanoparticles embedded in transparent glass are presented. The AFM measurements reveal the presence of small islands of several nm in diameter, which correspond to the nanoparticles of CdSe. The UV–VIS absorbance spectrum displayed the first exciton peak at 520 nm. Calculated size of nanoparticles is about 2.6 nm. The PL measurements display one main broad emission band at ∼2.14 eV which is identified as basic interband transition in CdSe nanoparticle. The energy of basic transition in spherical CdSe quantum dot in effective

mass approximation is calculated. Based on this model, the average radius of CdSe QD is found to be ∼ 3 nm.

References

Ahmadi, T.S., Wang, Z.L., Green, T.C., Henglein, A., El-Sayed, M.A.: Shape-controlled synthesis of colloidal platinum nanoparticles. Science **272**, 1924–1926 (1996)

Bruchez Jr., M., Moronne, M., Gin, P., Weiss, S., Alivisatos, A.P.: Semiconductor nanocrystals as fluorescent biological labels. Science **281**, 2013–2016 (1998)

Chan, W.C.W., Nie, S.M.: Quantum dot bioconjugates for ultrasensitive nonisotopic detection. Science **281**, 2016–2018 (1998)

Dayneko, S., Linkov, P., Martynov, I., Tameev, A., Tedoradze, M., Samokhvalov, P., Nabiev, I., Christyakov, A.: Photoconductivity of composites based on CdSequantum dots and low-gap polymers. Physica E **79**, 206–211 (2016)

Debgupta, J., Sadananda, M., Kalita, H., Mohammed, A., Patra, A., Pillai, V.: Photophysical and photoconductivity properties of thiol-functionalized grapheme-CdSe QD composites. RCS Adv. **4**, 13788–13795 (2014)

Hegazy, M., Abd, El-Hameed A.: Characterization of CdSe-nanocrystals used in semiconductors for aerospace applications: production and optical properties. NRIAG J. Astron. Geophys. **3**, 82–87 (2014)

Klein, D.L., Roth, R., Lim, A.K.L., Alivisatos, A.P., McEuen, P.: A single-electron transistor made from a cadmium selenide nanocrystal. Nature **389**, 699–701 (1997). https://doi.org/10.1038/39535

Kongkanand, A., Tvrdy, K., Takechi, K., Kuno, M., Kamat, P.V.: Quantum dot solar cells. Tuning photoresponse through size and shape control of CdSe-TiO$_2$ architecture. J. Am. Chem. Soc. **130**, 4007–4021 (2008)

Kostić, R., Stojanović, D.: Nonlinear absorption spectra for intersubband transition of CdSe/ZnS spherical quantum dots. J. Nanophotonic **5**, 051810 (2011)

Mekhlouf, S.E., Boukenter, A., Ferrari, M., Goutaland, F., Ollier, N., Ouerdane, Y.: UV assisted local crystallization in Er^{3+} doped oxy-fluoride glass. J. Non-Cryst. Solids **353**, 506–509 (2007)

Oertel, D. C., Bawendi, M. G.: Photodetectors based on treated CdSe quantum-dot films. Appl. Phys. Lett. **87**, 213505 (2005)

Poole Charles Jr., P., Owen Frank, J. (ed.): Introduction to Nanotechnology, vol. 1, pp. 1–20. Wiley, Hoboken (2003)

Sahin, M., Nizamoglu, S., Kavruk, A.E., Demir, H.V.: Self-consistent computation of electronic and optical properties of a single exciton in a spherical quantum dot via matrix diagonalization method. J. Appl. Phys. **106**, 043704 (2009)

Schoss, D., Mews, A., Eychmuller, A., Weller, H.: Quantum-dot quantum well CdS/HgS/CdS: theory and experiment. Phys. Rev. B **49**, 17072–17078 (1994)

Srivastava, P., Singh, K.: Synthesis of CdSe nanoparticles by solvothermal route: structural, optical and spectroscopic properties. Adv. Mater. Lett. **3**, 340–344 (2012)

Wang, C., Shim, M., Guyott-Sionnest, P.: Electrochromic nanocrystal quantum dots. Science **91**, 2390–2392 (2001)

Woo, W.K., Shimizu, K.T., Jarosz, M.V., Neuhauser, R.G., Leatherdale, C.A., Rubner, M.A., Bawendi, M.G.: Reversible charging of CdSe nanocrystals in a simple solid-state device. Adv. Mater. **14**, 1068–1071 (2002)

Yu, D., Wehrenberg, B. L., Jha, P., Ma, J., Guyot-Sionnest, P.: Electronic transport of n-type CdSe quantum dot films: effect of film treatment. J. Appl. Phys. **99**(10), 104315 (2006)

Yu, W., Qu, L., Guo, W., Peng, X.: Experimental determination of the extinction coefficient of CdTe, CdSe, and CdS nanocrystals. Chem. Mater. **15**, 2854–2860 (2003)

Improvement of magneto-optical quality of high purity Bi$_{12}$GeO$_{20}$ single crystal induced by femtosecond pulsed laser irradiation

G. S. I. ABUDAGEL[a], S. PETRIČEVIĆ[a], P. MIHAILOVIĆ[a], A. KOVAČEVIĆ[b], J. L. RISTIĆ-DJUROVIĆ[b], M. LEKIĆ[b], M. ROMČEVIĆ[b], S. ĆIRKOVIĆ[b], J. TRAJIĆ[b,*], N. ROMČEVIĆ[b]

[a]School of Electrical Engineering, University of Belgrade, Bulevar kralja Aleksandra 73, 11000 Belgrade, Serbia
[b]Institute of Physics, University of Belgrade, Pregrevica 118, 11080 Belgrade, Serbia

Femtosecond pulsed laser irradiation can improve optical properties of Bi$_{12}$GeO$_{20}$ single crystals. We investigate if the effect occurs if the crystals are grown from high purity components. The samples are irradiated by a femtosecond pulsed laser beam of increasing power. The maximal transmittance of 44% occurs at the irradiating laser power of 451 mW. After irradiation, intensity of Raman spectra peaks increase, except for the peak at 203 cm^{-1}, whose intensity decreases. The irradiation also changes the sample colour. Although the Verdet constant does not change, the absorption coefficient decreases significantly, which leads to magneto-optical quality improvement of approximately 70%.

1. Introduction

Bismuth germanium oxide (Bi$_{12}$GeO$_{20}$) from the sillenite group of cubic crystals is commonly abbreviated as BGO or s-BGO. Due to its fitting optical characteristics, such as photoconductivity, photochromism, photorefractivity, piezoelectricity, as well as to electro-optic and magneto-optic effects it supports [1, 2], it has been used in a wide range of optical applications and devices [2–6]. Its cubic cell unit is composed of two formula units, namely of 24 Bi, 40 O and 2 Ge. The Ge atoms positioned in the centre and the vertices of a cube are tetrahedrally coordinated by the oxygen atoms, whereas the Bi atoms are heptacoordinated [7–9]. There are numerous studies that considered properties of doped and un-doped BGO, see for example [10–18], as well as those investigating property changes induced by a wide variety of exposure types such as thermal treatments, particle beams or light treatments [3, 12–16, 19–25].

BGO is a good example of a Faraday rotator crystal possibly applicable in sensor systems. In order to evaluate usability of a crystal for sensing purposes not only its Faraday rotation capability, but its ability to be integrated into a sensing optical system must be considered. In general, in fiber-optic sensing systems optical beams used to sense the measured quantity are guided through the fibers, giving rise to the absorption coefficient as the most important optical property. Crystals with high absorption coefficient are in general less useful for sensor systems because they absorb much of the light and cause low signal-to-noise ratio at the receiving photo diode. If the magnetic field is to be detected, the intensity of light caused by magnetic field modulation is proportional to the Verdet constant, whereas the intensity of light reaching the

photodiode as well as the photocurrent is inversely proportional to the crystal absorption. The noise in a fiber optic sensing system is predominantly determined by the noise in the processing electronics and can be expressed as the noise present in the photocurrent. Therefore, the signal-to-noise ratio of the magnetic field sensor is proportional to the Verdet constant and inversely proportional to the absorption coefficient of a crystal. Consequently, due to its proportionality to the signal-to-noise ratio, the magneto-optical quality of a crystal defined as a ratio of the Faraday rotation, which is proportional to the Verdet constant, and the absorption coefficient can be used as a measure of a crystal's applicability in a magnetic field sensing system.

When Bi$_{12}$GeO$_{20}$ crystals were exposed to pulsed laser beam irradiation, there are examples of laser beam operating in the nanosecond [3], picosecond [23–25], or femtosecond range [26]. In [26] it was determined that femtosecond pulsed laser irradiation of increasing power causes significant changes in the transmittance, transmission spectra, sample colour, Raman spectra, X-ray diffraction pattern, Verdet constant, magneto-optical property, and absorption coefficient of lower quality black Bi$_{12}$GeO$_{20}$ single crystals. Here we analyze if the same increasing power pattern of femtosecond pulsed laser irradiation has similar effect on the high quality yellow Bi$_{12}$GeO$_{20}$ single crystals, i.e., on the crystals that were grown from the components whose purity is higher than that of the black crystals, and whose magneto-optical quality is the maximal obtainable by the applied crystal growth technique.

2. Experimental procedure

2.1. Preparation of crystal samples

Single crystals of $Bi_{12}GeO_{20}$ were grown in the air by the Czochralski technique using the MSR 2 crystal puller, Eurotherm temperature controller and the calculated critical crystal diameter, critical rotation rate and pulling rate, as explained in detail in [17, 26]. The system provided small fluctuations in crystal diameter size as well as in melting temperature. The $Bi_{12}GeO_{20}$ seed was oriented in the $\langle 111 \rangle$ direction and the charge was a mixture of Bi_2O_3 and GeO_2 in the stoichiometric ratio 6:1. The light yellow crystal samples were obtained using the Bi_2O_3 and GeO_2 purity of 99.999 wt.% and 99.9999 wt.%, respectively. Crystal samples of size 4 mm × 4 mm × 10 mm were cut from the boule and mechanically as well as chemically polished. The technique used to prepare the samples insured maximal sample quality within the limits corresponding to their purity [17].

2.2. Crystal irradiation and characterization

The equipment used to produce the femtosecond pulsed laser beam and establish its wavelength was the Coherent Mira 900F femtosecond laser, Coherent Verdi V-10 pump laser that provided a 532 nm continuous wave pump beam, and Ocean Optics HR2000CG UV-NIR spectrometer. Crystal samples were irradiated along the crystal growth direction (z), i.e. along the samples' longest axis. The irradiating laser beam radius provided partial irradiation of the exposed crystal facet. The beam wavelength was 800 nm, whereas its power was increased from 50 mW to 950 mW and was adjusted by a graded filter. The pulses were 90 fs long and had repetition rate of 76 MHz. The samples were irradiated by each beam power for 3 s. The beam power was measured with the Ophir power meter with the thermal and photometric heads. In order to enable comparison of the irradiation effects on the single crystal samples of different purity, i.e., on yellow and black $Bi_{12}GeO_{20}$ samples, the irradiation conditions were intentionally chosen to be identical to those applied to the lower purity black crystals in [26].

The sample colour was calculated from the transmission spectra measured by the Beckman Coulter DU 720 General Purpose UV/VIS spectrometer.

The micro-Raman spectra were recorded at room temperature in the spectral range between 100 and 1100 cm^{-1} with 1 cm^{-1} resolution using the backscattering configuration and the 532 nm line of Verdi G optically pumped semiconductor laser as an excitation source, and the Jobin Yvon T64000 spectrometer, which has nitrogen cooled charge-coupled-device detector.

The Faraday rotation and optical activity were measured by Δ/Σ method at the wavelength of $\lambda = 632.8$ nm. After the BGO crystal the orthogonal polarizations of the light beam were separated by the $CaCO_3$ crystal into two parallel beams 3 mm apart. The quadrant photodiode connected into transimpedance stages was used for optoelectronic conversion. This method is described in more details in [26].

3. Results and discussion

The irradiation pattern applied here to the higher purity yellow crystals is identical to the one utilized in [26] to irradiate black crystals grown from the components of lesser purity. Consequently, the obtained results can be compared and the differences can be attributed solely to different sample purity. With the increase of irradiating laser power, the transmittance of irradiated sample undergoes initial growth followed by a decrease, as can be seen in Fig. 1. Comparison with the dependence corresponding to the black crystal given in [26] reveals that the transmittance curves for the black as well as for the yellow crystal has the same shape and that the slopes of the two curves appear to be approximately equal. The curve corresponding to the yellow crystal is shifted to the larger values by approximately 18.8% compared to the curve corresponding to the black crystal. For the yellow crystal, the maximal transmittance of 44.0% occurs at the irradiating laser power of 451 mW, whereas the lower purity black crystal was reported in [26] to have the smaller maximal transmittance value of 25.1% corresponding to 455 mW. It seems that both curves exhibit local irregularities which occur at 197.4–249.7 mW, 552–605 mW and 800–857 mW for the black crystal and at 593–641 mW for the yellow crystal. It is possible that the irregularity in the yellow sample curve for large values of incident power P_0 is not visible because it is outside the considered range of irradiating laser power, or due to insufficient measurement accuracy achieved for yellow crystal data points above 700 mW.
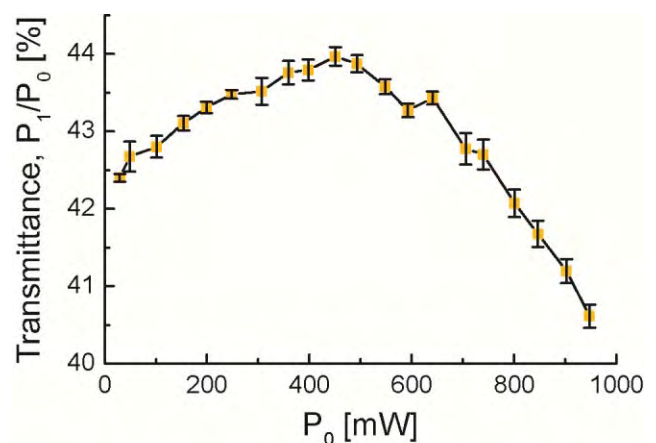

Fig. 1. Change of crystal transmittance with increase of irradiating laser power. For each value of the incident power P_0, a sample is irradiated by the femtosecond laser beam for 3 s. The transmittance is given as P_1/P_0, where P_1 is the transmitted power. The error bars were calculated from the uncertainties of measured values of the incident and transmitted power, ΔP_0 and ΔP_1.

The sample colours before and after irradiation were calculated using the CIE chromaticity coordinates and are given in Fig. 2. Comparison with the results corresponding to the black crystal given in [26] revealed that the change of black crystal colour was more pronounced than that of the yellow crystal presented here.

The Raman spectra of unirradiated and irradiated samples are recorded at room temperature in the spectral range from 150 to 800 cm^{-1} and are shown in Fig. 3. The results obtained for unirradiated crystals are in agreement with those given in [8, 17]. After irradiation the intensity of the $F(TO)$ peak at 203 cm^{-1} decreased, whereas all other peaks became more pronounced. Despite the difference in purity between the yellow samples studied here and the black crystals considered in [26] the Raman spectra of unirradiated crystals do not differ significantly. As reported in [26], irradiation of the black crystal caused all the peaks of symmetry type E, i.e., the peaks at 234, 454, and 619.6 cm^{-1}, to disappear and intensity increase of all other peaks. The change in the same Raman spectrum peaks of $Bi_{12}GeO_{20}$ was reported in [16]; however, the most, medium, and least intense peaks correspond to the annealed, doped, and untreated samples, respectively.
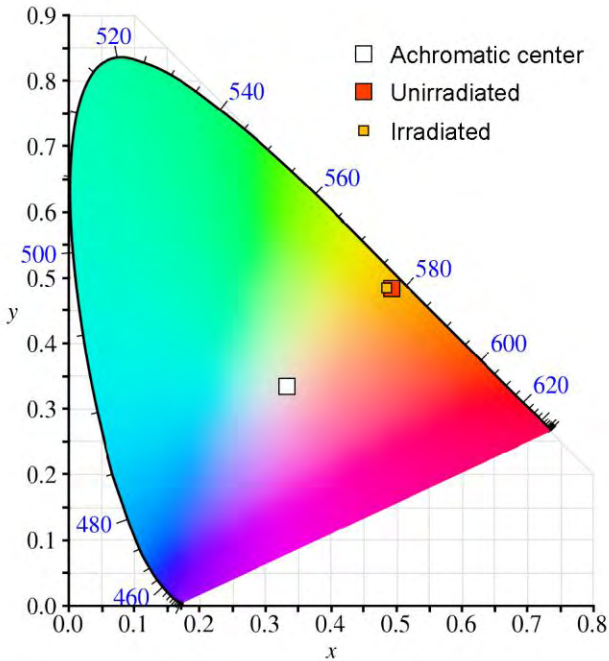
Fig. 2. Colours of irradiated and unirradiated samples in CIE chromaticity diagram.
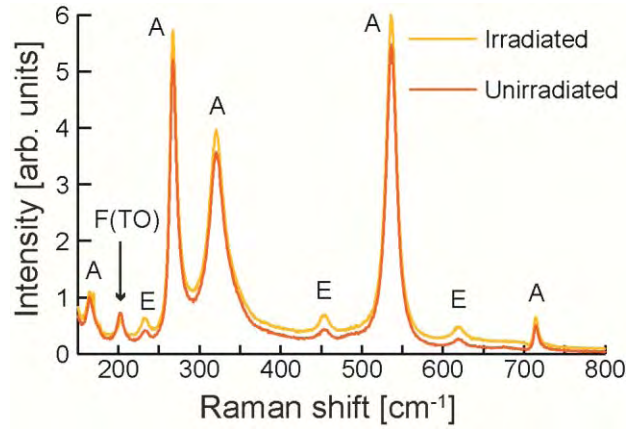
Fig. 3. Raman spectra. Irradiation caused a small upward shift of the crystal spectrum except for the F(TO) type peak at 203 cm^{-1}.

The Verdet constant is calculated from

$$V = \frac{\theta_{0AC}}{B_0 l} = \frac{1}{2B_0 l} \sin^{-1}\left(\frac{U_1 - U_2}{U_1 + U_2}\right)_{0AC} \quad (1)$$

where θ_{0AC} is the amplitude of the AC signal, B_0 is the amplitude of the magnetic induction, whereas U_1 and U_2, are the output signal voltages obtained after transimpedance stages from the vertically and horizontally polarized components, respectively. The FFT was used to separate spectral components of U_1 and U_2. The Faraday rotation was determined from the magnitude of the 50 Hz component.

The absorption coefficients were obtained by measuring the difference in beam intensities at the quadrant photodiode [26] with and without BGO crystal in the beam path. The reflection on the BGO crystal was calculated using the normal incidence and BGO refraction index of $n_{BGO} = 2.55$.

The absorption coefficient, α, was calculated from the beam intensities with and without the crystal present in the beam path, $I(x)$ and $I(0)$, and the known crystal length $l = 9.8$ mm as

$$I(l) = I_0 e^{-\alpha l} \Rightarrow \alpha = -\frac{1}{l}\ln\frac{I(l)}{I_0} \quad (2)$$

The magneto-optical quality is calculated by dividing the Verdet constant by the absorption coefficient. The obtained results are given in Table 1.

Table 1. Magneto-optical properties of irradiated and unirradiated high purity crystal samples.

Property	Unirradiated sample	Irradiated sample
Verdet constant ($rad\ T^{-1}m^{-1}$)	72	72
Absorption coefficient (cm^{-1})	0.58	0.34
Magneto-optical quality ($rad\ T^{-1}$)	1.24	2.1

The data given in Table 1 show the effects of femtosecond laser irradiation on the magneto-optical properties of the high purity BGO crystal. The irradiation caused 41.4% decrease in the absorption coefficient and did not influence the Faraday constant. Consequently, the increase in crystal transparency resulted in a significant 70% increase in the magneto-optical quality. As explained earlier, increase in crystal transparency is an important gain from the point of view of a sensor system since the system-level signal-to-noise ratio is directly proportional to the magneto-optical quality of a crystal. Therefore, it is expected that the signal-to-noise ratio of a sensor system would be improved by the same amount as the improvement in the magneto-optical quality induced by the irradiation. Consequently, it can be concluded that the femtosecond pulsed laser irradiation affects the crystal in a positive manner.

4. Conclusions

Femtosecond pulsed laser irradiation of increasing power caused significant changes in optical properties of $Bi_{12}GeO_{20}$ single crystals grown from the components of high purity, as was the case in [26] when the component purity was not so high. The transmittance dependence on the applied irradiation power had the same shape regardless of the purity of the components the crystals were grown from. The curve corresponding to the higher purity crystal, i.e., the yellow crystal, is shifted to the larger values by approximately 18.8%. For the black and yellow crystal, the maximal transmittance of 25.1% and 44.0% occurred at 455 mW and 451 mW, respectively. The Raman spectra peaks became somewhat stronger, except for the E type peaks at 234, 454, and 619.6 cm^{-1} in the lower purity black crystal, which disappeared and the yellow crystal peak at 203 cm^{-1} whose intensity decreased. Irradiation also caused slight colour change of the yellow crystal and significant change of the black crystal colour. The Verdet constant did not change; however, the absorption coefficient significantly decreased leading to equally significant increase of the magneto-optical quality of the sample. Consequently, it can be concluded that optical properties of high quality $Bi_{12}GeO_{20}$ single crystals can be improved by irradiation with the femtosecond pulsed laser beam.

References

[1] M. Simon, F. Mersch, C. Kuper, Phys. Status Solidi A. **159**(2), 559 (1997).

[2] V. M. Skorikov, Yu. F. Kargin, A. V. Egorysheva, V. V. Volkov, M. Gospodinov, Inorg. Mater. **41**(1), S24 (2005).

[3] R. A. Ganeev, A. I. Ryasnyansky, B. Palpant, S. Debrus, J. Appl. Phys. **97**, 104303 (2005),

[4] P. Yeh, Introduction to Photorefractive nonlinear optics, first ed., Wiley-Interscience, New York, 1993.

[5] M. J. Weber, J. Lumin. **100**, 35 (2002).

[6] M. Itoh, T. Katagiri, H. Mitani, M. Fujita, Y. Usuki, Phys. Status. Solidi B, **245**(12), 2733 (2008).

[7] S. C. Abrahams, P. B. Jamieson, J. L. Bernstein, J. Chem. Phys. **47**(10), 4034 (1967).

[8] V. I. Burkov, V. S. Gorelik, A. V. Egorysheva, Y. F. Kargin J. Russ. Las. Res. **22**, 243 (2001).

[9] S. F. Radaev, V. I. Simonov, Y. F. Kargin, Eur. J. Solid. State Inorg. Chem. **29**(2), 383 (1992).

[10] N. C. Deliolanis, I. M. Kourmoulis, G. Asimellis, A. G. Apostolidis, E. D. Vanidhis, N. A. Vainos, J. Appl. Phys. **97**(2), 023531 (2005).

[11] C. G. P. Moraes, F. A. A. Jesus, Z. S. Macedo, Adv. Cond. Matter. Phys. **2014**, 968349 (2014), http://dx.doi.org/10.1155/2014/968349.

[12] O. Peña-Rodríguez, J. Olivares, I. Bányász, Opt. Mater. **47**, 328 (2015).

[13] V. M. Skorikov, I. S. Zakharov, V. V. Volkov, E. A. Spirin, Inorg. Mater. **38**(2), 172 (2002).

[14] Z. S. Macedo, C. S. S. Oliveira, A. C. Hernandes, J. Appl. Phys. **102**(3), 034105 (2007).

[15] H. Marquet, J-C. Merle, J-G. Gies, Opt. Mater. **14**, 277 (2000).

[16] P. S. Yu, L. B. Su, H. L. Tang, X. Guo, H. Y. Zhao, Q. H. Yang, J. Xu, Sci. China Tech. Sci. **54**(5), 1287 (2011).

[17] Z. Ž. Lazarević, P. Mihailović, S. Kostić, M. J. Romčević, M. Mitrić, S. Petričević, J. Radunović, M. Petrović-Damjanović, M. Gilić, N. Ž. Romčević, Opt. Mater. **34**, 1849 (2012).

[18] S. Kumaragurubaram, S. Moorthy Babu, C. Subramanian, P. Ramasamy, Indian J. Eng. Mater. Sci. **7**(5-6), 331 (2000).

[19] A. Cremades, J. Piqueras, A. Remón, J.A. García, M. T. Santos, E. Diéguez, J. Appl. Phys. **83**(12), 7948 (1998).

[20] A. Cremades, M. T. Santos, A. Remón, J. A. García, E. Diéguez, J. Piqueras, J. Appl. Phys. **79**(9), 7186 (1996).

[21] I. Stefaniuk, P. Potera, I. Rogalska, D. Wróbel, Current Topics in Biophysics **33**, 231 (2010).

[22] N. Benjelloun, M. Tapiero, J. P. Zielinger, F. Marsaud, J. C. Launay, J. Appl. Phys. **64**(8), 4013 (1988).

[23] R. A. Ganeev, A. I. Ryasnyansky, R. I. Tugushev, M. K. Kodirov, F. R. Akhmedjanov, T. Usmanov, Opt. Quant. Electron. **36**(9), 807 (2004).

[24] M. Sylla, D. Rouède, R. Chevalier, X. Nguyen Phu, G. Rivoire, Opt. Commun. **90**, 391 (1992).

[25] B. Taheri, S. A. Holmstrom, R. C. Powell, J. J. Song, A. M. F. I. Földvári, A. Péter, Opt. Mater. **3**, 251 (1994).

[26] A. Kovačević, J. L. Ristić-Djurović, M. Lekić, B. Hadžić, G. S. I. Abudagel, S. Petričević, P. Mihailović, B. Matović, D. Dramlić, L. M. Brajović, N. Romčević, Mater. Res. Bull. **83**, 284 (2016).

_____
[*]Corresponding author: jelena@ipb.ac.rs

Kinetics of Solid-State Synthesis of Quaternary Cu_2FeSnS_4 (Stannite) Nanocrystals for Solar Energy Applications

P. Baláž[a,*], M. Baláž[a], A. Zorkovská[a], I. Škorvánek[b], Z. Bujňáková[a] and J. Trajić[c]

[a]Institute of Geotechnics of Slovak Academy of Sciences, Watsonova 45, 04001 Košice, Slovakia
[b]Institute of Experimental Physics of Slovak Academy of Sciences, Watsonova 47, 04353 Košice, Slovakia
[c]Institute of Physics Belgrade, Pregrevica 118, 11080 Belgrade, Serbia

In this study we demonstrate the use of elemental precursors (Cu, Fe, Sn, S) to obtain stannite forms by a solid-state one-pot mechanochemical synthesis. In the processing route, we report the kinetics of the synthesis. For the characterization of the unique nanostructures, X-ray diffraction, specific surface area measurements and SQUID magnetometry methods were applied. CFTS polymorphs with the tetragonal body-centered structure with the average crystallite size 18–19 nm were obtained. The weak ferromagnetic properties of the quaternary nanocrystals after maximum milling time were also documented.

1. Introduction

There is a general paradox in present research and application of chalcogenide solar materials. On one side, $CuIn_{1-x}Ga_xSe_2$ (CIGS) thin film solar cells attracted a big attention owing to their high power conversion efficiency and good stability. On the other side, these materials represent the potential environmental problem because of Se toxicity, In and Ga limited availability and high price [1–4]. Quaternary semiconductor nanocrystals provide promising alternatives to conventional photovoltaic materials because of their environmental acceptance (application of S instead of toxic Se), cheapness and availability (application of earth-abundant Fe, Zn and Sn instead of scarce In and Ga). For example kesterite (CZTS) and stannite (CFTS) possess many advantageous characteristics for photovoltaic applications, such as composition from the abundant and non-toxic elements, suitable band gap, high absorption coefficient and high radiation stability [3, 5, 6].

Stannite Cu_2FeSnS_4 has been recently prepared by several techniques such as solution-based synthesis, hot injection and microwave irradiation [7–15]. However, these techniques are complex, time-consuming, need high temperature and toxic organic solvents.

In this study, we attempt to synthesize CFTS phase by a novel solid-state reaction using a high-energy planetary milling. The structural, optical and magnetic properties including kinetics of the phase evolution are investigated.

2. Experimental

The solid-state synthesis of CFTS was realized in a planetary mill Pulverisette 6 (Fritsch, Germany) under the following conditions: loading — 50 balls ($d = 10$ mm)

of tungsten carbide, volume of milling pot from tungsten carbide — 250 mL, input mass of sample mixed from Cu, Fe, Sn and S elements in a stoichiometric ratio of Cu_2FeSnS_4 — 5 g, ball-to-powder ratio — 70, milling speed — 500 min^{-1}, milling time — 1–120 min, milling atmosphere — argon.

The crystal structure was characterized by using a D8 Advance Bruker X-ray diffractometer (Bruker, Germany) in the Bragg–Brentano geometry working with a Cu K_α radiation ($\lambda = 0.15406$ nm) and a scintillation detector. The data were collected over the angular range $10° < 2\theta < 100°$ with scanning steps of $0.02°$ and a measurement step time interval of 6 s. For the data processing, the commercial Bruker tools have been used. Specifically, for the phase identification, the Diffrac^{plus} Eva and the ICDD PDF2 database were utilized.

For the determination of the elemental sulphur content, the Soxhlet extractor, with CS_2 as the extraction solvent, in which elemental sulphur is dissolved, was used. The non-reacted sulphur present in the extracted CFTS sample remains in the thimble. The amount of the non-reacted sulphur dissolved in CS_2 is calculated from the weight difference of the distillation flask before the experiment and after the evaporation of solvent.

A nitrogen adsorption apparatus NOVA 1200e Surface Area & Pore Size Analyzer (Quantachrome Instruments, United Kingdom) was employed to record the specific surface area (S_{BET}) values, which were calculated using the Brunauer–Emmett–Teller (BET) equation. The measurements were performed at the liquid nitrogen temperature.

The magnetic measurements were performed by a Magnetic Property Measuring System model MPMS-XL-5 (Quantum Design, USA) equipped with 5 T superconducting magnet. The magnetization curves as a function of the applied field have been collected at room temperature.

---

*corresponding author; e-mail: balaz@saske.sk

3. Results and discussion

3.1. Structural analysis

The XRD patterns of the starting mixture (Cu, Fe, Sn and S powders) milled for 20–120 min are shown in Fig. 1.
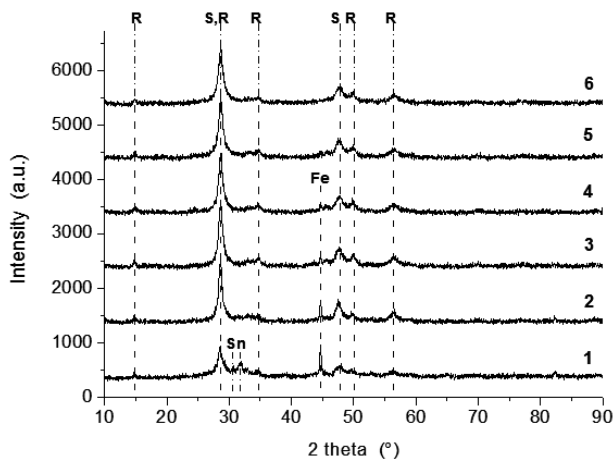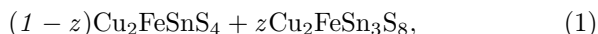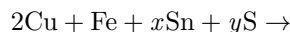

Fig. 1. XRD patterns of the CFTS samples, milling time, t_M: 1 — 20 min, 2 — 30 min, 3 — 45 min, 4 — 60 min, 5 — 90 min, 6 — 120 min; R — rhodostannite $Cu_2FeSn_3S_8$, S — stannite Cu_2FeSnS_4, Fe — elemental iron, Sn — elemental tin.

In principle, the mechanochemical synthesis can be described by a hypothetical Eq. (1):

$$2Cu + Fe + xSn + yS \rightarrow$$

$$(1 - z)Cu_2FeSnS_4 + zCu_2FeSn_3S_8, \qquad (1)$$

where $x = 1$ and 3; $y = 4$ and 8 for stannite and rhodostannite formation, respectively, and $z = 0 \div 1$. At the beginning of the mechanochemical synthesis, the peaks of the non-reacted Sn and Fe precursors can be traced (plot 1). However, with the progress of reaction, only the peaks of the non-consumed Fe are visible (plots 2–4). Later on, only the peaks corresponding to stannite Cu_2FeSnS_4 (S, JCPDS 44-1476) and rhodostannite $Cu_2FeSn_3S_8$ (R, JCPDS 85-0378) are visible (plots 5,6). In this case, the observed peaks can be assigned to the (112), (204) and (312) planes of the tetragonal crystals. Both tetragonal phases show the presence of crystallites with the sizes calculated by the Rietveld analysis 18.3 nm and 18.9 nm for stannite and rhodostannite, repectively. The new phenomenon of stannite → rhodostannite transformation can be traced as a consequence of milling (Fig. 2).

The amounts 76% stannite and 24% rhodostannite have been calculated for the sample milled for 120 min (Fig. 1, plot 6). In nature, rhodostannite is a replacement product of stannite [16]. This transformation may happen also with synthetic crystals by the application of high-energy milling, which often leads to the products with extraordinary properties [17]. As stated in [18], high local pressures and contact surface of the milled solids,
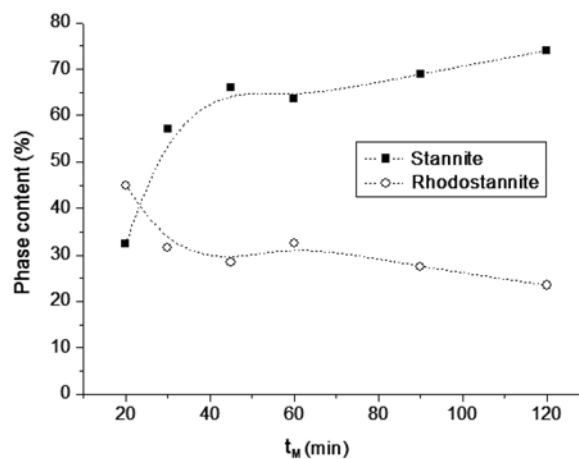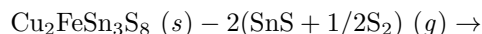

Fig. 2. Stannite, Cu_2FeSnS_4 → rhodostannite, $Cu_2SeSn_3S_8$ transformation in dependence on milling time, t_M.

as well as volume defects (e.g. strain) are responsible for such transformations. We speculate that during milling, SnS and S_2 are liberated from rhodostannite, according to a hypothetical Eq. (2):

$$Cu_2FeSn_3S_8 \ (s) - 2(SnS + 1/2S_2) \ (g) \rightarrow$$

$$Cu_2FeSnS_4 \ (s). \qquad (2)$$

This is supported by findings in [19], where SnS as volatile compound, in which tin is present as Sn(II) ion, is formed from kesterite structure, and, together with sulphur, is liberated into gas phase.

The kinetics of the solid-state reaction of Cu, Fe, Sn and S elements yielding quaternary nanocrystals is depicted in Fig. 3.
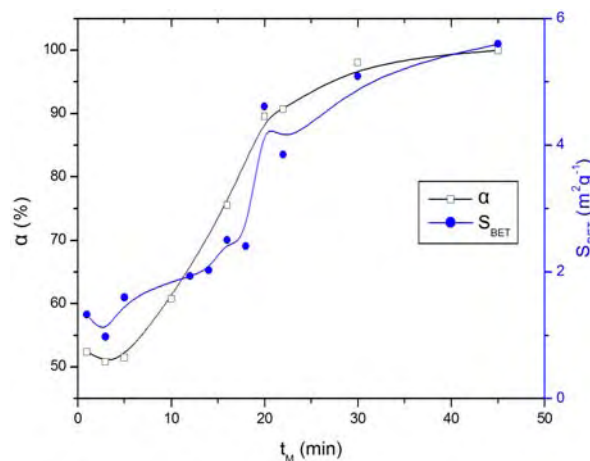

Fig. 3. Conversion degree of reaction, α and specific surface area, S_{BET} vs. milling time, t_M.

The Soxhlet method (see Sect. 2), by which the amount of non-consumed sulphur, as a measure of the progress of the mechanochemical synthesis, can be determined, has been applied for the determination of the conversion degree, α. The synthesis is very fast and the values

$\alpha \approx 50\%$ can be obtained right few moments after its initiation. A sigmoidal shape of $\alpha(t_M)$ dependence proves the acceleration of the synthesis at $t_M \approx 15$ min. Later on, the reaction does proceed less quickly and at $t_M \geq 45$ min, practically no non-reacted sulphur has been detected, which means its total consumption with full conversion of the precursors to stannnite polymorphs. The synthesis reaction (2) is topochemical, which is supported by the very similar course of $S_{\text{BET}}(t_M)$ plot, which hints to the decisive role of the surface defects created during the synthesis.

3.2. Magnetic properties

Figure 4 shows that the magnetization values for $M(H)$ curves taken at 300 K are well-saturated after the application of magnetic fields with the magnitude higher than 1 T. In principle, the magnetic data can also be used for progress evaluation of reaction (2). The final products of this reaction, namely stannite and rhodostannite, are weak magnetic (paramagnetic) substances at a room temperature [11, 20]. Therefore, the differences in the saturation magnetization of the samples milled for different times are caused mainly by the different amount of the non-consumed iron, which is the only ferromagnetic component in these materials at 300 K. For longer milling times, the saturation magnetization rapidly decreases, indicating that significant amount of elemental Fe has been already consumed by the mechanochemical reaction.
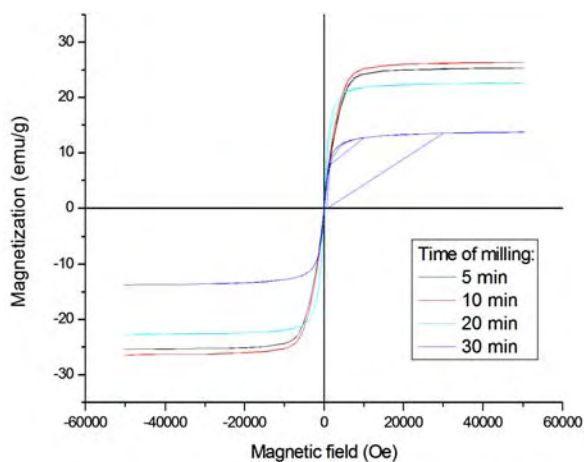

Fig. 4. Magnetization vs. magnetic field for the CFTS samples milled for different times.

4. Conclusions

The simple one-pot solid-state synthesis of CFTS quaternary nanocrystals with the properties suitable for the application in solar cell materials has been demonstrated. Stannite, Cu_2FeSnS_4 and rhodostannite, $Cu_2FeSn_3S_8$ with crystallite sizes 18–19 nm were obtained. The influence of mechanical treatment is manifested by stannite-rhodostannite transformation. The

newly revealed phenomena broaden the scope of quaternary nanocrystals application.

References

[1] W. Hsu, C.M. Sutter-Fella, M. Hettick, L.T. Cheng, S.W. Chan, Y.F. Chen, Y.P. Zeng, M. Zheng, H.P. Wang, C.C. Chiang, A. Javey, *Sci. Rep.* **5**, (2015).

[2] Q. Guo, G.M. Ford, W.C. Yang, B.C. Walker, E.A. Stach, H.W. Hillhouse, R. Agrawal, *J. Am. Chem. Soc.* **132**, 17384 (2010).

[3] S. Delbos, *EPJ Photovolt.* **3**, 35004 (2012).

[4] X.B. Song, X. Ji, M. Li, W.D. Lin, X. Luo, H. Zhang, *Int. J. Photoenergy* 613173 (2014).

[5] J.J. Scragg, *Copper Zinc Tin Sulfide Thin Films for Photovoltaics*, Springer-Verlag, Berlin 2011.

[6] S. Siebentritt, S. Schorr, *Prog. Photovolt.* **20**, 512 (2012).

[7] L.H. Ai, J. Jiang, *Nanotechnology* **23**, 495601 (2012).

[8] W. Wang, H.L. Shen, H.Y. Yao, J.Z. Li, *Mater. Lett.* **125**, 183 (2014).

[9] M. Cao, C. Li, B.L. Zhang, J. Huang, L.J. Wang, Y. Shen, *J. Alloys Comp.* **622**, 695 (2015).

[10] C. Li, M. Cao, J. Huang, L.J. Wang, Y. Shen, *Mater. Sci. Semicond. Process.* **31**, 287 (2015).

[11] Y. Cui, R.P. Deng, G. Wang, D.C. Pan, *J. Mater. Chem.* **22**, 23136 (2012).

[12] X.K. Meng, H.M. Deng, J. He, L. Sun, P.X. Yang, J.H. Chu, *Mater. Lett.* **151**, 61 (2015).

[13] C. Huang, Y. Chan, F.Y. Liu, D. Tang, J. Yang, Y.Q. Lai, J. Li, Y.X. Liu, *J. Mater. Chem. A* **1**, 5402 (2013).

[14] C. Yan, C. Huang, J. Yang, F.Y. Liu, J. Liu, Y.Q. Lai, J. Li, Y.X. Liu, *Chem. Commun.* **48**, 2603 (2012).

[15] B.B. Zhou, X.N. Yan, P. Li, L.B. Yang, D.Y. Yu, *Eur. J. Inorg. Chem.* **2015**, 2690 (2015).

[16] H. Hey, *Mineral. Mag.* **37**, 954 (1970).

[17] P. Baláž, M. Achimovičová, M. Baláž, P. Billik, Z. Cherkezova-Zheleva, J.M. Criado, F. Delogu, E. Dutková, E. Gaffet, F.J. Gotor, R. Kumar, I. Mitov, T. Rojac, M. Senna, A. Streletskii, K. Wieczorek-Ciurowa, *Chem. Soc. Rev.* **42**, 7571 (2013).

[18] E.G. Avvakumov, *Methods in Chemical Processes Activation*, Nauka, Novosibirsk 1979.

[19] J.J. Scragg, T. Ericson, T. Kubart, M. Edoff, C. Platzer-Bjorkman, *Chem. Mater.* **23**, 4625 (2011).

[20] M. Womes, J.C. Jumas, J. Olivierfourcade, F. Aubertin, U. Gonser, *Chem. Phys. Lett.* **201**, 555 (1993).

Optical properties of $Cd_{1-x}Mn_xS$ nanoparticles: off-resonance Raman spectroscopy

M. PETROVIĆ, M. ROMČEVIĆ, R. KOSTIĆ, N. ROMČEVIĆ, W. D. DOBROWOLSKI[a], M. GILIĆ, B. HADŽIĆ, J. TRAJIĆ, D. STOJANOVIĆ, Z. LAZAREVIĆ
Institute of Physics, Pregrevica 118, Belgrade, 11080 Serbia
[a]Institute of Physics PAS, Lotnikow 32/46, Warsaw, 02-668 Poland

$Cd_{1-x}Mn_xS$ nanoparticles (x=0.05-0.4) with average particle size of about 2.2nm were synthesized using the colloidal chemistry method and characterized by Raman scattering measurements. The dominant Raman line of $Cd_{1-x}Mn_xS$ nanoparticles was at about $300 cm^{-1}$ showing asymmetric broadening for $\omega < 300 cm^{-1}$. Significant change in the line intensity for different Mn content x and excitation wavelength λ was noticed.

1. Introduction

$Cd_{1-x}Mn_xS$ nanoparticles (NPs) with size quantum confinement belong to the diluted magnetic semiconductor quantum dot class of materials that has been widely studied in the last few years. The study of diluted magnetic semiconductors, such as $Cd_{1-x}Mn_xS$ quantum dots, is strongly motivated due to the localization of magnetic ions in the same places as the free-like electron and hole carriers occurring in these nanomaterials [1,2]. This interesting phenomenon causes unique properties in diluted magnetic semiconductors dots that can be explored in different technological applications, such as wavelength tunable laser [3], solar cells [4,5], spintronic devices [6], etc. $Cd_{1-x}Mn_xS$ is a typical example of diluted magnetic semiconductor. Mn^{2+} ions can be incorporated in $A^{II}B^{VI}$ semiconductor host in large proportions without substantially altering the crystallographic quality of the material. Finally, Mn^{2+} ion is electrically neutral in an $A^{II}B^{VI}$ host, thus avoiding the formation of any acceptor or donor impurities in the crystal.

Vibrational spectroscopy (Raman spectroscopy) is a powerful, non-destructive technique sensitive to local environment, ideal for *in site* probing during growth and device fabrication and operation [7]. Similar as for the bulk materials, Raman spectroscopy provides information about optical vibrational modes of semiconductor nanoparticles [8-10].

In this paper, we present a continuation of our effort to understand the properties of powders consisting of nanosized diluted magnetic semiconductors prepared using colloidal chemistry method. The influence of the composition and the excitation wavelength on the Raman active vibrations were studied in detail.

2. Synthesis and characterization

Colloidal dispersions consisting of $Cd_{1-x}Mn_xS$ NPs were prepared by mixing a solution containing $Cd(NO_3)_2$ and $MnSO_4$ with a solution containing Na_2S in the presence of surface active agent hexametaphosphate $(NaPO_3)_6$. The concentration of cations $([Cd^{2+}] + [Mn^{2+}])$ was constant $(2\times10^{-3}M)$, while S^{2-} ions were used in excess $(2.4\times10^{-3}M)$. The concentration of $(NaPO_3)_6$ was $2\times10^{-2}M$. Light and air were excluded during the preparation of this colloid. After precipitation of colloidal particles, the solvent was removed by vacuum evaporation at room temperature. The obtained yellow powders could be redisolved in water to give a colloid with the same structured absorption spectrum as the solution before evaporation. The content of Mn^{2+} ions was up to x=0.3 and was checked out by X-ray dispersive fluorescence analysis technique. This technique gives results with uncertainty of 10%.

The X-ray diffraction analysis of $Cd_{1-x}Mn_xS$ NPs showed hexagonal wurtzite crystal structure. UV-Vis absorption spectra were recorded on Perkin-Elmer Lambda 5 instrument. A blue shift of the absorption onset of the $Cd_{1-x}Mn_xS$ nanoparticles compared to the bulk $Cd_{1-x}Mn_xS$ was about 0.3eV. The radius of the particles was calculated using an effective mass approximation model [11]. The calculated value for the particle size of $Cd_{1-x}Mn_xS$ nanoparticles was found to be 2.2nm. The results of experimental and theoretical studies of the Raman active vibrations in nanosized CdS crystals we reported in Ref. [12].

3. Results and discussion

The unpolarized Raman spectra were excited by 488, 496.5, 501.7 and 514.5nm lines of an argon laser in the

back-scattering geometry. The Jobin Yvon U-1000 monochromator, with a conventional photo counting system was used. Measurements were performed in spectral region from 150 to 450cm^{-1} at room temperature. The main feature in measured Raman spectra was mode at $\approx$300cm^{-1}. Raman mode at $\approx$300cm^{-1} is slightly asymmetric and broadened toward lower frequencies and can be well identified as LO type phonon mode confined in a spherical nanocrystal.

All Cd$_{1-x}$Mn$_x$S NPs samples showed significant changes in experimental Raman line shape, mainly in intensity, as a function of excitation energy. For each Mn content (x), the intensity of the line decreases with the increase of the excitation wavelength λ, where the rate of the decrease depends on the Mn content (x). As an example, the Raman spectra of Cd$_{0.9}$Mn$_{0.1}$S sample for various excitation wavelengths (λ= 488, 496.5, 501.7 and 514.5nm) are presented in Fig.1. The ratio of Raman intensities (I$_{488}$/I$_{514}$) of mode at about 300cm^{-1} for various contents of Mn^{2+} is given in Fig. 2. This picture summarizes the change in the intensity for all contents (x=0; 0.05; 0.1; 0.15; 0.3) and applied excitations. From Fig. 2 it is clear that the ratio of Raman intensities changes nonlineary as a function of Mn^{2+} content and has a maximum at x=0.1. The observed effect can be explained by the fact that the band gap energy of Cd$_{1-x}$Mn$_x$S NPs is a function of particle size and content of Mn^{2+}.

Decrease of semiconductor nanocrystals size leads to an increase in band gap energy. For a fixed size of Cd$_{1-x}$Mn$_x$S nanoparticles the band gap energy is a function of Mn^{2+} content and has a minimum around x=0.1 [13]. Because of that, among the Cd$_{1-x}$Mn$_x$S NPs with different Mn^{2+} content, the nanocrystals with x=0.1 are the closest to the resonant regime, and potentially have the strongest intensity of Raman line. The experimental data confirmed that the strongest intensity of Raman line is for the x=0.1 sample for all applied excitation energies.

The Cd$_{1-x}$Mn$_x$S NPs were not theoretically treated at this moment, because it is complicate to distinguish the influence of size and Mn^{2+} content on the phonon properties. In the Mn^{2+} doped bulk CdS samples new impurity modes appear between TO-LO frequencies of CdS [14,15]. The TO-LO modes originating from the impurities are not well resolved for the samples with low Mn^{2+} content.

4. Conclusion

We investigated Raman spectra of Cd$_{1-x}$Mn$_x$S nanoparticles synthesized using colloidal chemistry method and small enough to show effects due to the phonon confinement. In the Raman spectra an asymmetric line was observed at about 300cm^{-1}. Registered nonlinear change in intensity for different Mn^{2+} content x and excitation energies is connected to nonlinear changes of energy gap.

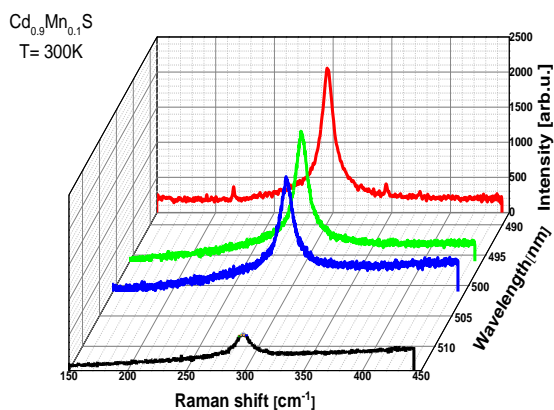*Fig. 1. Raman spectra of the Cd$_{0.9}$Mn$_{0.1}$S nanoparticles at different laser excitations (488, 496.5, 501.7 and 514.5nm).*

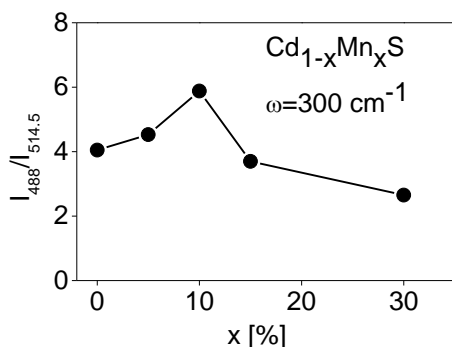*Fig. 2. Ratio of Raman intensities (I$_{488}$/I$_{514}$) as a function of Mn^{2+} content.*

References

[1] P. I. Archer, S. A. Santangelo, D. R. Gamelin, Nano. Lett. **7**, 1037 (2007).

[2] R. Beaulac, P. I. Archer, S. T. Ochsenbein, D. R. Gamelin, Adv. Funct. Mater. **18**, 3873 (2008).

[3] D. J. Norris, A. L. Efros, S. C. Erwin, Science. **319**, 1776 (2008).

[4] I. Gur, N. A. Fromer, M. L. Geier, A. P. Alivisatos, Science. **310**, 462 (2005).

[5] S. C. Erwin, L. Zu, M. L. Haftel, A. L. Efros, T. A. Kennedy, D. J. Norris, Nature. **436**, 91 (2005).

[6] H. J. Yu, X. Liu, K. E. Kweon, J. Joo, J. Park, K. T. Ko, D. W. Lee, S. Shen, K. Tivakornsasithorn, J. S. Son, J.-H. Park, Y.-W. Kim, G. S. Hwang, M. Dobrowolska, J. K. Furdyna, T. Hyeon, Nature Materials. **9**, 47 (2010).

[7] P. Moriarty, Rep. Prog. Phys. **64**, 297 (2001).

[8] M. P. Chamberlain, C. Trallero-Giner, M. Cardona, Phys. Rev. B **51**, 1680 (1995).

[9] E. Roca, C. Trallero-Giner, M. Cardona, Phys. Rev. B **49**, 13074 (1994).

[10] A. G. Rolo, M. I. Vasilevskiy, M. J. M. Gomes, O. V. Vikhrova, Yu. P. Rakovich, M. V. Artemyev, Proc. Mater. Res. Soc. Symp. **571**, 217 (2000).

[11] L. E. Brus, J. Chem. Phys. **80**, 4403 (1984).

[12] R. Kostic, N. Romcevic, Phys. Stat. Sol. (c) **1**(11), 977 (2004).

[13] L. Levy, D. Ingert, N. Feltin, M. P. Pileni, J. Cryst. Growth **184/185**, 377 (1988).

[14] E.-K. Suh, A. K. Arora, A. K. Ramdas, S. Rodriguez, Phys. Rev. B **45**, 3360 (1992).

[15] S. Venugopalan, A. Petrou, R. R. Galaska, A. K. Ramdas, S. Rodriguez, Phys. Rev. B **25**, 2681 (1982).

_____

[*]Corresponding author: milicap@ipb.ac.rs

Growth, characterization and optical quality of calcium fluoride single crystals grown by the Bridgman method

HANA IBRAHIM ELSWIE[a], SLOBODANKA KOSTIĆ[b], VESNA RADOJEVIĆ[a], NEBOJŠA Ž. ROMČEVIĆ[b],
BRANKA HADŽIĆ[b], JELENA TRAJIĆ[b], ZORICA Ž. LAZAREVIĆ[b,*]
aFaculty of Technology and Metallurgy, University of Belgrade, Belgrade, Serbia
bInstitute of Physics, University of Belgrade, P.O. Box 68, Belgrade, Serbia

Calcium fluoride - CaF_2 single crystals were grown using the Bridgman technique. By optimizing growth conditions, <111>-oriented CaF_2, crystals up to 20 mm in diameter were grown. Number of dislocations in CaF_2 crystals which were made by the method of Bridgman was 5×10^4 - 2×10^5 per cm^2. In this paper we used XRD, Raman spectroscopy and the measurement of transmission in the mid IR-range to investigated structural and optical properties of obtained CaF_2 single crystals.

1. Introduction

A calcium fluoride (here after abbreviated as CaF_2) single crystal has excellent transmission characteristics down to the vacuum ultraviolet region, and it is utilized as a lens material in the wafer-stepper of semiconductor lithography technology together with synthetic quartz. CaF_2 single crystals of more than 10 in diameter are required for the lens materials. Such large CaF_2 single crystals are grown by the Czochralski method [1, 2] or the vertical Bridgman method [3, 4]. Extremely high material performances are required for the lens material in the wafer-stepper to achieve high resolution of lithography. Among them, the reduction of birefringence caused by the residual stress is one of the technical problems. In the Czochralski method, residual stress is induced in the crystal by thermal stress, where as, in the vertical Bridgman method, residual stress is induced not only by thermal stress but also due to mechanical stress caused by the contact of the crystal and crucible. Generally as-grown single crystals with larger diameter have larger residual stress, which results in larger birefringence in as-grown crystals. Therefore, annealing after single-crystal growth is in dispensable process, when CaF_2 single crystals are used for the lens material in the wafer-stepper. Such annealing reduces the residual stress and suppresses the birefringence at a low level, but a very long annealing period is required to reduce the birefringence to the target value. Numerical simulations of residual stress and birefringence play an important role for searching effective annealing conditions.

CaF_2 is an ionic crystal with the fluorite structure. The lattice is a face centered cubic (*fcc*) structure with three sublattices. The unit cell of the material is most easily described as a simple cubic lattice formed by the F^- ions where a Ca^{2+} ion is contained in every second cube.

The remaining empty cubes (called interstitial or hollow sites) are important for defect formation and diffusion, but also for the accommodation of unwanted impurities like rare earth ions and dopants. The lattice constant is $a = 5.4626$ Å [5] (Fig. 1).

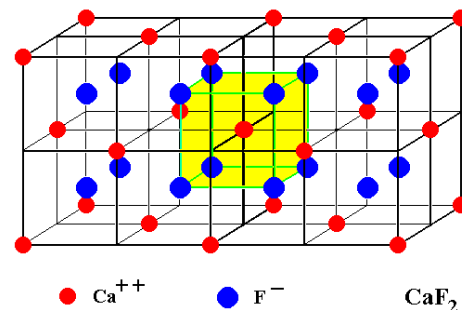*Fig. 1. Unit cell representation of CaF_2 structure*

Single crystal CaF_2 used in the optical device can be of natural origin - fluorite, under which name is often referred to in literature [6] and synthetic single crystal CaF_2 which is usually obtained growth from the melt. By its chemical and physical properties of the single crystal CaF_2 is very different from other materials that have been developed techniques to obtain single crystals. The relatively high melting point (over 1300 °C), high chemical aggressiveness of fluorine at these temperatures, relatively small chemical compounds CaF_2 stability at high temperatures and very strong ability to react CaF_2 with traces of water vapor, require the use of special growth conditions to obtain quality crystals. Therefore, the growth of a single crystal CaF_2 may take place either in vacuum or in an inert gas atmosphere (argon or helium) at purity of at

least 99.99% in order to prevent the presence of traces of moisture or oxygen.

The aim of the present work was to obtain single crystal CaF_2 optical quality. The structural and optical properties obtained crystal was characterized using XRD, Raman and FTIR spectroscopic characterization.

2. Experimental procedures

The Bridgman method of crystal growth is relatively simple and allows operation in a vacuum, and also in an inert atmosphere. In this method, the crucible uses a cylindrical shape with a conical bottom. The procedure consisted of the following: the crucible cylindrical shape with melted batch CaF_2 down from the upper hot chamber of the furnace in the cooler lower chamber of the same furnace. The bottom of the crucible was in the shape of a cone and that in the formation of germs and begins the process of crystallization. The crucible was from spectroscopically pure graphite [2-8]. One of the main drawback of this method is that in the course of growth can be seen the process of crystal growth, so that if it comes to the appearance of polycrystalline, this can be concluded only after the completion of the process of growth and cooling crystals.

To obtain single crystals of CaF_2 by the Bridgman method in a vacuum has been used device BCG 356. Initial samples of single crystals were mostly clear and transparent, but some were cracked. Because of the small temperature gradient there were a sudden crystallization process and the appearance of dendrites in the lower part of the crucible, and therefore made changes to the structure of the crucible. With this change we have achieved that cone of the lower part of the crucible is in the form of a tube. Therefore we have achieved that by the sudden crystallization takes an extended part of the crucible, thus avoiding the occurrence of dendrites. The crystals that were obtained on the crucible constructed in this way were of better quality. However, when grinding the upper surface of the crystal, because the dirt that clung to that, there have been cracks crystal along a plane of cleavage.

Experiments have been performed with CaF_2 in the form of a powder. Since this device works in a vacuum, there was a danger that the air contained in the powder CaF_2, when you turn on the vacuum pump, disperses the powder throughout the apparatus. Therefore, the CaF_2 powder was compaction and sintered in the form of pills. With such obtained pills could easily and quickly be filled crucible. Power generator was initially $P_{gen} = 3.8$ kW, and was later increased to $P_{gen} = 3.94$ kW. The crystal growth rates were 6 mm h^{-1}, 12 mm h^{-1}, 24 mm h^{-1} and 48 mm h^{-1}.

The observations relating to the dislocation were recorded by observing an etched surface of CaF_2 crystal, using a Metaval of Carl Zeiss Java metallographic microscope with magnification of 270x. To test the dislocations were used CaF_2 samples that are obtained by cleaving the crystals CaF_2 per plane splitting <111>. The samples were etched with concentrated sulfuric acid from

10 to 30 min. It has been shown that the best results are obtained on the sample crystal is etched for 15 min.

The crystal structure of CaF_2 single crystal was approved using the X-ray diffractometer (XRD, Model Philips PW 1050 diffractometer equipped with a PW 1730 generator, 40 kV x 20 mA, and using CuKα radiation of 1.540598 Å at the room temperature. Measurements were done in 2θ range of 10-90° with scanning step width of 0.05° and 10 s scanning time per step.

The Raman scattering measurements of CaF_2 crystal was performed in the backscattering geometry at room temperature in the air using a Jobin-Yvon T64000 triple spectrometer, equipped with a confocal microscope (100x) and a nitrogen-cooled charge coupled device detector (CCD). The spectra have been excited by a 514.5 nm line of Coherent Innova 99 Ar$^+$ - ion laser with an output power of less than 20 mW to avoid local heating due to laser irradiation. Spectra were recorded in the range from 100 - 800 cm^{-1}.

The transmission a spectrum of CaF_2 sample (powdered and pressed in the disc with KBr) was obtained by transmission Fourier transforms infrared (FTIR) Hartmann&Braun spectrometer, MB-series. The FTIR spectrum was recorded between 4000 and 400 cm^{-1} with a resolution of 4 cm^{-1}.

3. Results and discussion

CaF_2 single crystals are obtained by the vertical Bridgman method in vacuum. Experiments were carried out with the crystal growth rate of 6-48 mm h^{-1}. The best result was obtained with a crystal growth rate of 6 mm h^{-1}. If the growth rate of the single crystal CaF_2 larger, experiments showed that these crystals contain more stress and that in this case it is more likely to obtain polycrystals. Stresses in single crystals we have tried to eliminate annealing of crystals. The process of annealing was carried out on the plate and bulk crystal CaF_2. The temperature of annealing of the plate was at 1000 °C for 3 h, and the temperature of annealing of the bulk crystal was at 1000 °C and 1080 °C for 1 - 3 h. Annealing is carried out under an inert atmosphere of argon. It was noticed that after annealing, plate CaF_2 did not have enough stress. Annealing bulk single crystal CaF_2 had less stress than non-annealing. The obtained single crysta of CaF_2 was 20 mm in diameter and 90 mm in length. A polished plate of CaF_2 with a diameter of 20 mm is displayed in Fig. 2.
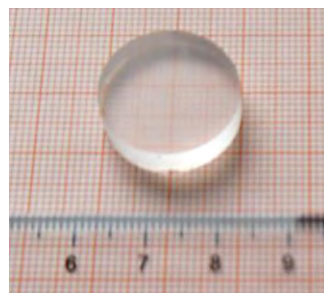

Fig. 2. Photographs of Bridgman-grown CaF$_2$ single crystals

The general conclusion is that in all samples was observed relatively high dislocation density (ranging from 60000 to 140000) as a consequence of greater internal stresses, which have emerged in the process of cooling. From the Fig. 3 it can be observed dislocations on CaF_2 single crystal. Etch pits have the shape of a three-sided pyramid. Number of dislocations in CaF_2 crystals which were made by the method of Bridgman was $5 \cdot 10^4$ - $2 \cdot 10^5$ per cm^2 (Fig. 3).
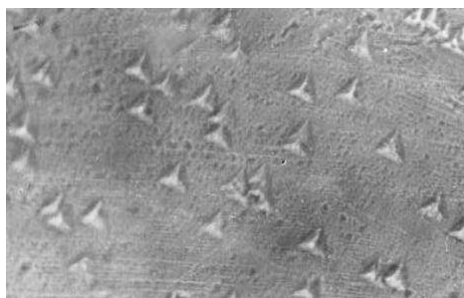

Fig. 3. The microscopic image of the surface CaF_2 crystal plate in the direction ‹111›. Magnification of 270x

The sample of CaF_2 single crystal was of cubic structure with the *Fm3m* space group [9]. XRD pattern (Fig. 4) was indexed by using JCPDS database (card no. 87-0971). The XRD pattern was found to match exactly with those reported in the literature [10, 11]. The displayed peaks correspond to (*h k l*) values of (1 1 1), (2 2 0), (3 1 1), (4 0 0), (3 3 1) and (4 2 2). Using the (*h k l*) values of different peaks, the lattice constant (*a*) of the sample was calculated. Their lattice parameter was calculated from the equation of plane spacing for cubic crystal system and Bragg's law for diffraction [12]. The lattice parameter was 5.452±0.011 Å, calculated from the obtained XRD diagram, which was in good agreement with the literature [5, 13].
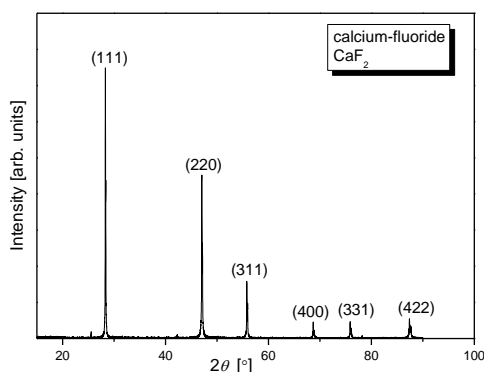

Fig. 4. X-ray diffraction pattern of the CaF_2 powdered sample

Three atoms in cubic O_h^5 (*Fm3m*) primitive cell of the CaF_2 crystal are given nine fundamental vibrations, described by the following O_h-irreducible representations (at *k* = 0): $\Gamma = 2T_{1u} + T_{2g}$. According to several comprehensive work (see, e.g. [14-19]), their distribution

among optical and acoustical are: the triply degenerate T_{2g} optical phonon is Raman active and IR inactive; one of the T_{1u} representations (triply degenerate as well) corresponds to the zero frequency acoustic mode, while the other T_{1u} species is actually split into a double degenerate transverse optical mode and a nondegenerate longitudinal optical mode, all the above are IR active. The room-temperature first order T_{2g} one-band spontaneous Raman scattering spectra of CaF_2 crystal is shown in Fig. 5. In this single allowed SRS-promoting optical mode with frequency ω_{SRS} = 319.7 cm^{-1} Ca^{2+} cation remains stationary and the neighboring substitutional fluoride F^{-1} ions vibrate against each other [19-21].
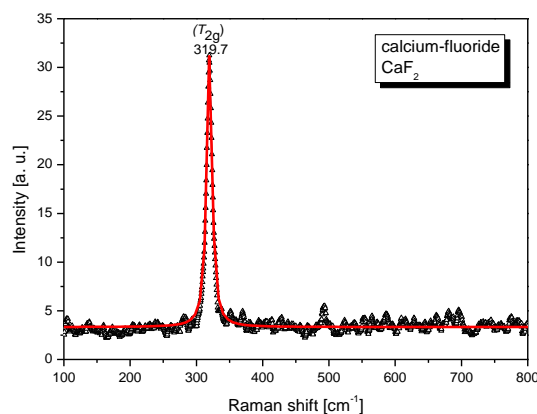

Fig. 5. Raman spectra of the CaF_2 single crystal at room temperature

FTIR transmission was measured in order to check the purity of the obtained CaF_2. As shown in Fig. 6, the sharp peaks of the absorption at 2854 cm^{-1} and 2936 cm^{-1} are assigned to the symmetric and antisymmetric stretching vibration of $-CH_2$ groups [22]. Also, the spectra shows two broad IR absorption peaks at ~3432 cm^{-1} and 1628 cm^{-1} are assigned to the symmetrically stretching vibration and antisymmetric stretching vibration of hydroxyl groups -OH, implying the presence of H_2O molecules [23, 24]. The peak at 671 cm^{-1} in the FTIR spectra was assigned to the Ca-F stretching vibration of CaF_2 [25]. The band at ~2357 cm^{-1} is due to KBr pellets used for recording FTIR spectrum [26].
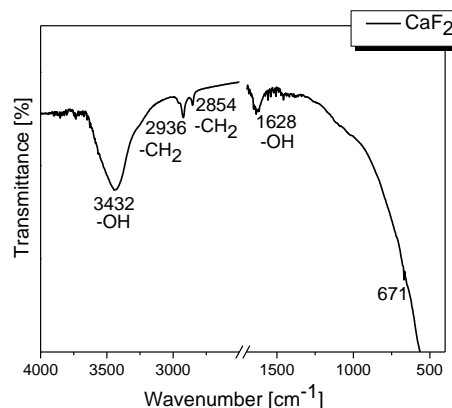

Fig. 6. FTIR spectra of CaF_2

The properties of the crystal, such as density of dislocations, cystallinity, and impurities concentrations, determine the optical quality.

4. Conclusions

CaF_2 single crystals in diameter of 20 mm are obtained by the vertical Bridgman method in vacuum. The crystal growth rate was 6.0 mm h^{-1}. Number of dislocations is of the order of 5×10^4 - 2×10^5 per cm^2. The crystal structure was confirmed by XRD. The Raman T_{2g} optical mode at 319.7 cm^{-1} was observed. The FTIR transmission spectra indicate that there are some amounts of -CH2, -OH or water molecules and organic groups adhering to the surfaces. Based on our work and observations during the experiment, it could be concluded that the obtained transparent single crystal CaF_2 of good optical quality, which was the goal of our work.

Acknowledgements

References

[1] L. Su, Y. Dong, W. Yang, T. Sun, Q. Wang, J. Xu, G. Zhao, Mater. Res. Bull. **40**, 619 (2005).

[2] H. Yanagi, T. Nawata, Y. Inui, Y. Hatanaka, E. Nishijima, T. Fukuda, Proc. SPIE 5377, Optical Microlithography XVII, 1886 (May 28, 2004); doi:10.1117/12.556614.

[3] N. Senguttuvan, M. Aoshima, K. Sumiya, H. Ishibashi, J. Crys. Growth **280**, 462 (2005).

[4] J. Xu, M. Shi, B. Lu, X. Li, A. Wu, J. Crys. Growth **292**, 391 (2006).

[5] G. Scholz, I. Dörfel, D. Heidemann, M. Feist, R. Stösser, J. Solid State Chem. **179**, 1119 (2006).

[6] I. V. Stepanov, P. P. Feofilov, Artificial fluorite. In Rost kristalov (Vol. I), Moscow, Russia: Akademia Nauk SSSR. (in Russian), 1957, p. 229.

[7] G. V. Molev, V. E. Bozherolnog, J. Cryst. Growth **19**, 117 (1973).

[8] K. Recker, R. Leckebusch, J. Cryst. Growth **9**, 274 (1971).

[9] L. Gerward, J. S. Olsen, S. Steenstrup, M. Malinowski, S. Åsbrink, A. Waskowska, J. Appl. Crystallogr. **25**, 578 (1992).

[10] B.-C. Hong, K. Kawano, J. Alloys Compd. **408-412**, 838 (2006).

[11] N. D. Alharbi, J. Nanomaterials **2015**, Article ID 136957, 8 pages, http://dx.doi.org/10.1155/2015/136957.

[12] S. Biswas, S. Kar, S. Chaudhuri, J. Cryst. Growth **299**, 94 (2007).

[13] L. G. DeShazer, S. C. Rand, B. A. Wechsler, in: M. J. Weber (ed.) Handbook of Laser Science and Technology, **V**, Optical Materials: Part 3(CRC Press, Boca Raton, FL), 1988, pp.281.

[14] R. K. Chang, B. Lacina, P. S. Pershan, Phys. Rev. Lett. **17**, 755 (1966).

[15] J. R. Ferraro, H. Horan, A. Quattrochi, J. Chem. Phys. **55**, 664 (1971).

[16] D. G. Mead, G. R. Wilkison, J. Phys. C **10**, 1063 (1977).

[17] D. J. Oostra, H. W. den Hartog, Phys. Rev. B **29**, 2423 (1984).

[18] P. C. Ricci, A. Casu, G. de Giudici, P. Scardi, A. Anedda, Chem. Phys. Let. **444**, 145 (2007).

[19] A. A. Kaminskii, S. N. Bagayev, H. J. Eichler, H. Rhee, K. Ueda, K. Takaichi, K. Oka, H. Shibata, Y. Hatanaka, Y. Matsumoto, Laser Phys. Lett. **8**, 385 (2006).

[20] L. Su, J. Xu, W. Yang, X. Jiang, Y. Dong, Chinese Optics Letters **3**, 219 (2005).

[21] J. P. Russell, Proceedings of the Physical Society **85**, 194 (1965).

[22] J. Song, G. Zhi, Y. Zhang, B. Mei, Nano-Micro Lett. **3**, 73 (2011).

[23] L. Zhou, D. Chen, W. Luo, Y. Wang, Y. Yu, F. Liu, Mater. Lett. **61**, 3988 (2007).

[24] G. A. Kumar, C. W. Chen, J. Ballato, R. E. Riman, Chem. Mater. **19**, 1523 (2007).

[25] K. Tahvildari, M. Esmaeili Pour, Sh. Ghammamy, H. Nabipour, Int. J. Nano Dim. **2**, 269 (2012).

[26] C. Pandurangappa, B. N. Lakshminarasappa, B. M. Nagabhushana, J. Alloys Compd. **489**, 592 (2010).

*Corresponding author: lzorica@yahoo.com

Structural Properties of Cu-Se-CuSe$_2$ Thin Films

M. Gilić, M. Petrović, B. Hadžić, M. Romčević, J. Trajić, N. Romčević and Z. Lazarević

Abstract This paper describes the structural and optical properties of Cu-Se-CuSe$_2$ thin films. The surface morphology of thin films was investigated by atomic force microscopy (AFM) and scanning electron microscopy (SEM). Formation of thin films is concluded to proceed unevenly, in the form of islands which later grew into agglomerates. The structural characterization of Cu-Se-CuSe$_2$ thin film was investigated using X-ray diffraction pattern (XRD). The presence of two-phase system is observed. One is the solid solution of Cu in Se and the other is low-pressure modification of CuSe$_2$. The Raman spectroscopy was used to identify and quantify the individual phases present in the films. Red shift and asymmetry of Raman mode characteristic for CuSe$_2$ enable us to estimate nanocrystal dimension. In the analysis of the far-infrared reflection spectra, numerical model for calculating the reflectivity coefficient of layered system, which includes film with nanocrystallite inclusions (modeled by Maxwell–Garnet approximation) and substrate, has been applied. UV–VIS spectroscopy and photoluminescence spectroscopy are employed to estimate direct and indirect band gap of CuSe$_2$.

M. Gilić (✉) · M. Petrović · B. Hadžić · M. Romčević · J. Trajić ·
N. Romčević · Z. Lazarević
Institute of Physics, University of Belgrade, Belgrade, Serbia
e-mail: martina@ipb.ac.rs

M. Petrović
e-mail: milicap@ipb.ac.rs

B. Hadžić
e-mail: branka@ipb.ac.rs

M. Romčević
e-mail: romcevic@ipb.ac.rs

J. Trajić
e-mail: jelena.trajic@ipb.ac.rs

N. Romčević
e-mail: romcevi@ipb.ac.rs

Z. Lazarević
e-mail: zorica.lazarevic@ipb.ac.rs

1 Introduction

Nanostructures—either thin films, nanorods, nanotubes or quantum dots—have received growing interest as a result of their fascinating properties and applications that are superior to their bulk counter parts. Materials of nanoscopic dimensions have received rapid advance and widespread interest in the last decade [1–6]. As for copper selenides, they are metal chalcogenide semiconductors that exist in many phases and crystallographic forms: different stoichiometric such as CuSe (mineral klockmannite), Cu_2Se, $CuSe_2$ (mineral marcasite), Cu_3Se_2 (mineral umangite), Cu_5Se_4 (mineral athabaskite), Cu_7Se_4 as well as in non-stoichiometric form as $Cu_{2-x}Se$ (mineral berzelianite) and can be constructed into several crystallographic forms (monoclinic, cubic, tetragonal, orthorhombic, hexagonal, etc.). The phase diagram of copper–selenium system [7] shows us that the thermal stability of these compounds is highly dependent on the stoichiometric form.

Cu-Se thin films are p-type semitransparent highly conducting semiconductors [8, 9] that found numerous applications in devices such as thin film solar cells, photodetectors, superionic materials, optical filters [10, 11]. Moreover, $CuSe_2$ is superconductor at low temperatures with a transition temperature $T_C \sim 2.4$ K [12]. $CuSe_2$ is reported to be weak ferromagnetic below 31 K [13, 14] implying the possible coexistence of ferromagnetism and superconductivity in this compound.

The optical and electrical properties of copper selenide films depend on the used fabrication method due to compositional complexity of this compound, and possible phase transitions. Numerous methods have been reported for the deposition of these films of different crystalline modifications and varying stoichiometry. These methods can be primarily categorized in two processes. One is solution-based process: chemical bath deposition [9, 15], solution growth [8], hydrothermal method [16], etc. Another one is vacuum based process: vacuum evaporation techniques [17–20].

This paper reports optical and structural characterization of $Cu-Se-CuSe_2$ thin films of three different thicknesses. These films are obtained by rather simple and low-cost vacuum evaporation technique, using Mo boat onto glass substrate at room temperature. Characterization was performed using XRD, SEM, Raman, far-infrared reflection, UV–VIS and photoluminescence measurements. The structure of the obtained films is discussed on the basis of XRD data along with SEM measurements. The above properties have been reviewed with respect to the results of the Raman and far-infrared spectroscopy. Optical properties i.e. band gap determination was done with help of UV–VIS and photoluminescence measurements.

2 Samples Preparation

Thin films were obtained by evaporating commercially high purity CuSe powder (99.99 %) bought at Aldrich. The powder was deposited onto a highly pre-cleaned glass substrates with use of Mo boat. The procedure was done in a high—vacuum environment with typical background pressures of 3 mPa. The deposition rate, 10 nm/s, was monitored by quartz crystal thickness monitor—FTM4, Edwards. The final thicknesses of the films were found to be 56 nm (film1), 79 nm (film2) and 172 nm (film3).

3 Results and Discussion

3.1 Scanning Electron Microscopy

Scanning electron microscopy (SEM) images were obtained for Cu-Se-CuSe$_2$ thin films deposited on glass substrate in order to study the surface morphology and agglomeration of the samples. SEM imaging was done using scanning electron microscope equipped with a high brightness Schottky Field Emission gun (FEGSEM, TESCAN) operating at 4 kV. The samples were coated with gold/palladium to make them conductive.

Top view and tilted micrographs of thin films are presented in Fig. 1. From top view micrographs we may observe that the surface of our samples is relatively uneven and rather rough, with presence of cracks and voids. Formation of thin films is concluded to proceed unevenly, in the form of islands which later grew into agglomerates. Agglomerated clusters of few hundreds nanometers in diameter are distributed non-uniformly along the surface. In order to obtain the film thicknesses, the samples are tilted at 30°. The estimated thicknesses are: $\sim$56 nm for film1, $\sim$78 nm for film2 and $\sim$171 nm for film3. The thickness values estimated by SEM analysis match the ones obtained during the preparation of thin films.

3.2 XRD

The structural characterization of thin film was investigated by using X-ray diffraction pattern. X-ray diffraction measurements were performed on a Philips 1050 X-ray powder diffractometer using a Ni-filtered CuK$_\alpha$ radiation and Bragg-Brentano focusing geometry. The patterns were taken in the 10–80° 2θ range with step of 0.05° and exposure time of 6 s per step.

X-ray diffraction patterns of our samples are presented in Fig. 2. There is wide diffraction structure in region 20–40° characteristic for nanocrystal materials. Good defined peaks are signs of crystal structure formation.
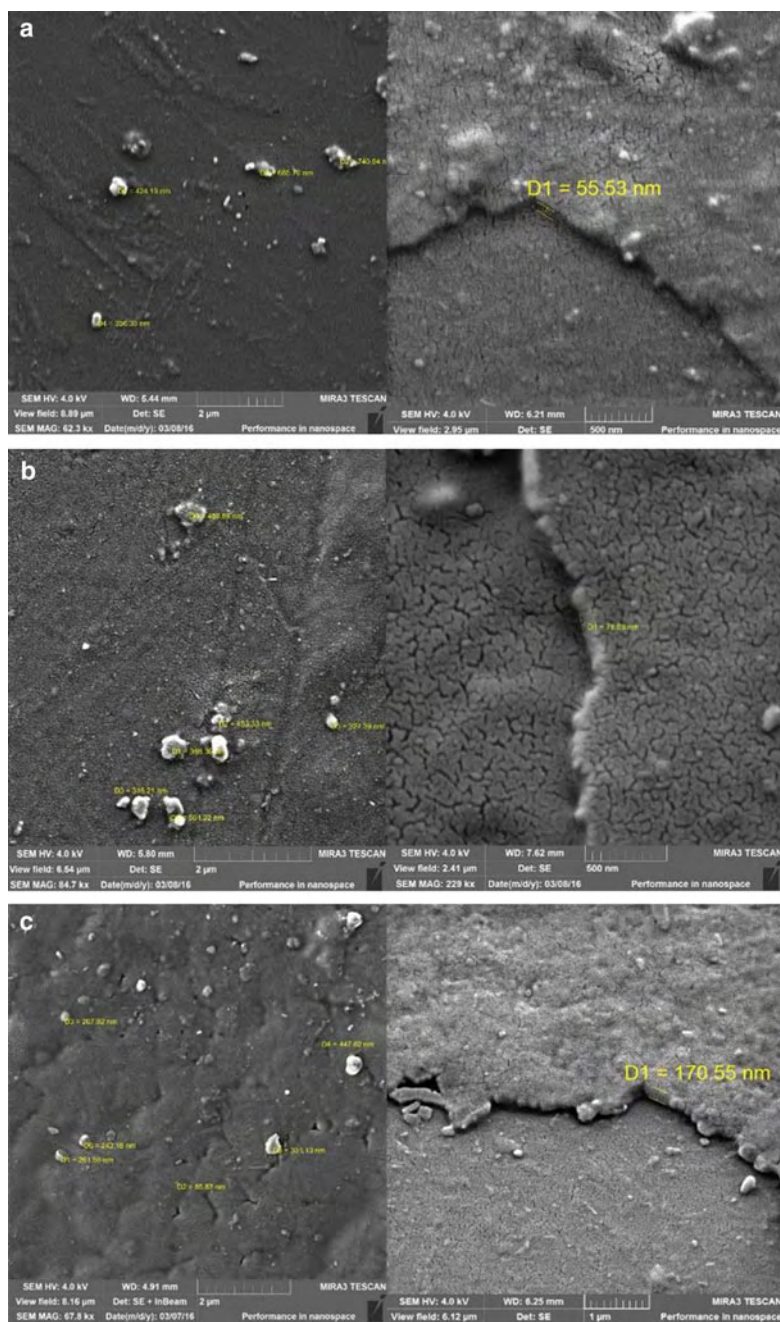
Fig. 1 Top view and tilted micrographs of **a** film1, **b** film2, **c** film3 at room temperature using SEM
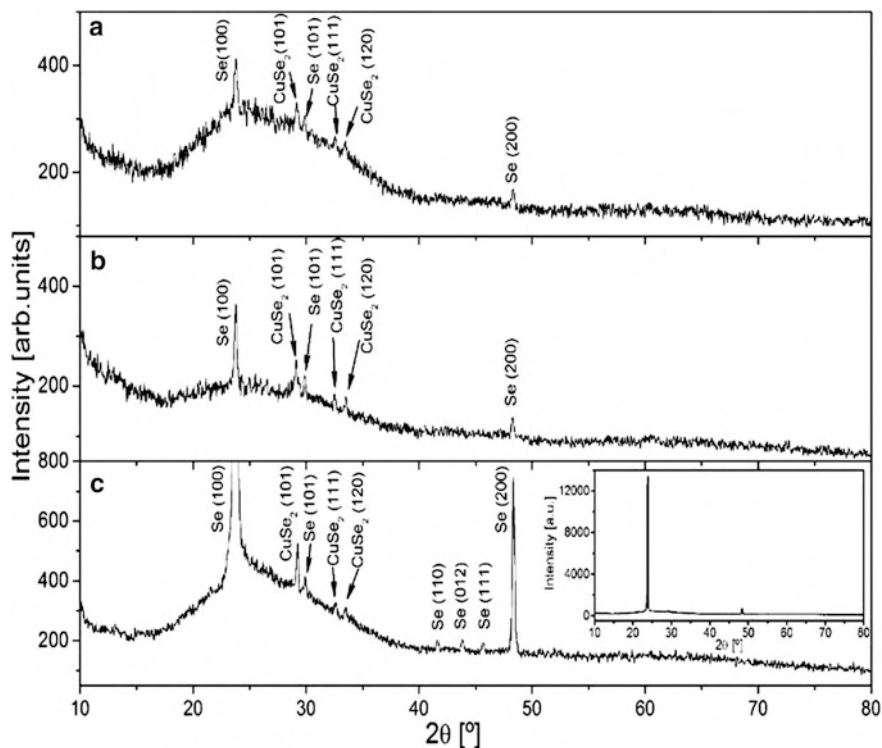
Fig. 2 XRD spectra of **a** film1 **b** film2 and **c** film3; inset: full intensity spectrum of film3

Reflections are clearly seen at Bragg angles (2θ) of about 24°, 29°, 30°, 32.6°, 33.4°, 42°*, 44°*, 46°* and 48.5°. Reflections at angles with asterisk are noticed only for the sample film3. The inset in Fig. 2c presents the full intensity spectrum of film3. The intensities of peaks that rise up with film thickness are signs of the crystal growth. The structural phase analysis was performed on the obtained diffractograms by using EVA 9.0 computing program. It has been observed that the two-phase samples are obtained. Two crystal structures were identified. More prominent one is hexagonal selenium and less prominent is orthorhombic marcasite structure of CuSe₂.

The dominant phase is solid solution of Cu in Se. Namely, according to phase diagrams in works of Chakrabarti and Laughlin [21] and Heyding [7], selenium and copper make solid solution even at 67 % of Se. Selenium, the solvent, has hexagonal structure [22] which is by no means the only stable phase of Se under normal conditions of temperature and pressure, with $Z = 3$ atoms per unit cell.

Selenium atoms are arranged in helical chains which are oriented along the c-axis of the hexagonal elementary cell (Fig. 3a). One chain is always surrounded by six chains in corners of a hexagon to yield the 3D structure (Fig. 3b). The bonding of atoms within a given chain is covalent where as the bonding between neighboring chains is by weaker Van der Waals forces. Reflections at 24° (100), 30° (101), 42°* (110), 44°*(012), 46°*(111) and 48.5° (200) are attributed to this phase.

The second one is low-pressure modification of $CuSe_2$, with Bragg reflections at 29° (101), 32.6° (111) and 33.4° (120) [PDF-2 74-0280]. This modification of $CuSe_2$ has the orthorhombic marcasite structure with $Z = 2$ formula units per unit cell [23], Fig. 4. In this structure each Cu atom is surrounded by six Se atoms in a distorted octahedral arrangement, in plane by 4Se with Cu-Se distance 2.62 Å and out of plane by two more Se neighbors with Cu-Se distance 2.60 Å. These octahedra are corner-sharing in the (ab) plane and edge-sharing along c axis. Each Se atom is in a distorted tetrahedral configuration, surrounded by three Cu neighbors and one *Se* neighbor (*Se-Se* distance 2.29 Å).

Small intensity of Bragg reflections characteristic for $CuSe_2$ indicates small amount of $CuSe_2$, probably in a form of crystallites of very small dimension. The absence of great number of peaks characteristic for the diffractograms of these phases indicates there is no random distribution of crystallites, but the preferentially oriented structures—which indeed was expected for thin films.

3.3 Raman Spectroscopy

The micro-Raman spectra were taken in the backscattering configuration and analyzed by Jobin–Yvon T64000 spectrometer, equipped with nitrogen cooled charged-coupled-device detector. As an excitation source we used the 532 nm line
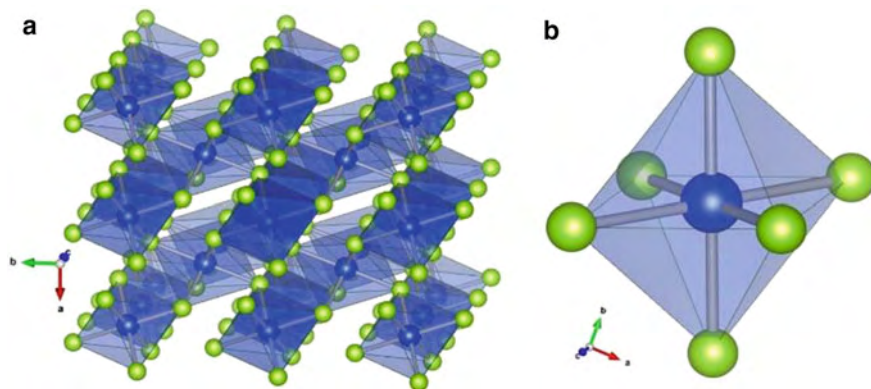

Fig. 3 Crystal structure of hexagonal Se; **a** atoms oriented along c-axis; **b** one chain surrounded by six nearest-neighbor helices
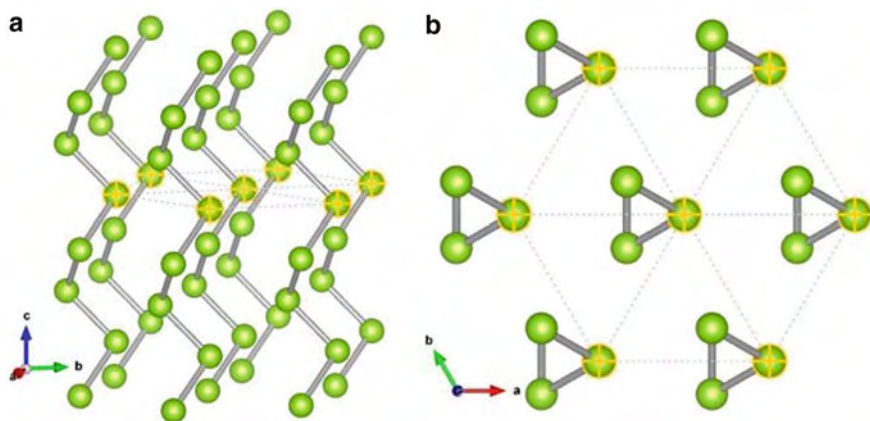
Fig. 4 Crystal structure of orthorhombic CuSe$_2$; *blue spheres*—copper ions, *green spheres*—selenium ions; **a** 2 × 2 × 2 unit cells—coordination polihedra around Cu^{2+} ions; **b** one separated coordination polyhedron around Cu^{2+} ion

of Ti: Sapphire laser, with laser power 20 mW. The measurements were performed in the spectrum range 100–400 cm^{-1}.

The Raman spectra of Cu-Se-CuSe$_2$ thin films of different thickness are shown in Fig. 5. Experimental Raman scattering spectra (presented as open dots) are analyzed by the deconvolution to Lorentzian curves. The dominant structure is in region 230–240 cm^{-1}. Ten modes can be reconstructed.

Eight modes (thick green lines on Fig. 5a) are recognized as fundamental and second order modes of hexagonal selenium and listed in Table 1. Factor-group analysis predicts three fundamental Raman active modes. The dominant structure is mainly formed of two fundamental selenium modes of close energy that are assigned as E^2 (~ 232 cm^{-1}) and A_1 (~ 236 cm^{-1}) modes of hexagonal Se structure. Mode at ~ 143 cm^{-1} is identified as E^1 mode. Low intense mode at ~ 105 cm^{-1} is identified as A_2 mode. This fundamental mode is IR active and Raman forbidden. This mode was already registered in hexagonal Se Raman spectra [24]. Wide structures of small intensity at ~ 185, ~ 208, ~ 287 and ~ 354 cm^{-1} are assigned as second order modes and listed in Table 1, as in [24].

Two modes of low intensity, denoted with blue lines in Fig. 5, are in spectral region close to dominant selenium fundamental modes. These two lines i.e. Raman active modes are associated to CuSe$_2$. The more intense one is at ~ 255, ~ 252 and ~ 251 cm^{-1} for samples film1, film2 and film3 respectively. In Raman spectra of marcasite type CuSe$_2$ one expects dominant scattering structure centered at ~ 260 cm^{-1} mostly from A_g^1 stretching mode activity. A_g^1 phonon branch goes down in all directions in Brillouin zone (BZ). In the case of very small particles i.e. nanoparticles, effects of confinement is to push A_g^1 mode to lower frequencies. In nanocrystals optical modes are confined, bulk selection rules are ruined, high surface to volume ratio increases the role of surface properties, but there is

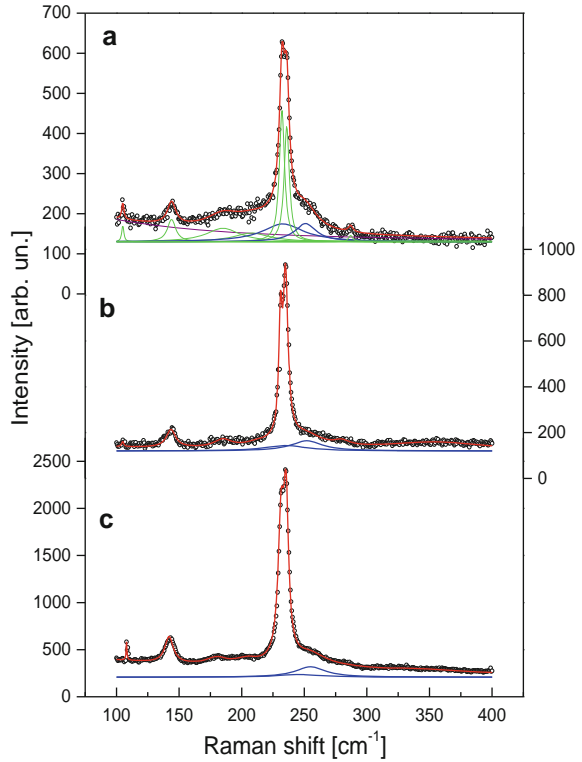**Fig. 5** Raman spectra of Cu-Se-CuSe$_2$ thin films of different thicknesses: **a** film1; **b** film2; **c** film3

Table 1 Position of registered Raman (infrared) active modes (cm^{-1}) of hexagonal Se

Film1	Film2	Film3	[24]	Assignment
Fundamental modes				
105 (105)	105 (105)	108 (105)	102	A$_2$ (IR)
144 (152)	143.5 (–)	142.6 (–)	143	E^1 (Raman, IR)
232 (230)	232 (230)	232 (230)	233	E^2 (Raman, IR)
236	236	236	237	A$_1$ (Raman)
Second order modes				
185	185	183	183	–
208 (200)	208 (200)	206 (205)	206	2A$_2$ (IR)
287 (272)	280 (280)	273 (270)	273	2E^1 (Raman, IR)
345 (350)	345 (358)	345 (358)	345	–

fundamental track of bulk properties. As A$_g^1$ dispersion relation decreases in all directions in BZ, we expect the frequencies of confined mode to be below 260 cm^{-1}. Analysis of the Raman spectra presented in Fig. 5 concerns to the spectral region below 260 cm^{-1} (ω_{Ag}^1).

A continuum model of the optical phonon confinement in nanocrystal is used. Parameters were transferred from the bulk phonon dispersion curves. It is limited to nanoparticles of regular shape. Although this is not the case in real nano-crystallites, we present results of calculation for ideal spherical CuSe$_2$ nanocrystals. One small spherical CuSe$_2$ crystal, isotropic and homogeneous inside, is considered. This consideration of confined optical vibrations in nanocrystals is based on macroscopic equation for the relative displacement of the positive and negative ions [25, 26]. This equation is solved in spherical coordinates. The spherically symmetric solutions of equation must belong to the irreducible representations of the three-dimensional rotation-inversion group $O(3)$ labeled as D_l^g (even) and D_l^u (odd upon inversion). Raman transition operator for allowed scattering belongs to D_0^g and D_2^g [27]. Frequencies of the spherical ($l = 0$) and spheroidal quadrupolar modes ($l = 2$) can be calculated and generally observed by resonant Raman scattering.

If we assume, as in [28, 29], that at the surface of the sphere all components of displacement are almost zero, the electrostatic potential and the normal component of the electric displacement are continuous. Then one can obtain frequencies of the Raman active modes ($l = 0$ and $l = 2$, $n = 1, 2, 3, …$), l and n being the spherical quantum numbers. The most important contribution to one-phonon Raman scattering corresponds to $l = 0$. This mode is excited for parallel polarizations of the incident and scattered light. The corresponding frequencies are:

$$\omega_n^2 = \omega_o^2 - \beta \left(\frac{\mu_n}{r} \right)^2 \tag{1}$$

ω_0 is the optical bulk frequency i.e. $\omega_0 = 260$ cm^{-1} in CuSe$_2$, r is the radius of the sphere, μ_n is the nth node of the Bessel spherical function j_1 ($\mu_1 < \mu_2 < \mu_3 < …$). Frequency shift (difference between ω_n and ω_0) for fixed r depends on $\beta \cdot \beta_1 = 1.5 \ 10^3$ m/s for bulk CuSe$_2$. ω_n increases as the radius of the dot (r) increases, and in the limit: $r \rightarrow \infty$ frequencies ω_n converge to ω_0. Figure 6 presents the optical vibration modes frequencies dependence ($l = 0$, $n = 1, 2, 3$) on the radius of CuSe$_2$ nanocrystals. The smaller the radius the lower is the frequency of confined mode. As for intensity, this model predicts the most intensive peak in Raman spectra to be the mode ω_n ($n = 1$).

Exact positions of modes at ~ 251, ~ 252 and ~ 255 cm^{-1} (Table 2 and Fig. 5), for three samples: film1, film2 and film3 respectively, are marked with stars in Fig. 6. These modes are tentatively assigned as $l = 0$, $n = 1$. It is evident that experimental values determine nanocrystals dimension. Modes at frequencies ~ 233, ~ 235 and ~ 246 cm^{-1} (Table 2 and Fig. 5), for samples film1, film2 and film3 respectively, fall on the calculated curves. These modes are tentatively assigned as $l = 0$, $n = 2$. Nanocrystals dimension established by $l = 0$, $n = 1$ modes is definitely confirmed. Despite the situation that in reality there is nanocrystal size distribution, nanocrystal shape irregularity, inhomogeneity inside, Raman spectroscopy enable detection of average particle size as: $r \sim 3.3$ nm (film1), $r \sim 3.4$ nm (film2) and $r \sim 4.3$ nm (film3).
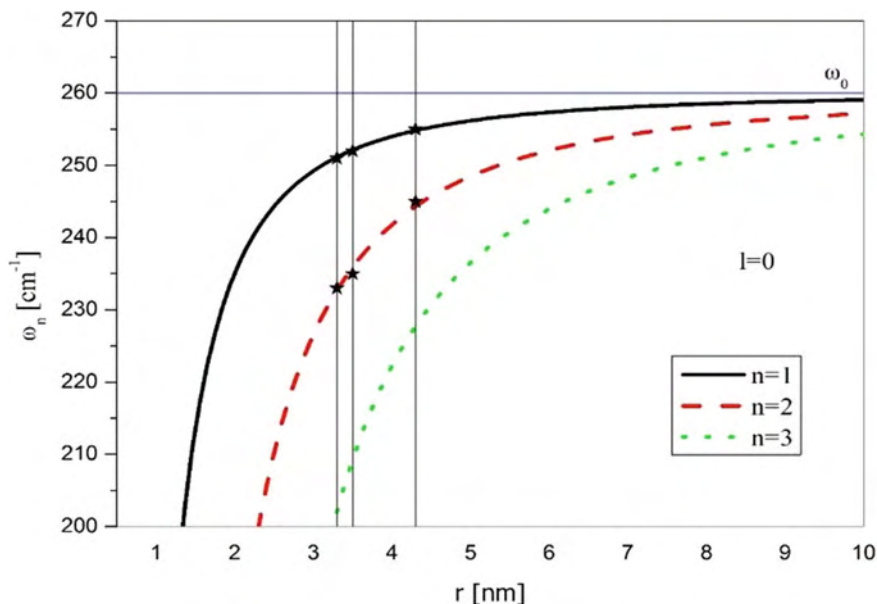
Fig. 6 The radial dependence of $l = 0$ optical modes for $CuSe_2$ spherical nanocrystals

Table 2 Position of registered Raman (IR) active modes (cm^{-1}) of marcasite $CuSe_2$

$l = 0$	Film1	Film2	Film3	[30, 31]	Assignment
$n = 1$	251 (251)	252 (252)	255 (255)	260	A_g^1
$n = 2$	233	235	243		

The mode originating from $CuSe_2$ is broadened and shifted toward lower frequencies in comparison to the bulk system [30, 31]. Shift toward lower frequencies is characteristic for modes of decreasing phonon dispersion relation in bulk. The results of Raman spectroscopy are in good agreement with XRD results. The presence of two crystal phases in synthesized film, the hexagonal Se and orthorhombic $CuSe_2$, is confirmed once again. Small amount of $CuSe_2$ evidenced by XRD is confirmed by low intensity of $CuSe_2$ modes.

3.4 Far-Infrared Spectroscopy

The far-infrared measurements were carried out with a BOMEM DA-8 FIR spectrometer. A DTGS pyroelectric detector was used to cover the wave number range from 90 to 600 cm^{-1}.

The penetration depth of the infrared electromagnetic waves into a nontransparent crystal is approximately 3 μm. Thickness of our films is from 56 to 172 nm, so reflectivity spectra contain information about films together with information about substrate. Three-layer structure is schematically presented in Fig. 7, where medium 1 is air with dielectric function ε_1 ($\varepsilon_1 = 1$), medium 2 is thin Se-CuSe$_2$ mixture layer with corresponding dielectric function ε_2 and medium 3 is glass substrate with dielectric function ε_3. In this case:

$$R_A = \frac{A_r}{A_i} = \frac{\mathbf{r}_{12}e^{-i\alpha} + \mathbf{r}_{23}e^{i\alpha}}{e^{-i\alpha} + \mathbf{r}_{13}\mathbf{r}_{23}e^{i\alpha}} \tag{2}$$

where A_i and A_r are amplitudes of incident and reflection beams, $r_{ij} = (n_i - n_j)/(n_i + n_j) = (\sqrt{\varepsilon_i} - \sqrt{\varepsilon_j})/(\sqrt{\varepsilon_i} + \sqrt{\varepsilon_j})$ are Fresnel coefficients, n_i is complex refractive index of corresponding medium, ε_i complex dielectric constant and $\alpha = 2\pi\omega d(\varepsilon_2)^{1/2}$ is the complex phase change related to the absorption in the medium 2 with the thickness d. The corresponding reflectance (R) is:
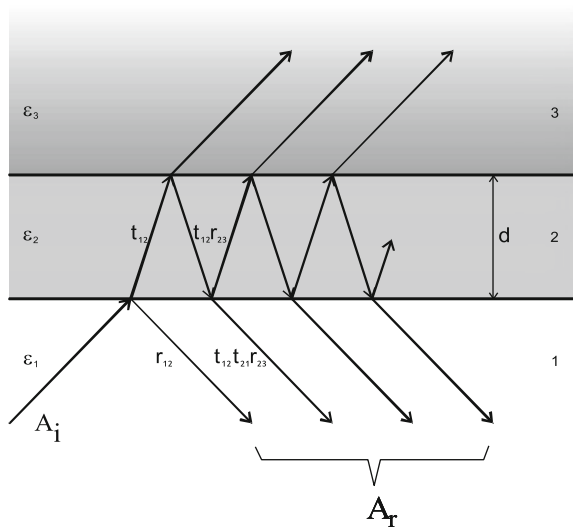
$$R = |R_A| \tag{3}$$

The dielectric function of homogeneous medium is:

$$\varepsilon(\omega) = \varepsilon_\infty \prod_{k=1}^{k=N} \frac{\omega_{LOk}^2 - \omega^2 + i\gamma_{LOk}\omega}{\omega_{TOk}^2 - \omega^2 + i\gamma_{TOk}\omega} \tag{4}$$

where ω_{TO} and ω_{LO} are the transversal and longitudinal optical vibrations, and γ_{TO} and γ_{LO} are damping parameters.

Fig. 7 Schematic presentation of a three-layer structure

The Se-CuSe$_2$ thin films we threat as a mixture of uniformly distributed spherical inclusions of CuSe$_2$ in homogeneous Se. Namely, when visible light interacts with semiconducting nanoparticles (characteristic size L, dielectric function ε'') which are distributed in a medium with the dielectric constant ε', the heterogeneous composite can be treated as a homogeneous medium, and so-called effective medium theory applies.

There are many mixing models for the effective dielectric permittivity of such a mixture [32]. XRD and Raman measurements imply that the structure of our films can be treated as Se film with separated nanocrystals of CuSe$_2$ inside. We decided to use Maxwell–Garnet model for present case, as we did in our previous works [3, 33–36]. For the spherical inclusions case, the prediction of the effective permittivity of mixture ε_{eff} according to the Maxwell–Garnet mixing rule reads [37, 38]:

$$\varepsilon_2 = \varepsilon_{\text{eff}} = \varepsilon' + 3f\varepsilon' \frac{\varepsilon'' - \varepsilon'}{\varepsilon'' + 2\varepsilon' - f(\varepsilon' - \varepsilon'')} \tag{5}$$

Here, spheres of permittivity ε'' are located randomly in homogeneous environment of permittivity ε'. Spheres of permittivity ε'' occupy a volume fraction f. ε' and ε'' are also in form of Eq. (4).

The far-infrared reflection spectra of Se-CuSe$_2$ thin films mixture on glass are presented in Fig. 8. Film thickness increases from the bottom to the top of the Figure. Experimental data are presented by circles, while the solid lines are calculated spectra obtained by a fitting procedure based on the previously presented model.

The far-infrared reflectivity spectrum of the glass substrate is shown in Fig. 8 (bottom). The calculated spectrum, presented by solid line, was obtained using the dielectric function given by Eq. (4). As a result of the best fit we obtained two modes (N = 2). Frequencies of these two modes are $\omega_{TO1} = 438 \text{ cm}^{-1}$, $\omega_{LO1} = 439 \text{ cm}^{-1}$ and $\omega_{TO2} = 471 \text{ cm}^{-1}$, $\omega_{LO2} = 523 \text{ cm}^{-1}$. Frequency values of these modes have remained the same during the fitting procedure for all thin film samples. As the thickness of the film increases, these substrate reflectivity structures become weaker. As concerns fitting procedure, this weakening is the consequence of increasing the film thickness d.

As we know, there are three infra-red active modes: A$_2$, E^1 and E^2. We assumed permittivity of Se ε' in form given by Eq. (4) at positions $\omega_{A2} \sim 105 \text{ cm}^{-1}$, $\omega_{E1} \sim 152 \text{ cm}^{-1}$ and $\omega_{E2} \sim 230 \text{ cm}^{-1}$ (N = 3). To achieve coinciding with the experimental spectra, we modeled, permittivity of CuSe$_2$ ε'' in form given by Eq. (4) (N = 1) at positions 250–255 cm^{-1}. Volume fraction f is of the order of few percentages. Effective permittivity of film is $\varepsilon_2 = \varepsilon_{\text{eff}}$ given by Eq. (5). Additional parameter is the thickness d of the film. Reflectance of the whole structure was calculated by using Eqs. (2) and (3). The best fitting parameters are listed in Tables 1 and 2.

FIR reflectivity measurements are in accordance with the XRD and Raman spectroscopy results. Synthesized films are thin and CuSe$_2$ particles are small. There is certain roughness of the sample surface, and that is why the most phonon

Fig. 8 Far-infrared
reflectivity spectra of
Se-CuSe$_2$ thin films mixture
on glass substrate.
Reflectivity spectra from the
bottom to the *top*: glass
substrate; film1; film2; film3
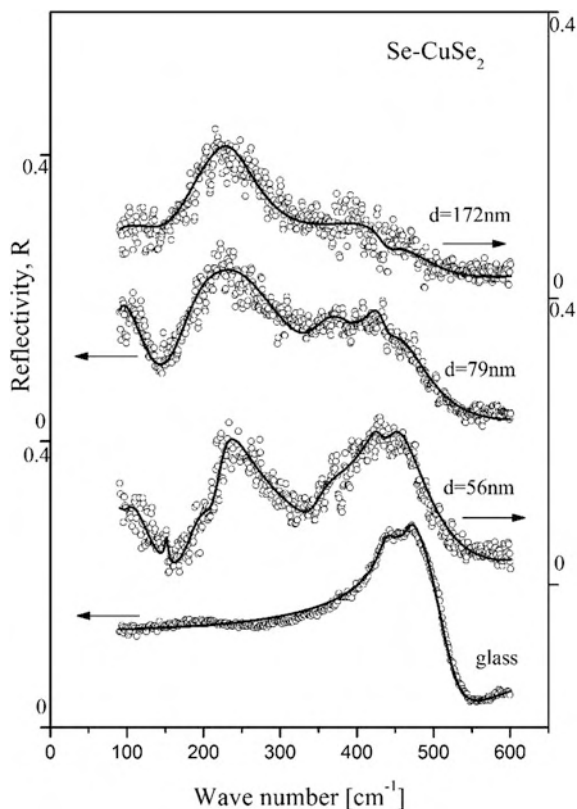
structures in FIR reflectivity spectra are wide and of low intensity. In the central
region, 200–300 cm^{-1}, the modes overlap each the other. As a result there is wide
and complex structure in this spectral region. Low reflectivity level and high noise
compared to it, results in the shape of experimental spectra presented in Fig. 8.
Phonon characteristics are practically transferred from Raman measurements. After
careful and demanding fitting procedure we achieved that calculated FIR reflectivity
spectra reproduce experimental results completely. FIR results, in this case, are used
as kind of control and confirmation of samples structure established by XRD and
Raman spectroscopy.

3.5 UV–VIS Spectroscopy

The UV–VIS diffusion reflectance and transmittance spectra were recorded in the
wavelength range of 300–1000 nm on a Shimadzu UV-2600 spectrophotometer

equipped with an integrated sphere. The diffuse reflectance and transmittance spectra were measured relative to a reference sample of $BaSO_4$.

In this study we used Tauc plot for the determination of optical band gap from diffuse reflectance measurements. The determination of band gap in semiconductors is significant for obtaining the basic solid state physics. The relation expression proposed by Tauc, Davis and Mott [39–41] is following:

$$\alpha h v = A(h v - E_g)^{1/n} \tag{6}$$

where h is a Planck's constant, A is the transition probability constant depending on the effective mass of the charge carriers in the material, E_g is the band gap, hv is the photon energy and α is absorption coefficient which is defined as the relative rate of decrease in light intensity along its propagation path, i.e. a property of a material that defines the amount of light absorbed by it. The value of n denotes the nature of the transition. In case of direct transitions n equals 1/2 and 3/2 for allowed and forbidden transitions, respectively. As for indirect transitions, n equals 2 and 3 for allowed and forbidden transitions, respectively. Since $CuSe_2$ exhibits both direct and indirect allowed transitions, $n = 1/2$ and $n = 2$.

Then, the acquired diffuse reflectance spectra are converted to Kubelka–Munk function [42]:

$$\alpha = \frac{(1 - R)^2}{2R} \tag{7}$$

So using this function, a plot of $(\alpha h v)^{1/n}$ against hv is obtained. The energy band gap is determined by extrapolating the linear portion of $(\alpha h v)^{1/n}$ versus hv to the energy axis at $(\alpha h v)^{1/n} = 0$. The intercept of these plots on the energy axis gives the energy band gap. Such plots are given in Fig. 9. Direct transitions (left part of Fig. 9) reveal band gap for both selenium and $CuSe_2$, while indirect transitions (right part of Fig. 9) reveal band gap for $CuSe_2$ only.

The experimentally determined values of energy gaps for $CuSe_2$ show slight decrease with film thickness and their values range from 2.75 to 2.72 eV for direct transitions, and from 1.75 to 1.71 eV in the case of indirect transitions. As for selenium, estimated band gaps follow the same trend with film thickness and range between 2.33 and 2.36 eV. The estimated band gap positions of each sample are given in Table 3. The difference in film thicknesses causes the small difference in band gaps in second decimal place and they follow the well-established trend—the smaller the thickness, the wider is the band gap. Also, their values are quite wider than the ones that can be found in literature.

References report a large range of energy band gap values for Cu-Se. For direct transitions that values usually go between 2 and 3 eV. Bari et al. [43] obtained the value of 2.51 eV for the sample thickness of 150 nm, and with the increase of film thickness they reported the decrease of band gap width. Grozdanov [44], Garcia et al. [15] and Sakr et al. [45] obtained the value of 2.33, 2.13–2.38 and 2.74 eV respectively. The latter is very similar to the results obtained in this paper. Rajesh
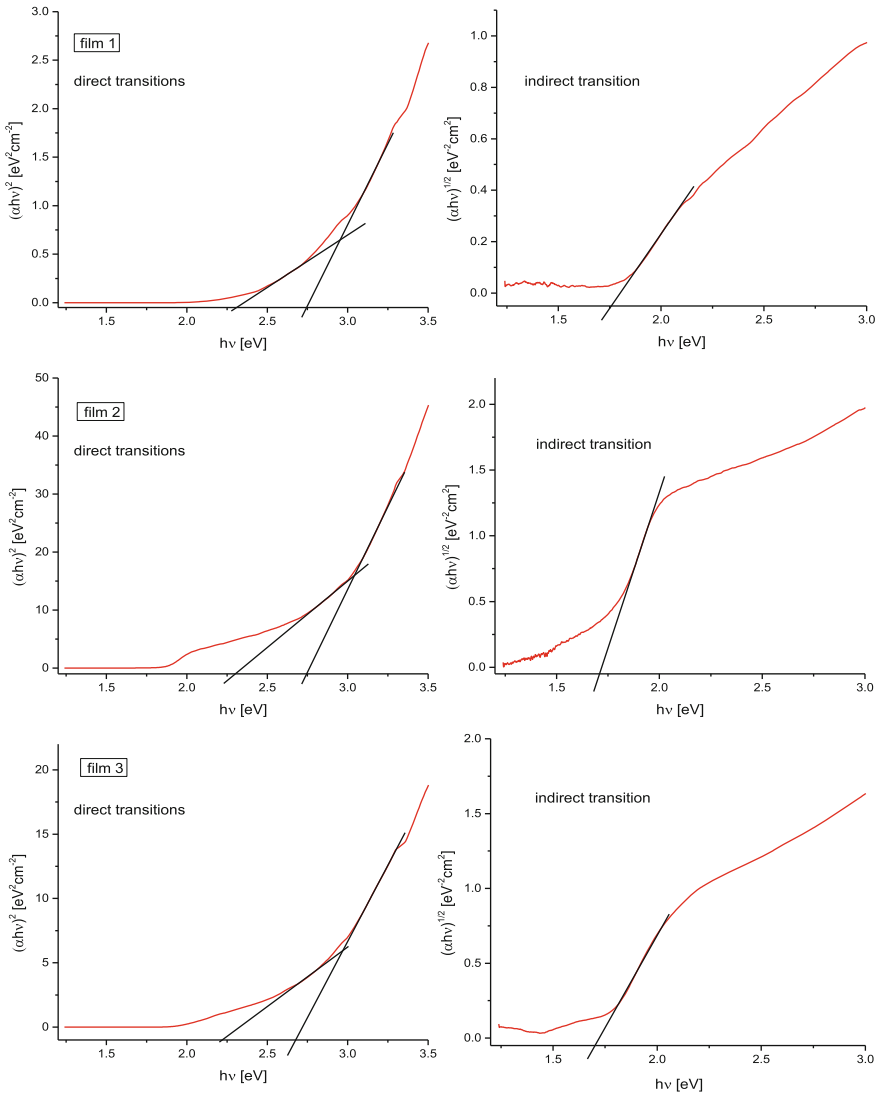
Fig. 9 Dependence of the $(\alpha h\nu)^2$ of the photon energy (hν)—*left side*, and dependence of the $(\alpha h\nu)^{1/2}$ of the photon energy (hν)—*right side*

Table 3 The estimated band gap energies of complex thin films

	Film1	Film2	Film3
CuSe$_2$ direct transition (eV)	2.75	2.74	2.72
CuSe$_2$ indirect transition (eV)	1.75	1.72	1.71
Se direct transition (eV)	2.36	2.34	2.33

et al. [46] got a diversity of band gaps ranging from 1.95 (the thickest film) to 3.70 eV (the thinnest film). As for indirect transitions, they received less attention. In [15] the obtained values are 1.22–1.34 eV, whereas in [47] the value is about 1.4 eV. The values we obtained, ∼1.7 eV, are wider than reported in literature. In our opinion, the larger indirect band gap values are due to quantum confinement effect [48, 49] where by the electrons are localized in individual crystallites.

As for selenium, the direct band gap is reported to be about 2 eV for the bulk [50, 51] and 2.20–2.06 for the thin films of thickness 130–290 nm [52]. Our films are thinner than the ones mentioned in the literature and it is not surprising that we obtained wider band gap values, about 2.3 eV.

3.6 Photoluminescence Spectroscopy

Photoluminescence measurements were obtained by Jobin–Yvon U1000 spectrometer, equipped with RCA-C31034A photomultiplier with housing cooled by Peltier element, amplifiers and counters. As an excitation source, the 488 nm laser line of Argon laser was used.

Photoluminescence spectra can be used for investigation the possible outcomes of photo-induced electrons and holes in a semiconductor, since photoluminescence emission results from the recombination of free charge carriers. A semiconductor is characterized with the electronic band structure and its main features—the valence band or the highest occupied molecular orbital (HOMO) and the conduction band or the lowest unoccupied molecular orbital (LUMO). The difference between the valence band and the conduction band in the means of energy is called band gap (Eg). We talk about two types of photoluminescence phenomenon according to its attributes and formation mechanism: the band-to-band photoluminescence and the excitonic photoluminescence [53]. The band-to-band PL spectrum regards the separation situation of photo-generated charge carriers. The excitonic PL spectrum, however, cannot directly reflect the separation situation of photo-induced carriers. If discrete energy levels are present in the band gap, these may dominate the optical spectrum. PL measurements then yield information about the energetic positions of the electronic states in the gap. Such localized states can originate from various types of imperfections like vacancies, interstitial atoms, atoms at surfaces and grain boundaries. However, it is often difficult to determine the exact position and origin of these states.

Photoluminescence spectra of Cu-Se-CuSe$_2$ thin films on various temperatures are presented in Fig. 11. At room temperature (Fig. 10) in all spectra, the band in red area at about 1.63 eV is clearly seen. According to the UV–VIS results (see previous chapter), we can attribute this mode to band-to-band transition for indirect transition in CuSe$_2$. In green area, a broad band is observed at 2.32 eV which originates from direct transitions in selenium (also see prev. chapter).

Fig. 10 Photoluminescence spectra of Cu-Se-CuSe$_2$ thin films at room temperature
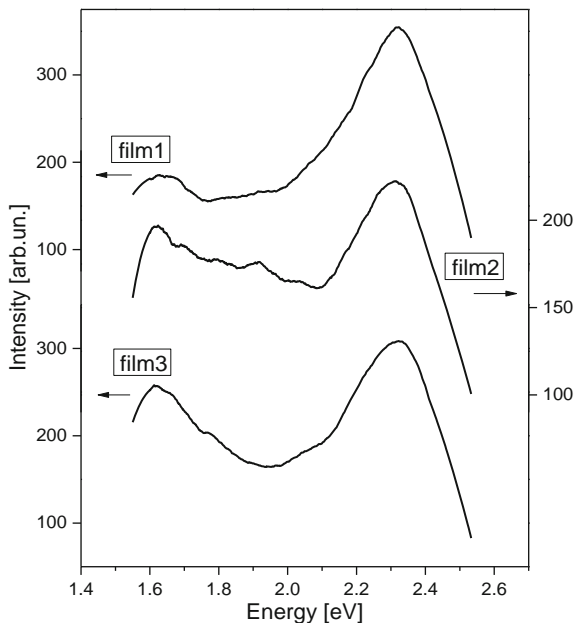
At lower temperatures (Fig. 11a–c) there are several peaks in green, yellow and cyan areas of the spectra, which in our opinion belong to dislocation luminescence or defect luminescence. The mode at $\sim$1.8 eV is clearly seen. According to literature data [51] this band is attributed to selenium defect mode-negative U-center. This mode is expected to appear at 0.5 eV from the band edges. In all spectra, the uprise of peak intensity with lowering temperature is observed.

Temperature dependence of a PL emission bands is shown in Fig. 12. We observe blue shift with increasing temperature for all bands. Shrinking of the band gap with lowering temperature is observed.

A model is proposed by Shen et al. [54] to explain those discrepancies. It involves surface electron accumulation as a result of severe band bending in nanorods. However, the same trend is observed in thin film samples (including ours), whose curvature-less surface does not support a spatial charge separation such as in 1D nanostructures. Wei et al. [55] gave more exact explanation of this phenomenon in their work. They began the analysis by making difference between E_{PL} and E_g:

$$E_{PL}(n, T) = E_g(n, T) + E_{Fn}(n, T) - E_{Fp}(n, T) \tag{8}$$

where E_{Fn} and E_{Fp} are the electron and hole quasi-Fermi levels measured from bottom of conduction band and top of valence band, respectively. So the

Fig. 11 Photoluminescence spectra of Cu-Se-CuSe$_2$ thin films at various temperatures: **a** film1, **b** film2, **c** film3
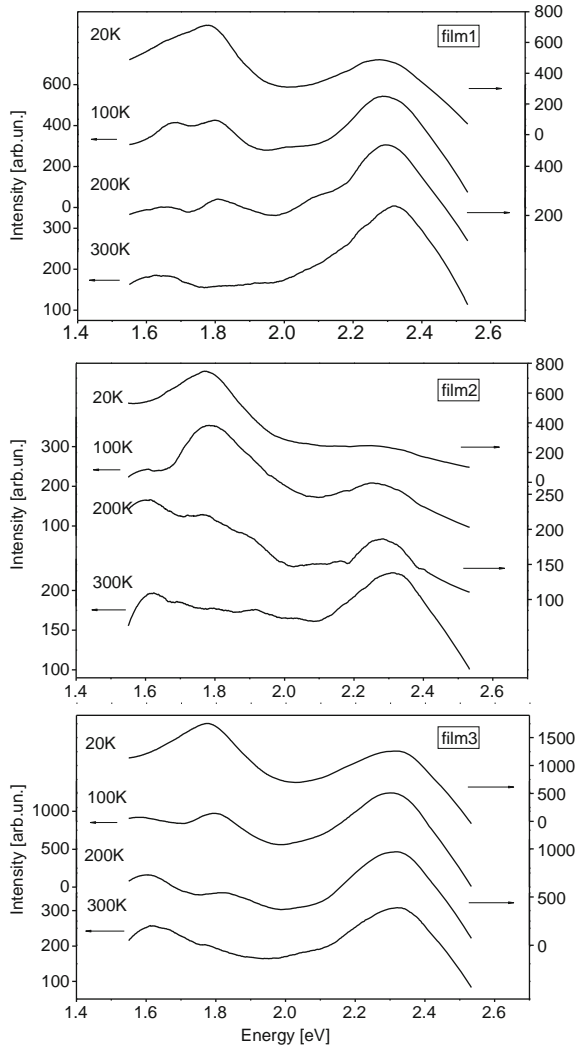
temperature dependence of the band gap shift is the competition between the lattice dilation dE_g/dT on one hand, and the sum $(dE_{Fn}/dT - dE_{Fp}/dT)$ on the other. The former results in conventional red shift of the band gap with increasing temperature, and the latter gets a blue shift. The resulting shift depends on the magnitude of these two contributions. Usually when the electron density n is high, the thermal response in the material is governed by electronic rather than photonic interactions, the sum $(dE_{Fn}/dT - dE_{Fp}/dT)$ becomes dominant thus the blue shift of E_{PL} is observed, as in our case.
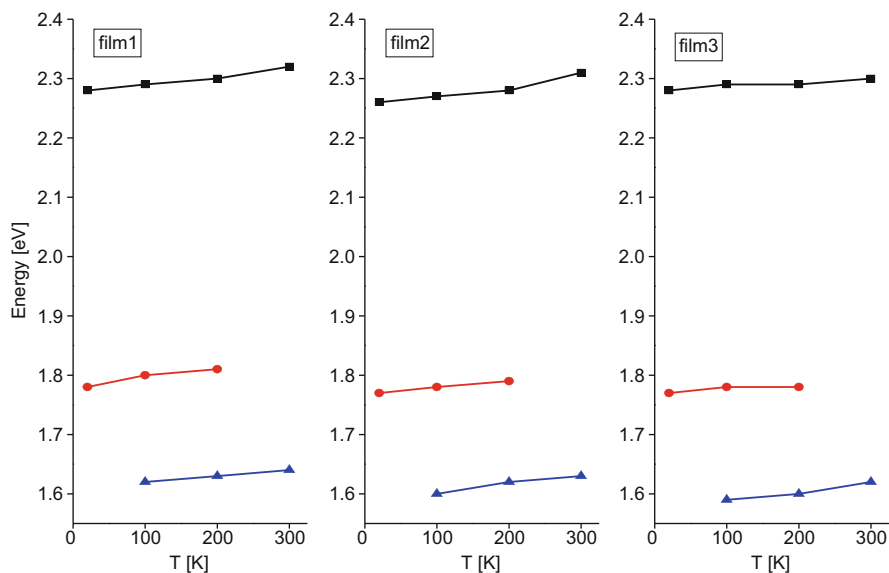
Fig. 12 Temperature dependence of photoluminescence emission bands

4 Conclusions

The optical and structural parameters have been studied for Cu-Se-CuSe$_2$ thin films. The surface morphology of thin films was investigated by AFM and SEM. X-ray diffraction results indicate that thin films have two phases, the solid solution of Cu in Se and the low-pressure modification of CuSe$_2$.

Raman active modes of hexagonal Se are clearly seen and assigned. We tentatively assign modes at 251–255 and 233–243 cm^{-1} as $l = 0$, $n = 1$ and $n = 2$ confined CuSe$_2$ A_g^1 mode. Although assumed model concerns to an ideal spherical nanocrystal, it works well in real samples where there is nanocrystal size distribution, shape irregularity, inside inhomogeneity. Raman spectroscopy enables detection of average particle size as: $r \sim 3.3$ nm (film1), $r \sim 3.4$ nm (film2) and $r \sim 4.3$ nm (film3). Infrared active modes of hexagonal Se that dominate in the reflectivity spectra are identified. Presence of CuSe$_2$ nanocrystals in predominantly Se film was modeled by effective medium theory. Calculated FIR reflectivity spectra reproduce completely experimental ones. FIR reflectivity results confirm the sample structure established by XRD and Raman spectroscopy.

UV–VIS reflectance measurements revealed values for both direct and indirect band gap in CuSe$_2$: ~ 2.7 and 1.7 eV respectively, and direct band gap in Se at ~ 2.3 eV for. The existence of indirect band gap in CuSe$_2$ on this value, somehow wider then in literature, is confirmed by photoluminescence measurements. A band

at ~ 1.8 eV, registered by PL measurements at low temperatures, is attributed to defect level of selenium-negative U-center. In this paper we proved that simple and low-cost technique as vacuum evaporation is capable of producing a high-quality thin films.

References

1. M. Gilic, J. Trajic, N. Romcevic, M. Romcevic, D. Timotijevic, G. Stanisic, I. Yahia, Optical properties of CdS thin films. Opt. Mat. **35**, 1112–1117 (2013)
2. N. Romcevic, M. Petrovic-Damjanovic, M. Romcevic, M. Gilic, L. Klopotowski, W. Dobrowolski, J. Kossut, I. Jankovic, M. Comor, Magnetic field influence on optical properties of $Cd_{1-x}Mn_xS$ (x = 0; 0.3) quantum dots: Photoluminescence study. J. Alloy. Comp. **553**, 75–78 (2013)
3. M. Gilic, N. Romcevic, M. Romcevic, D. Stojanovic, R. Kostic, J. Trajic, W. Dobrowolski, G. Karczewski, R. Galazka, Optical properties of CdTe/ZnTe self-assembled quantum dots: Raman and Photoluminescence spectroscopy. J. Alloy. Comp. **579**, 330–335 (2013)
4. M. Rabasovic, D. Sevic, J. Krizan, M. Rabasovic, S. Savic-Sevic, M. Mitric, M. Petrovic, M. Gilic, N. Romcevic, Structural properties and luminescence kinetics of white nanophosphor YAG:Dy. Opt. Mat. **50**, 250–255 (2015)
5. B. Hadzic, N. Romcevic, M. Romcevic, I. Kuryliszin-Kudelska, W. Dobrowolski, M. Gilic, M. Petrovic Damjanovic, J. Trajic, U. Narkiewicz, D. Sibera, Raman study of surface optical phonons in ZnO(Co) nanoparticles prepared by calcination method. J. Optoelectron. Adv. Mat. **16**, 508–512 (2014)
6. M. Petrović, N. Romčević, M. Romčević, G. Stanišić, D. Vasiljević-Radović, J. Trajić, Z. Lazarević, S. Kostić, Spectroscopy characterization of MnSe nanoclasters randomly distributed in HgMnTe single crystal. J. Crystal Growth **338**, 75–79 (2012)
7. R.D. Heyding, The copper/selenium system. Can. J. Chem. **44**, 1233–1236 (1966)
8. S. Gosavi, N. Deshpande, Y. Gudage, R. Sharma, Physical, optical and electrical properties of copper selenide (CuSe) thin films deposited by solution growth technique at room temperature. J. Alloy. Comp. **448**, 334–338 (2008)
9. P. Hankare, A. Khomane, P. Chate, K. Rathad, K. Garadkar, Preparation of copper selenide thin films by simple chemical route at low temperature and their characterization. J. Alloy. Comp. **469**, 478–482 (2009)
10. V.J. Fulari, V.P. Malekar, S.A. Gangawane, Measurement of properties of copper telluride thin films using holography. Prog. Electromagn. Res. C **12**, 53–64 (2010)
11. H.M. Pathan, C.D. Lokhande, D.P. Amalnerkar, T. Seth, Modified chemical deposition and physicochemical properties of copper (I) selenide thin films. Appl. Surf. Sci. **211**, 48–56 (2003)
12. Y. Takana, N. Uchiyama, S. Ogawa, N. Mori, Y. Kimishima, S. Arisawa, A. Ishii, T. Hatano, K. Togano, Superconducting properties of $CuS_{2-x}Se_x$ under high pressure. Phys. C **341**, 739–740 (2000)
13. G. Krill, P. Panissod, M.F. Lapierre, F. Gautier, C. Robert, M.N. Eddine, Magnetic properties and phase transitions of the metallic CuX_2 dichalcogenides (X = S, Se, Te) with pyrite structure. J. Phys. C **9**, 1521–1533 (1976)
14. M. Kontani, T. Tutui, T. Moriwaka, T. Mizukoshi, Specific heat and NMR studies on the pyrite-type superconductors CuS_2 and $CuSe_2$. Phys. B **284**, 675–676 (2000)

15. V. Garcia, P. Nair, M. Nair, Copper selenide thin films by chemical bath deposition. J. Cryst. Growth **203**, 113–124 (1999)
16. A. Sobhani, M. Salavati-Niasari, A new simple route for the preparation of nanosized copper selenides under different conditions. Ceram. Inter. **40**, 8173–8182 (2014)
17. P. Peranantham, Y. Jeyachandran, C. Viswanathan, N. Praveena, P. Chitra, D. Mangalaraj, S. K. Narayandass, The effect of annealing on vacuum-evaporated copper selenide and indium telluride thin films. Mater. Charact. **58**, 756–764 (2007)
18. H. Okimura, T. Matsumae, Electrical properties of Cu$_{2-x}$Se thin films and their application for solar cells. Thin Solid Films **71**, 53–59 (1980)
19. G.G. Rusu, M. Rusu, M. Girtan, Optical characterization of vacuum evaporated CdZnTe thin films deposited by a multilayer method. Vacuum **81**, 1476–1482 (2007)
20. A.M. Hermman, L. Fabick, Research on polycrystalline thin-film photovoltaic devices. J. Crys. Growth **61**, 658–664 (1983)
21. D.J. Chakrabarti, D.E. Laughlin, The Cu-Se (Copper-Selenium) System. Bull. Alloy Phase Diagrams **2**, 305–315 (1981)
22. P. Cherin, P. Unger, The crystal structure of trigonal selenium locality: synthetic. Inorg. Chem. **6**, 1589–1591 (1967)
23. G. Gattow, Z. Arong, Allg. Chem. **340** (1965) (Calculated from ICSD using POWD-12++, 1997)
24. G. Lucovsky, A. Mooradian, W. Taylor, G.B. Wright, R.C. Keezer, Identification of the fundamental vibrational modes of trigonal, α-monoclinic and amorphous selenium. Solid State Commun. **5**, 113–117 (1967)
25. M.P. Chamberlain, C. Trallero-Giner, M. Cardona, Theory of one-phonon Raman scattering in semiconductor microcrystallites. Phys. Rev. B **51**, 1680–1693 (1995)
26. R. Roca, C. Trallero-Giner, M. Cardona, Polar optical vibrational modes in quantum dots. Phys. Rev. B **49**, 13704–13711 (1994)
27. E. Duval, Far-infrared and Raman vibrational transitions of a solid sphere: selection rules. Phys. Rev. B **46**, 5795–5797 (1992)
28. C. Trallero-Giner, A. Debernardi, M. Cardona, E. Menendez-Proupin, A.I. Ekimov, Optical vibrons in CdSe dots and dispersion relation of the bulk material. Phys. Rev. B **57**, 4664–4669 (1998)
29. J. Trajic, R. Kostic, N. Romčević, M. Romčević, M. Mitric, V. Lazovic, P. Balaz, D. Stojanovic, Raman spectroscopy of ZnS quantum dots. J. Alloy. Comp. **637**, 401–406 (2015)
30. C. Sourisseau, R. Cavagnat, M. Fouassier, The vibrational properties and valence force fields of FeS$_2$, RuS$_2$ Pyrites and FeS$_2$ Marcasite. J. Phys. Chem. Solids, **52**, 537–544 (1991)
31. X. Wu, M. Kanzaki, S. Qin, G. Steinle-Neumann, L. Dubrovinsky, Structural study of FeP$_2$ at high pressure. High Press. Res. **29**, 235–244 (2009)
32. K. Karkkainen, A. Saviola, K. Nikoskinen, in *IEEE Transaction on Geosciences and Remote Sensors*, vol. 39, pp. 1013–1018 (2001)
33. M. Gilic, M. Petrovic, R. Kostic, D. Stojanovic, T. Barudzija, M. Mitric, N. Romcevic, U. Ralevic, J. Trajic, M. Romcevic, I. Yahia, Structural and optical properties of CuSe$_2$ nanoparticles formed in thin solid Cu-Se film. Infrared Phys. Technol. **76**, 276–284 (2015)
34. J. Trajic, M. Gilic, N. Romcevic, M. Romcevic, G. Stanisic, Z. Lazarevic, D. Joksimovic, I. Yahia, Far-infrared investigations of the surface modes in CdS thin films. Phys. Scr. **T162**, 014031–014034 (2014)
35. J. Trajić, N. Romčević, M. Gilić, M. Petrović Damjanović, M. Romčević, V.N. Nikiforov, Optical properties of PbTe0.95S0.05 single crystal at different temperatures: far-infrared study. J. Optoelectron. Adv. Mat. **6**, 543–546 (2012)
36. R. Kostić, M. Petrović-Damjanović, N. Romčević, M. Romčević, D. Stojanović, M. Čomor, Far-infrared spectroscopy of Cd$_{1-x}$Mn$_x$S quantum dots. J. Alloy. Comp. **521**, 134–140 (2012)
37. J.C.M. Garnett, Colours in metal glasses and in metallic films. Trans. R. Soc. CCIII, 385–420 (1904)

38. A. Saviola, I. Lindell, in *PIER 6 Progress in Electromagnetic Research*. Dielectric properties of heterogeneous materials (Amsterdam, Elsevier), pp. 101–51
39. J. Tauc, R. Grigorovici, A. Vancu, Optical properties and electronic structure of amorphous Germanium. Phys. Status Solidi **15**, 627 (1966)
40. J. Tauc, F. Abeles, in *Optical Properties of Solids* (North Holland, 1972)
41. E. Davis, N. Mott, Conduction in non-crystalline systems V. Conductivity, optical absorption and photoconductivity in amorphous semiconductors. Phil. Mag. **22**, 903–922 (1970)
42. P. Kubelka, F. Munk, Ein Beitrag zur Optik der Farbanstriche. Z. Tech. Phys. **12**, 593–601 (1931)
43. R. Bari, V. Ganesan, S. Potadar, L. Patil, Structural, optical and electrical properties of chemically deposited copper selenide films. Bull. Mater. Sci. **32**, 37–42 (2009)
44. I. Grozdanov, Electroconductive copper selenide films on transparent polyester sheets. Synth. Metals. **63**, 213 (1994)
45. G. Sakr, I. Yahia, M. Fadel, S. Fouad, N. Romcevic, Optical spectroscopy, optical conductivity, dielectric properties and new methods for determining the gap states of CuSe thin films. J. Alloy. Comp. **507**, 557–562 (2010)
46. D. Rajesh, R. Chandrakanth, C. Sunandana, Annealing effects on the properties of copper selenide thin films for thermoelectric applications. J. Appl. Phys. **4**, 65–69 (2013)
47. V.M. Bhuse, P.P. Hankare, K.M. Garadkar, A.S. Khomane, A simple, convenient, low temperature route to grow polycrystalline copper selenide thin films. Mater. Chem. Phys. **80**, 82–87 (2003)
48. G. Hodes, A. Albu-Yayor, F. Decker, P. Motisuke, High thin-film yield achieved at small substrate separation in chemical bath deposition of semiconductor thin films. Phys. Rev. B **36**, 4215–4219 (1987)
49. V. García, M. Nair, P. Nair, R. Zingaro, Chemical deposition of bismuth selenide thin films using N,N-dimethylselenourea. Semicond. Sci. Technol. **12**, 645–649 (1997)
50. S. Kasap, J.B. Frey, G. Belev, O. Tousignant, H. Mani, L. Laperriere, A. Reznik, J.A. Rowlands, Amorphous selenium and its alloys from early xeroradiography to high resolution X-ray image detectors and ultrasensitive imaging tubes. Phys. Status Solid **246**, 1794–1801 (2009)
51. M. Benkhedir, Defect levels in amorphous selenium bandgap. Katholieke Universiteit Leuven PhD Thesis (2006)
52. M. Singh, K. Bhahada, Y. Vijay, Optical band gap of $In_{0.1}Bi_{1.9}Te_3$ thin films. Indian J. Pure Appl. Phys. **43**, 129–135 (2005)
53. F.B. Li, H.Z. Li, Photocatalytic properties of gold/gold ion-modified titanium dioxide for wastewater treatment. Appl. Catal. A **228**, 15–23 (2002)
54. C.H. Shen, H.Y. Chen, H.-W. Lin, S. Gwo, A.A. Klochikhin, V.Y. Davydov, Structure and photoluminescence properties of epitaxially oriented GaN nanorods grown on Si (111) by plasma-assisted molecular-beam epitaxy. Appl. Phys. Lett. **88**, 253104–253112 (2006)
55. P. Wei, S. Chattopadhyay, F. Lin, C. Hsu, S. Jou, J. Chen, P. Huang, H. Hsu, H. Shih, K. Chen, L. Chen, Origin of the anomalous temperature evolution of Photoluminescence peak energy in degenerate InN nanocolumns. Opt. Express. **17**, 1160–11697 (2009)

Optical Properties of Plastically Deformed Copper: Ellipsometry and Raman Study

M. Gilić, M. Petrović, B. Hadžić, Z.Ž. Lazarević, M. Romčević,
J. Trajić and N.Ž. Romčević

Abstract In this paper, we used Raman spectroscopy and spectroscopic ellipsometry to investigate optical properties of plastically deformed copper. Chemically pure copper prepared in a sample of square cross section (10×10 mm^2) and about 50 mm long was extremely plastically deformed with the repeated application of Equal Channel Angular Pressing. Information about microstructure with ultrafine grains is obtained by atomic force microscopy. The structure of the sample surface —the copper oxide and surface roughness over-layer—was registered by spectroscopic ellipsometry. By Raman spectroscopy, two types of lines are registered: narrow, with the width ~7 cm^{-1}; and wide, ~40 cm^{-1}, which implies that nano-sized crystal structures related to three-dimensional amorphous boundary spaces exist in the specimen.

Keywords Copper · Amorphization · Plastic deformation · Spectroscopic ellipsometry · Raman spectroscopy

1 Introduction

In last two decades, a great interest has been expressed in research regarding a severe plastic deformation technique called Equal Channel Angular Pressing (ECAP). Vast number of papers has been published in wake of pioneering work of Valiev et al. [1] and Segal [2]. The reason for this interest lies in the fact that metals and alloys that endured ECAP exhibit a very small grain size and, as a consequence, their tensile strength is remarkably improved. All relevant work about this severe plastic deformation technique is summarized in the [3]. In the studies of [4] and [5], a model is developed that describes how, in severely deformed materials, grain subdivision

M. Gilić (✉) · M. Petrović · B. Hadžić · Z.Ž. Lazarević · M. Romčević ·
J. Trajić · N.Ž. Romčević
Institute of Physics, University of Belgrade, Belgrade, Serbia
e-mail: martina@ipb.ac.rs

occurs by the formation of cell blocks separated by sets of dislocations. Within these cells, there are regions relatively free of dislocations, which are bounded with low-angle boundaries. Cell blocks become narrower and narrower with increasing the degree of deformation, which leads to transformation of cell boundaries into high-angle boundaries. This fact, often observed in plastically deformed metals and alloys, seems to explain the formation of very small grains [6, 7].

On the other hand, copper is used in a vast variety of products in both domestic and industrial domains as a thermal and electrical conductor, as well as a constituent of various metal alloys [8]. Among metals, only silver has higher electrical conductivity, but copper is much cheaper and more abundant. Due to this property, copper has been used widely as an electrode in electrochemical studies [9]. Since it is both ductile and malleable copper is easy to treat. The ease with which it can be drawn into wire makes it useful for electrical work, in addition to its excellent electrical properties. Copper can be machined, although it is usually necessary to use an alloy for complicated parts, to get really good mixed characteristics. Good thermal conduction makes it useful for heat sinks and in heat exchangers. Copper has good corrosion resistance, nevertheless not as good as gold. It has excellent brazing and soldering properties and can also be welded, and the best results are obtained with gas metal arc welding [10].

The colour of copper samples is usually reddish to brownish due to the existence of thin layers on their surface (mostly oxide), which are formed gradually when gases (especially oxygen) react with them in the air. Still, the colour of the clean surface is much brighter (pink or bright brown). Copper has its characteristic colour because of its unique band structure. Copper, caesium, and gold are the only three elemental metals with a natural colour other than grey or silver [11]. The usual grey colour of metals depends on their "electron sea", which is capable of absorbing and re-emitting photons over a wide range of frequencies.

In this paper, we present the results of AFM, spectroscopic ellipsometry, and Raman spectroscopy measurements of plastically deformed copper.

2 Experimental

2.1 Samples Preparation

A chemically pure copper sample (99.99), prepared as a specimen of square cross section (10×10 mm^2) and about 50 mm long, was extremely plastically deformed with the repeated application of Equal Channel Angular Pressing (ECAP). ECAP, which is known as one of the discontinuous processes of severe plastic deformation, was applied as an effective technique for producing bulk nano-scaled structures.

The experiments were performed in our experimental hydraulic press (VEB WEMA 250 MP), equipped with a tool for Equal Channel Angular Pressing (ECAP). The tool consists of two intersecting channels of the same cross

Fig. 1 Obtaining samples: **a** Cu 1.1P; **b** Cu 1.2V
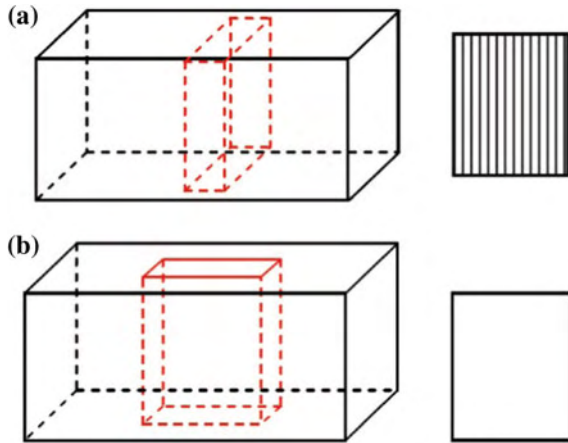
section (10×10 mm^2) that meet at the angle $2\Phi = 90°$. The geometry of the tool provides that the material is deformed by simple shear at ideal, frictionless conditions. The cross section of the specimen remains almost equal before and after each step of the process; thus, it is possible to subject one specimen to ECAP several times in order to reach high degrees of plastic deformation. In our case, the sample of chemically pure copper was subjected eight times to the ECAP process at room temperature (20 °C). This processing, performed at low homologous temperatures, led to a subdivision of the initially coarse-grained microstructure into a hierarchical system of cell blocks and dislocation cells. With increasing strain of the material, the size of both of these constituents decreased.

Two samples were prepared for microstructure investigation: Cu 1.1P—cross-sectional surface and Cu 1.2V—longitudinal section surface, Fig. 1.

2.2 Devices and Measurements

The surface morphology of thin films was investigated by atomic force microscopy (AFM). AFM imaging was done using the NTEGRA Prima system from NT–MDT. Typical tip curvature radius was 8–10 nm. All AFM measurements were performed at room temperature and under ambient conditions.

The ellipsometric measurements were performed using a variable angle spectroscopic ellipsometer (VASE) SOPRA GES5-IR in the rotating polarizer configuration. The data were collected over the range 1.5–4.2 eV with the step of 0.05 eV for three different angles of incidence 65°, 70°, and 75°. The 70° angle was chosen for its maximum sensitivity of the ellipsometric data.

The fitting of the model to the experimental data was done using the Levenberg–Marquardt algorithm, to minimize the value of the following merit function [12, 13]:

$$\chi^2 = \frac{1}{2N - P - 1} \sum_{i=1}^{N} \frac{\left(<\tan(\psi)>_{\text{exp}} - <\tan(\psi)>_{\text{cal}} \right)^2}{\sigma_{1,i}^2}$$
$$+ \frac{\left(<\cos(\Delta)>_{\text{exp}} - <\cos(\Delta)>_{\text{cal}} \right)^2}{\sigma_{2,i}^2} \tag{1}$$

where N is the total number of data points; P is the number of fitted parameters; $<\tan(\psi)>$ exp, $<\tan(\psi)>$ cal and $<\cos(\Delta)>$ exp, $<\cos(\Delta)>$ cal represent the experimental and calculated values of ellipsometric quantities, $\tan(\psi)$ and $\cos(\Delta)$; and σ_i is the error of each measured quantity. All calculations were made using Winelli_II, Version 2.0.0.0.

The micro-Raman spectra were taken in the backscattering configuration and analyzed by Jobin Yvon T64000 spectrometer, equipped with nitrogen-cooled charge-coupled device detector. As an excitation source, we used the 514.5-nm line of an Ar-ion laser. The measurements were performed at different laser power.

3 Results and Discussion

3.1 Atomic Force Microscopy

The surfaces of the samples have been investigated using atomic force microscopy (AFM). Figure 2a shows a typical picture of a started Cu sample. Figure 2b, c shows typical topological morphology in two directions (longitudinal and transverse). On the transverse surface, more contour particles can be seen, which probably correspond to the nano-sized crystalline phases. Contrary to this, on the longitudinal surface, there are essentially less phases, which could be compared to the phases formed on the transverse surface.
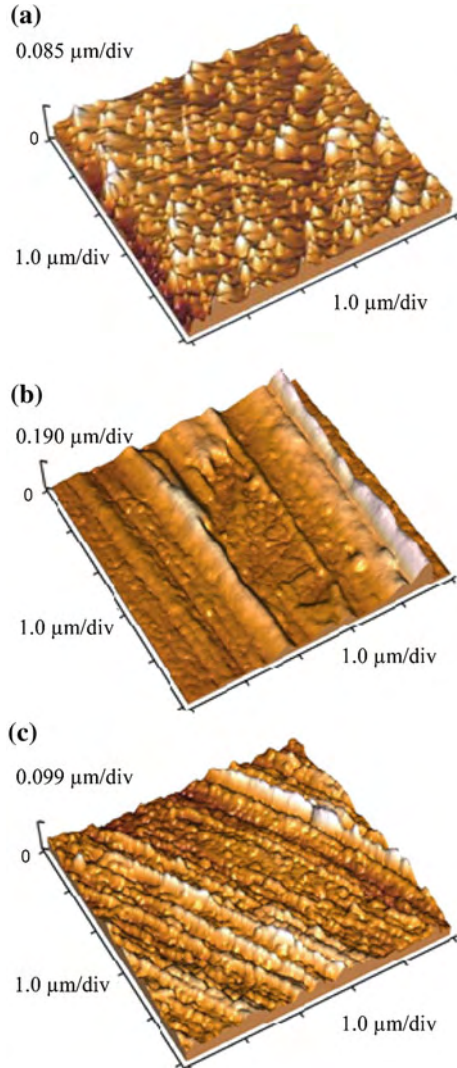
3.2 Spectroscopic Ellipsometry

Spectroscopic ellipsometry (SE) is a surface-sensitive, non-destructive optical technique used to characterize surface changes, optical constants of bulk or layered materials, over-layer thicknesses, multi-layer structures, and surface or interface roughness [13]. Ellipsometry measures $\tan(\psi)$ and $\cos(\Delta)$ spectra which are, respectively, the amplitude and projected phases of the complex ratio:

$$\rho = r_p/r_s = \tan(\psi)e^{i\Delta} \tag{2}$$

where r_p and r_s are the complex reflectance coefficients of light, polarized parallel (p), and perpendicular (s) to the plane of incidence, respectively. Ellipsometric

Fig. 2 AFM image of surface
of the **a** pure Cu; **b** Cu 1.2V;
c Cu 1.1P sample

(a)

0.085 µm/div

0

1.0 µm/div

1.0 µm/div

(b)

0.190 µm/div

0

1.0 µm/div

1.0 µm/div

(c)

0.099 µm/div

0

1.0 µm/div

1.0 µm/div

quantities ψ and Δ are sensitive to changes of different parameters such as surface
conditions, over-layer structure, and dielectric function of the material and others.

When it is exposed to oxygen, copper oxidizes naturally to copper (I) oxide
(Cu_2O). The influence of the surface roughness also has to be taken into account.
Figure 3 presents both real and imaginary parts of pseudodielectric function for the
bulk copper and samples Cu 1.1P and Cu 1.2V. Therefore, the ellipsometric spectra
($\tan(\psi)$, $\cos(\Delta)$) of the two samples Cu 1.1P and Cu 1.2V were fitted using a
two-film model: Cu as a substrate, an over-layer of Cu_2O, and a surface roughness
layer, Fig. 4c. The surface roughness over-layer is composed of the bulk copper

Fig. 3 a Real and **b** imaginary part of pseudodielectric function for Cu1.1P (*squares*), Cu1.2V (*triangles*), and bulk copper (*solid line*)
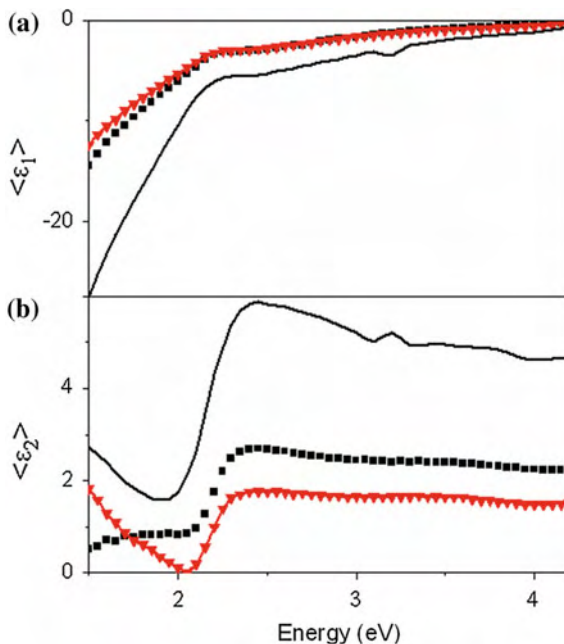
oxide and an ambient. Using Bruggeman effective medium approximation [6], we calculated the volume fraction of the constituents.

Figure 4a presents the experimental and the best fitting data of the sample Cu 1.1P. The thickness of the Cu_2O is ~ 1.5 nm, and the roughness over-layer, with 80 % of Cu_2O and 20 % of void, is ~ 25.6 nm. For the energies above 2 eV, this fit is better than for the energies around and below this value. This may indicate that the dielectric function of the sample substrate is different from the one of the bulk copper taken from Palik [14] and that these changes are due to plastic deformation.

The best fit to the model of the sample Cu 1.2V is presented in Fig. 4b. The thickness of the copper oxide is ~ 1.7 nm, and the roughness over-layer, with 81 % of the oxide and 19 % of the void, is ~ 35 nm. Comparing these two fits, one can see that, in the case of the Cu 1.1P sample, the model with Cu_2O and surface roughness is better suited than in the case of the Cu 1.2V sample.

3.3 Raman Spectroscopy

Pure copper in principle crystallized in the face-centred cubic type structure (O_h space group symmetry), so the first-order Raman modes are not active. However, plastic deformation of the sample and the penetration of oxygen into the sample (and creating CuO) cause the appearance of Raman active modes. Factor group analysis for CuO yields [15]:

Fig. 4 a Experimental data (*dots*) and fitted data (*solid line*) of the sample Cu 1.1P; **b** experimental data (*dots*) and fitted data (*solid line*) of the sample Cu 1.2V; **c** sketched model
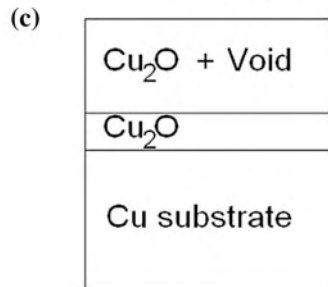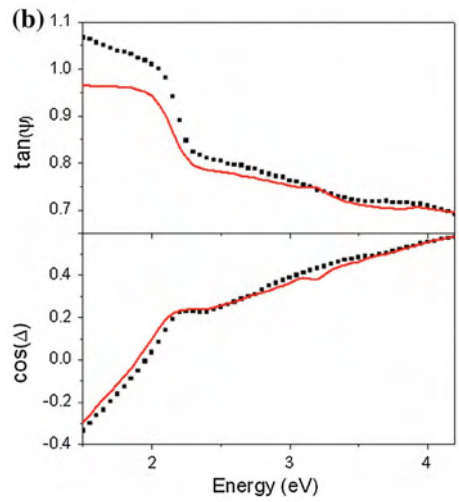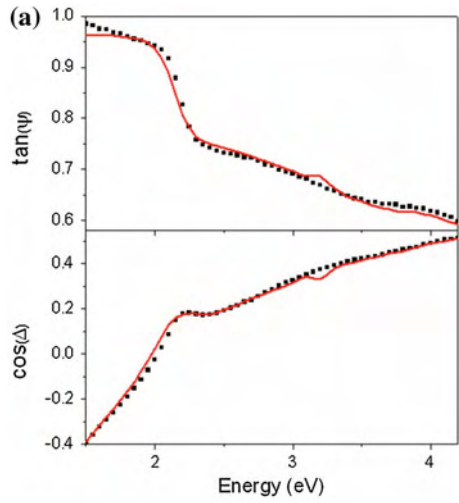
$$Cu(C_i): \Gamma = 3A_u + 3B_u \tag{3}$$

$$O(C2): \Gamma = A_g + 2B_g + A_u + 2B_u \tag{4}$$

$$\Gamma CuO = A_g + 2B_g + 4A_u + 5B_u \tag{5}$$

Of these modes, $1A_u(T_y)$ and $2B_u(T_x, T_z)$ are acoustical modes, so that the total of vibrational modes ($q = 0$) and their activity is:

$$\Gamma_{CuO}^{vib} = A_g(R) + 2B_g(R) + 3A_u(IC) + 3B_u(IC) \tag{6}$$

Thus, three Raman (A_g, B_g) and six infrared (A_u, B_u) active modes are to be expected in the spectra of CuO.

The Raman spectra of Cu 1.2V and Cu 1.1P are presented in Figs. 5 and 6. In addition to a very narrow line (with a width of ~ 2 cm^{-1}), two types of lines are clearly visible in the spectra: narrow (~ 7 cm^{-1}) and wide (~ 40 cm^{-1}) lines. To demonstrate the nature of these very narrow lines in the range up to 120 cm^{-1}, the spectrum of nitrogen is given on the insert of Fig. 5. It is obvious that the positions of these narrow lines from the insert match corresponding lines registered in the spectrum on Figs. 5 and 6. So it can be concluded that they are the parasite lines. The narrow lines are well defined, so we used the deconvolution method in analysis of the wide lines. Raman scattering spectra are often analyzed with the help of a Lorentzian function or by the convolution of a Lorentzian and Gaussian curves [16]. As the quality of the spectra in Figs. 5 and 6 is such that it allows only a qualitative analysis with a partial discussion of the trend, we assumed that all lines are of the Lorentzian type. A typical line shape obtained in this way is also shown in Figs. 5 and 6. Dashed lines correspond to the Rayleigh scattering and

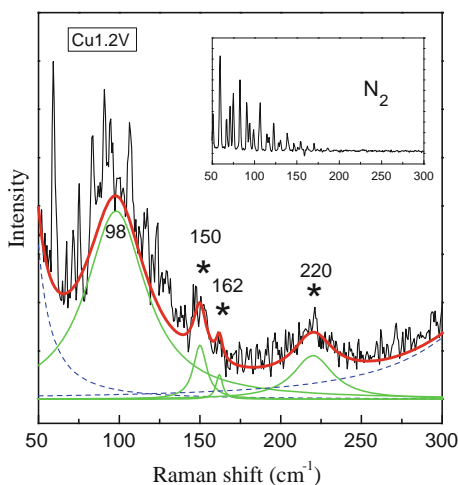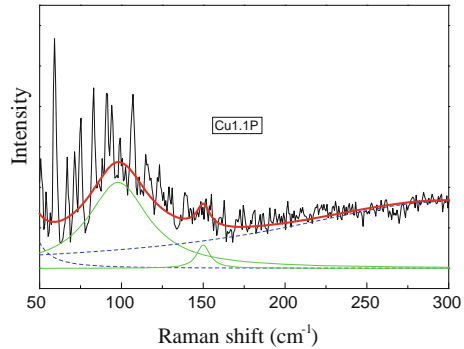Fig. 5 Raman spectra of Cu 1.2V sample. *Inset* Raman spectra of N$_2$

Fig. 6 Raman spectra of Cu
1.1P sample

luminescence [17]. Well-resolved peaks appear at about 98, 150, 162, and
220 cm^{-1} for the sample Cu 1.2V (Fig. 5) and at 98 and 150 cm^{-1} are observed for
the sample Cu 1.1P (Fig. 6). Differences in the spectra originated from the different
deformation.

Narrow lines, which are marked by stars in Fig. 5, originated from the crystal
structures Cu and CuO. The appearance of CuO modes, as we have already said, is
a consequence of the oxygen penetration in the sample. The registered lines orig-
inate from Cu–Cu and Cu–O [15]. The wide line is a consequence of the amorphous
state. Namely, the wide line at 98 cm^{-1} originated from CuO that became amor-
phous. In this range, the CuO phonon state density is large [15], and therefore, the
line is no longer narrow.

The mode at 220 cm^{-1} is probably a consequence of the multi-phonon process.
The absence of those structures in the Cu 1.1P Raman spectra points to the influ-
ence of material treatments on the structure of Cu and CuO. The existence of two
types of lines indicates that nano-sized crystal structures of both Cu and CuO
related to three-dimensional amorphous boundary spaces exist in the specimen,
which indicates that the plastic deformation of the sample did not lead to total
amorphization of the specimen.

4 Conclusion

In our research, we investigated optical properties of two samples of plastically
deformed copper: Cu 1.1P—cross-sectional surface and Cu 1.2V—longitudinal
surface. The two-film model was used to calculate the thickness of spontaneously
formed copper oxide and surface roughness (ellipsometric measurements). In
Raman spectra, two types of lines are registered: narrow (with width of ~7 cm^{-1})
and wide (~40 cm^{-1}). Narrow lines originate from crystal phases of Cu and CuO.
Wide line at 98 cm^{-1} originates from CuO that became amorphous. The existence
of two types of lines indicates that nano-sized crystal structures of both Cu and CuO

are surrounded in all three dimensions with amorphous phases, which implies that the plastic deformation of the sample did not lead to total amorphization of the specimen.

References

1. R. Valiev, A. Korznikov, R. Mulykov, Structure and properties of ultrafine-grained materials produced by severe plastic deformation. Mater. Sci. Eng. A **168**, 141–148 (1993)
2. V. Segal, Materials processing by simple shear. Mater. Sci. Eng. A **197**, 157–164 (1995)
3. R. Valiev, T. Langdon, Principles of equal-channel angular pressing as a processing tool for grain refinement. Prog. Mater. Sci. **51**, 881–981 (2006)
4. Q. Liu, N. Hansen, Macroscopic and microscopic subdivision of a cold-rolled single crystal of cubic orientation. Proc. R. Soc. **A454**, 2555–2591 (1998)
5. B. Bay, N. Hansen, D. Huges, D. Kuhlmann-Wilsdorf, Overview no. 96 evolution of f.c.c. deformation structures in polyslip, Acta Merallurgica Materialia, **40**, 205–219 (1992)
6. Y. Iwahashi, Z. Horita, M. Nemoto, T. Langdon, The process of grain refinement in equal-channel angular pressing. Acta Mater. **46**, 3317–3331 (1998)
7. C. Xu, M. Furukawa, Z. Horita, T. Langdon, Developing a model for grain refinement in equal-channel angular pressing. Mater. Sci. Forum **503–504**, 19–24 (2006)
8. N. Habbache, N. Alane, S. Djerad, L. Tifouti, Leaching of copper oxide with different acid solutions. Chem. Eng. J. **152**, 503–508 (2009)
9. G. Karim-Nezhad, R. Jafarloo, P. Seyed Dorraji, Copper (hydr)oxide modified copper electrode for electrocatalytic oxidation of hydrazine in alkaline media, Electrohimica Acta **54**, 5721–5726 (2009)
10. W.F. Smith, J. Hashemi, *Foundations of Materials Science and Engineering*, 4th edn. (McGraw-Hill, Boston, 2006)
11. C. William, C. Robert, *Chambers's Information for the People.L*, 5th edn. (W. & R. Chambers, Edinburgh, 1884)
12. M. Losurdo, Relationships among surface processing at the nanometer scale, nanostructure and optical properties of thin oxide films. Thin Solid Films **455–456**, 301–312 (2004)
13. R.M.A. Azzam, N.M. Bashara, *Ellipsometry and Polarized Light* (North-Holland, Amsterdam, 1977)
14. E.D. Palik, *Handbook of Optical Constants of Solids* (Academic Press, Waltham, 1985)
15. G. Kliche, Z.V. Popovic, Far-infrared spectroscopic investigations on CuO. Phys. Rev. B **42**, 10060–10066 (1990)
16. Z.Ž. Lazarević, S. Kostić, M.J. Romčević, J. Trajić, B. Hadžić, D. Stojanović, N.Ž. Romčević, Study of Bi12SiO20 single crystals obtained by Czochralski method. Optoelectron. Adv. Mater.—Rapid Commun. **5**, 150–152 (2011)
17. B.N. Henry, in *Raman Spectroscopy: Sixty Years On*, vol. 10, ed. by J.R. During (Elsevier, Amsterdam, 2008)

Optical Properties and Electron–Phonon Interactions of $CdTe_{1-x}Se_x(In)$ Single Crystal

M. Petrović, J. Trajić, M. Gilić, M. Romčević, B. Hadžić, Z. Lazarević and D. Stojanović

Abstract The far-infrared reflectivity spectra of $CdTe_{0.97}Se_{0.03}$ and $CdTe_{0.97}Se_{0.03}(In)$ single crystals were measured at different temperatures. The analysis of the far-infrared spectra was carried out by a fitting procedure based on the dielectric function which includes spacious distribution of free carrier as well as their influence on the plasmon–phonon interaction. We found that the long wavelength optical phonon modes of $CdTe_{1-x}Se_x$ mixed crystals exhibit a two-mode behavior. The local In mode at about 160 cm^{-1} is observed. In both samples, a surface layer with a low concentration of free carriers is formed.

Keywords Semiconductors · Electron–phonon interactions · Light absorption and reflection

1 Introduction

The optical, structural, and electrical properties of II–VI compound semiconductors with band gap energies ranging from 0 to 4 eV are appealing for ultrasensitive multiplexing/multicolor applications in a variety of emerging areas of biotechnology, nanoscale optoelectronics, and nanophotonics. By varying the composition and controlling the lattice constants in ternary or quaternary alloys, we can achieve greater flexibility of tuning emission and absorption wavelengths for high-efficiency solid-state light emission sources.

These compounds crystallize in zinc-bland and wurtzite structure. These structures are the two combinations of the tetrahedral sp^3 bonded lattice sites with the outermost cations d-states influencing the bonding. These states lie in or close to the energy regime of the usual valence states which affect the band structure and optical

M. Petrović (✉) · J. Trajić · M. Gilić · M. Romčević · B. Hadžić · Z. Lazarević · D. Stojanović
Institute of Physics, University of Belgrade, Belgrade, Serbia
e-mail: milicap@ipb.ac.rs

properties. Intermediate values of energy gaps, lattice parameters, and other properties can be obtained by forming ternary and quaternary compounds. Ternary compounds have been extensively studied by vibration spectroscopy with a emphasize on nanometer-size-related effects [1–5].

The subject of this paper is $CdTe_{1-x}Se_x$ mixed crystal doped with In. In this work, the reflectivity spectra of the $CdTe_{0.97}Se_{0.03}$ and $CdTe_{0.97}Se_{0.03}(In)$ at different temperatures have been present. These spectra were analyzed using the dielectric function which includes plasmon–phonon interaction [6]. As the result of the best fit, the TO and LO local mode frequencies were determined. The model of phonon mode behavior for these mixed crystals based on Genzel's model [7] was used.

2 Experimental

Single crystals of $CdTe_{1-x}Se_x$ were grown by the Bridgman method at the Institute of Physics, Polish Academy of Sciences, Warsaw.

Far-infrared reflection spectra were measured at 80 and 300 K in the spectral range from 80 to 650 cm^{-1}, carried out with a BOMEM spectrometer.

3 Results and Discussion

The far-infrared reflection spectra of $CdTe_{0.97}Se_{0.03}$ single crystal sample are shown in Fig. 1. The experimental data are represented by circles. In the spectra, two dominant structures at about 140 and 170 cm^{-1} are clearly visible. As we will show later, the feature at about 140 cm^{-1} corresponds to the longitudinal–transverse (LO–TO) splitting of the CdTe-like mode. The feature at about 170 cm^{-1} is related to the CdSe-like mode.

The theoretical model for the bulk dielectric function has been discussed by several authors [8, 9]. We note briefly that the low-frequency dielectric properties of CdTe and CdSe have been described with not less than two classical oscillators ($l \geq 2$) corresponding to the TO modes, superimposed by a Drude part that takes into account the free carrier contribution [10]:

$$\varepsilon_S(\omega) = \varepsilon_\infty + \sum_{k=1}^{l} \frac{\varepsilon_\infty \left(\omega_{LOk}^2 - \omega_{TOk}^2 \right)}{\omega_{TOk}^2 - \omega^2 - i\gamma_{TOk}\omega} - \frac{\varepsilon_\infty \omega_P^2}{\omega(\omega + i\gamma_P)} \tag{1}$$

where ε_∞ is the bound charge contribution and is considered as a constant, ω_{LOk} and ω_{TOk} are the longitudinal and transverse optical phonon frequencies, and ω_P is the plasma frequency, while γ_{LOk} and γ_{TOk} indicate the damping of uncoupled

Fig. 1 Far-infrared reflection spectra of CdTe$_{0.97}$Se$_{0.03}$ at different temperatures. The experimental spectra are presented by *circle*. The *solid* and *dashed lines* are calculated spectra obtained by fitting procedure based on the model given by Eqs. (1) and (2)
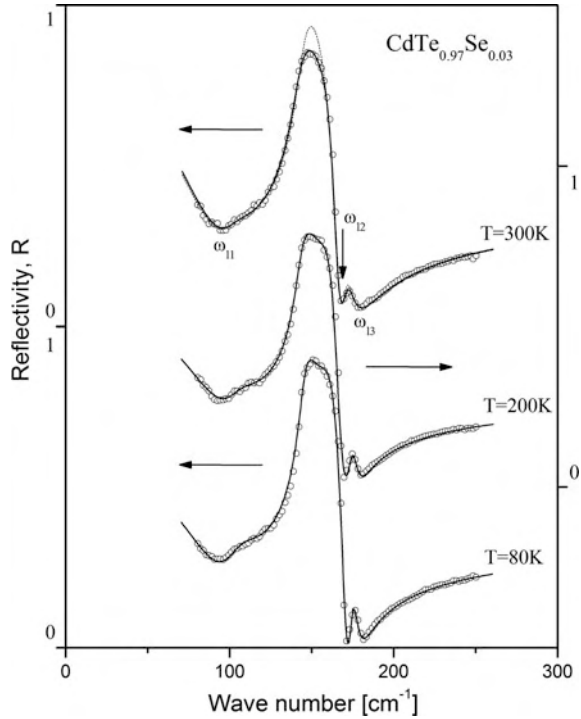
modes of the host crystal and the γ_P value describes the plasmon mode damping coefficient. As a result, a combined plasmon–LO phonon modes (ω_{lj}) were observed. In the experimental spectra, only coupled mode positions are observable. Therefore, the LO mode could be determined only if the influence of the free carrier contraction will be eliminated [11]. In the analysis of reflectivity spectra of CdTe$_{1-x}$Se$_x$, we have decided to use dielectric function which takes into account the existence of plasmon–LO phonon interaction in advance [11]:

$$\varepsilon(\omega) = \varepsilon_\infty \frac{\prod_{j=1}^{m+n} \left(\omega^2 + i\gamma_{lj}\omega - \omega_{lj}^2\right)}{\omega^m \prod_{i=1}^{m} (\omega + i\gamma_{Pi}) \prod_{i=1}^{n} (\omega^2 + i\gamma_{ti}\omega - \omega_{ti}^2)} \qquad (2)$$

$$\times \prod_{k=1}^{s} \frac{\omega^2 + i\gamma_{LOk}\omega - \omega_{LOk}^2}{\omega^2 + i\gamma_{TOk}\omega - \omega_{TOk}^2} \times \frac{\omega^2 + i\gamma_L\omega - \omega_L^2}{\omega^2 + i\gamma_{0k}\omega - \omega_0^2}$$

The first term in Eq. 2 represents coupling m plasmons and n phonons, while the second term represents uncoupled modes of the crystal (s), while $l = n + s$. The ω_{lj} and γ_{lj} parameters of the first numerator are eigenfrequencies and damping coefficients of the longitudinal plasmon–n phonon waves. The parameters of the first denominator correspond to the similar characteristics of the transverse (TO) vibrations.

The second term represents uncoupled crystal mode, where the ω_{LOk} and ω_{TOk} are the longitudinal and transverse frequencies, while γ_{LOk} and γ_{TOk} are damping of uncoupled modes. In the case of plasmon–LO phonon coupling, $m = 1$ and $n = 1$. The third term in Eq. 2 represented indium local phonon, where ω_0 is local phonon characteristic frequencies and ω_L is connected to the intensity of local mode oscillator ($s(\omega_0) \sim (\omega_L^2 - \omega_0^2)$).

We have decided to use dielectric function which takes into account the existence of plasmon–two different LO phonon interaction in the analysis of the reflectivity spectra $CdTe_{1-x}Se_x$ which corresponds to $l = 2$ in dielectric function given by Eq. 1. As we already observed, the coupled mode positions are defined as the solutions of the real part of Eq. 1 ($Re\{\varepsilon_s = 0\}$). In this case, there are three coupled modes, which can be calculated by solving the equations:

$$\omega^6 - A\omega^4 - B\omega^2 - C = 0 \tag{3}$$

where:

$$A = \omega_{LO1}^2 + \omega_{LO2}^2 + \omega_P^2 \tag{4}$$

$$B = \omega_{LO1}^2 \cdot \omega_{LO2}^2 + \omega_P^2(\omega_{TO1}^2 + \omega_{TO2}^2) \tag{5}$$

$$C = \omega_{TO1}^2 \cdot \omega_{TO2}^2 \cdot \omega_P^2 \tag{6}$$

On the other hand, if we use the dielectric function defined by Eq. 2, the values of initial ω_{LO1} and ω_{LO2} (which are two different phonons) and ω_P modes can be determined by:

$$\omega_P = \frac{\omega_{l1}\omega_{l2}\omega_{l3}}{\omega_{t1}\omega_{t2}} \tag{7}$$

$$\omega_{LO1,2} = \frac{1}{2}(\omega_{l1}^2 + \omega_{l2}^2 + \omega_{l3}^2 - \omega_P^2)$$
$$\pm \sqrt{\left(\frac{1}{4}\left(\omega_{l1}^2 + \omega_{l2}^2 + \omega_{l3}^2 - \omega_P^2\right)^2 - \omega_{l1}^2\omega_{l2}^2 - \omega_{l2}^2\omega_{l3}^2 - \omega_{l1}^2\omega_{l3}^2 + \omega_P^2\left(\omega_{t1}^2 + \omega_{t2}^2\right)\right)} \tag{8}$$

Dashed lines in Fig. 1 (T = 300 K) obtained by a fitting procedure based on the model given by Eq. 2 for the case $m = 1$, $n = 2$ and $s = 1$. The first term in Eq. 2 (where $n = 2$) represents the structures at about 140 and 170 cm^{-1} and can be identified as some of the lattice vibrations modes of $CdTe_{1-x}Se_x$. A difference between theoretical spectra and experimental data for wave numbers from 140–160 cm^{-1} to 170–175 cm^{-1} was noted. This imperfection was improved by using the modified dielectric function (2). In $CdTe_{1-x}Se_x$ mixed crystal [12], a surface layer with a low concentration of free carriers could be formed. This means that first term in Eq. 2 must be used twice, for each layer (each plasma frequencies)

Fig. 2 The eigenfrequencies of the plasmon–phonon modes for single crystal $CdTe_{0.97}Se_{0.03}$. The *solid lines* calculated spectra [Re $\{\varepsilon_s\} = 0$; ε is given by Eq. (1)]; ●—ω_{l1}, ω_{l2} and ω_{l3}; □—ω_{LO1} and ω_{LO2}; *—ω_{TO1} and ω_{TO2}
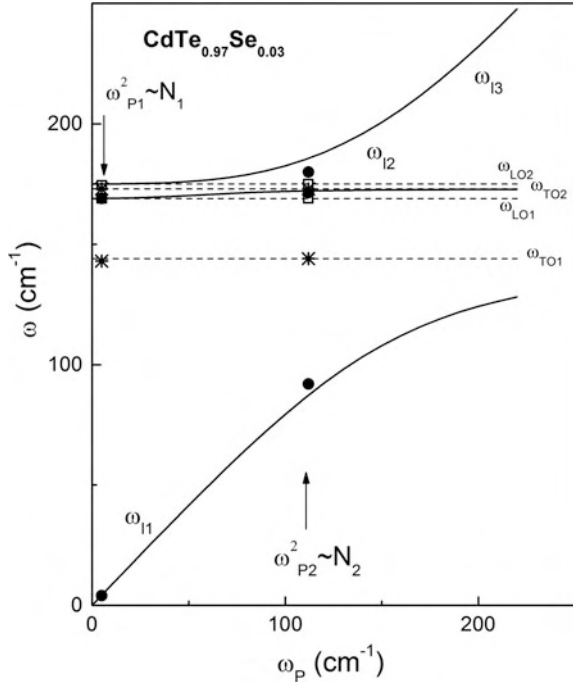

separately. The excellent agreement between the experimental data and theoretical spectra (solid line) is obtained.

As a result of the best fit, we obtained the frequencies of plasmon–phonon coupled modes (ω_{l1}, ω_{l2}, and ω_{l3}) and TO optical phonons (Eq. 2). Values for ω_{LO1}, ω_{LO2}, and ω_P are calculated from Eqs. 3–8. The characteristic parameters obtained by described procedure are shown in Fig. 2, where the solid lines are obtained using Eq. 3, the solid circles (●) refer to eigenfrequencies spectra ω_{lj} ($j = 1, 2$ and 3), values corresponding ω_{TO1} and ω_{TO2} are given by stars (*), and the open squares (□) represent the calculated values for ω_{LO1} and ω_{LO2} (Eq. 8). The agreement of the plasmon–LO phonon mode frequencies obtained theoretically with the experimentally ones is very good. The plasma frequency (Eq. 7)) of surface layer (ω_{P1}, where $\omega_{P1} \sim N_1^{1/2}$) is lower than the plasma frequencies inside the sample (ω_{P2}, $\omega_{P2} \sim N_2^{1/2}$), what is expected for this type of material.

To study the phonon mode behavior for the ternary compounds $CdTe_{1-x}Se_x$, we used the model based on Genzel's model [7]. This model gave good results in previous studies [13–15] for describing the phonon behavior in the ternary mixed crystals. In our calculations, the basic assumptions of REI model (random element isodisplacement model) [16] were applied. Namely, in the $AB_{1-x}C_x$ type of mixed crystals, the crystal lattice of a mixed system comprises two sublattices: one of them filled by A atoms only and second filed by B and C atoms, randomly distributed. The local electric field (E_{loc}) was taken into account, and a connection between the

Fig. 3 Concentration
dependence of the frequency
of the optical mode
CdTe$_{1-x}$Se$_x$ single crystals
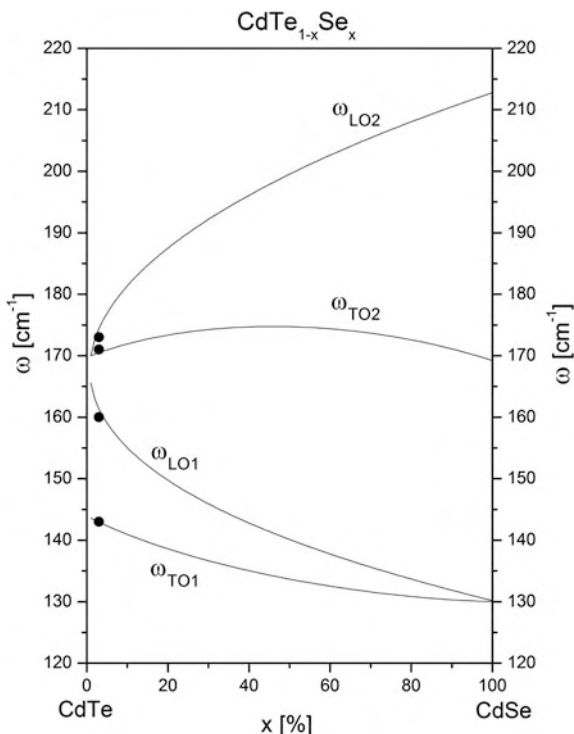
microscopic and macroscopic parameters was made using the Born–Huang pro-
cedure, where the dependence of the force constant between first neighbors on
concentration (x) was neglected, but the second-neighbor force constant was
involved. The curves shown in Fig. 3 were obtained using this model. The
experimental values for the TO and LO modes are marked by full circles. The
results shown in Fig. 3 suggest that the phonons in CdTe$_{1-x}$Se$_x$ exhibit the
two-mode behavior, according to Genzel's notation [7], i.e., each TO–LO mode
pair for the end members degenerates to an impurity mode. The agreement between
the experimental and theoretical results is very good, with regard to the approxi-
mations on which these models are based.

The far-infrared reflection spectra of the CdTe$_{0.97}$Se$_{0.03}$(In) single crystal sample
are shown in Fig. 4. The experimental data are represented by circles. The solid line
is obtained using the same procedure we described for Fig. 1. We used dielectrical
function given by Eq. 2, where $m = 1$, $n = 2$, and $s = 1$ with one local mode. Surface
layer with the lowest free carrier concentration than the rest part of the sample is
considered. The excellent agreement between the experimental data and theoretical
spectra (full line) is obtained.

Fig. 4 Far-infared reflection spectra of $CdTe_{0.97}Se_{0.03}(In)$ single crystals at temperature 80, 150, and 300 K. The experimental spectra are presented by *circles*. The *solid lines* are calculated spectra obtained by fitting procedure based on the model given by Eq. (2)
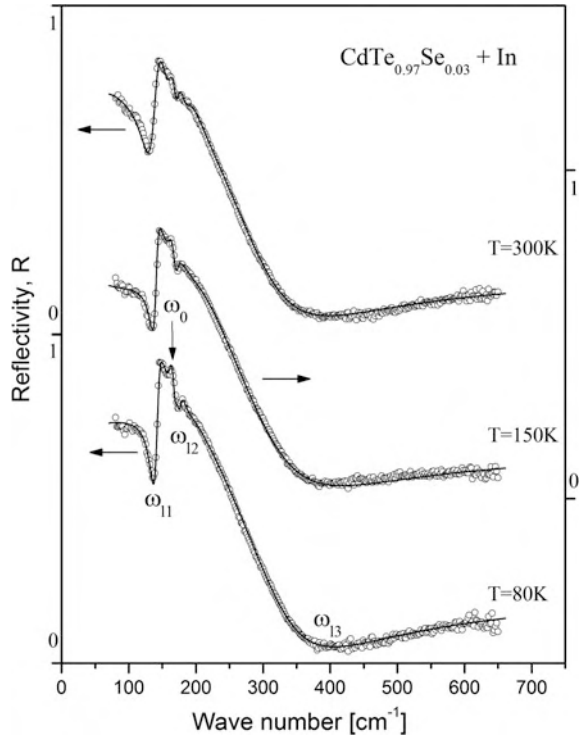
Doping $CdTe_{0.97}Se_{0.03}$ with In causes two consequences:

1. Local phonon mode appearance: Indium in $CdTe_{1-x}Se_x$ system is substitution impurity mode. The impurity mode can arise due to the difference between masses and force constants of the impurity ion and the ion of the host material [17], or their appearance can be caused by more complex mechanism of electron–phonon interaction [18]. In our case, $CdTe_{1-x}Se_x$ substitutes Cd. Difference between masses of Cd and In ions is very small; consequently, local mode is situated very close to CdTe LO phonon mode. In Fig. 4, it is visible as independent mode (ω_0) at about 160 cm^{-1}.

2. Free carrier concentration at all mixed crystal, including surface layer increase, what is seen in Fig. 4 as a global minimum shift to higher wave numbers. Figure 5 is obtained using the same procedure we used for Fig. 2. The plasma frequency (Eq. 7) of surface layer (ω_{P1}') is lower than the plasma frequencies inside the sample (ω_{P2}'); hence, the plasma frequency (free carrier concentration) increased at doped sample.

Fig. 5 The eigenfrequencies of the plasmon–phonon modes for single crystal $CdTe_{0.97}Se_{0.03}(In)$. The *solid lines* are calculated spectra $[Re\{\varepsilon_s\} = 0; \varepsilon$ is given by Eq. (1)]; ●—ω_{l1}, ω_{l2}, and ω_{l3}; □—ω_{LO1} and ω_{LO2}; ∗—ω_{TO1} and ω_{TO2}
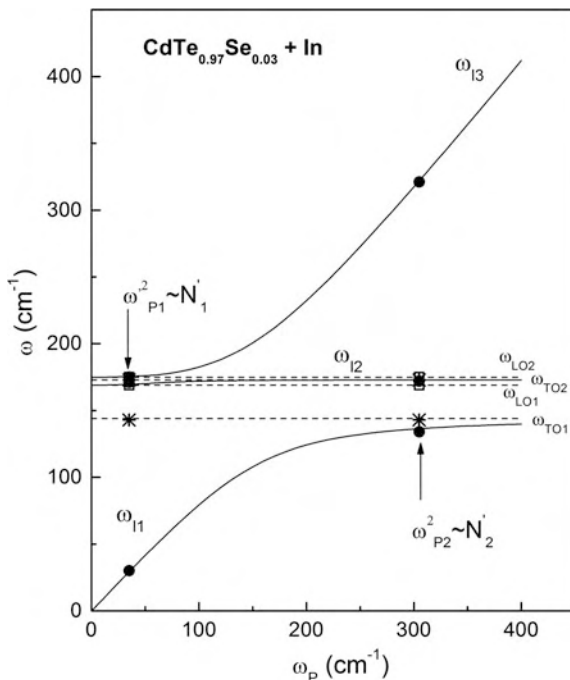
4   Conclusions

In this paper, we used far-infrared reflectivity measurements to obtain phonon properties of the ternary $CdTe_{0.97}Se_{0.03}$ and $CdTe_{0.97}Se_{0.03}(In)$ single crystals. We found that the long wavelength optical phonon modes of mixed crystals exhibit a two-mode behavior. In doped sample, the local In mode at about 160 cm^{-1} is observed. In both samples, a surface layer with a low concentration of free carriers is formed.

References

1. A. Tu, P.D. Persans, Raman scattering as a probe of composition in II-VI ternary semiconductor-glass composites. Appl. Phys. Lett. **58**, 1506–1508 (1991)
2. A. Mlayah, A.M. Brugman, R. Carles, J.B. Renucci, M.Y. Valakh, A.V. Pogorelov, Surface phonons and alloying effects in (CdS)x (CdSe)1 − x nanospheres. Sol. St. Commun. **90**, 567–570 (1994)

3. A. Roy, A.K. Sood, Surface and confined optical phonons in CdSxSe$1 − x$ nanoparticles in a glass matrix. Phys. Rev. B **53**, 12127–12129 (1996)
4. A. Ingale, K.C. Rustagi, Raman spectra of semiconductor nanoparticles: disorder-activated phonons, Phys. Rev. B, **58**, 7197–1201 (1998)
5. Yu.M. Azhniuk, A.G. Milekhin, A.V. Gomonnai, V.V. Lopushansky, V.O. Yukhymchuk, S. Shulze, E.I. Zenkevich, D.R.T. Zahn, Resonant Raman studies of compositional and size dispersion of CdS$_{1-x}$Se$_x$ nanocrystals in a glass matrix. J. Phys. Condens. Matter **16**, 9069–9073 (2004)
6. A.A. Kukharskii, Plasmon-phonon coupling in GaAs. Solid State Commun. **13**, 1761–1764 (1973)
7. L. Genzel, T.P. Martin, C.H. Perry, Model for long-wavelenght optical-phonon modes of mixed crystals. Phys. Status Solidi B **62**, 83–86 (1974)
8. E. Burstein, A. Pinczuk, R.F. Wallis, in D.L. Carter, R.T. Bate (Eds.), The Physics of Semimetals and Narrow-Gap Semicon, (Pergamon, New York, 1971), 251–267
9. M.A. Kinch, D.D. Buss, Far I.R. determination of the transverse optic lattice mode in PbTe at low temperature. Solid State Commun. **8**, 1275–1279 (1970)
10. V. Gopal, Analysis of the infrared plasma reflectivity spectra of semiconductors. Infrared Phys. **18**, 121–127 (1978)
11. A.A. Kukharskii, Solid State Commun. **11**, 319–324 (1972)
12. D. Jovanovic, D. Milivojevic, M. Romcevic, B. Babic-Stojic, N. Romcevic, Optical and magnetic properties of Hg1-xMnxSe alloys. Mater. Sci. Forum **494**, 277–281 (2005)
13. N. Romcevic, M. Romcevic, A. Golubovic, A. Le Vai Khoi, D. Mycielski, D. Jovanovic, S. Stojanovic, S. Djuric Nikolic, Far-infrared and Raman spectroscopy of Cd1-xMnxTe1-ySey: phonon properties. J. Alloy Compd. **397**, 52–57 (2005)
14. N. Romcevic, M. Romcevic, V. Le Khoi, A. Mycielski, V.A. Kulbachinskii, P.D. Maryanchuk, I.A. Churilov, Plasmon-two phonon interaction in PbTe$_{0.95}$S$_{0.05}$ alloy. Phys. Stat. Sol. (c) **1**, 977–1002 (2004)
15. S. Perkowitz, R.H. Shoskley, G.L. Person, Far-infrared study of free carriers and the plasmon-phonon interaction in CdTe. Phys. Rev. B **9**, 545–549 (1974)
16. M. Cardona, G. Gunterodt (Eds.), *Light Scattering in Solids IV*, vol. 54 (Springer, Berlin, 1984), 63–128
17. A. A. Maradudin, in F. Seitz, D. Turnball (Eds.), *Theoretical and Experimental Aspects of the Effects of Point Defects and Disorder on the Vibrations of Crystals*[*]*—1 Solid, State. Physics*. vol. 19 (Academic, New York, 1966)
18. N. Romcevic, J. Trajic, A.T. Kuznetsova, M. Romcevic, B. Hadzic, D.R. Khokhlov, Far-infrared study of impurity local modes in Ni- doped PbTe. J. Alloys Compd. **442**, 324–329 (2007)

Vibrational Spectroscopy of SOP Modes in ZnO Doped with CoO, MnO and Fe$_2$O$_3$

B. Hadžić, N. Romčević, J. Trajić, R. Kostić, G. Stanišić and D. Timotijević

Abstract Nanocrystalline samples of ZnO doped with CoO, MnO and Fe$_2$O$_3$ were synthesized by traditional wet chemical method followed by calcinations. Samples where characterized by X-ray diffraction to determine composition of the samples (ZnO, Co$_3$O$_4$, Mn$_3$O$_4$, ZnMn$_2$O$_4$, ZnMnO$_3$, ZnFe$_2$O$_4$ and Fe$_2$O$_3$) and the mean crystalline size (from 8 to 156 nm, depending on the sample). In this paper we report the experimental Raman scattering spectra (from 100 to 1600 cm^{-1} and from 200 to 1600 cm^{-1}) with surface optical phonons (SOP) in range of 496−575 cm^{-1}. This shows the change of position of SOP modes with crystalline size and change of intensity of SOP modes with change of concentration of doping elements. The phonon of registered phase's exhibits effects connected to phase concentration, while the SOP phonon mode exhibit significant confinement effect.

Keywords Nanostructured materials · Optical properties · Light absorption and reflection

1 Introduction

Nanostructures made of zinc oxide (ZnO), a wide direct band gap semiconductor of 3.37 eV with large exciton binding energy of 60 meV, have recently attracted a lot of attention due to their proposed applications in low-voltage and short-wavelength electro-optical devices, transparent ultraviolet protection films, gas sensors and others. In recent years, the study of transition metal (Fe, Co, Ni, V, Cr, etc.) doped ZnO based diluted magnetic semiconductors (DMSs) has increased due to its application in magnetoelectronic and spintronic devices, with many reports about high temperature ferromagnetism in these materials [1–6].

As an ideal, sensitive, non-destructive, rapid and powerful technique Raman spectroscopy often has been method of choice to identify the microscopic vibration

B. Hadžić (✉) · N. Romčević · J. Trajić · R. Kostić · G. Stanišić · D. Timotijević
Institute of Physics, University of Belgrade, Belgrade, Serbia
e-mail: branka@ipb.ac.rs

caused by the slight structural distortion in bulk as well as in thin films and nanostructured samples both pure and doped. Raman scattering in case of ZnO and ZnO-related compounds has been used to study local atomic arraignment, dopant incorporation, electron-phonon coupling, multi phonon process and others [7–12].
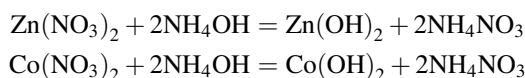
Existence of surface optical phonons (SOP) in ZnO nanostructures has been expected due to their large surface-to-volume ratio. That's why in determination of sample properties the state of surface atoms is important. When dimensions becomes extremely small surface modes are only modes that persist, so having this in mind we can say that presence of Raman forbidden SOP modes is related to loss of long-range order and symmetry breakdown in ZnO shell [13]. In many papers all of this can be found, predicted theoretically and/or detected experimentally for ZnO nanostructures [14].

The aim of this work is to give complete picture how preparation method and doping elements influence on sample as well as SOP modes characteristics, by applying micro-Raman spectroscopy, along with Co, Mn and Fe ions position in ZnO lattice, the formation of existing phases, and the samples quality in dependence of doping elements concentrations.

2   Samples and Characterization

The nanocrystalline samples of ZnO doped with $CoO/MnO/Fe_2O_3$ were synthesized by use of wet chemical method followed by calcination. In this method a mixture of cobalt and zinc hydroxides was obtained by addition of an ammonia solution or 2 M solution of KOH to the 20 % solution of a proper amount of $Zn(NO_3) \times 6H_2O$ and $Co(NO_3) \times 4H_2O/Mn(NO_3) \times 4H_2O/Fe(NO_3) \times 4H_2O$ in water:

- In the case of samples doped with CoO

$$Zn(NO_3)_2 + 2NH_4OH = Zn(OH)_2 + 2NH_4NO_3$$
$$Co(NO_3)_2 + 2NH_4OH = Co(OH)_2 + 2NH_4NO_3$$

- In the case of samples doped with MnO

$$Zn(NO_3)_2 + 2NH_4OH = Zn(OH)_2 + 2NH_4NO_3$$
$$Mn(NO_3)_2 + 2NH_4OH = Mn(OH)_2 + 2NH_4NO_3$$

- In the case of samples doped with Fe_2O_3
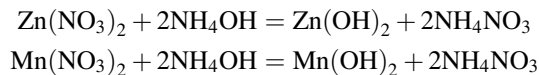
$$Zn(NO_3)_2 + 2NH_4OH = Zn(OH)_2 + 2NH_4NO_3$$
$$Fe(NO_3)_2 + 2NH_4OH = Fe(OH)_2 + 2NH_4NO_3$$
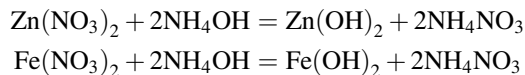
Next, the obtained hydroxides were filtered, dried at 70 °C and calcined at 300 °C during one hour. Nanopowders obtained on this way were pressed into indium panel.

This method allowed obtaining the series of samples with nominal concentration of doping element from 5 % to 95 %. Here we will present the results of micro-Raman spectroscopy for most emblematic samples of 5–95 % range as well as changes of relative intensity of modes with concentration of doping element.

Morphology of the samples was investigated using scanning electron microscope (SEM). On SEM images for lower concentration of doping element can be easily distinguish two types of particles, one bigger than 100 nm, which belongs to ZnO phase and other much smaller, that belongs to formed phases of doping element. With doping element concentration increase the size of particles becomes similar, while further increase to the highest level of dopant concentration leads to dominance of smaller particles that belongs to formed phases.

Secondly, we used X-ray diffraction (XRD) ($Co_{K\alpha}$ radiation, X'Pert Philips) to determine the phase composition of all our samples. In the case of ZnO doped with CoO XRD analysis revealed the presence of crystalline phases of spinel structure Co_3O_4 (ICSD: 80-1540) and hexagonal ZnO. On this way obtained XRD parameters allowed us, using Scherrer's formula [15], to determine a mean crystalline size in these samples. The mean crystalline size ã, in this case, are between 14 and 55 nm for Co_3O_4 phases and from 43 till 156 nm for ZnO phases. These results, the phase composition and the mean crystalline size are gathered in Table 1. The presence of ZnO phase has been registered in samples doped with 60 % of CoO and more, but the results obtained for their crystallite size are unreliable, that's why it hasn't been shown in Table 1. On the same way we obtained these information for samples doped with MnO as well as with Fe_2O_3. In the case where MnO was dopant phase composition investigation revealed the presence of hexagonal ZnO, along with spinel structures of Mn_3O_4, $ZnMn_2O_4$ and $ZnMnO_3$. The mean crystalline size ã of these phases are between 9 and 13 nm for $ZnMnO_3$ phases, from 24 to 47 nm for Mn_3O_4 phases and above 100 nm for ZnO and $ZnMn_2O_4$ phases. The results of XRD measurements are gather in Table 2. Sign "+" in this table means that it's been register presence of these particles but it wasn't possible to determinate their size.

In the case of ZnO doped with Fe_2O_3 the phase composition investigation revealed the presence of hexagonal ZnO, spinel structures of $ZnFe_2O_4$ and rhombohedral Fe_2O_3. The mean crystalline size ã of these phases are between 26 and 51 nm for ZnO phases, from 8 to 12 nm for $ZnFe_2O_4$ phases and at approximately 23, 24 nm for Fe_2O_3 phases. The results of XRD measurements are gather in Table 3. Sign "+" in this table means that it's been register presence of these particles but it wasn't possible to determinate their size, while "×" means that these particles should be registered but they haven't and "−"means that the presence of these particles haven't been register. Most of this is clearly visible in Fig. 1 where are shown XRD spectra's for presented samples.

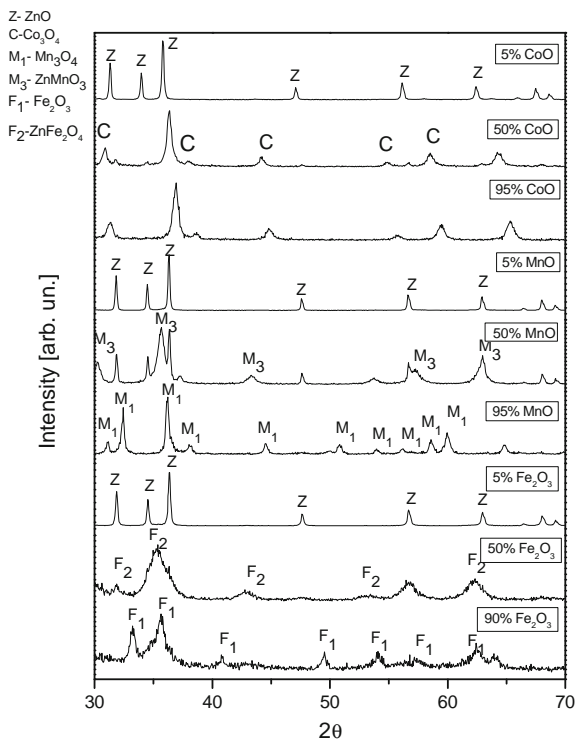**Table 1** XRD analysis results for ZnO doped with CoO

	ã [nm] ZnO phase	ã [nm] Co_3O_4 phase
5 wt%	156	55
10 wt%	118	50
20 wt%	57	21
30 wt%	101	30
40 wt%	80	17
50 wt%	43	21
60 wt%	–	14
70 wt%	–	15
80 wt%	–	21
90 wt%	–	25
95 wt%	–	20

Table 2 XRD analysis results for ZnO doped with MnO

Wt% ZnO	Wt% MnO	Mn_3O_4 phase	$ZnMn_2O_4$ phase	$ZnMnO_3$ phase	ZnO phase
95	5			+	+
90	10			+	+
80	20			9 nm	
70	30			10 nm	above 100 nm
60	40			9 nm	above 100 nm
50	50			13 nm	above 100 nm
40	60	24 nm	+		
30	70	37 nm	+		
20	80	45 nm			
10	90	47 nm			
5	95	43 nm			

Table 3 XRD analysis results for ZnO doped with Fe_2O_3

Wt% of ZnO	Wt% of Fe_2O_3	ã [nm] ZnO phase	ã [nm] $ZnFe_2O_4$ phase	ã [nm] Fe_2O_3 phase
95	5	+	10	–
90	10	+	8	–
80	20	+	8	–
70	30	51	11	–
60	40	26	12	–
50	50	×	8	–
40	60	×	12	–
30	70	×	12	–
20	80	×	12	×
10	90	–	×	24
5	95	–	–	23

Fig. 1 XRD spectra's for all presented samples

3   Surface Optical Phonons

Briefly we will present main ideas about concept of surface optical phonons (SOP). Reduction of the particles dimensions to nanoscale, and presence of imperfections, impurity and others, results in breakdown of phonon momentum selection rules, that's why some new forbidden vibration modes whose phonons have $l \neq 0$ contribute to Raman scattering, as in our case [7, 16–18]. SOP modes appear in samples whose particles size is smaller than the wavelength of incident laser beam and that these modes arise in polar crystals [13]. Here we will be focused on Bruggerman formula and it mixing rule [19–21] which is much more appropriate for our samples because in it doesn't exist restrictions for volume fraction, what makes it more suitable for high concentration of inclusions. The effective dielectric function according to the Bruggeman mixing rule is given by:

$$(1-f)\frac{\varepsilon_1 - \varepsilon_{eff}}{\varepsilon_{eff} + g(\varepsilon_1 - \varepsilon_{eff})} + f\frac{\varepsilon_2 - \varepsilon_{eff}}{\varepsilon_{eff} + g(\varepsilon_2 - \varepsilon_{eff})} = 0 \qquad (1)$$

where, g is a geometric factor who depends on the shape of the inclusions. In the case of two-dimensional circles g = 1/2, while for the three dimensional spherical particles g = 1/3.

In our samples nanoparticles are clusterized, occupy a significant volume and aren't well-separated in air, that's why they satisfy the Bruggeman formula conditions with g = 1/3 appliance.

When are ZnO nanoparticles in case, in a region of appearance of SOPs, we have two phonons $\omega_{A_1LO} = 577$ cm^{-1}, $\omega_{A_1TO} = 379$ cm^{-1}, $\omega_{E_1TO} = 410$ cm^{-1}, $\omega_{E_1LO} = 592$ cm^{-1}, with dielectric permittivity $\varepsilon_\infty = 3,7$ [26–28]. In our case we can neglect influence of the plasmon-phonon interaction because of low free carriers concentration and low mobility. Nanoparticles of our samples are randomly distributed in space and accordingly to the incident light. Not all of symmetry phonons typical for ZnO are register in Raman spectra, which indicates that those Raman unregister symmetry phonons participate in SOP creation, what will be shown later. The excitation of extraordinary phonons results in Raman intensity given with:

$$I \sim \text{Im}\left(\frac{-1}{\varepsilon_{eff}}\right) \tag{2}$$

This type of calculation predicts appearance of one asymmetric peak in the area of Bruggerman formula applicability with wavenumbers below $\omega_{E_1}(LO)$. Obtained experimental spectra of ZnO doped with CoO nanopowders shows good agreement with this calculations. That's why the great difference in the intensity and line shape of simulated SOP modes, as we shall see later, is mainly the results of variation in main volume fraction and damping rate.

4   Results and Discussion

The micro-Raman spectra were taken in the backscattering configuration and analyzed using Jobin Yvon T64000 spectrometer, equipped with nitrogen cooled charge-coupled-device detector. As excitation source we used the 514.5 nm line of an Ar-ion laser. The measurements were performed at 20 mW laser power.

For analysis of Raman spectra we have assumed that all phonon lines are of Lorentzian type which is one of common type of lines for this kind of analysis, other common type of line is Gaussian [22]. We used Eqs. 1 and 2 to calculate SOP lines, with $\varepsilon_1 = 1$.

In Figs. 2, 4 and 6 are presented Raman spectra for three most emblematic samples of each dopant type, while in Figs. 3, 5 and 7 are presented changes of SOP modes with concentration for each dopant type. As we already mention, XRD reveals presence of ZnO, Co_3O_4, Mn_3O_4, $ZnMn_2O_4$, $ZnMnO_3$, $ZnFe_2O_4$ and Fe_2O_3 respectively. For analysis of vibration properties of nanoparticles is crucial understanding of vibration properties of bulk material. That's why we start analysis

of obtained Raman spectra with brief report about structural and vibration properties of all potentially present phases in the samples. We expect that bulk modes will be shifted and broadening as a consequence of miniaturization.

ZnO, basic material in our samples, is a semiconductor with a wurtzite crystal structure. With four atoms per primitive cell, this hexagonal structure belongs to C_{6v}^4 space group and all atoms occupy C_{3v} sites. As it has been seen many times [23, 24] ZnO have four Raman active modes (A_1, E_1 and $2E_2$) where A_1 and E_1 are polar modes and they split into transverse (TO) and longitudinal (LO) phonons. This TO and LO phonons have different frequencies due to macroscopic electric fields (associated with the LO phonons) and anisotropy caused by the short-range interatomic forces. The TO-LO splitting is larger than the A_1-E_1 splitting due to anisotropy caused by dominances of electrostatic forces in the short-range force region. In bulk ZnO A_1 atoms move parallel to the c-axis and E_1 perpendicular to c-axis for the lattice vibration. Often, two nonpolar Raman active modes, are assigned with $E_2^{(1)}$(low) and $E_2^{(2)}$(high). Frequencies of ZnO Raman active modes and their assignation are 102 cm^{-1} ($E_2^{(1)}$ (low)), 379 cm^{-1} (A_1(TO)), 410 cm^{-1} (E_1(TO)), 437 cm^{-1} ($E_2^{(2)}$ (high)), 541 cm^{-1} (A_1(LA)), 577 cm^{-1} (A_1(LO)) and 592 cm^{-1} (E_1(LO)), while modes on 330, 660 and 1153 cm^{-1} are multi phonon modes [23, 24].

Co_3O_4 belongs to O_h^7 space group and crystallizes in the normal spinel structure $Co^{2+}(Co^{3+})_2O_4^{2-}$ where Co^{2+} and Co^{3+} are placed at tetrahedral and octahedral sites, respectively. His primitive unit cell contains 14 atoms and it has 5 Raman active modes A_{1g} at 691 cm^{-1}, E_g at 482.4 cm^{-1} and three F_{2g} at 194.4 cm^{-1}, 521.6 cm^{-1} and 618.4 cm^{-1} [25].

The hausmannite Mn_3O_4 ($MnMn_2O_4$ in spinel notation) is a normal tetragonal spinel structure with space group D_{4h}^{19}. The elementary unit cell contents four formula units i.e. $Mn_4Mn_8O_{16}$. Factor-group analysis predicts 14 Raman-active modes ($2A_{1g} + 2B_{1g} + 4B_{2g} + 6E_g$) [26]. To the same space group belongs $ZnMn_2O_4$ too. We have to mention that it hasn't been measured Raman spectra with all 14 Raman-active modes yet. The biggest numbers of measured Raman-active modes are 5 and those 5 haven't been identified (assigned) still, except characteristic mode at 653 cm^{-1} for all the spinel structures. It is assigned to the A_{1g} mode, which corresponds to the Mn-O breathing vibration of divalent manganese ions in tetrahedral coordination. In the vibrational modes of species A_{1g} and E_g, only motions of the oxygen atoms are involved [26]. In Mn_3O_4 related publications it can be observed large variation of A_{1g} peak position from 650 cm^{-1} till 668 cm^{-1}. Those Raman active modes for Mn_3O_4 are at 310 cm^{-1}, 357 cm^{-1}, 485 cm^{-1}, 579 cm^{-1} and 653 cm^{-1} [26–28] while for $ZnMn_2O_4$ are at 300 cm^{-1}, 320 cm^{-1}, 382 cm^{-1}, 476 cm^{-1} and 678 cm^{-1} [26–28].

$ZnFe_2O_4$ spinel has cubic structure that belongs to the space group O_h^7(Fd3 m). The full unit cell contains 56 atoms (Z = 8), the smallest Bravais cell only consists of 14 atoms (Z = 2). The factor group analysis predicts 5 Raman active modes in $ZnFe_2O_4$ spinel [9] at 221 cm^{-1} (F_{2g}(1)), 246 cm^{-1} (E_g), 355 cm^{-1} (F_{2g}(2)), 451 cm^{-1} (F_{2g}(3)) and 647 cm^{-1} (A_{1g}). In the cubic spinel's, including ferrites, the modes at above 600 cm^{-1} mostly correspond to the motion of oxygen atoms in
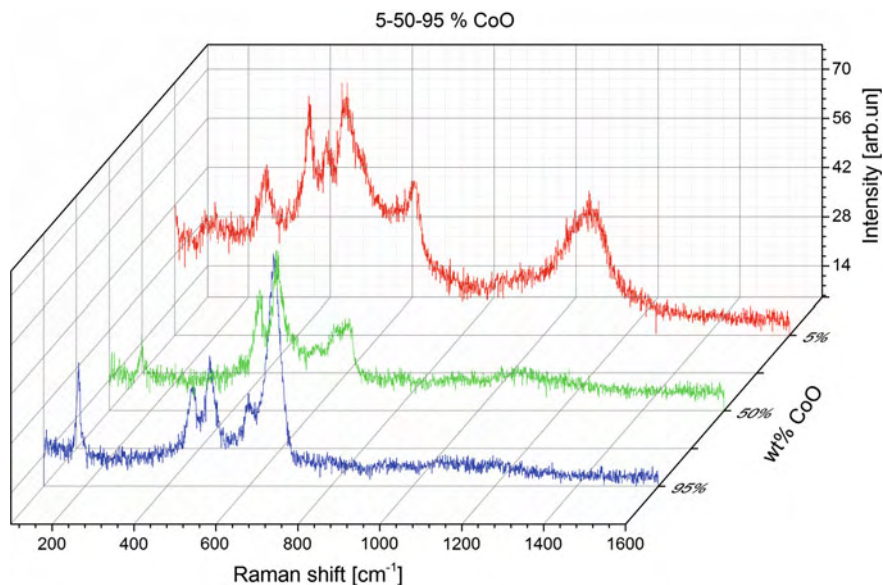
Fig. 2 Raman spectra of ZnO doped with 5, 50 and 95 % of CoO

tetrahedral AO_4 group. The other lower frequency modes represent the characteristic of the octahedral BO_6 sites.

Fe_2O_3 crystallize in the rhombohedric (trigonal) system with space group D_{3d}^6. Primitive unit cell contains two formula units (Z = 2). The factor group analysis predicts 7 Raman active modes, $2A_{1g}$ at 225 cm^{-1} and 498 cm^{-1}, and $5E_g$ at 246 cm^{-1}, 294 cm^{-1}, 300 cm^{-1}, 412 cm^{-1} and 613 cm^{-1} [9]. There is, as addition to these first order Raman spectra, multi phonon peak at 1320 cm^{-1}. When symmetry rules are broken can be visible Raman forbidden mode at 660 cm^{-1}.

In Fig. 2 are given Raman spectra of ZnO doped with 5 %, 50 % and 95 % of CoO. On these spectra are evident existence of single and multi phonons modes characteristic for ZnO, such as 379 cm^{-1} (A_1(TO)), 437 cm^{-1} ($E_2^{(2)}$), 577 cm^{-1} (A_1(LO)), and multi phonons at 330, 660 and $\sim$1110 cm^{-1}. From all these modes characteristic for ZnO one is the most obvious. That is the mode at 437 cm^{-1}. His sharp peak is clearly visible on Raman spectra for smaller concentration of doping element (CoO) and with increase of CoO concentration his intensity decrease. All others phonons modes of ZnO behave on the same way as the mode at 437 cm^{-1}. Beside these modes characteristic for ZnO in these samples we also notice existence of typical modes for Co_3O_4 phase, such as 194 cm^{-1} (F_{2g}), 482 cm^{-1} (E_g), 521 cm^{-1} (F_{2g}), 618 cm^{-1} (F_{2g}) and 691 cm^{-1} (A_{1g}). Opposite from ZnO modes, Co_3O_4 modes increase their intensity with increase of concentration of CoO. The most evident Co_3O_4 modes on these spectra are 482 cm^{-1}, 521 cm^{-1} and 691 cm^{-1}. Here we need to emphasis that position of peaks centers are on smaller frequencies, which is a consequence of nanosized structure of this samples but in good
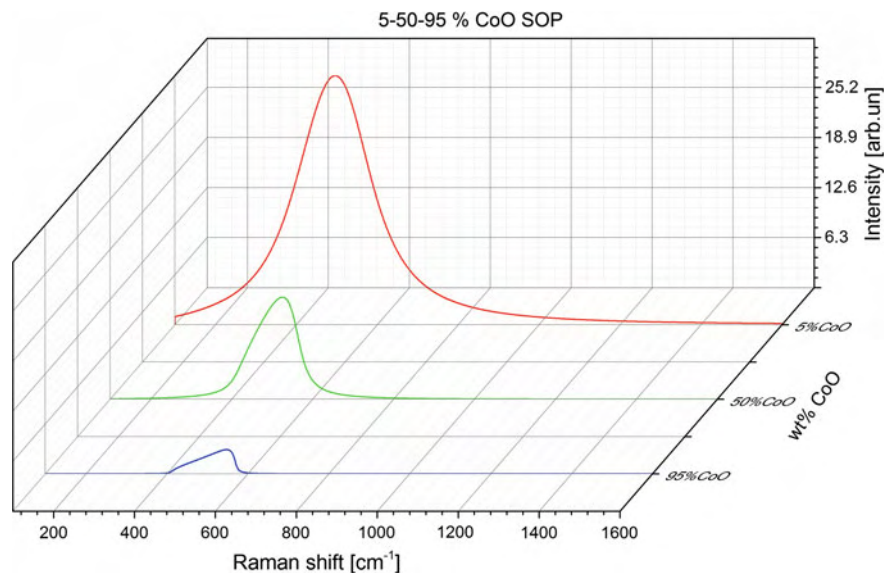
Fig. 3 SOP modes of ZnO doped with 5, 50 and 95 % of CoO

agreement with earlier reported Raman frequencies for bulk crystals, gather in work of M. Bouchard at all [29]. These results of Raman spectroscopy are in good agreement with previously done XRD analysis. Apart all modes that we have mention, is also evident existence of additional structure. This structure is SOP mode and they, as we already mention, originate from ZnO nanoparticles due to nanosize structure of samples. Change of characteristic SOP modes with concentration of doping element (CoO) for three chosen spectra is shown on Fig. 3. From this figure it's clearly visible that the change in position of SOP modes directly follows the decrease of crystalline size of ZnO. Along this, on Fig. 3 we can notice that intensity of SOP modes decrease with increases of doping element CoO. This change of intensity of SOP modes is similar to the change of intensity of ZnO modes and opposite to the change of intensity of Co_3O_4 modes, which is one more proof that SOP modes originate from ZnO.

In Fig. 4 are given Raman spectra of ZnO doped with 5 %, 50 % and 95 % of MnO. Sharp and narrow peak, clearly visible on spectra doped with 5 % of MnO, whose position is in that spectra on 436 cm^{-1} is obviously $E_2^{(2)}$ mode of ZnO. With increase of doping element, intensity of this peak decrease, due to ZnO origin. Beside this $E_2^{(2)}$ mode, also are visible ZnO modes at 379 cm^{-1} $A_1(TO)$, 541 cm^{-1} $A_1(LO)$ and 577 cm^{-1} $A_1(LO)$. Multi phonon 2LO ZnO modes at ~ 330 and ~ 1150 cm^{-1} are clearly visible too, while multi phonon mode 660 cm^{-1} is in the shadow of sharp peak at approximately 679 cm^{-1}, typical for spinel structure, whose origin in this case is from $ZnMn_2O_4$. On these spectra, with smaller dopant concentration, are also visible $ZnMnO_3$ modes on 448 and 610 cm^{-1} and Mn_3O_4
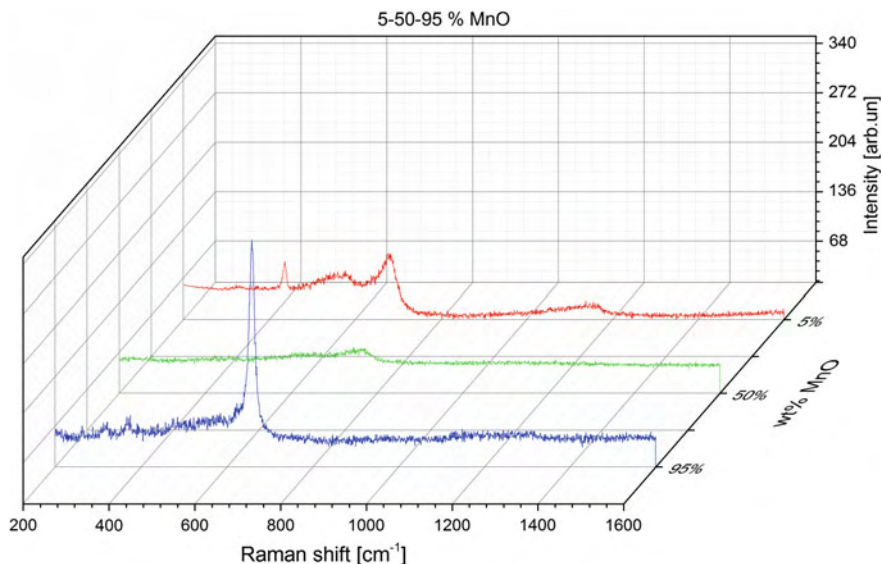
Fig. 4 Raman spectra of ZnO doped with 5, 50 and 95 % of MnO

mode on 485 cm^{-1}. For higher dopant concentration on spectra dominate sharp and narrow peak at approximately 650 cm^{-1}, typical for spinel structure and his origin is from Mn_3O_4. Beside this peak, also in sample doped with 95 % of MnO is visible Mn_3O_4 peak at 480 cm^{-1}. Presence of basic material ZnO is visible by modes at approximately 427 cm^{-1} $E_2^{(2)}$, 535 cm^{-1} A_1(LO) and multi phonon 2LO mode at 1150 cm^{-1}. $ZnMn_2O_4$ mode is represented with peaks at approximately 318, 380 and 476 cm^{-1}. Beside all these peaks of phases registered by XRD we also notice peaks that belongs to MnO phase such as peak on approximately 250 cm^{-1} and 590 cm^{-1}. Existence of MnO phase hasn't been register by XRD analysis. Here are also most of center peak position on something smaller frequencies as a consequence of nanosized structure of samples but generally in good agreement with previously reported Raman frequencies in works [24–26]. Low Raman activity of Mn_3O_4 on the one hand and the sensitivity of Raman analysis to the surface of the samples on the other hand could be reason for the difference between the Raman and XRD analysis for all concentration of dopant. Change of characteristic SOP modes with concentration of doping element (MnO) is shown on Fig. 5. On this figure we can notice that intensity of SOP modes decrease with increases of MnO concentration. This change of intensity of SOP modes is similar to the change of intensity of ZnO modes and opposite to the change of intensity of Mn_3O_4, $ZnMn_2O_4$ and $ZnMnO_3$ modes, like in case where dopant was CoO.

In Fig. 6 are given Raman spectra of ZnO doped with 5, 50 and 90 % of Fe_2O_3. Sharp and narrow peak, clearly visible on spectra doped with 5 % of Fe_2O_3, whose position is in that spectra on 437 cm^{-1} is obviously $E_2^{(2)}$ mode of ZnO. With increase of doping element, intensity of this peak decrease, due to ZnO origin.
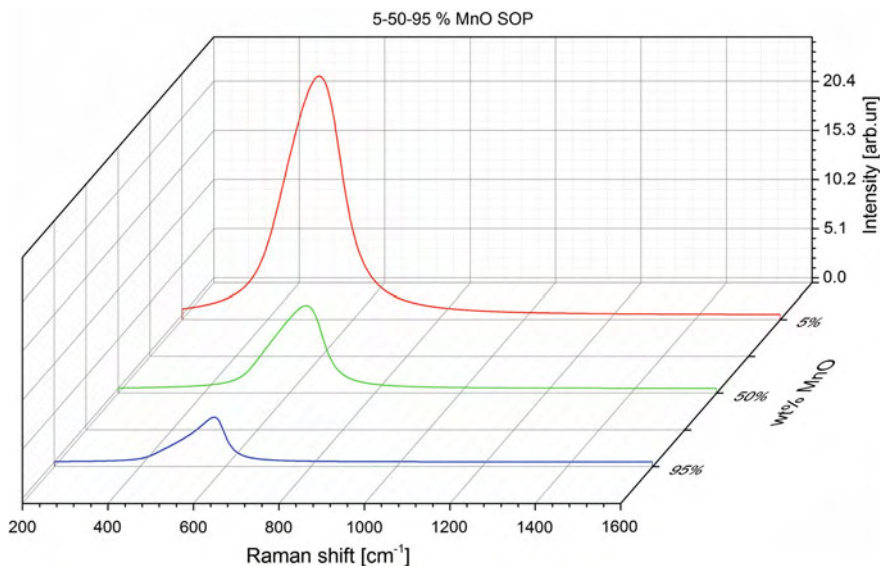
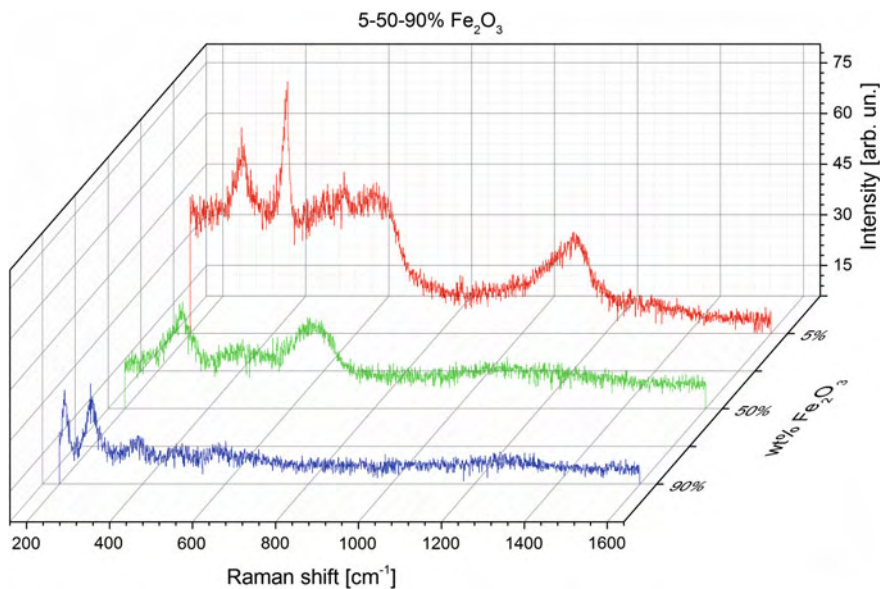**Fig. 5** SOP modes of ZnO doped with 5, 50 and 95 % of MnO

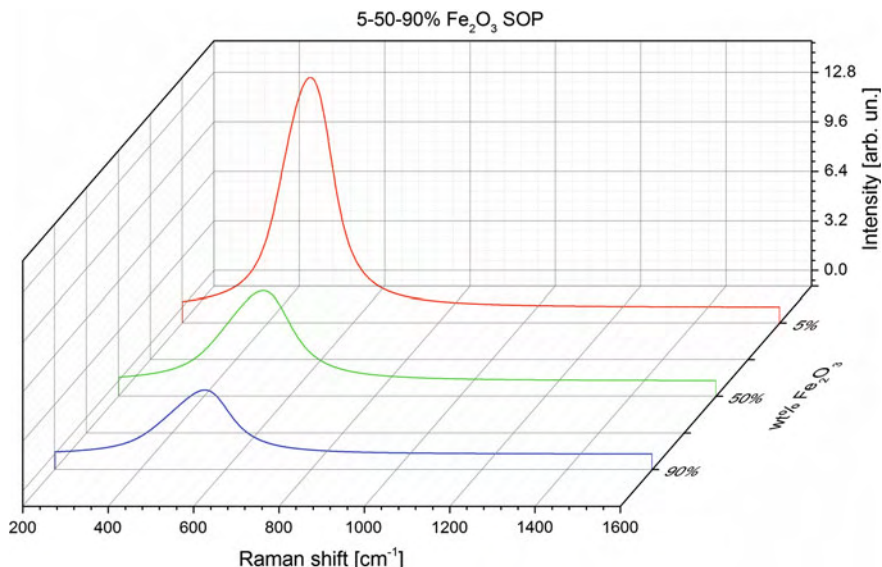**Fig. 6** Raman spectra of ZnO doped with 5, 50 and 90 % of Fe_2O_3

Fig. 7 SOP modes of ZnO doped with 5, 50 and 90 % of Fe$_2$O$_3$

Beside this E$_2^{(2)}$ mode, also are visible ZnO modes at 379 cm^{-1} A$_1$(TO), 577 cm^{-1} A$_1$(LO) and 592 cm^{-1} E$_1$(LO). Multi phonon 2LO ZnO modes at ∼330 and ∼1150 cm^{-1} are clearly visible too, while multi phonon mode 660 cm^{-1} with ZnFe$_2$O$_4$ peak at 647 cm^{-1} form one wide structure. Also on these spectra we can notice ZnFe$_2$O$_4$ modes at 246 cm^{-1} E$_g$, 355 cm^{-1} F$_{2g}$ and 451 cm^{-1} F$_{2g}$. Also we can notice peaks that belong to Fe$_2$O$_3$ phase as well, at 294 cm^{-1} E$_g$ and 498 cm^{-1} A$_g$. In spectra with 90 % of Fe$_2$O$_3$ we can easily notice Fe$_2$O$_3$ peaks at 225 cm^{-1} A$_g$, 294 cm^{-1} E$_g$, 412 cm^{-1} E$_g$ and 498 cm^{-1} A$_g$ along with two multi phonon peaks at 660 cm^{-1} and 1324 cm^{-1}. Also here are evident two ZnFe$_2$O$_4$ peaks at 355 cm^{-1} F$_{2g}$ and 451 cm^{-1} F$_{2g}$, while existence of ZnO modes are represented with four weak peaks at 437 cm^{-1} E$_2^{(2)}$, 577 cm^{-1} A$_1$(LO), 592 cm^{-1} E$_1$(LO) and multi phonon peak 660 cm^{-1}. Generally, with Raman spectroscopy in these spectra have been register existence of phases which haven't been register by XRD such as existence of Fe$_2$O$_3$ phase on lower dopant concentration and existence of ZnO and ZnFe$_2$O$_4$ phases for highest dopant concentration. Here are, as well as in case where CoO and MnO was dopants, most of center peak position on something smaller frequencies as a consequence of nanosized structure of samples but generally in good agreement with reported Raman frequencies in works [9, 23, 24]. Change of characteristic SOP modes with concentration of Fe$_2$O$_3$ is shown in Fig. 7. In this figure. we can notice that intensity of SOP modes decrease with increases of Fe$_2$O$_3$ concentration. This change of intensity of SOP modes is similar to the change of intensity of ZnO modes and opposite to the change of intensity of ZnFe$_2$O$_4$ and Fe$_2$O$_3$ modes, as well as in cases where doping elements was CoO and MnO.

5 Conclusions

The phase composition nanocrystalline samples of ZnO doped with CoO, MnO and Fe_2O_3 prepared by traditional wet chemistry method followed by calcinations was determined by X-ray diffraction. The crystalline phases of ZnO, Co_3O_4 Mn_3O_4, $ZnMn_2O_4$, $ZnMnO_3$, $ZnFe_2O_4$ and Fe_2O_3 were identified in samples. Crystallite size of all registered phases doesn't have monotonous dependence.
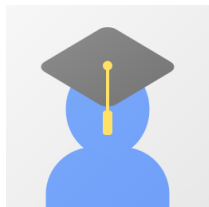
By Raman spectroscopy are registered peaks from all phases found by XRD in all samples, along with peaks that belong to MnO phase, in samples doped with MnO, whose presence hasn't been registered with XRD, as well as in case of samples doped with Fe_2O_3 where this Fe_2O_3 phase was register even for samples with smaller dopant concentration. Raman peaks of these phases are shifted and broadening compared to bulk modes. Due to nanosize structure of samples in presented Raman spectra's are also evident surface optical phonon (SOP) modes from ZnO nanoparticles. Relative intensity of ZnO and SOP modes decreases with increases of dopant concentration, while relative intensity of Co_3O_4, Mn_3O_4, $ZnMn_2O_4$, $ZnMnO_3$, $ZnFe_2O_4$ and Fe_2O_3 increases with increases of dopant concentration.

References

1. Y. Zhang, L. Wu, H. Li, J. Xu, L. Han, B. Wang, Z. Tuo, E. Xie, Influence of Fe doping on the optical property of ZnO films. JALLCOM **473**, 319–322 (2009)
2. Y. Chen, D.M. Bagnall, H. Koh, K. Park, K. Higara, Z. Zhu, T. Yao, Plasma assisted molecular beam epitaxy of ZnO on c-plane sapphire: growth and characterization. J. Appl. Phys. **84**, 3912–3918 (1988)
3. J. Nemeth, G. Rodriguez-Gattorno, A. Diaz, I. Dekany, Synthesis of ZnO nanoparticles on a clay mineral surface in dimethil sulfoxide medium. Langmuir **20**, 2855–2860 (2004)
4. J.M.D. Coey, M. Venkatesan, C.B. Fitzgerald, Donor impurity band exchange in dilute ferromagnetic oxides. Nat. Mater. **4**, 173–179 (2005)
5. T. Dietl, High temperature ferromagnetism and nano-scale phase separations in diluted magnetic semiconudtors and oxides. Acta Phys. Pol. A **111**, 27–46 (2007)
6. C. Sudakar, J.S. Thakur, G. Lawes, R. Naik, V.M. Naik, Ferromagnetism induced by planar nanoscale CuO inclusions in Cu-doped ZnO thin films. Phys. Rev. B **75**, 054423–054426 (2007)
7. J. Xu, W. Ji, X.B. Wang, H. Shu, Z.X. Shen, S.H. Tang, Temperature dependence of the Raman scatering spectra of Zn/ZnO nanoparticles. J. Raman Spectrosc. **29**, 613–615 (1998)
8. H. Zeng, W. Cai, B. Cao, J. Hu, Y. Li, P. Liu, Surface optical phonon Raman scattering in Zn/ZnO core-shell structured nanoparticles. Appl. Phys. Lett. **88**, 181905–3 (2006)

9. N. Romčević, R. Kostić, B. Hadžić, M. Romčević, I. Kuryliszin-Kudelska, W. Dobrowolski, U. Narkievicz, D. Sibera, Raman scattering from ZnO incorporating Fe nanoparticles: vibrational modes and low-frequency acoustic modes. JALLCOM **507**, 386–390 (2010)

10. M. Millot, J. Gonzalez, I. Molina, B. Salas, Z. Golacki, J.M. Broto, H. Rakoto, M. Gorian, Raman spectroscopy and magnetic properties of bulk ZnO: Co single crystal. JALLCOM **423**, 224–227 (2006)

11. R.P. Wang, G. Xu, P. Jin, Size dependence of electron-phonon coupling in ZnO nanowires. Phys. Rev. B **69**, 113303–113304 (2004)

12. R.Y. Sato-Berrú, A. Vázquez-Olmos, A.L. Fernández-Osorio, S. Sotres-Martínez, Micro-Raman investigationof transition-metal-doped ZnO nanoparticles. J. Raman Spectrosc. **38**, 1073–1076 (2007)

13. G. Irmer, Raman scattering of nanoporous semiconductors. J. Raman Spectrosc. **38**, 634–646 (2007)

14. P.-M. Chassaing, F. Demangeot, V. Paillard, A. Zwick, N. Combe, C. Pages, M.L. Kahn, A. Maisonnat, B. Chaudret, Surface optical phonons as a probe of oraganic ligands on ZnO nanoparticles: An investigation using a dielectric continuum model and Raman spectrometry. Phys. Rev. B **77**, 153306–153404 (2008)

15. A.L. Patterson, The diffraction of X-rays by small crystalline particles. Phys. Rev. **56**, 972–977 (1939)

16. H. Zeng, W. Cai, B. Cao, J. Hu, Y. Li, P. Liu, Surface optical phonon Raman scattering in Zn/ZnO core-shell structured nanoparticles. Appl. Phys. Lett. **88**, 181905–5 (2006)

17. A. Ghosh, R.N.P. Choudhary, Phonon assisted photoluminescence and surface optical mode of Zn embedded ZnO nanostructure. J. Phys. D: Appl. Phys. **42**, 075416–6 (2009)

18. F. Friedrich, N.H. Nickel, Resonant Raman scattering in hydrogen and nitrogen doped ZnO. Appl. Phys. Lett. **91**, 111903–3 (2007)

19. D.A.G. Bruggeman, Berechnung verschiedener physikalischer Konstanten von heterogenen Substanzen. Ann. Phys. **24**(5), 636–664 (1935)

20. J. Saarinen, E.M. Vartiainen, K. Peiponen, On tailoring of nonlinear spectral properties of nanocomposites having Maxwell Garnett of Bruggeman structure. Opt. Rev. **10**(2), 111–115 (2003)

21. X.C. Zeng, D.J. Bergman, P.M. Hui, D. Stroud, Effective-medium theory for nonlinear composites Phys. Rev. B **38**, 10970–10973 (1988)

22. H. Idink, V. Srikanth, W.B. White, E.C. Subbarao, Raman study of low temperature phase transitions in Bismuth titanate, $Bi_4Ti_3O_{12}$. J. Appl. Phys. **76**, 1819–1823 (1994)

23. N. Ashkenov, B.N. Mbenkum, C. Bundesmann, V. Riede, M. Lorenz, D. Spemann, E.M. Kaidashev, A. Kasic, M. Shubert, M. Grundmann, Infrared dielectric functions and phonon modes of high-quality ZnO films. J. Appl. Phys. **93**, 126–133 (2003)

24. E.F. Venger, A.V. Melnichuk, L. Lu Melnichuk Yu A. Pasechuk, Anisotropy of the ZnO single crystal reflectivity in the region of residual rays. Phys. Stat. Solidi B **188**, 823–831 (1995)

25. V.G. Hadjiev, M.N. Iliev, I.V. Vegilov, The Raman spectra of Co_3O_4. J. Phys. C: Solid State Phys. **21**, L199–L201 (1988)

26. C.M. Julien, M. Massot, C. Poinsignon, Lattice vibrations of manganese oxides: part I. Periodic structures. Spectrochim. Acta Part A **60**, 689–700 (2004)

27. K. Polychronopoulou, F. Cabello Galisteo, M. Lopez Granados, J. L.G. Fierro, T. Bakas, A. M. Efstathiou, Novel Fe-Mn-Zn-Ti-O mixed-metal oxides for the low-temperature removal of H_2S from gas streams in the presence of H_2, CO_2, and H_2O. J. Catal. **236**, pp. 205–220 (2005)

28. L. Malavasi, P. Galinetto, M.C. Mozzati, C.B. Azzoni, G. Flor, Raman spectroscopy of AMn_2O_4 (A = Mn, Mg, Zn) spinels. Phys. Chem. Chem. Phys. **4**, 3876–3880 (2002)

29. M. Bouchard, A. Gambardella, Raman microscopy study of synthetic cobalt blue spinels used in the field of art. J. Raman Spectrosc. **41**, 1477–1485 (2010)

Jelena Trajić

Associate Research Professor

physics

НАСЛОВ	НАВЕЛО	ГОДИНА
Raman spectroscopy of ZnS quantum dots J Trajić, R Kostić, N Romčević, M Romčević, M Mitrić, V Lazović, P Balaž, ... Journal of Alloys and Compounds 637, 401-406	36	2015
Far-infrared study of impurity local modes in Ni-doped PbTe N Romčević, J Trajić, TA Kuznetsova, M Romčević, B Hadžić, ... Journal of alloys and compounds 442 (1-2), 324-327	28	2007
Surface optical phonons in ZnO (Co) nanoparticles: Raman study B Hadžić, N Romčević, M Romčević, I Kuryliszyn-Kudelska, ... Journal of alloys and compounds 540, 49-56	27	2012
Raman spectroscopy of optical properties in CdS thin films J Trajić, M Gilić, N Romčević, M Romčević, G Stanišić, B Hadžić, ... Science of Sintering 47 (2), 145-152	26	2015
Plasmon–phonon and plasmon–two different phonon interaction in Pb1−xMnxTe mixed crystals J Trajić, N Romčević, M Romčević, VN Nikiforov Materials Research Bulletin 42 (12), 2192-2201	16	2007
Optical properties of PbTe: Mn J Trajić, M Romčević, N Romčević, S Nikolić, A Golubović, S Durić, ... Journal of alloys and compounds 365 (1-2), 89-93	16	2004
Raman spectra of Pb1− xMnxTe alloys N Romčević, A Golubović, M Romčević, J Trajić, S Nikolić, S Đurić, ... Journal of alloys and compounds 402 (1-2), 36-41	15	2005
Pb1-x Mnx Te and PbTe1-xSx compounds and their optical properties J Trajić, A Golubović, M Romčević, N Romčević, S Nikolić, VN Nikiforov Journal of the Serbian Chemical Society 72 (1), 55-62	13	2007
Structural and optical properties of CuSe2 nanocrystals formed in thin solid Cu–Se film M Gilić, M Petrović, R Kostić, D Stojanović, T Barudžija, M Mitrić, ... Infrared Physics & Technology 76, 276-284	10	2016
Raman spectroscopy of PbTe1− xSx alloys N Romčević, J Trajić, M Romčević, A Golubović, S Nikolić, VN Nikiforov Journal of alloys and compounds 387 (1-2), 24-31	9	2005
Optical properties and plasmon–Two different phonons coupling in ZnGeAs2+ Mn M Romčević, N Romčević, W Dobrowolski, L Kilanski, J Trajić, ... Journal of alloys and compounds 548, 33-37	8	2013

НАСЛОВ	НАВЕЛО	ГОДИНА
Far-infrared study of impurity local modes in Co-doped PbTe J Trajić, N Romčević, M Romčević, D Stojanović, R Rudolf, ... Journal of alloys and compounds 493 (1-2), 41-46	8	2010
Optical Properties of CuSe Thin Films–Band Gap Determination M Petrović, M Gilić, J Ćirković, M Romčević, N Romčević, J Trajić, I Yahia Science of Sintering 49 (2)	7	2017
Kinetics of solid-state synthesis of quaternary Cu2FeSnS4 (stannite) nanocrystals for solar energy applications P Baláž, M Baláž, A Zorkovská, I Škorvánek, Z Bujňáková, J Trajić Acta Phys Pol A 131, 1153-1155	7	2017
Far-infrared spectra of dysprosium doped yttrium aluminum garnet nanopowder J Trajić, MS Rabasović, S Savić-Šević, D Ševic, B Babić, M Romčević, ... Infrared Physics & Technology 77, 226-229	7 *	2016
Far-infrared spectroscopy of CdTe1− xSex (In): Phonon properties M Petrović, N Romčević, J Trajić, WD Dobrowolski, M Romčević, B Hadžić, ... Infrared Physics & Technology 67, 323-326	7	2014
Optical and Magnetic Properties of PbTe (Ni) N Romčević, J Trajić, M Romčević, D Stojanović, T Kuznetsova, ... Acta Physica Polonica A 4 (115), 805-807	6	2009
Structural properties of Eu3+ doped Gd2Zr2O7 nanopowders: Far-infrared spectroscopy J Mitrić, J Križan, J Trajić, G Križan, M Romčević, N Paunović, B Vasić, ... Optical Materials 75, 662-665	5	2018
Far-infrared investigations of the surface modes in CdS thin films J Trajić, M Gilić, N Romčević, M Romčević, G Stanišić, Z Lazarević, ... Physica Scripta 2014 (T162), 014031	5	2014
Optical properties of plastically deformed copper J Trajić, R Rudolf, I Anžel, M Romčević, N Lazarević, M Mirić, Z Lazarević, ... Acta Physica Polonica A 117 (5), 791-793	5	2010
Plasmon: Two phonon interaction in PbMnTe and PbTeS alloys J Trajić, N Romčević, M Romčević, VN Nikiforov Journal of the Serbian Chemical Society 73 (3), 369-376	5	2008
Far-infrared spectra of mesoporous ZnS nanoparticles J Trajić, M Romčević, N Romčević, B Babić, B Matović, P Baláž Optical Materials 57, 225-230	4	2016
Raman spectra of CdTe/ZnTe self-assembled quantum dots N Romčević, M Romčević, R Kostić, D Stojanović, G Karczewski, ... Microelectronics Journal 40 (4-5), 830-831	4	2009
Improvement of magneto-optical quality of high purity Bi12GeO20 single crystal induced by femtosecond pulsed laser irradiation GSI Abudagel, S PETRIČEVIĆ, P MIHAILOVIĆ, A KOVAČEVIĆ, ... Optoelectronics and Advanced Materials, Rapid Communications 11 (7-8)	3	2017
Defects in Cd1− xMnxGeAs2 lattice M Romcevic, N Romcevic, J Trajic, L Kilanski, W Dobrowolski, ... Journal of Alloys and Compounds 688, 56-61	3	2016

НАСЛОВ	НАВЕЛО	ГОДИНА
Study of Bi12SiO20 single crystals obtained by Czochralski method ZŽ Lazarević, S Kostić, MJ Romčević, J Trajić, B Hadžić, D Stojanović, ... Optoelectron. Adv. Mater.—Rapid Commun 5, 150-152	3	2011
Photoluminescence spectroscopy of CdSe nanoparticles embedded in transparent glass M Gilic, R Kostic, D Stojanovic, M Romcevic, B Hadzic, M Petrovic, ... Optical and Quantum Electronics 50 (7), 1-8	2	2018
Structural Properties of Cu-Se-CuSe$_2$ Thin Films M Gilić, M Petrović, B Hadžić, M Romčević, J Trajić, N Romčević, ... Proceedings of the IV Advanced Ceramics and Applications Conference, 235-256	2	2017
Off-resonant Raman spectroscopy of ZnS quantum dots R Kostić, D Stojanović, J Trajić, P Balaž Proceedings of the IV Advanced Ceramics and Applications Conference, 203-215	2	2017
Spectroscopy study of Bi12GeO20 single crystals ZŽ LAZAREVIĆ, S Kostić, V Radojević, MJ Romčević, B Hadžić, J Trajić, ... Optoelectronics and Advanced Materials-Rapid Communications 7 (January …	2	2013
Far-infrared phonon spectroscopy of Pb1− xMnxTe layers grown by molecular beam epitaxy N Romčević, AJ Nadolny, M Romčević, T Story, B Taliashvili, A Milutinović, ... Journal of alloys and compounds 438 (1-2), 34-40	2	2007
Plasmon-two phonon interaction in PbTe$_{0.95}$S$_{0.05}$ alloy N Romčević, J Trajić, M Romčević, VN Nikiforov physica status solidi (c) 1 (11), 2832-2835	2	2004
Structural Properties of Pb1-xMnxTe Alloys A Golubović, S Nikolić, J Trajić, S Djurić, NŽ Romčević, MJ Romčević, ... Materials Science Forum 453, 99-102	2	2004
Surface optical phonon (SOP) mode in ZnS/Poly (methylmethacrylate) nanocomposites M Curcic, B Hadzic, M Gilic, V Radojevic, A Bjelajac, I Radovic, ... Physica E: Low-dimensional Systems and Nanostructures 115, 113708	1	2020
Influence of Preparation Method on SOP Modes in ZnO Doped with CoO Nanoparticles B Hadžić, M Romčević, J Trajić, G Stanišić, D Timotijević Proceedings of the IV Advanced Ceramics and Applications Conference, 217-234	1	2017
Optical properties of Cd1-xMnxS nanoparticles: off-resonance Raman spectroscopy M PETROVIĆ, M ROMČEVIĆ, R KOSTIĆ, N ROMČEVIĆ, WD Dobrowolski, ... Optoelectronics and Advanced Materials-rapid communications 10 (March-April …	1	2016
Vibrational Spectroscopy of SOP Modes in ZnO Doped with CoO, MnO and Fe$_2$O$_3$ B Hadžić, N Romčević, J Trajić, R Kostić, G Stanišić, D Timotijević Proceedings of the III Advanced Ceramics and Applications Conference, 159-172	1	2016
Raman study of surface optical phonons in ZnO (Co) nanoparticles prepared by calcinations method B HADŽIĆ, N ROMČEVIĆ, M ROMČEVIĆ, I KURYLISZYN-KUDELSKA, ... Journal of Optoelectronics and Advanced Materials 16 (5-6), 508-512	1	2014

НАСЛОВ	НАВЕЛО	ГОДИНА
Spectroscopy characterization of MnSe nanoclasters randomly distributed in HgMnTe single crystal M Petrović, N Romčević, M Romčević, G Stanišić, D Vasiljević-Radović, ... Journal of crystal growth 338 (1), 75-79	1	2012
Optical properties of plastically deformed copper: an ellipsometric study N Romcevic, R Rudolf, J Trajic, M Romcevic, B Hadzic, ... Materiali in tehnologije 45 (5), 463-465	1	2011
Phonons investigation of ZnO@ ZnS core-shell nanostructures with active layer B Hadzic, B Matovic, M Randjelovic, R Kostic, M Romcevic, J Trajic, ... Journal of Raman Spectroscopy 52 (3), 616-625		2021
Plasmon–Phonon interaction in ZnSnSb2+ Mn semiconductors M Romcevic, N Paunovic, U Ralevic, J Pesic, J Mitric, J Trajic, L Kilanski, ... Infrared Physics & Technology 108, 103345		2020
Far-infrared spectroscopy of laser power modified MnO nanoparticles B. Babic, B.Hadzic, I. Kuryliszyn-Kudelska, N. Paunovic, B. Vasic, W.D ... Optoelectronics and Advanced Materials-Rapid Communications 13, 376-379		2019
Far infrared spectra of Si doped PbTe single crystals J. Trajic, N. Paunovic, M. Romcevic, V.E. Slynko, Jasna L. Ristic-Djurovic ... Optical Materials 91, 195-198		2019
Optical properties of the mechanochemically synthesized Cu2FeSnS4 (stannite) nanocrystals: Raman study J. Trajic, M. Romcevic, M. Petrovic, M. Gilic, P. Balaz, A. Zorkovska, N ... Optical Materials 75, 662-665		2018
Far-infrared study of the mechanochemically synthesized Cu2FeSnS4 (stannite) nanocrystals J. Trajic, M. Romcevic, N. Paunovic, M. Curcic, P. Balaz, N. Romcevic Infrared Physics & Technology 90, 66–69		2018
Surface optical phonon – Plasmon interaction in nanodimensional CdTe thin Films J. Mitric, N. Paunovic, M. Mitric, B. Vasic, U. Ralevic, J. Trajic, M ... Physica E: Low-dimensional Systems and Nanostructures 104, 64-70		2018
Growth, characterization and optical quality of calcium fluoride single crystals grown by the Bridgman method HI Elswie, S Kostić, V Radojević, NŽ Romčević, B Hadžić, J Trajić, ... Optoelectronics and Advanced Materials-Rapid Communications 10 (7-8), 522-525		2016
Optical Properties of Plastically Deformed Copper: Ellipsometry and Raman Study M Gilić, M Petrović, B Hadžić, ZŽ Lazarević, M Romčević, J Trajić, ... Proceedings of the III Advanced Ceramics and Applications Conference, 173-182		2016
Optical Properties and Electron–Phonon Interactions of $CdTe_{1-X}Se_X$(In) Single Crystal M Petrović, J Trajić, M Gilić, M Romčević, B Hadžić, Z Lazarević, ... Proceedings of the III Advanced Ceramics and Applications Conference, 183-191		2016
Self-polarization in spherical quantum dot DP Stojanović, RS Kostić, JM Trajić		2015

НАСЛОВ	НАВЕЛО	ГОДИНА

Tehnika 70 (5), 747-751

Galvanomagnetic and optical properties of chromium doped PbTe

J. Trajić, N. Romčević, M. Romčević, D. Stojanović, L.I. Ryabova, D.R. Khokhlov
Journal of Alloys and Compounds 602 (2014), 300-305

2014

Plasmon–ionized impurity–phonon interaction in PbTe doped with Ni

J TRAJIĆ, N ROMČEVIĆ, M ROMČEVIĆ, Z LAZAREVIĆ, TA Kuznetsova, ...
Optoelectronics and Advanced Materials-Rapid Communications 7 (July-August …

2013

Infrared and Raman Spectroscopy Study of Antimony Doped Barium Titanate Prepared from Organometallic Complex

ZŽ Lazarević, NŽ Romčević, MJ Romčević, J Trajić, MM Vijatović, J Bobić, ...
International Journal of Modern Physics B 24 (06n07), 676-681

2010

Ellipsometric Measurements of Plastically Deformed Copper

M Mirić, R Rudolf, I Anžel, B Hadžić, M Romčević, J Trajić, N Romčević
Acta Physica Polonica A 116 (4), 715-717

2009

Selected Papers Presented at the Tenth Annual Conference of the Materials Research Society of Serbia, YUCOMAT 2008, Herceg Novi, Montenegro, September 8-12, 2008

Ž Nikitović, V Stojanović, ZL Petrović, R Kostić, D Stojanović, ...
Acta Physica Polonica A 115 (4)

2009

Photoluminescence Spectroscopy of CdTe/ZnTe Self-Assembled Quantum Dots

N Romcevic, M Romcevic, R Kostic, D Stojanovic, A Milutinovic, J Trajic, ...
International Journal of Photoenergy 2009

2009

Investigation of photoconductivity in n-type Galium doped PbTe

D Stojanović, N Romčević, J Trajić, B Hadžić, M Romčević, DR Khokhlov
Science of Sintering 39 (2), 169-175

2007

RAMANOVA SPEKTROSKOPIJA CD1-XMNXS NANOČESTICA

N Romčević, R Kostić, M Romčević, J Trajić
Proc. 50th ETRAN Conference 4

2006

Surface Optical Phonon in Europium doped Yttrium Orthovanadate Nanopowders

J Mitrić, N Paunović, J Ćirković, M Gilić, J Trajić, M Romčević, N Romčević
14 th Photonics Workshop, 22

Far-infrared and Raman Spectroscopy of CdTe 0.97 Se 0.03 (In)

N Romcevic, M Romcevic, J Trajic, D Stojanovic, Z Lazarevic, B Hadzic, ...

FAZNI PRELAZ KOD PbTe0. 95S0. 05 MONOKRISTALA: ULTRAZVUýNA MERENJA

J Trajić, N Romčević, M Romčević, VN Nikiforov, AN Vasilev
Tc 900, 3.64

На основу члана 22. става 2. члана 70. став 6. и члана 86. став 1. и 2. Закона о научноистраживачкој делатности ("Службени гласник Републике Србије", број 110/05 и 50/06 – исправка и 18/10), члана 50. став 1. Закона о изменама и допунама Закона о научноистраживачкој делатности ("Службени гласник Републике Србије", број 112/15), члана 2. става 1. и 2. тачке 1 – 4.(прилози), члана 31. став 1., члана 37. и 38. Правилника о поступку и начину вредновања и квантитативном исказивању научноистраживачких резултата истраживача ("Службени гласник Републике Србије", број 38/08) и захтева који је поднео

Институт за физику у Београду

Комисија за стицање научних звања на седници одржаној 28.09.2016. године, донела је

ОДЛУКУ
О СТИЦАЊУ НАУЧНОГ ЗВАЊА

Др Јелена Трајић
стиче научно звање
Виши научни сарадник
Р е и з б о р

у области природно-математичких наука - физика

О Б Р А З Л О Ж Е Њ Е
Институт за физику у Београду

утврдио је предлог број 200/1 од 09.02.2016. године на седници Научног већа Института и поднео захтев Комисији за стицање научних звања број 237/1 од 17.02.2016. године за доношење одлуке о испуњености услова за реизбор у научно звање *Виши научни сарадник*.

Комисија за стицање научних звања је по претходно прибављеном позитивном мишљењу Матичног научног одбора за физику на седници одржаној 28.09.2016. године разматрала захтев и утврдила да именована испуњава услове из члана 70. став 6. и члана 86. став 1. Закона о научноистраживачкој делатности ("Службени гласник Републике Србије", број 110/05 и 50/06 – исправка и 18/10), члана 2. става 1. и 2. тачке 1 – 4.(прилози), члана 31. став 1., 37. и 38. Правилника о поступку и начину вредновања и квантитативном исказивању научноистраживачких резултата истраживача ("Службени гласник Републике Србије", број 38/08) за реизбор у научно звање *Виши научни сарадник,* па је одлучила као у изреци ове одлуке.

Доношењем ове одлуке именована стиче сва права која јој на основу ње по закону припадају.

Одлуку доставити подносиоцу захтева, именованој и архиви Министарства просвете, науке и технолошког развоја у Београду.

ПРЕДСЕДНИК КОМИСИЈЕ   **МИНИСТАР**

Др Станислава Стошић-Грујичић,   Младен Шарчевић

научни саветник

Анекс III Уговора о реализацији Пројекта ИИИ 45003 у 2014. години

У складу са чл. 10, 97, 98. и 104. Закона о научноистраживачкој делатности („Службени гласник РС", бр. 110/05, 50/06-испр. и 18/10 - у даљем тексту: Закон), сагласно Акту о избору, вредновању и финансирању Програма ОИ/ТР/ИИИ број 451-01-967/2010-01 од 20. маја 2010. године - у даљем тексту: Акт, а на основу тачке 2. Одлуке о распореду средстава за финансирање истраживања по пројектима одобреним у оквиру програма ОИ/ТР/ИИИ у периоду од 1. маја до 31. децембра 2014. године, број 451-03-694/2014-14 -1 од 29. априла 2014. године,

уговорне стране:

1) РЕПУБЛИКА СРБИЈА – Министарство просвете, науке и технолошког развоја, Београд, Немањина 22-26, ПИБ 102199748, матични број: 17329235 (у даљем тексту: Министарство), које представља министар просвете, науке и технолошког развоја,

и

2) РЕАЛИЗАТОРИ ИСТРАЖИВАЊА - учесници у реализацији научноистраживачког пројекта:

2. 1) Иновациони центар Електротехничког факултета у Београду д.о.о., ПИБ 104385708, матични број:20146125, рачун КЈС број 840-0000000091723-51, кога заступа др Бранимир Рељин , директор

2. 2) Мегатренд универзитет, Факултет за међународну економију, ПИБ 100024624, матични број:17251716, рачун КЈС број 840-0000000246763-46, кога заступа др Бранислав Пелевић , декан

2. 3) Мегатренд универзитет, Факултет за пословне студије, ПИБ 104042065, матични број:17241117, рачун КЈС број 840-0000000442763-60, кога заступа др Ана (Ланговић) Милићевић , декан

2. 4) Универзитет у Београду, Грађевински факултет, ПИБ 100251144, матични број:07006454, рачун КЈС број 840-0000001437660-59, кога заступа др Душан Најдановић , декан

2. 5) Универзитет у Београду, Електротехнички факултет, ПИБ 101206130, матични број:07032498, рачун КЈС број 840-0000001438660-66, кога заступа др Бранко Ковачевић , декан

2. 6) Универзитет у Београду, Институт за нуклеарне науке "Винча", ПИБ 101877940, матични број:7035250, рачун КЈС број 840-0000000011723-73, кога заступа др Борислав Грубор , директор

2. 7) Универзитет у Београду, Институт за физику, ПИБ 100105980, матични број:7018029, рачун КЈС број 840-0000000020723-39, кога заступа др Александар Богојевић , в.д. директор

2. 8) Универзитет у Београду, Машински факултет, ПИБ 100209517, матични број:07032501, рачун КЈС број 840-0000001876660-28, кога заступа др Милорад Милованчевић , декан

2. 9) Универзитет у Београду, Стоматолошки факултет, ПИБ 100125119, матични број:07001991, рачун КЈС број 840-0000001122660-85, кога заступа др Мирослав Вукадиновић , декан

2. 10) Универзитет у Београду, Технолошко-металуршки факултет, ПИБ 100123813, матични број:07032552, рачун КЈС број 840-0000001441660-87, кога заступа др Ђорђе Јанаћковић , декан

2. 11) Универзитет у Новом Саду, Факултет техничких наука, ПИБ 100724720, матични број:08067104, рачун КЈС број 840-0000001710660-30, кога заступа др Раде Дорословачки , декан

2. 12) Универзитет Унион, Рачунарски факултет, ПИБ 102971356, матични број:17489453, рачун КЈС број 840-0000000296763-08, кога заступа Др Драган Милетић , декан

закључују

Анекс III
основног уговора о реализацији Пројекта ИИИ у периоду мај -децембар 2014. као четврте године истраживања у циклусу 2011-2015. године

Члан 1.

Овим анексом се мења и допуњује основни Уговор о реализацији Пројекта ИИИ, тако што се уређују међусобна права и обавезе уговорних страна и Руководиоца Пројекта у реализацији и финансирању научноистраживачког пројекта: "Оптоелектронски нанодимензиони системи - пут ка примени", евиденциони број ИИИ 45003 (у даљем тексту: Пројекат ИИИ) у периоду мај-децембар 2014. као четврте године истраживања у текућем циклусу 2011-2015. године.

Финансирање реализације Пројекта ИИИ у периоду јануар-април 2014. године извршено је у складу са одлуком број 451-03-694/2014-14 од 30. јануара 2014. године.

Реализатори истраживања на Пројекту ИИИ по овом анексу су правна лица из члана 104. став 1. Закона.

Члан 2.

Укупан обим истраживања на Пројекту ИИИ у 2014. години износи 389 истраживачких месеци (од којих у периоду јануар-април 2014. године пројектно финансирано 130 истраживач месеци).

Руководилац Пројекта ИИИ је др Небојша Ромчевић, научни саветник запослен у научноистраживачкој организацији: Универзитет у Београду, Институт за физику (у даљем тексту: Руководилац Пројекта).

Одлуку о одређивању другог лица за Руководиоца Пројекта доноси министар, уз прибављено образложено писано мишљење руководилаца свих Реализатора истраживања.

Пројекат ИИИ чине следећи потпројекти:
- Потпројекат 1: "Синтеза наноматеријала и структура", чији је руководилац Душанка Стојановић, виши научни сарадник
- Потпројекат 2: "Теорија оптичких особина наноструктура", чији је руководилац Милан Тадић, редовни професор
- Потпројекат 3: "Електронски принципи формирања и функционисања наноструктура ", чији је руководилац Ивана Радисављевић, научни сарадник
- Потпројекат 4: "Примена рачунара у повезивању теоријских, експерименталних и примењених истраживања", чији је руководилац Стеван Милинковић, редовни професор
- Потпројекат 5: "Карактеризација наночестица и наноструктура", чији је руководилац Јелена Трајић, виши научни сарадник
- Потпројекат 6: "Испитивање електричних карактеристика нових материјала и пројектовање сензора са оптичким влакнима", чији је руководилац Милош Сланкаменац, доцент
- Потпројекат 7: "Наноструктурни оптоелектонски сензорски системи", чији је руководилац Пеђа Михаиловић, ванредни професор

Члан 3.

Овим анексом се утврђује следећи износ и структура буџета Пројекта ИИИ за 2014. годину:

1) Накнаде за рад истраживача, односно сарадника ангажованих на Пројекту ИИИ (у даљем тексту: истраживач) у бруто износу, одређене множењем одобрених

УГОВОР О ДОПУНСКОМ РАДУ

На основу члана 202. Закона о раду, **Рачунарски факултет у Београду**, ул. Кнез Михаилова 6/6 кога заступа в.д. декана др Драган Милетић ЈМБГ 2103955722214(даље: **послодавац**) и др Јелена Трајић ЈМБГ 1907964715040 ул. Катанићева 9 а са пребивалиштем у Београду, (даље: **извршилац посла**), закључују

УГОВОР О ДОПУНСКОМ РАДУ

Члан 1

Извршилац посла преузима обавезу да за послодавца обавља послове извођења наставе за предмет Карактеризација полупроводника на програму докторских студија Рачунарско инжењерство.

Извршилац посла ће наведене послове обављати у седишту послодавца, односно у Београду, Кнез Михаилова 6/6.

Члан 2

Послове из члана 1. извршилац посла ће обављати највише 1 (један) радни дан у недељи у трајању од 5 часова.

Евиденцију о радним сатима ће водити послодавац, а извршилац посла ће давати сагласност на ту евиденцију својим потписом.

Члан 3

Послодавац ће извршиоцу посла на име обављеног рада исплатити износ који ће бити одређен анексом овог уговора.

Члан 4

Овај уговор почиње да важи од школске 2014/15 године.

По истеку наведеног периода послодавац и извршилац посла могу наставити даљу сарадњу која ће бити дефинисана анексом уговора.

Члан 5

Евентуалне спорове по овом уговору уговорне стране решаваће споразумно, а спорове који се не могу решити споразумно, решаваће надлежни суд у Београду.

Члан 6

Овај уговор сачињен је у 2 истоветна примерка од којих по 1 примерак задржава свака уговорна страна.

У Београду дана 19.11.2013. године.

ИЗВРШИЛАЦ ПОСЛА   ПОСЛОДАВАЦ

Др Јелена Трајић   Др Драган Милетић

(https://www.cost.eu)

CA18112 - Mechanochemistry for Sustainable Industry

Home (https://www.cost.eu) > Browse Actions (https://www.cost.eu/?page_id=89) > Mechanochemistry for Sustainable Industry

🌐 www.mechsustind.eu (http://www.mechsustind.eu)

⬇ Downloads   👥 Team

| Description | Parties | **Management Structure** |

Action Leadership Positions

Action Chair	Dr Evelina COLACINO ⌄ (145460)
Action Vice Chair	Prof Lucia MAINI ⌄ (121694)
WG 1 - Lab-scale syntheses	Dr Bilge BAYTEKIN ⌄ (168310)
WG 2 - Mechanistic investigations and in-situ monitoring	Dr Ivan HALASZ ⌄ (144075)
WG 3 - "The engineering perspective"	Dr Deborah CRAWFORD ⌄ (148617)
Grant Holder Scientific Representative	Prof Lucia MAINI ⌄ (121694)
Science Communication Manager	Dr Felipe GARCIA ⌄ (148375)
STSM Coordinator	Dr Matej BALÁŽ ⌄ (148203)
ITC Conference Manager	Dr Vania ANDRE ⌄ (148240)

Management Committee

Country	MC Member

Latvia	Dr Edgars ELSTS ⌄ (16 028)
Latvia	Dr Kirill SHOBIN ⌄ (220535)
Malta	Dr Liana VELLA ZARB ⌄ (9153)
Malta	Prof Ulrich BAISCH ⌄ (81473)
Moldova	Dr Evghenii HAREA ⌄ (105031)
Montenegro	Prof Vanja ASANOVIĆ ⌄ (242875)
Netherlands	Mr Pietro RANDO ⌄ (205044)
Netherlands	Prof Floris RUTJES (0)
North Macedonia	Prof Aleksandar CVETKOVSKI ⌄ (192860)
North Macedonia	Prof Kiril LISICHKOV ⌄ (157888)
Norway	Prof Eva RAULS ⌄ (229930)
Poland	Prof Dariusz MATOGA ⌄ (147531)
Poland	Prof Janusz LEWINSKI ⌄ (149167)
Portugal	Dr Fátima PIEDADE ⌄ (135219)
Portugal	Dr Vania ANDRE ⌄ (148240)
Romania	Dr Marieta MURESAN-POP ⌄ (149022)
Romania	Prof Ede BODOKI ⌄ (108243)
Serbia	Dr Jasmina GRBOVIC NOVAKOVIC ⌄ (39205)
Serbia	Dr Jelena TRAJIĆ ⌄ (203353)
Slovakia	Dr Matej BALÁŽ ⌄ (148203)
Slovakia	Prof Radovan SEBESTA ⌄ (6271)
Slovenia	Dr Miroslav HUSKIC ⌄ (21421)
Slovenia	Dr Thomas WILHELM ⌄ (181385)
Spain	Ms Daily RODRÍGUEZ ⌄ (121036)
Spain	Prof José Carlos MENÉNDEZ RAMOS ⌄ (133175)
Sweden	Dr Niclas SOLIN ⌄ (223547)
Switzerland	Dr Fabrice GALLOU ⌄ (223992)

PROGRAM

&

ZBORNIK APSTRAKATA

Programski odbor

Kopredsednici

dr Nebojša Romčević, Kristal infiz doo

Dragan Ignjatijević, Spektroskopija infiz doo

Članovi

prof. Zoran V Popović, Institut za fiziku

prof. Jovan Radunović, Elektrotehnički fakultet

prof. Dejan Živković, Inovacioni centar elektrotehničkog fakulteta

prof. Daniel W Dobrowolski, IFPAN, Warsaw, Poland

dr Ivan Pipi, Instituto di Fisica Aplicata - Nello Carrara, Italy

Organizacioni odbor

Dr Maja Romčević, Institut za fiziku

Dr Radoš Gajić, Institut za fiziku

Dr Jelena Trajić, Institut za fiziku

Dr Radmila Kostić, Institut za fiziku

Dr Dušanka Stojanović, Institut za fiziku

Zorica Lazarević, Institut za fiziku

2

PROGRAM

&

ZBORNIK APSTRAKATA

Програмски одбор:

III Саветовања - Трансфер технологија и знања из Научно-истраживачких организација у мала и средња предузећа (Врдник, 29. јуни - 01. јули 2010.)

Копредседници:

др Небојша Ромчевић, научни саветник Института за физику, директор Кристал Инфиз доо

дипл. инж. Драган Игњатијевић, директор Спектроскопија Инфиз доо.

Чланови одбора:

Проф. Зоран В. Поповић, дописни члан САНУ

Проф. Дејан Живковић, Иновациони Центар Електротехнички факултет, Београд
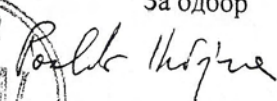
Др Драган Поповић, директор Института за физику

Prof Daniel W Dobrowolski, Institute of Physics Polish Academy of Science, Warsawa, Poland

Dr Ivan Pipi, Instituto di Fisica Aplicata - Nello Carrara, Italy.

Dr Jelena Trajić, Института за физику

Dr Dušanka Stojanović, Института за физику.

За одбор

др Небојша Ромчевић

директор, Кристал инфиз доо

Univerzitet u Beogradu

Fakultet za fizičku hemiju

Martina D. Gilić

Optičke osobine nanodimenzionih sistema formiranih u plastično deformisanom bakru, tankim filmovima CdS i heterostrukturama CdTe/ZnTe

doktorska disertacija

Beograd, 2014

Физички факултет

Универизитет у Београду

докторска дисертација

Вибрациона спектроскопија $Pb_{1-x}Mn_xTe$ добијеног епитаксијом молекулског снопа и нанодимензионог ZnO допираног Mn, Co и Fe

Бранка Б. Хаџић

Београд, 2009

Физички факултет

Универизитет у Београду

магистарска теза

Вибрациона спектроскопија $Pb_{1-x}Mn_xTe$ добијеног Брицмановим методом и епитаксијом молекулског снопа

Бранка Б. Хаџић

Београд, 2007

Megatrend univerzitet, Beograd

Fakultet za poslovne studije, Beograd

Andrea D. Bučalina

KOMPARATIVNA ANALIZA SAVREMENIH SVETSKIH TOKOVA U UPRAVLJANJU INVESTICIJAMA U NANOTEHNOLOŠKE PROIZVODE

-doktorska disertacija-

Beograd, 2013.

Mentor: prof. dr Nataša Bogavac Cvetković,

Fakultet za poslovne studije, Beograd

Članovi komisije: prof. dr Ana Milićević,

Fakultet za inženjerski menadžment, Beograd

dr Jelena Trajić, viši naučni saradnik

Institut za fiziku, Zemun

Datum odbrane doktorske disertacije:.................................

Datum promocije:...............................

Doktorat nauka: multidisciplinarna oblast – Ekonomija, Menadžment

Subject **NCN: SONATA BIS Invitation to review grant proposal for the National Science Center, Poland**

From National Science Centre, Poland <osf_administracja@opi.org.pl>

To <jelena@ipb.ac.rs>

Reply-To <ewelina.szymanska-skolimowska@ncn.gov.pl>

Date 2017-11-29 09:56

Jelena Trajić

Dear Prospective Reviewer,

We would like to invite you to review a research proposal submitted to the executive government agency of National Science Centre (Narodowe Centrum Nauki - NCN; http://www.ncn.gov.pl).

Proposal's data:
Funding scheme SONATA BIS, Raman spectroscopy of acoustic and optical phonons confined in colloidal II-VI nanocrystal heterostructures, dr inż. Grzegorz Zatryb, Wrocław University of Science and Technology, No. 384143, Panel ST3

We would greatly appreciate your reply within the next 3 days about your intention to review the proposal. Should you choose to accept our invitation, please complete the evaluation form no later than **18th December, 2017** using the OSF electronic submission system (https://osf.opi.org.pl).
If you cannot evaluate this proposal we would be grateful for suggesting an alternate qualified reviewer.

We offer remuneration of PLN 400,00 gross (equivalent of c.a. EUR 100 gross) for a completed review of the proposal.

For detailed instructions regarding the use of the system please see Guidelines for the Written Review.

Please do not hesitate to contact us if you require any further information regarding the mission statement of the Centre or the reviewing process.

Kind regards,
dr inż. Ewelina Szymańska-Skolimowska
Discipline Coordinator
National Science Centre
ewelina.szymanska-skolimowska@ncn.gov.pl

--
Utworzono / Created: 2017-11-29, 09:56:44

Subject	**Review submitted**
From	Narodowe Centrum Nauki <osf_administracja@opi.org.pl>
To	<jelena@ipb.ac.rs>
Reply-To	<jelena@ipb.ac.rs>
Date	2017-12-16 13:17

Dear Reviewer,

We appreciate your participation in the evaluation process. You have finished all the necessary steps and your review is now correctly submitted in the system.

Coordinator of the peer review process.

--
Utworzono / Created: 2017-12-16, 13:17:52

Subject	**Thank you for the review of OM-D-18-02178R1**
From	Alok Srivastava <eesserver@eesmail.elsevier.com>
Sender	<eesserver@eesmail.elsevier.com>
To	<jelena@ipb.ac.rs>
Reply-To	Alok Srivastava <srivastava@ge.com>
Date	2019-01-22 20:37

*** Automated email sent by the system ***

Ms. Ref. No.: OM-D-18-02178R1
Title: Stabilized Blue Emitting ZnS@SiO2 Quantum Dots
Optical Materials

Dear Dr. Jelena Trajic,

Thank you for taking the time to review the above-referenced manuscript. You can access your
comments and the decision letter when it becomes available.

To access your comments and the decision letter, please do the following:

1. Go to this URL: https://ees.elsevier.com/om/

2. Enter your login details

3. Click [Reviewer Login]

If you have not yet activated or completed your 30 days of access to Scopus and ScienceDirect,
you can still access them via this link:

http://scopees.elsevier.com/ees_login.asp?journalacronym=OM&username=jelena@ipb.ac.rs

You can use your EES password to access Scopus and ScienceDirect via the URL above. You can
save your 30 days access period, but access will expire 6 months after you accepted to review.

Thank you again for sharing your time and expertise.

Yours sincerely,

Veeraiah Nalluri, Ph.D
Associate Editor
Optical Materials

****
For further assistance, please visit our customer support site at http://help.elsevier.com
/app/answers/list/p/7923. Here you can search for solutions on a range of topics, find answers
to frequently asked questions and learn more about EES via interactive tutorials. You will also
find our 24/7 support contact details should you need any further assistance from one of our
customer support representatives.

Subject APYA: Thank you for the review of APYA-D-19-00171R1

From Stela Canulescu <em@editorialmanager.com>

Sender <em.apya.4337.61ad2e.bfa008e3@editorialmanager.com>

To J Trajic <jelena@ipb.ac.rs>

Reply-To Stela Canulescu <stec@fotonik.dtu.dk>

Date 2019-03-05 00:16

```
Ref.:
Ms. No. APYA-D-19-00171R1
Facile deposition and study of substrate temperature effect on the structure and physical
properties of Cu2FeSnS4 (CFTS) thin films
Applied Physics A

Dear Dr. Trajic,

Thank you for your review of this manuscript.

You can access your review comments and the decision letter (when available) by logging onto
the Editorial Manager site.

Your username is: JTrajic

If you forgot your password, you can click the 'Send Login Details' link on the EM Login page
at https://www.editorialmanager.com/apya/

Thank you very much.

Kind regards,

Dr. Stela Canulescu
Member of the Board of Editors
Applied Physics A

We really value your feedback! Please spend 1 minute to tell us about your experience of
reviewing - click https://springernature.eu.qualtrics.com/jfe/form/SV_cNPY5OM4ZC3PkON?J=339

Recipients of this email are registered users within the Editorial Manager database for this
journal. We will keep your information on file to use in the process of submitting, evaluating
and publishing a manuscript. For more information on how we use your personal details please
see our privacy policy at https://www.springernature.com/production-privacy-policy. If you no
longer wish to receive messages from this journal or you have questions regarding database
management, please email our publication office, stating the journal name(s) and your email
address(es):
PublicationOfficeSPS@springernature.com

_____
In compliance with data protection regulations, you may request that we remove your personal
registration details at any time.  (Use the following URL: https://www.editorialmanager.com
/apya/login.asp?a=r) Please contact the publication office if you have any questions.
```

Subject **JAP: MS #JR17-2798R Review Received for REVISED manuscript**

From <jap-edoffice@aip.org>

To <jelena@ipb.ac.rs>

Date 2017-07-20 15:52

Dear Dr. Trajic:

Thank you for your review of the revised manuscript "Study on physical model of infrared dielectric constant of Zinc sulfide" by Huasong Liu, Shida Li, Xiao Yang, Dandan Liu, Yiqin Ji, Feng Zhang, and Deying Chen [Paper #JR17-2798R], which we have safely received.

A copy of this review is attached for your reference.

Sincerely,

Journal of Applied Physics Editorial Office

AIP Publishing
1305 Walt Whitman Road
Suite 300
Melville, NY 11747-4300 USA

phone: +1-516-576-2910
e-mail: jap-edoffice@aip.org

Manuscript #JR17-2798R:

Does the manuscript present original and timely results that significantly advance the knowledge in applied physics: Yes

Does the manuscript report on convincing and rigorous data methods and analysis: Yes

(Confidential)If accepted for publication should this manuscript be given wider publicity because of its outstanding quality: Yes

Is the manuscript clearly written in correct English well organized and free from ambiguities: Yes

Is the title descriptive of the contents concise interesting and free of acronyms: Yes

Does the abstract adequately and clearly describe the contents (problem approach findings) of the paper: Yes

Are the figures in the manuscript necessary adequate well presented and clearly labeled: Yes

Is the reference list appropriate: Yes

REMARKS to AUTHOR(s):

Comments to the Editor (Confidential):
Dear Editor,
The authors fulfill my remarks. By my opinion, manuscript should be published.
Sincerely,
dr Jelena Trajić

Recommendation (Confidential) for The Editor: Publish as is

Want to Review Revision (confidential): Yes

Subject	**Thank you for Reviewing #JEMS-D-19-00064R1**
From	Journal of Electronic Materials (JEMS) <em@editorialmanager.com>
Sender	<em.jems.0.623252.b8d69480@editorialmanager.com>
To	J. Trajic <jelena@ipb.ac.rs>
Reply-To	Journal of Electronic Materials (JEMS) <neeraj.poduval@springernature.com>
Date	2019-03-28 15:19

Dear Dr. Trajic,

Thank you for your review of the manuscript JEMS-D-19-00064R1 for Journal of Electronic
Materials.

We greatly appreciate your assistance in this important process and we hope that you will
consider future requests to review manuscripts submitted to Journal of Electronic Materials.

With kind regards,
Springer Journals Editorial Office
Journal of Electronic Materials

We really value your feedback! Please spend 1 minute to tell us about your experience of
reviewing - click https://springernature.eu.qualtrics.com/jfe/form/SV_cNPY5OM4ZC3PkON?J=11664

Recipients of this email are registered users within the Editorial Manager database for this
journal. We will keep your information on file to use in the process of submitting, evaluating
and publishing a manuscript. For more information on how we use your personal details please
see our privacy policy at https://www.springernature.com/production-privacy-policy. If you no
longer wish to receive messages from this journal or you have questions regarding database
management, please contact the Publication Office at the link below.

_____
In compliance with data protection regulations, you may request that we remove your personal
registration details at any time. (Use the following URL: https://www.editorialmanager.com
/jems/login.asp?a=r) Please contact the publication office if you have any questions.

Subject   **Re: recenzija za Sci Sinter**

   From   Nina Obradovic <nina.obradovic@itn.sanu.ac.rs>

     To   Jelena Trajic <jelena@ipb.ac.rs>

   Date   2016-06-07 13:44

---

hvala najlepse!

On 07.06.2016. 13:19, Jelena Trajic wrote:

> Draga Nina,
>
> U prilogu vam saljem recenziju.
>
> Pozdrav,
> Jelena Trajic
>
> On 02 Jun 2016 12:12, Nina Obradovic wrote:
>> Draga Jelena,
>>
>> u prilogu ti saljem rad tvoje koleginice Maje, molim te da mi
>> posaljes svoje misljenje o radu i popunjen rec list u roku od mesec
>> dana.
>>
>> Unapred hvala,
>>
>> srdacan pozdrav,
>>
>> Nina

--
Dr. Nina Obradović
Senior Research Associate
Institute of Technical Sciences of SASA
Knez Mihailova 35/IV
11000 Belgrade, SERBIA
Phone: +381 11 2027203
Mob.:+381 69 1250603
e-mail: nina.obradovic@itn.sanu.ac.rs
http://www.itn.sanu.ac.rs/ninaobradovic_eng.html

Subject	**Thank you for the review of MSB-D-17-01399R1**
From	Materials Science & Engineering B <eesserver@eesmail.elsevier.com>
Sender	<eesserver@eesmail.elsevier.com>
To	<jelena@ipb.ac.rs>
Reply-To	Materials Science & Engineering B <msb@elsevier.com>
Date	2017-10-18 22:03

Dear Dr. Trajic,

Thank you for taking the time to review the above-referenced manuscript. We will be adding your comments to those of the editor and sending them on to the author.

Thank you again for sharing your time and expertise.

Yours sincerely,

Prashant Kumta, PhD
Editor-in-Chief
Materials Science and Engineering B

****
For further assistance, please visit our customer support site at http://help.elsevier.com/app/answers/list/p/7923
Here you can search for solutions on a range of topics, find answers to frequently asked questions and learn more about EES via interactive tutorials. You will also find our 24/7 support contact details should you need any further assistance from one of our customer support representatives.

Subject **Thank you for the review of OM-D-16-00872R2**

From Alok Srivastava <srivastava@ge.com>

Sender <ees.om.3f0e.3b9871.76c179c0@eesmail.elsevier.com>

To <jelena@ipb.ac.rs>

Date 2016-08-27 20:54

Ms. Ref. No.: OM-D-16-00872R2
Title: Optical and morphological characteristics of zinc selenide-zinc sulfide solid solution crystals
Optical Materials

Dear Dr. Jelena Trajic,

Thank you for taking the time to review the above-referenced manuscript. You can access your comments and the decision letter when it becomes available.

To access your comments and the decision letter, please do the following:

1. Go to this URL: http://ees.elsevier.com/om/

2. Enter your login details

3. Click [Reviewer Login]

If you have not yet activated or completed your 30 days of access to Scopus and ScienceDirect, you can still access them via this link:

http://scopees.elsevier.com/ees_login.asp?journalacronym=OM&username=jelena@ipb.ac.rs

You can use your EES password to access Scopus and ScienceDirect via the URL above. You can save your 30 days access period, but access will expire 6 months after you accepted to review.

Thank you again for sharing your time and expertise.

Yours sincerely,

Maurizio Ferrari
Handling Editor
Optical Materials

****
For further assistance, please visit our customer support site at http://help.elsevier.com /app/answers/list/p/7923. Here you can search for solutions on a range of topics, find answers to frequently asked questions and learn more about EES via interactive tutorials. You will also find our 24/7 support contact details should you need any further assistance from one of our customer support representatives.

Subject	**Thank you for your review of RA-ART-11-2016-026489**
From	RSC Advances <onbehalfof+advances+rsc.org@manuscriptcentral.com>
Sender	<onbehalfof+advances+rsc.org@manuscriptcentral.com>
To	<jelena@ipb.ac.rs>
Reply-To	<advances@rsc.org>
Date	2016-11-19 23:02

IP8 webmail

19-Nov-2016

Dear Dr Trajic:

TITLE: Achieving Rough Sphere-shape ZnS with Superior Attenuation Electromagnetic Absorption Performance

Thank you for your recent review and your support as a reviewer for RSC Advances.

Do you have an ORCID iD? ORCID (Open Researcher and Contributor iD) is a unique researcher identifier that allows you to link your research output and other professional activities in a single record.   If you associate your ORCID iD with your account on our system, and you publish an article in any of the Royal Society of Chemistry's journals, your ORCID will be linked to the article and displayed alongside the final published version. You may also choose to have your ORCID record updated automatically with details of the publication.
To create a new ORCID iD record or to link your user account to an existing ORCID iD, simply click this link: https://mc.manuscriptcentral.com/rscadv?URL_MASK=7380b0047fe54d37b196c5a5e6d33cd9

As a reviewer you are entitled to a 25% discount on books published by the Royal Society of Chemistry. To receive this discount, enter the promotional code JLREF25 when purchasing from our online bookshop (pubs.rsc.org/bookshop). Please contact booksales@rsc.org if you have any problems.

Thank you for your support as a reviewer for the Royal Society of Chemistry. By providing a review for RSC Advances you are part of the world's leading chemistry community.

Best wishes,
Juan Giner-Casares
Associate Editor, RSC Advances